

به نام خدا



مرکز دانلود رایگان مهندسی متالورژی و مواد

www.Iran-mavad.com



HANDBOOK OF THERMAL ANALYSIS

www.iran-mavad.com Edited by
T. Hatakeyama and Zhenhai Liu

مرجع دانشجوین و مهندسين مواد

Handbook of Thermal Analysis

This page intentionally left blank

Handbook of Thermal Analysis

Edited by

T. HATAKEYAMA

National Institute of Materials and Chemical Research, Ibaraki, Japan

ZHENHAI LIU

Changchun Institute of Applied Chemistry, Changchun, China

JOHN WILEY & SONS

Chichester • New York • Weinheim • Brisbane • Singapore • Toronto

www.iran-mavad.com

مرجع دانشجویان و مهندسين مواد

Copyright © 1998 John Wiley & Sons Ltd,
Baffins Lane, Chichester,
West Sussex PO19 1UD, England

National 01243 779777
International (+ 44) 1243 779777
e-mail (for orders and customer service enquiries): cs-books@wiley.co.uk
Visit our home Page on <http://www.wiley.co.uk>
or <http://www.wiley.com>

All Rights Reserved. No part of this book may be reproduced, stored in a retrieval system, or transmitted in any form or by any means, electronic, mechanical, photocopying, recording, scanning or otherwise, except under the terms of the Copyright, Designs and Patents Act 1988 or under the terms of a licence issued by the Copyright Licensing Agency, 90 Tottenham Court Road, London W1P 9HE, without the permission in writing of the Publisher

Other Wiley Editorial Offices

John Wiley & Sons, Inc., 605 Third Avenue,
New York, NY 10158-0012, USA

WILEY-VCH Verlag GmbH, Pappelallee 3,
D-69469, Weinheim, Germany

Jacaranda Wiley Ltd, 33 Park Road, Milton,
Queensland 4064, Australia

John Wiley & Sons (Asia) Pte Ltd, 2 Clementi Loop #02-01,
Jin Xing Distripark, Singapore 129809

John Wiley & Sons (Canada) Ltd, 22 Worcester Road,
Rexdale, Ontario M9W 1L1, Canada

Library of Congress Cataloging-in-Publication Data

Hatakeyama, T.
Handbook of thermal analysis / T. Hatakeyama, Liu Zhenhai.
p. cm.
Includes bibliographical references and index.
ISBN 0-471-98363-2 (alk. paper)
1. Thermal analysis. I. Liu, Zhenhai. II. Title.
QD79.T38 1998
543'.086—dc21 98-5979
CIP

British Library Cataloguing in Publication Data

A catalogue record for this book is available from the British Library

ISBN 0 471 98363 2

Typeset in 10/12 pt Palatino by Mathematical Composition Setters Ltd, Salisbury
Printed and bound in Great Britain by Bookcraft (Bath) Ltd
This book is printed on acid-free paper responsibly manufactured from sustainable forestry,
in which at least two trees are planted for each one used for paper production

Contents

List of Contributors	xiii
Preface	xvii
Acknowledgements	xix
Part I Thermal Analysis	
1 Introduction	3
1.1 Purpose and Scope	3
1.2 Short History of Thermal Analysis	3
1.3 Terminology	4
1.3.1 Changes and Developments in the Nomenclature of Thermal Analysis	4
1.3.2 Definition and Classification of Thermal Analysis	4
1.3.3 Some General TA terms	5
1.4 Characteristics and Data Reporting for Thermal Analysis	6
1.4.1 Characteristics of Thermal Analysis	6
1.4.2 Data Reporting of Thermal Analysis	7
1.5 Calibration of Temperature and Enthalpy	8
1.5.1 Temperature Calibration of Thermogravimetry	8
1.5.1.1 Curie Point Method	8
1.5.1.2 Dropping Weight Method	8
1.5.2 Temperature Calibration of DTA and DSC	8
1.5.3 Enthalpy Calibration of DTA and DSC	9
1.5.4 Calorimetric Calibration of DSC	11
1.5.5 Temperature and Size Calibration of TMA	11
1.6 Standard Test Methods for Thermal Analysis	12
1.7 References	13
2 Conformation of TA Apparatus	15
2.1 General Scope	15
2.1.1 Basic Conformation	15
2.1.2 Commercial Apparatus	15
2.1.3 Computer Software	16
2.2 Standard TA Apparatus	17
2.2.1 Thermogravimetry (TG)	17
2.2.1.1 Simultaneous Measurements	17

2.2.1.2	Basic Configuration	17
2.2.1.3	Microbalance	17
2.2.1.4	Commercial TG	18
2.2.1.5	Crucible	18
2.2.1.6	Atmosphere	19
2.2.1.7	Temperature Calibration	19
2.2.1.8	High-resolution TG	19
2.2.2	Differential Thermal Analysis (DTA) and Differential Scanning Calorimetry (DSC)	19
2.2.2.1	Heat-flux DSC	19
2.2.2.2	Triple-cell Heat-flux DSC	20
2.2.2.3	Power Compensation DSC	21
2.2.2.4	Temperature Modulated DSC (MDSC)	21
2.2.2.5	High-sensitivity DSC (HS-DSC)	23
2.2.2.6	High-pressure DTA	23
2.2.2.7	Sub-ambient Operation	24
2.2.3	Thermomechanometry	24
2.2.3.1	Thermomechanical Analysis (TMA)	24
2.2.3.2	Dynamic Mechanical Analysis (DMA)	25
2.2.4	Thermodilatometry	26
2.2.4.1	Linear Expansion Coefficient Measurement	27
2.3	Light, Electric, Acoustic TA	27
2.3.1	Alternating Current Calorimetry (ACC)	27
2.3.1.1	Apparatus	27
2.3.1.2	Measurements	27
2.3.2	Thermostimulated Current Measurements (TSC)	28
2.3.2.1	Apparatus	28
2.3.2.2	Experimental Procedure	28
2.3.2.3	Thermal Sampling	28
2.3.3	Thermoluminescence (TL)	29
2.3.3.1	Electron Traps	29
2.3.3.2	Oxyluminescence	29
2.3.3.3	Apparatus and samples	29
2.3.3.4	Measurements	29
2.3.3.5	TL Glow Curve	30
2.3.4	Thermal Diffusivity Measurement by Temperature Wave Analysis (TWA)	30
2.3.4.1	Theory	30
2.3.4.2	Apparatus	31
2.3.4.3	Samples	31
2.3.4.4	Measurements	31
2.3.4.5	TWA curves	32
2.4	Simultaneous TA Analysis	32
2.4.1	Thermomicroscopy	32
2.4.2	X-ray DSC	33
2.4.3	TA-EGD-EGA Coupled Simultaneous Technique	33
2.4.3.1	1 DTA/DSC-EGD Coupled Technique	34
2.4.3.2	DTA-EGD-GC On-line Coupled Simultaneous Technique	35
2.4.3.3	TG-DTA-MS Coupled Technique	36
2.4.3.4	TG-Fourier Transform Infrared Spectroscopy (FTIR)	37
2.4.3.5	DTA-NDIR Coupled Technique	38

2.4.3.6	TG-DTA-TGT Coupled Technique	38
2.4.4	Opto-thermal Transient Emission Radiometry (OTTER)	39
2.5	Automated TA Systems	39
2.6	Installation and Maintenance	39
2.7	References	40
3	Effect of Experimental Conditions on TA Measurements, Kinetics of TA and Expression of TA Data	42
3.1	Effect of Experimental Factors	42
3.1.1	Heating Rate	42
3.1.2	Mass and Particle Size of Sample	43
3.1.3	Atmosphere	44
3.1.4	Buoyancy, Convection Currents and Turbulence	45
3.1.5	Sample Container, Temperature Gradient and Reaction Extent in Various Parts of Sample Vessel	45
3.1.6	Packing Density of Sample	46
3.2	Resolution of Apparatus	47
3.3	Kinetics of Thermal Analysis	47
3.3.1	Determination of Kinetic Parameters for Reaction	47
3.3.1.1	Determination of Apparent Activation Energy by Ozawa Method (Ozawa-Flynn-Wall Method)	47
3.3.1.2	Determination of Apparent Activation Energy by Kissinger Method	48
3.3.1.3	Determination of Kinetic Parameters by Freeman and Carroll Method	48
3.3.1.4	Determination of Kinetic Parameters by using Peak Values	49
3.3.2	Reaction Mechanism	49
3.3.3	Mechanism of Isothermal Reaction in Solid State	50
3.3.4	Non-isothermal Crystallization Kinetics of Polymers by DSC Measurement	51
3.3.4.1	Ziabicki Method	51
3.3.4.2	Ozawa Method	52
3.3.4.3	Modified Ozawa Method	52
3.3.4.4	Modified Avrami Method	53
3.3.5	General Description of Kinetics of Resin Curing Under Isothermal Conditions	53
3.3.6	Methods for Determining Kinetic Parameters of Thermosetting Reactions of Resins	55
3.3.6.1	Freeman-Carroll Method	55
3.3.6.2	Ellerstein Method	55
3.3.6.3	Barton Method	56
3.3.6.4	Method Based on Maximum Values	56
3.3.7	Some Advances in Thermal Analysis Kinetics	56
3.3.7.1	Kinetic Model Functions	57
3.3.7.2	New Method of Non-isothermal Kinetic Analysis of TA Data	57
3.3.7.3	Controlled Transformation Rate Thermal Analysis (CRTA) Method	60
3.4	Expression of TA Curves and Determination of Termination Point for Transition or Reaction	61
3.4.1	TA Curves and Their Expression	61
3.4.2	Determination of the Terminated Point of a DTA Curve for Transition or Reaction	62
3.4.3	Determination of Thermal Time Constant and Lowest Separation Temperature for a DTA Curve	62

3.5	Quantitative Treatments of TG Data	63
3.5.1	Multi-step Reactions	63
3.5.2	Dynamic Rate Controlled Method	64
3.6	Standard Mathematical Software	65
3.7	References	65
4	TA Measurement of Various Transitions	66
4.1	Glass Transition	66
4.1.1	Determination of Glass Transition Temperature by DTA or DSC	66
4.1.2	Effect of Plasticizers and Random Copolymers	67
4.1.3	Effect of Relative Molecular Mass	68
4.1.4	Effect of Cross-linking Density	68
4.1.5	Effect of Crystallinity	68
4.1.6	Enthalpy Relaxation	68
4.1.7	Macromolecular Constants C_1 and C_2 in the WLF Equation	70
4.1.8	Relaxation Activation Energy of Polymers in the Glass Transition Region	71
4.1.9	Characteristic Temperature, Free Volume Fraction and Thermal Expansion Coefficient of Polymers	71
4.2	Crystallization and Melting	72
4.2.1	Determination of Melting and Crystallization Temperatures by DTA or DSC	72
4.2.1.1	Melting Temperature	73
4.2.1.2	Crystallization Temperature	73
4.2.2	Thermodynamic Equilibrium Melting Temperature of Polymer Crystals	74
4.2.3	Determination of Heats of Fusion and Crystallization of Polymers	74
4.2.4	Melting Enthalpy of Perfect Polymer Crystals by DSC	76
4.2.5	Melting Enthalpy of Perfect Polymer Crystals by Solvent Dilution	76
4.2.6	Isothermal Crystallization of Polymers	77
4.2.7	Determination of Isothermal Crystallization Rate by DSC	78
4.2.8	Measurement of Heat of Isothermal Crystallization	78
4.2.8.1	Apparatus Constant Determination	78
4.2.8.2	Measurement of Heat of Crystallization	78
4.2.9	Transition Regions of Polymers Melt-crystallized Isothermally	78
4.2.10	Surface Free Energies of Developing Polymer Crystals During Isothermal Crystallization	80
4.2.11	Transport Activation Energy of Polymer Segments During Isothermal Crystallization Measured by DSC and Polarizing Optical Microscopy	80
4.2.12	Growth Rate of Polymer Spherulites Crystallized Isothermally from the Melt by Polarizing Optical Microscopy	81
4.2.13	Overall Kinetic Parameters of Polymers Crystallized Isothermally from the Melt	82
4.2.14	Overall Growth Rate of Polymer Spherulites Crystallized from the Subcooled Melt	82
4.2.15	Determination of Crystallinity of Polymers (Dynamic Heating Method)	83
4.2.16	Determination of Crystallinity of Polymers (Isothermal Crystallization Method)	84
4.2.17	Crystallinity of Poly(ethylene terephthalate) (PET) Molded Under Different Conditions	84
4.2.18	Density, Melting Temperature and Degree of Crystallinity of Polyethylene	85
4.2.19	Multiple Melting Peaks of Polyethylene	85
4.2.20	Polymorphism of Dotriacontane	86

4.2.21	Thermotropic Liquid Crystals	87
4.2.22	Thermotropic Polymeric Liquid Crystals	88
4.2.22.1	Temperature Region of Liquid Crystals	88
4.2.22.2	Main-chain Liquid Crystalline Polymer	88
4.2.22.3	Side-chain Liquid Crystalline Polymer	89
4.2.23	Determination of SFI of Fat	89
4.2.24	Wax Content of Lubricants	90
4.2.25	Heat of Transition of Lipids	90
4.2.26	Denaturation of Proteins	90
4.2.27	Phase Diagram for Binary System	91
4.3	Miscibility and Phase Behavior of Polymer Blends	92
4.3.1	Miscibility and Phase Separation in Amorphous Polymer Blends	92
4.3.2	Miscible Blends Containing a Crystalline Polymer	93
4.3.3	Miscible Blends Containing two Crystalline Polymers	95
4.3.4	Phase Separation in Crystalline Polymer Blends	96
4.3.5	Upper and Lower Critical Solution Temperature	99
4.3.6	Folded Surface Free Energy in Miscible Polymer Blends by Isothermal Melt Crystallization	100
4.2.7	Growth Rate of Miscible Polymer Blend Spherulites Crystallized Isothermally from the Melt by Polarizing Optical Microscopy	101
4.3.8	Determination of the Composition of Polymer Blends	101
4.4	Thermomechanometry	102
4.4.1	Measurement of Anisotropy of Polymer Films Using TMA	102
4.4.2	Restriction on Deformation of Polyethylene Films by Reinforcing Agents	103
4.4.3	Penetration and Tension Measurements of Polymer Film by TMA	103
4.4.4	Dynamic Mechanical Spectra of Polymers	104
4.4.5	Activation Energy of Secondary Relaxation in Polymers	105
4.4.6	Master Curve of Polymers Using Dynamic Mechanical Spectra	106
4.4.7	DMA of Polymers in Humid Conditions	107
4.5	Measurement of Water Content	107
4.5.1	Bound Water Content of Polymers Determined by DSC	107
4.5.1.1	Determination of Dry Sample Mass	107
4.5.1.2	Determination of Freezing, Freezing Bound and Non-freezing Water	108
4.5.2	Bound Water Content of Polymers Determined by TG	108
4.5.3	Phase Diagram of Water–Polymer Systems	109
4.5.4	DSC Measurement of Mixtures of Water and Ethanol	110
4.5.5	Free and Bound Water in Biopolymers	111
4.5.6	Measurement of Water in Manganese Dioxide	111
4.5.7	Pressurized Dehydrolysis of Hydrated Aluminum Oxide	112
4.6	Thermal Analysis of Metals and Alloys	112
4.6.1	Determination of Thermodynamic Parameters of Phase Transitions for Metals and Alloys	112
4.6.1.1	Crystallization and Melting of Metals and Alloys	112
4.6.1.2	Martensitic Transformation of Shape Memory Alloy	113
4.6.1.3	Glass Transition of Amorphous Alloys	114
4.6.1.4	Magnetic Transition of Metals and Alloys	115
4.6.1.5	Determination of an Equilibrium Phase Diagram	116
4.6.1.6	Mixing Enthalpy and Entropy of Metallic Liquids by Measurements and Calculation	117

4.6.2	Determination of Kinetic Parameters for Phase Transformations of Metals and Alloys	117
4.6.2.1	Stable, Metastable and Unstable Phase Diagrams	117
4.6.2.2	Determination of Activation Energy for Phase Transformation	118
4.6.2.3	Determination of Time–Temperature Transformation Diagram (TTT diagram), Continuous-temperature Transformation Diagram (CTT diagram) and Critical Cooling Rate	123
4.6.3	Determination of Specific Heats of Metals and Alloys	120
4.6.3.1	Measuring Methods for Specific Heats and Estimation of Measuring Error	120
4.6.3.2	Determination of Specific Heats of Metastable Solids (Nanostructured Crystals, Amorphous Alloys, Superheated Crystals)	121
4.6.3.3	Determination of Specific Heats of Undercooled Liquids	122
4.6.4	Properties of Anti-oxidation of Metals and Alloys	123
4.6.5	Determination of Thermal Expansion Coefficients	123
4.7	Miscellaneous	124
4.7.1	Cryobehavior of Suspended Single Cells by Low-temperature DSC	124
4.7.2	Thermal Analysis of Mixed Fat	125
4.7.3	DSC Measurement of Edible Meat	125
4.7.4	Thermal Analysis of Silicone Rubber	126
4.8	References	126
5	Application of TA to Chemical Reactions	129
5.1	Thermal Stability	129
5.1.1	Relative Thermal Stability of Polymeric Materials	129
5.1.2	Estimation of Thermal Index of Electrical Insulating Material by the Toop Method	129
5.1.3	Estimation of Thermal Index of Electrical Insulating Materials by the TG-secant Method	131
5.1.4	Determination of Oxidative Induction Time of Organic Materials	132
5.2	Cross-linking and Polymerization Reactions	133
5.2.1	The Contents, Construction and Significance of Time–Temperature–Transformation Isothermal Cure Diagram	133
5.2.2	Curing and Glass Transition of Epoxy Resin	135
5.2.3	Thermal Analysis of Photopolymerization	135
5.3	Evaluation of Catalysts in the Solid State	136
5.3.1	Evaluation of Catalysts in the Solid State by the DTA–EGD–GC On-line Coupled Simultaneous Technique	136
5.3.1.1	Spinel-type Catalyst	136
5.3.1.2	Screening of Oxidative Activity of CuO Catalysts	137
5.3.1.3	Screening of Perovskite-type Catalysts Containing Rare Earths	138
5.3.1.4	Screening of Calcination Conditions of Multi-component Catalysts	139
5.3.1.5	Screening of Activity of Supported Methanation Catalysts	140
5.3.1.6	Examination of Poisoning Effect of SO ₂ on Methanation Catalysts	140
5.3.1.7	Examination of Burned Coke of Catalyst	141
5.3.2	Evaluation of Metal Catalysts by Pressure DTA	141
5.4	TA of Wood	142
5.4.1	Thermal Decomposition of Cellulose by TG–DTA–FTIR	142
5.4.2	Thermal Decomposition of Lignin by TG–DTA–FTIR	143

5.4.3	Thermal Decomposition of Wood by TG–DTA–FTIR	144
5.4.4	Acid Hydrolysis of Cellulose	144
5.4.5	Oxidative Stability of Rosins	145
5.4.6	Combustion Characteristics of Flame-retarded Wood	145
5.5	TA of Explosives and Coals	146
5.5.1	Monitoring the Instantaneous Change of Energy-stored Materials	146
5.5.2	DSC Measurement of Self-reacting Substances	147
5.5.3	Proximate Analysis of Coal and Coke	148
5.5.4	Determination of Heat Content of Coal	148
5.6	Quantitative Analysis of Minerals and Determination of Coexistence of Minerals by TG	149
5.6.1	Quantitative Analysis of Minerals by Thermogravimetry	149
5.6.2	Determination of Composition of Minerals Showing Isomorphism	149
5.7	Miscellaneous	150
5.7.1	Thermal Decomposition of Heat-conductive Oil	150
5.7.2	Measurement of the Content of Carbon Black in Rubber	151
5.7.2.1	Continuous Heating Method	151
5.7.2.2	Double Heating Method	151
5.7.3	Measurement of Oxidation of Oils and Fats	152
5.7.4	Measurement of Reaction of Metals with Gases	152
5.7.5	Determination of the Degree of Conversion of Gypsum to Plaster of Paris by DSC	152
5.8	References	153
6	TA Measurement of Physical Characterization Parameters of Substances	155
6.1	Thermodynamic Parameters	155
6.1.1	Determination of Heat Capacity by DSC	155
6.1.1.1	Scanning Method	155
6.1.1.2	Enthalpy Method	156
6.1.2	Determination of Coefficient of Linear Expansion by TMA	156
6.1.3	Determination of Thermal Conductivity	157
6.1.4	Determination of Thermal Diffusivity	158
6.2	Purity Determination	159
6.3	Thermoporosimetry	161
6.4	References	161
 Part II Thermal Analysis Curves		
7	Thermal Analysis Curves of Polymers	165
7.1	Appendix: Transition Maps of Representative Polymers	206
7.2	References	210
8	Thermal Analysis Curves of Foods and Food Additives	212
8.1	Thermal Analysis Curves of Foods	212
8.2	Thermal Analysis Curves of Food Additives	223
8.3	References	237
9	Thermal Analysis Curves of Plant Materials	239

10 Thermal Analysis Curves of Minerals	247
10.1 Thermal Analysis Curves of Natural Elements	247
10.2 Thermal Analysis Curves of Halide Minerals	252
10.3 Thermal Analysis Curves of Sulfide Minerals	256
10.4 Thermal Analysis Curves of Oxide Minerals	271
10.5 Thermal Analysis Curves of Sulfate Minerals	280
10.6 Thermal Analysis Curves of Carbonate Minerals	293
10.7 Thermal Analysis Curves of Borate Minerals	301
10.8 Thermal Analysis Curves of Phosphate Minerals	308
10.9 Thermal Analysis Curves of Arsenide Minerals	312
10.10 Thermal Analysis Curves of Silicate Minerals	315
10.11 References	336
11 Thermal Analysis Curves of Energetic Materials	337
11.1 References	375
12 Thermal Analysis Curves of Inorganic Materials	378
12.1 Thermal Analysis Curves of Complexes of Rare Earth Bromides with Glycine and/Alanine	378
12.2 Thermal Analysis Curves of Complexes of Transition Metals with Schiff Bases	386
12.3 Thermal Analysis Curves of Other Complexes	391
12.4 References	401
13 DTA–EGD–GC Coupled Simultaneous Thermal Analysis Curves	402
13.1 Solid Catalysts	403
13.2 Anti-oxidant Additive in Petroleum	410
13.3 Coal	413
13.4 Minerals	418
13.5 References	423
Appendix 1 Specific Heat Capacity of Pure α-Alumina in the Temperature Region from 120 to 780 K	424
Appendix 2 An Approximate Expression of Specific Heat Capacity of Pure α-Alumina	425
Appendix 3 Physical Constants and Conversion Tables	426
Index of Contributors	428
General Index	429
Materials Index	441

List of Contributors

Editors

Hatakeyama, Tatsuko and Liu Zhenhai

Editorial Advisory Board

Cai Gencai[†], Cai Zhenqian, Huang Kelong,
Sun Tongshan and Liu Jingjian

List of Contributors

Cai Gencai [†]	University of Science and Technology of East China, Analysis and Research Centre, Shanghai 200237, China
Cai Zhenqian	Nanjing University of Science and Technology, Department of Environmental Science and Engineering, Nanjing 210014, China
Cong Guangmin	Guangzhou Institute of Chemistry, Chinese Academy of Sciences, Guangzhou 510650, China
Guo Quipeng	University of Science and Technology of China, Department of Polymer Science and Engineering, Hefei 230026, China
Hashimoto, Toshimasa	Tokyo Institute of Technology, Ohokayama Meguro-ku, Tokyo 152, Japan
Hatakeyama, Hyoe	Fukui University of Technology, Gakuen, Fukui 910, Japan
Hatakeyama, Tatsuko	National Institute of Materials and Chemical Research, Tsukuba, Ibaraki 305, Japan

[†]Deceased

xiv	List of Contributors
He Guanhu	Institute of Metal Research, Chinese Academy of Sciences, Shenyang 110015, China
Hua Rong	Changchun Institute of Applied Chemistry, Chinese Academy of Sciences, Changchun 130022, China
Huang Kelong	University of Science and Technology of Changchun, Department of Material Science, Changchun 130023, China
Huang Yuhui	Guangzhou Institute of Chemistry, Chinese Academy of Sciences, Guangzhou 510650, China
Jian Qing	Jilin University of Technology, Department of Material Science and Engineering, Changchun 130025, China
Jian Yinshan	University of Science and Technology of Changchun, Department of Material Science, Changchun 130023, China
Ling Yue	Nanjing University of Science and Technology, Department of Environmental Science and Engineering, Nanjing 210014, China
Liu Jingjian	Changchun Institute of Applied Chemistry, Chinese Academy of Sciences, Changchun 130022, China
Liu Yan	Nanjing University of Science and Technology, Department of Environmental Science and Engineering, Nanjing 210014, China
Liu Zhenhai	Changchun Institute of Applied Chemistry, Chinese Academy of Sciences, Changchun 130022, China
Lu Zhenrong	Suzhou University, Central Laboratory, Suzhou 215006, China
Nishinari, Katatsuyoshi	Osaka City University, Department of Food and Nutrition Sumiyoshi-ku, Osaka 558, Japan
Niu Chunji	Changchun Institute of Applied Chemistry, Chinese Academy of Sciences, Changchun 130022, China
Peng Xinsheng [†]	Changchun Institute of Applied Chemistry, Chinese Academy of Sciences, Changchun 130022, China
Qian Yixiang	Shanghai Institute of Petrochemical Industry, Shanghai 201208, China
Qu Guijie	Changchun Institute of Applied Chemistry, Chinese Academy of Sciences, Changchun 130022, China
Quinn, Francis X.	L'Oreal, 1 Avenue Eugene Shueller, Aulnay sous Bois 93601, France
Sun Tongshan	Shandong University, Department of Chemistry, Jinan 250100, China

Wang Zenglin	Changchun Institute of Applied Chemistry, Chinese Academy of Sciences, Changchun 130022, China
Wei Xueli	Institute of Metal Research, Chinese Academy of Sciences, Shenyang 110015, China
Yang Shulin	Nanjing University of Science and Technology, Department of Environmental Science and Engineering, Nanjing 210014, China
Ye Chunmin	Changchun Institute of Applied Chemistry, Chinese Academy of Sciences, Changchun 130022, China
Ye Su	Research Institute for Chemical Processing Utilization of Forest Products, Chinese Academy of Forestry, Nanjing 210042, China
Zhang Hongfang	Changchun Institute of Applied Chemistry, Chinese Academy of Sciences, Changchun 130022, China
Zhao Min	Jilin University of Technology, Department of Material Science and Engineering, Changchun 130025, China

This page intentionally left blank

Preface

Thermal analysis (TA) has been widely used in various fields in the last forty years and a large variety of thermal analyzers is commercially available all over the world. TA apparatus equipped with microprocessors and easy-to-use software has increased the number of users. At present, it is very difficult to find ordinary substances and industrial products which have not yet been the target of thermal analysis.

This handbook is designed to provide general information on basic principles of TA and a variety of applications. It consists of the following three parts: Part I deals with information on transition, reaction and characteristic parameters of substances. It introduces general principles, data treatment, experimental procedure and data analysis. Part II describes about 1000 typical thermal analysis curves with brief explanations of various materials, such as polymers, minerals, explosives, foods, inorganic compounds, and application of simultaneous techniques for those same substances. It also includes TA charts which have mainly been contributed by institutes and universities in China.

Part III cites various data tables relating to thermal analysis.

In 1994, the editors of this handbook, Liu Zhenhai and T. Hatakeyama published *Handbook of Thermal Analysis*, Chemical Industry Press, Beijing. Dr J. Deeny of John Wiley & Sons recommended that the handbook should be translated from Chinese to English. The editors and Dr Deeny discussed the matter and decided on a complete revision of the handbook. At the same time, the completely revised handbook will be published in both the United Kingdom and China in English and Chinese.

We are grateful to the contributors and to C. Langham and S. Hirose who kindly helped us to write and edit this handbook. We would like to extend special thanks to Hyoe Hatakeyama, who made many valuable suggestions. We would also like to thank Wang Qihua (Mrs Liu) for her encouragement.

This handbook is the merging of results from China and Japan. We hope readers will find it helpful. As Lao Tsu said that 'the wide road has no special entrance.'

[†]T. Hatakeyama (Tokyo)
Liu Zhenhai (Changchun)

[†]Dr Hatakeyama is now at: Faculty of Home Economics, Otsuma Women's University, 12 Sanban-cho, Chiyoda-ku, Tokyo 102-8357, Japan.

This page intentionally left blank

Part I

Thermal Analysis

This page intentionally left blank

Introduction

1.1 Purpose and Scope

The term thermal analysis (TA) is frequently used to describe analytical experimental techniques which investigate the behavior of a sample as a function of temperature. The ability of TA to characterize, quantitatively and qualitatively, a huge variety of materials over a considerable temperature range has been pivotal in its acceptance as an analytical technique. TA is widely used in basic research and other applications by numerous scientists and engineers all over the world. A number of TA books, general and specific, have been published in various languages, including English, Chinese and Japanese [1–32].

This handbook is designed to provide general information on the basic principles of TA and a variety of its applications. It is composed of two parts. Part I deals with information on the transition, reaction and characteristic parameters of substances. It introduces general principles, data treatment, experimental procedures and data analysis. Part II presents about 1000 typical thermal analysis curves, with brief explanations, for a wide variety of materials, such as polymers, foods, woods, minerals, explosives, inorganic compounds, and their coupled simultaneous curves. TA charts have been contributed by Institutes and Universities in China. Part III cites various data tables relating to thermal analysis. The Appendices include a comparison of TA terms in three languages, a survey of standard reference materials and TA conversion tables.

1.2 Short History of Thermal Analysis

BC 600–18th century

Early stages of the history of phase transition phenomena related to heat can be found in Ref. 33

1887 Le Châtelier introduced the use of heating rate curves to identify clays [34–37]

1899 Roberts-Austen introduced the differential temperature method [38]

1903 The term thermal analysis was first used by Tammann [39]

1904 Kumakov [40] developed a versatile photographic recorder which was utilized in differential thermal analysis (DTA) by the Russian school [41]

1915 Honda [42, 43] laid the broad foundations of modern thermogravimetry, introducing the thermobalance

1919 International Union of Pure and Applied Chemistry (IUPAC) was established

1945 The first commercial thermogravimeter was produced [35]

1960s Introduction of elaborate differential thermal analyzers [35]

1964 Development of differential scanning calorimetry by Watson *et al.* [43]

1965 Japanese Society of Thermal Analysis and Calorimetry was established [44]

1965 The first International Conference on Thermal Analysis was held in Aberdeen, Scotland [45]

- 1968 The 2nd International Conference on Thermal Analysis was held in Boston, USA, and at the same time the International Confederation for Thermal Analysis (ICTA) was established. ICTA has since been renamed the International Confederation for Thermal Analysis and Calorimetry (ICTAC)
- 1969 *Journal of Thermal Analysis* was first published
- 1970 *Thermochimica Acta* was first published
- 1975 *Journal of the Society of Thermal Analysis and Calorimetry, Japan* was first published
- 1979 Committee for Thermochemistry, Thermodynamics and Thermal Analysis was established in China. This committee was subsequently renamed the Commission on Solution Chemistry, Chemical Thermodynamics, Thermochemistry and Thermal Analysis of the Chinese Chemical Society (CSTTT CCS), and since then the Committee for Chemical Thermodynamics and Thermal Analysis [46]
- 1980 The first Chinese Symposium on Thermochemistry, Thermodynamics and Thermal Analysis was held in Xi'an [46].
- 1986 The first Sino-Japanese Joint Symposium on Calorimetry and Thermal analysis was held in Hangzhou, November 1986 [46].

1.3 Terminology

1.3.1 Changes and Developments in the Nomenclature of Thermal Analysis

Changes and developments are illustrated schematically in Scheme 1.1.

1.3.2 Definition and Classification of Thermal Analysis

The definition given in the first report on nomenclature for thermal analysis (Part I) is as follows:

Thermal analysis A general term covering a group of related techniques whereby the depen-

dence of the parameters of any physical property of a substance on temperature is measured.

This definition has certain shortcomings and it is recommended that it be replaced by (see Part IV):

Thermal analysis A group of techniques in which a physical property of a substance is measured as a function of temperature whilst the substance is subjected to a controlled temperature program.

In addition to being more accurate, this definition has the advantage that it can be adapted to define all thermoanalytical techniques by alteration of only a few words in each instance, such as:

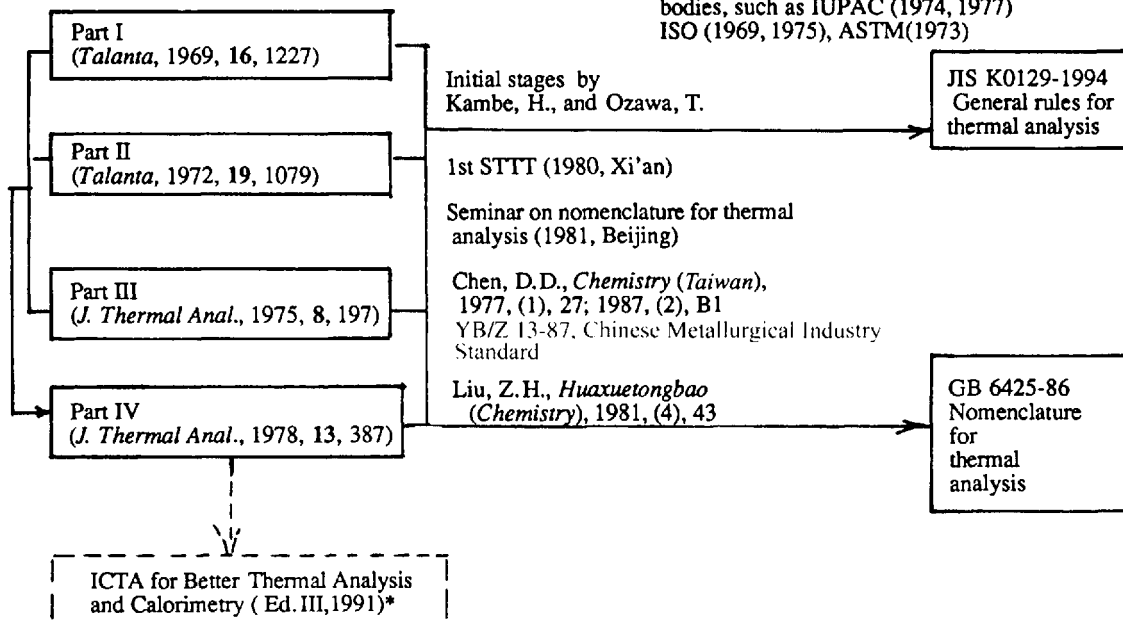
Thermogravimetry (TG) A technique in which the mass of a substance is measured as a function of temperature whilst the substance is subjected to a controlled temperature program. The record is the thermogravimetric or TG curve.

Differential thermal analysis (DTA) A technique in which the temperature difference between a substance and a reference material is measured as a function of temperature whilst the substance and reference material are subjected to a controlled temperature program. For the DTA curve, the temperature difference (ΔT) should be plotted on the ordinate with endothermic reactions downwards.

Differential scanning calorimetry (DSC) A technique in which the difference in energy inputs into a substance and a reference material is measured as a function of temperature whilst the substance and reference material are subjected to a controlled temperature program. Two modes, power-compensation DSC and heat-flux DSC, can be distinguished, depending on the method of measurement used. Usually, for the power-compensation DSC curve, heat flow rate should be plotted on the ordinate with endothermic reactions upwards, and for the heat-flux DSC curve with endothermic reactions downwards.

Dynamic thermomechanometry (or dynamic mechanical analysis, DMA) A technique in which the dynamic modulus and/or damping of a substance under oscillatory load is measured as a function of temperature whilst the substance is subjected to a controlled temperature program.

Parts I - IV are accepted by international and national bodies, such as IUPAC (1974, 1977) ISO (1969, 1975), ASTM(1973)



*This part has not yet been accepted.

Scheme 1.1 Changes and developments in the nomenclature for thermal analysis

A new definition was proposed by Gimzewski [47] in 1991, but it has not yet been accepted. According to his proposal, thermal analysis is defined as a group of techniques in which a property of the sample is monitored against time or temperature while the temperature of the sample, in a specified atmosphere, is programmed.

On the basis of the physical properties determined, thermal analysis techniques can be classified as outlined in Table 1.1

1.3.3 Some General TA Terms

Curve The curve describes the relationship between physical quantities and temperature or time under a controlled temperature program. The physical quantity should be plotted on the ordinate decreasing downwards and temperature (T) or time (t) on the abscissa increasing from left to right.

Derivative techniques are not defined, since

derivative curves can be calculated or recorded for most measurements.

Differential This refers to the difference between two physical quantities (e.g. the temperatures of sample and reference material for DTA) under a controlled temperature program.

Derivative The derivative expresses the rate of change of physical quantity against temperature or time.

Subscripts The use of double subscripts, such as T_{sp} , T_{co} , should be avoided. If the subscript relates to an object, it should be a capital letter, e.g. m_s represents the mass of the sample, T_R the temperature of the reference material. If the subscript relates to a phenomenon occurring, it should be lower case, e.g. T_g represents the glass transition temperature, T_c the temperature of crystallization, T_m the temperature of melting, T_s the temperature of a solid-state transition.

Heating rate The heating rate can be expressed either as dT/dt , when a true derivative is intended, or as β in $K\ min^{-1}$. The heating rate

Table 1.1 Classification of thermal analysis techniques

Physical property	Derived technique(s)	Acceptable abbreviation
Mass	Thermogravimetry	TG
	Isobaric mass-change determination	
	Evolved gas detection	EGD
	Evolved gas analysis	EGA
	Emanation thermal analysis	
Temperature	Thermoparticulate analysis	
	Heating-curve determination	
	Differential thermal analysis	DTA
Enthalpy	Differential scanning calorimetry	DSC
Dimensions	Thermodilatometry	
Mechanical characteristics	Thermomechanical analysis	TMA
	Dynamic thermomechanometry	
Acoustic characteristics	Thermosonimetry	
Optical characteristics	Thermoacoustimetry	
Electrical characteristics	Thermooptometry	
Magnetic characteristics	Thermoelectrometry	
	Thermomagnetometry	

so expressed need not be constant and can be positive or negative.

1.4 Characteristics and Data Reporting for Thermal Analysis

1.4.1 Characteristics of Thermal Analysis

The characteristics of TA are summarized as follows:

1. The sample can be analyzed over a wide temperature range using various temperature programs under dynamic and isothermal conditions. On this account, it is convenient to determine the kinetic parameters under non-isothermal conditions.
2. Any physical form of sample (solid, liquid, gel) in various shapes (powder, films, granules, fiber, fabrics, plate, etc.) is applicable.
3. A small amount of sample is required (0.1 μg –10 mg).
4. The time required for measurements ranges from several minutes to several hours.
5. The atmosphere in the vicinity of the sample can be defined.

6. Samples can be annealed, aged or cured and their previous thermal history can be erased in the TA instruments.
7. Measuring techniques and handling of samples are not difficult.
8. A wide variety of TA instruments are commercially available and the price is moderate.

In addition to the above-mentioned advantages, the following factors should be taken into consideration.

1. TA data is indirect. It is necessary to correlate with data obtained by direct methods, such as spectroscopic and morphological observations in order to elucidate the molecular processes.
2. TA experiments are carried out under non-equilibrium conditions. On this account, the observed transition temperature is not the equilibrium transition temperature.
3. The precise sample temperature during measurements is unknown owing to the conformation of the temperature sensor. The thermal gradient in the sample cannot be measured.
4. The sensitivity and precision of measurements of physico-chemical changes are relatively low compared with spectroscopic techniques.

It is recommended that the standard experiment should be performed in comparison with related standards when a suitable standard can be found. If not, the principles and the basic hypothesis of the TA method should be taken into consideration in order to choose suitable experimental conditions. For example, when the purity of the substance is determined based on Van't Hoff's equation under dynamic conditions by DSC, the melting curve of the samples should be scanned very slowly (e.g. $0.5^{\circ}\text{C min}^{-1}$), since Van't Hoff's equation is assumed to apply under quasi-equilibrium conditions.

1.4.2 Data Reporting of Thermal Analysis [48]

Data on thermal analysis should generally include the following identifications and/or statements:

1. The definitive name of all substances (sample, reference, diluent, etc.) and an empirical formula or equivalent compositional information should be given.
2. The source of substances, details of their histories, pretreatments and chemical purity as far as is known should be stated.
3. The temperature environment of the sample during measurements, including initial temperature, final temperature and rate of temperature change over the range of interest, even if linear, should be clear.
4. The sample atmosphere by pressure, composition and purity and whether the atmosphere is static, self-generated or dynamic, should be stated. If possible, the ambient atmospheric pressure and humidity should be specified. When the pressure is other than atmospheric pressure, details of the controlling method should be given.
5. The mass, dimensions and geometry of the sample are necessary.
6. The abscissa scale of the TA curve should be time or temperature at a specified location. Time or temperature is plotted to increase from left to right.
7. The ordinate scale depends on each thermal analysis (see Table 1.1).
8. Faithful reproduction of all original records that are presented should be ensured.

In DTA and DSC, it is recommended that the following be added.

1. Dimensions, geometry and materials of the sample holder and the method of loading the sample should be given (not necessary when commercially available apparatus is used and the name of manufacturer and the model are stated).
2. Methods used to identify intermediates or final products should be stated.
3. Whenever possible, each thermal effect should be identified and supplementary supporting evidence stated.
4. Apparatus including the model, the geometry and materials of thermocouples and the locations of the differential and temperature-measuring devices should be given.
5. The ordinate scale should indicate the temperature difference ΔT or the heat-flux rate dQ/dt . Preferred plotting will indicate an upward deflection as the positive temperature differential (exothermic) and a downward deflection as the negative temperature differential (endothermic) with respect to the reference for DTA and heat-flux DSC, and an upward deflection as the positive direction (endothermic) for power compensation DSC.

In addition, for TG the following apply:

1. The ordinate scale should indicate the mass change, mass loss should be plotted downwards and deviations from this practice should be clearly marked.
2. If derivative thermogravimetry is employed, the method of obtaining the derivative should be indicated and the units of the ordinate specified (modern instrumentation calculates TG derivatives automatically and in that case users ordinarily use the system as a 'black box').

For TMA the following are recommended:

1. Types of deformation (tensile, torsional, bending, etc.) and the dimensions, geometry and materials of the loading elements should be stated.

2. The ordinate scale in specific terms should be identified, if possible. Increases in expansion, elongation or extension (in the static procedure) and torsional displacement should be plotted upwards and increased penetration or deformation in flexure should be plotted downwards.

1.5 Calibration of Temperature and Enthalpy

1.5.1 Temperature Calibration of Thermogravimetry

1.5.1.1 Curie Point Method

Ferromagnetic material becomes paramagnetic and the measured magnetic force is effectively reduced to zero at the Curie point of a ferromagnetic material. If a ferromagnetic material is placed in a thermobalance crucible, which itself is in a constant magnetic field, the thermobalance will record a mass which is the sum of the true mass of the material and a magnetic mass due to the interaction between the ferromagnet and the permanent magnet field. As the ferromagnet is heated through its Curie point, the magnetic mass decreases to zero and the balance registers an apparent mass loss (or mass gain, depending on the configuration). If several ferromagnetic standard reference samples are placed in the crucible at once, a multipoint calibration curve can be obtained over a wide temperature range.

Blaine and Fair [49] determined new estimates

for the 'true' magnetic transition temperatures of the ICTA Certified Magnetic Reference Material GM 761, using a six-point calibration method. The experimental results were corrected, using a linear calibration curve, to produce the new estimates of the magnetic transition temperatures presented in Table 1.2. The precision of these values varies with the transition temperature range of each particular material, but has a pooled standard deviation of $\pm 2^\circ\text{C}$.

1.5.1.2 Dropping Weight Method

A small inert platinum weight is suspended within the thermobalance sample container by a fusible link composed of a temperature calibration material [50, 51]. The weight is either caught in the sample container, producing an 'action/reaction' response on the TG curve, or dropped through a hole in the bottom of the sample container, producing a discontinuous weight loss. The fusible links are constructed from wires of diameter 0.25 mm or smaller of indium, tin, lead, zinc, aluminum, silver or gold. The calibration data for these metals using the weight-drop method are given in Table 1.3.

Temperature calibration is considered to be accurate to within $\pm 2^\circ\text{C}$ over the range 25–1200 $^\circ\text{C}$, with an individual measurement precision of $\pm 1.1^\circ\text{C}$.

1.5.2 Temperature Calibration of DTA and DSC

Thermal analysis techniques are a class of analytical methods whereby where the nature of a sample is investigated in response to a

Table 1.2 New estimates of magnetic transition temperatures for Certified Magnetic Reference Material GM 761 [49]

Material	Transition temperature/ $^\circ\text{C}$		Deviation/ $^\circ\text{C}$
	Experimental	Lit.	
Permanorm 3	259.6 ± 3.7	266.4 ± 6.2	-6.8
Nickel	361.2 ± 1.3	354.4 ± 5.4	6.8
Mumetal	403.0 ± 2.5	385.9 ± 7.2	17.1
Permarnorm 5	431.3 ± 1.6	459.3 ± 7.3	-28.0
Trafoperm	756.2 ± 1.9	754.3 ± 11.0	2.2

Table 1.3 Fusible link temperature calibration data [52]

Material	Observed temperature °C	Corrected temperature °C	Lit. temperature °C	Deviation from lit. value/°C
Indium	159.90 ± 0.97	154.20	165.63	-2.43
Lead	333.02 ± 0.91	331.05	327.50	3.55
Zinc	418.78 ± 1.08	419.68	419.58	0.10
Aluminum	652.23 ± 1.32	659.09	660.37	-1.28
Silver	945.90 ± 0.52	960.25	961.93	-1.68
Gold	1048.70 ± 0.87	1065.67	1064.43	1.24

temperature program, hence it is necessary to increase the precision of the temperature measurement. This kind of experiment is not carried out in an equilibrium state, but under heating or cooling dynamic conditions, forming a temperature gradient between the furnace and the sample, and within the sample itself. Owing to limitations of instrument configuration, the temperature sensor (thermocouple) is not in contact with the sample. The measured value of temperature for the same transition or reaction depends on the instrument and the experimental conditions, e.g. sample mass, heating rate, shape and material of the container and packing mode.

To establish a common basis for thermal analysis experiments, a series of ICTA (International Confederation for Thermal Analysis)–NBS (National Bureau of Standards) Standard Reference Materials were proposed via common experiments. These Standard Reference Materials have now been re-named ICTA Certified Reference Materials (CRM) and catalogued by the NBS (now NIST) as GM-758, GM-759 and GM-760 (see Table 1.4). The temperature standards of CRM are not the true transition temperatures of these materials, e.g. the difference between the extrapolated onset T_c of a CRM and the equilibrium transition temperature is usually $\pm 3^\circ\text{C}$.

These sets of materials have been adopted by a number of national and international organizations, among them the International Standards Organization (ISO), the International Union for Pure and Applied Chemistry (IUPAC) and the American Society for Testing and Materials (ASTM).

The choice of material was restricted to those having first-order solid-state phase changes in the appropriate temperature ranges. Melting points were excluded because several types of specimen holders in common use could not retain liquids. A number of recognized melting point standards (e.g. Pb, Zn) may contaminate thermocouples and sample holders through alloy formation, and decomposition processes were considered to be unsuitable because the atmosphere could not be controlled in many types of apparatus.

The potential system for DTA temperature standards should show high chemical stability (the material should not change during storage) and chemical inertness (the material should not affect materials normally employed in instrument construction) and should conform to the following. Transitions should be characterized adequately by equilibrium thermodynamic methods. Other thermal effects should occur at temperatures removed from the transition of interest. Materials should not require pretreatment. Materials can be heated in normal atmospheres without secondary effects. Materials should be available commercially in high purity. Naturally occurring materials are not favored because of inhomogeneity. Expensive and relatively rare materials would be unsuitable for eventual large-scale distribution.

1.5.3 Enthalpy Calibration of DTA and DSC

The relationship between the peak area (A) of the DTA or DSC curve, corresponding to an

Table 1.4 Mean temperature results (°C) [52]

Compound or element	T_c	Heating			Cooling		
		N^a	Onset	Peak	N^a	Onset	Peak
KNO_3	127.7	63	128 ± 5 (112–149)	135 ± 6 (126–160)	31	122 ± 4 (112–128)	119 ± 4 (110–126)
In	157	59/60	154 ± 6 (140–162)	159 ± 6 (140–171)	29/27	154 ± 4 (146–163)	150 ± 4 (139–155)
Sn	231.9	57/59	230 ± 5 (217–240)	237 ± 6 (226–256)	22/18	203 ± 16 (168–222)	203 ± 17 (176–231)
$KClO_4$	299.5	67/66	299 ± 6 (280–310)	309 ± 8 (296–330)	31	287 ± 4 (278–296)	283 ± 5 (274–295)
Ag_2SO_4	430	64	424 ± 7 (400–439)	433 ± 7 (405–452)	30/27	399 ± 14 (337–413)	399 ± 15 (336–419)
SiO_2	573	66	571 ± 5 (552–581)	574 ± 5 (560–588)	34/36	572 ± 3 (565–577)	569 ± 4 (550–575)
K_2SO_4	583	67	582 ± 7 (560–598)	588 ± 6 (575–608)	30/31	582 ± 4 (572–587)	577 ± 8 (551–587)
K_2CrO_4	665	63	665 ± 7 (640–678)	673 ± 6 (656–692)	31	667 ± 5 (652–675)	661 ± 8 (630–671)
$BaCO_3$	810	71	808 ± 8 (783–834)	819 ± 8 (800–841)	29	767 ± 13 (742–790)	752 ± 16 (714–779)
$SrCO_3$	925	67/66	928 ± 7 (905–948)	938 ± 9 (910–961)	31/30	904 ± 15 (875–944)	897 ± 13 (868–920)
SiO_2 in 4 : 1 mixture		42/40	572 ± 6 (560–583)	575 ± 5 (56–590)	22/23	574 ± 3 (570–583)	570 ± 4 (563–582)
K_2SO_4 in 4 : 1 mixture		32/39	582 ± 5 (572–595)	586 ± 6 (574–600)	22/23	584 ± 4 (570–595)	582 ± 4 (570–594)

^a N = number of observations.

enthalpy change (ΔH) for a mass (m) of sample, is

$$A = + \Delta H m K \quad (1.1)$$

where K is the calibration constant in $cm^2 J^{-1}$. In order to determine K , a standard of high purity and accurately known enthalpy of fusion (ΔH_f) is required. Indium, for which $\Delta H_f = 28.5 J g^{-1}$ and the melting point is 156.5 °C, is often employed for this purpose. Accordingly, a known amount of indium (5–10 mg) is scanned in a differential thermal analyzer or differential scanning calorimeter operating under fixed conditions. On the basis of the area under the peak, the calibration constant, K (in $cm^2 J^{-1}$) can be determined. Knowing K , we can determine the enthalpy values for other unknown materials. The values

of melting points and enthalpies of known materials are listed in Table 1.5.

Basically, there are three approaches to peak area measurement: (a) the 'cut and weigh' method, which is accurate to within ±5%; (b) the planimeter method, which is accurate to within ±1%; (c) the integrator method, which is more accurate than method (b). It should be noted that when computer-equipped apparatus is used, enthalpy calculations are carried out automatically if the apparatus is correctly calibrated using calibration reference materials.

The higher the temperature in DTA measurements, the smaller is the peak area for the same heat quantity owing to heat radiation, hence the melting point of chosen calibration material

Table 1.5 Melting points and enthalpies of enthalpy calibration reference materials [53]

Compound or element	Melting point °C	Enthalpy of fusion J g ⁻¹
Naphthalene	80.3	149.0
Benzoic acid	122.4	148.0
Indium	156.6	28.5
Tin	231.9	60.7
Lead	327.5	22.6
Zinc	419.5	113.0
Aluminum	660.2	396.0
Silver	690.8	105.0
Gold	1063.0	62.8

should be close to the temperature range of interest to be investigated.

1.5.4 Calorimetric Calibration of DSC

The heat of transition of a sample can be expressed as follows when it is determined by DSC:

$$\Delta H = (1/m) \int_{t_e}^{t_f} (dQ/dt) dt \quad (1.2)$$

where ΔH is the transition enthalpy, m sample mass, t time, dQ/dt heat flux difference. and subscripts e and f represent the extrapolated onset and final point of the peak, respectively. If the left-hand side of equation 1.1 is considered as ΔH_{ref} (ref = reference) and the right-hand side as ΔH_{meas} (m = measured), both sides can be equalized by introducing a proportionality constant, K , to give

$$\Delta H = (K/m) \int_{t_e}^{t_f} (dQ/dt) dt \quad (1.3)$$

For calibration,

$$K = \Delta H_{ref}/\Delta H_{meas} \quad (1.4)$$

must be determined. The calibration can be carried out using materials whose transition enthalpies are well established [54]. The proportionality constant K is independent of temperature. The value was determined to be

$K = 1.046 \pm 3\%$ by using 12 compounds with 15 transitions in the temperature range 0–670 °C and a ΔH range of 0.3–40 kJ mol⁻¹. The experiments were conducted under the following conditions: Du Pont Thermal Analyzer 1090, aluminum pan or gold pan (for K₂CrO₄), sample size 10–20 mg, heating rate 2–10 °C min⁻¹ and Ar purge gas (50 ml min⁻¹).

1.5.5 Temperature and Size Calibration of TMA [6]

Temperature calibration is carried out using two standard metals whose melting temperature is known. Ordinarily, indium, tin, lead and zinc are used. Melting temperatures of the metals are given in Table 1.5. Two metals should be selected whose melting temperatures (T'_h and T'_l) are either side of the transition temperature of the sample (T_s). Heating the standard metal with 0.1 mm thickness using the same experimental conditions as for a sample is tested. The temperature at which the probe is displaced due to melting of the metal is defined as the transition temperature of standard metals. T_s is calculated using the following equation:

$$T_s = T_i - \Delta T_l - (T_i - T_l)[(\Delta T_h - \Delta T_l)/(T_h - T_l)] \quad (1.5)$$

where T_s is transition temperature of the sample, T_i the temperature of displacement of the sample i , T_h the melting temperature of the standard metal at the high temperature side, T_l that at the low temperature side, $\Delta T_h = T'_h - T_h$, $\Delta T_l = T'_l - T_l$, T'_h is the temperature of displacement of the standard metal at the high temperature side and T'_l is that at the low temperature side.

Dimensional calibration is carried out using standard materials of which the expansion coefficient is known: boronsilicate glass (NIST SRM 7) and molten quartz (NIST SRM 39) are usually used. The calibration factor Δa can be obtained as follows:

$$\Delta a = a_{std} - (a_{std})_{app} \quad (1.6)$$

where a_{std} is the reported value of the expansion coefficient and $(a_{std})_{app}$ is the measured value of the standard material.

1.6 Standard Test Methods for Thermal Analysis

To satisfy the need for industrial standards, data comparisons between laboratories and for the

computer storage and search surveys, a series of important thermoanalytical standardizations (see Table 1.6), with uniform experimental conditions, calibration of instruments, data handling, etc., have been proposed by the American

Table 1.6 ASTM, JIS, DIN and Chinese GB standards for thermal analysis

No.	Standard
ASTM	
E 472-79	Standard Practice for Reporting Thermoanalytical Data
E 473-82	Standard Definitions of Terms Relating to Thermal Analysis
D 4092-82	Standard Definitions and Descriptions of Terms Relating to Dynamic Mechanical Measurements on Plastics
E 474-80	Standard Method for Evaluation of Temperature Scale for Differential Thermal Analysis
E 914-83	Standard Practice for Evaluating Temperature Scale for Thermogravimetry
D 3418-82	Standard Test Method for Transition Temperatures of Polymers by Thermal Analysis
E 794-81	Standard Test Method for Melting Temperatures and Crystallization Temperatures by Thermal Analysis
E 793-81	Standard Test Method for Heats of Fusion and Crystallization by Differential Scanning Calorimetry
D 3417-82	Standard Test Method for Heats of Fusion and Crystallization of Polymers by Thermal Analysis
D 3895-80	Standard Test Method for Oxidative Induction Time of Polyolefins by Thermal Analysis
E 537-76	Standard Method for Assessing the Thermal Stability of Chemicals by Methods of Differential Thermal Analysis
E 487-79	Standard Test Method for Constant-temperature Stability of Chemical Materials
E 698-79	Standard Test Method for Arrhenius Kinetic Constants for Thermal Unstable Materials
D 3850-79	Standard Test Method for Rapid Thermal Degradation of Solid Electrical Insulating Materials by Thermogravimetric Method
E 659-78	Standard Test Method for Autoignition Temperature of Liquid Chemicals
D 3947-80	Standard Test Method for Specific Heat of Aircraft Turbine Lubricants by Thermal Analysis
E 831-81	Standard Test Method for Linear Thermal Expansion of Solid Materials by Thermodilatometry
D 2236-81	Standard Test Method for Dynamic Mechanical Properties of Plastics by Metals of a Torsional Pendulum
E 14-63	Standard Recommended Practice for Thermal Analysis of Metals and Alloys
JIS	
K 0129-1994	General Rules for Thermal Analysis
K 7120-1987	Testing Methods of Plastics by Thermogravimetry
K 7121-1987	Testing Methods for Transition Temperatures of Plastics
K 7122-1987	Testing Methods for Heat of Transition of Plastics
K 7123-1987	Testing Methods for Specific Heat Capacity of Plastics
R 3251-1990	Measuring Method of the Linear Thermal Expansion Coefficient for Low Expansion Glass by Laser Interferometry
H 7101-1989	Method for Determining the Transformation Temperatures of Shape Memory Alloys
DIN	
51005	Terms
51006	Thermogravimetry
51008	Determination of Melting Temperatures
Chinese National Standards	
GB 6425-86	Nomenclature for Thermal Analysis
GB/T 13464-92	Thermal Analysis Test Method for Thermal Stability of Materials

Society for Testing Materials (ASTM), Japanese Industrial Standards (JIS), Deutsche Industrie Normen (DIN) and Chinese National Standards (Chinese GB).

1.7 References

- 1 Slade Jr. P. E., and Jenkins, L. T. (Eds), *Techniques and Methods of Polymer Evaluation*, New York, Marcel Dekker. Vol. 1 *Thermal Analysis*, 1966; Vol. 2, *Thermal Characterization Techniques*, 1970.
- 2 Porter, R. S., and Johnson, J. F. (Eds), *Analytical Calorimetry*. New York, Plenum, Vol. 1, 1968; Vol. 2, 1974.
- 3 Mackenzie, R. C. (Ed.), *Differential Thermal Analysis*. London, Academic Press. Vol. 1, 1970; Vol. 2, 1972.
- 4 Wendlandt, W. W., *Thermal Methods of Analysis*. 2nd edn. New York, Wiley, 1974.
- 5 Kambe, H. (Ed.), *Thermal Analysis*. Tokyo, Kodansha, 1975 (in Japanese).
- 6 Keattch, C. J., and Dollimore, D., *An Introduction of Thermogravimetry*, 2nd edn. London, Heyden, 1975.
- 7 Turi, E. A. (Ed.), *Thermal Characterization of Polymeric Materials*. Orlando, Academic Press, 1981.
- 8 Chen Jianbang, *Thermal Analysis and its Application to Ceramics*. Beijing, Chinese Building Industry Press, 1981 (in Chinese).
- 9 Kambe, H. (Ed.), (Liu Zhenhai, transl.), *Thermal Analysis*. Beijing, Chemical Industry Press, 1982 (in Chinese).
- 10 Mrevlishvili, G. M., *Low Temperature Calorimetry of Biopolymers*. Tbilisi, Metznieva, 1984 (in Russian).
- 11 Zhang Zhongli, et al., *Thermal Apparatus in Analysis*. Beijing, Mechanical Industry Press, 1984 (in Chinese).
- 12 Society of Thermal Analysis and Calorimetry Japan, *Fundamentals and Applications of Thermal Analysis*. Tokyo, Kagaku Gijutsu, 1985 (in Japanese).
- 13 Chen Jinghong and Li Chuanru, *Thermal Analysis and Its Applications*. Beijing, Science Publishers, 1985 (in Chinese).
- 14 Dodd, J. W., and Tonge, K. H., *Thermal Methods*. Chichester, Wiley, 1987.
- 15 Li Yuzeng, *Thermal Analysis*. Beijing, Qing-Hua University Press, 1987 (in Chinese).
- 16 Brown, M., *Introduction to Thermal Analysis*. New York, Chapman and Hall, 1988.
- 17 Society of Thermal Analysis and Calorimetry Japan, *Fundamentals and Applications of Thermal Analysis*, 2nd edn. Tokyo, Kagaku Gijutsu, 1989 (in Japanese).
- 18 Wunderlich, B., *Thermal Analysis*. Boston, Academic Press, 1990.
- 19 Saito, A., *Fundamental of Thermal Analysis*. Tokyo, Kyoritsu, 1990 (in Japanese).
- 20 Gao Jiawu, et al., *Thermal Analysis Curves of Polymeric Materials*. Beijing, Science Press, 1990 (in Chinese).
- 21 Xu Guohua, Yuan Jing, et al., *Common Apparatus of Thermal Analysis*. Shanghai, Shanghai Science and Technology Press, 1990 (in Chinese).
- 22 Charsley, E. L., and Warrington, S. B. (Eds), *Thermal Analysis—Techniques and Applications*. Cambridge, Royal Society of Chemistry, 1991.
- 23 Liu Zhenhai (Ed.), *General Thermal Analysis*. Beijing, Chemical Industry Press, 1991 (in Chinese).
- 24 Cai Zhengqian, *Thermal Analysis*. Beijing, Higher Education Press, 1991 (in Chinese).
- 25 Kambe, H., and Ozawa, T. (Eds), *Thermal Analysis*. Tokyo, Kodansha, 1992 (in Japanese).
- 26 Mrevlishvili, G. M., and Uedaira, H. (Ueadiar, H., transl.), *Low Temperature Calorimetry of Biopolymers*. Sapporo, Hokkaido University Press, 1992 (in Japanese).
- 27 Bershtein, V. A., and Egorov, V. M. (Kemp, T. J., transl.), *Differential Scanning Calorimetry of Polymers*. New York, Ellis Horwood, 1994.
- 28 Society of Thermal Analysis and Calorimetry Japan, *Fundamentals and Applications of Thermal Analysis*, 3rd edn. Tokyo, Realize, 1994 (in Japanese).
- 29 Liu Zhenhai and Hatakeyama, T. (eds), *Handbook of Thermal Analysis*. Beijing, Chemical Industry Press, 1994 (in Chinese).
- 30 Hatakeyama, T., and Quinn, F. X., *Thermal Analysis*. Chichester, Wiley, 1994.
- 31 Shen Xing, *Differential Thermal Analysis, Thermogravimetric Analysis and Kinetics of Isothermal Reaction in the Solid State*. Beijing, Metallurgical Industry Press, 1995 (in Chinese).
- 32 Thermal Analysis Application Group, *Applied Thermal Analysis*. Tokyo, Daily Industry News Paper 1996 (in Japanese).
- 33 Proks, I., in Chvoj, Z., Sestak, J., and Triska, A. (eds), *Kinetic Phase Diagrams—Nonequilibrium Phase Transitions*. Amsterdam, Elsevier, 1991, Ch. 1.
- 34 Le Chatelier, H., *Bull. Soc. Fr. Min. Cristallogr.*, 1887; 10: 204.
- 35 Brief history of thermal analysis is reviewed by Wendlandt, W. W., and Gallagher, P. K., in Turi, E. A. (Ed.), *Thermal Characterization of Polymeric Materials*. London, Academic Press, 1981; (more than 200 references are cited).
- 36 Concise history of thermal analysis in Europe and Japan is introduced by Saito, A., *Fundamentals of Thermal Analysis for Material Science*. Tokyo, Kyoritsu, 1990, Ch. 1 (in Japanese).

- 37 Short history of thermal analysis in Europe, China and Japan and details of present status (statistical data on publications) are summarized by Liu Zhenhai, *Introduction to Thermal Analysis*. Beijing, Chemical Industry Publisher, 1991, Ch. 1 (in Chinese).
- 38 Roberts-Austen, W. C., *Metallographist*, 1889, 2, 186.
- 39 Tammann, G. Z., *Z. Anorg. Chem.*, 1903, 37, 303.
- 40 Tammann, G. Z., *Z. Anorg. Chem.*, 1905, 45, 24.
- 41 Kurnakov, N. S., *Z. Anorg. Chem.*, 1904, 42, 184.
- 41 Saito, H., *Thermobalance Analysis*. Tokyo, Technical Book Publisher, 1962.
- 42 Keattch, C. J., in Society of Thermal Analysis and Calorimetry (Ed.), *Heat, Temperature Measurements and Thermal Analysis 1977*. Tokyo, Science Technology Publisher, 1977, p. 65.
- 43 Watson, E. S., O'Neill, M. J., Justin, J., and Brenner, N., *Anal. Chem.*, 1964, 36, 1233.
- 44 Hatakeyama, T., *Netsu Sokutei*, 1989, 16, 237 (in Japanese).
- 45 Mackenzie, R. C., *J. Thermal Analysis*, 1993, 40, 5.
- 46 Liu Zhenhai, *Netsu Sokutei*, 1991, 18, 252 (in Japanese).
- 47 Gimzewski, *Better Thermal Analysis and Calorimetry*, 3 edn.
- 48 ASTM E472-79.
- 49 Blaine, R. L., and Fair, P. G., *Thermochim Acts*, 1983, 67, 233.
- 50 McGhie, A. R., *Anal Chem.*, 1983, 55, 987.
- 51 McGhie, A. R., Chiu, Fair, P. G., and Blaine, R. L., *Thermochim Acta*, 1983, 67, 241.
- 52 Certificate for ICTA Certified Reference Materials for Differential Thermal Analysis from 125 to 940 °C.
- 53 Dodd, J. W., and Tonge, K. H., *Thermal Methods*. London, Wiley, 1987, p. 142.
- 54 Breuer, K. H., and Eysel, W., *Thermochim Acta*, 1982, 57, 317.

Conformation of TA Apparatus

2.1 General Scope

2.1.1 Basic Conformation

The general conformation of thermal analysis (TA) apparatus, consisting of a physical property sensor, a controlled-atmosphere furnace, a temperature programmer and a recording device, is illustrated in Figure 2.1. The most common forms of TA are shown in Chapter 1 (Table 1.1)

Modern TA apparatus is generally interfaced to a computer (workstation) which oversees the operation of the instrument, controlling the temperature range, heating and cooling rate, flow of purge gas and data accumulation and storage. Various types of data analysis can be performed by the computer. A trend in modern TA is to use a single workstation to operate several instruments simultaneously, as shown in Figure 2.2.

TA instrumentation without a computer is also used where the analog output signal is plotted

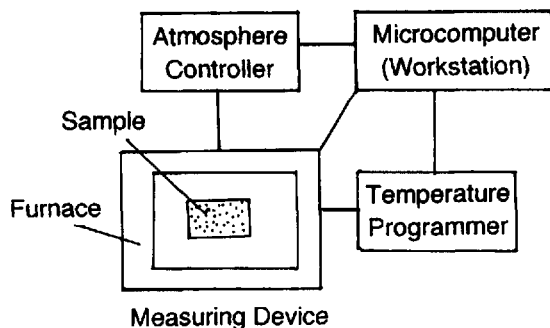


Figure 2.1 Block diagram of TA instrument

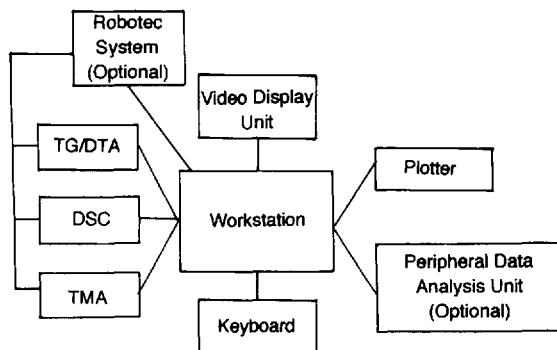


Figure 2.2 Simultaneous operation of TA instruments using a computer (workstation)

using a chart recorder. Data are accumulated on chart paper and calculation is performed manually. The quality of the data obtained is not diminished in any way. The accuracy of the results is the same provided that the apparatus is used properly and the data are analyzed correctly.

2.1.2 Commercial Apparatus

Table 2.1 shows TA apparatus which is commercially available. There are a variety of standard types, such as the thermogravimeter (TG), differential thermal analyzer (DTA), differential scanning calorimeter (DSC), thermomechanical analyzer (TMA) and viscoelastic measurement analyzer (the term thermomechanometry is sometimes used for measurements including TMA, DMA and other viscoelastic measurements) including a dynamic mechanical analyzer

(DMA), all of which operate in a normal temperature region. The temperature region in Table 2.1 represents average values for commercially available apparatus. Detailed specifications of each analyzer are given in Sections 2.2, 2.3 and 2.4.

Table 2.2 lists commercially available TA apparatus that is non-standard. Simultaneous TA analysis which combines TA apparatus with other analytical instrumentation, such as mass spectrometers, Fourier transform infrared spectrometers, X-ray analyzers and gas chromatographs, is widely used.

Table 2.1 Standard thermal analyzers which are commercially available

Thermal analyzer	Temperature region °C
TG (high-temperature use)	Ambient to ~1600
TG-DTA (standard use)	Ambient to 1000
DTA (high-temperature use)	Ambient to 1600
Heat-flux type DSC (standard)	-150 to 750
Heat-flux type DSC (highly sensitive)	-100 to 100
TMA	-150 to 700
DMA	-150 to 500
Viscoelastic measurement apparatus	-150 to 500

Table 2.2 Non-standard thermal analyzers which are commercially available

High-pressure DTA
TG-gas chromatograph (TG-GC)
TG-Fourier transform infrared spectrometer (TG-FTIR)
TG-mass spectrometer (TG-MS)
TG-mass spectrometer-gas chromatograph (TG-MS-GC)
DTA-X-ray diffractometer
DTA-polarizing light microscope (DTA-POL)
High-sensitive DSC
Thermally stimulated current analyzer (TSC)
Alternating current calorimeter (ACC)
Thermoluminescence analyzer (TL)
Fourier transform dielectric spectrometer
Viscoelastic measurement analyzer at constant humidity
Dielectric measurement analyzer (simultaneously with viscoelastic measurement)
Alternating current thermal diffusivity measurement analyzer

In cases where TA apparatus is used in special conditions, such as at high pressure (above 10 MPa), high temperature (above 1700 °C) and a large sample mass (above several grams), it is necessary for users to assemble the apparatus themselves.

2.1.3 Computer Software

Commercially available software for TA apparatus performs a number of tasks (Table 2.3).

Table 2.3 Commercially available TA software

TA instrument	Software function
General (DTA, DSC, TG, TMA, DMA)	Variation of signal amplitude Signal and temperature calibration Accumulation and storage of data Baseline smoothing ^a Display and calculation of transition temperatures Display of multiple curves Curve subtraction Derivative TA curve Baseline correction ^a
DSC	Display and calculation of transition enthalpy Heat capacity determination Purity calculation Reaction rate calculation Temperature modulation
TG	Conversion from mass change to % mass change Reaction rate calculation Heating rate control harmonized with mass change
TMA, DMA	Thermal expansion coefficient calculation Display of stress-strain curve Display of creep curve Display of stress-relaxation curve Arrhenius plot and associated parameters Calculation and display of master curve Heating rate control harmonized with sample deformation

^aIf a large amount of smoothing or baseline correction is necessary, it is better to review the sample preparation and the experimental conditions to improve the data rather than correct the data by computer.

Software for more specialized purposes is generally written by the user. Data analysis using computer software is more convenient than manual analysis. However, it is necessary to understand the characteristics of TA data before using the software.

2.2 Standard TA Apparatus

2.2.1 Thermogravimetry (TG)

Thermogravimetry is a technique which measures the mass change of a sample as a function of temperature in the scanning mode or as a function of time in the isothermal mode. Thermal events do not bring about a change in the mass of the sample, such as melting crystallization and glass transition, but thermal changes accompanying mass change, such as decomposition, sublimation, reduction, desorption, absorption and vaporization, can be measured by TG.

2.2.1.1 Simultaneous Measurements

Many instrument manufacturers produce simultaneous TG-DTA apparatus. The advantage of such apparatus is not only that the sample and experimental conditions are identical but also that standard reference materials for DTA and DSC can be used for temperature calibration (see Section 2.2.1.7).

The gaseous products evolved during TG measurements are analyzed by coupling an appropriate instrument to the TG apparatus. Mass spectrometers (TG-MS), Fourier transform infrared spectrometers (TG-FTIR) and gas chromatographs (TG-GC) will be described in Section 2.4.

2.2.1.2 Basic Configuration

TG curves are recorded using a thermobalance. The principle elements of a thermobalance are an electronic microbalance, a furnace, a temperature programmer, an atmospheric controller and an instrument for simultaneously recording the output from these devices. A schematic illustration of a thermobalance is shown in Figure 2.3. Usually a computer stores a set of mass and

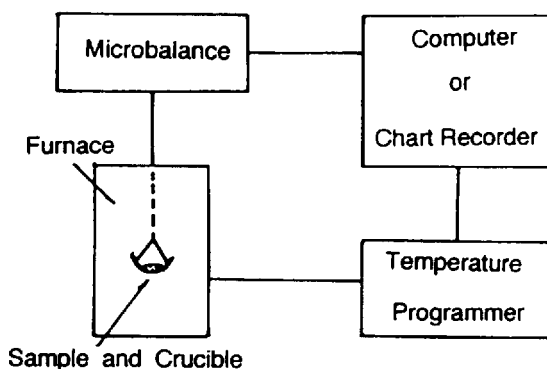


Figure 2.3 Block diagram of a thermobalance

temperature data as a function of time and then, after completing data acquisition, time is converted to temperature.

2.2.1.3 Microbalance

Various designs of microbalance are commercially available, including beam, spring, cantilever and torsion balances, as shown schematically in Figure 2.4.

The furnace heating coil is wound non-inductively to avoid magnetic interactions between the coil and the sample. Coils are made from various materials, such as nichrome ($T < 1300$ K), platinum ($T > 1300$ K), platinum-10% rhodium ($T < 1800$ K) and silicon carbide ($T < 1800$ K). The furnaces consisting of an infrared (IR) ray heater instead of a standard coil heater are also used. An IR furnace is routinely used up to 1800 K. Using an elliptical reflector or parabolic reflector, IR

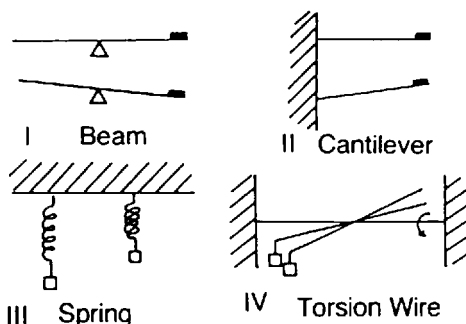


Figure 2.4 Various types of microbalance: (I) beam; (II) cantilever; (III) spring; (IV) torsion wire

rays are focused on the sample holder. This IR furnace enables the temperature to be raised to 1800 K in a few minutes. On this account, it is convenient for use for isothermal measurements.

2.2.1.4 Commercial TG

A sample holder may be one of three types according to the arrangement of the balance and furnace; (1) below the balance, (2) above the balance or (3) parallel to the balance. The below-balance type is usually used for a simple TG measurement (not a simultaneous measurement). Figure 2.5 shows a typical arrangement of a commercial TG apparatus with the sample holder position below the balance.

The above-balance type and the parallel-balance type of TG are commonly used for simultaneous measurements in TG and differential thermal analysis (DTA). Representative arrangements of commercial TG-DTA apparatus of these types are shown in Figures 2.6 and 2.7, respectively. The TG furnace shown in Figure 2.7 is equipped with an IR ray heater.

Some characteristics of commercially available TG and TG-DTA models are shown in Appendix A.

2.2.1.5 Crucible

A variety of crucible sizes, shapes and materials are used. Examples are shown in Figure 2.8. There

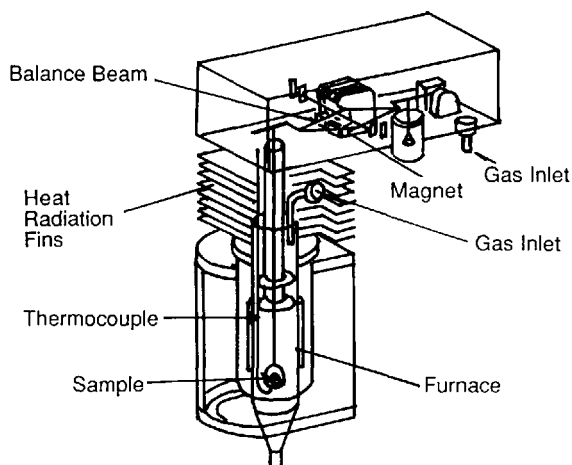


Figure 2.5 The below-balance type TG (reproduced by permission of Shimadzu)

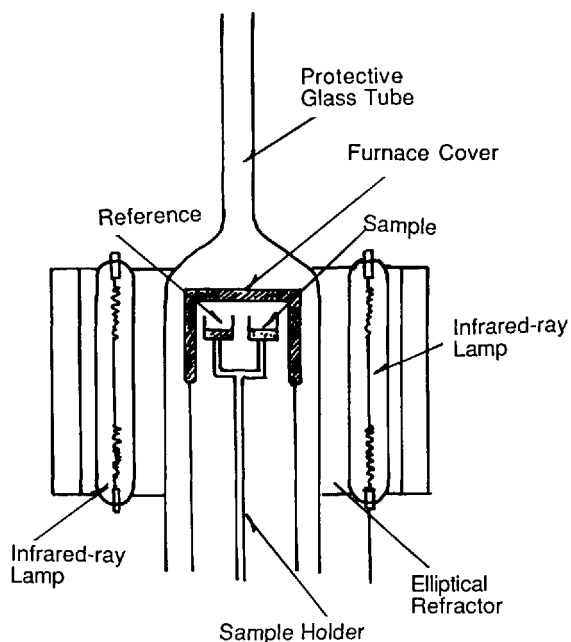


Figure 2.6 The above-balance type TG equipped with infrared ray heater (reproduced by permission of Sinku Riko)

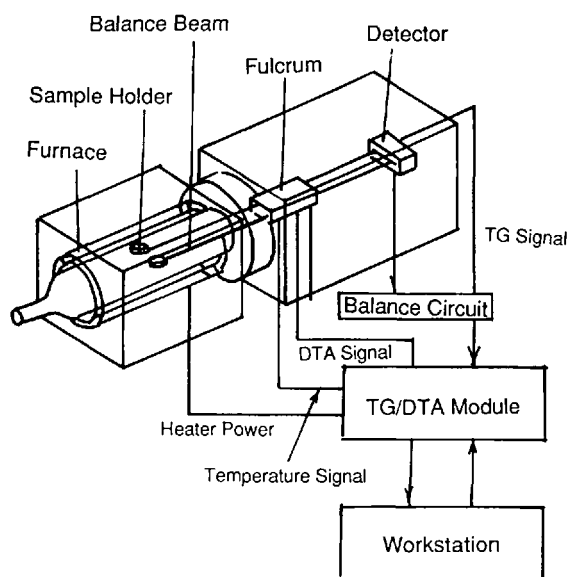


Figure 2.7 The parallel-balance type TG (reproduced by permission of Seiko Instruments)

must be no chemical reaction between the crucibles and the samples. Crucibles are typically made from platinum, aluminium, quartz or alumina (a ceramic), but crucibles made from

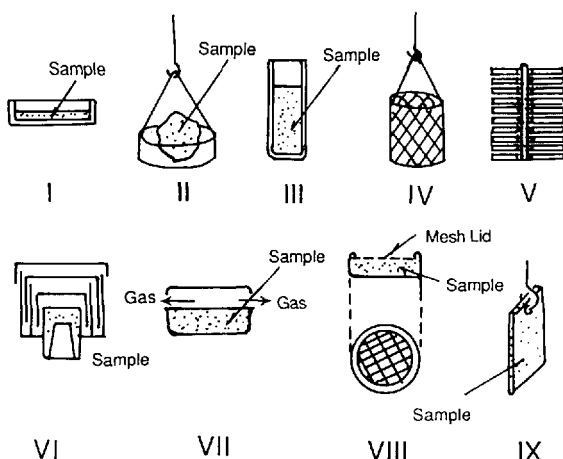


Figure 2.8 Typical crucibles used in TG (reproduced by permission of Kyoritus) [1]. I, Plate; II, hanger; III, cylinder; IV, basket; V, multi-plates; VI, labyrinth; VII, crucible with a hole; VIII, crucible with mesh lid; IX, without crucible

other materials are available. Crucibles are chosen according to the purpose of each experiment.

2.2.1.6 Atmosphere

TG is measured under various atmospheric conditions, such as static, flowing and dynamic conditions. In static conditions, the gas composition around the sample varies when a gas generating reaction occurs. On this account, the reaction rate of the sample varies in accordance with the partial pressure of the gas. Usually, dynamic gas flow is recommended. Gases employed in TG analysis are air, Ar, Cl_2 , CO_2 , H_2 , HCN, H_2O , N_2 , O_2 and SO_2 . It is strongly recommended that a safety officer be consulted to ensure the safe use and proper disposal of harmful gases such as Cl_2 , HCN and SO_2 .

2.2.1.7 Temperature Calibration

The Curie point of a ferromagnetic material is defined as the temperature at which the ferromagnetic material becomes paramagnetic and the measured magnetic force is reduced to zero. When a ferromagnetic material in a constant magnetic field is heated through its Curie point, the magnetic mass decreases to zero and the balance indicates the apparent mass loss. This change is used for temperature calibration TG. A practical method is shown in Chapter 1, Section 1.4.1.

2.2.1.8 High-resolution TG

In order to increase the resolution of TG curves, it is necessary to change the heating rate in coordination with the decrease in mass. This technique is called controlled rate thermogravimetry (CRTG). Several kinds of technique for controlling the temperature, such as step-wise isothermal control, dynamic rate control and constant decomposition rate control, are employed. The above technique is mainly achieved using software with commercial TG apparatus [2].

2.2.2 Differential Thermal Analysis (DTA) and Differential Scanning Calorimetry (DSC)

Theoretical analysis of classical DTA, heat-flux DSC and power compensated DSC is summarized Ref. 3. References 4–12 are useful for readers who concerned with mathematical modeling.

2.2.2.1 Heat-flux DSC

Apparatus—Heat-flux DSC is illustrated schematically in Figure 2.9. The sample holder unit is placed at the center of the furnace. The sample is sealed in a sample pan and placed in one side of the holder, and an inert reference material (exhibiting no phase change over the entire temperature range of the experiment) is likewise inserted in the other side of the holder. The temperature difference between the sample and reference is measured by thermocouples, attached to the base of each side of the holder, as a function of the furnace temperature. A second series of thermocouples measures the temperature of the furnace and of the heat-sensitive plate.

DTA curve—Heating the furnace at a programmed rate raises the temperature of the sample and the reference. When the sample undergoes a phase transformation, energy is absorbed or liberated, altering the heat flux through the heat-sensitive plate and inducing a temperature difference between the sample and the reference. A DTA curve plots this tempera-

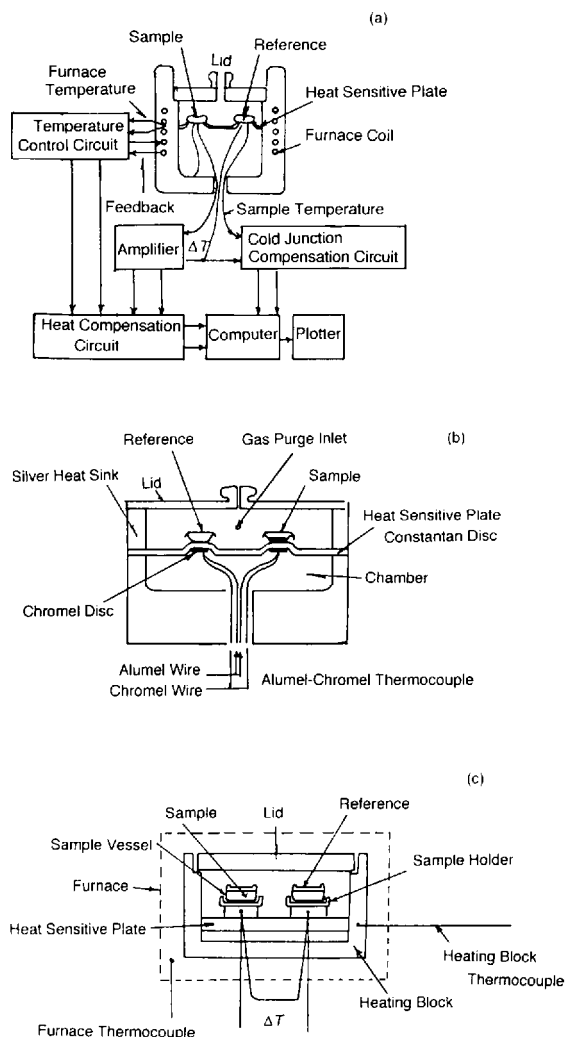


Figure 2.9 (a) Schematic diagram of quantitative DTA apparatus; (b) TA Instruments design (reproduced by permission of TA Instruments); (c) Seiko Instruments design (reproduced by permission of Seiko Instruments)

ture difference as a function of the programmed furnace temperature in the scanning mode, or as a function of time in the isothermal mode (Figure 2.10).

Characteristics—Transition temperatures are measured precisely using the DTA. The transition enthalpy is estimated from the DTA curve using the heat capacity of the heat sensitive plate as a function of temperature. The maximum sensitivity of quantitative DTA is typically 35 mW.

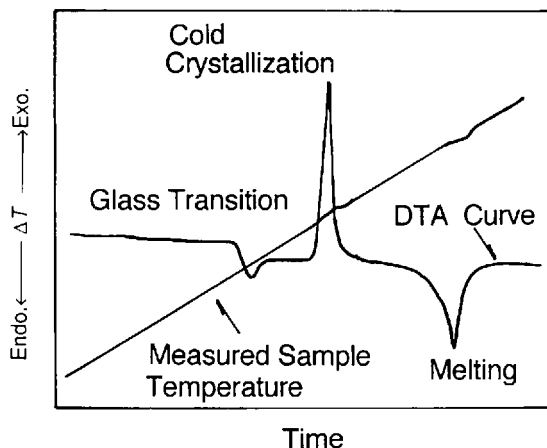


Figure 2.10 Schematic illustration of the measured sample temperature as a function of time for a polymer subjected to a linear heating ramp, and the corresponding DTA curve

A linear instrument baseline is easily obtained because the relatively large furnace heats the atmosphere surrounding the sample holder unit. However, the time required to stabilize the instrument for an isothermal measurement is considerable for both heating and cooling experiments.

Calibration—Temperature and energy calibrations are carried out using standard reference materials (see Chapter 1, Sections 1.4.1 and 1.4.3).

Sample vessels—Sample vessels (open and sealed types) are commercially available in various shapes made from a range of materials, including aluminum, carbon, gold, platinum, silver and stainless steel (Figure 2.11).

2.2.2.2 Triple-cell Heat-flux DSC[13]

Triple-cell DTA instruments are employed to determine transition enthalpies accurately at temperatures >1000 K where the radiative effects from the furnace can no longer be neglected. The operating principle is the same as in heat-flux DSC with the difference that an empty sample vessel, the sample and the reference material are measured simultaneously. Radiative effects are reduced by inserting high thermal conductivity adiabatic shields between the furnace and

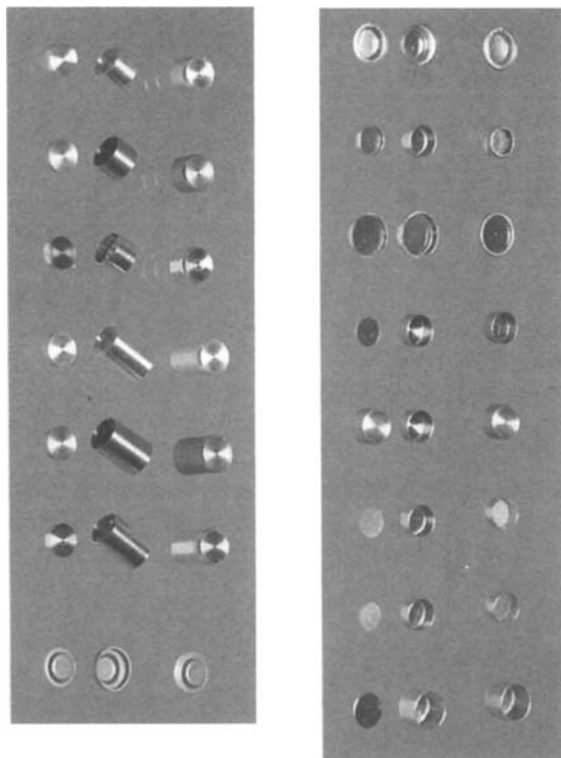


Figure 2.11 Various types of sample vessels

sample holder unit, giving a DSC curve repeatability of $\pm 3\%$ up to 1500 K.

2.2.2.3 Power Compensation DSC

In a power compensation differential scanning calorimeter (DSC), the base of the sample holder unit is in direct contact with a reservoir of coolant (Figure 2.12). The sample and reference holders are individually equipped with a resistance sensor, which measures the temperature of the base of the holder, and a resistance heater. Upon detection of a temperature difference between the sample and reference, due to a phase change in the sample, electrical power is supplied so that the temperature difference falls below a threshold value, typically <0.01 K.

A DSC curve plots the power input per unit time, which is proportional to the heat capacity of the sample, as a function of either the programmed temperature or time. The maximum sensitivity of a power compensation DSC is 35 mW. Temperature and energy calibrations are

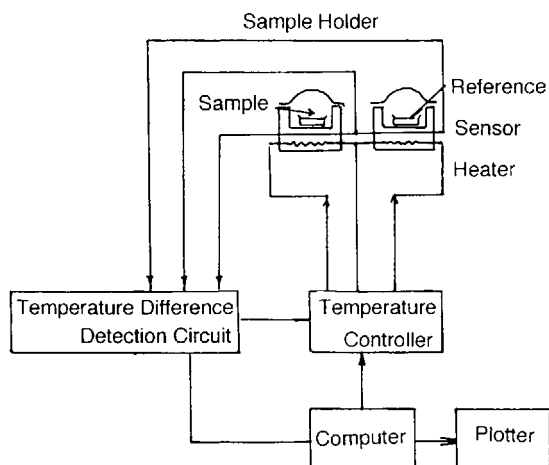


Figure 2.12 Block diagram and schematic diagram of power compensation DSC system (reproduced by permission of Perkin-Elmer)

carried out using standard reference materials (Chapter 1, Sections 1.5.2 and 1.5.3).

Compared with a heat-flux DSC, higher scanning rates can be used with a power compensation DSC, with a maximum reliable scanning rate of 60 K min^{-1} . Maintaining the linearity of the instrument baseline can pose problems at high operating temperatures or in the sub-ambient mode.

2.2.2.4 Temperature Modulated DSC (TMDSC)

TMDSC is a recently suggested technique, and discussions of its attributes are continuing [14–23].

In TMDSC, a perturbation in the form of an oscillating sine wave of known frequency is applied to the linear temperature control program. This variation can be applied in principle to heat-flux DSC and to power compensation DSC instruments. The thermal response is analyzed using Fourier transformation, with the component in-phase with the temperature oscillation thought to be caused by reversible or equilibrium changes in the sample, and the out-of-phase component associated with non-reversible changes.

A general comparison of DSC and TMDSC is presented in Table 2.4.

Table 2.4 Comparison of DSC and TMDSC

DSC		TMDSC
Experimental parameters	Heating rate: isothermal to 60 K min ⁻¹	Heating rate: isothermal to 10 K min ⁻¹ Temperature modulation amplitude: ± 0.01 –10 K Temperature modulation period: 10–100 s
Data obtained	Total heat flow	Total heat flow Modulated heat flow Reversing heat flow Non-reversing heat flow Heat capacity

The signal deconvolution method employed to extract the reversing and non-reversing heat flows implicitly assumes that the response of the rate of the kinetic process to temperature is linear for this type of measurement. In addition, it is hypothesized that the function which describes the kinetics of any transformation in the sample is given by the sum of the average underlying kinetic function plus a sinusoidal contribution which has the same form and frequency as the temperature modulation, with no phase difference. Although these assumptions may be true for the baseline or for a glass transition, they are not valid for sample fusion.

Furthermore, the temperature modulation generally cannot be maintained during fusion because of the large amount of energy absorbed during the phase transformation. This change in energy flux leads to an uncontrolled deviation in the temperature modulation and therefore all parameters determined using this modulation (heat capacity, reversible and non-reversible heat flow, modulated heat flow) are meaningless.

When studying fusion by TMDSC the following experimental precautions must be taken:

1. Modulation amplitude set for 'heat-only'.
2. 4 complete modulation cycles over the fusion peak.
3. Modulation period: 60 s when using N₂ purge gas, 50 s with He.
4. The temperature modulation signal must be monitored as a function of temperature. This is most conveniently done by simultaneously observing the total heat flow signal and the

modulation temperature amplitude as a function of temperature. The measurement is valid only as long as these signals correspond precisely.

Given the experimental difficulties and the fact that a clear methodology for interpreting the results obtained does not currently exist, TMDSC studies of sample fusion should be analyzed with caution.

MDSC can be useful in resolving polymer glass transitions, which are otherwise difficult to analyze owing to concomitant solvent (or other volatile component) evaporation. The polymer glass transition is resolved in the reversing heat flow signal, while the contribution from the volatile component is observed in the non-reversing heat flow.

Within the limitations described below, heat capacity can be determined in a single measurement using TMDSC:

1. The heat capacity measured by TMDSC varies greatly with the temperature modulation period. The extent of this variation over a broad range of modulation periods (10–100 s) must be established by the user and the definitive measurement ultimately performed at a modulation period which lies in the plateau region, where $\Delta C_p \pm 3\%$.
2. The sample mass must be sufficiently low that the sample can instantaneously follow the imposed temperature modulation, and not be limited by the thermal conductivity of the sample. However, the sample mass must be

great enough to avoid errors due to exaggerated baseline curvature.

2.2.2.5 High-sensitivity DSC (HS-DSC)

Two types of HS-DSC are currently available. The first is based on the heat-flux DSC design, where the sensitivity is improved by (i) increasing the quantity of sample used, (ii) employing several thermocouples connected in series to measure the sample and reference temperatures and (iii) increasing the volume of the heat sink to minimize temperature fluctuations. The maximum sensitivity of this design of apparatus is between 1.0 and 0.4 mW.

The Privalov calorimeter is an example of an adiabatic HS-DSC, and is shown schematically in Figure 2.13 [24–26]. Heating elements are placed in the sample and reference holders, which in turn are surrounded by two adiabatic shields. Electrical power is supplied to minimize any temperature difference developed between the sample and reference due to a change of phase. An HS-DSC curve plots the heat capacity of the sample as a function of the programmed temperature. The maximum sensitivity of a Privalov HS-DSC is 0.4 mW. Energy calibration is carried out by supplying a known quantity of electrical power and measuring the heat capacity change of pure water or a buffered saline solution.

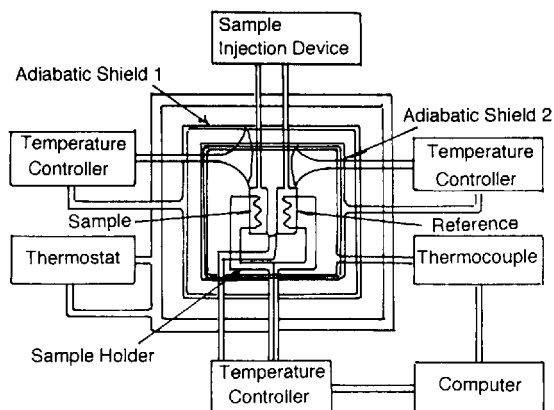


Figure 2.13 Schematic diagram of Privalov adiabatic HS-DSC system (reproduced by permission of the Russian Academy of Natural Science)

2.2.2.6 High-pressure DTA

Figure 2.14 shows a schematic diagram of a commercial high-pressure DTA. The assembly of the system is designed to operate at a maximum working pressure of 7 MPa and to attain a vacuum of under 1 Pa. The pressure enclosure consists of a base, metal cylinder and top plate surrounding the DSC sample holder. Gas is introduced from a high-pressure gas tube into the enclosure through the inlet valve as shown.

A high-pressure DTA assembled by the user is illustrated schematically in Figure 2.15 [27, 28]. The pressure in the sample holder unit is increased by an electrical or mechanical pump, using either dimethylsilicone (maximum pressure 600 MPa) or kerosene (maximum pressure 1000 MPa) as the pressure medium. The temperature range of this instrument is 230–670 K at a heating rate of 1–5 K min⁻¹. The phase transition behavior of various polymers is measured using the above type of high-pressure DTA [29–31].

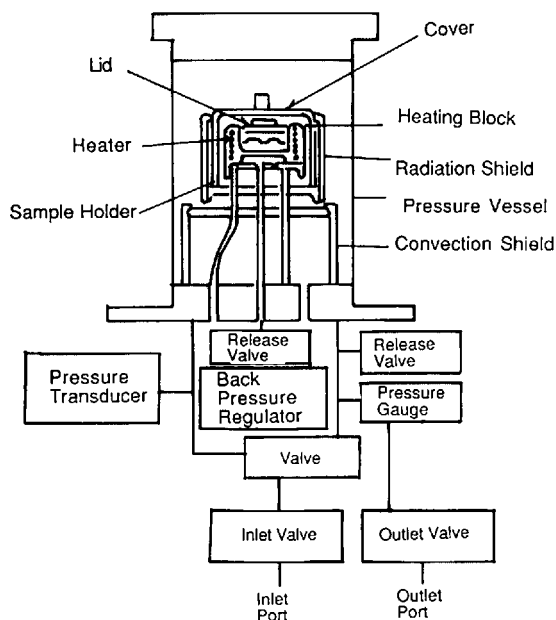


Figure 2.14 Schematic diagram of a commercial high-pressure DTA apparatus (reproduced by permission of TA Instruments)

Commercial high-pressure DTA instruments use an inert purge gas to attain a maximum operating pressure of 10 MPa. The DTA heating curves of polyethylene measured over a range of pressures are presented in Figure 2.16.

2.2.2.7. Sub-ambient Operation

When measurements are made at temperatures below 40 °C, the sample holder assembly is cooled using a cooling apparatus. The most

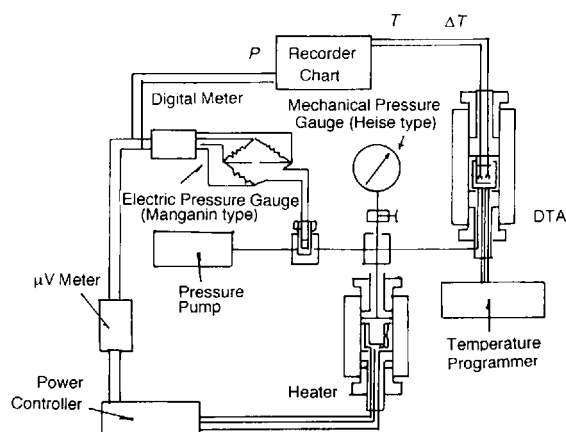


Figure 2.15 Schematic diagram of a high-pressure DTA apparatus (reproduced by permission of Y. Maeda)

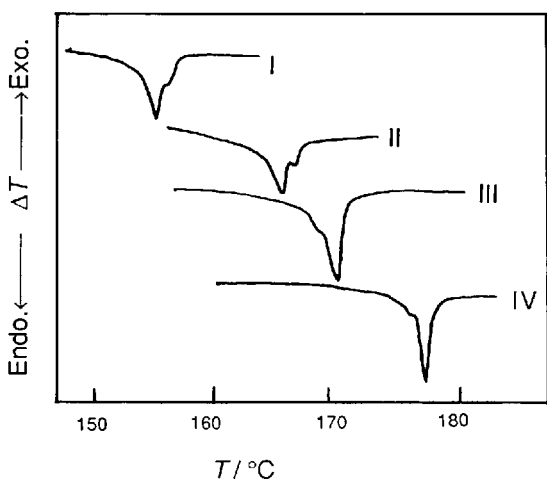


Figure 2.16 DTA heating curves of polyethylene recorded at various pressures: (I), 0.1; (II), 100; (III), 200; (IV), 350 MPa (reproduced by permission of Y. Maeda)

common types of cooling apparatus are illustrated in Figure 2.17. The coolant can be one of the following mixtures, where the lower operational temperature limit is given in parentheses: water-crushed ice (−12 °C), dry ice-acetone (−30 °C), dry ice-methanol (−30 °C) or liquid nitrogen (−130 °C).

2.2.3 Thermomechanometry

2.2.3.1 Thermomechanical Analysis (TMA)

Thermomechanical analysis (TMA) is a technique that measures the deformation of a substance under non-oscillatory load or strain as a function of temperature or time. Therm dilatometry (see Section 2.2.4) is a technique that measures dimensional changes of a sample as a function of temperature or time. Both of these techniques can be applied using the same apparatus. The sample is heated or cooled at a certain rate, or is maintained isothermally at a fixed temperature.

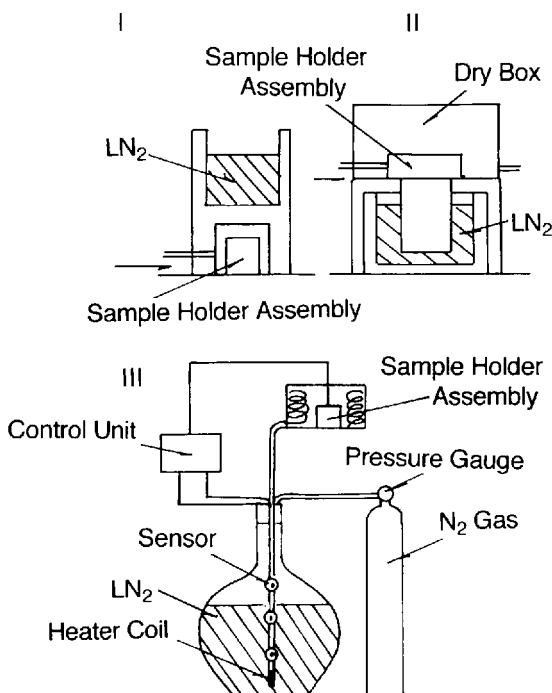


Figure 2.17 Types of DSC cooling apparatus

The measurements can be taken under a variety of atmospheres including *in vacuo*, various gases and aqueous solutions. Samples can be solid (including not only film but also powder, thin-layered film, fiber), liquid or gel. TMA is used to measure linear expansion, compression, elongation, bending, swelling penetration, etc.

Basic configuration—TMA commonly consists of a stress generator, displacement detector, furnace, furnace temperature controller, temperature programmer and temperature detector. In a modern TA system, the sample holder part is connected to the workstation which is used in TG DTA, DSC, etc., as shown in Figure 2.1. A typical arrangement of TMA is shown in Figure 2.18.

Some characteristics of commercially available TMA apparatuses are shown in the Appendices.

Sample probe—In order to measure dimensional changes of samples under stress or strain, various types of sample probes are used. TMA probes and deformation modes for specific applications are shown in Figure 2.19.

Temperature and size calibration—Temperature and size calibration of TMA are carried out using melting of pure metals (see Chapter 1, Section 1.4.5).

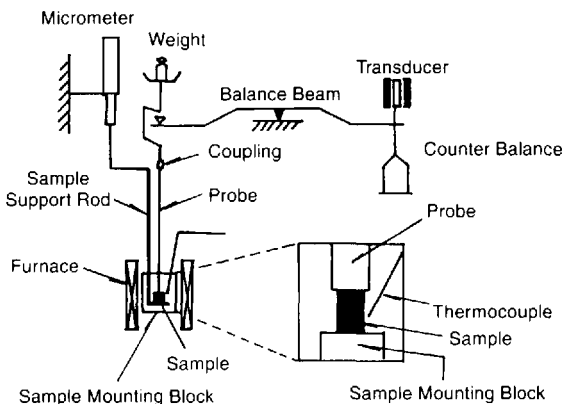


Figure 2.18 A typical arrangement of TMA (reproduced by permission of Ulvac Sinku-Riko)

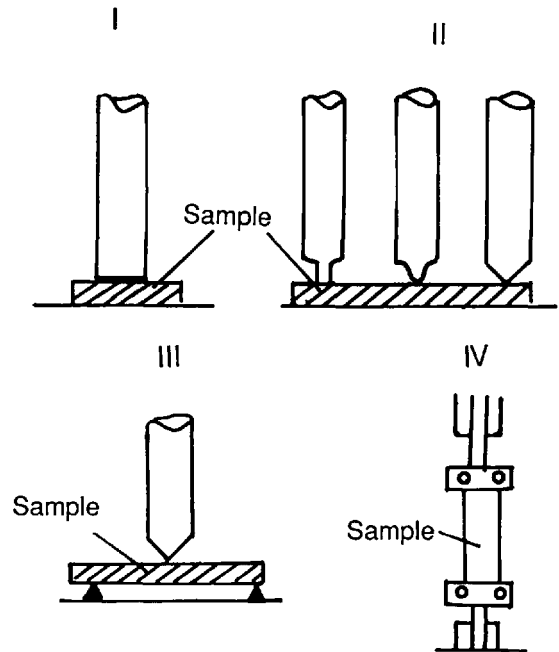


Figure 2.19 Various types of TMA probes: I, expansion mode; II, compression mode; III, bending mode; IV, stretching mode

2.2.3.2 Dynamic Mechanical Analysis (DMA)

Theory [32–34]—A sinusoidally varying stress of frequency ω , applied to a sample which is clamped into a rigid frame, produces a sinusoidally varying strain, where the stress proceeds the strain by a phase angle δ . Thus,

$$\sigma(t) = \sigma_0 \sin(\omega t + \delta) \quad (2.1)$$

$$\gamma(t) = \gamma_0 \sin(\omega t) \quad (2.2)$$

where σ_0 and γ_0 denote the maximum stress and strain amplitudes, respectively. These quantities are related by

$$\sigma(t) = E^*(\omega)\gamma(t) \quad (2.3)$$

where $E^*(\omega)$ is the dynamic modulus, often expressed as

$$E^*(\omega) = E'(\omega) + iE''(\omega) \quad (2.4)$$

$E'(\omega)$ and $E''(\omega)$ denote the dynamic storage modulus and the dynamic loss modulus, respectively. The phase angle δ is calculated using

$$\tan \delta = E'/E'' \quad (2.5)$$

Apparatus—Apparatus is categorized by differences in $\sigma(t)$ application, i.e. bending, stretching, torsion, etc. A block diagram of a commercial DMA using oscillatory bending force is shown in Figure 2.20.

DMA curve and transition map [35]—DMA curves of poly(vinyl alcohol) showing E' , E'' and $\tan \delta$ as a function of temperature over a range of values of ω are presented in Figure 2.21. This technique is particularly suited to studying glass transitions, side-chain or main-chain motions and local mode relaxations in polymers from which samples of appropriate dimensions can be prepared. From the variation in the temperature at which a feature (peak, inflection, shoulder) in the $\tan \delta$ plot of a DMA curve as a function of ω is observed, a transition map ($\log \omega$ versus $1/T$) can be compiled. If the locus of the transition map is a straight line, the activation energy for the phenomena responsible can be calculated using the Arrhenius equation. Where the locus is non-linear, the Williams-Landel-Ferry (WLF) equation can be employed to calculate characteristic parameters. A transition map of poly(vinyl alcohol) compiled from the data in Figure 2.21 is presented in Figure 2.22. Activation energies in this case can be calculated for the α (motion in the crystalline regions), β (glass transition) and γ (local mode relaxation) transitions

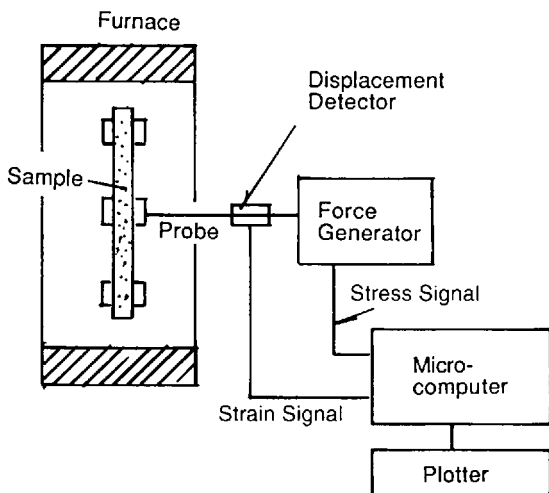


Figure 2.20 Block diagram of a DMA using bending force

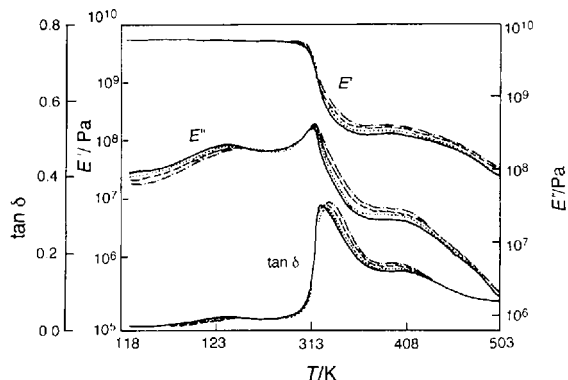


Figure 2.21 DMA curves poly(vinyl alcohol). Frequency: —, 0.5; ···, 1.0; ---, 5.0; - · -, 10 Hz

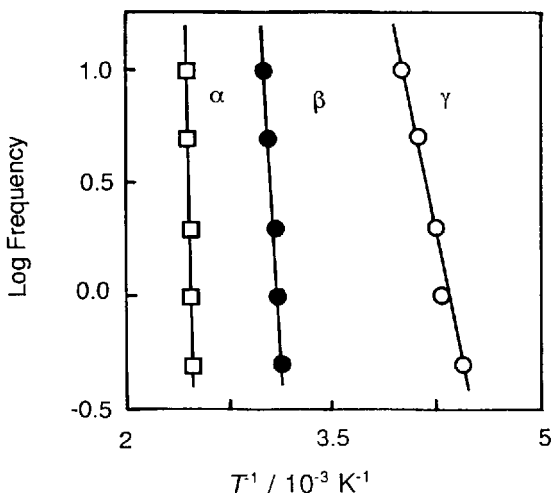


Figure 2.22 Transition map of poly(vinyl alcohol). α , Motion in crystalline region; β , glass transition; γ , local mode relaxation

using the Arrhenius equation. Transition maps of various polymers are shown in Part II, Chapter 7.

2.2.4 Thermodilatometry

Formerly, dilatometry was commonly used to measure sample volume as a function of temperature. Glass capillary dilatometers were designed and built by individual researchers using mercury as the filling medium [36]. Mercury is no longer used in volumetric experiments. Dilatometry is not as widely practised as before, in part because an alternative filling agent has not been found, and has been largely

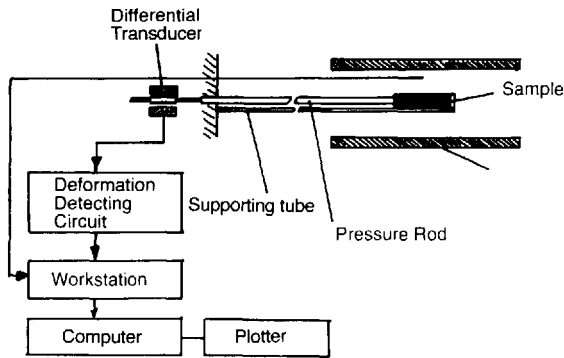


Figure 2.23 Apparatus for linear expansion coefficient measurement using a differential transducer (reproduced by permission of Ulvac Sinku Riko)

supplanted by TMA. Instead of the sample volume, the linear expansion coefficient is measured using TMA (Section 6.1.2).

2.2.4.1 Linear Expansion Coefficient Measurement

The precise value of the linear expansion coefficient can be measured using the apparatus shown in Figure 2.23 from -17 to 1000°C , with a sample size of $8\text{--}10$ mm diameter and $55\text{--}50$ mm length. Dimensional changes are detected in the range of $\pm 1\text{ }\mu\text{m}$ to $\pm 2500\text{ }\mu\text{m}$.

2.3 Light, Electric, Acoustic TA

2.3.1 Alternating Current Calorimetry (ACC)

2.3.1.1 Apparatus

Alternating current calorimetry (ACC) measures the alternating temperature change produced in a sample by an alternating heating current, from which the heat capacity of the material can be estimated. Assuming that heat does not leak from the sample during heating and at constant current amplitude and frequency, the amplitude of the alternating temperature (T_{ac}) of the sample is given by [37, 38]

$$T_{ac} = (Q/i\omega C) \cdot \exp(i\omega t) \quad (2.6)$$

where C is the heat capacity of the sample, $Q \exp(i\omega t)$ the heat flux and ω the angular frequency.

A block diagram of an AC calorimeter is presented in Figure 2.24. The output of a white light source is modulated with a variable-frequency beam chopper so that a square wave is produced which illuminates one surface of the sample. The fluctuating alternating temperature is measured on the other surface using a thermocouple. The variation in T_{ac} as a function of time for materials corresponds to large and small heat capacity. Owing to recent improvements in the design of lock-in amplifiers which can operate at low frequencies, ACC can be applied to a broad range of materials, including polymers [38]. ACC is applied to solution samples [39, 40]. ACC is operated at low temperature [41] and under high pressure [42].

2.3.1.2 Measurements

The operating temperature range is typically $100\text{--}1000\text{ K}$ using samples of area $30\text{--}50\text{ mm}^2$ and thickness $0.01\text{--}0.3\text{ mm}$. The temperature resolution is $\pm 0.0025\text{ K}$ for $T < 770\text{ K}$ and $\pm 0.025\text{ K}$ for $T > 770\text{ K}$. The sample holder is purged with

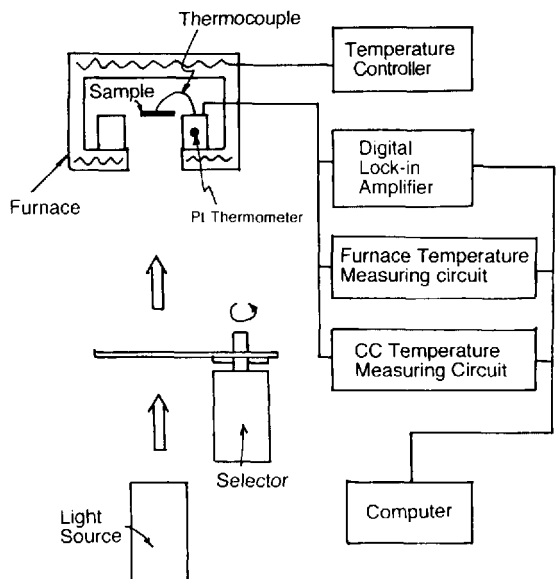


Figure 2.24 Block diagram of ACC (reproduced by permission of Ulvac Shinku Riko)

a dry inert gas. Alumel–chromel or chromel–constantan thermocouples of 0.002 mm diameter are used as a support of metal samples. When organic substances are measured, samples are dissolved in an organic solvent and spread on a thin metal support (stainless-steel film), which is then placed in an evacuated oven to dry the sample. The thermocouple is fixed to the metal support in this case. For polymers, the accuracy of the C_p measurement: is $\pm 2\%$ in absolute value. Fine graphite powder in sol form is sprayed on the illuminated surface of the polymer to ensure complete absorption of the impinging light.

2.3.2 Thermostimulated Current Measurement (TSC)

When a high electric field is applied to a flat insulator, such as polymeric films, electron trapping, the mobile ions and permanent dipole polarization easily occur in these materials. This polarization can be nullified by short circuiting and accelerated by increasing the temperature. A current spectrum can be obtained during the heating process after a flat insulator has been polarized at a constant electrical field E_p at a chosen polarization temperature T_p and then frozen by cooling. This analysis is called thermostimulated current (TSC), thermocurrent or thermal depolarization current measurement. Originally TSC was applied to measure charge detrapping in inorganic compounds, such as semiconductors, glasses and alkali metal halide crystals.

The TSC spectra of polymers have several peaks associated with structural transitions, even though the current is typically of the order of picoamperes. On this account, TSC is a powerful and sensitive method for polymer analysis. In the last 25 years, TSC analysis has been applied to the study of molecular relaxation processes in polymers, including copolymers, polymer blends and, composite materials [43–46]. TSC of polymers is also sensitive to additives, dopants, plasticizers, water and low molecular weight organics.

2.3.2.1 Apparatus

Figure 2.25 shows a typical experimental set up for TSC measurements. It is constructed with

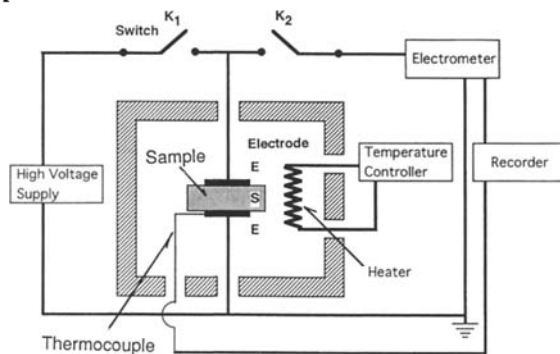


Figure 2.25 Block diagram of TSC apparatus

a d.c. power supply, sensitive electrometer, temperature program controller, recorder and sample cell. The standard sample shape has to be a flat plate because of applying a uniform electrical field.

2.3.2.2 Experimental Procedure

A typical experimental procedure for TSC is as follows.

1. A flat film shaped polymer sample is set between two metal electrodes and then heated above its main transition temperature, which is defined as the polarization temperature T_p .
2. A high electric field E_p is applied for polarizing at T_p for a chosen time t_p and then the sample is cooled to a temperature T_0 where the transition is finished.
3. The external field is removed and an electrometer is connected to both sides of the sample to measure the current.
4. The sample is heated at a constant rate ϕ , typically 10 K min^{-1} , and the depolarization current is observed as a function of temperature.
5. In the case of polymers, the TSC peak temperature corresponds to the molecular mobility of the polymer structure because the rate of depolarization is related to the relaxation times of the internal motions.

2.3.2.3 Thermal Sampling

A single relaxation process is normally assumed when analyzing the shape of the TSC curve, and the activation energy can be estimated using the

Arrhenius equation from the initial gradient of the TSC curve. However, it is unreasonable to assume that a single relaxation process is responsible for the complex TSC curves recorded for polymers. In order to deconvolute these curves into individual relaxation peaks, the 'thermal sampling' approach is used. The temperature and applied field diagram are shown in Figure 2.25 compared with the standard TSC method. The sample is polarized at T_p for a time t_p (about 5 min), then cooled to a chosen depolarization temperature T'_p generally 5 K below the original T_p . Then E_p is cut off and the temperature is held without a polarization field for the same time as the polarization. After quenching to a further low temperature, the sample is reheated and TSC is observed. This procedure is repeated with the varying T_p , so that one obtains a set of individual peaks as shown in Figure 2.26. If the polarization is due to the distribution of relaxation times, the thermal sampling technique can be applied to the experimental production of the relaxation spectra.

2.3.3 Thermoluminescence (TL)

2.3.3.1 Electron Traps

Thermoluminescence (TL) has been used to

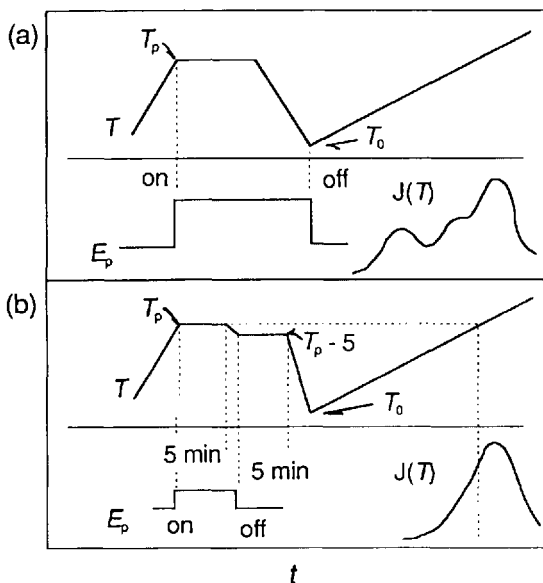


Figure 2.26 Temperature and applied field diagram for the thermal sampling method

estimate the energy depths of trapped electrons in insulators including polymers as with the TSC method. At the same time, applications to polymers have provided a useful tool for studies on polymer chain molecular motions. In its early stages of development, a detailed review of TL applications in the field of polymer science was given by Partidge [47].

A typical TL glow curve can be obtained when an insulator is heated at a constant rate after being irradiated by a high-energy beam, such as UV radiation, X-rays or γ -rays. The trapped electrons in the specimen are generated by the radiation. There are three different types of electron traps: dielectric cavity traps, neutral molecules with a positive electron affinity and free radicals. When the excited specimen is heated, a TL glow is observed owing to the recombination of detrapped electrons [48–50].

2.3.3.2 Oxyluminescence

Polymers at elevated temperatures luminesce owing to oxidation. When polymers are heated in air or an oxygen atmosphere at high temperature, light emission caused by oxidation is observed as a function of temperature. This phenomenon is called oxyluminescence (OL). The OL curves can be attributed to the degradation of each polymer so that the amount of light emission usually increases with increase in temperature.

2.3.3.3 Apparatus and Samples

The TL apparatus is illustrated in Figure 2.27. The main parts of the apparatus consist of a photomultiplier tube as high-sensitivity light detector enclosed in a light-tight box and a sample cell controlled at a constant heating rate, typically $5\text{--}10\text{ K min}^{-1}$, is employed, except in experiments to determine the heating rate contribution. Excitation is carried out, for example, by irradiation with X-rays from a Cu tube at 30 kV and 50 mA. In order to obtain reliable and reproducible results, the irradiated samples are kept in a dark, cold location until taken for measurement.

2.3.3.4 Measurements

Typically samples are shaped into disks about

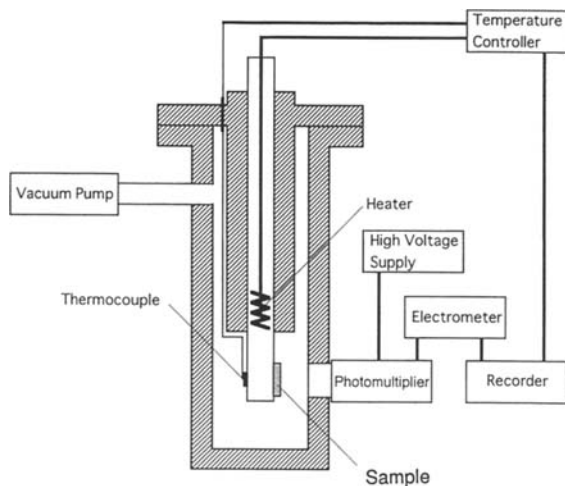


Figure 2.27 Block diagram of TL apparatus

100 μm thick and irradiated at low temperature using dry-ice or liquid nitrogen. Even if a sample cannot be formed into a disk shape, samples in any form, such as powder, fiber and small sections, can be measured. All measurements are carried out in an atmosphere of nitrogen or under reduced pressure, except when studying the oxidation effect. For spectral emission distribution measurement, a series of band pass filters are employed, because sufficient intensity is not obtained with a monochromator.

2.3.3.5 TL Glow Curve

The pattern of TL glow curves, in both shape and intensity, vary in a characteristic manner, reflecting the higher order structure of the polymer molecules. The TL peak in a glow curve can be attributed to the molecular relaxation of each sample.

2.3.4 Thermal Diffusivity Measurement by Temperature Wave Analysis (TWA)

The temperature modulation technique is advantageous for observing the complex physical properties in the relaxation region. The temperature wave analysis (TWA) method is a non-steady-state method for measuring the thermal diffusivity of materials.

When a temperature wave is generated at the front surface of a thin, flat sample, it passes through the thickness direction, then a phase delay and decay of the amplitude of the temperature wave occur according to the thermal diffusivity, sample thickness and frequency. The thermal diffusivity value is obtained by analyzing the temperature wave behavior measured as a function of frequency. In TWA, the thermal diffusivity is continuously measured as a function of temperature at constant heating or cooling in a wide temperature range, including the melting, crystallization and glass transition temperatures.

2.3.4.1 Theory [51–55]

Figure 2.28 shows a schematic diagram of the sample film and the backing substrate contacting at $x = 0$ and $x = d$. Assuming that the heat flow occurs only in the thickness direction, and the substrate is semi-infinite, the temperature oscillations at infinity are obtained. When the sample thickness is larger than thermal diffusion length, the phase shift of the temperature wave $\Delta\theta$ between two surfaces of the sample is given as

$$\Delta\theta = (\pi f/\alpha)^{1/2}d - (\pi/4) \quad (2.7)$$

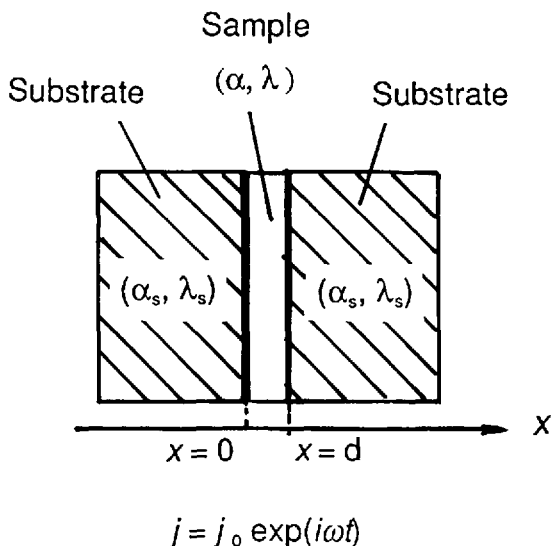


Figure 2.28 Schematic diagram of sample film and the backing substrate α , α_s , thermal diffusivity of sample and substrate, respectively; λ , λ_s , thermal conductivity of sample and substrate, respectively

From this equation, a linear relationship is obtained when $\Delta\theta$ is plotted against $f^{1/2}$, where f is frequency. If the sample thickness has been estimated by another method, the thermal diffusivity value can be calculated from its gradient.

Equation 2.6 can be rewritten using the frequency of the temperature wave as follows:

$$\alpha = \pi f [d/(\Delta\theta + \pi/4)]^2 \quad (2.8)$$

From this equation, α is determined from $\Delta\theta$, which is the measured value at a constant frequency. When the sample temperature is scanned at constant heating or cooling rate, we can obtain α directly as a function of temperature, if the experiment is performed under carefully controlled conditions.

2.3.4.2 Apparatus

A schematic diagram of the TWA system is illustrated in Figure 2.29(a). Thin sputtered gold layers were used as a temperature wave generator. The detecting resistance sensor is magnified as shown in Figure 2.29(b). When a sine wave current is supplied to the heater, a temperature wave is generated at the front surface of the sample and propagates through the sample. The amplitude of the input temperature wave was chosen according to the sample conditions, thickness and thermal diffusivity. Typically the temperature variations are controlled to within 0.5 K in the front surface, then the temperature variation of the rear surface is approximately 0.001 K. The temperature variation at the rear surface is detected by the variation of the electrical resistance of the sensor. The a.c. component of the resistance variation is amplified and analyzed using a lock-in amplifier.

2.3.4.3 Samples

In this method, there are no limitations on the sample thickness, sample size and electrode size and shape. Typically, a sample film of 5 × 10 mm and 10–100 μm thick is placed between the two glass slides on which the sensor and heater are sputtered with gold (1 × 4 mm). The thickness of the sample is maintained by the spacers and shrinkage and deformation during the measurement can be avoided.

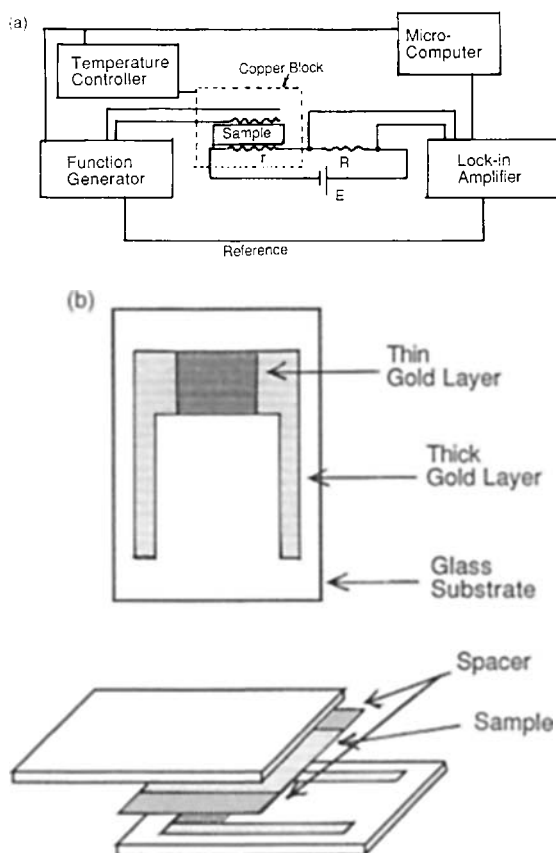


Figure 2.29 Schematic illustration of the TWA system: (a) block diagram; (b) magnified illustration of temperature wave generator and detecting resistance sensor

2.3.4.4 Measurements

A thermocouple is inserted into a dummy sample, which is located symmetrically with the sample on the hot stage. The temperature of the hot stage is kept constant and the phase shifts are measured as a function of frequency for the determination of exact thermal diffusivity. In the case of TWA, the temperature is scanned at a constant rate from 0.1 to 10 K min⁻¹. A thin synthetic sapphire plate is used as a reference material to check the thermal diffusivity value.

With this TWA technique, the thermal diffusivity can be obtained at a constant scanning rate over a wide temperature range including the phase transition region of the polymer, while the frequency range of the temperature wave can be chosen in the range 1 Hz–5 kHz. The glass

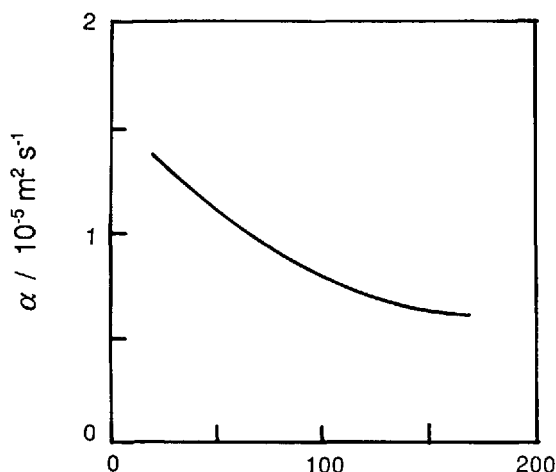


Figure 2.30 TWA curve of a synthetic sapphire plate

transition, the first-order transition and the cold crystallization temperatures are clearly obtained from both the change of phase delay and amplitude decay of the temperature wave.

2.3.4.5 TWA Curves

Figure 2.30 shows the α value of a synthetic sapphire plate as a function of temperature, which indicates a monotonic decrease with increase in temperature. The value of α at 25 °C is in good agreement with the literature values. It is confirmed that the time constant of the sensor or total measurement system is adequate in the experimental frequency range up to 2 kHz.

2.4 Simultaneous TA Analysis

Various types of TA apparatus can be combined so that several physical properties can be measured simultaneously [56]. Table 2.3 lists the most commonly available simultaneous analysis instruments.

2.4.1 Thermomicroscopy

Thermomicroscopy is the simultaneous characterization of a sample by optical methods as the sample is subjected to a controlled temperature

program. Alterations in surface structure alone rarely generate enthalpic variations large enough to be detected by DSC, but can induce large changes in the reflected light intensity (RLI) from the surface. A simultaneous DSC–RLI instrument is schematically illustrated in Figure 2.31, where the light source can be either a filament lamp or a laser. Measurements of the transmitted light intensity (TLI) can be more easily correlated with DSC data as TLI reflects the effect of the sample bulk on the impinging light [Figure

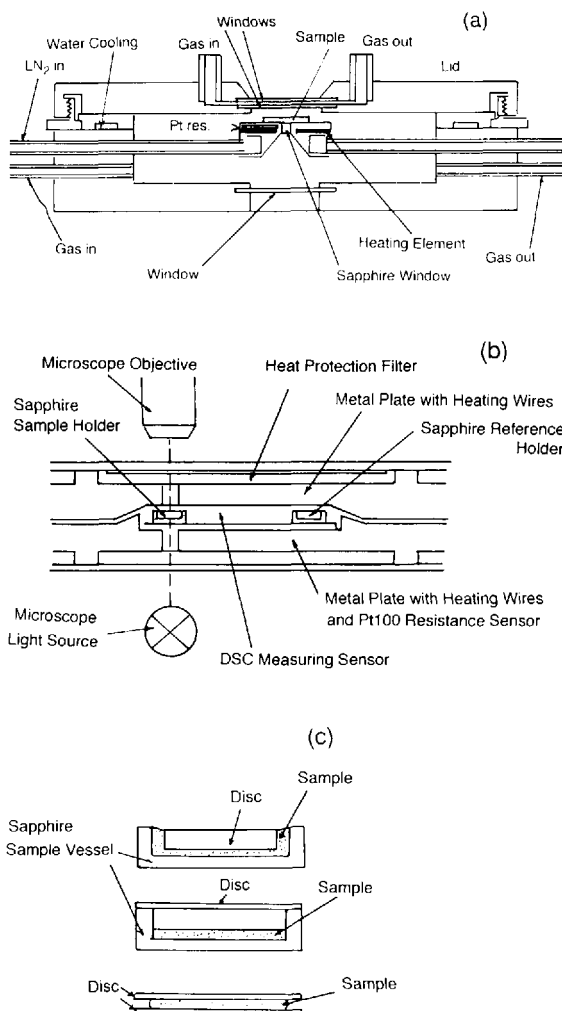


Figure 2.31 (a) Microscope stage for transmitted light (reproduced by permission of Japan High-Tec); (b) simultaneous DSC–transmitted light apparatus; (c) sapphire sample holder of (b) (reproduced by permission of Mettler-Toledo)

2.31(b)]. This method, although confined to transparent materials, is widely used to investigate the nucleation, growth kinetics and high-order structure of liquid crystals. Owing to design constraints, the enthalpic sensitivity of simultaneous DSC-TLI instruments is lower than of DSC-RLI and lower again than that of standard DSC instruments.

Thermomicroscopy can be used to study the following solid-phase transformations, melting, crystallization, liquid crystallization, gel to liquid crystal transformations, decomposition, surface oxidation, swelling, shrinking, surface melting, cracking, bubbling, color changes and texture changes.

2.4.2 X-ray DSC

Simultaneous X-ray DSC instruments, based on those developed for DSC-TLI, are available covering a broad range of X-ray scattering angles [synchrotron orbital radiation (SOR) $0.05^\circ < 2\theta < 0.5^\circ$; small-angle X-ray scattering (SAXS), $0.25^\circ < 2\theta < 10^\circ$; wide-angle X-ray diffraction (WAXD), $5^\circ < 2\theta < 70^\circ$]. Within this range, structural features ranging in size from 0.1 to 500 nm can be studied. Sample pans for X-ray-DSC analysis are made from materials of high X-ray transparency and low diffuse scattering with few Bragg reflections, such as aluminum, graphite and boron nitride.

Owing to the high X-ray flux in SOR experiments, time-resolved X-ray analysis is possible. However, in this case care must be taken to avoid radiation induced decomposition of the sample.

2.4.3 TA-EGD-EGA Coupled Simultaneous Technique

The reaction processes of substances cannot be analyzed by simple DTA/DSC or TG when thermal transition and the mass change due to reaction overlap. If DTA/DSC or TG is coupled with an evolved gas detector (EGD) and/or evolved gas analyzer (EGA), the reaction process can clearly be detected. Among various thermal analysis coupled simultaneous techniques [56], DTA/DSC or TG coupled with EGD and/or EGA is extensively used. TA-EGD-EGA coupled

simultaneous techniques [57–60] were developed in the 1980s.

An analytical scheme for the TA-EGD-EGA coupled simultaneous technique is shown in Figure 2.32. The evolved gas from TA (DTA/DSC or TG) is introduced into the EGA system after passing through the EGD system. The evolved gas is directly introduced to a thermal conductivity detector (TCD), avoiding second reactions. Two methods are used for the TA and EGA coupled simultaneous technique: (1) on-line coupled simultaneous technique in series and (2) off-line combined method. In technique (1), TA is connected serially with a Gas chromatograph (GC) [61–65], mass spectrometer (MS) [57, 64, 65], Fourier transform infrared (FTIR) spectrometer [66, 67], non-dispersive IR (NDIR) spectrometer [68, 69] or thermo-gas-titrimetric apparatus (TGT) [58, 70–72] via an interface. Sampling is carried out continuously and the evolved reaction gas from TA is analyzed. The above analysis can also be carried out using a sampling valve which collects the reacted evolved gas intermittently and repeatedly. An evolved gas sampler consisting of an evolved gas trap unit (ambient temperature *ca* 75 °C) is used for intermittent sampling [73]. When the TA experiment is finished, the evolved gas is absorbed in each absorbing tube, then the carrier gas is passed to the evolved gas injector unit (ambient temperature *ca* 220 °C) connected to an EGA system (GC, MS, IR, etc.) for analysis.

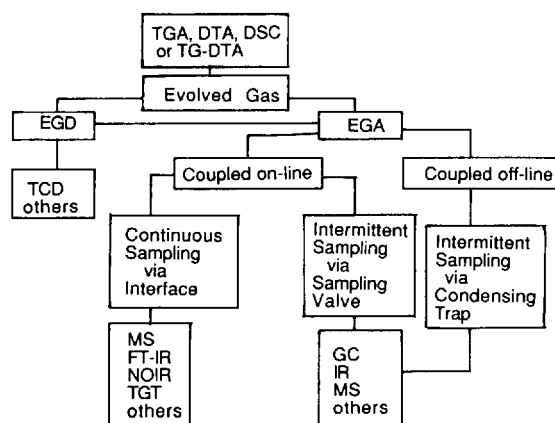


Figure 2.32 Analytical scheme for the TA-EGD-EGA coupled simultaneous technique

2.4.3.1 DTA/DSC–EGD Coupled Technique

The DTA/DSC–EGD coupled simultaneous technique and relevant equipment have been investigated since 1979 [62, 74, 75]. The Model CDR-1 power compensation DSC analyzer (ambient temperature *ca* 720 °C) was developed by the Tian Ping Instrumental Factory (Shanghai, China). The EGD detector is a thermal conductivity detector (TCD) in the GC analyzer. The CDR-1 DSC analyzer coupled with GC was constructed using a specially designed gas conduit. A schematic diagram of the on-line coupled simultaneous DTA/DSC–EGD apparatus is shown in Figure 2.33.

Simultaneity of DTA/DSC and EGD—

When no gas is evolved from the sample during heating, the bridge circuit is balanced and the output signal remains at zero. The EGD curve is smooth, and the corresponding DTA/DSC curve is recorded. As soon as the chemical reaction occurs in the sample, the evolved gas is transported by the carrier gas, the thermal conductivity of the detectable arm of the TCD is changed depending on the reference arm of the TCD, the bridge circuit is unbalanced and the EGD signal deviates from zero. The EGD curve is recorded relative to the DTA curve. The simultaneity of DTA and EGD was examined using the thermal

decomposition reaction of standard material and reliable results were obtained [62, 74, 75] (see Chapter 13).

Quantitative method of EGD(OEGD)—

TCD signal is markedly affected by various factors, such as the bridge current and cell temperature of EGD system, the thermal conductivity and the flow rate of the carrier gas. When the experimental conditions are maintained at a constant, the size and direction of the TCD exported signal is related to the thermal conductivity and concentration of the evolved component which is transported in the carrier gas, but the signal is not related to the source of the sample. Hence the same evolved gas produced by the thermal decomposition of different samples can be quantified precisely. This quantitative method is termed quantitative evolved gas detection (QEGD).

Figure 2.34 shows the calibration line of the EGD–H₂O peak with four carrier gases, Ar, N₂, air and H₂. This figure represents the relationship between the peak area (or mass in mg) of evolved H₂O from the calibrated the H₂O mass for the calibrated sample/CaC₂O₄·H₂O and the calculated value of sample/CaC₂O₄·H₂O having

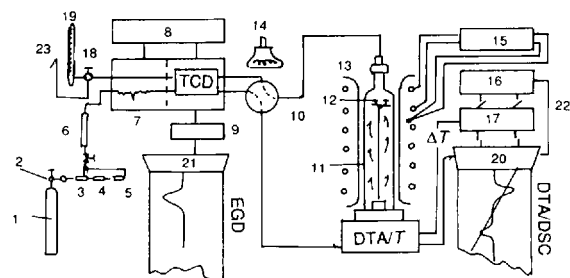


Figure 2.33 On-line coupled simultaneous DTA/DSC–EGD apparatus. 1, Gas cylinder; 2, reducer valve; 3, gas drying; 4, governor valve; 5, buffer; 6, float meter; 7, pre-heater; 8, controlled temperature unit; 9, bridge; 10, four-way valve; 11, gas conduit; 12, crucible; 13, furnace; 14, infrared lamp; 15, controlled temperature programmer; 16, power compensation unit; 17, DTA amplifier unit; 18, three-way valve; 19, soap film flow meter; 20, recorder for DTA/DSC; 21, recorder for EGD; 22, selective switch; 23, tail gas

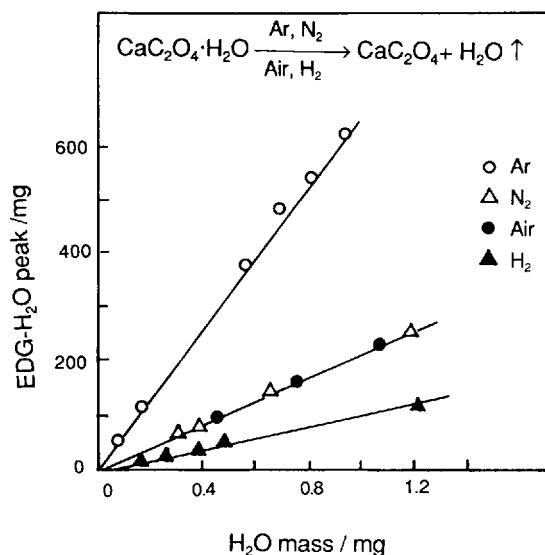


Figure 2.34 Calibration line of EGD–H₂O peak (mg). Calibrated sample, CaC₂O₄·H₂O; DTA, 100 V; heating rate, 20 °C min⁻¹; atmosphere, Ar, N₂, H₂O; flow rate, 20 ml min⁻¹; TCD, 100 mA/115 °C; H₂O mass, mg

different mass. As shown in the figure, good linearity is achieved.

For the examination of the QEGD method, the application of different samples containing hydrous and hydroxylic compounds in different carrier gases is tested. The above different samples liberate H_2O by thermal decomposition during heat treatment. From the calibration line, the EGD- H_2O peak can be obtained. The accuracy was $<10\%$ [62, 74, 75]. The experimental results indicated that its simultaneity, linearity and quantity correspond to those of the same type of commercial instruments [73, 76].

Using the above method, the calibration line of the EGD- CO peak and the EGD- CO_2 peak from the calibrated sample/ CaC_2O_4 and $CaCO_3$ are shown in Figures 2.35 and 2.36, respectively.

It is indicated (see the reaction equation in Figure 2.36) that the $CaCO_3$ formation is accompanied by the release of CO , but the second reaction of the gas phase with the O_2 in the carrier gas (air) is produced immediately after the primary decomposition product of CO . The resultant product is CO_2 . Using the calibration lines of EGD- H_2O , EGD- CO and EGD- CO_2 , the amounts of H_2O , CO and CO_2 which were released in the thermal decomposition of different samples can be detected by QDTA.

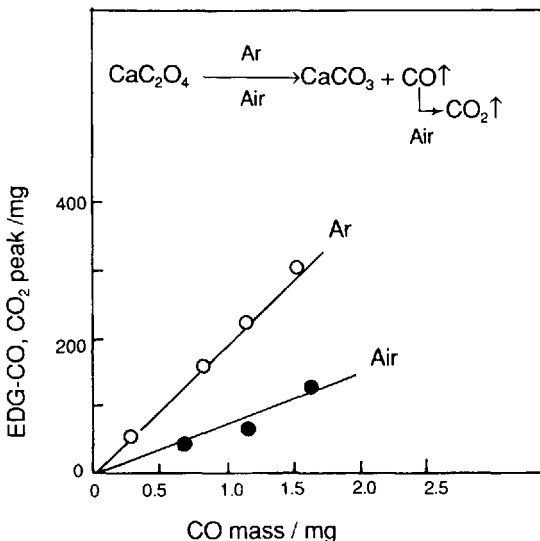


Figure 2.35 Calibration line of EGD- CO peak (mg). Calibrated sample, CaC_2O_4 . Test conditions as in Figure 2.34

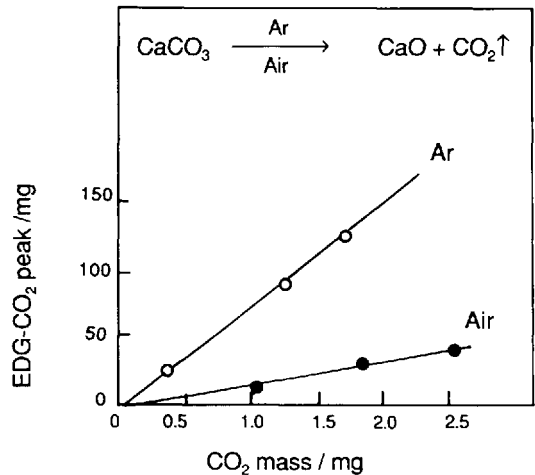


Figure 2.36 Calibration line of EGD- CO_2 peak (mg). Calibration sample, $CaCO_3$. Test conditions as in Figure 2.33

2.4.3.2 DTA-EGD-GC On-line Coupled Simultaneous Technique

For extended applications, a DTA/DSC-EGD-GC on-line coupled simultaneous technique and relevant apparatus were established in the 1980s [63]. The CDR-1 DSC analyzer was replaced by the Model CRY-1 DTA (ambient temperature ca $1200^\circ C$) for the purpose of high-temperature measurements. The scheme of the DTA-EGD-GC on-line coupled simultaneous apparatus is shown in Figure 2.37. DTA and a EGD-GC

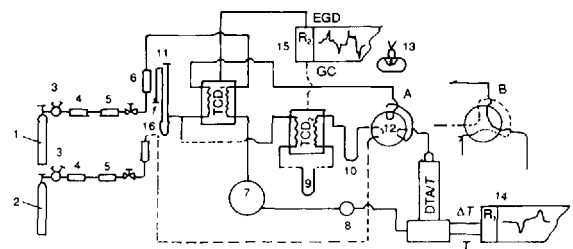


Figure 2.37 Schematic diagram of the DTA-EGD-GC on-line coupled simultaneous apparatus (reproduced by permission of Tian Ping Instrumental Factory, China). 1, Gas cylinder for DTA system; 2, carrier gas for GC system; 3, reducer valve; 4, gas drying; 5, governor valve; 6, float meter; 7, six-way valve; 8, gasifier; 9, 5A molecular sieve; 10, 401 organic support; 11, soap film flow meter; 12, sampling valve; 13, infrared lamp; 14, recorder for DTA/T; 15, recorder for EGD-GC; 16, tail gas

unit with a binary flow and binary thermal conductivity detectors, TCD₁ and TCD₂, connected by a specially designed gas conduit and other accessories were constructed.

Chromatographic columns filled with 401 organic support and 5A molecular sieve were connected in series. A single column filled with Porapak-QS or 401 organic support was also used. The peak height detected by TCD₁ represents the EGD curve and that detected by TCD₂ represents the gas chromatogram. When the thermal decomposition reaction of the sample occurs, the EGD curve traces the variations in the DTA. According to the variations in the DTA-EGD curves, the reaction gas evolved can be intercepted at any temperature on-line for GC analysis by a sampling valve from state A to state B (see Figure 2.37). The gas chromatogram at this reaction temperature is recorded. After GC analysis is finished, the sampling valve is restored (i.e. from state B to state A) to repeat the GC analysis. Hence the evolved gas at different reaction temperatures of the sample during heating can be intercepted intermittently many times for GC analysis.

The functioning of the DTA-EGD-GC on-line coupled simultaneous apparatus is as follows:

1. The EGD curve traces the variation in the DTA curve and the features of the thermal variations of DTA can be directly revealed, whether it is due to a physical process or a chemical reaction.
2. According to the variations in the DTA-EGD curves, the relevant component of the reaction gases evolved at any temperature can be intercepted intermittently and analyzed by GC using a sampling valve at different time intervals.
3. The information and data from four aspects of DTA-EGD-GC and *T* (temperature of reaction and thermal effects, etc.) can be obtained by one measurement from a single sample at the milligram level under the same conditions.
4. The DTA-EGD-GC on-line coupled simultaneous apparatus provides a micro-scale, precise and rapid experimental method for studying the reaction process of solid sub-

stances during thermal decomposition, tracing the variations in the composition of the reaction gases evolved and investigating the mechanism of gas-solid phase thermal reactions in an inert gas or reactive gases.

During the last two decades, the DTA-EGD-GC on-line coupled simultaneous apparatus has been applied in the following fields: solid catalysts [77–79], anti-oxidation additives in petroleum [80], thermal characteristics of coal [81–83], mineralogy [60, 84–87], organometallic chemistry [88–90], polymer chemistry [91], pharmaceutical chemistry [92], environmental protection chemistry and the thermal behavior of all kinds of chemical compounds [62, 63]. Numerous DTA-EGD-GC curves are shown in Chapter 13.

2.4.3.3 TG-DTA-MS Coupled Technique

MS—MS is a highly sensitive technique for identifying unknown compounds. When bombarded with electrons, all substances ionize and fragment in a unique manner. The mass spectrum, which records the masses and relative abundances of the ion fragments, gives a fingerprint for each compound. MS, using quadrupole mass spectrometers, is the most commonly used EGA technique.

TG-DTA-MS—A TG-MS instrument is shown in Figure 2.38. The evolved gas components are detected in the gaseous state at the temperature and pressure in the vicinity of the ion source. The entire mass spectrum, or selected regions of the spectrum, can be recorded continuously and the amount of sample can be of the order of nanograms. The greatest difficulty in coupling a mass spectrometer with a TA instrument is the very large pressure difference between the instruments.

Mass ion chromatograms of poly(vinyl chloride) are shown in Figure 2.39. The major components of peak I are HCl and C₆H₆, and numerous kinds of hydrocarbons are observed in peak II.

A TG-DTA-MS coupled simultaneous apparatus employing a quadrupole mass spectro-

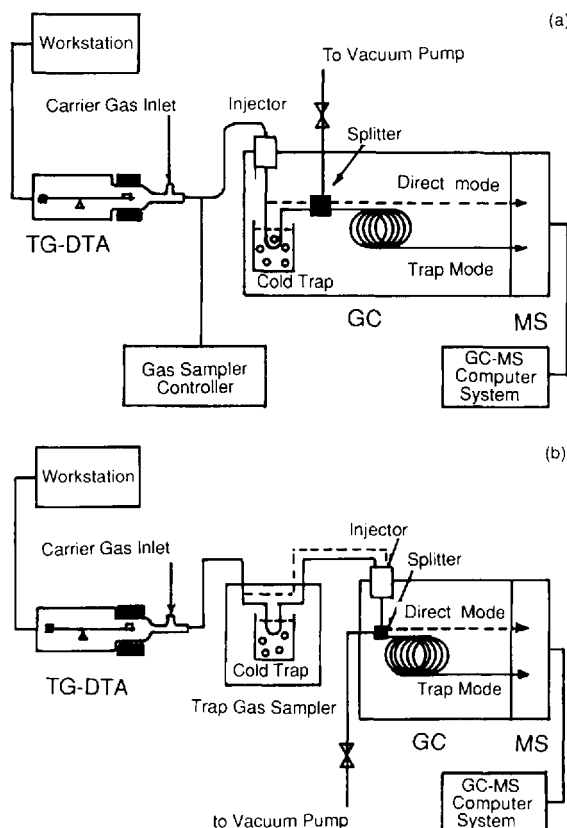


Figure 2.38 Schematic diagram of a simultaneous TG-DTA-MS apparatus. (a) One-channel interface; (b) four-channel interface (reproduced by permission of Rigaku)

meter (QMS 511, mass numbers 1–511) was developed by Netzsch (Model STA 429). The heating element of the TG-DTA apparatus is equipped with a high-temperature tube furnace with coiled SiC, with operating temperatures up to 1500 °C. The gas evolved from the sample can be analyzed under atmospheric pressure or high vacuum [92].

2.4.3.4 TG-Fourier Transform Infrared (FTIR) Spectroscopy

Apparatus—The structure of a TG-DTA-FTIR instrument is shown in Figure 2.40. For optimum performance the lowest purge gas flow rate possible increases the concentration of product gases, while avoiding secondary gas-phase

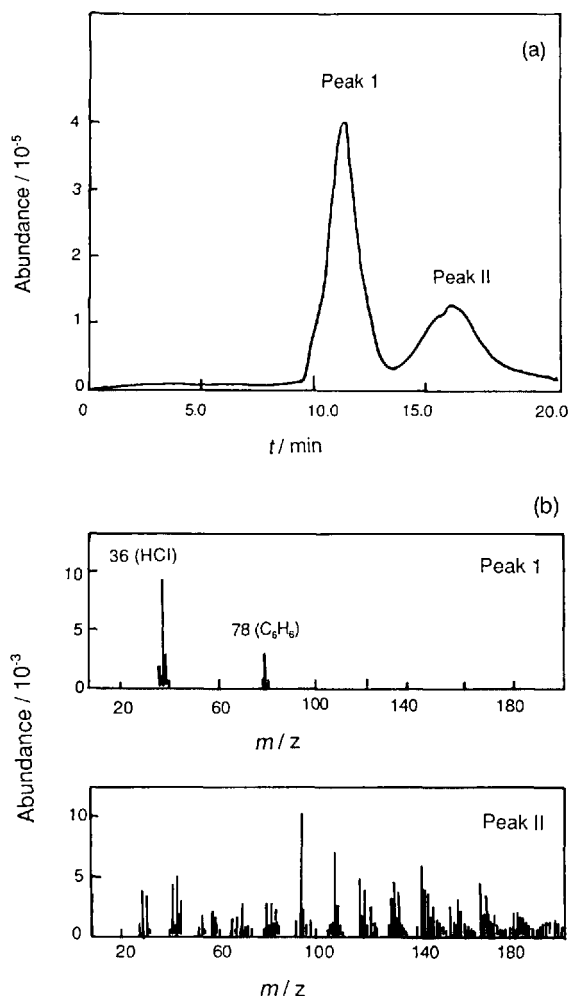


Figure 2.39 Mass ion chromatograms of poly(vinyl chloride) (reproduced by permission of Rigaku)

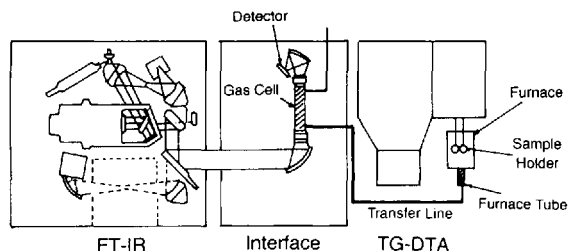


Figure 2.40 Block diagram of TG-DTA-FTIR instrument

reactions. Corrosive and reactive decomposition products are more easily handled by the TG-FTIR coupling mechanism compared with TG-MS. In Figure 2.41 the decomposition of

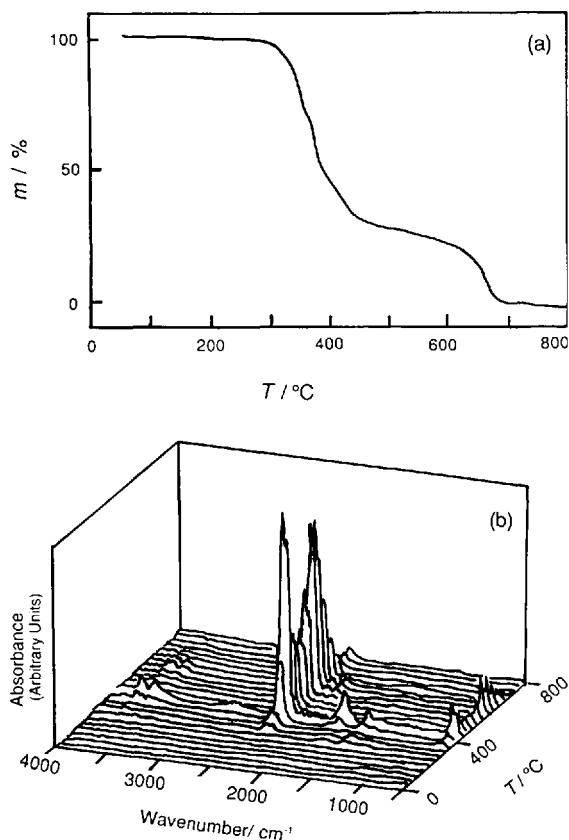


Figure 2.41 (a) TG curve of glucose; (b) three dimensional diagrams (intensity, wavenumber and TG temperature) of FTIR spectra of gases evolved from glucose (reproduced by permission of K. Nakamura)

glucose as revealed using TG-DTA-FTIR is shown.

2.4.3.5 DTA-NDIR Coupled Technique

A non-dispersive IR (NDIR) detector permits the continuous detection of a certain selected constituent in mixed gases. This apparatus was constructed for practical purposes at the Institute of Geological Sciences (London) [68]; a detector for five evolved gases, such as H_2O , CO_2 , CO , SO_2 and O_2 , is coupled to a DTA furnace, realizing a coupled simultaneous DTA-NDIR determination. NDIR detection limits are an order of magnitude lower than those for an X-ray diffractometer. Details can be found elsewhere [68, 69, 93].

2.4.3.6 TG-DTA-TGT Coupled Technique

For the quantitative analysis of a certain component in mixed gases, an automatic titration technique for evolved gases from TA connected with the process of continuous titration was developed [58, 70–72, 94]. This technique is known as thermo-gas titration (TGT). Detected curves (TGT curve) and derivative curves (DTGT curve) can be obtained. The TG-DTA-TGT coupled simultaneous technique and relevant equipment were also established in the 1980s [70]. This technique is based on the direct determination of CO_2 and SO_3 (SO_2) and on the indirect determination of H_2O . A schematic diagram of the TG-DTG-DTA-TGT coupled simultaneous apparatus [71] is shown in Figure 2.42.

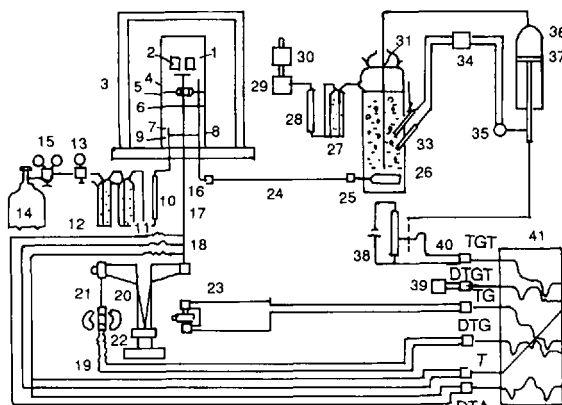


Figure 2.42 Schematic diagram of the TG-DTA-TGT coupled simultaneous apparatus. 1, Crucible for sample; 2, crucible for reference material; 3, electric furnace; 4, corundum bell; 5, upper corundum diaphragm disk; 6, middle corundum diaphragm disk; 7, corundum gas inlet tube; 8, corundum gas outlet tube; 9, lower corundum diaphragm disk; 10, gas flow meter; 11, bottle filled with silica gel for gas drying; 12, bottle filled with soda asbestos (ascarite) for gas purification; 13, governor valve for the control of carrier gas flow; 14, gas cylinder; 15, reducer valve of the gas cylinder; 16, boring of the furnace stand; 17, corundum tube for holding the thermocouples; 18, thermocouples; 19, flexible conductor; 20, balance; 21, coil of the deriving unit; 22, magnets of the deriving unit; 23, differential former; 24, capillary tube for gas conduction; 25, absorption vessel; 26, glass filter; 27, bottle filled with silica gel for drying; 28, gas flow meter; 29, control unit for gas flow; 30, vacuum pump; 31, inlet tube for the titrant; 32, reference calomel electrode; 33, glass electrode; 34, pH-meter switch; 35, servomotor of the automatic burette; 36, cylinder of the automatic burette; 37, piston of the automatic burette; 38, potentiometer; 39, deriving device; 40, pens of the recorder; 41, chart of the recorder

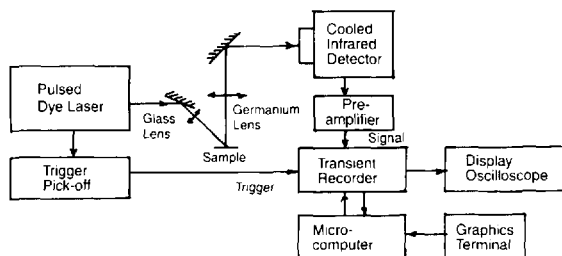


Figure 2.43 Block diagram of OTTER apparatus

2.4.4 Opto-thermal Transient Emission Radiometry (OTTER)

An OTTER apparatus is illustrated schematically in Figure 2.43. Briefly, a laser pulse impinges upon the sample surface, inducing a thermal emission transient which is detected in the form of a temperature decay curve using a wideband infrared detector. The shape of the temperature decay curve is determined by (1) the penetration depth of the incident laser pulse into the sample, (2) the thermal diffusivity of the sample and (3) the transparency of the sample at the emitted thermal infrared wavelength.

The thermal emission transient originates from a narrow region near the sample surface (typically <100 nm). The characteristic parameters of the temperature decay curve (thermal diffusivity and absorption coefficients) are estimated by non-linear least-squares fitting of the curve to theoretical models. This technique has been used to study the water concentration gradient of skin [95]

2.5 Automated TA Systems

An automated sample supplier can be fitted to the TA unit when large numbers of samples are to be routinely measured. Samples are handled and placed in the instrument by a robot arm, and removed after measurements have been completed. Robot arms are commercially available for DSC, TG-DTA and TMA instruments. An automated sample supplier is shown in Figure 2.44.

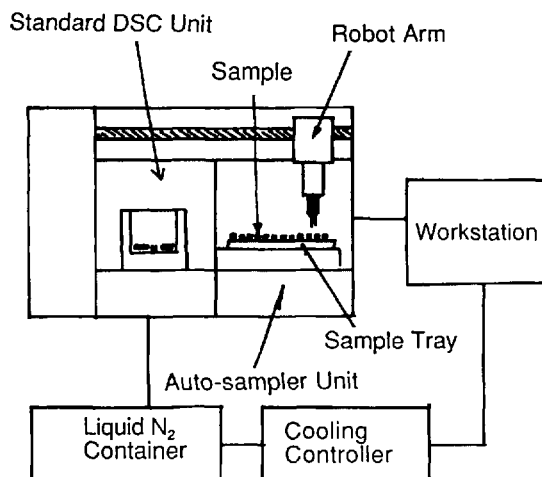


Figure 2.44 Schematic diagram of automated DSC sample supplier (reproduced by permission of Seiko Instruments)

2.6 Installation and Maintenance

The following points should be considered when installing a DSC or DTA instrument:

1. Place the instrument on a level surface approximately 1 m above floor level.
2. Maintain the ambient laboratory temperature between 288 and 303 K and the relative humidity $< 75\%$.
3. A voltage regulator should be used to isolate the instrument from voltage fluctuations, and the electric supply should be latched to avoid uncontrolled powering up of the apparatus following a power failure.
4. Avoid exposure to direct sunlight or air currents.
5. Avoid exposure to magnetic and electric fields, microwaves or other high-frequency signals.
6. Isolate the instrument from mechanical vibrations.

In order to maintain the instrument in good condition a number of elementary precautions should be taken:

Beginners:

1. Read the instruction manuals carefully and discuss your proposed experiments with an experienced user before commencing.

2. Familiarize yourself with those precautions necessary to avoid serious damage to the instrument.
3. Immediately contact an experienced user if the apparatus displays any unusual response.

Advanced users:

1. Record all users' names, sample names, dates and experimental conditions after each series of measurements has been completed.
2. Maintain a small purge gas flow through the instrument even when it is not in use.
3. Contact your repair engineer immediately in the event of instrument failure.

2.7 References

- 1 Saito, Y., *Fundamental Thermal Analysis*, Tokyo, Kyoritsu, 1990.
- 2 Arii, T., Kishi, A., and Fujii, N., *Netsu Sokutei*, 1996, **23**(1), 5.
- 3 Saito, K., Atake, T., and Saito, Y., *Netsu Sokutei*, 1987, **14**, 2.
- 4 Smyth, H. T., *J. Am. Ceram. Soc.*, 1951, **34**, 221.
- 5 Boersma, S. L., *J. Am. Ceram. Soc.*, 1955, **38**, 281.
- 6 Ozawa, T., *Bull. Chem. Soc. Jpn.*, 1966, **39**, 2071.
- 7 Gray, A. P., Porter, R. S., and Johnson, J. F. (Eds), in *Analytical Calorimetry*, New York, Plenum Press, 1968.
- 8 Adam, G., and Muller, F. H., *Kolloid. Z. Z. Polym.*, 1963, **192**, 29.
- 9 Mraw, S. C., *Rev. Sci. Instrum.*, 1982, **53**, 228.
- 10 Saito, Y., Saito, K., and Atake, T., *Thermochim. Acta*, 1986, **99**, 299.
- 11 Saito, Y., Saito, K., and Atake, T., *Thermochim. Acta*, 1986, **104**, 275.
- 12 Saito, Y., Saito, K., and Atake, T., *Thermochim. Acta*, 1986, **107**, 277.
- 13 Takahashi, Y., and Asou, M., *Thermochim. Acta*, 1993, **223**, 7.
- 14 Reading, M., Elliott, D., and Hill, V. L., *J. Thermal Anal.*, 1993, **40**, 949.
- 15 Gill, P. S., Sauerbrunn, S. R., and Reading, M., *J. Thermal Anal.*, 1993, **40**, 931.
- 16 Ozawa, T., and Kanari, K., *Thermochim. Acta*, 1995, **253**, 183.
- 17 Schawe, J. E. K., *Thermochim. Acta*, 1995, **260**, 1.
- 18 Schawe, J. E. K., *Thermochim. Acta*, 1995, **261**, 183.
- 19 Van Assche, G., Van Hemelrijck, A., Rahier, H., and Van Mele, B., *Thermochim. Acta*, 1995, **268**, 121.
- 20 Schawe, J. E. K., *Thermochim. Acta*, 1995, **271**, 127.
- 21 Schawe, J. E. K., and Hohne, G. W. H., *J. Thermal Anal.*, 1996, **46**, 893.
- 22 Hensel, A., Dobbertin, J., Swawe, J. E. K., Boller, J., and Schick, C. J., *Thermal Anal.*, 1996, **46**, 935.
- 23 Varma-Nair, M., and Wunderlich, B., *J. Thermal Anal.*, 1996, **46**, 879.
- 24 Privalov, P. L., and Khechinashiili, N. N., *J. Mol. Biol.*, 1974, **86**, 665.
- 25 Privalov, P. L., Plotnikov, V. V., and Filimonov, V. V., *J. Chem. Thermodyn.*, 1975, **7**, 41.
- 26 Privalov, P. L., *Adv. Protein Chem.*, 1979, **23**, 167.
- 27 Takamizawa, K., *Thermochim. Acta.*, 1978, **25**, 1.
- 28 Takamizawa, K., Nagao, Y., Irii, D., and Urabe, Y., *Thermochim. Acta.*, 1985, **88**, 205.
- 29 Maeda, Y., and Karaz, F. E., and MacKnight, W. J., *J. Appl. Polym. Sci.*, 1986, **32**, 1986.
- 30 Maeda, Y., and Watanabe, J., *Macromolecules*, 1993, **26**, 401.
- 31 Maeda, Y., and Blumstein, A., *Mol. Cryst. Liq. Cryst.*, 1991, **195**, 169.
- 32 Gross, B., *Mathematical Structure of the Theories of Viscoelasticity*, Paris, Hermann, 1953.
- 33 Tobolsky, A., *Properties and Structure of Polymers*, London, Wiley, 1960.
- 34 Ferry, J. D., *Viscoelastic Properties of Polymers*, New York, Wiley, 1961.
- 35 Wada, Y., *Properties of Polymers in the Solid State*, Tokyo, Baifukann, 1981, p. 381.
- 36 Hatakeyama, T., and Quinn, F. X., *Thermal Analysis*, Chichester, Wiley, 1994.
- 37 Hatta, I., and Ikushima, A., *Jpn. J. Appl. Phys.*, 1981, **20**, 1995 (review paper; 72 relevant references are cited).
- 38 Futatsugi, M., Fukuzono, T., and Saruyama, Y., *Polym. Commun.*, 1989, **30**, 22.
- 39 Imaizumi, S., Suzuko, K., and Hatta, I., *Rev. Sci. Instrum.*, 1983, **54**, 1180.
- 40 Imaizumi, S., and Garland, C. W., *J. Phys. Soc. Jpn.*, 1967, **56**, 3887.
- 41 Suzuki, T., Tsuboi, T., and Takaki, H., *Jpn. J. Appl. Phys.*, 1982, **21**, 368.
- 42 Polandov, I. N., Chernenko V. A., and Novik, V. K., *High Temp. High Press.*, 1981, **13**, 399.
- 43 Van Turnhout, J., *Thermally Stimulated Discharge of Polymer Electrets*, Amsterdam, Elsevier, 1975.
- 44 Bucci, C., Fieschi, R., and Guidi, G., *Phys. Rev.*, 1966, **148**, 816.
- 45 Lacabanne, C., Chatain, D., Guillet, J., Seytre, G., and May, J. F., *J. Polym. Sci. Polym. Phys. Ed.*, 1975, **13**, 445.
- 46 Hashimoto, T., Shirakai, M., and Sakai, T., *J. Polym. Sci., Polym. Phys. Ed.*, 1978, **16**, 1965.
- 47 Partridge, R. H., *Radiation Chemistry of Macromolecules*. New York, Academic Press, 1972.
- 48 Hashimoto, T., Sakai, T., and Iguschi, M., *J. Phys. D.*, 1979, **12**, 1567.
- 49 Ashby, G. E., *J. Polym. Sci.*, 1961, **50**, 99.
- 50 Wendlandts, W. W., *Thermochim. Acta*, 1983, **71**, 129.

- 51 Kurihara, T., Morikawa, J., and Hashimoto, T., *Int. J. Thermophys.*, 1997, **181**, 505.
- 52 Hashimoto, T., Matsui, Y., Hagiwara, A., and Miyamoto, A., *Thermochim. Acta*, 1990, **163**, 317.
- 53 Hashimoto, T., and Tsuji, T., *J. Thermal Anal.*, 1993, **40**, 721.
- 54 Morikawa, J., Kobayashi, A., and Hashimoto, T., *Thermochim. Acta*, 1995, **267**, 289.
- 55 Morikawa, J., Tan, J., and Hashimoto, T., *Polymer*, 1995, **361**, 4439.
- 56 *Thermal Analysis, Proceedings of 4th ICTA*, Budapest, 1974.
- 57 Barnes, P. A., *Thermochim. Acta*, 1987, **114**, 1.
- 58 Paulik, J., Paulik, F., and Arnold, M., *J. Thermal Anal.*, 1987, **32**, 301.
- 59 Mackenzie, R. C., *J. Thermal Anal.*, 1975, **197**, 8.
- 60 Cai Gencai, *J. Thermal Anal.*, 1995, **45**, 167.
- 61 Pannetier, G., and Djega-Mariadassou, G., *Bull. Soc. Chim. Fr.*, 1965, 2089.
- 62 Cai Gencai, *J. East China Inst. Chem. Technol.*, 1981, **1**, 115.
- 63 Cai Gencai, *J. East China Instit. Chem. Technol.*, 1982, **1**, 87.
- 64 Emmerich, W.-D., and Kaisersberger, E., in *Proceedings of 5th ICTA*, 1977, p. 67.
- 65 Charsley, E. L., Manning, N. J., and Warrington, S. B., *Thermochim. Acta*, 1987, **114**, 47.
- 66 Roush, P. B., *Am. Lab.*, 1983, **10**, 90.
- 67 Khorami, J., Chauvette, G., Lemieux, A., et al., *Thermochim. Acta*, 1986, **103**, 221.
- 68 Morgan, D. J., *Anal. Proc.*, 1984, **21**, 3.
- 69 Morgan, D. J., *Thermochim. Acta*, 1988, **135**, 207.
- 70 Paulik, J., Paulik, F., and Arnold, M., *J. Thermal Anal.*, 1982, **25**, 327.
- 71 Paulik, F., Paulik, J., and Arnold, M., *J. Thermal Anal.*, 1984, **29**, 333.
- 72 Paulik, J., Paulik, M., and Arnold, M., *J. Thermal Anal.*, 1984, **29**, 345.
- 73 *Thermal Analysis Instrument 30 Series*, Shimadzu, Kyoto.
- 74 Cai Gencai, *Chem. Technol. Pet.*, **7**, 468.
- 75 Cai Gencai, *Anal. Apparatus*, 1982, **4**, 10.
- 76 Emmerich, W.-D., and Bayreuther, K., *Thermal Analysis, Proceedings of 4th ICTA*, Budapest, 1974, Vol.3, p. 1017.
- 77 Cai Gencai, *J. East China Inst. Chem. Technol.*, 1983, **4**, 579.
- 78 Cai Gencai, *J. Fuel Chem. Technol.*, 1989, **13**, 357.
- 79 Cai Gencai and Zhu Xiaolin, *J. East China Inst. Technol.*, 1987, **13**, 437.
- 80 Cai Gencai, *J. East China Inst. Chem. Technol.*, 1987, **13**, 438.
- 81 Cai Gencai, *J. Fuel Chem. Technol.*, 1989, **17**, 329.
- 82 Cai Gencai, *J. Fuel Chem. Technol.*, 1992, **20**, 318.
- 83 Cheng Jingmei, Ren Deqing, Cai Gencai and Huang Yinghua, *J. East China Univ. Sci. Technol.*, 1997, in press.
- 84 Cai Gencai, *Acta Mineral. Sin.*, 1989, **9**, 330.
- 85 Cai Gencai, *J. East China Inst. Chem. Technol.*, 1992, **18**, 404.
- 86 Cai Gencai, *J. East China Univ. Sci. Technol.*, 1995, **21**, 256.
- 87 Cai Gencai, *J. East China Univ. Sci. Technol.*, 1995, **21**, 262.
- 88 Cai Gencai, Qian Yanlong, Huang Jilng, Huang Jiazhen, et al., *J. East China Univ. Sci. Technol.*, 1997, **23**, in press.
- 89 Cai Gencai, Qian Yanlong, Hang Jiling, Hang Jiazhen et al., *J. East China Univ. Sci. Technol.*, 1997, **23**, in press.
- 90 Cheng Jinghong, He Zijian, Li Jiansheng and Cai Gencai, in *Proceedings of the 2nd Symposium on STTT of the Chinese Chemical Society*, 1984, p. 439.
- 91 Pan Weipen, Whiteley, M. J., Seragelden, M. A., and Cai Gencai, *Thermochim. Acta*, 1990, **173**, 83.
- 92 429/TG-DTA-MS. Netzsch.
- 93 Milodowski, A. E., and Morgan, D. J., *Nature*, 1980, **266**, 248.
- 94 Paulik, J., Paulik, F., and Arnold, M., in *Thermal Analysis, Proceedings of International Conference, Kingston*, 1982, Vol. 1, p. 621.
- 95 Imhof, R. E., Birch, D. J. S., Thornley, F. R., Gilchrist, J. R., and Strivens, T. A., *J. Phys. E. Sci. Instrum.*, 1984, **17**, 521.

Effect of Experimental Conditions on TA Measurements, Kinetics of TA and Expression of TA Data

3.1 Effect of Experimental Factors

3.1.1 Heating Rate

Experimental results of thermal analysis are markedly affected by heating rate. In general, the effect of heating rate can be summarized as follows.

(A) The heating rate influences the temperature distribution inside the sample. Figure 3.1 shows an example of a temperature gradient in low-density polyethylene with a thickness of 10 mm. When the heating rate is $2.5\text{ }^{\circ}\text{C min}^{-1}$, the temperature difference inside and outside the sample is negligible. In contrast, the temperature difference is $10\text{ }^{\circ}\text{C}$ at $40\text{ }^{\circ}\text{C min}^{-1}$ [1].

(B) When a chemical reaction, for example a thermal decomposition reaction, is measured by TG, DTA (or DSC), the initial temperature T_i , peak temperature T_p and final temperature T_f shift to the high temperature side with increasing heating rate. For example, when the CO_2 elimination reaction of siderite is measured in an N_2 atmosphere at a heating rate ranging from 1 to $20\text{ }^{\circ}\text{C min}^{-1}$, T_i shifts from 400 to $480\text{ }^{\circ}\text{C}$ and T_f from 500 to $610\text{ }^{\circ}\text{C}$ [2]. Several kinetic methods have been established (e.g. Kissinger method, Ozawa-Flynn-Wall method) based on the scanning rate dependence of TA data (see Section 3.3.1).

(C) When the heating rate is high, the reaction takes place with greater speed in the higher temperature region. The reaction finishes within a narrow temperature interval, and on this account the derivative curves (e.g. DTG, DTA, DSC curves) become sharper.

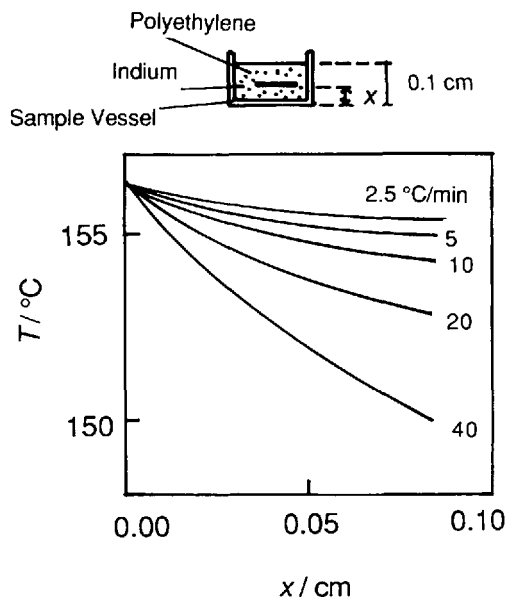


Figure 3.1 Melting temperature of indium, sandwiched between polyethylene films, as a function of the distance (x) from the base of the sample vessel to the indium sample and as a function of heating rate

(D) When multiple reactions are observed, individual reactions are clearly resolved by slower heating rates for DTA curves. The inflection on the TG curve which is observed at a high heating rate changes into a more pronounced horizontal mass plateau at a low heating rate. When the heating rate is controlled dynamically and continuously in response to the reaction of the sample, sharper resolution can be observed, as shown in Figure 3.2 (see Section 3.5.2).

(E) The peak areas of DTA curves are reported to be equal to within $\pm 3\%$, when the scanning rate is changed. However, the area decreased slightly with decreasing heating rate. This tendency was reported in the endothermic reaction of dehydration of kaolin with heating rates from 5 to $20^\circ\text{C min}^{-1}$ [3].

The heating rate influences the phase transition of polymers in a complex manner, e.g. recrystallization is frequently accompanied by a melting process at a low heating rate, and superheating takes place at high heating rate. Since contradictory thermal behavior occurs simultaneously in the same temperature range, it is necessary to choose a suitable heating rate for TA experiments. In some cases, it is recommended to follow related standards. If there is no special requirement, it is common to choose 5 or $10^\circ\text{C min}^{-1}$ [1].

3.1.2 Mass and Particle Size of Sample

When the amount of sample is small, the temper-

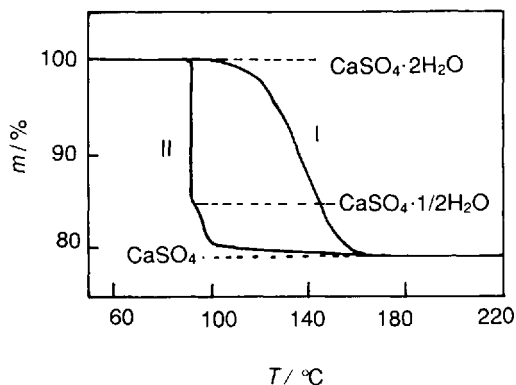


Figure 3.2 Comparison of resolution of TG curves of dehydration of $\text{CaSO}_4 \cdot 2\text{H}_2\text{O}$ obtained by standard heating at 5°C min^{-1} (I) and by the dynamic rate controlled method (II)

ature gradient from outside to inside the sample decreases. Atmospheric gas makes the temperature surrounding the sample uniform and reduces the temperature difference between the sample and sample holder. Hence temperature scanning rate can be linear, despite the thermal irregularity caused by endo- or exothermic heat from the sample. Figure 3.3 shows the relationship between melting peak temperature (T_{pm}) of hexacosane (purity 99.4%) and sample mass in the microgram range. The melting temperature of the sample mass from 0.0003 to 0.0500 mg is observed to be constant.

The peak area, A , of the DTA curve is dependent on the mass of sample, m . The heat of reaction or transition ΔH is given by:

$$A = (Gm\Delta H)/k \quad (3.1)$$

where G is the calibration factor and k the thermal conductivity.

The particle size of the sample influences the TA results. For example, thermo-oxidation of polybuta-1,2-diene gives an exothermic peak at around 200°C . The smaller the particle size, the larger was the exothermic peak area of the DTA curve. In general, both the initial and final thermal decomposition temperatures decrease with decreasing particle size of the sample. Decomposition of a sample with a large particle size is slower than that of a sample with a large specific surface area. TG curves of two samples of whewellite, $\text{CuC}_2\text{O}_4 \cdot \text{H}_2\text{O}$, one a single crystal and the other a powder, were measured *in vacuo*. As shown in Figure 3.4, the dehydration

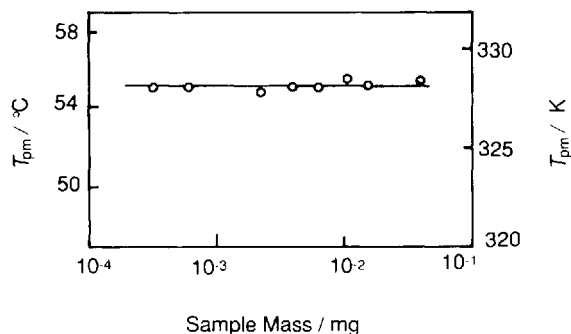


Figure 3.3 Relationship between T_{pm} and mass of hexacosane

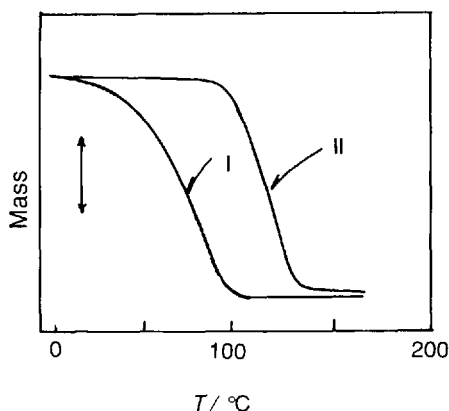


Figure 3.4 TG curve for dehydration of whewellite with different particle sizes (sample mass 6 mg). Heating rate, $2^{\circ}\text{C min}^{-1}$. The arrow in the figure shows 0.2 mg. I, Powder; II, Single crystal

of the powder material starts at a temperature much lower than that of the single crystal [4].

3.1.3 Atmosphere

In order to confirm the physico-chemical origins of thermal events, the atmosphere is often varied. For example, a sample was measured by DTA or DSC in air and an exothermic peak was observed, then the same sample was measured in an inert atmosphere. The result obtained will be different according to the origin of the thermal event: (1) when the exothermic peak remains unchanged the exotherm is attributable to crystallization or curing, (2) when the exothermic peak changes into an endothermic peak it is a decomposition reaction and (3) when there is no peak or a small exothermic peak, it is a kind of oxidative reaction of metals. By changing the atmosphere, the difference between thermal-decomposition and thermo-oxidative decomposition of organic polymers can be distinguished.

For the reaction of a self-generated atmosphere, if the gases produced have not been removed in time, the reaction shifts to the higher temperature side. For example, water vapor inhibits the dehydration reaction of $\text{CaSO}_4 \cdot 2\text{H}_2\text{O}$ and the reaction temperature increases in comparison with the results obtained in air. The dehydration process becomes a multiple process owing to water

vapor, and double peaks are observed on the DTA curve (see Figure 3.5 [5]).

The thermal decomposition of CaCO_3 indicates that the rate of reaction is dependent on how quickly heat is supplied to the system. The rate of thermal decomposition of CaCO_3 depends on the kind of atmosphere, with a higher rate of decomposition in He, followed by N_2 and Ar. This order agrees well with the order of the thermal conductivities of the gases.

Concerning the effect of CO_2 pressure on the shape of the DTA curve of dolomite, Criado [6] suggested several equations and obtained theoretical curves for the reaction rate of the thermal decomposition of CaCO_3 versus temperature at different pressures of CO_2 . The abrupt narrowing of the DTA peaks is explained as being due to a change in pressure and not reaction mechanism.

Important points concerning the atmospheric factors can be summarized as follows:

(A) *Static or dynamic atmosphere.* Under static conditions, gaseous products cannot be removed rapidly from the vicinity of the sample. This leads to a partial pressure of the products and the reaction temperature is increased. Under dynamic or flowing conditions, evolved gases can be removed from the vicinity of the sample, and the partial pressure of the products decreases.

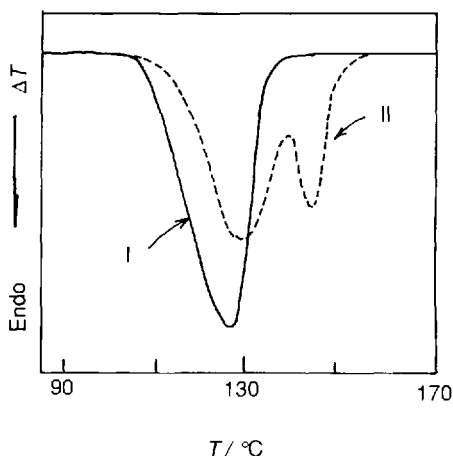


Figure 3.5 DTA curves of $\text{CaSO}_4 \cdot 2\text{H}_2\text{O}$ in (I) air and (II) water vapor [5]

(B) *kinds of atmosphere.* The gases employed in TA experiments are categorized in several classes: (1) oxidizing atmosphere, O_2 , air; (2) reducing atmosphere, H_2 , CO; (3) non-interactive atmosphere, He, N_2 , Ar; (4) self-generated gases from samples or gases produced by reaction of the sample with the atmosphere, such as CO_2 , water vapor and mixtures of gases; and (5) corrosive gases, such as Cl_2 , F_2 , SO_2 , HCN. When these kinds of dangerous and harmful gases are used, safety should be ensured in order to prevent explosions and poisoning. (When a hazardous gas is used, it is recommended that the person in charge of safety at the institution concerned is informed. It is necessary to understand relevant regulations and rules in each country.) The above atmospheres can be controlled with variations in pressure, including *in vacuo*.

(C) *Flow rate.* The flow rate of the atmosphere affects the decomposition temperature of the sample, precision of determination of temperature, flatness of the baseline and peak areas of DTA or DSC curves.

(D) *Miscellaneous.* It should be noted that if a reaction between the atmosphere and a thermocouple and the sample container, gas pipe or other parts of the apparatus occurs, damage to the apparatus will be caused. In addition, the effects of the partial pressure of gaseous products (especially water vapor), thermal conductivity, etc., should be monitored carefully.

3.1.4 Buoyancy, Convection Currents and Turbulence

Buoyancy exerted on the sample decreases with increasing temperature, since the density of the gas-purged intermediate space surrounding the sample holder decreases with increasing temperature. This causes an apparent mass gain.

An apparent mass loss is caused by the upper flowing stream of gas in the vicinity of the sample holder. The upper flowing stream can be reduced by changing the configuration of the sample holder (see Section 2.2.1). It is also important that the size and shape of the sample crucible are adjusted appropriately. In some cases, it is recommended that a small hole is made in the crucible (Figure 3.6).

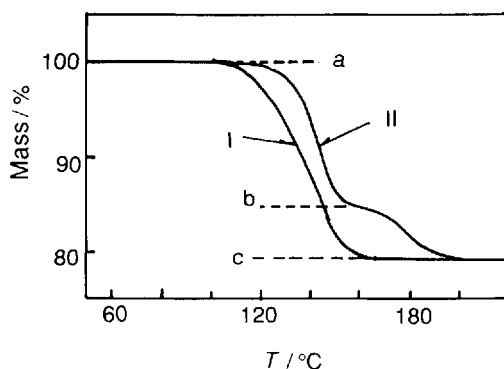


Figure 3.6 TG curves of hydration of $CaSO_4 \cdot 2H_2O$. I, Open type crucible; II, sealed crucible with pinhole

However, it is difficult to obtain a TG curve without apparent mass changes over the entire temperature range, although the mass change of a modern thermobalance can be controlled within a very small range.

3.1.5 Sample Container, Temperature Gradient and Reaction Extent in Various Parts of Sample Vessel

The choice of vessels, having different shapes and being made from various materials, is based on the nature of the sample and the experimental conditions and requirements. Figure 3.7 shows

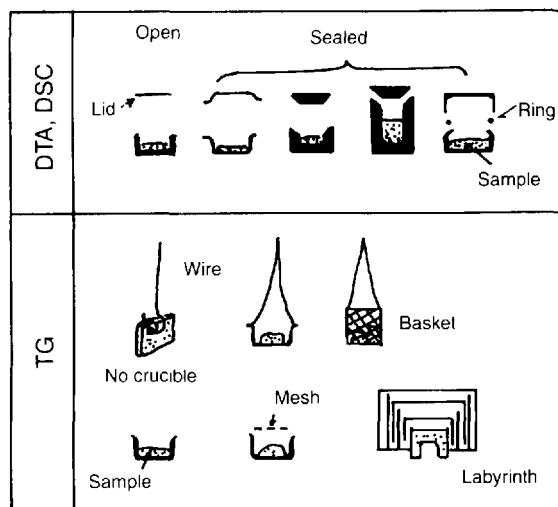


Figure 3.7 Representative sample vessels for DSC and DTA and crucible for TG

representative sample vessels for DSC and DTA and a crucible for TG. The vessels can be made from various materials, such as platinum, silver, nickel, aluminum, stainless steel and quartz. The mass of commercially available sample vessels ranges from 10 to 300 mg. The suitable temperature ranges, thermal conductivities and thermal radiation of various materials are different. The maximum temperature of operation should be chosen to be lower than the maximum safe operating temperature of various materials. If the vessel melts on the sample holder, alloying will occur and the sample holder will be irreparably damaged. The maximum safe operating temperatures of various materials used for making sample vessels are listed in Table 3.1.

One of the basic requirements for vessel materials is that they are non-interactive with the sample and its products. If possible, a small, shallow pan should be used as a sample vessel. This shape is favorable for diffusion of gases liberated from the sample, rapid heat transfer and homogeneous heating. In the case of vaporization or sublimation during heating, a sealed vessel should be used, but then the state of the atmosphere will be changed.

The maximum temperature gradient between the wall of the sample holder and center of the sample can be calculated according to the following equations [7]. For a disk:

$$Y_m = [(\Delta H G \phi) / \lambda]^{1/2} (S/2) \quad (3.2)$$

Table 3.1 Maximum operating temperatures of sample vessels made from various materials

Material	Maximum recommended operating temperature/°C
Aluminum	560
Aluminum nitride	480 (air) 980 (N ₂)
Carbon	230 (air) 880 (N ₂) 1830 (Ar, He)
Gold	930
Platinum	1630
Silver	830
Stainless steel ^a	130

^a With rubber ring.

For a cylinder:

$$Y_m = [(\Delta H G \phi) / 2\lambda]^{1/2} \tau \quad (3.3)$$

where S is the sample thickness, τ the diameter of the vessel, ΔH the enthalpy of the reaction, G the heat capacity of the sample, ϕ the heating rate and λ the thermal conductivity.

The extent of reaction varies depending on the location of the sample in the vessel. This is clearly seen in the following example of the thermal decomposition reaction of zinc hydroxide carbonate [4]. The reaction was carried out in a flowing air atmosphere using a hemispherical Pt/Ph crucible of 16 mm diameter \times 8 mm, a heating rate of 0.5 °C min⁻¹, annealed isothermally at 185 °C for 5 h. The reacted sample taken from various parts of sample vessel was analyzed by X-ray diffractometry. The amounts of ZnO in the sample were 50% in concentric zones, 70% at the surface layer and about 25% at the bottom zone.

3.1.6 Packing Density of Sample

Loosely packed, coarse materials contain vacant space which reduces the thermal conductivity of the sample. Smaller particles allow dense packing, resulting in higher thermal conductivity. The appearance of TG, DTA and DSC curves changes as a result of the difference in packing density. Figure 3.8 shows a polymeric sample; one form is loosely packed and the other is densely packed. Different temperatures of melting are observed over a whole range of scanning rate.

Packing density affects sample contact with the atmosphere. For example, the second step of

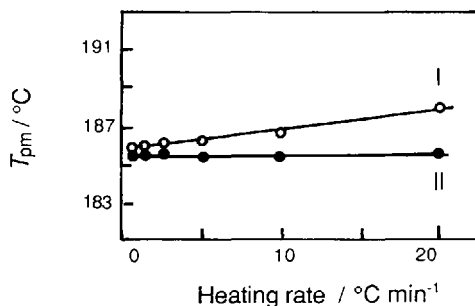
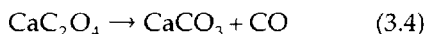


Figure 3.8 Melting temperature of polyoxymethylene as a function of heating rate. I, Loosely packed sample; II, densely packed sample

the reaction of $\text{CaC}_2\text{O}_4 \cdot \text{H}_2\text{O}$ in air is elimination of CO:



The exothermic peak of the DTA curve of a loosely packed sample was observed at 511.8 °C. Air easily diffused into the sample inside and hence an oxidative atmosphere was sufficiently provided. In contrast, the DTA curve of densely packed samples showed an endothermic peak at 513.5 °C because oxygen was not supplied inside of the sample.

3.2 Resolution of Apparatus

The ability of apparatus to resolve two or more thermal events which occur in a close temperature range is important. In order to evaluate the resolution of various types of apparatus, it is recommended that the melting of a 4 : 1 mixture (by mass) of silica and potassium sulfate is measured. This composition gives two approximately equally sized peaks separated by about 11 °C.

To provide a measure of the resolution of two peaks, the baseline separation method is used [8]. The percentage resolution (R) is defined as

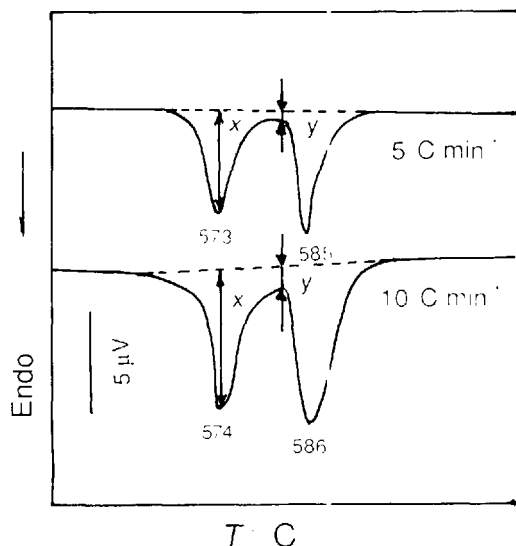


Figure 3.9 Resolution of DTA curve. Apparatus, Beijing Optical Instrument Factory DTA-TG Analyzer Model 4.1; sample mass, 300 mg

follows:

$$R = 100[1 - (y/x)] \quad (3.5)$$

where x is the height of the SiO_2 peak and y is the minimum deviation of the experimental curve from the baseline in the region between the peaks as shown in Figure 3.9.

From the DTA data in Figure 3.9, R values of 95.8% at a heating rate of 5 °C min⁻¹ and 94.7% at 10 °C min⁻¹ were obtained.

3.3 Kinetics of Thermal Analysis

3.3.1 Determination of Kinetic Parameters for Reaction

3.3.1.1 Determination of Apparent Activation Energy by Ozawa Method (Ozawa–Flynn–Wall Method) [9]

This method is applicable to the integral-type DTA curves. It is especially suitable for mass-loss reactions on heating, such as thermal degradation of polymers and the process of releasing small molecules due to physical or chemical changes. A group of TG curves measured at more than four heating rates is necessary, as shown schematically in Figure 3.10. The TG curves shift to higher temperature with increasing heating rates. A group of the parallel curves will be obtained if the reaction mechanism is not changed.

At the same conversion (m^* in Figure 3.10), the following expression can be obtained from the P function of Doyle's approximate expression:

$$d(\log \phi)/d(1/T) \approx 0.4567(E/R) \quad (3.6)$$

In Figure 3.10, temperature, T_1, T_2, \dots (in kelvin), corresponds to the heating rate ϕ_1, ϕ_2, \dots at the same conversion m^* , E is the apparent activation energy in kJ mol^{-1} and R is the gas constant, $8.314 \text{ J mol}^{-1} \text{ K}^{-1}$. The data for mass loss 30% for a modified polyamide by arylonitrile–butadiene epoxy resin are given in Table 3.2.

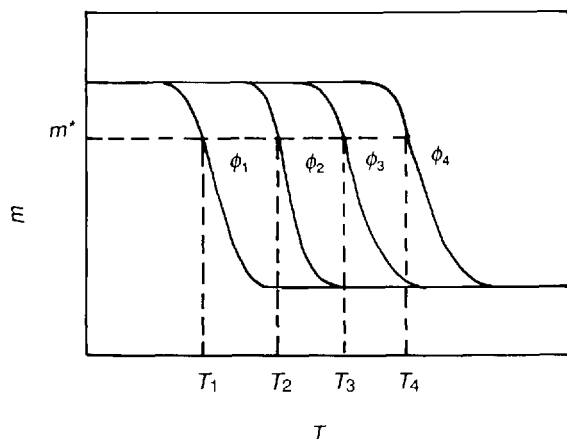


Figure 3.10 Schematic representation of the Ozawa method

According to equation 3.6, the plot of $\log \phi$ versus $1/T$ at a given conversion gives a straight line on the basis of the data in Table 3.2, and the activation energy E can be estimated from the slope:

$$E = \frac{d(\log \phi)/d(1/T)}{R/0.4565} = 135 \text{ J mol}^{-1} \quad (3.7)$$

(correlation coefficient $r = 0.992$)

When the apparent activation energy is not constant for a process, this method cannot be applied,

Table 3.2 The data for mass loss 30% at different heating rates for modified polyamide

Heating rate, ϕ K min^{-1}	Log ϕ	Temperature at mass loss 30%K	$T^{-1}/10^{-3} \text{ K}^{-1}$
1	0	726	1.377
2	0.3	754	1.326
5	0.7	787	1.271
10	1	803	1.245

Table 3.3 Peak temperatures of DTA curves for polyarylsulfone at different rates

Heating rate, ϕ K min^{-1}	T_p/K	$T_p^{-1}/$ 10^{-3} K^{-1}	$T_p^2/$ 10^2 K^2	$(\phi/T_p^2)/$ $10^{-6} \text{ K}^{-1} \text{ min}^{-1}$	$\text{Log}(\phi/T_p^2)$
2	842	1.188	7090	2.82	-5.550
5	891	1.122	7939	6.30	-5.201
10	927	1.079	8593	11.63	-4.934
20	974	1.027	9487	21.10	-4.676

since the process does not consist of a single unit process. Even if the reaction obviously consists of two or more steps, the equation is applicable when the E value for each process is stable.

3.3.1.2 Determination of Apparent Activation Energy by Kissinger Method [10]

In this method, from the correlation between peak temperature T_p and heating rate ϕ for more than four thermal analysis curves of derivative type (such as DTA and DTG curves), the apparent activation energy can be determined according to the equation

$$[d(\ln \phi/T_p^2)]/d(1/T_p) = -E/R \quad (3.8)$$

where E is the apparent activation energy and R is the gas constant, $8.314 \text{ J mol}^{-1} \text{ K}^{-1}$.

Taking DTA curves for polyarylsulfone as an example, the peak temperatures at different heating rates are listed in Table 3.3.

From the slope of the plot of $\log(\phi/T_p^2)$ vs T_p^{-1} , based on the data in Table 3.3, E can be estimated according to the equation

$$E = -[d(\log \phi/T_p^2)]/d(1/T_p)R \times 2.303$$

$$= 105 \text{ kJ mol}^{-1} \quad (r = 0.999) \quad (3.9)$$

Although four thermal analysis curves are necessary for this method, the calculation is simple.

3.3.1.3 Determination of Kinetic Parameters by Freeman and Carroll Method [11]

This method is known as the difference-differential method. From one thermal analysis curve (e.g. a TG curve), first determining mass-loss

conversion and rate, reciprocal of temperature at some points on the TG curve and then their differences between two adjacent points, kinetic parameters can be obtained schematically according to following equation:

$$-(E/2.3R)[\Delta(1/T)/\Delta \log C] \\ = [\Delta \log(dC/dt)/\Delta \log C] - n \quad (3.10)$$

where C is the concentration of reacting species, dC/dt the mass-loss rate at time t , T the temperature (K), n the order of reaction, E the activation energy (kJ mol^{-1}) and R the gas constant ($8.314 \text{ J mol}^{-1} \text{ K}^{-1}$).

The data in Table 3.4 are examples for the dehydration reaction $\text{Mg}(\text{OH})_2$.

From the plot of $[\Delta \log(dC/dt)/\Delta \log C]$ vs $[\Delta(1/T)/\Delta \log C]$, the slope of the straight line is -0.677×10^4 ($r = 0.998$), so $E = 0.677 \times 10^4 \times 2.3 \times 8.314 = 130 \text{ kJ mol}^{-1}$ and $n = 0.82$ (≈ 1) from the intercept of the straight line. When the mass-loss rate obviously changed, the selected temperature interval should be decreased.

3.3.1.4 Determination of Kinetic Parameters by Using Peak Values [12, 13]

The TG curve peak temperature T_p and the amount of reacting species C_p at which the maximum mass-loss rate occurs are defined as shown in Figure 3.11.

According to the equation

$$\log(dC/dt) = \log A + (E/R) \{ C_p / [(dC/dt)_p T_p^2] \} \\ \log C - 1/2.303T \quad (3.11)$$

taking a series of values $T_1, C_1, (dC/dt)_1; T_2, C_2, (dC/dt)_2; \dots$, the pre-exponential factor A and the activation energy E can be estimated from the

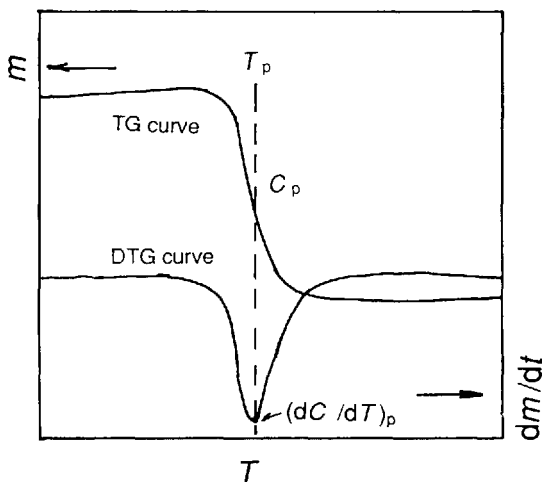


Figure 3.11 Definition of characteristic quantities at the maximum mass-loss rate

intercept and slope of the plot

$$\log(dC/dt) \text{ vs } [C_p / \{(dC/dt)_p T_p^2\}] \\ \log C - 1/2.303T \quad (3.12)$$

in the above equation, where dC/dt is the mass-loss rate, $dC/dt = \phi dC/dT$ (ϕ = heating rate), R is the gas constant ($8.314 \text{ J mol}^{-1} \text{ K}^{-1}$), C is the amount of reacting species and T is temperature (K). Knowing the E values, the order of reaction can be obtained according to the following equation:

$$E = -[RT_p^2 n (dC/dT)_p] / C_p \quad (3.13)$$

If $n = 1$,

$$E = -[RT_p^2 / C_p] (dC/dT)_p \quad (3.14)$$

3.3.2 Reaction Mechanism

The reactions of many substances are complex, including phase boundary reactions, nucleation

Table 3.4 TG data for the dehydration reaction of $\text{Mg}(\text{OH})_2$

Temperature range/K	$\Delta(1/T) \times 10^5$	$\Delta \log C$	$\Delta \log(dC/dt)$	$\Delta(1/T) 10^4 / \Delta \log C$	$\Delta \log(dC/dt) / \Delta \log C$
666–684	–3.95	–0.053	0.220	7.45	–4.15
684–702	–3.75	–0.093	0.193	4.03	–2.08
702–720	–3.56	–0.165	0.097	2.16	–0.59
720–738	–3.39	–0.376	–0.097	0.90	0.26

and growth of solid products and diffusion of gas products. Among these factors, the slowest process is the major factor on which the reaction mechanism depends. In an infinitesimal time interval, the non-isothermal reaction process can be considered as an isothermal one and the reaction rate may be expressed as

$$d\alpha/dt = A \exp(-E/RT)f(\alpha) \quad (3.15)$$

where α is the fraction reacted in time t and the function $f(\alpha)$ depends on the reaction mechanism and the geometry of the reacting particles (see Table 3.5).

Integrating equation 3.15 at a constant heating rate $\phi = dT/dt$, we obtain

$$\int_0^{\alpha} d\alpha/f(\alpha) = g(\alpha) = (AE/R\phi)p(\chi) \quad (3.16)$$

where $\chi = E/RT$, the fraction α of the sample has reacted at temperature T . The function $p(\chi)$ can be expressed by some approximate equations. Taking the logarithm of equation 3.16:

$$\log g(\alpha) - \log p(\chi) = \log(AE/R\phi) \quad (3.17)$$

The right-hand side of equation 3.17 is independent of temperature, whereas the left-hand side is temperature dependent. To a first approximation,

the function $\log p(\chi)$ is a linear function of $1/T_a$ if χ is sufficiently large, and thus $\log(\alpha) \sim 1/T_a$ also should be a straight line for the correct mechanism function, but sometimes the correlation coefficients of the straight lines obtained for different mechanism functions only have a slight difference, in which case it is necessary to determine the reaction mechanism in terms of other supplementary method.

3.3.3 Mechanism of Isothermal Reaction in Solid State

Based on the standard equation for the analysis of nucleation and growth processes, the kinetics of isothermal solid-state reactions can be represented by the following equation [15]:

$$\ln[-\ln(1 - \alpha)] = \ln k + m \ln t \quad (3.18)$$

where α is the fraction reacted in time t , k is a constant which depends in part on the nucleation frequency and linear rate of grain growth and m is a constant that can vary according to the geometry of the system or mechanism of the reaction (see Table 3.6). The designation and the mechanism represented by m are the same as those in Table 3.5.

Table 3.5 Commonly used functional forms of $f(\alpha)$ [14]

Designation	Functional form	Rate-controlling process
D_1	$\alpha^2 = kt$	One-dimensional diffusion
D_2	$(1 - \alpha)\ln(1 - \alpha) + \alpha = kt$	Two-dimensional diffusion, cylindrical symmetry
D_3	$[1 - (1 - \alpha)^{1/3}]^2 = kt$	Three-dimensional diffusion, spherical symmetry, Jander equation
D_4	$[1 - (2/3)\alpha] - (1 - \alpha)^{2/3} = kt$	Three-dimensional diffusion, spherical symmetry, Ginstling-Brounshtein equation
F_1	$-\ln(1 - \alpha) = kt$	Random nucleation, one nucleus on each particle
A_2	$[-\ln(1 - \alpha)]^{1/2} = kt$	Random nucleation Avrami equation 1
A_3	$[-\ln(1 - \alpha)]^{1/3} = kt$	Random nucleation, Avrami equation 2
R_2	$1 - (1 - \alpha)^{1/2} = kt$	Phase boundary reaction, cylindrical symmetry
R_3	$1 - (1 - \alpha)^{1/3} = kt$	Phase boundary reaction, spherical symmetry

Table 3.6 Values of m for solid-state reaction rate equation [15]

Designation	m
D_1	0.62
D_2	0.57
D_3	0.54
D_4	0.57
F_1	1.00
R_2	1.11
R_3	1.07
Zero order	1.24
	equation form $a = kt$
A_2	2.00
A_3	3.00

When $\ln[-\ln(1-\alpha)]$ is plotted against $\ln t$, if the range of α is limited to 0.15–0.50, the kinetic data give a linear plot with slope m . Dehydroxylation of kaolinite was carried using 91 mg of sample at 427 °C *in vacuo*, and $t_{0.5} = 97$ min was obtained. A linear plot with a slope (m) of 0.56 was produced, indicating a diffusion-controlled reaction. It is attributable to either D_2 or D_4 as shown in Table 3.6.

3.3.4 Non-isothermal Crystallization Kinetics of Polymers by DSC Measurement

The kinetics of the isothermal crystallization of polymers have been thoroughly studied. However, practical processes such as extrusion, molding, injection and film production usually proceed under non-isothermal crystallization conditions. In order to obtain products with better properties, it is necessary to have quantitative evaluations of the non-isothermal crystallization process. A few methods have been developed to study the kinetics of non-isothermal crystallization by DSC for polymers.

The following methods for the measurement of the kinetics of non-isothermal crystallization are briefly introduced.

3.3.4.1 Ziabicki Method [16]

The crystallization process of polymers can be

described by first-order kinetics:

$$d\alpha/dt = (1-\alpha)K(T) \quad (3.19)$$

where α is the relative crystallinity and $K(T)$ is a rate constant dependent only on temperature. It is assumed that the shape of the plots of rate constant $K(T)$ versus temperature T can be expressed by a Gaussian function:

$$K(T) = K_p \exp[-4 \ln 2 (T - T_m)^2 / D^2] \quad (3.20)$$

The kinetic crystallizability G is given as follows:

$$G = \int_{T_g}^{T_m} K(T) dT = \sqrt{\pi/\ln 2} K_p D/2 \quad (3.21)$$

where K_p is the maximum value of the rate constant corresponding to the temperature T_p , D is the width of the crystallization exotherm at half-height, T_m is the melting temperature and T_g is the glass transition temperature. The parameter G characterizes the degree of crystallinity per unit cooling rate obtained over the crystallization range $T_m \sim T_g$. Considering the effect of the cooling rate, the final form of G is

$$G_c = G/(dT/dt) \quad (3.22)$$

A typical DSC crystallization curve for nylon 1010 is shown in Figure 3.12.

The parameters T_p and $D = T_{D_2} - T_{D_1}$ can easily be determined directly from Figure 3.12.

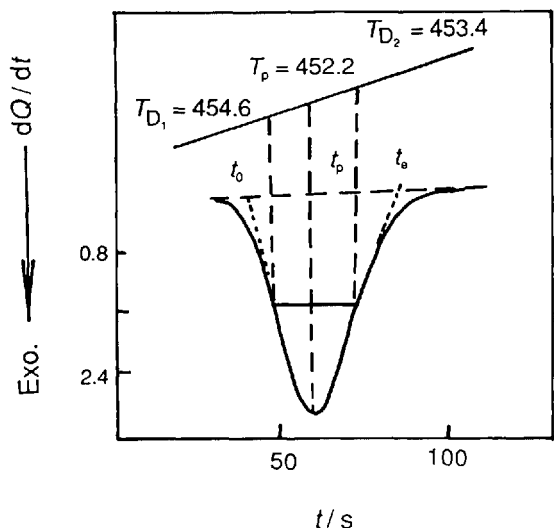


Figure 3.12 DSC curve for non-isothermal crystallization of nylon 1010 at a cooling rate $\phi = 5 \text{ K min}^{-1}$

According to T_p and D , the parameters $K(T)$, G and G_c can now be calculated from equations 3.20–3.22 and are listed in Table 3.7.

3.3.4.2 Ozawa Method [17, 18]

Ozawa extended Avrami's theory to crystallization under non-isothermal conditions in a crystallization process at a constant rate.

More than four DSC curves at different cooling rates were measured for the melt sample heat-treated at above the melting temperature for a given time, and the kinetic parameters can be obtained according to the equation [17]:

$$\log\{\ln[1 - \alpha(T)]\} = \log k - m \log \phi \quad (3.23)$$

where $\alpha(T)$ is the amount of sample crystallized at a given temperature T , which can be expressed by the partial area of the DSC curve at a certain time [Figure 3.13(a)], k is the rate constant of crystallization, m is the Ozawa exponent, which depends on the crystallization mechanism, including different nucleation and crystal growth as well as crystalline morphology (Table 3.8), and ϕ is the cooling rate.

If we plot $\log\{-\ln[1 - \alpha(T)]\}$ against $\log \phi$ at a given temperature, a straight line can be obtained, and m and k can be calculated from the slope and the intercept [Figure 3.13(b)]. If the slopes of the line are the same for different temperatures, the mechanism of crystallization has not changed (Table 3.8).

The half-time of crystallization is given by

$$t_{1/2}(T) = [\ln 2/K(T)]^{1/m} \quad (3.24)$$

3.3.4.3 Modified Ozawa Method [19]

Combining the Avrami and Ozawa equations

and taking account of $t = |T_0 - T_1|/\phi$, where T_0 is the initial temperature and T_1 is the temperature at a certain time t , a new crystallization kinetic equation under certain temperature conditions

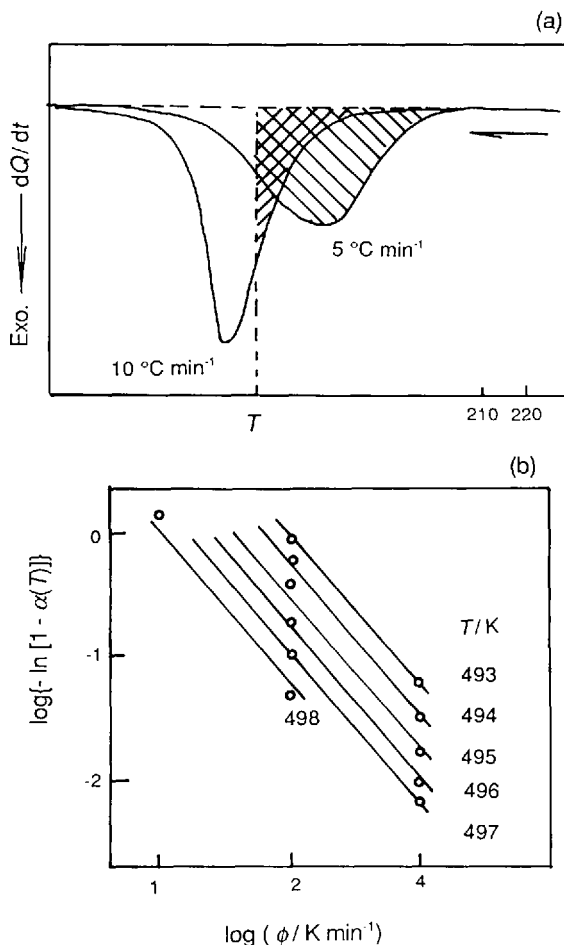


Figure 3.13 (a) DSC curves with different cooling rates and (b) plot of $\log\{-\ln[1 - \alpha(T)]\}$ against $\log \phi$ of poly(ethylene terephthalate) (PET)

Table 3.7 Kinetic parameters for non-isothermal recrystallization of nylon 1010

Parameter	Cooling rate, dT/dt K min ⁻¹				
	2.5	5	10	20	40
$\tau_{0.5}/\text{min}^{-1}$	0.228	0.957	1.266	2.304	3.359
Half-height width, D/K	2.18	2.36	3.95	5.10	8.37
Rate constant, K_p/s^{-1}	0.0048	0.0183	0.0152	0.0278	0.0415
Kinetic crystallizability, G/K s ⁻¹	0.001	0.046	0.032	0.075	0.184
G_c	0.264	0.552	0.192	0.225	0.276

Table 3.8 Exponent of Ozawa equation (m) and crystallization mechanism

Type of crystallization	Nucleation	m
Fibrillar	Athermal	≤ 1
Fibrillar, branching	Athermal	1
		increasing with time
Spherical, diffusion controlled	Athermal	3/2
Fibrillar	Thermal	≤ 2
Circular lamellar	Athermal	≤ 2
Fibrillar, branching	Thermal	2
		increasing with time
Truncated sphere	Athermal	2–3
Spherical, diffusion controlled	Thermal	5/2
Spherical	Athermal	3
Truncated sphere	Thermal	3–4
Spherical	Thermal	4
Solid sheaf	Athermal	≥ 5
Solid sheaf	Thermal	≥ 6

has been derived as follows:

$$\log \phi = \log F(T) - a \log t \quad (3.25)$$

where $a = n/m$, n is the Avrami's exponent and m is the Ozawa exponent, $F(T) = [K(T)/Z_i]^{1/m}$. It represents the value which is needed to achieve a certain cooling rate per unit time; Z_i is the Avrami rate constant. From equation 3.25, a plot of $\log \phi$ against $\log t$ is a straight line with an intercept $\log F(T)$ and a slope a (Figure 3.14)

3.3.4.4 Modified Avrami Method [20]

The modified Avrami equation could be derived

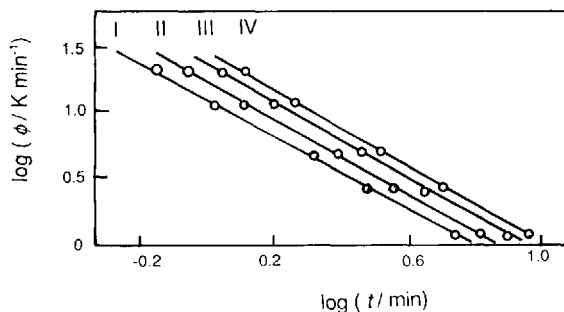


Figure 3.14 Plot of $\log \phi$ versus $\log t$ for a PEO-PBHE blend (60:40) with different relative crystallinities. α = (I) 27.1, (II) 46.8, (III) 71.6 and (IV) 86.4%.

from the modified first-order kinetic model to describe the crystallization of polymers. The modified Avrami equation is

$$d\alpha/dt = K\alpha^m(1-\alpha) \quad (3.26)$$

where α is the relative crystallinity at time t , K is the rate constant of crystallization at a given temperature and the exponent m depends on certain nucleation and growth mechanisms. The relationship between m and the Avrami exponent n is $m = (n-1)/n$. From equation 3.26, a plot of $\ln[1/(1-\alpha)(d\alpha/dt)]$ versus $\ln \alpha$ should yield a straight line with a slope m and an intercept $\ln K$ (Figure 3.15).

3.3.5 General Description of Kinetics of Resin Curing Under Isothermal Conditions

Kinetic modeling of thermosetting resins provides valuable information regarding the durability of materials and the optimization of processing conditions. For example, the experimental conditions for an epoxy-amine mixture are as follows: (1) samples should be prepared using fresh resin systems; (2) the mixture is prepared at room temperature by adding the amine curing agent to the epoxy with continuous stirring until a clear homogeneous solution is obtained; (3) the solution should be degassed

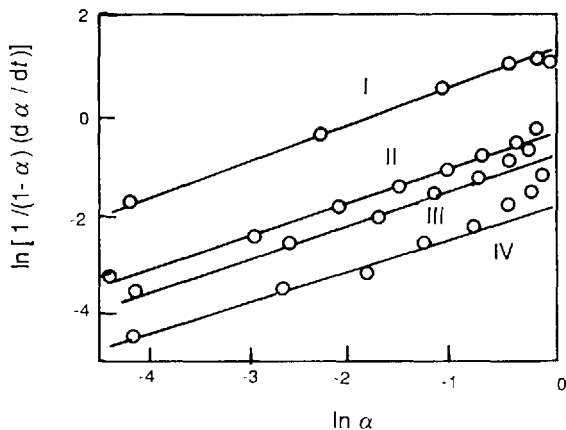


Figure 3.15 Plot of $\ln[1/(1-\alpha)(d\alpha/dt)]$ versus $\ln \alpha$ for PET. Roman numerals represent PET prepared using different catalysts

under vacuum; (4) the product should then be transferred immediately to DSC pans and analyzed or stored at low temperature until needed for analysis.

Typical experimental conditions and procedure [21] are sample size 5–10 mg and flow rate of nitrogen 30 ml min⁻¹. For iso-thermosetting experiments on a resin, the DSC sample holder should be preheated to the desired isothermal temperature. The easiest method of determining the four appropriate isothermal temperatures is as follows: (1) a sample of the thermoset is heated in the DSC at a rate of 5 °C min⁻¹, obtaining a heating DSC curve; (2) the isothermal temperatures are selected in the range between 10 °C below the onset of the curve (e.g. 85 °C) and the midpoint of the peak maximum (e.g. 120 °C); and (3) the isothermal temperatures selected should be separated by 5–10 °C (in this case 85, 90, 100 and 110 °C, respectively).

The thermosetting reaction of the resin follows *n*th-order (equation 3.27) or autocatalyzed (equation 3.28) kinetics.

$$d\alpha/dt = K(1 - \alpha)^n \quad (3.27)$$

$$d\alpha/dt = K'\alpha^m(1 - \alpha)^n \quad (3.28)$$

where $d\alpha/dt$ is the rate of conversion, proportional to the fraction of unreacted material, α is the fractional conversion of reactants consumed after time t , n and m are the reaction orders and k and k' are the specific rate constants.

Systems obeying *n*th-order kinetics have a maximum rate of heat evolution at time $t = 0$, and an autocatalyzed thermoset show its maximum heat evolution at 30–40% of the cure reaction.

The two basic parameters ΔH_t and dH/dt are required to solve the kinetic expression. As shown in Figure 3.16, ΔH_t represents the partial heat of cure of the sample and dH/dt represents the heat flow rate at time t . These values are then converted into fractional quantities by dividing them by the total heat of cure, ΔH_T :

$$d\alpha/dt = (dH/dt)/\Delta H_T \quad (3.29)$$

$$\alpha = \Delta H_t/\Delta H_T \quad (3.30)$$

Based on several assumptions, the following rate expression has been developed for epoxy–

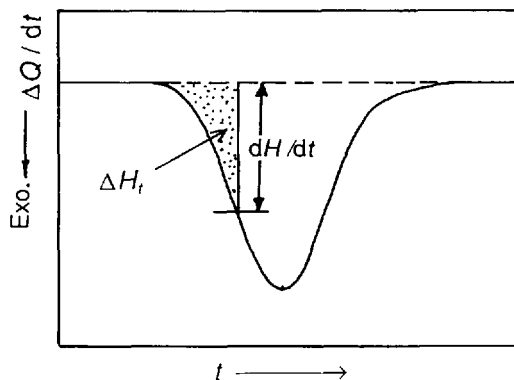


Figure 3.16 Schematic DSC curve for iso-thermosetting reaction of resin

amine systems [22, 23]:

$$d\alpha/dt = (\alpha K_a + K_c)(1 - \alpha)(B - \alpha) \quad (3.31)$$

$$(d\alpha/dt)/[(1 - \alpha)(B - \alpha)] = \alpha K_a + K_c \quad (3.32)$$

where $d\alpha/dt$ is the cure rate (s⁻¹), α is the fractional conversion of the epoxide, K_a is the specific autocatalyzed rate constant at temperature T (s⁻¹), K_c is the specific catalyzed rate constant at temperature T (s⁻¹) and B is the ratio of amine to epoxide equivalents initially in the system. K_a and K_c can be obtained from slope and intercept of the $(d\alpha/dt)/[(1 - \alpha)(B - \alpha)]$ vs α plot. B can be estimated from the extent of conversion, α_p , at the iso-thermosetting exothermic peak maximum:

$$B = (2\alpha_p - 3\alpha_p^2)/(1 - 2\alpha_p) \quad (3.33)$$

The activation energies associated with the autocatalyzed and catalyzed reactions, E_a and E_c , may be determined from rate constants in several isothermal experiments based on the Arrhenius equation:

$$K_a = Z_a \exp(-E_a/RT) \quad (3.34)$$

$$K_c = Z_c \exp(-E_c/RT) \quad (3.35)$$

where Z is the pre-exponential factor, E the activation energy (kJ mol⁻¹), R the gas constant (8.314 J mol⁻¹ K⁻¹) and T the temperature (K).

When reversion occurs at a curing degree $\alpha > 0.5$, the reaction rate decreases markedly because the glass transition temperature approaches the cure temperature. The reaction becomes diffusion controlled rather than

kinetically controlled, and on this account, the reaction rate drops substantially.

3.3.6 Methods for Determining Kinetic Parameters of Thermosetting Reactions of Resins

3.3.6.1 Freeman–Carroll Method

In order to estimate both E and n , the following Freeman–Carroll relationship can be applied, using data obtained from a single dynamic DSC curve of resin curing [24]:

$$\Delta \ln(dH/dt)/\Delta \ln(A - a) = n - \{[(E/R)\Delta(1/T)]/\Delta \ln(A - a)\} \quad (3.36)$$

where dH/dt is the heat flow rate ($\text{mJ}^{-1} \text{s}$), T is temperature (K), A is the total area of the exothermal peak of the DSC curve (cm^2), a is the partial area of the DSC curve at temperature T (cm^2), E is the activation energy (kJ mol^{-1}), n is the reaction order and R is the gas constant ($8.314 \text{ J mol}^{-1} \text{ K}^{-1}$).

In addition to the total area A , at least 10–20 sets of heat flow rates dH/dt and partial areas at different temperatures should be tabulated for a single DSC curve, and calculating the differences between two neighboring points, E and n can be obtained from the slope and intercept of the $\Delta \ln(dH/dt)/(\Delta \ln(A - a))$ vs $\Delta(1/T)/\Delta \ln(A - a)$ plot.

3.3.6.2 Ellerstein Method

The kinetic parameters can be determined from a dynamic DSC curve for resin curing by using the following equation [25]:

$$T^2(S/h) = (E/R) - nT^2(h/r) \quad (3.37)$$

$$h = (dH/dt)/\phi$$

$$S = (h_2 - h_1)/dT \quad (3.38)$$

$$r = H_T - H$$

where dH/dt is the heat flow rate (mJ s^{-1}), ϕ is the heating rate (K min^{-1}), H_T is the total heat quantity corresponding to the total area of the exothermal peak of the DSC curve, H is the

quantity of heat corresponding to the partial area of the DSC curve at temperature T , E is the activation energy (kJ mol^{-1}), n is the reaction order and R is the gas constant ($8.314 \text{ J mol}^{-1} \text{ K}^{-1}$).

The total and partial quantities of heat measured at different temperatures are calculated from a heating DSC curve, as shown in Figure 3.17, and E and n values can be obtained from the intercept and slope of the $T^2(S/h)$ vs $T^2(h/r)$ plot.

From the $T^2(S/h)$ vs $T^2(h/r)$ plot for the curing reaction of hydroxyl-terminated poly(tetrahydrofuran) telechelic oligomer with styrene illustrated in Figure 3.18 at a heating rate of

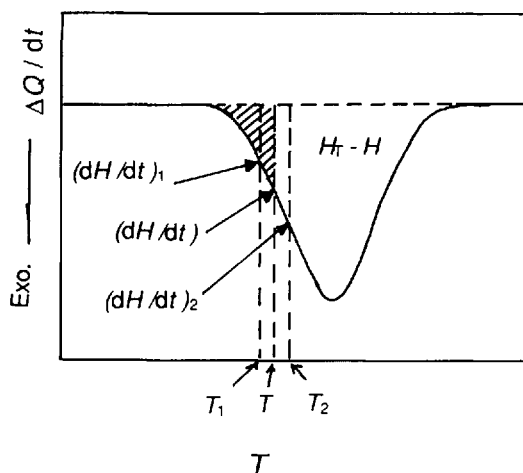


Figure 3.17 Heating DSC curve of curing reaction for resin

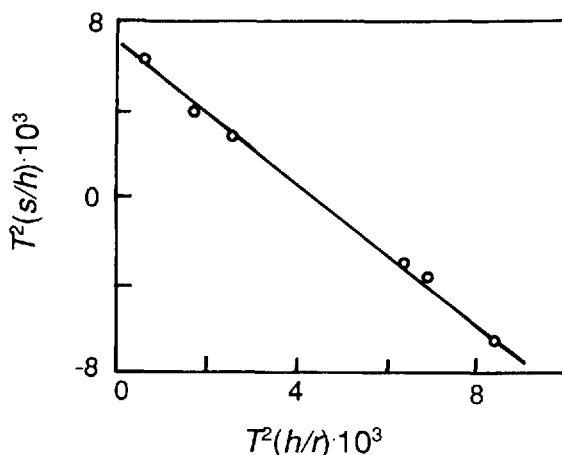


Figure 3.18 $T^2(S/h)$ vs $T^2(h/r)$ plot for the curing reaction of hydroxyl-terminated poly(tetrahydrofuran) telechelic oligomer with styrene

5 K min⁻¹, the kinetic parameters were obtained as $n = 1.6$ and $E = 59.3$ kJ mol⁻¹.

3.3.6.3 Barton Method

The activation energy E can be estimated from two dynamic DSC experiments at different heating rates. If the values of da/dt and temperature are known at a fixed conversion a , E can be obtained according to the Barton equation [26]:

$$\ln(r_1/r_2) = E/R(1/T_2 - 1/T_1) \quad (3.39)$$

where r_1 and r_2 are conversion rates da/dt at a particular iso-conversion degree, subscripts 1 and 2 refer to the heating rates ϕ_1 and ϕ_2 , respectively, T_1 and T_2 are temperatures at a particular iso-conversion degree corresponding to heating rates ϕ_1 and ϕ_2 , E is the activation energy and R is the gas constant (8.314 J mol⁻¹ K⁻¹).

As shown in Figure 3.19, at iso-conversion degree 30%, the temperatures and conversion rates corresponding to heating rates ϕ_1 and ϕ_2 were T_1 , T_2 and r_1 , r_2 , respectively. Substituting the above estimated values into equation 3.39, the value of E can be determined.

3.3.6.4 Method Based on Maximum Values

For a curing reaction of a resin under dynamic conditions, the conversion degree α_p at the maximum conversion rate is independent of the heating rate ϕ . From DSC curves measured at

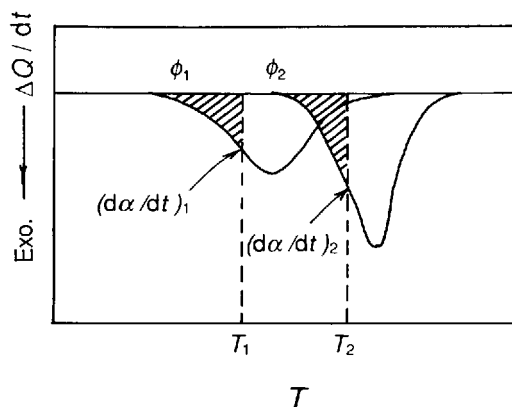


Figure 3.19 DSC curves for resin curing at different heating rates

different heating rates, the activation energy E can be estimated by using the iso-conversion degree method (i.e. the Ozawa method, see Section 3.3.1). The pre-exponential factors for n th-order and autocatalyzed reactions can be calculated from heating rates ϕ , temperatures T_p and conversion degrees α_p at maximum conversion rates according to the following equations [27]:

for n th-order reaction:

$$Z = [\phi E \exp(E/RT_p)]/RT_p^2 [n(1 - \alpha_p)]^{n-1} \approx \phi E \exp(E/RT_p)/RT_p^2 \quad (3.40)$$

for autocatalyzed reaction:

$$Z = [\phi E \exp(E/RT_p)]/RT_p^2 (2\alpha_p - 2B\alpha_p - 3\alpha_p^2 - B) \quad (3.41)$$

where B is a stoichiometric parameter, e.g. the ratio of equivalents of amine hydrogens to epoxide.

The kinetic parameters can be estimated according to Kissinger's method [27] from the dependence of the exothermal peak temperature of DSC curves on heating rate. Knowing the reaction order, the maximum point of the DSC curve, dH/dt vs T , is used to obtain the ratio E/n from the expression [28]:

$$(E/n) = [RT_p^2/(H_T - H_p)\phi](dH/dt)_p \quad (2.42)$$

where ϕ is the heating rate (K min⁻¹), H_T is the total heat quantity, H_p is the partial heat quantity at the maximum point, T_p is the peak temperature and $(dH/dt)_p$ is the heat flow rate at maximum point.

3.3.7 Some Advances in Thermal Analysis Kinetics [29–43]

In thermal analysis, the reactions studied are almost invariably heterogeneous and the reaction temperature is usually being continuously increased or decreased according to some set (usually linear) program. Many methods for the analysis of the non-isothermal kinetic data have been developed and numerous papers have appeared and are still appearing on this topic. On the other hand, it is a field of considerable controversy. All controversies regarding the versatility or otherwise of non-isothermal kinetics stem from the applicability of the Arrhenius

equation, which was based on sound theoretical principles and was derived from the kinetic theory of gases, to solid-state kinetics [29]. In addition, whether the kinetic model functions $f(\alpha)$ derived on the basis of the physico-geometric assumption of regularly shaped sample bodies can describe extremely complicated real heterogeneous systems remains a questionable point [30, 31]. Fortunately, a great deal of effort has been directed at improving thermoanalytical kinetic methods. As space is limited, what follows is only a brief introduction to some advances in this field. More detailed information can be found in the references cited.

3.3.7.1 Kinetic Model Functions [30–35]

Since the traditional kinetic models of solid-state reactions are often based on a formal description of geometrically well defined bodies treated under strictly isothermal conditions, they are evidently not appropriate to describe the real process, which requires account to be taken of irregularity of shape, polydispersity, shielding and overlapping, unequal mixing anisotropy and so on, for sample particles under reaction. One of the measures which has been taken to solve the problem is to introduce an accommodation function $a(\alpha)$ [32]. The discrepancy between the idealized $f(\alpha)$ and the actual kinetic model function $h(\alpha)$ can be expressed as

$$h(\alpha) = f(\alpha)a(\alpha) \quad (3.43)$$

The kinetic expression $h(\alpha)$ can be considered as a distorted case of homogeneous-like kinetics and of $f(\alpha)$, with a possible $a(\alpha)$ to decrease the difference of the idealized $f(\alpha)$ from the practical process. In the case of a more complicated process, it would be useful to find an empirical function $h(\alpha)$ containing the smallest possible number of constants, so that there is some flexibility sufficient to describe real TA data as closely as possible. An empirical kinetic model was proposed by Sestak and Berggren [33], and was later simplified by Gorbachev [34], the final form of which is

$$h(\alpha) = \alpha^m(1 - \alpha)^n \quad (3.44)$$

which is usually cited in the literature as the Sestak–Berggren SB(m, n) kinetic model, with m and n taken as kinetic parameters which describe the shape of measured TA curves. This kinetic model function has attracted increasing interest in recent years. [35]

3.3.7.2 New Method of Non-isothermal Kinetic Analysis of TA Data [30, 31, 36, 37]

It was shown that both the activation energy and pre-exponential factor in the kinetic equations commonly used are mutually correlated, known as the 'kinetic compensation effect (KCE)'. In other words, any change in the activation energy is 'compensated' by the change of $\ln A$. From this point of view, it seems that the methods of kinetic analysis aiming to ascertain all kinetic parameters from only one experimental TA curve are problematic. This problem cannot be solved even using the most sophisticated non-linear regression algorithms unless the kinetic models (or at least one kinetic parameter) are *a priori* known.

Taking into account these facts, a completely new method of kinetic analysis of TA data was proposed by Malek and Smrcka [36, 37]. This method allows the determination of the most suitable kinetic model and the calculation of a complete set of kinetic parameters. For the same reason as above, here we merely outline the main procedures, equations and figures involved in the method, and the reader is referred to the original papers for further details.

Calculation of the activation energy, E —The calculation of the activation energy is based on multiple scan methods where several measurements at different heating rates are needed, i.e. the iso-conversion methods: the Ozawa–Flynn–Wall method, the Kissinger–Akahira–Sunose method and the expanded Friedman method. The first two are described in Section 3.3.1. The expanded Friedman method is expressed in the form

$$\ln(da/dt) = \ln[Af(\alpha)] - E/RT \quad (3.45)$$

where α is the degree of conversion, da/dt the rate of reaction, A the pre-exponential factor and E the activation energy. The slope of $\ln(da/dt)$ versus $1/T$ for the same value of α gives the value of the activation energy. By repeating the procedure for various values of α , the method allows one to check the invariance of E with respect to α , which is one of the basic assumptions in kinetic analysis.

Determination of the kinetic model function, $f(\alpha)$ —Once the activation energy has been determined, it is possible to search for the most suitable kinetic models which are listed in Table 3.9. Two special functions, $Y(\alpha)$ and $Z(\alpha)$, which can easily be obtained by simple transformation of the experimental data, are defined for this purpose. These two functions can be formulated as follows:

$$Y(\alpha) = (da/dt)e^x \quad (3.46)$$

$$Z(\alpha) = \pi(x)(da/dt)T/\beta \quad (3.47)$$

where $x = E/RT$ is the reduced activation energy, β the heating rate and $\pi(x)$ an approximation of the temperature integral, and its rational expression by Senum and Yang is recommended because it gives errors lower than $10^{-5}\%$ for $x > 20$:

$$\pi(x) = (x^3 + 18x^2 + 88x + 96)/(x^4 + 20x^3 + 120x^2 + 240x + 120) \quad (3.48)$$

The function $Y(\alpha)$ is proportional to the kinetic model function $f(\alpha)$. Thus, by plotting the $Y(\alpha)$ dependence, normalized within the interval $(0, 1)$, the shape of the function $f(\alpha)$ is obtained, which is characteristic for each kinetic model as shown in Figure 3.20 and Table 3.10. From this point of view, the following rules can be formu-

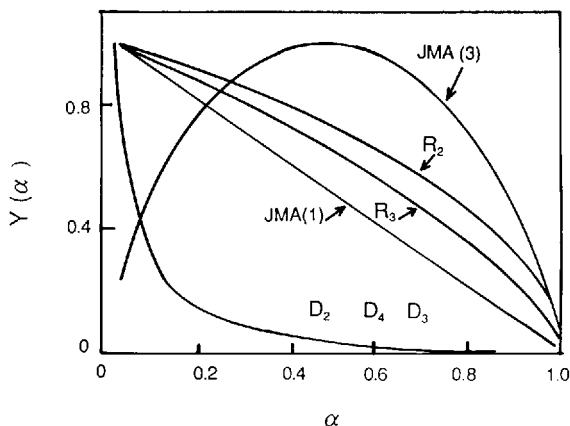


Figure 3.20 Typical shapes of the function $Y(\alpha)$ for several kinetic models (reproduced by permission of Elsevier Science Publishers from *Solid State Ionics*, 1993, 63–65, 251)

Table 3.10 Properties of the function $Y(\alpha)$ for the basic kinetic model

Model	$Y(\alpha)$
JMA(n)	Concave for $n < 1$ Linear, for $n = 1$ Maximum for $n > 1$
R_2	Convex
R_3	Convex
D_2	Concave
D_3	Concave
D_4	Concave

lated:

- (a) If the $Y(\alpha)$ function decreases steadily it has a maximum α_i at $\alpha_m = 0$. This function can be convex [$Y(\alpha_i) > \alpha_i$], linear [$Y(\alpha_i) = \alpha_i$] or concave [$Y(\alpha_i) < \alpha_i$]. A convex dependence corresponds to the RO ($n < 1$) model, a linear dependence to the JMA(n) model and a

Table 3.9 Basic kinetic model functions

Model	Symbol	$f(\alpha)$
Johnson–Mehl–Avrami equation	JMA(n)	$n(1-\alpha)[\ln(1-\alpha)]^{1-1/n}$
Reaction order equation	RO(n)	$(1-\alpha)^n$
Two-dimensional diffusion equation	D_2	$1/[-\ln(1-\alpha)]$
Jander equation	D_3	$3(1-\alpha)^{2/3}/2[1-(1-\alpha)^{2/3}]$
Ginstling–Brounshtein equation	D_4	$(3/2)[(1-\alpha)^{-1/3}-1]$
Sestak–Berggren equation	SB(m, n)	$\alpha^m(1-\alpha)^n$

concave dependence to the D_2 , D_3 , D_4 or RO ($n > 1$) model.

- (b) If there is a maximum of the $Y(\alpha)$ function at $\alpha_m \in (0, 1)$, the kinetic data can be described by the SB(m, n) or JMA($n > 1$) model.

The curve of $Z(\alpha)$ has a maximum at α_p^∞ which also corresponds to the maximum of a TA peak for $x_p \rightarrow \infty$. This parameter has a characteristic value for the D_2 , D_3 , D_4 and JMA(n) models, as summarized in Table 3.11.

It is evident that the shape of the function $Y(\alpha)$ and the maximum, α_p^∞ , of the function $Z(\alpha)$ can be used to guide the choice of a kinetic model. Both parameters α_m and α_p^∞ are especially useful in this respect. Their combination allows the determination of the most suitable kinetic model, as shown by the scheme in Figure 3.21.

Calculation of kinetic exponents, n (or m)—To calculate the kinetic exponents for the RO(n), JMA(n) or SB(m, n) model, the appropriate

Table 3.11 Characteristic values of the parameter α_p^∞

Model	α_p^∞
JMA(n)	0.632
D_2	0.834
D_3	0.704
D_4	0.776

ate equations, described below, can be selectively employed depending on the kinetic model determined in the above step.

(a) *RO(n) model.* The kinetic exponents for this model can be calculated iteratively using the equation

$$\alpha_p = 1 - \{1 + [(1 - n)/n]x_p\pi(x_p)\}^{1/(n-1)} \quad (3.49)$$

(b) *JMA(n) model.* If the $Y(\alpha)$ function has a maximum at $\alpha_m \in (0, \alpha_p)$ (i.e. $n > 1$), the kinetic exponent n can be calculated using the equation

$$n = 1/[1 + \ln(1 - \alpha_m)] \quad (3.50)$$

If there is no maximum of the $Y(\alpha)$ function, the n value can be obtained from the slope of the plot of $\ln[-\ln(1 - \alpha)]$ vs $1/T$, which is nE/R . An alternative method of calculation is based on the following equation:

$$n = [1 - x_p\pi(x_p)]/[\ln(1 - \alpha_p) + 1] \quad (3.51)$$

It is recommended that an average of the two values obtained using both methods is taken, since this gives a good approximation of the kinetic exponent.

(c) *SB (m, n) model.* The kinetic parameter ratio, $p = m/n$, is calculated using the following equation:

$$p = \alpha_m/(1 - \alpha_m) \quad (3.52)$$

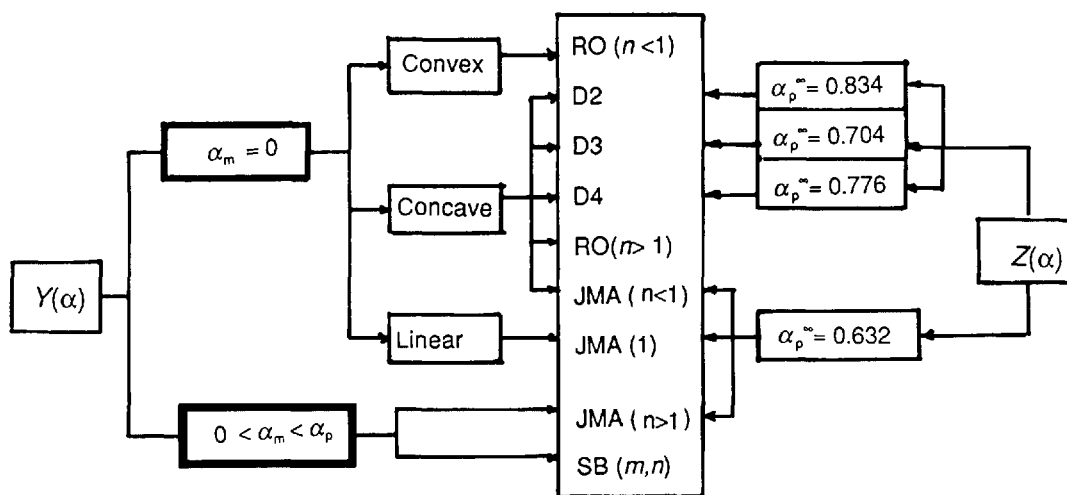


Figure 3.21 Schematic diagram of the kinetic model determination (reproduced by permission of Elsevier Science Publishers from *Solid State Ionics*, 1993, 63–65, 251)

and n can be obtained using the equation

$$\ln[(d\alpha/dt)e^x] = \ln A + n \ln[\alpha^n(1 - \alpha)] \quad (3.53)$$

that is, the kinetic parameter n corresponds to the slope of the linear plot of $\ln[(d\alpha/dt)e^x]$ vs $\ln[\alpha^n(1 - \alpha)]$ for $\alpha \in (0.2, 0.8)$. Then the second kinetic exponent is $m = pn$.

(d) *Calculation of the pre-exponential factor, A.* Knowing the value of the activation energy and the kinetic model, the pre-exponential factor is calculated using either the equation

$$A = [-\beta x_p / T_p f'(a_p)] \exp(x_p) \quad (3.54)$$

or

$$a = Y(\alpha)/f(\alpha) \quad (3.55)$$

The latter can be used to check the constancy of A during the course of a reaction by comparing the value of A at different α .

Tables 3.12 and 3.13 show the results of the non-isothermal decomposition kinetics of two series of complexes: dinitrato(N,N,N',N' -tetra- n -butyl aliphatic diamide)uranyl(II) [38] and dinitrato(di- N -alkyl caprolactams)uranyl(II) [39] using the method of Málek *et al.*

3.3.7.3 Controlled Transformation Rate Thermal Analysis (CRTA) Method [40, 43]

The controlled transformation rate thermal analysis (CRTA) technique was first developed by Rouquerol [40, 41] and allows the reaction rate, instead of the heating rate, to be kept constant in TA measurements. It has been found that the CRTA method can reduce the influence of heat and mass transfer phenomena on the forward solid-state reaction compared with the conventional thermal methods. Moreover, it has been suggested that the CRTA technique has a higher resolving power than conventional DTA-TG for separating overlapping processes and, at the same time, has a higher efficiency for discriminating the actual kinetic models obeyed by the reaction. Hence, it has been claimed that the CRTA method shows numerous advantages over the conventional approach, which explains its recent commercialization by a number of manufacturers of thermobalances and dilatometers, including Netzsch, Setaram and TA Instruments [42].

Compared with the conventional thermoanalytical methods, the CRTA technique can provide

Table 3.12 Kinetic parameters and mechanism of the thermal decomposition for complexes $\text{UO}_2[\text{Bu}_2\text{NCO}(\text{CH}_2)_n\text{CONBu}_2](\text{NO}_3)_2$ with $n = 1, 2, 3, 4, 6, 7$ or 10

No.	Complex	$E/\text{kJ mol}^{-1}$	$\text{Ln}(A/\text{s}^{-1})$	Model	m	n
1	$n = 1$	152	30.68	RO		-1.15
2	$n = 2$	172	38.72	SB	0.374	1.483
3	$n = 3$	175	35.78	SB	0.968	1.326
4	$n = 4$	170	33.28	SB	0.280	0.747
5	$n = 6$	193	20.00	SB	0.127	0.248
6	$n = 8$	186	35.73	SB	0.293	0.754
7	$n = 10$	182	32.98	SB	0.083	0.393

Table 3.13 Kinetic parameters and models for thermal decomposition of complexes $\text{UO}_2(\text{NO}_3)_2[\text{CH}_2(\text{CH}_2)_4\text{CONR}]_2$

Complex	$E/\text{kJ mol}^{-1}$	Model	m	n	$\text{Ln } A$
$\text{R} = \text{C}_2\text{H}_5$	87.31	SB	0.874	0.936	20.2
$\text{R} = \text{C}_4\text{H}_9$	91.68	SB	0.836	0.947	21.1
$\text{R} = \text{C}_6\text{H}_{13}$	97.53	SB	0.264	0.789	22.4
$\text{R} = \text{C}_8\text{H}_{17}$	112.9	SB	0.228	0.584	25.3
$\text{R} = \text{C}_{10}\text{H}_{21}$	115.7	SB	0.202	0.579	24.8
$\text{R} = \text{C}_{12}\text{H}_{23}$	112.9	SB	0.197	0.992	22.7

more reliable results of kinetic analysis, particularly, in cases where the sample mass is large, and if the reaction produces gaseous products.

The kinetic equation

$$da/dt = Af(a)\exp(-E/RT) \quad (3.56)$$

can be rewritten as

$$\ln[1/f(a)] = \ln(A/C) - E/RT \quad (3.57)$$

in the CRTA method, where da/dt is a constant, C . Then the activation energy can be calculated using one of the following approaches:

1. Plots of $\ln[1/f(a)]$ vs $1/T$ are constructed for every trial of the mechanism function $f(a)$. The E and A values obtained with the largest linear regression coefficient should be chosen and the corresponding $f(a)$ is the most suitable mechanism function.
2. TA measurements are performed at various reaction rates, C_i , and then many sets of data of T_i and C_i at a given value are obtained. The plot of $\ln C_i$ vs $1/T_i$ gives the E value.
3. The activation energy E can also be determined by the rate-jump method of CRTA. In the rate-jump method, the reaction rate is cycled between two predetermined values by increasing the gas flow towards the exterior of the reaction chamber in that ratio, and by measuring the resulting temperature limits. Each set of two successive rates with the corresponding temperatures allows an independent calculation of E from the equation

$$E = R[T_1 T_2 / (T_1 - T_2)] \ln(C_1 / C_2) \quad (3.58)$$

where T_1 and T_2 correspond to the same degree of reaction.

It is found that the activation energy E determined from the rate-jump method of CRTA is

nearly constant irrespective of the sample size within a sample mass range of 20–200 mg for the thermal decomposition of dolomite, as shown in Table 3.14 [43].

3.4 Expression of TA Curves and Determination of Termination Point for Transition or Reaction

3.4.1 TA Curves and Their Expression

TA curves can be categorized into two types, derivative (e.g. DTA curve, DTG curve) and integral (e.g. TG curve). As shown in Figure 3.22, derivative TA curves are expressed with the following parameters: T_i , initial temperature; T_o , extrapolated onset temperature; T_p , peak temperature; and T_f , final temperature. The true final temperature of reaction is T^*_{if} , not T_f , owing to the

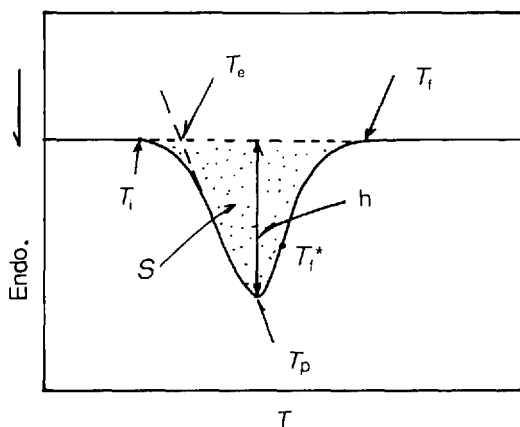


Figure 3.22 Schematic DTA curve of chemical reaction or physical transition

Table 3.14 Effect of the sample size on activation energies E of the thermal decomposition of dolomite determined from the rate-jump method of CRTA

	Sample mass/mg			
Parameter	20	50	100	200
Rate-jump ratio	3.7–5.5	3.4–5.0	3.2–4.2	3.5–4.5
$E/\text{kJ mol}^{-1}$	201 ± 26	194 ± 13	190 ± 13	180 ± 15

thermal lag of the process. Among the above temperatures, the repeatability of T_i and T_f is relatively poor depending on the sensitivity of the instrument. In general, the repeatability of T_e and T_p is good. The peak height h and peak area S are in proportion to the reaction rate and reaction heat, respectively. The reaction shifts to higher temperature with increasing heating rate. Sharper transition curves are obtained by rapid heating or cooling.

As shown in Figure 3.23, a multi-step process may easily be distinguished from a derivative curve (DTG curve), taking into account the lowest point (as indicated by the arrow). Maximum reaction rates for multi-step processes are also easily obtained.

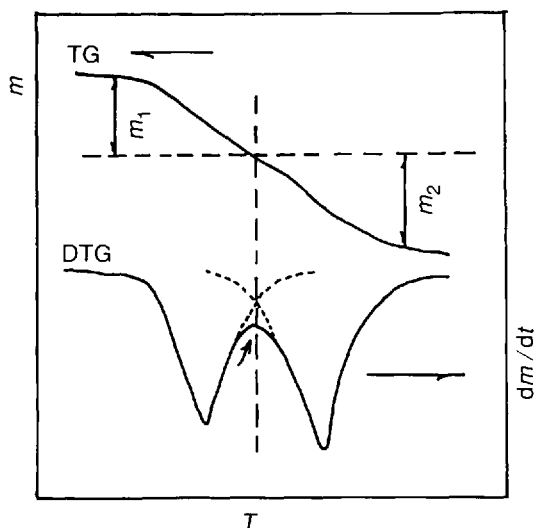


Figure 3.23 Schematic TG and DTG curves of transition or chemical reaction or physical transition

3.4.2 Determination of the Terminated Point of a DTA Curve for Transition or Reaction [44]

After the completion of melting for a crystalline sample, the temperature difference ΔT decreases according to an exponential function (as seen in Figure 3.24), which can be expressed as

$$[\Delta T - (\Delta T)_a] = (\Delta T)_h \exp[-(1/\tau)(t - t_p)] \quad (3.59)$$

where $\tau = RC_s$, R is thermal resistance and C_s is the heat capacity of the sample; for the definition of other quantities, see Figure 3.24.

From equation (3.59), the $\ln[\Delta T - (\Delta T)_a]$ vs $(t - t_p)$ plot should be a straight line. As shown in Figure 3.24, from the high-temperature side of melting to the peak top of the DTA curve, the point from which the straight line deviates is the terminated point of melting (C point) according to equation (3.59). The straight line continues until $t = t_p$, and the intercept equals $\ln(\Delta T)_h$. The peak top is the terminated point of the melting process, as for melting DTA curves for high-purity metals (e.g. Pb, In). The terminated point of melting for polyethylene is located on the DTA curve where the curve has decreased to one third of $(\Delta T)_h$.

3.4.3 Determination of Thermal Time Constant and Lowest Separation Temperature for a DTA Curve

The DTA curve can be expressed by the following equation [45]:

$$R(dH/dt) = (T_s - T_r) + R(C_s - C_r)(dT_r/dt) + RC_s[d(T_s - T_r)/dt] \quad (3.60)$$

where R is thermal resistance, $(K s J^{-1})$, dH/dt heat flow rate $(J s^{-1})$, t time (s) (counted from the initial temperature of the peak), RC_s thermal time constant (s), T_s and T_r temperatures of sample and reference, respectively (K) and C_s and C_r heat

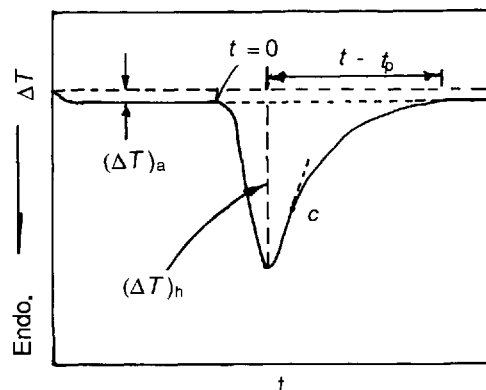


Figure 3.24 DTA curve of endothermic transition

capacities of sample and reference with container and holder, respectively (J K^{-1}).

The term $T_s - T_r$ in equation (3.60) is the temperature difference between the sample and reference, i.e. the ordinate value of the DTA curve at any point. The term $R(C_s - C_r)(dT_r/dt)$ is the baseline displacement from the zero level, and is dependent on the heat capacity difference between the sample and reference, the thermal resistance of the system and the heating rate. The term $RC_s d(T_s - T_r)/dt$ is the slope of the curve at any point multiplied by the time constant RC_s of the system (see Figure 3.25).

On the DTA curve in Figure 3.25, point *a* is the initial point of a transition, *b* is the top point, with corresponding time t_p , and *c* is the terminated point. Assuming at $t = 0$, $\Delta T = \Delta T_p$ (in the case of the peak top to the terminated point, for example, the DTA curve of melting for high-purity indium), $\Delta T = \Delta T_c$ (in the case of point *c* as terminated point, for the DTA curve of polyethylene melting), for these two cases RC_s can be obtained by using the following relationships:

$$\ln \Delta T_p - \ln \Delta T = (1/RC_s)t \quad (3.61)$$

$$\ln \Delta T_c - \ln \Delta T = (1/RC_s)t \quad (3.62)$$

By plotting $\ln \Delta T_p - \ln \Delta T$ vs t or $\ln \Delta T_c - \ln \Delta T$ vs t , we can obtain RC_s from the slope of the straight line. The data determined from the melting of indium are given in Table 3.15, resulting in $RC_s = 6.1649$ with correlation coefficient $r = 0.9967$.

Gray's definition of the least separation temperature L is

$$L = [0.693RC_s + (t_p/2)](dT_r/dt) \quad (6.63)$$

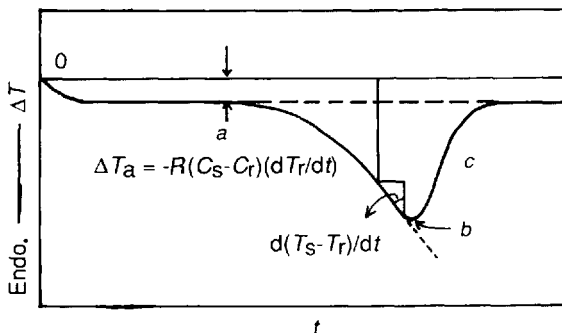


Figure 3.25 Schematic DTA curve used for equation 3.60

Table 3.15 Data for determination of RC_s from DTA curve for melting of indium (heating rate 20 K min^{-1} , size of sample 17.13 mg) [46]

t/s	$\Delta T/\text{mm}$	$\ln \Delta T$	$\ln \Delta T_p - \ln \Delta T$
0	68	4.220	
2	58.5	4.069	0.151
4	45.5	3.818	0.402
6	35	3.55	0.665
8	25	3.219	1.001
10	20	2.996	1.224
12	13	2.565	1.655
14	10	2.303	1.917
16	7.2	1.974	2.246
18	5.2	1.649	2.571
20	4.0	1.386	2.834
22	2.5	0.916	3.304
24	1.5	0.405	3.815

where L is the least temperature interval of peak tops between two near peaks at 50% separation degree (K), t_p is the time calculated from the initial point to the peak top (s) and dT_r/dt is the heating rate (K s^{-1}).

For the melting of indium, substituting the experimental value $t_p = 24 \text{ s}$, L can be obtained as 5.42 K .

The R value has no effect on peak area, but it affects the peak shape to a large extent: the smaller the R value, the narrower and steeper is the peak. On this account, when R is small, adjacent peaks separate well. Therefore, the values of R , RC_s and L are important parameters for a differential scanning calorimeter or differential thermal analyzer.

3.5 Quantitative Treatments of TG Data

3.5.1 Multi-step Reactions

The desired reactions can be supported in terms of a comparison of calculated and determined values. Calcium oxalate monohydrate ($\text{CaC}_2\text{O}_4 \cdot \text{H}_2\text{O}$) is a typical example [47]. As shown in Figure 3.26, the mass-loss values determined by thermogravimetry for three well separated reactions of thermal decompositions are 12, 32 and 62%, which agree well with the following steps:

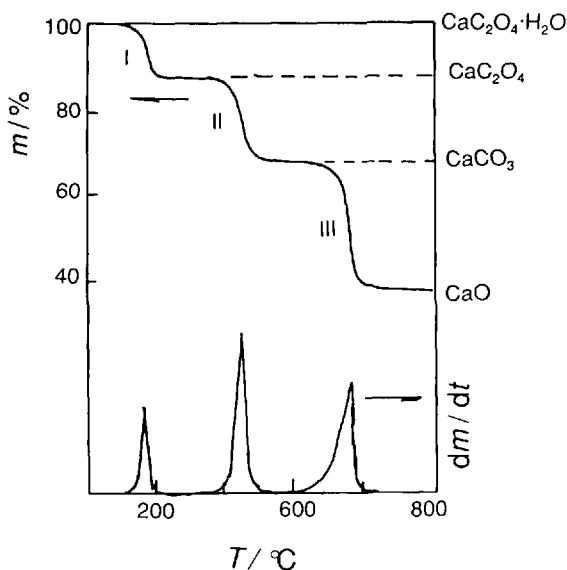
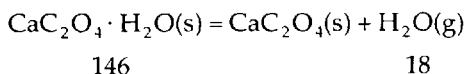


Figure 3.26 DTG/TG curves for $\text{CaC}_2\text{O}_4 \cdot \text{H}_2\text{O}$ (in air, at a heating rate of 3°C min^{-1})

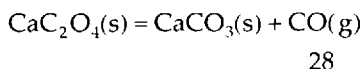
In step 1, hydrate water is lost, corresponding to



molecular mass:

$$\Delta m = (18/146) \times 100 = 12.3\%$$

In step 2, the anhydrous salt decomposes:

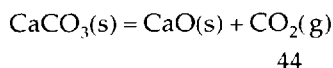


molecular mass:

$$\Delta m = (28/146) \times 100 = 19.2\%$$

$$\text{Total } \Delta m = 12.3 + 19.2 = 31.5\%$$

In step 3, the carbonate decomposes:



molecular mass:

$$\Delta m = (44/146) \times 100 = 30.1\%$$

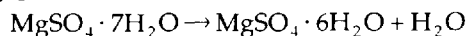
$$\text{Total } \Delta m = 12.3 + 19.2 + 31.5 = 61.6\%$$

For more complex reaction processes, in addition to the above calculation, it is necessary to check them with a structure analysis technique, such as X-ray diffraction.

3.5.2 Dynamic Rate Controlled Method

The heating rate of the sample is dynamically and continuously varied in response to the changes in the decomposition rate of the sample. It is reported that the dehydration of inorganic salts proceeds at nearly the same rate as that carried out under equilibrium conditions. Figure 3.27 shows a comparison between the TG curve for the dehydration of $\text{MgSO}_4 \cdot 7\text{H}_2\text{O}$ (heating rate $10^\circ\text{C min}^{-1}$) and the dynamic rate-controlled curve [48]. It can be seen that seven steps in dehydration are clearly separated:

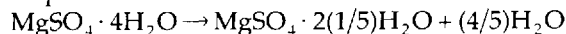
Step 1



Step 2



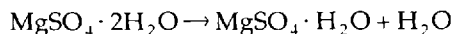
Step 3



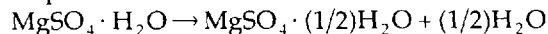
Step 4



Step 5



Step 6



Step 7

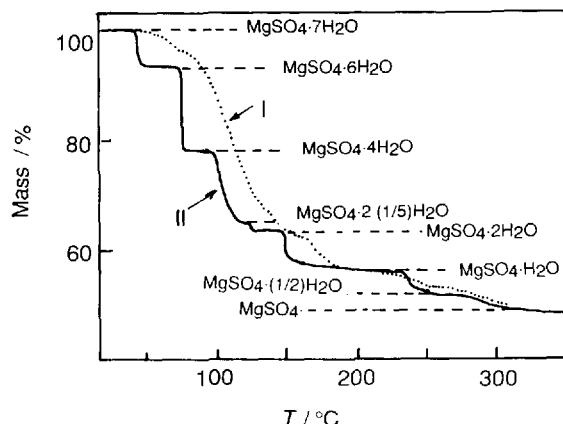
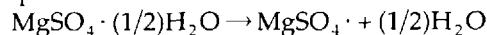


Figure 3.27 Comparison between (I) the TG curve for dehydration of $\text{MgSO}_4 \cdot 7\text{H}_2\text{O}$ (heating rate $10^\circ\text{C min}^{-1}$) and (II) the dynamic rate-controlled curve

3.6 Standard Mathematical Software

See Section 2.1.3.

3.7 References

- 1 Ichihara, S., in Society of Calorimetry and Thermal Analysis of Japan (Ed.), *Thermal Analysis Fundamentals and Applications*, 3rd edn. Tokyo, Realize, 1994, p.40.
- 2 Kotra, R. K., Gibson, E. K., and Urbancic, M. A., *Icarus*, 1982, **51**, 593.
- 3 Speil, S., Berkelhamer, L. H., Pask, J. A., and Davis, B., *US Bur. Mines Tech. Pap.*, 1945, 664.
- 4 Wiedemann, H. G., and Bayer, E., *Top. Curr. Chem.*, Berlin: 1978, **77**.
- 5 Momota, M., in Society of Calorimetry and Thermal Analysis of Japan (Ed), *Thermal Analysis fundamentals and Applications*, 3rd edn. Tokyo, Realize, 1994, p. 42.
- 6 Criado, J. M., *Thermochim. Acta*, 1977, **19**, 129.
- 7 Sestak, J., *Talanta*, 1966, **13**, 567.
- 8 Certificate for ICIA Certified Reference Materials for Differential Thermal Analysis from 125 to 940 °C.
- 9 Ozawa, T., *Bull. Chem. Soc. Jpn.*, 1965, **38**, 1881.
- 10 Kissinger, H. E., *Anal. Chem.*, 1957, **29**, 1702.
- 11 Freeman, E. S., and Carroll, B. J., *J. Phys. Chem.*, 1958, **62**, 394.
- 12 Reich, L., Leem H. T., and Levi, D. W., *J. Polym. Sci. B*, 1963, **1**, 535.
- 13 Fuoss, R. M., Sager, I. D., and Wilson, H. S., *J. Polym. Sci.*, 1964, **2**, 3147.
- 14 Wendlandt, W. W., *Thermal Analysis*, 3rd edn. New York, Wiley, 1986, p. 80.
- 15 Hancock, J. D., and Sharp, J. H., *J. Am. Ceram. Soc.*, 1972, **55**(2), 74.
- 16 Ziabicki, A., *Appl. Polym. Sym.*, 1967, **6**, 1.
- 17 Ozawa, T., *Polymer*, 1971, **12**, 150.
- 18 Xue Xiaofu, Yang Baoquan and Li Hongyun, *Acta Polym. Sin.*, 1993, (5), 589.
- 19 Liu Jieping, Mo Zhishen, and Qi Yuchen, *Acta Polym. Sin.*, 1993, **1**, 1.
- 20 Zhang Zhiying, *Chin. J. Polym. Sci.*, 1993, **11**, 125.
- 21 Sichina, W. J., *Du Pont Thermal Analysis Technical Literature*, No. TA-9. Wilmington, DE, Du Pont.
- 22 Horie, K., Mita, I., and Kambe, H., *J. Polym. Sci. Polym. Chem. Ed.*, 1970, **8**, 1357.
- 23 Sourour, S., and Kamal, M. R., *Thermochim. Acta*, 1976, **14**, 41.
- 24 Freeman, E. S., and Carroll, B., *J. Phys. Chem.*, 1958, **62**, 394.
- 25 Crane, L. W., Dynes, P. J., and Kaelable, D. H., *J. Polym. Sci., Polym. Lett. Ed.*, 1973, **11**, 533.
- 26 Barton, J. M., in Jen Chiu (Ed), *Polymer Characterization by Thermal Methods of Analysis*. New York, Marcel Dekker, 1974.
- 27 Kissinger, H. E., *Anal. Chem.*, 1957, **29**, 1702.
- 28 Peyser, P., and Bascom, W. D., *J. Appl. Polym. Sci.*, 1977, **21**, 2359.
- 29 Prasad, T. P., et al., *Thermochim. Acta*, 1992, **203**, 503.
- 30 Koga, N., et al., *Netsu Sokutei*, 1993, **20**, 210.
- 31 Sestak, J., and Malek, J., *Solid State Ionics*, 1993, **63-65**, 245.
- 32 Sestak, J., *J. Thermal Anal.*, 1990, **36**, 1977.
- 33 Sestak, J., and Berggren, G., *Thermochim. Acta*, 1971, **3**, 1.
- 34 Gorbachev, V. M., *J. Thermal Anal.*, 1980, **18**, 194.
- 35 Flynn, J. H., *Thermochim. Acta*, 1992, **203**, 519.
- 36 Malek, J., and Smrcka, V., *Thermochim. Acta*, 1991, **186**, 1353.
- 37 Malek, J., *Thermochim. Acta*, 1992, **200**, 257.
- 38 Lu Zhenrong, et al., *Thermochim. Acta*, 1995, **255**, 281.
- 39 Lu Zhenrong, et al., *J. Thermal Anal.*, 1995, **44**, 1391.
- 40 Rouquerol, J., *J. Thermal Anal.*, 1973, **5**, 203.
- 41 Rouquerol, J., *Thermochim. Acta*, 1989, **144**, 209.
- 42 Laureiro, Y., et al., *Thermochim. Acta*, 1996, **278**, 165.
- 43 Tanaka, H., *Netsu Sokutei*, 1992, **19**, 32.
- 44 Kambe, H., and Ozawa, T. (Eds), *Thermal Analysis*, new edn. 1992, p. 12 (in Japanese).
- 45 Gray, A. P., in Porter, R. F., and Johnson, J. M. (Eds), *Analytical Calorimetry*. New York, Plenum, 1968, p. 209.
- 46 Yu Boling and Jiang Jiaodong, *J. Beijing Inst. Clothing Technol.* 1991, **11**(2), 68 (in Chinese).
- 47 Dodd, J. W., and Tonge, K. H., *Thermal Methods*. Chichester, Wiley, 1987, p. 73.
- 48 Arai, A., Kanaya, T., Kishi, A., and Fujii, N., *Netsu Sokutei*, 1994, **21**, 151.

TA Measurement of Various Transitions

4.1 Glass Transition

4.1.1 Determination of Glass Transition Temperature by DTA or DSC

The heat capacity (C_p) of amorphous materials in the solid state is lower than that in the liquid state. On this account, a deflection of the baseline can be observed at the glass transition temperature (T_g). Occasionally, a small endothermic peak based on enthalpy relaxation (see Section 4.1.6) can be observed. Based on the C_p change, T_g can be determined experimentally using DTA or DSC. The T_g value depends markedly on the thermal history of the sample and the experimental conditions. The measurement should be performed with the same standardization procedure as in ASTM D 3418-82 and JIS K 7121-1987.

1. Before the measurement, maintain the sample at a temperature of $23 \pm 2^\circ\text{C}$ and a relative humidity of $50 \pm 5\%$ for more than 24 h (or under other desired conditions) for conditioning.
2. Weigh about 10 mg of the sample with a precision of 0.1 mg. If the sample contains a large amount of additive, 5–10 mg of pure sample (e.g. polymer) is sufficient. Since milligram quantities of sample are used, it is essential to ensure that the samples are homogeneous and representative.
3. Place the conditioned sample into the DSC or

DTA sample vessel. Heat the sample from ambient up to 30°C above the T_g final temperature for an amorphous polymer or 30°C above the T_m final temperature for a crystalline polymer. After maintaining this temperature for 10 min, cool to 50°C below the glass transition temperature.

4. After maintaining the apparatus at 50°C below the glass transition temperature, heat the sample at a rate of $20^\circ\text{C min}^{-1}$ up to 30°C above the end of the transition temperature. The sensitivity of the apparatus should be adjusted, resulting in more than a 10% deflection of full-scale of the recorder before and after the glass transition temperature. (Computer-equipped apparatus can carry out this process automatically).
5. The experiment should be performed under a nitrogen atmosphere with a continuous flow-rate of $10\text{--}50\text{ ml min}^{-1}$ to avoid oxidation.
6. The method of measuring the glass transition temperature is outlined in Figure 4.1.

A. mid-point glass transition temperature (T_{mg}): T_{mg} is the temperature at which the deviation of the DTA or DSC curve reaches 0.5 h (see Figure 4.1)

B. Extrapolated onset temperature of glass transition (T_{ig}): T_{ig} is the temperature at which the extrapolated baseline before the transition intersects the tangent drawn at the point of greatest slope on the step of the glass transition.

C. Extrapolated end temperature of glass transition (T_{eg}): T_{eg} is the temperature at which

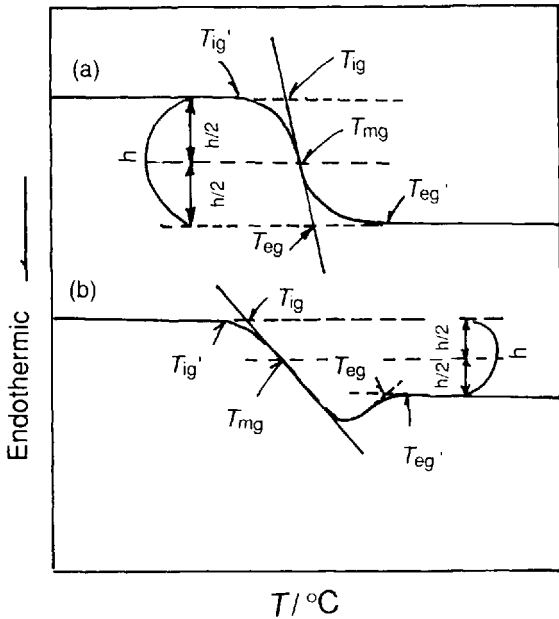


Figure 4.1 Determination of glass transition temperature: (a) step change before and after transition; (b) step change with a small peak before and after transition

the extrapolated baseline at the higher temperature side intersects the tangent drawn at the point of greatest slope on the step of the glass transition. When a peak appears at the higher temperature side of the step as in Figure 4.1, T_{eg} is the temperature at the intersection of the extended baseline at the higher temperature side with the tangent drawn at the point of greatest slope on the succeeding edge of the peak.

Repeatability: Duplicate determinations of glass transition temperatures on two specimens of the same sample by the same analyst should not differ by more than 2.5°C .

Reproducibility: Duplicate determinations of T_g s on specimens of the same sample analyzed in different laboratories should not differ by more than 4°C [1].

4.1.2 Effect of Plasticizers and Random Copolymers

When a plasticizer is blended into a polymer, the glass transition temperature (T_g) of the polymer decreases. The variation T_g for a mixture of poly(vinyl chloride) (PVC) and dioctyl phthalate

(DOP), a typical plasticizer, is shown in Figure 4.2(a).

If the plasticizer is miscible with a polymer, then a mixture of the two substances should yield a homogeneous blend with a single glass transition temperature. Ideally, the resulting T_g can be approximated by a simple relationship such as

$$1/T_g = m_1/T_{g_1} + m_2/T_{g_2} \quad (4.1)$$

where T_g is the glass transition temperatures of the mixture (K), m_1 and m_2 are the mass fractions

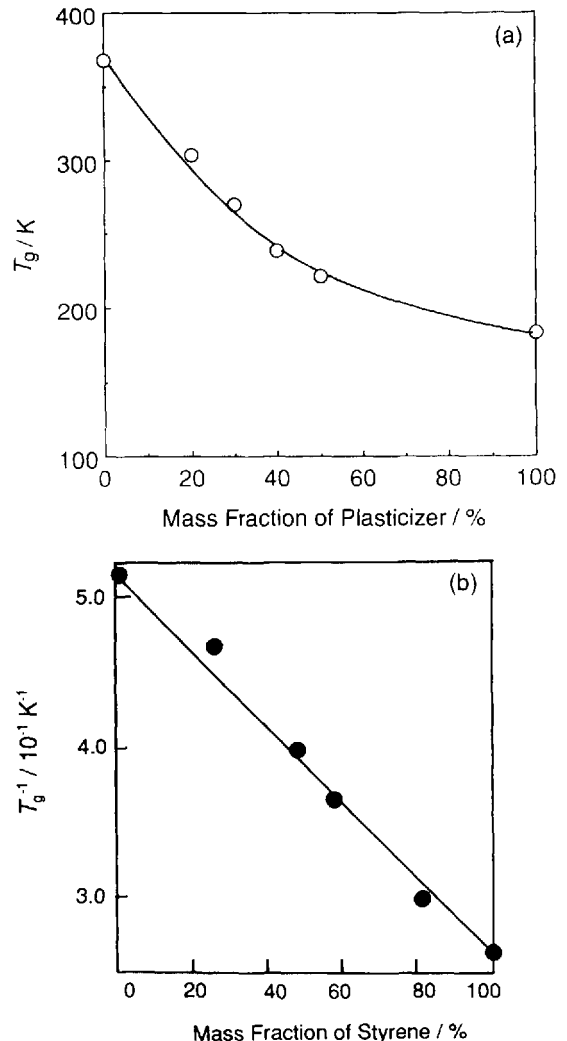


Figure 4.2 Relationship between (a) T_g of PVC and mass fraction of plastizer (DOP) (%) and (b) T_g of styrene-butadiene random copolymer and mass fraction of styrene

of the polymer and plasticizer, respectively, and T_{g1} and T_{g2} are glass transition temperatures of the polymer and the plasticizer, respectively (K). In the presence of the plasticizer, the glass transition temperature decreases. At the same time, the transition temperature region is broadened. For a random copolymer consisting of polymers 1 and 2 and miscible polymer blends, the relationship between the glass transition temperature and the copolymer composition follows the same rules as shown in equation 4.1 [see Figure 4.2(b)]. Both systems consist of two components, i.e. polymer-plasticizer and polymer 1-polymer 2. Many equations have been suggested for the calculation of the T_g of miscible polymer blends [2] (see Section 4.4).

4.1.3 Effect of Relative Molecular Mass

The glass transition temperature of polymers increases with increasing relative molecular mass in the low molecular mass region, i.e. from oligomer to $M_n \approx 1 \times 10^4$, and levels off in the high relative molecular mass region. The relationship between T_g of polystyrene and its relative molecular mass is shown in Figure 4.3 as an example [3-9].

The relationship between the glass transition temperature and relative molecular mass of a

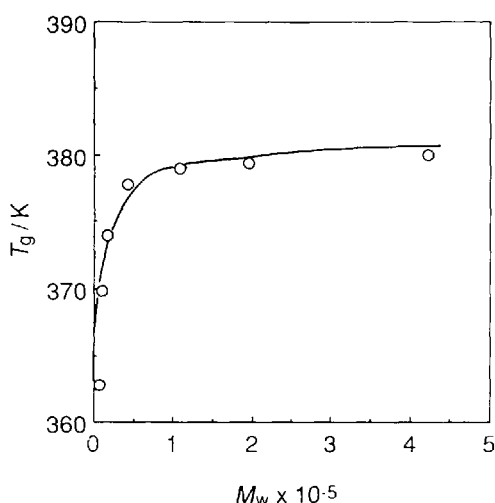


Figure 4.3 Relationship between T_g and M_w for polystyrene

polymer is expressed by the following equation;

$$T_g = T_g^* - C/M_w \quad (4.2)$$

where T_g is the glass transition temperature, T_g^* is the T_g of the polymer at infinite relative molecular mass, M_w is the weight-average relative molecular mass and C is a constant.

4.1.4 Effect of Cross-linking Density

The glass transition temperature of polymers increases with increasing cross-linking density. At the same time, the baseline change at T_g decreases and is difficult to detect by DSC, since molecular motion is restricted by junctions.

4.1.5 Effect of Crystallinity

The glass transition temperature is difficult to detect when the crystallinity of the sample increases. The deflection temperature at the baseline cannot be defined because the mobility of the molecules in the amorphous region is restricted by the presence of the crystalline region. In order to determine T_g , other TA methods, such as thermomechanometry, should be used.

When a crystalline polymeric sample is measured, the variation in T_g depends on the higher order structure. In some cases, T_g increases with increasing crystallinity, whereas in other cases it remains constant or decreases.

4.1.6 Enthalpy Relaxation

The glassy state of materials prepared under normal conditions is in a non-equilibrium state, in which an excess volume and enthalpy exist. When such a non-equilibrium glassy state is held at temperatures a few degrees lower than T_g , the excess thermodynamic properties decrease to those of an ideally equilibrium state. At the same time, the mechanical properties of the materials change [10].

For a quenched glass, only a step in the heat capacity is observed at T_g . For an annealed glass, however, not only a step but also a peak of heat capacity, which corresponds to the rapid recovery of the enthalpy, are observed at T_g . On annealing, the area of the endothermic peak

increases, and T_g of the sample shifts to a higher temperature (Figure 4.4).

Figure 4.5 shows the change in the specific heat capacity, which was obtained by DSC measurement, for quenched (solid line) and annealed (dashed line) samples. T_a and T_g represent the

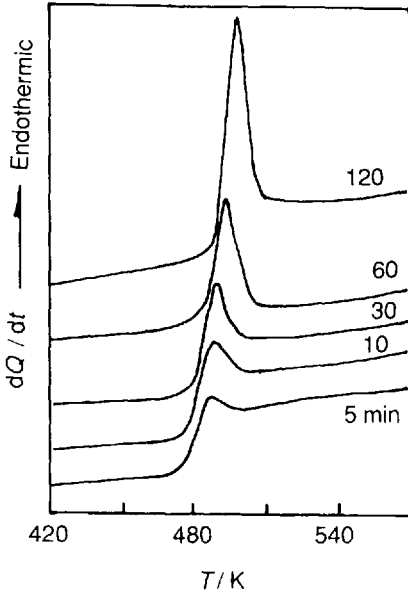


Figure 4.4 DSC curves of poly(phenylene oxide) annealed at 475 K for various time intervals. Numerals indicate annealing time

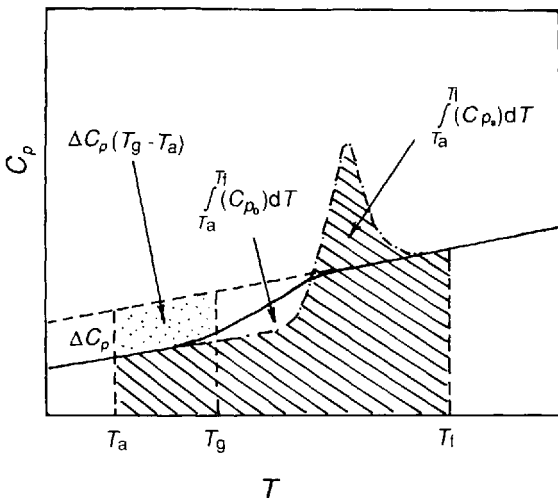


Figure 4.5 Schematic diagram of specific heat capacity change for quenched and annealed samples

annealing temperature and the glass transition temperature, respectively [11, 12].

The excess enthalpy, ΔH_0 of quenched glass can be expressed as

$$\Delta H_0 = \Delta C_p (T_g - T_a) \quad (4.3)$$

where ΔC_p represents the difference in specific heat capacities of the liquid state and the glassy state before and after the glass transition. The decreased enthalpy during annealing, i.e. the relaxation enthalpy, ΔH_d , can be expressed as follows:

$$\Delta H_d = \int_{T_a}^{T_l} (C_{p_a}) dT - \int_{T_a}^{T_l} (C_{p_0}) dT \quad (4.4)$$

where C_{p_a} and C_{p_0} represent the specific heat capacities of the annealed and the quenched samples, respectively. Therefore, the value of ΔH_d can be obtained by integrating two DSC curves for the annealed and the quenched samples in Figure 4.5 over the temperature range from T_a to T_l . Finally, the excess enthalpy, ΔH_l of a sample annealed at T_a for a time t is defined as

$$\Delta H_l = \Delta H_0 - \Delta H_d \quad (4.5)$$

The following equation can be used in order to compare the relaxation times of polymer glasses:

$$\Delta H_l = \Delta H_0 \exp(-t/\tau) \quad (4.6)$$

where τ is the relaxation time and t the annealing time at temperature T . Equation (4.6) can be rewritten as follows:

$$\ln(\Delta H_l/\Delta H_0) = -(t/\tau) + \text{constant} \quad (4.7)$$

From equation (4.7), the relaxation time, τ is obtained as follows:

$$\tau^{-1} = d[\ln(\Delta H_l/\Delta H_0)]/dt \quad (4.8)$$

The relaxation time, $\tau_{1/2}$ for which the enthalpy is reduced to half of the initial excess enthalpy, shows an Arrhenius temperature dependence, expressed as

$$(\tau_{1/2})^{-1} = A \exp(-E_a^*/RT) \quad (4.9)$$

where E_a^* is the apparent activation energy of enthalpy relaxation. The values of E_a^* , which were calculated from $\tau_{1/2}$, were about 300–400 kJ mol⁻¹ for several poly(alkyl methacrylates) [11].

4.1.7 Macromolecular Constants C_1 and C_2 in the WLF Equation

The temperature dependence of the relaxation time (τ) of polymers in the glass transition region cannot be described by the Arrhenius equation as the $\ln \tau$ versus $1/T$ plot is not linear. This means that the motional activation energy is not a constant but a function of temperature. In this situation, the temperature dependence of the relaxation time can be well described by the William-Landel-Ferry (WLF) equation as follows:

$$\log a_T = \log \left[\frac{\tau(T)}{\tau(T_0)} \right] = - \frac{C_1(T - T_0)}{C_2 + T - T_0} \quad (4.10)$$

where a_T is the shift factor and τ is the mean relaxation time calculated from $\tau = 1/(2\pi f)$, f being the frequency, and T_0 is a reference temperature. In order to match the experimental data with the WLF equation, equation (1) can be rearranged to the following form:

$$-\frac{1}{\log a_T} = \frac{1}{C_1} + \frac{C_2}{C_1} \frac{1}{T - T_0} \quad (4.11)$$

The constants in the WLF equation could be estimated according to the slope and intercept of the plot of $-1/\log a_T$ versus $(1/T - T_0)$. The values of C_1 and C_2 for some polymers in the glass state (C_{1g} and C_{2g}) are listed in Table 4.1.

The shift factor a_T could be measured by dynamic mechanical or dielectric relaxation spectroscopy.

As an example, the dependence of the dielectric relaxation time on T_g for the AB cross-linked copolymer (ABCP) of 50 : 50 polyurethane-styrene (COVTPU50St50) is shown in Figure 4.6 [13]. The plot of $-(\ln a_T)^{-1}$ versus $(T - T_0)^{-1}$ at T_g for the sample is shown in Figure 4.7. From this figure the constants in the WLF equation are estimated to be $C_1 = 12.4^\circ\text{C}$ and $C_2 = 56.4^\circ\text{C}$ for the polymer.

As is known, T_g has been selected as the reference temperature. Equation (4.10) is fitted in the temperature range from T_g to $T_g + 100^\circ\text{C}$. The average values of C_1 and C_2 were obtained by fitting data for a large number of polymers, and estimated to be 17.44°C and 51.6°C , respectively, when T_g was chosen as the reference tem-

Table 4.1 Parameters characterizing the temperature dependence of a_T for various polymers system

Polymer	$C_{1g}/^\circ\text{C}$	$C_{2g}/^\circ\text{C}$
<i>General</i>		
Polyisobutlene	16.6	104.4
Poly(vinyl acetate)	15.6	46.8
Poly(vinyl chloroacetate)	17.45	40.4
Polystyrene	13.3	47.5
Polystyrene	13.7	50.0
Poly- α -methylstyrene	13.7	49.3
Poly(methyl acrylate)	18.1	45.0
Poly-1-hexene	22.2	20.2
Polydimethylsiloxane	6.1	69.0
Polyacetaldehyde	14.5	24.0
Poly(propylene oxide)	16.2	24.0
Zinc phosphinate polymer	26.2	17.6
<i>Rubbers</i>		
EVEA rubber	16.8	53.6
Poly-1,4-butadiene	11.2	60.5
Poly-1,4-butadiene	11.3	60.0
Poly-1,4-butadiene	12.7	35.5
Styrene-butadiene copolymer	20.3	25.6
Butyl rubber	16.8	108.6
Ethylene-propylene copolymer	13.1	40.7
Ethylene-propylene copolymer	13.1	40.7
Polyurethane	15.6	32.6
<i>Methacrylate polymers</i>		
Methyl (atactic)	34.0	80.0
Methyl (conventional)	32.0	80.0
Ethyl	17.6	65.5
n-Butyl	17.0	96.6
n-Hexyl	17.8	129.4
n-Octyl	16.1	107.3
2-Ethylhexyl	20.2	119.9
<i>Diluted Systems</i>		
Poly(n-butyl methacrylate)	17.8	86.
in diethyl phthalate (50%)		
Poly(n-butyl methacrylate)	18.1	111.3
in diethyl phthalate (60%)		
Cellulose tributyrate	21.1	42.6
in dimethyl phthalate (21%)		
Cellulose tributyrate	23.3	38.6
in dimethyl phthalate (43%)		
Cellulose nitrate	26.2	53.5
in diethyl phthalate (23%)		
Poly(methyl methacrylate)	21.5	43.1
in diethyl phthalate (30%)		

perature. However, it is evident that the actual values vary from one polymer to another and the difference is too great to permit the use of these 'universals'. Universal values should not be used

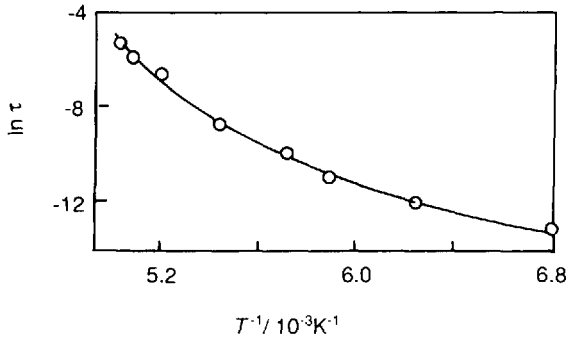


Figure 4.6 Dependence of relaxation time on T_g for the ABCP sample COVTU50St50 [13]

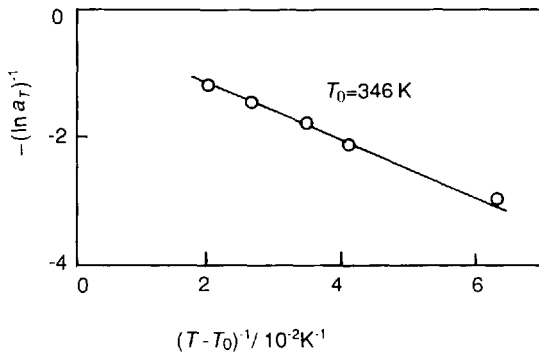


Figure 4.7 $-(\ln a_T)^{-1}$ versus $(T - T_0)^{-1}$ at T_g for sample ABCP of COVTU50St50 [13]

except when appropriate data cannot be found. The fixed values of $C_1 = 8.86^\circ\text{C}$ and $C_2 = 101.6^\circ\text{C}$ were used with the reference temperature $T_0 = T_g + (50-100^\circ\text{C})$. The WLF equation reads

$$\log a_T = -8.86(T - T_0)/(101.6 + T - T_0) \quad (4.12)$$

However, if possible, it is better to determine specific values of C_1 and C_2 by dynamic mechanical or dielectric relaxation analysis. Conversion from one reference T_0 to another T_1 can always be accomplished using the equation:

$$C_1^0 = C_1^1/(C_2^1 + T_0 - T_1) \quad (4.13)$$

$$C_2^0 = C_2^1 + T_0 - T_1 \quad (4.14)$$

4.1.8 Relaxation Activation Energy of Polymers in the Glass Transition Region

Using parameters calculated by the WLF equation [equation (4.10)], the relaxation activation

energy, E_a , can be calculated as follows:

$$E_a = \frac{d \ln a_T}{d(1/T)} = \frac{2.303C_1C_2RT^2}{(C_2 + T - T_0)^2} \quad (4.15)$$

where C_1 and C_2 are molecular parameters in the WLF equation and R is the gas constant.

The temperature dependence of the relaxation activation energy of hydroxy-terminated polybutadiene-methyl methacrylate AB cross-linked polymer in the glass transition region is shown in Figure 4.8. The parameters $C_1 = 8.77^\circ\text{C}$, $C_2 = 85.07^\circ\text{C}$ and $T_g = 340\text{ K}$ were measured by means of the dynamic mechanical spectra; 381 K was chosen as the reference temperature T_0 .

4.1.9 Characteristic Temperature, Free Volume Fraction and Thermal Expansion Coefficient of Polymers

The total volume of the polymer per gram, V , is the sum of the free volume, V_f and an 'occupied volume,' V_0 . The fractional free volume, f_s , a dimensionless number, is V_f/V . The relationship among f , a_f , C_1 and C_2 is

$$f_g = \frac{1}{2.303C_1} \quad (4.16)$$

where f_g is the fractional free volume of the polymer at the glass transition temperature.

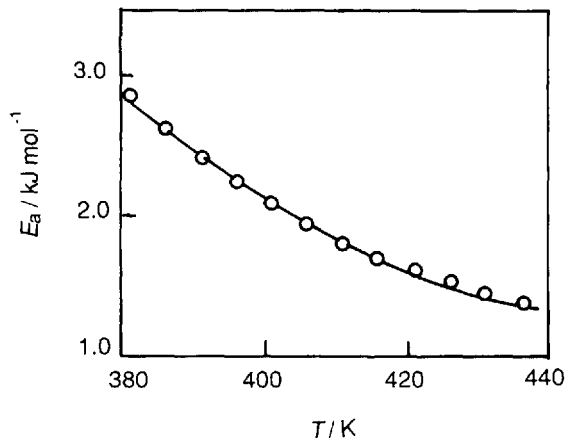


Figure 4.8 Relaxation activation energy of hydroxy-terminated polybutadiene-methyl methacrylate AB cross-linked polymer in the glass transition region as a function of temperature ($T_g = 340\text{ K}$, $T_0 = 380\text{ K}$) [14]

When $T > T_g$, f_s can be calculated as

$$f_s = f_g + \alpha_f(T - T_g) \quad (4.17)$$

where α_f is the thermal expansion coefficient of the fractional free volume:

$$\alpha_f = f_g/C_2 \quad (4.18)$$

where C_1 and C_2 are the molecular parameters in the WLF equation with the reference temperature T_g and f_s is the fractional free volume of the polymer in the rubber state. f_g and α_s can be calculated from equations (4.16), (4.17) and (4.18). C_1 and C_2 can be measured in terms of the WLF equation. The temperature dependence of the viscosity of the polymer, η , is as follows:

$$\log a_T = \log[\eta(T)/\eta(T_g)] = -\frac{C_1(T - T_g)}{C_2 + (T - T_g)} \quad (4.19)$$

The WLF equation can be used to describe the temperature dependence of η . T_2 , the characteristic temperature for the polymers, can be calculated as follows:

$$C_2 + T_2 - T_g = 0 \quad (4.20)$$

$$T_2 = T_g - C_2 \quad (4.21)$$

Equations (4.19) and (4.21) predict that the viscosity of the polymer becomes infinite at T_2 and all of the molecular motions were frozen in polymers. As an example, $C_1 = 8.77^\circ\text{C}$, $C_2 = 85.07^\circ\text{C}$, $T_g = 340\text{ K}$, $f_g = 0.0256$, $f_s = 0.0495$ at 381 K , $\alpha_f = 5.82 \times 10^{-4}\text{ K}^{-1}$ and $T_2 = 254.93\text{ K}$ were measured for an AB cross-linked polymer based on butadiene and PMMA [15].

4.2 Crystallization and Melting

4.2.1 Determination of Melting and Crystallization Temperatures by DTA or DSC

From the melting endothermic peak and the crystallization exothermic peak of DTA or DSC curves, transition temperatures can be determined. In order to erase the effect of the previous thermal history, such as superheating, super-

cooling and recrystallization during heating or cooling, the measurement should be performed using the same standardization procedure as in ASTM D 3418-82 and JIS K 7121-1987.

1. Before the measurement, maintain the sample at a temperature of $23 \pm 2^\circ\text{C}$ and a relative humidity of $50 \pm 5\%$ for more than 24 h for conditioning.
2. Weigh about 10 mg of the sample with a precision of 0.1 mg. If the sample contains a large amount of the additive, 5–10 mg of pure sample (e.g. polymer) is sufficient. Since milligram quantities of sample are used, it is essential to ensure that the samples are homogeneous and representative.
3. Place the conditioned sample into the pan of a DSC or DTA instrument. Heat the sample from ambient up to 30°C above the final temperature of the melting peak and maintain at this temperature for 10 min to ensure melting of the sample. Subsequently cool to at least 50°C below the final temperature of crystallization.
4. Melting and crystallization temperatures are determined as follows (see Figures 4.9 and 4.10);

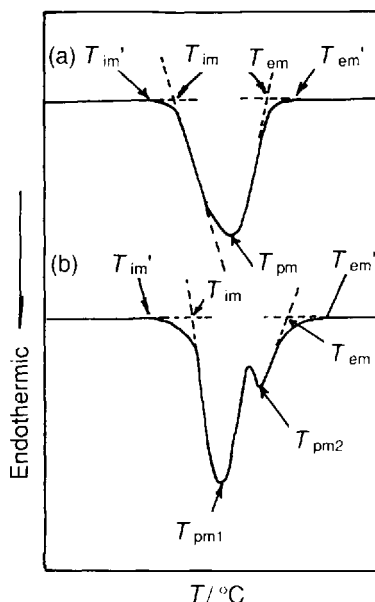


Figure 4.9 Determination of melting temperature: (a) single peak; (b) multiple peaks

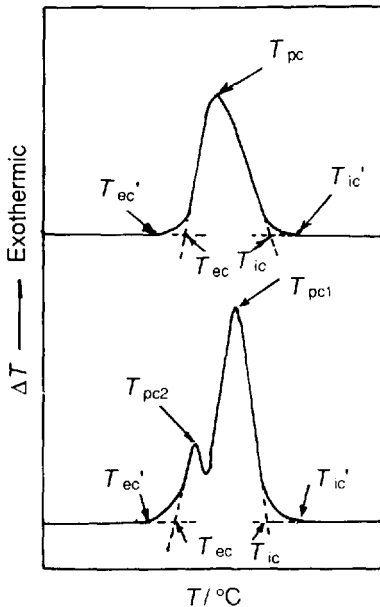


Figure 4.10 Determination of crystallization temperature: (a) single peak; (b) multiple peaks

A. Determination of melting temperature:

(a) Maintain the apparatus at about 100 °C below the melting temperature so that it is stable. (b) Heat the sample at a rate of 10 °C min⁻¹ up to 30 °C above the final temperature of melting. (c) When the melting temperature is determined using the sample conditioned by procedure (3), heat the sample at a rate of 10 °C min⁻¹ up to 30 °C above the melting peak temperature. (d) Accumulate data in a computer or record the DTA or DSC curve.

B. Determination of crystallization temperature: (a) Heat the sample up to about 30 °C above the final temperature of the melting peak by the above-mentioned procedure. (b) Maintain this temperature for 10 min, then cool to about 50 °C below the final temperature of the melting peak at a rate of 5 or 10 °C min⁻¹. (c) Accumulate data or record the cooling curve. (d) If the crystallization rate is slow and it is difficult to determine the completion of the crystallization peak on the lower temperature side, the experiment should be stopped. (e) The sensitivity should

be adjusted in order to obtain a peak height that is more than 25% of full scale (this is not necessary when computer-equipped apparatus is used). The flow rate of nitrogen should be appropriately controlled in the range 10–50 ml min⁻¹ and maintained at a constant value.

4.2.1.1 Melting Temperature

The peak temperature of melting (T_{pm}) is taken as the temperature of the peak on the melting DTA or DSC curve; the extrapolated onset temperature of melting (T_{im}) is the temperature at which the extrapolated baseline on the lower temperature side intersects the tangent drawn at the maximum rising slope of the peak; the extrapolated end temperature of melting (T_{em}) is given by the intersection of the tangent to the maximum falling slope of the peak and the extrapolated baseline on the higher temperature side. If there are more than two separate peaks of melting, the corresponding T_{pm} , T_{im} and T_{em} can be determined. In addition, when the melting takes place slowly, and it is difficult to determine the baseline on the lower temperature side, it is not necessary to determine T_{im} .

4.2.1.2 Crystallization Temperature

The peak temperature of crystallization (T_{pc}) is taken as the temperature at the top of the peak on the crystallization DTA or DSC curve; the extrapolated onset temperature of crystallization (T_{ic}) is defined as the intersection between the extrapolated baseline at the higher temperature and the tangent drawn at the point of greatest slope on the rising side of the crystallization peak. In the case of multiple peaks of crystallization, the corresponding characteristic temperature for each peak can be determined. In addition, if there are more than two overlapping peaks, T_{ic} , several T_{pc} s and T_{ec} s can be determined. Moreover, when the crystallization takes place continuously at a slower rate, it is difficult to determine the baseline on the lower temperature side and it is not necessary to determine T_{ec} .

Results of round robin tests on T_m and T_c can be found in Ref. 16.

4.2.2 Thermodynamic Equilibrium Melting Temperature of Polymer Crystals

The thermodynamic equilibrium melting point of polymer crystals can be measured by means of DSC and small-angle X-ray diffraction. The following procedure is recommended for the measurement of the equilibrium melting temperature of a polymer crystal, T_m^0 :

1. Calibrate the DSC instrument with temperature and heat flow scales following standard procedures.
2. Place 8 ± 2 mg of sample in a DSC vessel and quickly heat to a temperature T ($T > T_m^0$), which is held for about 10 min in order to erase all previous thermal and mechanical history.
3. Quench the sample (at a rate of $200^\circ\text{C min}^{-1}$, if possible) to the predetermined crystallization temperature T_c .
4. Record the heat generated during the development of the crystalline phase until a flat baseline is obtained.
5. Heat the sample from T_c at a heating rate of $20^\circ\text{C min}^{-1}$. The DSC curve is recorded and the melting temperatures T_m are obtained.
6. Plot T_m as a function of T_c .
7. The equilibrium melting temperature of the crystal, T_m^0 , is determined by the intersection between two straight lines to $T_m = T_c$ and the plot of T_m as a function of T_c according to the Hoffman–Weeks equation [17]:

$$T_m = T_m^0 [1 - 1/\gamma] + T_c/\gamma \quad (4.22)$$

where γ is the thickening factor. Multi-melting peaks are frequently observed on the DSC curves. This is caused by the polymorphism of the crystals and/or the crystals reorganized at T_c or during heating. On this account, the above extrapolation should be carried out carefully and correctly. Figure 4.11 shows the schematic relationship between T_m and T_c in order to obtain T_m^0 .

Another way to measure T_m^0 of polymer crystals is by extrapolation of the T_m versus $1/l$ to plot $1/l=0$, where l is the lamellae thickness of the crystals, which can be measured by small-angle

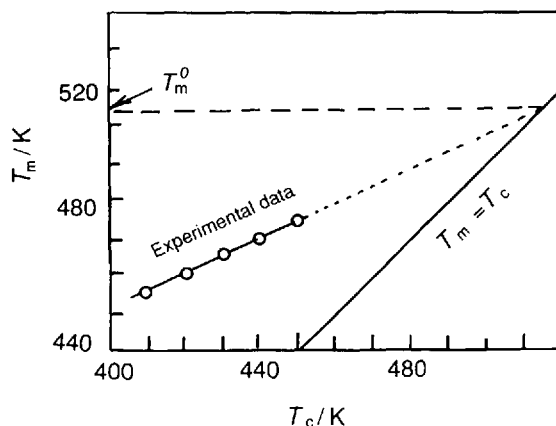


Figure 4.11 Schematic Hoffman–Weeks plots

X-ray diffractometry. The sample for an X-ray diffraction experiment is annealed under the same conditions as in DSC using an oil bath or heat oven because a large amount of the sample is necessary. Temperature-controlled systems equipped with an X-ray diffractometer can also be used (temperature-controlled sample holders ranging from liquid N_2 temperature to 700°C are commercially available). The measurement of T_m as a function of $1/l$ could follow the processes mentioned above. Additional steps are as follows:

1. Plot T_m as a function of $1/l$.
2. The melting point of the crystal of infinite l , T_m^0 , can be obtained by extrapolation to $1/l = 0$ in the equation

$$T_m = T_m^0 [1 - 2\sigma_e/[(\Delta H_f)l]] \quad (4.23)$$

The observed melting temperature T_m for a thin platelet is depressed below that of an infinite crystal by an amount $2\sigma_e/(\Delta H_f)$. This is equivalent to extrapolation to $T_m = T_c$, as mentioned above. As an example, T_m^0 of melt-crystallized polychlorotrifluoroethylene is estimated by extrapolation from the T_m versus $1/l$ plot as shown in Figure 4.12 and a value of 221.2°C was obtained. All the experiments should be conducted under N_2 gas. [18, 19]

4.2.3 Determination of Heats of Fusion and Crystallization of Polymers

The method involves the determination of the

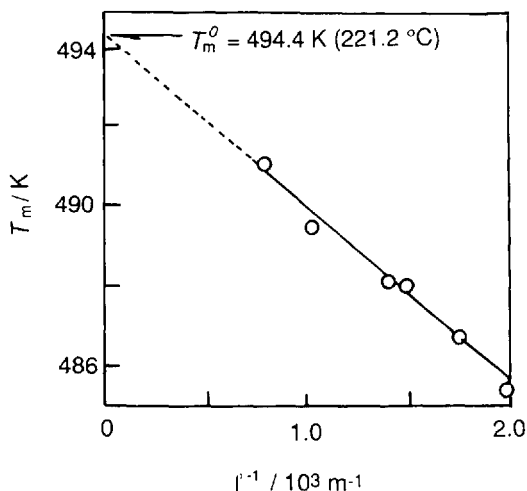


Figure 4.12 Plot of T_m as a function of $1/l$ for polychlorotrifluoroethylene

endotherm of fusion and exotherm of crystallization for polymers at a controlled heating or cooling rate in a controlled atmosphere by DSC. The data obtained are used in comparison with the results for standard materials measured under the same conditions. Experimental conditions, such as particle size of the sample, heating or cooling rate and pretreatment, influence the results. On this account, the experiment should be performed under the following conditions:

1. The size and shape of samples should be as follows: powder or granular form below 60 mesh; for thinner films, cut the disks to fit in the circular sample vessels; for molded or pelleted samples, cut the samples to fit the containers.
2. Before the measurement, maintain the sample for 24 h or more at temperature $23 \pm 2^\circ\text{C}$ and relative humidity $50 \pm 5\%$ for conditioning.
3. Weigh a container.
4. Weigh a homogeneous and representative sample of 5–10 mg to an accuracy of 0.01 mg, with a container.
5. Purge the sample holder with nitrogen (or other inert gas) at a flow rate of 50 ml min^{-1} .
6. (When computer-equipped apparatus is used, this step is not necessary; modern software shows curves on a reasonable scale automatically) Select appropriate x - and y -axis sensitivities to yield an area of $30\text{--}60 \text{ cm}^2$ under the fusion endotherm. If limited by the instrument, for certain sharp-melting materials, peak areas as small as $6\text{--}15 \text{ cm}^2$ may be used.
7. Heat the sample at a rate of $10^\circ\text{C min}^{-1}$ under a nitrogen atmosphere from ambient to 30°C above the melting point and maintain this temperature for 10 min to remove previous thermal history.
8. Cool to at least 50°C below the peak crystallization temperature at a rate of $10^\circ\text{C min}^{-1}$ and accumulate the data or record the cooling DSC curve. Use this curve for the calculation of heat of crystallization, ΔH_c .
9. After repeating procedures (6) and (7), measure and record the heating DSC curve at a heating rate of $10^\circ\text{C min}^{-1}$. Use this curve for the calculation of the heat of fusion, ΔH_f .
10. Choose a suitable standard material from those listed in Table 4.2, which has a first-order transition temperature nearest to that of the substance investigated, and measure the transition heat under the same conditions as mentioned above.
11. Calculate the heat of fusion and heat of crystallization as follows (using software, this process is carried out automatically when the

1. The size and shape of samples should be as follows: powder or granular form below 60 mesh; for thinner films, cut the disks to fit in the circular sample vessels; for molded or pelleted samples, cut the samples to fit the containers.
2. Before the measurement, maintain the sample for 24 h or more at temperature $23 \pm 2^\circ\text{C}$ and relative humidity $50 \pm 5\%$ for conditioning.

Table 4.2 Melting points and heats of fusion of standard materials

Standard materials	Melting point/ $^\circ\text{C}$	Heat of fusion/ kJ kg^{-1}
Benzzoic acid	122.4	142.04
Indium	156.4	28.45
Tin	231.9	59.50
Lead	327.4	22.92
Zinc	419.5	102.24

sample mass is given):

$$\Delta H = (AXY\Delta H_s m_s)/(mA_s X_s Y_s) \quad (4.24)$$

where ΔH is heat of fusion or crystallization of sample (kJ kg^{-1}), ΔH_s the heat of fusion or crystallization of the standard (kJ kg^{-1}), A the peak area of the sample (cm^2), A_s the peak area of the standard (cm^2), m the mass of the sample, (mg), m_s the mass of the standard (mg), Y the y -axis sensitivity of the sample (mW cm^{-1}), Y_s the Y -axis sensitivity of the standard (mW cm^{-1}), X the x -axis sensitivity (time base) of the sample (min cm^{-1}) and X_s the x -axis sensitivity (time base) of the standard (min cm^{-1}).

In order to measure the area of the fusion endotherm or crystallization exotherm (A and A_s), the following methods are used; (1) use a planimeter or (2) copy the peak of sample on to a known area, e.g. on graph paper, using a photocopying machine or by hand, cut off the peak using scissors, weigh the cut papers and calculate A and A_s . The average value of five measurements should be taken. Duplicate determinations of heats of fusion and crystallization on two specimens of the same sample by the same analyst or by different laboratories should not differ by more than 4.2 or 8.4 kJ kg^{-1} , respectively.

4.2.4 Melting Enthalpy of Perfect Polymer Crystals by DSC

The melting enthalpy of perfect polymer crystals, ΔH_f^0 , can be obtained using DSC and a hot stage equipped with a polarizing microscope, when the equilibrium melting point of the sample is known. The procedure for the measurement of ΔH_f^0 is recommended as follows:

1. The temperature and enthalpy of DSC should be calibrated following standard procedures. The temperature of the hot stage is calibrated by using a pure crystal with known melting temperatures.
2. Place a small piece of the film of crystalline polymer between two glass covers and melt the sample on a hot-plate.
3. Transfer the sample with the glass covers rapidly into the hot stage whose temperature

has been fixed at T_c . Isothermal crystallization of the sample is carried out in the hot stage.

4. Quench the sample to room temperature, cut it and then place a piece of the sample (about 8–10 mg) in the DSC pan.
5. Heat the sample and the melting enthalpy of the crystalline polymer can be measured from the DSC curves.
6. Repeat procedures (2)–(5) at various T_c 's.
7. Plot ΔH versus T_c and a straight line should be obtained.
8. By extrapolating T_c to T_m^0 of the polymer crystals, the melting enthalpy of the perfect polymer crystals can be obtained.

For the example, the melting enthalpy of isotactic polypropylene (iPP) was measured as a function of T_c . As shown in Figure 4.13, using the equilibrium melting point of iPP ($T_m^0 = 481 \text{ K}$), $\Delta H_f^0 = 148 \text{ J g}^{-1}$ was obtained.

4.2.5 Melting Enthalpy of Perfect Polymer Crystals by Solvent Dilution

The melting enthalpy of perfect polymeric crystals can be measured by DSC. When crystalline polymers absorb a small amount of the solvent, the equilibrium melting temperature of the pure polymeric crystals is depressed from T_m^0 to T_{mb}^0 :

$$1/T_{mb}^0 - 1/T_m^0 = R/\Delta H_f^0 V_1/V_2(\phi_2 - \chi\phi_2^2) \quad (4.25)$$

where T_{mb}^0 is the equilibrium melting temperature of the crystals sorbing the solvent, ΔH_f^0 is the melting enthalpy of perfect polymer crystals, $R = 8.314 \text{ J K}^{-1} \text{ mole}^{-1}$ is the gas constant, V_1 is the

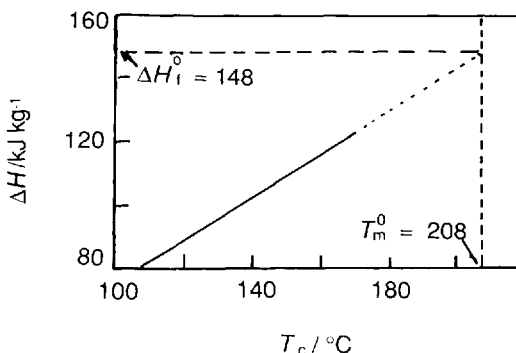


Figure 4.13 Equilibrium melting enthalpy of iPP [22]

molar volume of the crystallizable polymers, V_2 is the molar volume of the solvent, ϕ_2 is the volume fraction of the solvent absorbed, χ is the thermodynamic interaction parameter between the polymer and the solvent and T_{mb}^0 and T_m^0 can be measured by DSC as mentioned in Section 4.2.2. ΔH_f^0 values of several polymers have been measured using the above method [23].

4.2.6 Isothermal Crystallization of Polymers

DSC provides a rapid and sensitive evaluation of isothermal crystallization behavior. The sample of interest is annealed at a sufficiently high temperature for a period long enough to remove the previous thermal history. The sample is then rapidly cooled to the crystallization temperature, and the time period of exothermic crystallization is measured.

Crystallization behavior is affected by the temperature of crystallization, the nucleation properties of additives (such as dyes), the relative molecular mass distribution and co-existing monomers, etc. It is important to investigate the crystallization behavior of the polymers, since the properties of polymeric products, such as appearance, dimensional stability and thermal stability, are influenced by crystallization processes.

The temperature of isothermal crystallization of each polymer must be chosen taking into consideration the phase transition temperature of the particular polymer being studied. An example is shown using polyethylene with a melting point of 120 °C [24]. In this case, the following experimental conditions and procedure are used. A sample mass of 9.7 mg is used and the purge gas is nitrogen at a flow-rate of 50 ml min⁻¹. After a sufficient time has elapsed for the sample to be completely melted and annealed (nominally 10 min) at 155 °C, and the sample is cooled rapidly to the crystallization temperature, 127 °C. The crystallization process is observed as a function of time (Figure 4.14). The crystallization time is measured as the time elapsed from the onset of cooling to the peak of the crystallization time of 1.52 min.

Figure 4.15 shows the DSC curves of isothermal crystallization at different constant temperatures

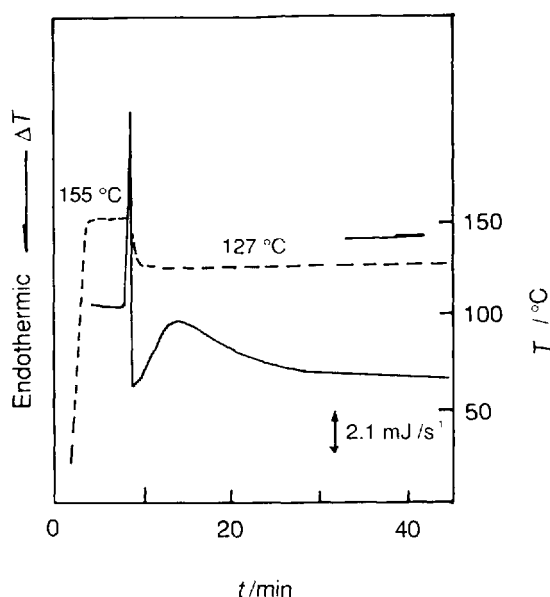


Figure 4.14 DSC curve for isothermal crystallization at 127 °C for polyethylene (sample mass 9.7 mg)

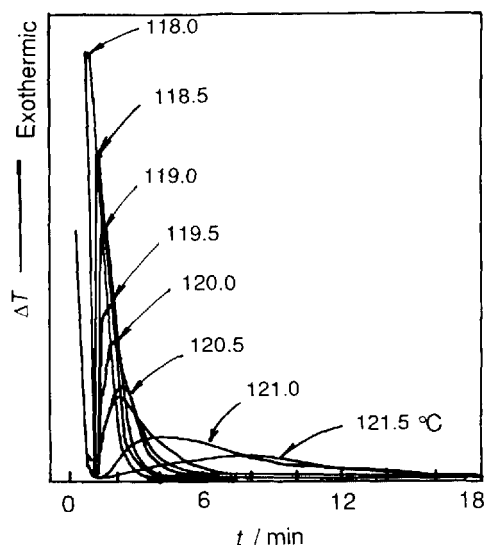


Figure 4.15 DSC curves for isothermal crystallization at different constant temperatures for HDPE. Sample mass, 5.4 mg; temperature lowered rapidly from 155 °C

for high-density polyethylene (HDPE) [25]. The time for crystallization to occur is closely dependent on the crystallization temperature, as shown in Figure 4.15.

In the temperature range 118.0–121.5 °C, the crystallization rate increases and the final

crystallization time decreases with decreasing crystallization temperature. From the experimental results it can be seen that a difference in crystallization temperature of 0.5 °C leads to an obvious change in crystallization rate. This indicates that the crystallization temperature should be strictly controlled in isothermal conditions.

4.2.7 Determination of Isothermal Crystallization Rate by DSC [26]

The isothermal crystallization rate for polymers can be determined by DSC. The experimental procedure is given below, using polypropylene samples as an example.

1. Place the sample in a sample vessel and dry it for about 1 day under a pressure of approximately 10 Pa.
2. Weigh the dried sample and seal the container.
3. Place the sample container in the sample holder of the DSC apparatus and heat the sample at a certain rate to a temperature above its melting point, e.g. heat the sample at 80 °C min⁻¹ to 230 °C.
4. Maintain the final temperature for 5 min or more in order to allow the sample to melt completely.
5. Allow the sample to cool at the same rate as that of heating, to the estimated crystalline temperature (115–135 °C).
6. Maintain the crystalline temperature, and obtain an isothermal crystallization DSC curve as shown in Figure 4.16.

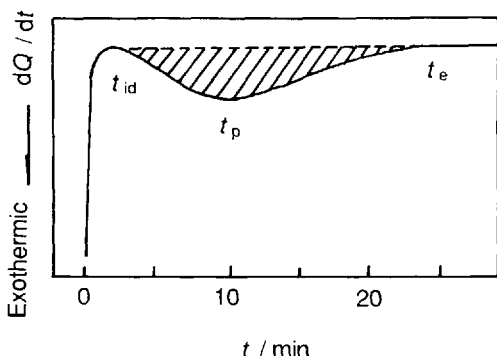


Figure 4.16 DSC curve for isothermal crystallization

If the crystallinity is supposed to be independent of the crystallization time, i.e. the heat given by per unit of crystal remains constant, the crystallinity of the sample can then be evaluated from the crystallization heat. The fraction of the uncrystallized sample, θ , at time t (min) can be expressed as

$$1 - \theta = \left[\int_0^t (dH_c/dt) dt \right] / \left[\int_0^{t_c} (dH_c/dt) dt \right] \quad (4.26)$$

where the crystallization heat, $\Delta H_c(t)$, is obtained from the area enclosed by the DSC curve in the time range 0– t (min).

The relationship between θ , and $\log t$ can be established from Figure 4.16 and equation (4.26) (isothermal crystallization curve). Generally, θ may be expressed as a function of t according to the Avrami equation:

$$\theta = \exp(-kt^n) \quad (4.27)$$

where k is the crystallization rate constant and n is the time exponent, depending on the nucleation mechanism and the nuclei growth geometry for the crystalline center; for the calculation of n , see Ref. 26.

4.2.8 Measurement of Heat of Isothermal Crystallization [26]

The isothermal crystallization heat of a polymer can be measured by DSC according to the following procedures.

4.2.8.1 Apparatus Constant Determination

1. Place two empty sample vessels in both the sample and reference holders.
2. Perform a heating run in the temperature range m.p. ± 40 °C, where m.p. is the melting point of a known pure substance (generally In).
3. The slope of the baseline should be adjusted.
4. Pack the pure substance in the sample vessel and heat it under the same conditions as in step (2), to measure the melting peak.
5. Calculate the apparatus constant using the equation

$$k = (\Delta H W_s S_s) / RA \quad (2.28)$$

where W_s is the mass of the pure substance (mg), S_s the chart paper speed (cm s^{-1}), R the response from the apparatus ($\text{mJ s}^{-1} \text{cm}^{-1}$), A the peak area (cm^2) and ΔH the transition enthalpy for the pure substance (mJ g^{-1}).

Modern apparatus normally performs the above procedure automatically. Even if the k value is included in the software provided, it is recommended to confirm the value in a certain time interval.

4.2.8.2 Measurement of Heat of Crystallization

The procedure for measuring the heat of isothermal crystallization is as described in Section 4.2.7.

As can be seen from Figure 4.17, t_{id} is the time when the crystal becomes observable, i.e. the induction period, t_p is the time of the maximum crystallization rate and t_e is the time when the crystallization is completed. It should be noted that sometimes t_e is difficult to determine if subordinate crystallization takes place. When a polymer has an extremely low subordinate crystallization rate, such as polypropylene, t_e is easily determined. In the hatched area in Figure 4.17, which is enclosed by the curve and the baseline to A' , the crystallization heat is as follows:

$$\Delta 2H_c = \frac{kR'A'}{W_s S_s} \quad (4.29)$$

where k is the apparatus constant obtained from equation (4.28), R the response of the DSC instrument during sample measurement ($\text{mJ s}^{-1} \text{cm}^{-1}$),

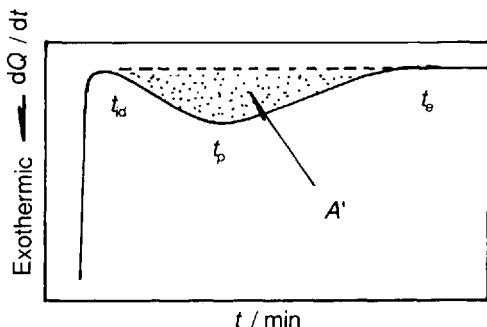


Figure 4.17 DSC curve for isothermal crystallization

W_s the mass of the dry sample (mg) and S_s the chart paper speed (cm s^{-1}). When calculation is made by computer, move the pointer carefully in order to choose the points t_{id} and t_e .

4.2.9 Transition Regions of Polymers Melt-crystallized Isothermally

When a polymer is isothermally crystallized from a subcooled melt at different T_c , transitions from regions I to II to III should be expected on increasing the ratio between the surface nucleation rate and the rate of spreading of the secondary nucleus on the substrate. The transitions of the regions and lateral and fold surface free energies of the developing crystals can be measured from the relationship between the linear growth rate of the spherulites, G , and the degree of undercooling:

$$\log G = C_1 - U^*/R(T_c - T_\infty) - K_g/fT_c\Delta T \quad (4.30)$$

where C_1 is a constant, T_c is the crystallization temperature, R is the gas constant, $T_0 = (T_g - 30) \text{ K}$, $f = 2T_c/(T_m^0 + T_c)$ is a correction factor for the temperature dependence of the enthalpy of fusion and $\Delta T = T_m^0 - T_c$ is the degree of supercooling.

Plotting $\log G + U^*/R(T_c - T_0)$ against $1/fT_c\Delta T$, straight lines result. As an example, the result for isotactic polypropylene is shown in Figure 4.18. According to the nucleation theories of melt-crystallized polymer developed at different

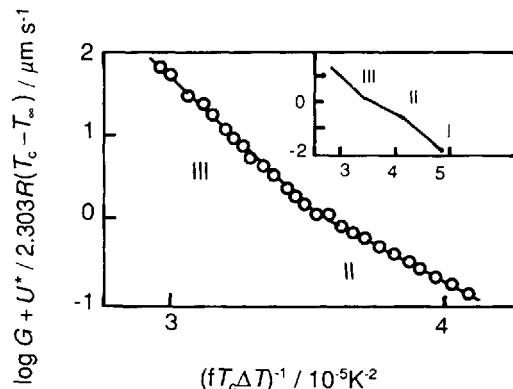


Figure 4.18 Plot of kinetic data for polypropylene according to equation (4.30)

degrees of undercooling, the curve should consist of three straight lines with the ratio of the slopes $K_{gI} : K_{gII} : K_{gIII} = 2 : 1 : 2$. $K_{gIII} = 7.28 \times 10^5 \text{ K}^2$, $K_{gII} = 3.68 \times 10^3 \text{ K}^2$ and $K_{gIII}/K_{gII} = 1.99$ can be calculated from Figure 4.18. The parameters for isotactic polypropylene were chosen as follows: $T_g = 252 \text{ K}$, $T_m^0 = 418 \text{ K}$ and $U^* = 6270 \text{ J mol}^{-1}$. Because there is a relationship among Avrami parameters, n , k and linear growth rate G :

$$G \propto k^{1/n} \quad (4.31)$$

$\log G$ in equation (4.30) could be substituted by the term $(1/n) \log k$. The slopes of the straight lines will not be changed. The measurement methods for G , k and n have been described in the sections mentioned above [27].

4.2.10 Surface Free Energies of Developing Polymer Crystals During Isothermal Crystallization

The lateral and fold surface free energies of the developing crystals during the isothermal crystallization of polymers, σ and σ_e , can be measured by DSC and/or polarizing optical microscopy according to the equation

$$K_g = C\sigma\sigma_e b_0 T_m^0 / K\Delta H_f^0 \quad (4.32)$$

where K_g is a constant related to crystallization regions for the same polymer, C is a parameter characteristic of the growth region ($C = 2$ in region II and 4 in regions I and III), b_0 is the layer thickness of the folded chain, T_m^0 is the thermodynamic equilibrium melting point of the polymer, K is Boltzmann's constant, ΔH_f^0 is the melting enthalpy of the perfect crystal and σ and σ_e are the lateral and fold surface free energies, respectively. The methods for the determination of the parameters K_g , ΔH_f^0 and T_m^0 have been described in Sections 4.2.2 and 4.2.4. The lateral surface free energy of the developing crystal, σ , can be calculated in terms of the Thomas–Staveley equation [28]:

$$\sigma = \beta \Delta H_f^0 A_0^{1/2} \quad (4.33)$$

where A_0 is the cross-sectional area of a chain in the polymeric crystal and β is a constant; $\beta = 0.1$ for polyalkenes and 0.24 for polyesters according

to Marand and Hoffman [29]. The fold surface free energy of the developing crystals, σ_e , can be calculated using the equation (4.32).

As an example, the σ_e of polypropylene has been determined as 0.122 J m^{-2} . The chosen parameters for isotactic polypropylene are as follows: $T_m^0 = 481 \text{ K}$, $b_0 = 6.56 \times 10^{-10} \text{ m}$, $A_0 \approx b_0^2$, $\Delta H_f^0 = 1.48 \times 10^8 \text{ J m}^{-3}$, $\sigma = 9.2 \times 10^{-3} \text{ J m}^{-2}$, $k = 1.38 \times 10^{-23} \text{ J K}^{-1}$ and $C = 2$ in region II and in regions I and III [30, 31]. The experimental procedure is the same as that described in Section 4.2.7.

4.2.11 Transport Activation Energy of Polymer Segments During Isothermal Crystallization Measured by DSC and Polarizing Optical Microscopy

The crystallization kinetics of heat polymers are governed by the energy barriers that must be overcome to form a critical nucleus on the crystal surface, ΔF^* , and to activate the transport of the segments across the solid–liquid interface, U^* . The accepted expression for the radial growth rate is

$$G = G_0 \exp(-U^*/RT) \exp(-\Delta F^*/kT) \quad (4.34)$$

where G_0 is a pre-exponential factor, R is the gas constant and k is Boltzmann's constant. It can be easily deduced that the growth rate of the spherulites is diffusion controlled at high undercooling and equation (4.34) can be simplified approximately as

$$G = G_0 \exp[-U^*/R(T_c - T_\infty)] \quad (4.35)$$

where T_c is the isothermal crystallization temperature and $T_\infty = T_g - 55$, T_g being the glass transition temperature of the polymer. By plotting $\log G$ against $1/(T_c - T_\infty)$, the transport activation energy of the polymer segments, U^* , can be calculated from the slope of the straight lines.

As an example, U^* of pure PEEK with different relative molecular mass measured by means of DSC is shown in Figure 4.19. The values of U^* ranged from 19.3 to 117.3 kJ mol^{-1} .

These results were measured by means of DSC. The relationship among Avrami parameters, k , n

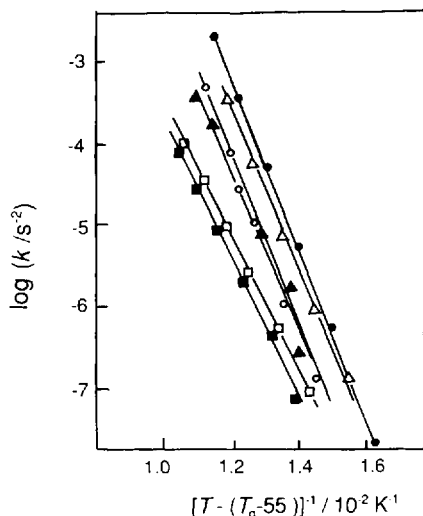


Figure 4.19 Plots of $\log k$ against $1/(T - T_\infty)$ for PEEK with different relative molecular mass [32]: molecular mass $M_w = (\bullet)$ 8300, (Δ) 18 000, (\circ) 135 000, (\blacktriangle) 32 000, (\square) 79 500, (\blacksquare) 55 500

and G is

$$G \propto (1/n) \log k \quad (4.36)$$

The experimental procedure for the measurement of n , k and G by DSC is the same as in Section 4.2.9. When a polarizing optical microscope is used, U^* measurement is effected as follows:

1. Calibrate the temperature scales following the standard procedure.
2. Place about 5 mg of sample powder or film between two glass covers.
3. Melt the sample on a hot-plate whose temperature is maintained over the T_m^0 of the polymer crystals, forming a homogeneous molten film.
4. Quench the sample in liquid nitrogen, obtaining a glassy polymeric film.
5. Place the sample in the hot stage whose temperature has been fixed at T_c , with $T_g < T_c < T_m$.
6. Monitor the radii of the spherulites as a function of crystallization time at T_c by using a polarizing optical microscope.
7. Measure the growth rate of the spherulites from the slope of the plot of radii of the spherulites against crystallization time.
8. Measure the glass transition temperature of the polymer by using DSC.
9. Plot $\log G$ against $1/(T_c - T_\infty)$, then U^* can be calculated from the slope of the straight lines.

4.2.12 Growth Rate of Polymer Spherulites Crystallized Isothermally from the Melt by Polarizing Optical Microscopy

The growth rate of polymer spherulites crystallized isothermally from the melt, G , can be measured by a polarizing optical microscope with a hot-stage. The crystallization temperature, T_c , was controlled by the hot-stage. The following procedure is recommended for the measurement of the spherulitic growth rate of polymers crystallized from the melt:

1. Calibrate the temperature of the hot-stage by using crystals, the melting points of which are known.
2. Maintain the temperature of the hot-stage fixed at T_c .
3. Place some powder or film of the sample between two glass covers.
4. Heat the sample on a hot-plate whose temperature is higher than that of the equilibrium melting point of the crystals. A homogeneous melt is obtained between the glass covers.
5. Transfer the molten sample to a glass slide that has been kept in the chamber of the hot stage of the microscope at T_c .
6. Monitor the radius of the spherulite, R , using a polarizing optical microscope, as a function of crystallization time, t .
7. The slope, dR/dt of the straight lines is the growth rate of the spherulites.

Plots of the growth rate of the spherulite versus crystallization temperatures, T_c , or degree of undercooling, ΔT , are shown in Figure 4.20.

Note that in order to monitor the radius of the spherulites (step 6), an ordinary camera or a video camera equipped with a light microscope is generally used. When a video camera is used, the size of the spherulites can easily be analyzed using a computer. Image analysis software is useful. Photographs taken as a function of times are also used. Monitoring can also be carried out by the standard method, i.e. a scale tip is inserted into the lens system and the size of spherulites can be read directly using a stop watch or digital timer.

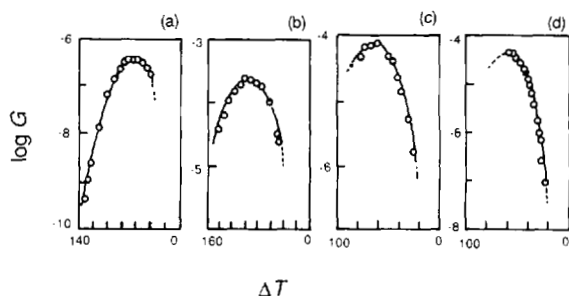


Figure 4.20 Plots of growth rate of the spherulite versus degree of undercooling, ΔT , under isothermal conditions [38]. (a) Isotactic polystyrene; (b) nylon 6; (c) polyoxypropylene; (d) polychlorotrifluoroethylene

4.2.13 Overall Kinetic Parameters of Polymers Crystallized Isothermally from the Melt

The overall kinetic parameters of polymers crystallized isothermally from the melt can be measured by DSC. The overall crystallization kinetics follow the Avrami equation:

$$\log \{-\ln[1 - \alpha(t)]\} = \log k + n \log t \quad (4.37)$$

where n , the Avrami index, and k , the kinetic rate constant depend on the nucleation and growth mechanism of the crystals. The experimental procedure has been described in Section 4.2.6. Both the relative degree of crystallinity $\alpha(t)$ and time t can be measured by analysis of the DSC curves of the polymer crystallized isothermally. Plots of $\log \{-\ln[1 - \alpha(t)]\}$ versus t are linear.

As an example, the experimental results are shown in Figure 4.21 and the values of n and k determined from the intercepts and slopes of these straight lines are given in Table 4.3 for polypropylene, a homopolymer (PP 1300). The n values vary between 2.2 and 2.4 almost irrespective of T_c .

4.2.14 Overall Growth Rate of Polymer Spherulites Crystallized from the Subcooled Melt

The overall growth rate of the spherulites of polymers crystallized from the melt under isothermal conditions can be measured by means

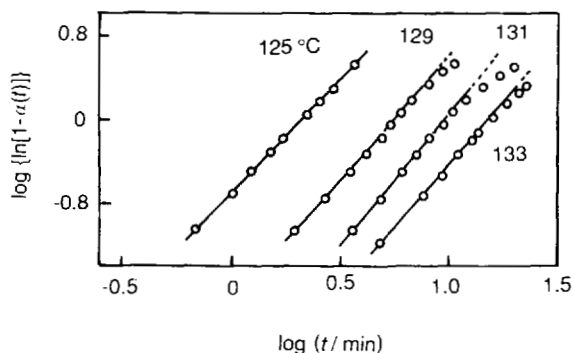


Figure 4.21 Plots of $\log \{-\ln[1 - \alpha(t)]\}$ against $\log t$ for isothermal crystallization of polypropylene [34]

Table 4.3 The Avrami parameters, n and k of polypropylene crystallized isothermally at various temperatures

$T_c / ^\circ\text{C}$	n	k / s^{-n}
133	2.3	1.7×10^{-2}
131	2.4	3.6×10^{-3}
129	2.3	1.9×10^{-2}
125	2.2	1.9×10^{-1}

of DSC. As mentioned above, the growth rate of a single spherulite can be determined using a polarizing optical microscope. However, DSC was used to measure the overall growth rate of the spherulites. In other words, the growth rate of the spherulites measured by DSC is the average value for the total spherulites in the sample. Good agreement between the two kinds of methods has been observed.

The equation commonly used to describe the linear growth kinetics is

$$G = G_0 \exp[-U^*/R(T_c - T_\infty)] \exp[-K_g/T_c(\Delta T)f] \quad (4.38)$$

where U^* is the activation energy for transport of the segments to the crystal front through the subcooled melt, $T_\infty = T_g - 50$, T_g is the glass transition temperature of the polymer, T_c is the crystallization temperature, $\Delta T = T_m^0 - T_c$ is the degree of undercooling, f is a correction factor for the temperature dependence of the enthalpy of fusion and can be expressed as $f = 2T_c/(T_m^0 + T_c)$, the factor K_g depends on the growth region and is related to the free energies of the developing

crystal, T_m^0 is the equilibrium melting point of the polymer and G_0 depends on the crystallization region. Some data on G_0 are given in Table 4.4 and they are suitable for nucleation controlling crystallization.

Usually, the measurement of the relative values of G is sufficient to evaluate the overall crystallization behavior and free energies under isothermal conditions. According to nucleation theories, a simple relationship between the linear growth rate of the spherulite, G , and the Avrami parameters n and k is

$$G = k^{1/n} \quad \text{or} \quad \log G = C_1 + (1/n)\log k \quad (4.39)$$

where C_1 is a constant. The parameters n and k can be determined by means of DSC as described in Section 4.2.13.

As an example, the plots of $(1/n)\ln K + U^*/[R(T_c - T_\infty)]$ versus $1/fT_c\Delta T$ for polypropylene and its composites are shown in Figure 4.22 [34].

4.2.15 Determination of Crystallinity of Polymers (Dynamic Heating Method)

The degree of crystallinity of a polymer affects a variety of physical properties, such as storage modulus, permeability, density and melting point. DSC provides a rapid method for determining polymer crystallinity based on the heat required to melt the polymer. This heat is reported as percentage crystallinity ratioed against the heat of fusion of a 100% crystalline sample of the same material. The heat of fusion

of a sample whose crystallinity is known is also used in order to obtain relative values.

The degree of crystallinity is calculated using the equation

$$\text{crystallinity}(\%) = (\Delta H_{\text{sample}}/\Delta H_{\text{std}}) \times 100\% \quad (4.40)$$

where ΔH is the heat of fusion of sample (J g^{-1}) and ΔH_{std} is the heat of fusion of 100% crystalline material (J g^{-1}).

A polyethylene sample analyzed over the temperature range from ambient to 180°C is shown in Figure 4.23 as an example. The value used here, 290 J g^{-1} , is the average value taken

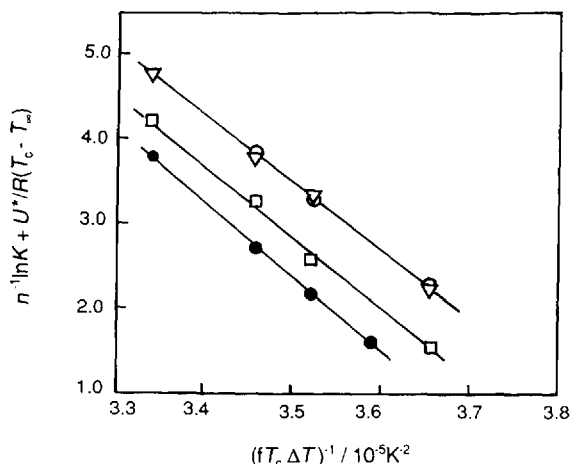


Figure 4.22 Plots of $n^{-1} \ln K + U^*/[R(T_c - T_\infty)]$ versus $(fT_c\Delta T)^{-1}$ for polypropylene (●), PP filled with La_2O_3 (□), PP filled with Y_2O_3 (▽), PP filled with mixture of rare earth oxides (○)

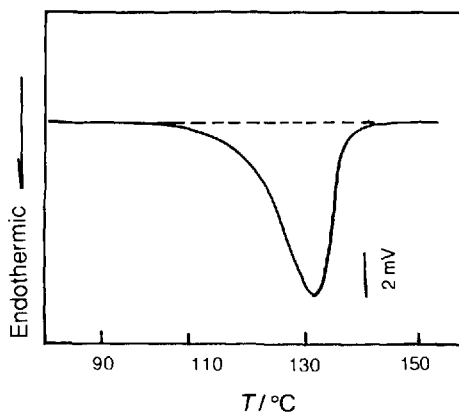


Figure 4.23 DSC melting curve of polyethylene [36] heating rate 5°C min^{-1} , nitrogen atmosphere)

Table 4.4 G_0 , T_g and T_m^0 of polymers with growth rate in a narrow temperature range [35].

Polymer	$G_0/\text{cm s}^{-1}$	T_m^0/K	T_g/K
<i>trans</i> -1,4-Polyisoprene	1.10×10^3	360.2	211
Poly(oxyethylene)	1.28×10^3	459.2	213
Polyethylene (spherulite)	2.24×10^3	417.8	231
Polyethylene (axialites)	4.40×10^9	417.8	231
Polyoxyethylene	1.15×10^5	348.4	206
Poly-1-butene (form II)	2.49	401	219
Selenium	4.58	492.4	300

from the literature and has a relative standard deviation of 5.2%.

4.2.16 Determination of Crystallinity of Polymers (Isothermal Crystallization Method)

The degree of crystallinity of polymers crystallized isothermally from the melt can be measured by DSC. The experimental procedure is described in Section 4.2.6. The relative degree of crystallinity $\alpha(t) = 1 - \theta$ was analyzed according to the usual procedure using equation (4.41).

The absolute degree of crystallinity of a polymer mixed with a non-crystallizable component was evaluated from the heat evolved during crystallization by using the relationship

$$\alpha(t) = \left[\int_0^t (dH/dt) dt \right] / [(1 - \phi)\Delta H_f^0] \quad (4.41)$$

where ΔH_f^0 is the heat of fusion for 100% crystalline polymer and ϕ the mass fraction of the non-crystallizable component in the mixture. When $\phi = 0$, $\alpha(t)$ is the degree of crystallinity of the polymer in its pure state.

As an example, the relative degree of crystallinity of pure isotactic polypropylene (PP) is shown in Figure 4.24 as a plot $\alpha(t)$ against time t . The isotactic PP sample, (PP 1300, obtained from Yanshan Petrochemical, Beijing, China) has a

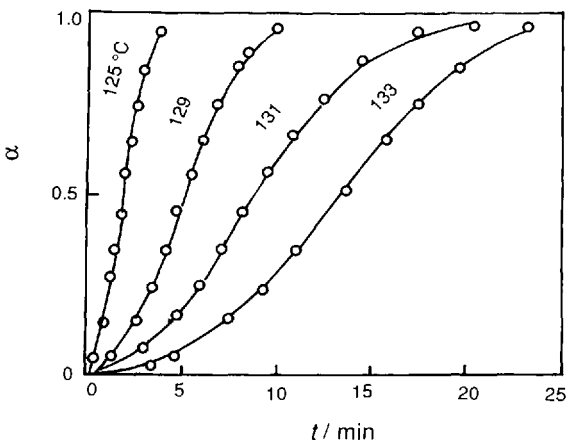


Figure 4.24 Development of relative degree of crystallinity with time for isothermal crystallization of isotactic PP [34]

melt flow-rate of 1.2 g per 10 min and a density of 0.91 g ml^{-1} at 25°C . The crystallization temperature, T_c , is indicated in Figure 4.24.

4.2.17 Crystallinity of Poly(ethylene terephthalate) (PET) Molded Under Different Conditions [37]

The properties of polymeric products vary with the conditions of processing. Whether the products are in the form of fiber, film or sheet, molecular orientation resulting from stretching increases the strength in an oriented direction. Molding methods and the processing conditions can be assessed by characterizing these polymeric materials using DSC.

Poly(ethylene terephthalate) (PET) is cited as an example. The DSC curve for melt-molded PET (Figure 4.25, curve I) exhibits a deviation from

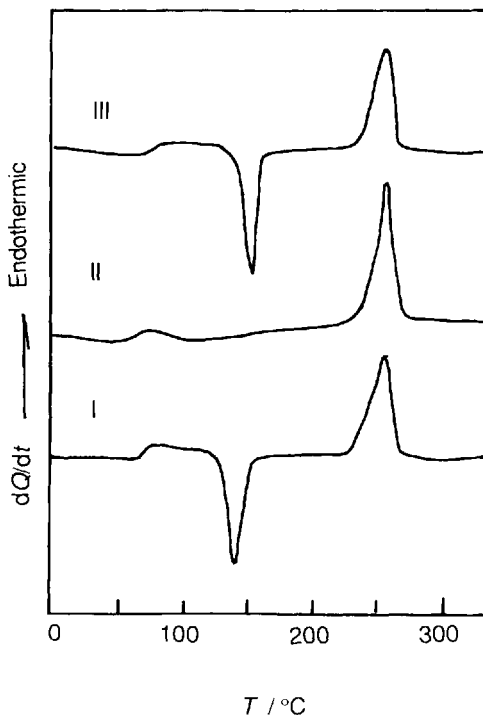


Figure 4.25 DSC curves for PET samples having various thermal histories. I, Melt-molded PET sample; II, double-stretcher formed PET sample; III, stretcher formed PET quenched from the molten state. Sample mass, 16mg; Heating rate, $10^\circ\text{C min}^{-1}$

the baseline due to glass transition and an exothermic peak due to the cold crystallization. Curve I shows that the sample is amorphous. When PET film is formed using a double stretcher, the deviation from baseline caused by the glass transition decreases and the cold crystallization peak disappears, as shown in curve II in Figure 4.25, indicating that the amorphous part is reorganized as a crystalline structure during the stretching process. When stretched PET is quenched to 0 °C from the molten state, glass transition and cold crystallization in the DSC curve appear once again, indicating that no crystallization occurs during rapid cooling and that the most frozen part of the sample remains in an amorphous state.

4.2.18 Density, Melting Temperature and Degree of Crystallinity of Polyethylene [38]

There are two types of polyethylene (PE): low density (LDPE) and high density (HDPE). The density of both types of PE is in the range 0.92–0.96 g cm⁻³. Figure 4.26 shows the DSC melting curves of (a) LDPE and (b) HDPE. Table 4.5 lists the density values. It can be seen that both the melting peak temperature and the heat of melting increase with increasing density. Good linearity between the heat of melting and density is observed, as shown in Figure 4.27.

The melting point and heat of melting of perfectly crystalline PE were reported to be 142 °C and 286.7 mJ mg⁻¹, respectively (the values may vary according to the literature). The degree of crystallinity for the sample can be evaluated from the ratio of the melting heat of the sample to the perfectly crystalline PE, as shown in Table 4.5.

4.2.19 Multiple Melting Peaks of Polyethylene [39]

The profile of the DSC curves for the melting of crystalline polymers is closely related to the conditions under which the crystal formed. For example, heat polyethylene to 120 °C and maintain it for a definite period of time. After the sample has completely melted, allow it to cool to

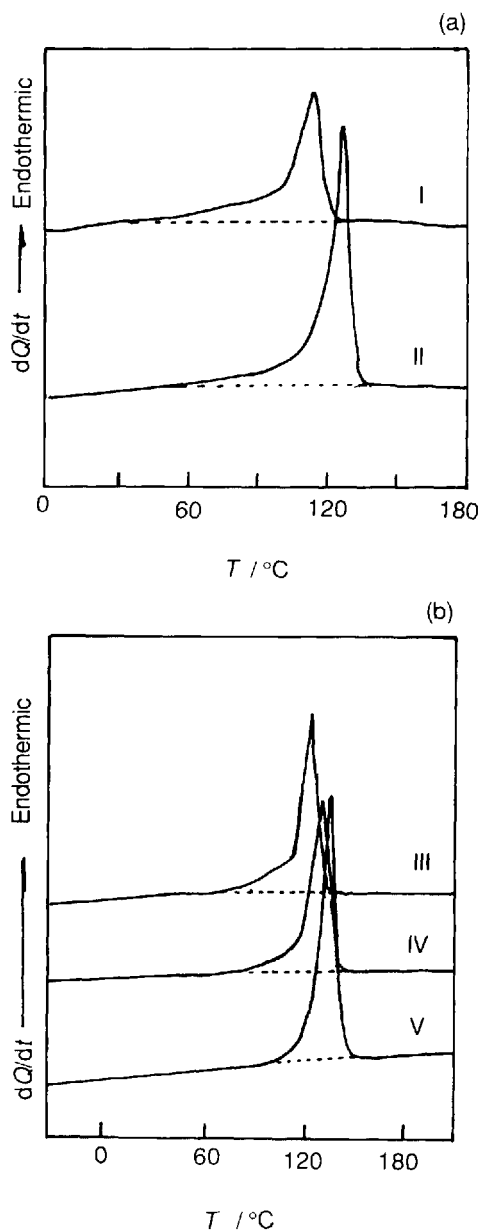


Figure 4.26 DSC melting curves for (a) LDPE and (b) HDPE. For I–IV see Table 4–5 Sample Mass, 10 mg; heating rate, 10 °C min⁻¹

110 °C. Maintain this temperature for 2 minutes, followed by rapid cooling to room temperature. Repeatedly treat the sample in the same way for several cycles, reducing the maximum temperature progressively by 5 °C in each cycle. The heating DSC curve for a sample subjected to such

a series of annealing cycles at successively lower temperatures exhibits multiple melting peaks, as shown in Figure 4.28, corresponding to the respective cycles. In other words, for PE, the melting process can clearly reveal the thermal history during the crystallization process.

4.2.20 Polymorphism of Dotriacontane

Long-chain hydrocarbons usually exhibit polymorphism depending on their thermal history. It is known that polymorphism plays an important role in the efficiency of pharmaceuticals and DSC is used for quality control. Figure 4.29 shows DSC heating curves of dotriacontane having a variety of thermal histories. The experimental conditions are as follows: sample mass, 0.1 mg;

heating rate, $0.5^{\circ}\text{C min}^{-1}$; cooling rate (after melting), $0.05, 0.5, 1.0$ and $10^{\circ}\text{C min}^{-1}$.

As shown in Figure 4.29, two peaks are observed on curve 1 and three peaks on each of curves II–V. The peaks are assigned as crystals A, B and C from the low to high temperature. The plots of the transition heats against the cooling rates for the respective samples are shown in Figure 4.30. It can be seen that the heat of transition of the A-type crystal increases with increasing cooling rate. In contrast, the heat of transition of the B-type crystal decreases with increasing cooling rate. This suggests that both A- and B-type crystals are thermodynamically quasi-stable.

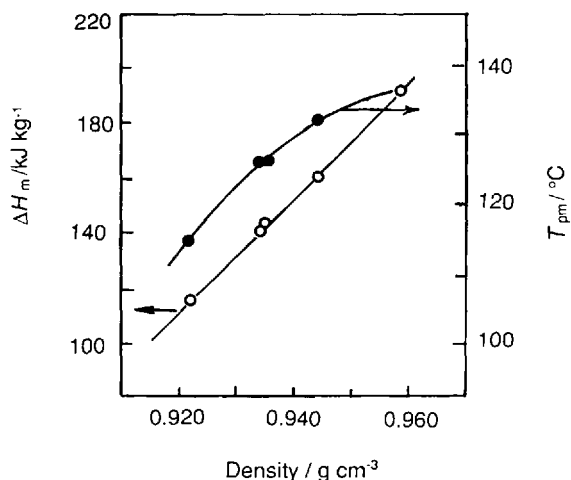


Figure 4.27 Relationship between heat of melting, peak temperature and density of PE

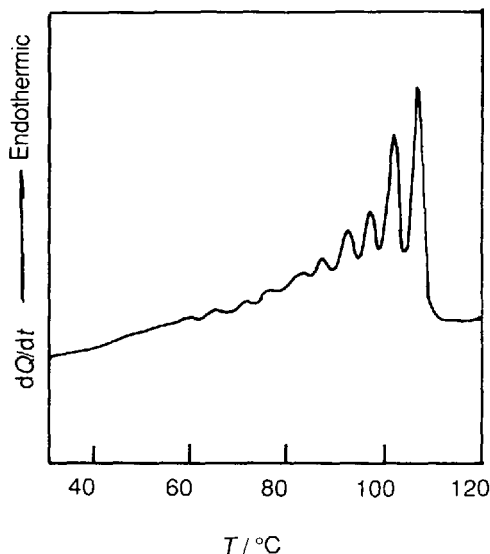


Figure 4.28 Multiple melting peaks on the DSC curve for a PE sample treated by a series of annealing cycles at successively lower temperatures [40]. Sample Mass, 10 mg; heating rate, $10^{\circ}\text{C min}^{-1}$; atmosphere, N_2

Table 4.5 Melting properties and degree of crystallinity for PE with different densities [38]

Sample No.	Density g cm^{-3}	Melting heat mJ mg^{-1}	Peak temperature $^{\circ}\text{C}$	Degree of crystallinity %
I	0.922	116.6	114.7	40.7
II	0.934	141.0	126.4	49.2
III	0.935	144.7	126.4	50.5
IV	0.944	160.0	132.2	55.8
V	0.958	191.8	137.0	66.9

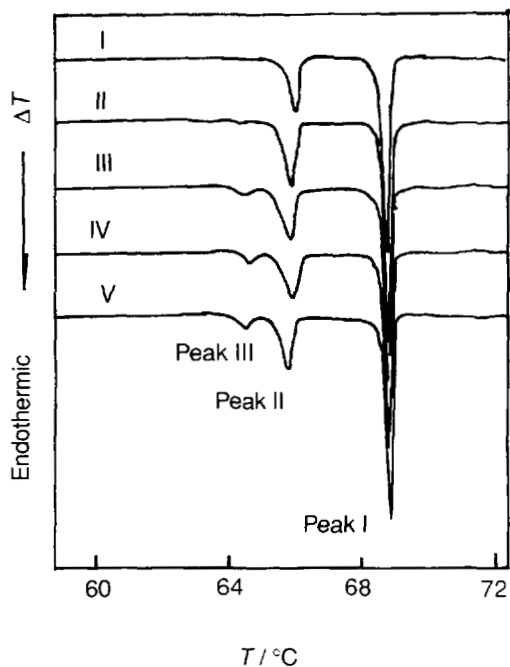


Figure 4.29 Heating DSC curves for dotriacontane cooled at various scanning rates [41]. I, Original sample not subjected to melting; II–V, the sample cooled at 0.05, III 0.5, IV 1.0 and V $10\text{ }^{\circ}\text{C min}^{-1}$

4.2.21 Thermotropic Liquid Crystals

There are some materials that exhibit more than one transition in changing from the solid to the liquid state. The molecular ordering in these mesophases lies between that of a solid and that of an isotropic liquid. This kind of material is known as a 'liquid crystal.' Liquid crystals show physical properties in both the solid and liquid states. There are two types of liquid crystal: one is lyotropic, whose phase transition is caused by changing the concentration or pH value of the solution, and the other is thermotropic, whose phase transition occurs on changing the temperature.

There is a large variety of thermotropic liquid crystals, and generally each of them may exhibit several mesophases as the temperature changes. The transition behavior of these mesophases is complex. DSC and DTA methods are particularly suitable for the detection and study of the mesophase.

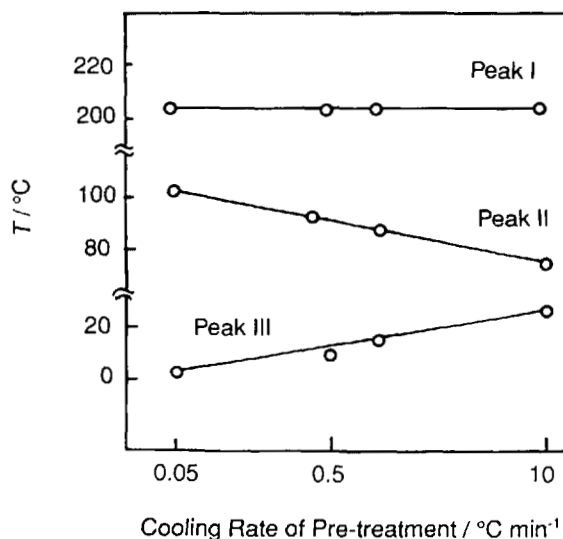


Figure 4.30 Relationship between heat of transition and cooling rate of pretreated dotriacontane

Figure 4.31 presents the DSC curves of di-4'-heptoxybenzal-1,4-phenylenediamine (HEPI-OBPD) [40]. The heating curve shows eight endothermic peaks corresponding to the following phase transitions: $C_4 \rightarrow C_3$ (peak 2); $C_3 \rightarrow C_2 \rightarrow C_1$ (peak 3); $C_1 \rightarrow S_K$ (peak 4); $S_K \rightarrow S_I$ (peak 5); $S_I \rightarrow S_1$ (peak 6); $S_1 \rightarrow S_C$ (peak 7); $S_C \rightarrow N$ (peak 8); and $N \rightarrow I$ (peak 9), where C, S, N, and I represent the crystal, smectic, nematic and isotropic phase, respectively. Only one peak

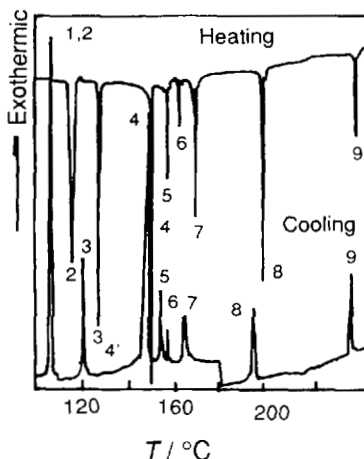


Figure 4.31 DSC curves for di-4'-heptoxybenzal-1,4-phenylenediamine [43]

(peak 3) is observed for the transitions $C_3 \rightarrow C_2$ and $C_2 \rightarrow C_1$ on the heating curve, which is, however, resolved into two peaks on the cooling curve. As the phase transitions for liquid crystalline materials usually occur continuously in such a narrow temperature range, raising the instrument resolution, using less sample mass and carrying out both heating and cooling scans are necessary to improve the results. Generally, except in the phase which is closest to the crystal transition, there is no significant supercooling for the other phase transitions.

X-ray diffractometry, polarization microscopy and mixture testing† are important in the identification of mesophases of liquid crystals; while DSC and DTA are the most valuable aids in revealing and confirming phase transition. Simultaneous polarization microscopy–DSC instruments are now commercially available.

DSC peak area (i.e. transition enthalpy) can be used, to some extent, to identify the mesophase near the transition temperature. Many studies have showed that the transition enthalpy (kJ mol^{-1}) for $N \rightarrow I$, for example, is 0.08–9.6; $S_A \rightarrow I$, 3–13; $S_C \rightarrow I$, 10–43; $S_A \rightarrow N$, 0.2–4.6; $S_C \rightarrow N$, 0.7–9.6; $S_B \rightarrow S_A$, 0.4–4.6; $S_B \rightarrow S_C$, 1.8–10; $S_C \rightarrow S_A$, 0.04–2.8; $S_F \rightarrow S_C$, 0.2–0.5; and so on. The melting enthalpy for crystals is usually higher than that for liquid crystals by at least 10–100-fold. A highly sensitive and reliable instrument is therefore necessary in order to observe calorimetrically the phase transition for liquid crystals.

4.2.22 Thermotropic Polymeric Liquid Crystals

Polymeric liquid crystals can be classified into either of two types, thermotropic and lyotropic, according to their formation conditions, or three types, main-chain, side-chain and complex liquid crystalline polymer (MCLCP, SCLCP and CLCP,

respectively), according to the location of the mesogenic moiety. DSC is the main technique used for thermal analysis of polymeric liquid crystals [43–45].

4.2.22.1 Temperature Region of Liquid Crystals

Liquid crystallinity is mainly exhibited in the following two temperature regions: (1) from T_g (glass transition temperature) to T_i (isotropic transition temperature, also known as the ‘clearing point’); (2) from T_m (melting point) to T_i , where several mesophases can usually be observed. Like ordinary polymers, the transition behavior of liquid polymers is also dependent on their thermal history and relative molecular mass. Therefore, only the samples with sufficient molecular mass and the same thermal history are suitable for the purpose of comparison and study. The transition temperatures for these substances rise with increase in the relative molecular mass, but remain approximately constant when the latter is more than 10 000. The transition heat shows a similar tendency. In addition, the transition entropy from mesophase to isotropic, ΔS_{1i} , is related to the order parameters.

4.2.22.2 Main-chain Liquid Crystalline Polymer

The transition temperature and transition heat for polyester MCLCP vary with the thermal treatment conditions. By changing the sample mass, heating rate and thermal treatment conditions, satisfactory results from DSC measurement for the rigid-rod MCLCP are usually obtainable. In some cases, self-polycondensation of polyesters proceeds continuously on thermal treatment by DSC. Thus, the relative molecular mass increases and a closer packed structure is obtained, resulting in more evident transition peaks. As the transition peaks on the DSC curve for the rigid-rod MCLCP are relatively small, careful inspection is necessary for their identification. When the sample is annealed at a temperature slightly below the isotropic transition temperature, more distinct peaks are frequently obtained.

† The method was established on the hypothesis that similar liquid crystals are compatible. A sample is mixed with an authentic sample and the two-component phase diagram of the mixture is established. When the phase transition temperature is maintained at a constant value by mixing, the sample can be identified as the same as the authentic material.

Like small molecule liquid crystals, the odd-even alternations in mesophase–isotropic temperatures (T_i), transition enthalpies (ΔH_i) and transition entropies (ΔS_i) can also be seen in rigid–flexible MCLCP as a function of the number of carbon atoms, n . In the flexible segment, among homologous series, the transition temperatures (including the melting point, T_m and the mesophase-to-isotropic transition temperature, T_i) of MCLCP with even n are higher than those of corresponding MCLCP with odd n . The plot of ΔH_i or ΔS_i versus n values shows two linear traces, with the even n one above and the odd n one below. The intercept and slope of these lines depend on the order and conformational changes of the sample during the mesophase-to-isotropic transition.

4.2.22.3 Side-chain Liquid Crystalline Polymer

Many SCLCP, in nature, are non-crystalline substances, so the glass transition temperature is dominated by the main-chain and the first-order transition from mesophase to isotropic for the side-chain mesogenic moiety can be observed on TA traces (Figure 4.32, curve a). These compounds sometimes exhibit liquid crystallinity (smectic, cholesteric or nematic phase, as shown in Figure 4.32, curve b). If the compounds have a long spacer group, the endothermic melting peak for the partially crystalline side-chain can be observed. In the case of coexistence of non-crystalline with liquid crystalline forms, the relative content of each component will vary with the thermal treatment. In addition, the mesophase structure can often be frozen into an amorphous glassy state by rapid cooling.

4.2.23 Determination of SFI of Fat [47]

The solid fat index (SFI) is an important physical characteristic of fat. The SFI is dependent on temperature and is defined by the DSC method [48] as

$$\text{SFI} = \int_{T_i}^T (dQ/dt) dT / \int_{T_i}^{T_f} (dQ/dt) dT \quad (4.42)$$

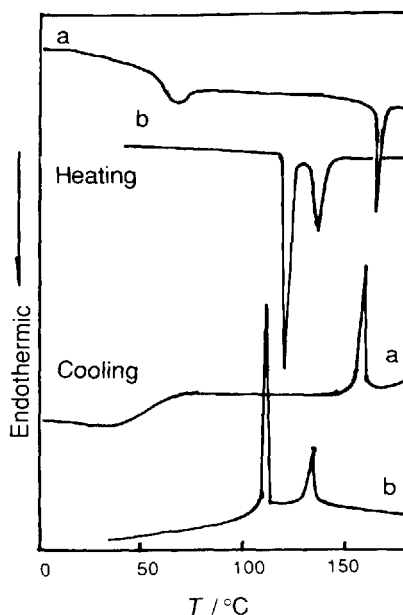
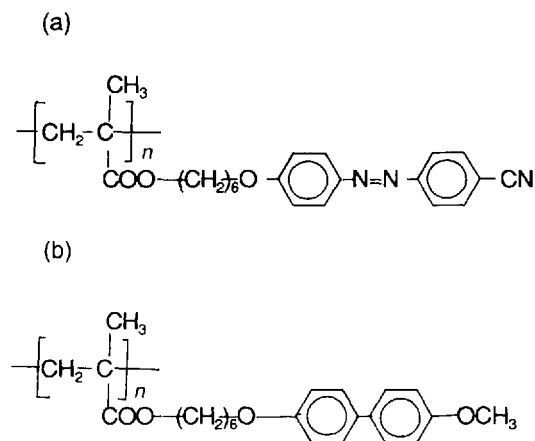


Figure 4.32 Phase transition of side-chain liquid crystalline polymer samples [46]. The structures of samples (a) and (b) are shown in Scheme 4.1. Sample mass, (a) 3.3 and (b) 9.0 mg, scanning rate (heating and cooling), $10^\circ\text{C min}^{-1}$

where, dQ/dt is the heat flux rate, T is any temperature, T_i is the initial melting temperature and T_f is the final melting temperature.

The SFI value can be obtained using the DSC method by dividing the partial peak area of the region defined by a temperature range from T_i to T by the total peak area. Figure 4.33 gives the



Scheme 4.1.

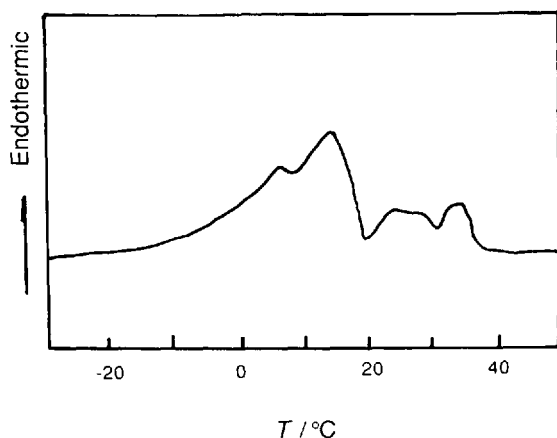


Figure 4.33 DSC curve for melting of beef tallow using the continuous heating technique

DSC curve for a beef tallow sample which demonstrates that the step heating method (Figure 4.34) gives a smaller error than continuous heating.

4.2.24 Wax Content of Lubricants

One major use of DSC in the petroleum industry is in the determination of the total wax content and crystallization temperature of lubricants. These two important parameters affect the low-temperature viscosity and lubricating ability of lubricants.

In order to determine the wax content of a lubricant by DSC, for example, for a

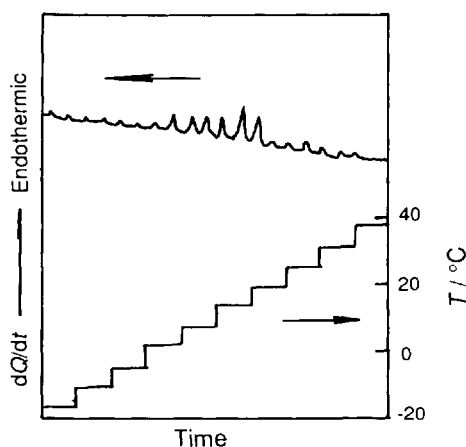


Figure 4.34 DSC curve for beef tallow using the step heating technique

high-melting wax, cool the sample of mass 20 mg at a rate of $10\text{ }^{\circ}\text{C min}^{-1}$ under a nitrogen atmosphere of flow-rate 50 ml min^{-1} from $70\text{ }^{\circ}\text{C}$ to $-70\text{ }^{\circ}\text{C}$, measure the crystallization exotherm and calculate the heat of crystallization from the area under the exothermic peak of the DSC curve. Ratioing this heat of crystallization to that obtained for a 100% wax sample yields the mass fraction of wax [49].

mass fraction of wax(%) =

$$(\Delta H_{\text{sample}} / \Delta H_{\text{stand}}) \times 100\%$$

where ΔH_{sample} is the heat of crystallization of the sample (Jg^{-1}) and ΔH_{stand} is the heat of crystallization of the standard (Jg^{-1}). The wax content of this sample was determined to be 42.3% by this method.

4.2.25 Heat of Transition of Lipids

Lipids are materials having both a hydrophobic and hydrophilic nature. Much work in recent years has been devoted to investigating the thermal phase transformation of lipids [48] relating to molecular arrangements in biological membranes [50]. Since these transitions are generally low-enthalpy, a differential scanning calorimeter with high sensitivity can be used to identify transitions in lipids and quantitate the energy associated with the transitions.

The procedure may be dependent on the particular system being studied. As an example, experimental conditions for the system of dimyristoylphosphatidylcholine (DMPC) are given in the caption of Figure 4.35.

The samples shown in Figure 4.35 were irradiated by ultrasonic waves in a flowing inert gas atmosphere in order to control the size of the vesicles. The main melting peak of sample I (without irradiation) is attributed to melting of multi-layered vesicles of diameter 300–1000 nm. With increasing irradiation time, the size of the vesicles decreases and multi-layer vesicles change into single-layer vesicles.

4.2.26 Denaturation of Proteins

The calorimetric recording of a dilute solution of lysozyme is shown in Figure 4.36 [52, 53].

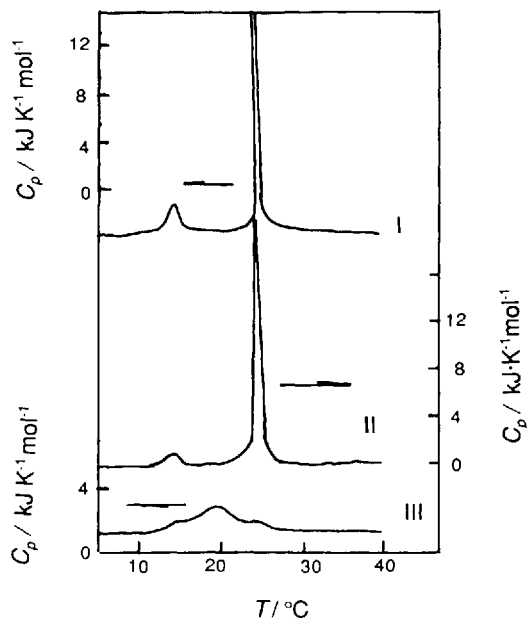


Figure 4.35 DSC curve of DMPC vesicles of various sizes [51]. Sample, DMPC vesicle suspension liquid; sample mass, lipid concentration 2 mmol L⁻¹; heating rate, 0.75 °C min⁻¹; atmosphere, N₂; sample vessel, tantalum-niobium alloy, 1.2 ml, sealed type; reference, buffer solution; vesicle size: I, 300–1000 nm, multi-layers; II, average 200 nm, 3–4 layers; III, 40 nm, single layer

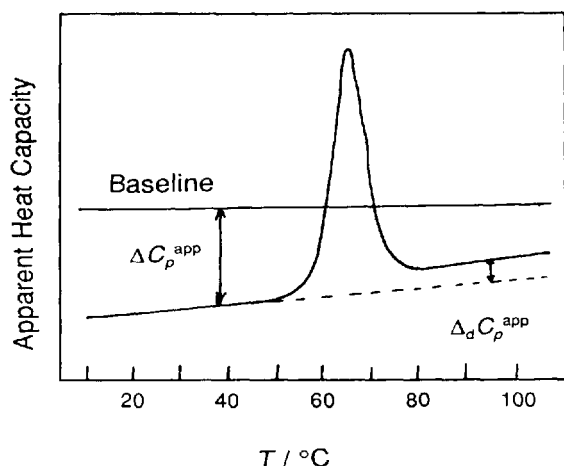


Figure 4.36 Apparent heat capacity of dilute lysozyme solution on heating. Sample concentration, 1.8 g l⁻¹; pH, 2.5; heating rate, 1 °C min⁻¹; sensitivity on heating, 4.18 × 10⁻⁵ J °C⁻¹

Measurements were carried out using a Privalov-type calorimeter (see Section 2.2.2) which has sufficiently high resolution and stability to measure the partial heat capacity of the protein in a dilute

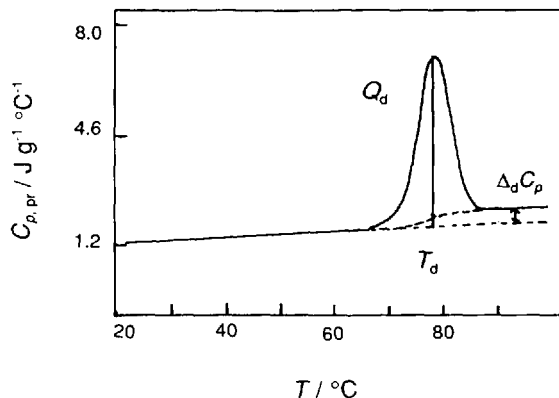


Figure 4.37 Temperature dependence of partial specific heat capacity of lysozyme in solution at pH 4.5. Sample concentration, 1.8 g l⁻¹; heating rate, 1 °C min⁻¹; sensitivity on heating, 4.18 × 10⁻⁵ J °C⁻¹

solution [54]. As shown in Figure 4.37, the heat capacity of the solution is lower than that of the same volume of pure solvent (shown as the baseline in Figure 4.36). From the distance between the baseline and recording curve of the solution (ΔC_p^{app}), the partial specific heat capacity of the protein, $C_{p,\text{pr}}(T)$, can be obtained using equation (4.43), if the specific partial volume of the protein, $V_{\text{pr}}(T)$, is known.

$$C_{p,\text{pr}}(T) = C_{p,\text{sol}}(T)[V_{\text{pr}}(T)/V_{\text{sol}}(T)] - \Delta C_p^{\text{app}}/m_{\text{pr}} \quad (4.43)$$

where m_{pr} is the amount of protein. The temperature dependence of the partial heat capacity of lysozyme in solution at pH 4.5 is shown in Figure 4.37. T_d is the mid-point of denaturation and Q_d is the heat of the denaturation process. The difference between the heat capacity (ΔC_p) of the native state (C_p^{N}) and that of denatured state (C_p^{D}) of protein at T_d , is expressed as $\Delta C_p(T_d) = C_p^{\text{D}}(T_d) - C_p^{\text{N}}(T_d)$. The enthalpy of denaturation (ΔH) can be obtained according to Kirchhoff's equation $d\Delta H/dT = \Delta_d C_p$.

4.2.27 Phase Diagram for Binary Systems

It is convenient to construct a phase diagram using DSC for multicomponent systems, such as alloys. The basic principle of the method is demonstrated using a binary system as an example.

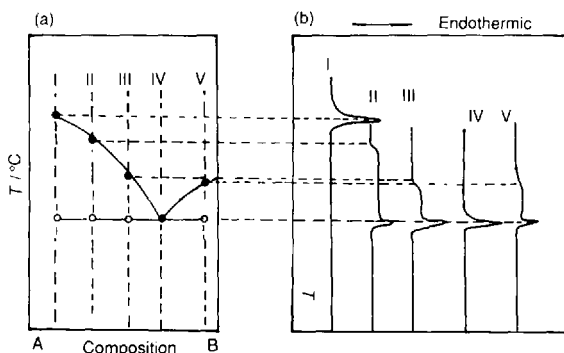


Figure 4.38 (a) Phase diagram and (b) DSC curves for a binary system with a co-crystallization point [55]

Figure 4.38(a) shows a phase diagram constructed using the DSC data given in Figure 4.38(b). In order to demonstrate clearly the relationship between (a) and (b), the coordinated axes in Figure 4.38(b) are unconventionally located, that is, the vertical coordinate is the temperature axis. The number of DSC curves corresponds to that shown in the diagram. A sharp endothermic peak due to the melting of the co-crystalline form can be observed in the DSC curves. In the phase diagram, the composition of sample 4 represents the co-crystallization point; the DSC baseline of these samples showed a continuous endothermic deviation at a temperature higher than the co-crystalline melting peak. The sample baseline does not become flat until liquidation finishes.

Once the phase diagram is established, an unknown composition ratio of two-component systems can also be evaluated from the temperature at which the DSC curve of the sample reaches the baseline from the endothermic direction.

4.3 Miscibility and Phase Behavior of Polymer Blends

In order to investigate miscibility and phase behavior of polymer blends, differential scanning calorimetry (DSC) has been frequently used for determination of glass transition temperature, crystalline melting temperature and other thermal properties.

4.3.1 Miscibility and Phase Separation in Amorphous Polymer Blends

Most miscible polymer blends are amorphous [56–58]. A miscible polymer blend possesses a homogeneous amorphous phase and hence will exhibit a single glass transition temperature (T_g) between the T_g s of the components.

Several theoretical and empirical equations have been used to describe the T_g -composition dependence of miscible blends. The two frequently used equations are the Fox equation [equation (4.44)] and the Gordon-Taylor equation [equation (4.45)]:

$$1/T_g = W_1/T_{g1} + W_2/T_{g2} \quad (4.44)$$

$$T_g = (W_1 T_{g1} + k W_2 T_{g2}) / (W_1 + k W_2) \quad (4.45)$$

where T_g is the glass transition temperature of the blend, T_{g1} and T_{g2} are the glass transition temperatures of components 1 and 2, respectively, W_1 and W_2 are the mass fractions of the components 1 and 2, respectively, and k is a constant.

Figure 4.39 shows the T_g data obtained by DSC for poly(*N*-vinyl-2-pyrrolidone) (PVP)–poly(vinyl chloride) (PVC) blends [58]. It can be seen that each blend has a single glass transition temperature which varies with blend composition. The appearance of one composition-dependent T_g reveals its single-phase nature, i.e. PVP is miscible with PVC over the entire composition

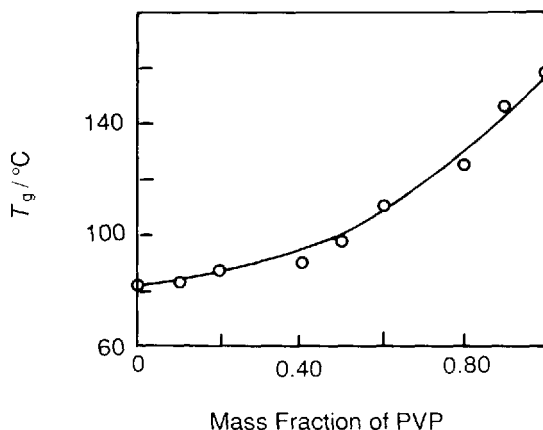


Figure 4.39 Composition dependence of T_g of PVP-PVC blends. The curve is as predicted by the Gordon-Taylor equation using a k value of 0.34

range. The curve in Figure 4.39 was drawn using the Gordon Taylor equation with a k value of 0.34 and fits the experimental data well.

In an amorphous polymer blend system, we can determine the phase boundary curve, i.e. a temperature versus composition phase diagram, by using DSC to follow the appearance of two separate T_g s at a certain annealing temperature. The phase diagram can also be obtained simply by optical observation. The temperature at which the first faint opalescence appears on heating is designated the cloud point.

All the PMMA–PVAc blends cast from chloroform were transparent at room temperature and were found to undergo phase separation at elevated temperatures. The cloud point curves are shown in Figure 4.40. An increase in the molecular mass of the PVAc decreases the cloud point temperature as expected. The minimum in the cloud point curve appears close to a 50:50 PMMA:PVAc mass ratio. This composition varies relatively little with molecular mass of PVAc as the latter is varied from 20 000 to 453 000.

4.3.2 Miscible Blends Containing a Crystalline Polymer

The miscibility of blends containing at least one crystalline component shows that they exhibit

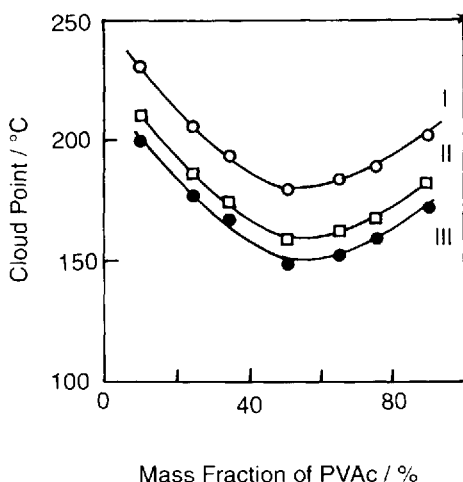


Figure 4.40 Plots of cloud points against composition for PMMA–PVAc blends. The weight-average molecular mass (M_w) of PMMA is 60 000. M_w of PVAc: I, 20 000; II, 170 000; III, 453 000

homogeneity in the amorphous phase, even if one or two separate crystalline phases are formed and even if each crystalline phase contains one polymer [59]. Based on this definition, a larger number of blends composed of an amorphous polymer and a semi-crystalline polymer have been judged to be miscible [60–62].

The thermal history has a profound influence on the DSC curves of polymer blends containing at least one crystalline component. In order to obtain T_g by DSC experiments, the samples are usually first heated to a temperature between the phase separation temperature and the melting point of the crystalline component and held for several minutes to remove the thermal history.

Plots of the T_g of PEO–PU blends as a function of composition are shown in Figure 4.41; the full curve is as predicted by the Fox equation [equation (4.44)]. The overall T_g variation indicates that these polymers are completely miscible at all compositions. The deviation of the experimentally obtained T_g s from the Fox equation at high PEO contents is due to crystallization during quenching. Crystallization for high PEO content blends was sufficiently rapid for it to be complete during the quenching after the first heating.

By measuring the area under the melting peak of DSC curves, it should be possible to evaluate the heats of fusion (ΔH_f) and crystallization (ΔH_c) in the blend. The fractional crystallinity, X_c was

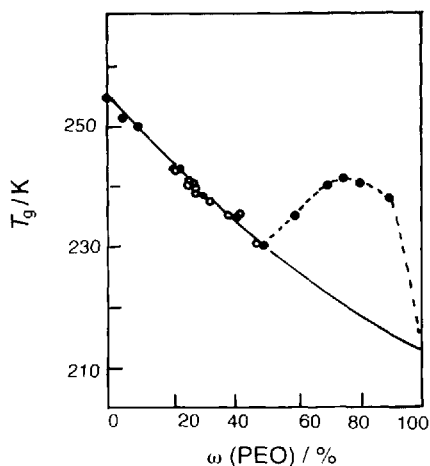


Figure 4.41 T_g s for PEO–PU blends plotted versus overall blend composition (filled circles) and versus calculated amorphous phase composition (open circles). The full curve is as predicted by the Fox equation. [equation (4.44)]

calculated from [63]:

$$X_c = (\Delta H_f - \Delta H_c) / \Delta H_f \quad (4.46)$$

where $\Delta H_f = 205 \text{ J g}^{-1}$ is the heat of fusion for 100% crystalline PEO [64]. Because of this crystallinity, the mass fraction of PEO in the amorphous phase, w' , does not equal the overall weight fraction of PEO in the blend, w . These quantities are related by

$$w' = (w - X_c) / (1 - X_c) \quad (4.47)$$

The open circles in Figure 4.41 represent a replot of the T_g values against the amorphous fraction of PEO. These data conform well to the Fox equation whereas the plot against overall PEO content does not.

Figure 4.42 shows the application of the Hoffman–Weeks procedure [17] to separate the morphological effect on melting point depression and to determine the equilibrium melting point of PEO in the blend and in the pure state. The observed melting temperature (T_m) of PEO and the PEO–PU blends increases linearly with increase in crystallization temperature for a wide range of undercooling. A depression of T_m , for the same T_c , is observed for blends. The analysis is based on the relationship

$$T_m = T_m^0 (1 - 1/\gamma) + T_c/\gamma \quad (4.48)$$

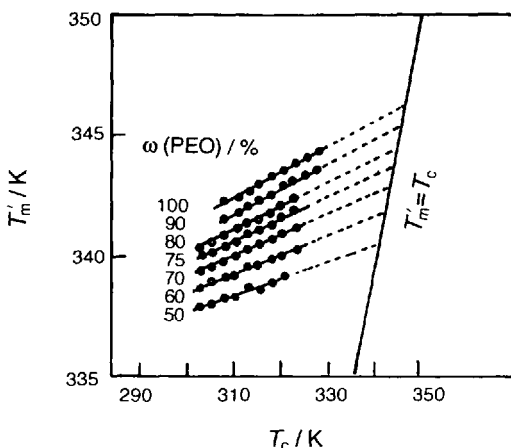


Figure 4.42 Hoffman–Weeks plot to obtain the equilibrium melting point for PEO in blends with PU. All samples were quenched from 100 °C to T_c and crystallized at T_c for 24 h

where T_m is the equilibrium melting temperature, T_m^0 is the observed melting point of PEO, T_c is the crystallization temperature at which annealing of the blends was performed and $1/\gamma$ is a morphological factor [65]. As shown in Figure 4.42, the T_m – T_c lines extrapolate to values of T_m that decrease with increasing content of PU. The values of the slopes $1/\gamma$ of the lines are almost independent of composition.

The findings that the morphological and stability parameter $1/\gamma$ is almost constant and independent of blend composition and that the T_m – T_c lines extrapolate to different equilibrium melting points strongly suggest that the melting point depression can be primarily ascribed to the diluent effect of the non-crystallizable polymer as the two components are miscible in the melt.

From this plot and extrapolating T_m to T_c , one obtains the T_m^0 and T_m^0 values as plotted in Figure 4.43, as suggested by the Nishi–Wang equation [66]:

$$(1 - T_m)/T_m^0 = -B\phi_1^2(V_{2U}/\Delta H_{2U}) \quad (4.49)$$

to obtain the interaction parameter B , where T_m^0 is the equilibrium melting temperature of the pure crystalline PEO, T_m is the value for a blend containing a ϕ_1 volume fraction of the amorphous component and $\Delta H_{2U}/V_{2U}$ characterizes the heat of fusion per unit volume for 100% crystalline PEO. The value of $\Delta H_{2U}/V_{2U}$ was

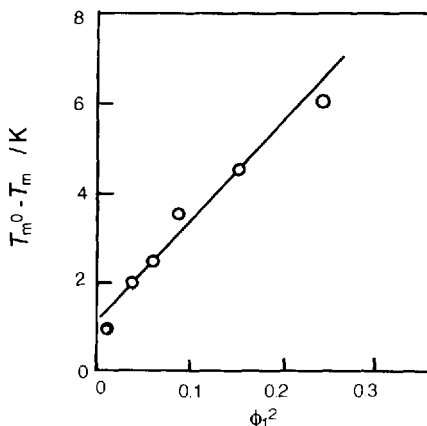


Figure 4.43 Melting point depression analysis to obtain the interaction energy density B for PEO–PU blends. The slope gives $B = -14 \text{ J cm}^{-3}$

calculated from the literature values [68] $V_{2U} = 38.9 \text{ cm}^3 \text{ mol}^{-1}$ and $\Delta H_{2U} = 8790 \text{ J mol}^{-1}$. The slope of the linear relationship in Figure 4.43 gives a value for $B = -14 \text{ J cm}^{-3}$.

The negative values found for B in the case of PEO-PU blends support the idea that these polymers are miscible in the molten state and the fact that the intercept of the Nishi-Wang plot is close to zero indicates that entropic effects contribute little to B .

4.3.3 Miscible Blends Containing Two Crystalline Polymers

Both poly(ϵ -caprolactone) (PCL) and poly [3,3-bis(chloromethyl)oxetane] (Penton) are crystalline polymers and the thermal behavior of the blends was investigated as a function of composition by using DSC [69].

The DSC curves of the quenched samples shown in Figure 4.44 reveal a single glass transition temperature which varies with blend composition. The appearance of a single T_g strongly suggests that the blend presents a homogeneous single amorphous phase, i.e. the two components are miscible in the amorphous phase.

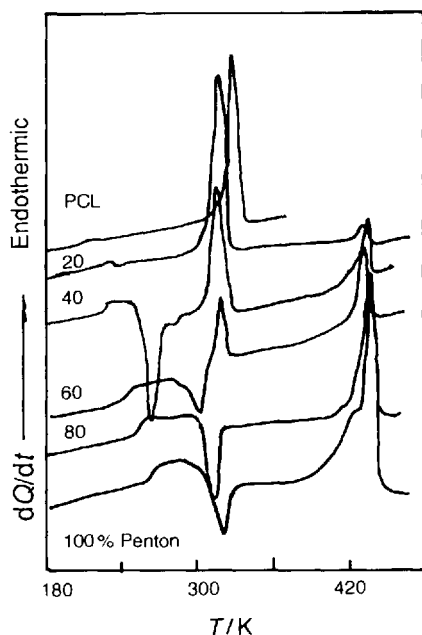


Figure 4.44 DSC curves for the quenched samples of PCL-Penton blends

The experimental data conform well to the Fox equation.

For pure PCL, no crystallization exotherm was observed, as can be seen in Figure 4.44, since crystallization was sufficiently rapid to occur completely during the quenching. However, for blends with mass fraction of Penton up to 60 %, a crystallization exotherm occurred and T_c increases with increase in Penton content. This phenomenon implies that the crystallization of PCL in the blend becomes progressively more difficult with increasing Penton content. Furthermore, the blend containing 80 % Penton did not show any crystallization exotherm of PCL. It is also noted that crystallization of Penton did not occur in the blends with Penton contents lower than 40 %. A decrease in the crystallization rates of both PCL and Penton in blends was also observed in the crystallization process during the cooling run.

The crystallinity indices of the PCL phase, $X_c(\text{PCL})$, and the Penton phase, $X_c(\text{Penton})$, in the PCL-Penton blends are presented in Figure 4.45 as functions of blend composition. The filled symbols denote the quenched samples and the open symbols the as-cast samples

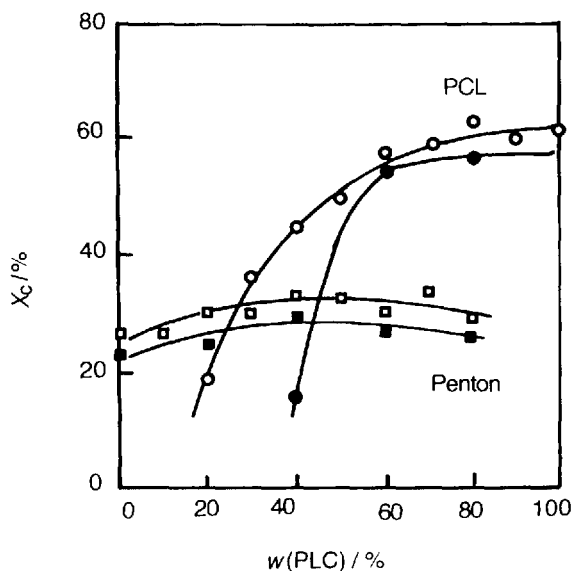


Figure 4.45 Crystallinity index X_c of PCL (circles) and Penton (squares) as a function of blend composition. The filled symbols denote the quenched samples and the open symbols the as-cast samples

and the open symbols the as-cast samples. The values of both the $X_c(\text{PCL})$ and $X_c(\text{Penton})$ for the as-cast samples are all higher than those for the quenched samples. Further the $X_c(\text{PCL})$ for both the quenched and the as-cast samples begins to decrease rapidly with Penton content at a 60 : 40 PCL–Penton composition. This could be considered to be due to the enhanced T_g value of the blend. Finally, the $X_c(\text{Penton})$ values do not decrease with the addition of PCL. This is because the T_g of the system does not increase with increasing PCL content.

The application of the Hoffman–Weeks procedure [17] was used to separate the morphological effect on melting point depression and to determine the equilibrium melting point of Penton in the blend and in the pure state. The interaction energy density B for the PCL–Penton blends was estimated to be -15 J cm^{-3} by using the Nishi–Wang plot [66] from the equilibrium melting point depression data. The negative B value confirms that these polymers are miscible in the molten state.

4.3.4 Phase Separation in Crystalline Polymer Blends

For blends containing one (or more) crystallizable component, it becomes difficult to follow the appearance of phase separation in an isothermal treatment or in a temperature scan since the magnitude and position of T_c can be strongly affected by the state of crystallization before or after the occurrence of phase separation. However, the changes in other thermal properties, such as enthalpy of crystallization and fusion and temperatures of crystallization and melting, can give some information on phase behavior, which can be taken as an indication of phase separation. Here, we describe an investigation of the phase behaviors in crystalline/miscible blends consisting of PEO and phenolphthalein poly(ether ether sulfone) (PES-C) [70]. In this system, it was difficult to determine the phase boundary, i.e. a temperature versus composition phase diagram, by using DSC to follow the appearance of two separate X_c s at a certain annealing temperature as conventionally shown by amorphous polymer blend systems, since PEO is a crystalline polymer

with a typically high degree of crystallinity. However, the changes in other thermal properties as functions of annealing temperatures can give some significant information, and the phase diagram was determined based on the analysis of thermal properties.

Miscible PES-C–PEO blends were prepared by solution casting from *N,N*-dimethylformamide, and were used throughout this study. The PES-C–PEO blends with $w(\text{PEO}) < 50\%$ were transparent at room temperature, but the blends containing $w(\text{PEO}) 50\%$ became increasingly opaque with increase in PEO content. The polarizing microscopic observation of all these blends with $w(\text{PEO}) < 50\%$ shows the typical morphology of spherulites. When heated up to 80°C , i.e. above the melting point of PEO (65°C), these opaque films all became clear. This observation indicates that the PES-C–PEO blends present a single homogeneous amorphous phase, i.e. phase separation did not occur, at least on a scale with dimensions of phase domains exceeding the wavelength of visible light.

When further heated up to 200°C , all the initially clear samples became turbid in succession, but the remixing did not occur when these samples were cooled due to kinetic effects. Careful microscopic observations revealed that the turbidity was caused by the formation of a phase-separated structure. These results suggest that the PES-C–PEO blends display LCST behavior, which means that there is a negative enthalpic contribution of mixing.

Figure 4.46 shows DSC curves of the PES-C–PEO blends. It can be seen that each blend displays a single glass transition temperature (T_g), intermediate between those of the two pure components and changing with the blend composition. According to the transparency of the sample and glass transition behavior, the conclusion can be reached that the PES-C–PEO blends are completely miscible in the amorphous state, i.e., possess a single, homogeneous, amorphous phase for all compositions below the temperature of phase separation.

As can be seen in Figure 4.46, no cold crystallization exotherm was observed for the pure PEO and the 20 : 80 PES-C–PEO blend, since crystallization was sufficiently rapid to occur completely

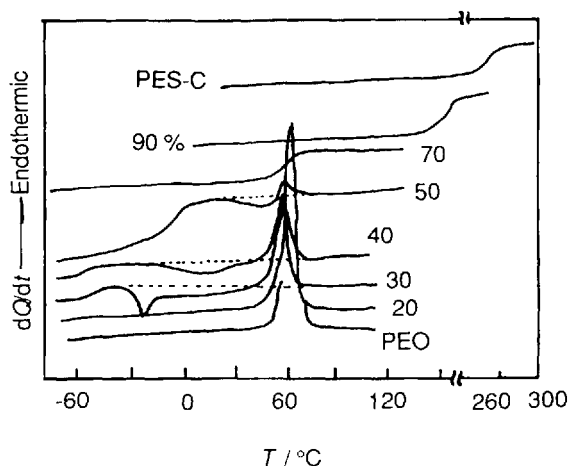


Figure 4.46 DSC curves of PES-C-PEO blends with different blend compositions after quenching. Heating rate, $20\text{ }^{\circ}\text{C min}^{-1}$. For ease of comparison, all curves are normalized to 1 mg of sample

during the quenching. However, for the blends with PES-C content from 30% to 50%, the crystallization temperature (T_c) increases with increasing PES-C content. This phenomenon indicates that crystallization of PEO becomes progressively difficult in the PES-C-rich blends. Furthermore, the blends with a PES-C content of 70 wt% or higher did not show any crystallinity. It was noted that the T_m of PEO in the blends apparently decreases with addition of PES-C to the system, which indicates that PES-C hinders the crystallization of PEO in the blends. This is a typical characteristic of a miscible blend composed of an amorphous polymer and a crystallizable polymer in which the T_g of the amorphous polymer is higher than that of the crystallizable component.

The interaction energy density B for the PES-C-PEO blends was estimated by using the Nishi-Wang plot [66] from the apparent melting point depression data. A tentative value of B was found to be -17 J cm^{-3} at $65\text{ }^{\circ}\text{C}$ for the PES-C-PEO. The negative B value suggests a negative free energy of mixing. It must be stressed that this estimate may be subject to some errors since the morphological effect on the melting point depression has not been excluded.

From the crystallinity of PEO as a function of blend composition, a dramatic decrease in crystallinity is observed when the content of PES-C is more than 20%, indicating a pronounced

inhibition of crystallization due to the presence of PES-C.

All these results clearly show that PES-C-PEO blends are miscible and exhibit an LCST behavior. However, as shown above, different thermal behaviors are shown by the miscible blends of PES-C and PEO, depending on the blend composition. Blends with different compositions display different changes in thermal properties when phase separation occurs. Therefore, the investigation of phase separation should be performed in the light of the blend compositions. The studies of phase separation process are discussed in detail as below.

A series of DSC curves for the 70:30 PES-C-PEO blend was obtained after annealing at temperatures between 80 and $200\text{ }^{\circ}\text{C}$ and then quenching to $-70\text{ }^{\circ}\text{C}$ (Figure 4.47). It can be seen that with annealing below $110\text{ }^{\circ}\text{C}$, the DSC scans show no obvious changes, but a significant difference was observed with annealing temperatures higher than $110\text{ }^{\circ}\text{C}$. Minor melting peaks of PEO appear in the DSC heating curves, and the area under the melting peaks increases with increasing annealing temperature, eventually maintaining a constant value when the annealing temperature is higher than $140\text{ }^{\circ}\text{C}$. The melting temperature (T_m) increases dramatically after annealing up to $110\text{ }^{\circ}\text{C}$ and thereafter only grad-

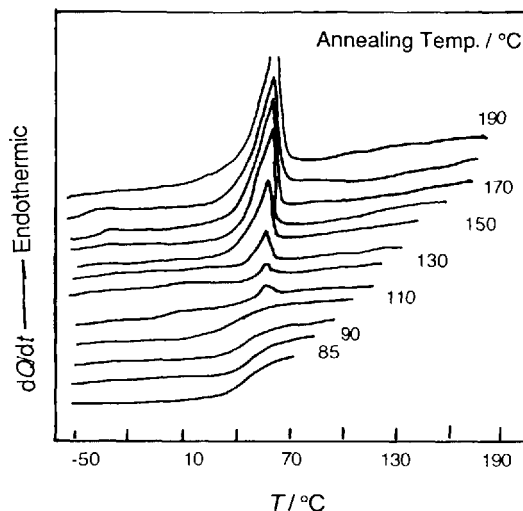


Figure 4.47 DSC curves for the 70:30 PES-C-PEO blend at various annealing temperatures between 85 and $190\text{ }^{\circ}\text{C}$. The annealing time was 5 min

ually increases. The appearance of the crystallization of PEO in the blends is indicative of the occurrence of phase separation, i.e. the PEO-rich phase has separated from the initial homogeneous amorphous PES-C-PEO mixture. With phase separation taking place, PEO gradually concentrates from the original homogeneous blends and both PEO-rich and PEO-lean phases are simultaneously formed, resulting in the appearance of crystallization and fusion of PEO during the process of quenching and heating. The higher the annealing temperature, the larger is the area under the melting peaks, which suggests that the phase separation occurs more completely. Hence the occurrence of melting at a particular annealing temperature should be considered as the beginning of phase separation.

From Figure 4.47, it is observed that the T_g s of the blends became broad in the vicinity of the onset of phase separation. The width of the glass transition may reflect the magnitude of local compositional fluctuations in the polymer blends, implying relative homogeneity or miscibility of the system. However, the transition temperatures do not change until the appearance of a minor melting peak in the DSC curve, indicating the occurrence of phase separation. With the phase separation occurring, the T_g s gradually shift to lower temperatures, although they increasingly become indistinguishable at higher annealing temperatures owing to the higher crystallinity after more complete phase separation. It is noted that the second T_g , i.e. that of the PES-C-rich phase, cannot be seen in Figure 4.47. However, there is an apparent deviation of the DSC curves from the baseline after the melting peaks of PEO. The higher the annealing temperature, the larger is the deviation, which suggests a broader range of glass transition of the PES-C-rich phase after the multi-stage thermal treatment. It should be pointed out that the heating rescan after the appearance of the melting peaks of PEO does not show the cold crystallization of PEO, which indicates that the crystallization of PEO in the newly separated PEO-rich phase mainly occurs during the quenching process.

For the 50 : 50 PES-C-PEO blend, an amorphous and homogeneous mixture was obtained after quenching from 80 to -70°C in terms of the

comparison of the area under the crystallization and melting peaks, since there are identical values of the enthalpy between the two transitions. Figure 4.48 shows a series of heating DSC curves for the 50 : 50 PES-C-PEO blend annealed at different temperatures between 80 and 130°C . Below 105°C , the endothermic enthalpy remains unchanged and equal to the exothermic enthalpy, which indicates that PEO crystallizes only during the heating run of DSC after quenching. When the annealing temperature is 105°C or above, both enthalpy values began to increase dramatically, and the enthalpy of fusion even began to surpass that of crystallization, in contrast to the cases at annealing temperatures below 105°C . At the same time, the cold crystallization temperatures (T_c) shifted to lower values whereas the melting temperatures (T_m) increased.

These results clearly indicate that, at annealing temperatures above 105°C , PEO began to crystallize not only during the heating scan but also during the quenching process. The shift of the crystallization peaks to lower temperature indicates that the composition might have changed somewhat during annealing. In other words, on annealing, two separate amorphous phases are formed, one the PES-C-rich phase and the other the PEO-rich phase. The PEO-rich phase can

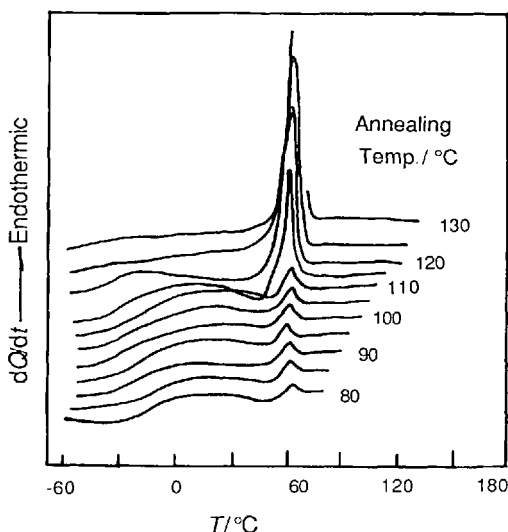


Figure 4.48 DSC curves for the 50 : 30 PES-C-PEO blend with various annealing temperatures between 85 and 130°C . The annealing time was 5 min

crystallize during the quenching process, and its thermal behavior is similar to that of the 30:70 PES-C-PEO blend (Figure 4.46). The cold crystallization of PEO occurs more easily, i.e. the hindrance effect of PES-C on PEO crystallization becomes smaller because the content of the amorphous component (PES-C) with higher T_g in the newly formed PEO-rich phase decreases. As a consequence, the enthalpy of crystallization and fusion increased, and T_m increased since more perfect crystals could be formed. It is assumed that the shift of the crystallization peak at a particular annealing temperature can correspond to the beginning of phase separation. Of course, the annealing time is an important factor which affects the shift and magnitude of the crystallization peak after the phase separation occurs.

4.3.5 Upper and Lower Critical Solution Temperature

When a homogeneous mixture solution is cooled, phase separation is induced at a certain temperature. This critical phase separation temperature is termed the 'upper critical solution temperature' (UCST). It is a convex upward curve in the plot of composition versus temperature (C - T plot) and its maximum point shifts to a higher temperature with increasing relative molecular mass of the polymer. However, for many polymer-solvent and polymer-polymer blend systems, a decrease in mutual solubility is also observed as the temperature increases. The critical phase separation temperature is called the 'lower critical solution temperature' (LCST). It is a convex downward curve in the C - T plot and the minimum point shifts to a lower temperature with increasing relative molecular mass of the blend components. LCST occurs at a higher temperature than UCST.

Polymer alloys and composites have become an attractive research field world-wide because of their practical and theoretical significance. Miscibility and phase separation are the key topics in this field. With the development of criterion techniques for miscibility, complicated phase diagrams for polymer blends were obtained which cannot be explained by the

unmodified Flory-Huggins theory, e.g. the LCST phase behavior of polymer-polymer blends. These difficulties led to the appearance of several newer theories, such as the equation of state and lattice fluid theories presented by Prigogine and Flory, etc., and the mean field theory, a Flory-Huggins-type theory. According to these theories, the Gibbs free energy of mixing, G_m , contains three different contributions: the combinatorial entropy of mixing, the exchange interaction and the free volume term. The first term becomes insignificant for high molecular mass polymer mixtures but for oligomer blends or polymer solution systems it causes UCST behavior. The free volume contribution is always positive and increases as a function of temperature. This term leads to LCST in polymer-polymer mixtures because of the difference in the thermal expansion coefficients of the pure components. A specific interaction is usually a prerequisite for the miscibility of homopolymer pairs but it is an exception for blends containing at least one random copolymer component.

McMaster [71] applied the equation of state theory to polymer blends and demonstrated that a system with a small positive exchange interaction energy parameter ($\chi_{1,2}$) and a very small free volume contribution can exhibit both UCST and LCST behavior. He also pointed out that such behavior is expected to be rare in polymer-polymer blends.

In practice, the existence of both UCST and LCST has been established for polymer-solvent systems. About 10 years ago, Schmitt discussed UCST, LCST and combined UCST and LCST behavior in blends of poly(methyl methacrylate) with poly(styrene-co-acrylonitrile) (PMMA-PSAN), Ueda and Karasz reported the existence of UCST in chlorinated polyethylene (CPE) blends using DSC, Inoue found that elastomer blends of *cis*-1,4-polybutadiene and poly(styrene-co-butadiene) exhibit both UCST and LCST behavior and Cong *et al.* [72] observed that blends of polystyrene and carboxylated poly(2,6-dimethyl-1,4-phenylene oxide) copolymers with a degree of carboxylation between molar fraction 8% and 10% exhibit both UCST and LCST behavior. They used DSC to establish the phase diagram.

The experimental procedures for thermally inducing phase separation of polymer blends by DSC technique are as follows.

1. A homogeneous blend sample was heated at a rate of $320\text{ }^{\circ}\text{C min}^{-1}$ to the selected annealing temperature and maintained at this temperature for a long enough time to establish phase equilibrium. Then the sample was rapidly quenched to liquid nitrogen temperature.
2. The annealed samples were scanned at the normal scanning rate for an assigned temperature.
3. Repeating the above procedures, a series of DSC curves corresponding to the different annealing temperatures were obtained.
4. Using the single T_g obtained from DSC curves as the criterion for a miscible blend, a phase diagram corresponding to different blend compositions and annealing temperatures was established.

Figures 4.49 and 4.50 show the DSC curves at different annealing temperatures and the phase diagram for a blend of polystyrene ($M_w = 115\ 000$) and carboxylated poly(phenylene oxide) (PPO) with molar fraction 8.0% carboxylation content.

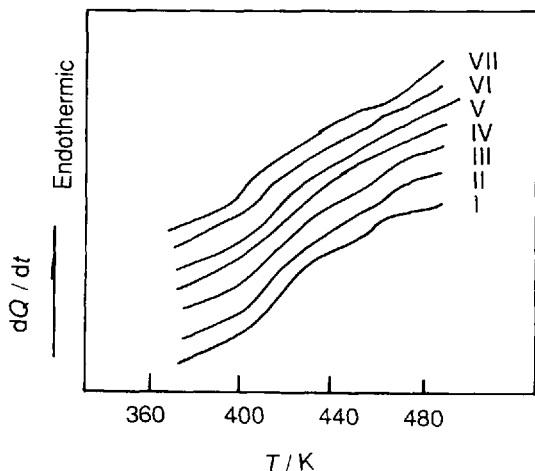


Figure 4.49 DSC curves for a $C^{8.0}\text{PPO-PS}_{115}$ blend for different annealing temperatures [72]: I, 150; II, 170; III, 190; IV, 200; V, 220; VI, 240; VII, 260 $^{\circ}\text{C}$. Sample: $C^{8.0}\text{PPO}$ means carboxylated PPO with a molar fraction 8.0% carboxylation contents and PS_{115} means PS with a relative molecular mass of 115 000 and $M_w/M_n = 1.05$. Measurements: Perkin-Elmer DSC4 heating rate, $20\text{ }^{\circ}\text{C min}^{-1}$; sample mass, ca 15 mg; atmosphere, N_2 annealing period, 20 min

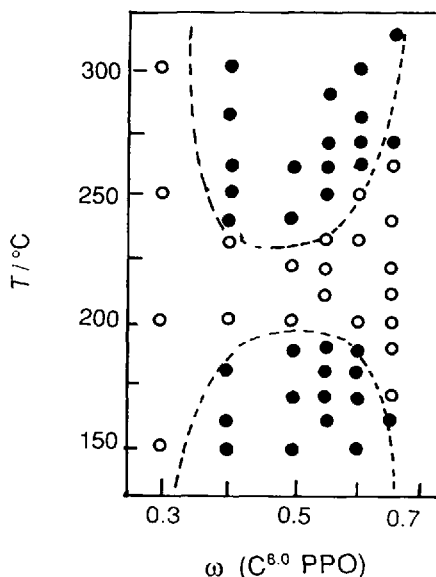


Figure 4.50 Phase diagram for a $C^{8.0}\text{PPO/PS}_{115}$ blend

In order to establish the phase diagram, the following points should be noted; (1) the equilibrium of polymer blends usually takes a long time, especially for polymers having soft and long chains, and therefore the annealing time required depends on the chemical structure of the polymer chains, i.e. the stiffer the chain the shorter is the annealing time required; and (2) it should be confirmed that the phase separation is reversible and the occurrence of an irreversible chemical reaction during annealing should be avoided.

4.3.6 Folded Surface Free Energy in Miscible Polymer Blends by Isothermal Melt Crystallization

The methods of measurement of the kinetic parameters of miscible or partially miscible polymer blends crystallized isothermally from the sub-cooled melt, K_g , n , k , σ_e and σ , are the same as those for homopolymers. However, the dilution effect of non-crystallizable molecules on the thermodynamics and the mobility of the constituents should be examined.

The theories of surface nucleation have been modified to account for the effect of the non-

crystallizable component on the linear growth rate of crystals developing in undercooled homogeneous blends. The equation commonly used to describe the linear growth kinetics is

$$G = \phi_2 G_0 \exp[-U^*/R(C_2 + T - T_g(\phi))] \times \exp[-rb_0\sigma_e T_m^0(\phi)/[kf\Delta H_m^0 T\Delta T(\phi)]] \times \exp[2\sigma T_m^0(\phi)\ln\phi_2/[b_0f\Delta H_m^0 T\Delta T(\phi)]] \quad (4.50)$$

G can be detected by using a polarizing optical microscope. If the experiments were carried out by means of DSC, the Avrami parameters, k and n , can be measured. Accordingly, equation (4.50) is modified to

$$\alpha = \ln K/n + U^*/R[C_2 + T_g(\phi)] - [1 + 2\sigma_e T_m^0(\phi)b_0f\Delta H_m^0 T\Delta T(\phi)]\ln\phi_2 = \ln G_0 - rb_0\sigma_e T_m^0(\phi)/kf\Delta H_m^0 T\Delta T(\phi) \quad (4.51)$$

By plotting α as a function of $1/\phi T_c \Delta T$ for each composition, one should obtain straight lines with slopes related to K_g , and hence the surface free energies of the lamella crystals. As an example, the kinetic data for partially miscible PEEK-PEK-C blends are shown in Figure 4.51.

$$K_g = Cb_0\sigma_e T_m^0/K\Delta H_f^0 \quad (4.52)$$

The symbols in equation (4.52) are explained in Section 4.2.10.

A fold surface free energy of $\sigma_e = (40 \pm 4) \times 10^{-7} \text{ J cm}^{-2}$ can be calculated for the PEEK crystals. The parameters are chosen as follows:

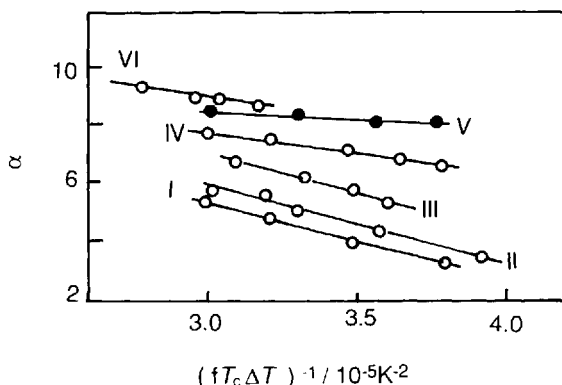


Figure 4.51 Plots of kinetic data according to equation (4.50). Mass fraction of PEK-C; I, 0; II, 5; III, 10; IV, 20; V, 40; VI, 60. The indicated compositions correspond to nominal values and not to the actual content of PEK-C in the crystalline phase [73]

$\sigma = 2.05 \text{ J m}^{-2}$, $\Delta H_f^0 = 130 \text{ J g}^{-1}$, $b_0 = 2.945 \times 10^{-10} \text{ m}$ and $T_m^0 = 639 \text{ K}$. From equation (4.50), the dilution effect of PEK-C on the crystallization of PEEK can be evaluated from $\ln\phi_2$ and the mobility of PEEK molecules from $T_g(\phi)$.

4.3.7 Growth Rate of Miscible Polymer Blend Spherulites Crystallized Isothermally from the Melt Measured by Polarizing Optical Microscopy [74]

The spherulitic growth rate of the miscible polymer blends crystallized isothermally from melt that consists of a crystallizable and a non-crystallizable component can be measured using a polarizing optical microscope with a hot stage. The crystallization temperature T_c was determined with the hot stage. The experimental procedure is the same as that for the homo-polymer mentioned above:

$$G = dR/dt \quad (4.53)$$

where R is radius of the spherulite and t is the crystallization time. G can be measured from the slope of the plot of R versus t .

As an example, the growth rate of the spherulites of PHB-CE2 blends is shown in Figure 4.52. G as a function of T_c and the compositions of the blends are shown in Figure 4.53.

4.3.8 Determination of the Composition of Polymer Blends

The composition of certain polymer blends (i.e. those whose parent polymers have sufficiently different melt temperatures), such as polyethylene-polypropylene, can be determined by DSC. The method is based on measurements of the heat of fusion of the respective parent polymers. The polymer crystallinity, upon which this heat of fusion is based, is sensitive to the thermal history. The apparatus should be calibrated using a known standard and, at the same time, the sample must be pre-heated in the same manner for correlations to be valid.

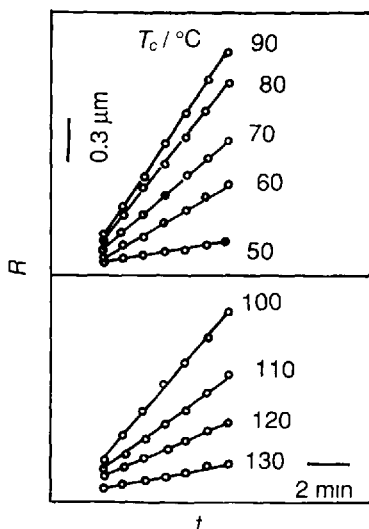


Figure 4.52 Growth rate of spherulites of PHB-CE2 blends

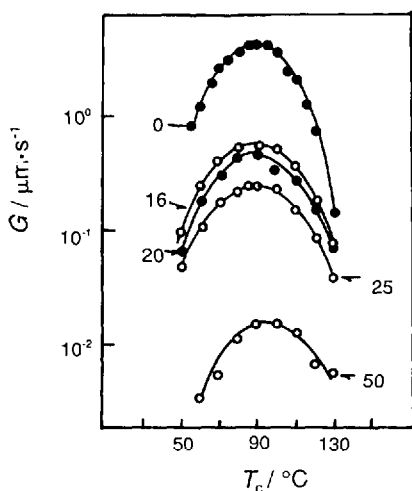


Figure 4.53 Plots of the growth rate of the spherulites against crystallization temperature T_c for PHB-CE blends with different compositions: neat PHB, PHB-CE1 blends (filled circles) and PHB-CE2 blends (open circles). Numerals on curves indicate the cellulose ester (CE) mass fraction

For polyethylene-polypropylene blends with melting temperatures around 140 and 170 °C the following experimental conditions may be used: sample size, 15 mg; temperature program, heating from 90 to 210 °C at 10 °C min⁻¹; and purge gas, N₂ at 50 ml min⁻¹.

A DSC curve produced using this procedure is shown in Figure 4.54. Using a suitable technique,

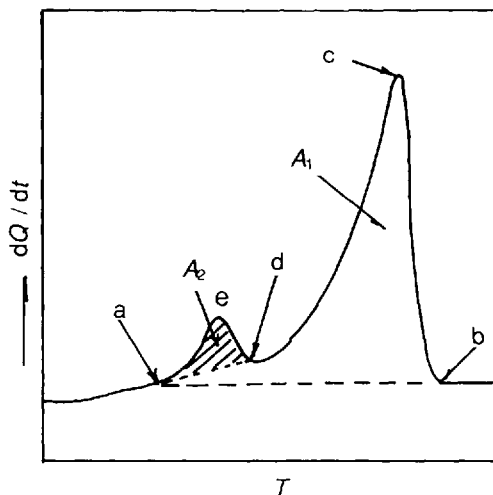


Figure 4.54 DSC curve for a PE-PP blend [75]. The known amount of PE in the blend is 14.0%

the area under the curves *adea* and *abcdea* in Figure 4.54 are integrated and the peak area fraction for the minor component, is calculated:

$$\text{area fraction} = (\text{adea}/\text{abcdea}) \times 100\% \quad (4.54)$$

Using the value of the area fraction, the mass fraction of PE in the blend is obtained from a previously prepared calibration graph shown in Figure 4.55. DSC measurements on an unknown sample should be carried out under conditions similar to those for the measurements of blends used for preparing the calibration graph. For example, the area fraction of PE shown in Figure 4.55 is

$$\text{area fraction} = \frac{5.94 \text{ cm}^2}{70.13 \text{ cm}^2} \times 100 = 8.5\%$$

and from the calibration graph the mass fraction of PE in the blend can be read as 14.1%.

4.4 Thermomechanometry

4.4.1 Measurement of Anisotropy of Polymer Films Using TMA

Thermomechanical analysis or thermomechanometry (TMA) is used to study the change in the dimensions of a sample as a

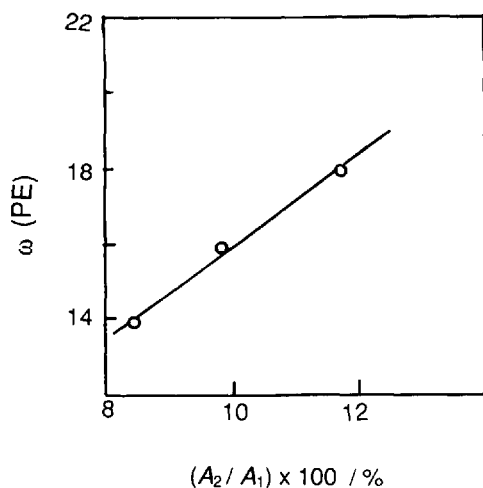


Figure 4.55 Calibration graph for PE-PP blends

function of temperature. This is demonstrated by TMA measurement of epoxy resin reinforced with glass-fiber. The TMA curves for epoxy resin reinforced with glass-fiber are given in Figure 4.56, which shows that the expansion coefficient for the sample varies with the direction. The inflection at about 130 °C observed for all three curves is attributed to the glass transition.

Generally, the physical properties of a polymeric film differ depending on the direction of stretching. This is caused by the orientation of the molecular chain in the stretching direction. Figure 4.57 shows the TMA curves for the PE

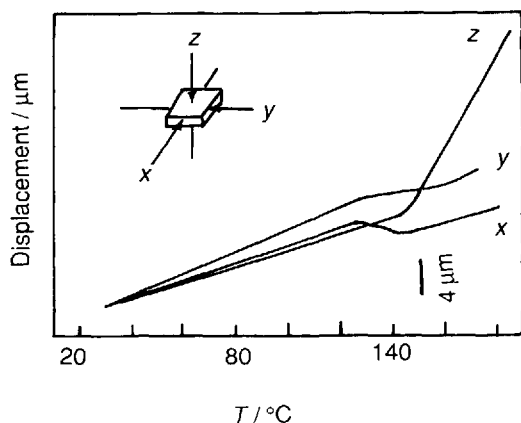


Figure 4.56 TMA curves in three directions for epoxy resin reinforced with glass-fiber [76]. Sample size, 7 × 7 × 1.6 mm; heating rate, 2.5 °C min⁻¹; load, 1 g; x, y and z, directions of stretching

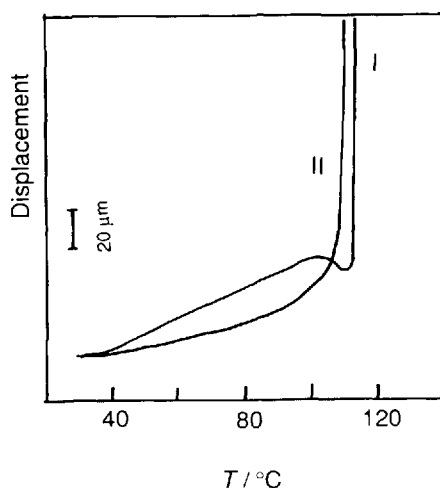


Figure 4.57 TMA curves for different directions of a polyethylene film. Sample size, 4–10 mm; heating rate, 5 °C min⁻¹; load, 2 g; I, in the direction of stretching; II, perpendicular to the direction of stretching

film obtained using a tension probe. It can be clearly seen that the thermal expansion and temperature of inflection depend markedly on the direction of measurement.

4.4.2 Restriction on Deformation of Polyethylene Films by Reinforcing Agents

Polyethylene film is extensively used as a packaging material. The mechanical properties of commercial films can generally be modified by adding suitable reinforcing agents.

Figure 4.58 represents the TMA curves for polyethylene films measured using a tension probe. The displacement decreases with increasing amount of reinforcing agent, indicating that reinforcing agents restrict the deformation of the sample. In Figure 4.58, shrinkage observed at about 105 °C is caused by the contraction of the stretched molecular chain and the abrupt elongation at about 110 °C is due to melting.

4.4.3 Penetration and Tension Measurements of Polymer Films by TMA

The softening temperature of a polymeric film is an important characteristic which can be

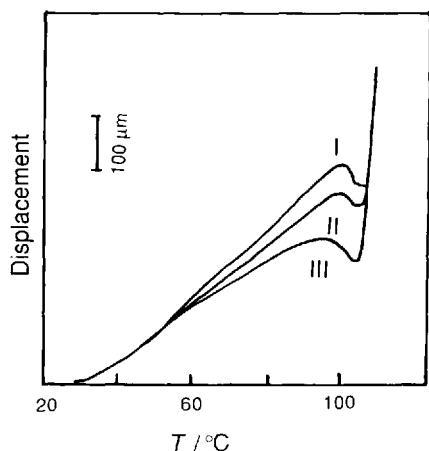


Figure 4.58 TMA curves for PE film using a tension probe [77]. Sample length, 2 mm; load, 2 g; heating rate, $5^{\circ}\text{C min}^{-1}$. Amount of reinforcing agent: I, 10%; II, 20%; III, 30%

evaluated by TMA penetration measurement. In this method, a probe with a small tip is placed on the sample film in the furnace and then heated under load. The probe will penetrate the sample when it starts to be softened and deformed. The initial deforming temperature is defined as the softening point, and the degree of deformation is dependent on various factors [78].

Figure 4.59 illustrates the results of penetration measurements for polyethylene (I), polypropylene (II) and Nylon (III) films. Figure 4.60 shows the TMA curves for polyethylene (PE) films measured using a tension probe at loads of 2, 3, 4 and

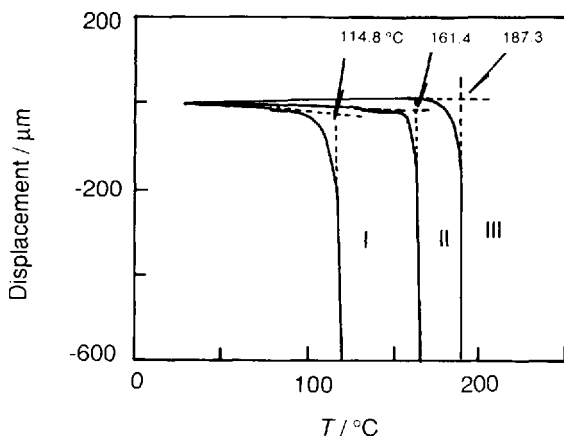


Figure 4.59 TMA curves for (I) PE, (II) PP and (III) nylon obtained using a penetration probe [79]. Load, 10 g; heating rate, $5^{\circ}\text{C min}^{-1}$

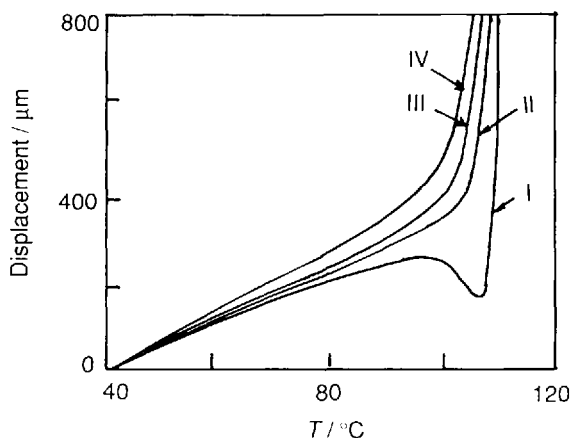


Figure 4.60 TMA curves for PE films measured using a tension probe at various loads [80]. Sample length, 10 mm. Load: I, 2 g; II, 3 g; III, 4 g; IV, 5 g

5 g. With increasing applied load, the transition temperature of PE film decreases, and at the same time the elongation increases. When the load is small, e.g. 2 g, contraction is observed. It is clear that the softening temperature may vary with the measurement conditions.

4.4.4 Dynamic Mechanical Spectra of Polymers

The dynamic mechanical properties of polymers are measured using various types of apparatus, as discussed in Chapter 2. By dynamic mechanical analysis, not only main chain motion but also the secondary relaxation can be detected. The mathematical structure of theories of dynamic viscoelastic properties has been presented [81,82] and application to polymers has been described [83].

Nylon 66-Poly(ether imide) (PEI) blend films were measured using a Rheometrics dynamic spectrometer in the shear mode operating at a frequency of 1 Hz and a constant strain of 0.1%. The dimensions of the test sample were $40 \times 12 \times 2$ mm. Nitrogen gas was circulated in the chamber to minimize degradation and chemical reaction during testing. The dynamic mechanical properties, shear storage modulus, G' , shear loss modulus, G'' , and the loss factor, $\tan \delta$, were measured at a heating rate of $3^{\circ}\text{C min}^{-1}$ over the temperature range -150°C to 300°C .

The shear storage moduli (G') of the blends are shown as a function of temperature in Figure 4.61 and the loss factor ($\tan \delta$) is shown in Figure 4.62. The three $\tan \delta$ peaks observed in PEI are denoted α , β and γ from high to low temperature. The α peak is attributed to the glass transition temperature, T_g , for the homopolymers. For the blend samples, the high $\tan \delta$ peak is attributed to the glass transition temperature of the PEI-rich phase and the lower $\tan \delta$ peak, $T_{g,2}$, that of the nylon 66-rich phase. The high T_g values of the blends are almost independent of composition. However, the lower T_g values of the blends increased with increasing content of PEI.

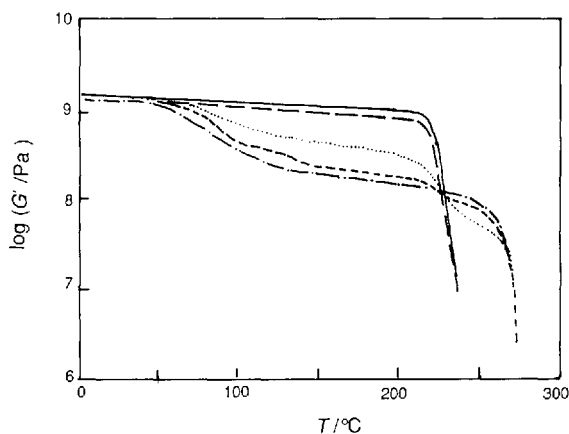


Figure 4.61 Shear storage modulus (G') curves for PEI, nylon 66 and PEV-nylon 66 blends [84]. PEI content (%): —, 100; — —, 90; ·····, 50; - - -, 10; — · —, 0

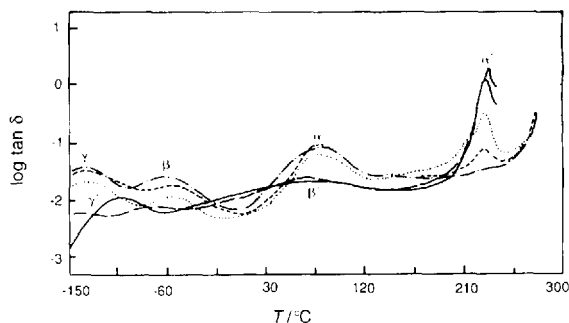


Figure 4.62 $\tan \delta$ versus temperature curves for PEI, nylon 66 and PEI-nylon 66 blends [84]. PEI content (%): —, 100; — —, 90; ·····, 50; - - -, 10; — · —, 0. PEI is commercially available as Ultem 1000 from GE with a density of 1.27 g cm^{-3}

The four secondary relaxations observed for the blends are denoted β , γ , β' and γ' . The secondary relaxation temperatures defined by the loss peaks are summarized in Table 4.6. The T_g values for the PEI phase were shifted to the high temperature side and the height of the loss peaks was reduced as the content of nylon 66 in the blends increased. T_{β} shifted to the high temperature side with increasing content of PEI in the blends, owing to the interaction between the two components in the blends. T_i relaxation is observed as a shoulder overlapping α' dispersion, as shown in Figure 4.62. T_i is located at about 213°C , regardless of the PEI content in the blends. It is assigned to the relaxation of the polymer chains at the interface region.

4.4.5 Activation Energy of Secondary Relaxation in Polymers

The activation energy of secondary relaxation in polymers can be measured by means of dynamic mechanical or dielectric relaxation spectroscopy. Dynamic mechanical or dielectric relaxation spectra of polymers can be obtained as a function of temperature at different frequencies. As an example, the dielectric relaxation behavior of the secondary relaxation in some AB cross-linked polymers is shown in Figure 4.63.

The Arrhenius plot of secondary relaxation in polymers is shown in Figure 4.64. It can be seen that a good linear relationship exists between the logarithmic relaxation time, $\log \tau$, and the

Table 4.6 Secondary relaxation temperatures ($^\circ\text{C}$) of the blends and homopolymers of PEI and nylon 66 [the numerals in the sample column indicate the PEI content (%)]

Sample	T_{β}	T_{γ}	T_i	$T_{\beta'}$	$T_{\gamma'}$
PEI 0	-62	-136			
PEI 5	-56	-130			
PEI 10	-54	-130	213		
PEI 15	-53	-133	213		
PEI 25	-52	-132	213		
PEI 50	-51	-134	213		
PEI 85				76	-75
PEI 90				79	-78
PEI 100				81	-101

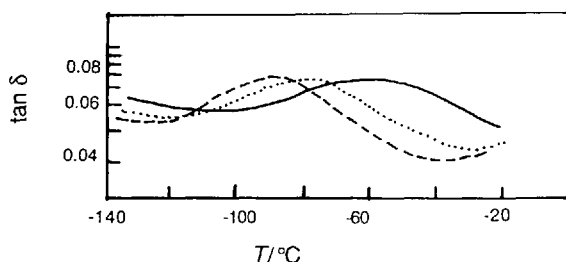


Figure 4.63 Dielectric loss spectra for the secondary relaxation regions in an AB cross-linked polymer [85], COVTPU50St50, at different frequencies: —, 1000 Hz; ·····, 110 Hz; ---, 30 Hz. COVTPU means vinyl-terminated polyurethane based on castor oil and 50 indicates a 50% mass fraction of the component in the AB cross-linked polymer

inverse of absolute temperature, a characteristic of the secondary relaxation in polymers. The activation energy of secondary relaxation in an AB cross-linked polymer, COVTPU50St50 (vinyl-terminated polyurethane, 50% mass fraction–polystyrene, 50% mass fraction), is calculated from Figure 4.64 to be 37.2 kJ mol^{-1} .

$$\tau = \tau_0 \exp(\Delta E^*/RT) \quad (4.55)$$

where τ_0 is the pre-exponential factor and R is the gas constant; τ can be calculated from $\tau = 1/2\pi f$ and f is the frequency. The value of the

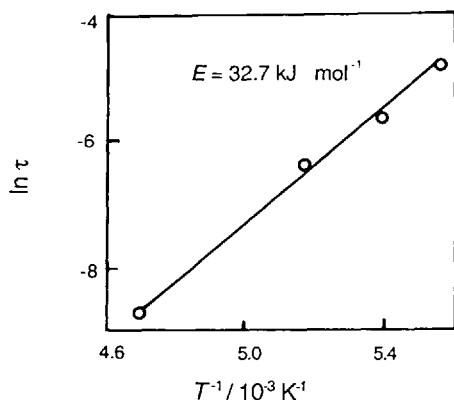


Figure 4.64 Arrhenius plot of secondary relaxation in the AB cross-linked polymer COVTPU50St50. Modern apparatus, such as a dynamic mechanical spectrometer and a dielectric measurement analyzer, are equipped with analytical software to calculate the activation energy

temperature, T , was decided using the dielectric relaxation spectra in Figure 4.63 where the peaks appear on the plots of $\tan \delta$ against temperature.

The dielectric measurement was carried out using a TRS-10C dielectric loss measuring apparatus (Japan Ando Electric). The heating rate was $2^\circ \text{C min}^{-1}$. The effective diameter of the electrode used was 3.8 cm, and a copper foil with a thickness of $22 \mu\text{m}$ was attached to the specimen in order to maintain close contact between the specimen and the surface of the electrode.

4.4.6 Master Curve of Polymers Using Dynamic Mechanical Spectra

Many viscoelastic parameters of polymers can be used to obtain master curves such as creep compliance J' , J'' , relaxation modulus E' , E'' , G' , G'' and loss factor $\tan \delta$. These viscoelastic variables of polymers are dependent on temperature, frequency and relaxation time. As an example, Figure 4.65 shows the experimental results and Figure 4.66 shows the master curve of PMMA. The parameter chosen is the storage moduli. The following procedure is recommended for the master curve measurement.

1. Measure the dynamic mechanical storage E' as a function of temperature at different frequencies.

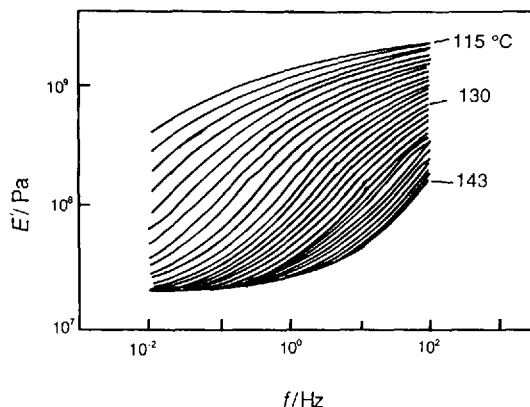


Figure 4.65 Plots of E' as a function of frequency at different temperatures for MMA

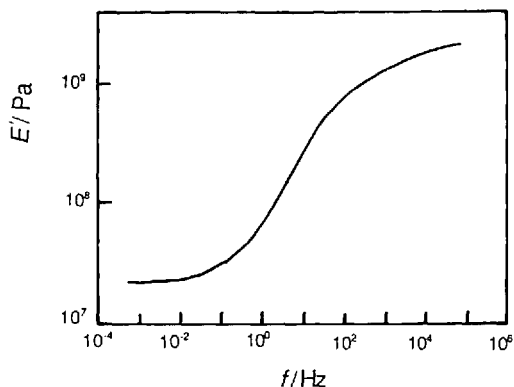


Figure 4.66 The master curve of E' as a function of frequency for PMMA ($T_g = 100^\circ\text{C}$) at $T_c = 130^\circ\text{C}$

2. Choose a reduced temperature T_0 ; $T_0 = 130^\circ\text{C}$ in Figure 4.76.
3. Calculate $E_r = E' T_0 \rho_0 / T \rho$, where the factor $T_0 \rho_0 / T \rho$ was applied in the reduced dynamic modulus E_r .
4. Exact matching of the shapes of adjacent curves is necessary, since T_g is one criterion for the applicability of reduced variables.
5. $\log a_T$ for each temperature ($T - T_0$) can be calculated by using the experimental curves.
6. The parameters, C_1 and C_2 in the WLF equation can be calculated by plotting $(-\log a_T)^{-1}$ against $(T - T_0)^{-1}$.
7. If C_1 and C_2 are known, the shift factor $\log a_T$ can be calculated from the WLF equation:

$$\log a_T = -C_1(T - T_0)/(C_2 + T - T_0) \quad (4.56)$$

These shift factors $\log a_T$ can be used to obtain the master curve.

4.4.7 DMA of Polymers in Humid Conditions

Molecular motion of hydrophilic polymers is enhanced in humid conditions and the transition temperature shifts to the low temperature side. A dynamic mechanical analyzer equipped with a humidity controller is used. The humidity controller is laboratory-assembled [86–88] or commercially available. The dynamic viscoelasticity of regenerated cellulose as a function of humidity is shown in Figure 4.67.

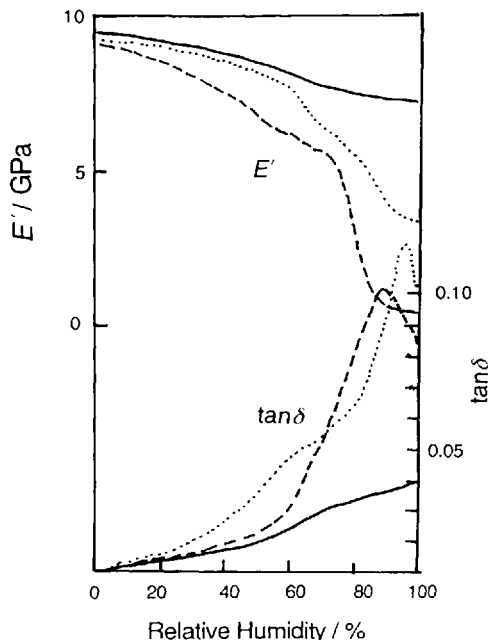


Figure 4.67 Dynamic viscoelasticity of regenerated cellulose as a function of humidity at 30°C (—), 50°C (.....) and 80°C (---)

4.5 Measurement of Water Content

4.5.1 Bound Water Content of Polymers Determined by DSC

Hydrated polymer systems have been widely investigated owing to the effect of water on the performance of commercial polymers and the crucial role played by water–polymer interactions in biological processes.

4.5.1.1 Determination of Dry Sample Mass

DSC is commonly used to determine the proportions of the various water fractions present in hydrated polymers. Hermetically sealed sample vessels are commonly used. If aluminum or silver sample vessels are to be used, they should be heated in an autoclave with a small amount of pure water at 373 K for several hours to prevent

the formation of aluminum hydroxide on the surface of the sample vessel.

All polymers contain a small amount of water which is absorbed during synthesis, processing or storage. This kind of closely associated water remains in the polymer matrix, even after heating the polymer at 100 °C under reduced pressure. It is important to establish the amount of this water fraction in order to determine the total amount of water present in the sample after hydration. To determine this intrinsic water content, the sample should be weighed as accurately as possible, noting that the sample will absorb water from the atmosphere during weighing. A microbalance with a sensitivity of the order of micrograms is necessary.

The sample vessel is pierced quickly, placed in the DSC at room temperature and heated at 10 °C min⁻¹. An endothermic deviation of the sample baseline due to the vaporization of water is observed. The presence of a very small amount of water can be detected by this procedure. The sample is heated until no deviation of the sample baseline is observed. The dried sample is then quickly reweighed and the intrinsic water content determined.

4.5.1.2 Determination of Freezing, Freezing Bound and Non-freezing Water

The uniformly hydrated sample is placed in the DSC at room temperature and cooled to -120 °C at 5–10 °C min⁻¹. The sample is held at -120 °C for 15 min and reheated to room temperature at the same rate. The temperature and number of crystallization exotherms observed depend on the nature of the polymer and the water content.

As shown in Figure 4.68, the first-order phase transition is not detected until a critical amount of water is added to a polymer (curve I). The amount of water is defined as non-freezing water content (W_{nf}) [89–92]. The maximum W_{nf} depends on the hydrophilicity of the polymer. When the water content in the polymer exceeds a critical amount, a small peak (peak II) is observed at a lower temperature than the crystallization peak of bulk water. The amount of water is categorized as freezing bound water content (W_{fb}).

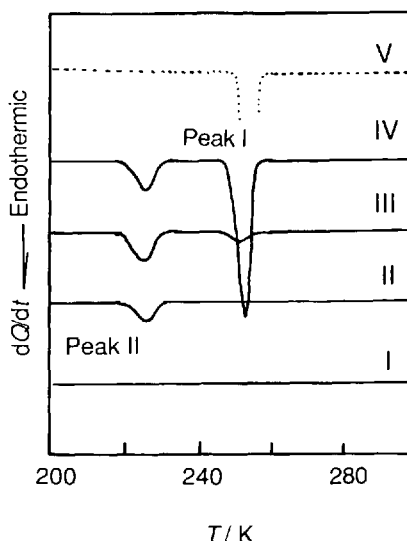


Figure 4.68 Schematic DSC cooling curves of water sorbed on hydrophilic polymers I, Non-freezing water (W_{nf}); II, W_{nf} + freezing bound water (W_{fb}), III, W_{nf} + W_{fb} + free water (W_f); IV, ...; V; bulk water

Free water (W_f) is shown as peak I on curves III and IV. W_f is the unbound water content in polymers whose transition temperature and enthalpy are equal to those of pure water (curve V).

$$W_c = W_{nf} + W_{fb} + W_f \quad (4.57)$$

Ordinarily, W_{fb} is small compared with W_{nf} and W_f . On this account, the total area of $W_f + W_{fb}$ per gram of dry sample (in Figure 4.69) is plotted as a function of W_c (g/g⁻¹). The intercept as indicated with the arrow in Figure 4.69 is adopted as W_{nf} .

4.5.2 Bound Water Content of Polymers Determined by TG

The mass of water, mass of dry sample, temperature of dehydration and rate of dehydration can be evaluated by TG. When TG-DTA is applied to water-sorbing samples, the heat of vaporization is simultaneously evaluated. For these measurements, an aluminum open-type crucible without a lid is usually used (see Section 2.2.1). The gas flow-rate markedly influences this type of measurement. Mass loss starts immediately after the water-sorbed sample is placed on the TG sample holder. The sample

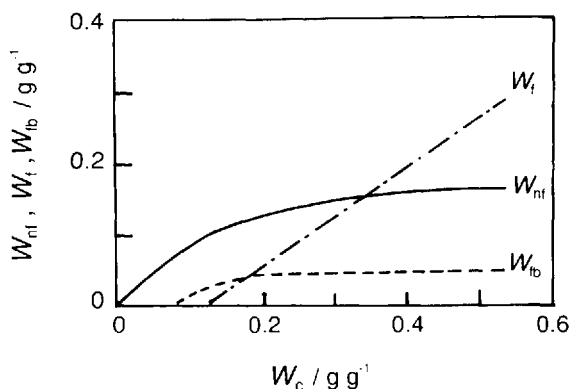


Figure 4.69 Schematic relationships between water content and free water, freezing bound water and non-freezing water content

mass increases when the sample is dry compared with the relative humidity at room temperature, or decreases if the sample sorbs a large amount of water compared with the relative humidity. On this account, it is difficult to attain equilibrated conditions at around room temperature. The following techniques are commonly applied: (1) the mass at the starting temperature is extrapolated from the TG curve at the steady state obtained on the high temperature side; (2) the sample is frozen in a coolant, picked up from the coolant, placed on the TG sample holder, and scanned immediately.

When water molecules co-exist with samples without any intermolecular interaction, the mass loss (TG) and vaporization peak (DTA) terminate at a temperature lower than 100 °C. In contrast, when water is tightly attached to polymers, mass loss is observed in two stages or multiple stages. Even if mass loss is observed in one stage on the TG curves, two or more peaks may be observed if the DTG curve (dm/dT) is deconvoluted. DTA endotherms due to vaporization also show multiple peaks.

Figure 4.70 shows schematic TG DTG curves of a polymer with non-freezing water (curve I) and a polymer with free and non-freezing water (curve II). The amount of each water fraction can be calculated from the area of each deconvoluted peak. The mass of water calculated from the vaporization method contains errors of several per cent in the repeatability, which are mainly due to setting the sample in the TG sample

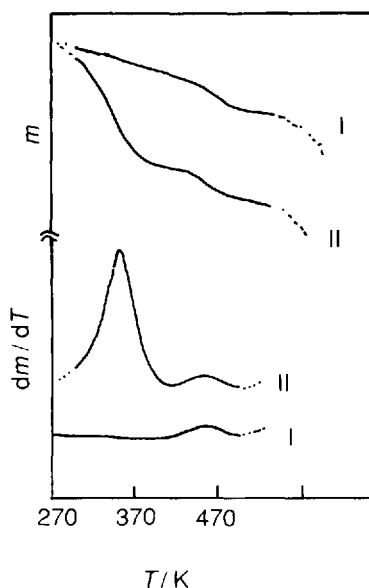


Figure 4.70 Schematic TG and DTG curves of water sorbed on hydrophilic polymers, I, Non-freezing water; II, free water and non-freezing water

holder. Results obtained by the TG method agree fairly well with those obtained by DSC [93].

4.5.3 Phase Diagram of Water–Polymer Systems

The transition temperature and enthalpy of solid water can be determined by the usual method (see Sections 4.2.1 and 4.2.3). Temperature calibration is usually carried out using melting and the crystal–crystal transition temperature of cyclohexane. A representative phase diagram using DSC is shown in Figure 4.71, where the water content (W_c) is expressed as mass of water/mass of dry sample. In the water–carboxymethylcellulose sodium salt system, glass transition (T_g), cold crystallization (T_{cc}), melting (T_m) of water and liquid crystallization (T^*) temperatures were observed. It is noteworthy that the bound water defined in Section 4.5.1 is in a thermodynamically non-equilibrium state. This suggests that the transition temperature depends on the measurement conditions and thermal history of the sample. The phase diagram established for water–polymer systems should be defined depending on the data from experimental conditions [94].

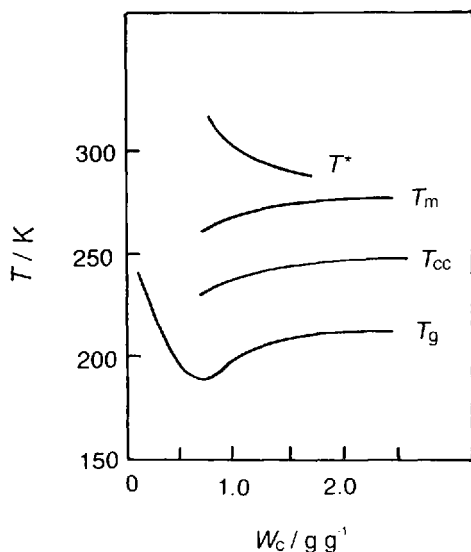


Figure 4.71 Phase diagrams of water-carboxymethylcellulose (CMC) sodium salt. Water content (W_c) = mass of water/mass of dry CMC, (g g^{-1}); heating rate, $10^\circ\text{C min}^{-1}$; sample mass, ca 5 mg; sample vessel, sealed-type aluminum

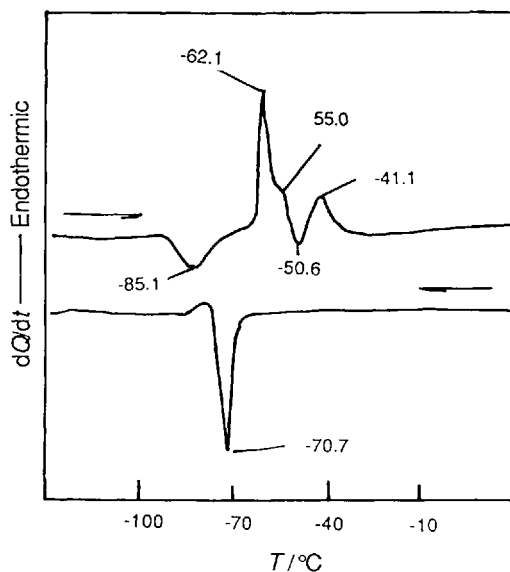


Figure 4.72 DSC curve for water-ethanol (40:60) mixture. Sample mass, 4.7 mg; scanning rate, 5°C min^{-1} ; sample vessel, sealed type

4.5.4 DSC Measurement of Mixtures of Water and Ethanol

Water-ethanol mixtures are measured by DSC as a practical application in brewing in order to estimate the degree of maturing of alcoholic drinks [95]. Figure 4.72 shows a DSC curve for a mixture of water and ethanol which was precooled from room temperature to -130°C prior to the heating run. The two peaks at about -62 and -41°C correspond to the melting of and recrystallization of water ethanol respectively; the shoulder peak at -55°C corresponds to the melting of the mixed solution. It is reported that, for whisky, the longer the storage period, the larger is the peak at -55°C (the size of this peak corresponds well with sampling tests carried out by brewers). The exothermic peaks at -85 and -50°C are recrystallization peaks for ethanol and water, respectively.

Figure 4.73 shows DSC curves, at a heating rate of 5°C min^{-1} , for samples which were cooled previously at various rates from room temperature. It is obvious that the precooling rate affects both the shape of the DSC curve and the temperature of the peaks, as indicated by A, B

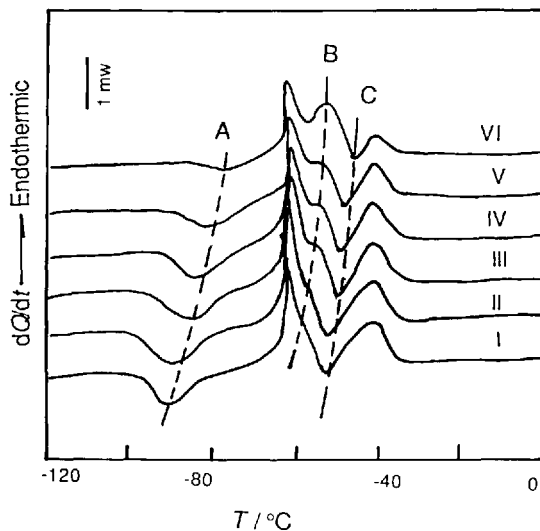


Figure 4.73 DSC curves for water-ethanol (40:60) mixture precooled at various cooling rates [96]: I, 20; II, 10; III, 5; IV, 2; V, 5; VI, $0.5^\circ\text{C min}^{-1}$. Sample mass, 4.7 mg; heating rate, 5°C min^{-1} ; sample vessel, aluminum sealed pan

and C. As shown in Figure 4.73, the lower the precooling rate, the larger is the melting peak at -55°C . It is noteworthy that the sample has to be precooled at the same rate before the DSC run.

4.5.5 Free and Bound Water in Biomaterials

Bound water is closely related to the physiological properties of biomaterials and affects the quality of foodstuffs and pharmaceuticals [97]. Figure 4.74 shows the DSC melting curves of the water in starch samples before and after gelatinization. Samples were measured using a hermetically sealed sample vessel. It can be clearly seen that the profile of the curve for the gelatinized starch is obviously different from that for the non-gelatinized starch. The sharp endothermic peak on both curves near 0 °C is due to the melting of the free water; the weak endothermic peak at about -5 °C on curve II is caused by the melting of bound water converted from part of the free water during gelatinization.

Figure 4.75 illustrates the DSC curves obtained for dextrin gel with various water contents. The endothermic peak at about 0 °C is attributed to the melting of the water and part of the water which begins to melt at approximately -10 °C can be attributed to bound water.

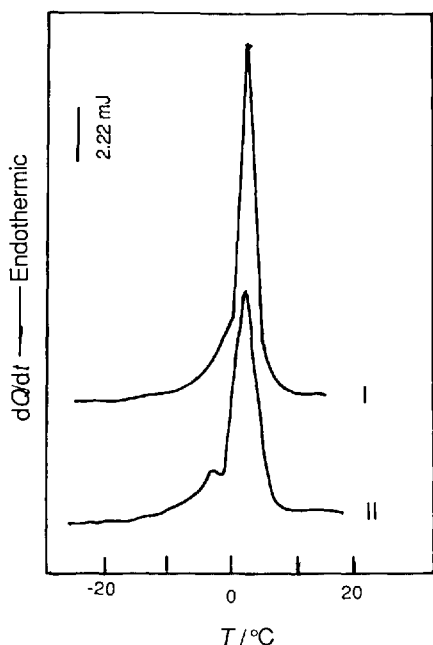


Figure 4.74 DSC curves for hydrous starch [98] I, before gelatinization; II, after gelatinization. Sample, starch with 50% of water; sample mass, 20 mg; heating rate, 2 °C min⁻¹

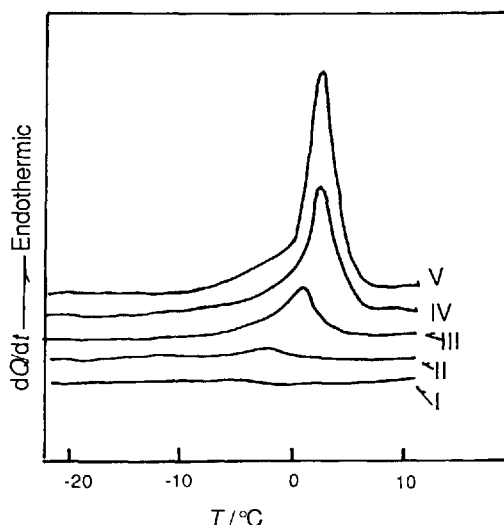
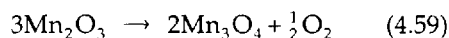
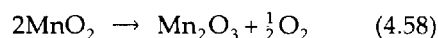


Figure 4.75 DSC curves for hydrous dextrin gel. Sample mass, 20 mg; heating rate, 2 °C min⁻¹. Water content: I, 2.5; II, 5; III, 10; IV, 15; V, 20 mg

4.5.6 Measurement of Water in Manganese Dioxide [99]

Manganese dioxide is widely used as a supporting electrolyte for cells. Since the negative electrode of cells is generally composed of alkalis, cells containing even a trace amount of water will self-discharge, produce gas and then deteriorate. Therefore, the quantitative determination of the water in MnO₂ is of great importance in stabilizing the cell power.

Figure 4.76 shows the TG-DTA curves for MnO₂ measured at ambient pressure. As shown by the TG curve, evaporation of water and then mass loss occur as soon as heating begins. The obvious mass losses at about 520 and 920 °C are attributed to the thermal decomposition reaction with the evolution of oxygen gas:



According to the above reactions, it is impossible to dry MnO₂ by heating it at ambient pressure. It was separately observed in a TG study that a pressure of 0.666 Pa, the water in MnO₂ does not completely evaporate until the temperature reaches 300 °C.

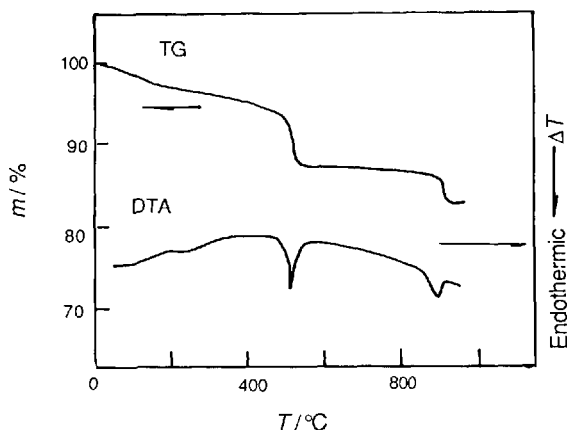


Figure 4.76 TG-DTA curve for MnO_2 at ambient pressure [99]. Sample mass, 40 mg; heating rate, 5°C min^{-1} ; atmosphere, air; flow-rate, 100 ml min^{-1}

4.5.7 Pressurized Dehydrolysis of Hydrated Aluminum Oxide

By pressurized dehydrolysis DSC (PDSC), the temperatures and the heat flows associated with transitions of materials can be measured as a function of time, temperature, purge gas composition and pressure (see Section 2.2.2). Figure 4.77 shows the PDSC curves of $\alpha\text{-Al}_2\text{O}_3 \cdot x\text{H}_2\text{O}$. The curves demonstrate that the dehydration peak of inter-layer water in $\alpha\text{-Al}_2\text{O}_3 \cdot x\text{H}_2\text{O}$ shifted to the higher temperature side as the pressure increased.

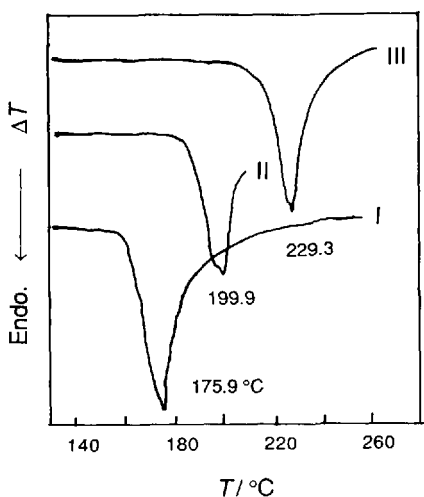


Figure 4.77 PDSC curves of $\alpha\text{-Al}_2\text{O}_3 \cdot x\text{H}_2\text{O}$ at various pressures: I, 0.5; II, 1.0; III, 2.0 MPa

4.6 Thermal Analysis of Metals and Alloys

4.6.1 Determination of Thermodynamic Parameters of Phase Transitions for Metals and Alloys

4.6.1.1 Crystallization and Melting of Metals and Alloys [100]

The crystallization of liquids or melting of crystals is an important phase transition. Melting temperatures are defined as shown in Figure 4.78 (see Sections 4.2.1 and 4.2.3).

By the determination of the melting point (T_m) and latent heat (Q), the melting entropy (S_m) and Gibbs free enthalpy difference of the transition are obtained. When $T < T_m$, the liquid crystallizes. If the volume difference of the Gibbs free enthalpy between the liquid and the crystal is ΔG_v , nuclei are spheres with a radius of r and the interface energy between the liquid and the crystals is σ , the Gibbs free enthalpy difference (ΔG) during nucleation is expressed as

$$\Delta G = (4/3)\pi r^3 \Delta G_v + 4\pi r^2 \sigma \quad (4.60)$$

If $\partial \Delta G / \partial r = 0$,

$$r_c = -2\sigma / S_m \Delta T \quad (4.61)$$

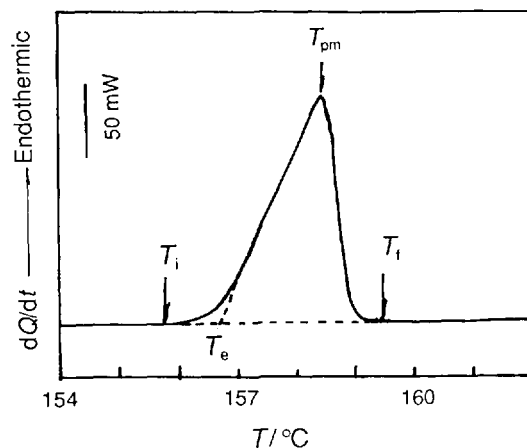


Figure 4.78 Melting DSC curve of indium. Sample mass, 20.398 mg; heating rate, 5°C min^{-1} ; $T_{pm} = 158.535^\circ\text{C}$; $Q = 572.742 \text{ mJ}$; $\Delta H = 28.081 \text{ J g}^{-1}$; height = 154.869 mW ; $T_c = 156.709^\circ\text{C}$

where $\Delta T = T_m - T$ is the degree of undercooling. When ΔT is small, the effect of the difference in specific heats between the liquid and the crystals (ΔC_p) on ΔG_v is negligible. ΔG shows a maximum at r_c . This positive ΔG is obtained by energy fluctuations of the system. Only when $r > r_c$ can nuclei grow with decreasing ΔG . When the compositions of the crystals and the liquid are different, diffusion and composition fluctuations are necessary in order to form and grow the nuclei. Thus, an induction time ($\tau_s \propto 1/\phi$) is required in the crystallization. ΔT increases with increasing ϕ . In equation (4.61), ΔT is the smallest value in thermodynamics. Owing to the existence of ΔT , T_m and $S_m = H_m/T_m$ cannot be measured by the crystallization of the liquid (H_m is the latent heat or enthalpy of the phase transition, which is equal to Q in this case).

During melting of the metals and alloys through heating, the liquid is formed on the surface of the crystalline specimen. Interfaces exist between the liquid and gas, and also between the liquid and the crystals. However, the interface between the crystals and the gas disappears. Combination of the above interface effects decreases ΔG . Hence, the formation of the liquid does not cause superheating. Through heating the crystals, T_m , H_m and S_m can be measured. The following experimental procedure is suggested:

1. A specimen of mass 5–10 mg is placed in the sample vessel and a constant argon gas flow is applied to avoid oxidation of specimens.
2. The specimen is heated at a rate of 20 K min^{-1} from $T_m - 200 \text{ K}$ to $T_m + 100 \text{ K}$ to measure T_m and H_m .

An example of melting for indium is shown in Figure 4.78.

4.6.1.2 Martensitic Transformation of Shape Memory Alloy [101]

During a solid-phase transformation, excess energetic terms are observed in addition to the transformation enthalpy. Even if there is no kinetic reason, ΔT is larger than that of the crystallization of the liquid. In order to obtain thermodynamic functions of the phase transfor-

mation, more thermodynamic data are necessary. Here, martensitic transformation of shape memory alloys is shown as an example of solid-phase transformations. When a shape memory alloy is deformed at lower temperature, a martensitic transformation occurs. After the alloy is heated to higher temperature accompanied by a reverse transformation, the original shape of the alloy is obtained. This effect is known as the shape memory effect.

Characteristics of this kind of transformation are that the composition of the alloy remains the same, the transformation can proceed in the reverse direction and coherent interfaces with a small σ arise during martensite formation. However, elastic energy, E_e is present because the lattice diameters and volumes of two phases are different E_e (to simplify, σ is included in E_e). The existence of E_e leads to the fact that M_s (subscripts i and f represent the start and finish temperatures of the phase transformation, respectively, and M stands for the martensitic transformation) is lower than the thermodynamic equilibrium temperature of two phases (T_0). During the reverse transformation, E_e promotes the phase transformation, which decreases the starting temperature of reverse transformation (A_i ; A stands for the austenite transformation) below T_0 . If E_e does not relax, $M_i = A_i$. However, during the reverse transformation, the distribution of E_e in the specimen is not homogeneous and the local E_e will quickly relax in an acoustic wave (E_t), which leads to an irreversible transformation. Since E_t is only a part of E_e , $M_i < A_i < T_0$, i.e. the transformation shows a hysteresis. Through measuring the transformation enthalpies Q^M , Q^A (to simplify, absolute values of Q and H are used; if they are negative, a negative sign is used), M_i , M_f , A_i and A_f , the above thermodynamic amounts can be calculated. The measurement and calculation methods are as follows:

1. A specimen of 40–50 mg with a shape represented by $r = 5.8 \text{ mm}$ and thickness $d = 0.2 \text{ mm}$ is placed in the sample vessel. A constant flow of argon gas is used to prevent the oxidation of the specimen.
2. The specimen is cooled at a rate of 20 K min^{-1}

- from $A_f + 20$ K to $M_f - 20$ K to measure M_i , M_f and Q^M .
3. The specimen is heated at a rate of 20 K min^{-1} from $M_f - 20$ K to $A_f + 20$ K to measure A_s , A_f and Q^A .
 4. The following equations are used to calculate the thermodynamic amounts:

$$T_0 = (M_i + A_f)/2 \quad (4.62)$$

$$\Delta S \approx Q^M/M_i \quad (4.63)$$

$$\Delta H = \Delta S T_0 \quad (4.64)$$

$$E_e = Q^M[(M_i + A_f)/(2M_i) - 1] \quad (4.65)$$

$$E_f = Q^A - Q^M \quad (4.66)$$

Figure 4.79 shows the measured curve for Cu-Al-Ni single crystals. If it is necessary to determine $E_e(x)$ and $E_f(x)$, where x is the transformation fraction, details can be found in the literature [102].

4.6.1.3 Glass Transition of Amorphous Alloys [103–105]

When the crystallization of liquid alloys can be prevented during cooling, glass or amorphous alloys are formed. A glass transition is a phase transition between a liquid and a glass, which

can be obtained by quenching the liquids or by a solid amorphization through diffusion of different elements at lower temperature or through mechanical alloying. The solid amorphization first leads to the formation of a supersaturated solution with a higher energetic state in comparison with glass. If long-distance diffusion of elements is impossible, this supersaturated solution is transformed to the glassy state to decrease the energetic state of the system. By thermal analysis, the glass transition temperature (T_g), the crystallization enthalpy of the liquid (H_x) and the activation energy for the glass transition (E_g) can be measured. The measurement of E_g will be introduced in Section 4.6.2.2.

A typical measuring curve for the glass transition is shown in Figure 4.80. In a binary system, diffusional crystallization is easier. Hence, glass crystallizes before a glass transition arises, and T_g cannot be observed. In this case, T_x (crystallization temperature of the glass) is used. The larger is T_g/T_m or T_x/T_m and the smaller is H_x , the greater is the glass-forming ability (GFA) of alloys. The relationship between H_x and H_m is as follows [102]:

$$H_x = H_m + \int_{T_m}^{T_x} C_p^{l-n} dt \quad (4.67)$$

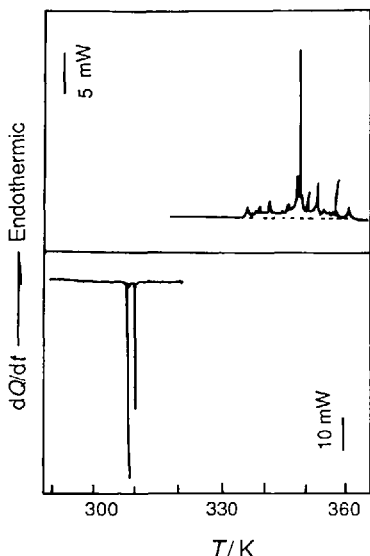


Figure 4.79 Martensitic and reverse transformations of Cu-Al-Ni single crystals

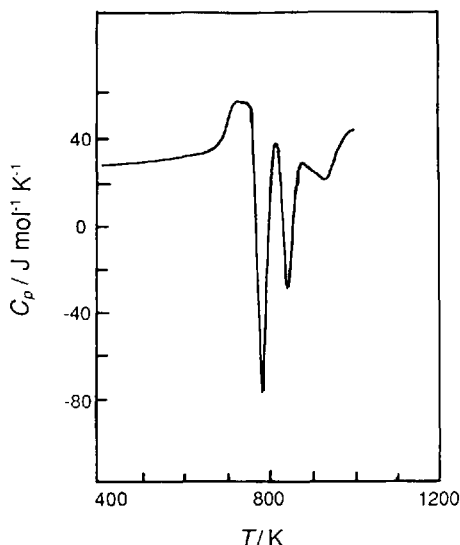


Figure 4.80 Glass transition of Zr-Al-Ni-Cu-Co alloys

where $\Delta C_p^{l-n} = C_p^l - C_p^n$ (C_p^l and C_p^n are the specific heat capacity of the liquid and the nanostructured crystals, respectively). Here C_p^n is used instead of the specific heat capacity of crystals (C_p^c) because the crystallized glass is nanostructured. In order to measure T_g , T_x and H_x the following approach is suggested:

1. A specimen in mass of 10 mg is placed in the sample holder. A constant flow of argon gas is used to prevent the oxidation of the specimen.
2. The specimen is heated to $T_g - 100$ K at a heating rate of 40 K min^{-1} , then cooled to ambient temperature with heating at $\phi = 200 \text{ K min}^{-1}$.
3. The specimen is heated through T_g and T_x at a heating rate of 40 K min^{-1} . The measurement is finished at $T = T_x + 100$ K. Then T_g , T_x and H_x are measured on the experimental curve.

Figure 4.81 shows a comparison between the measured $-H_x$ of Zr-Al-Ni-Cu-Co amorphous alloy and the calculated $H^{n-1}(-H_x)$. The results agree well. Since the temperature coefficient of the C_p^n function is very large, H_x does not increase as T_x increases.

4.6.1.4 Magnetic Transition of Metals and Alloys [106, 107]

At the Curie point of ferromagnetic materials, such as metals and alloys containing Fe, Co and Ni, the apparent mass of the specimen changes on the thermogravimetric (TG) curve (see Figure 4.82). Since the magnetic transition is a second-order phase transition, C_p changes at

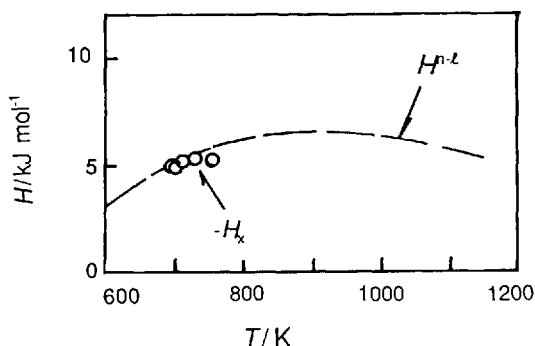


Figure 4.81 Comparison between the measured and calculated H_x [104]

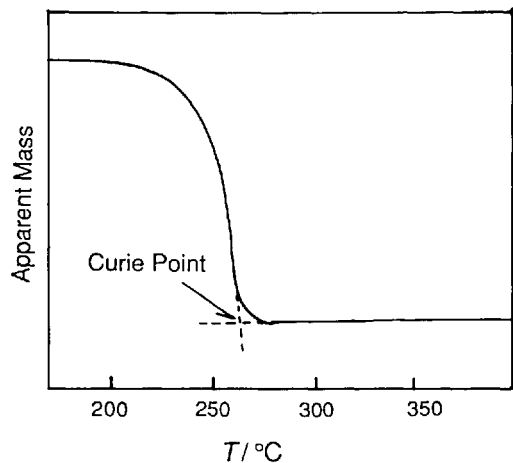


Figure 4.82 Curie transition of Fe-Si-B alloy

the transition. Hence the transition temperature can also be determined by C_p measurements.

Thermogravimetric method [106]—The TG method is performed as follows:

1. A specimen of mass 40 mg is placed in a sample holder of a thermogravimeter. The shape of the specimen is diameter $\phi = 5.8$ mm and $d = 0.2$ mm. A constant flow of argon is passed through the furnace to prevent the oxidation of the specimen.
2. A permanent magnet is placed around the sample holder.
3. The thermogravimetric curve is measured with a heating rate of 20 K min^{-1} and the Curie point of the specimen is defined as the onset point on the curve.

Figure 4.82 shows the measured result for Fe-Si-B alloy [106]. When the specimen is heated to the Curie point, the apparent mass of the specimen changes.

Specific heat method [108]—The steps in this method are as follows:

1. A specimen of mass 40 mg is placed in the sample holder of the DSC. The shape of the specimen is $\phi = 5.8$ mm and $d = 0.2$ mm. A constant flow of argon gas is passed through the furnace to prevent the oxidation of the specimen.

2. The specimen is heated at a heating rate of 40 K min^{-1} . The curve shows a sharp peak, as shown in Figure 4.83. The Curie point is defined as the peak.

Figure 4.83 shows the C_p s of Ni-Pd alloy. It should be noted that ΔH and ΔS still exist, although the magnetic transition is a second-order transition. The values of ΔH and ΔS are one or two orders of magnitude lower than those of the first-order transition. For example, $\Delta H = 0.22 \text{ kJ mol}^{-1}$ and $\Delta S = 0.48 \text{ J mol}^{-1} \text{ K}^{-1}$ for a solid solution of $\text{Ni}_{50}\text{Pd}_{50}$ at the magnetic transition.

4.6.1.5 Determination of an Equilibrium Phase Diagram [107]

DTA is a useful method for measuring an equilibrium phase diagram. For example, in order to establish a Gd-Co phase diagram, transformation temperatures of Gd_3Co are determined by DTA. The measuring method is as follows:

1. A specimen of mass 50 g is placed in an Al_2O_3 crucible with a flat bottom and a volume of 0.6 ml. The reference crucible is empty.
2. The furnace of the DTA is evacuated to 10^{-3} Pa, then argon gas is passed through the furnace, followed by evacuation again. This process is repeated twice to eliminate any remaining active gas.

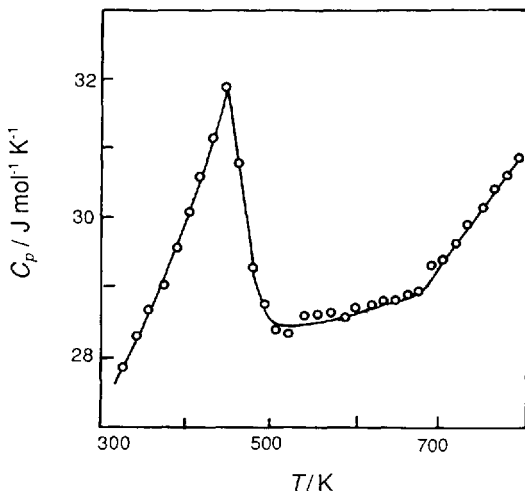


Figure 4.83 Specific heat measurement of Ni-Pd alloy [107]

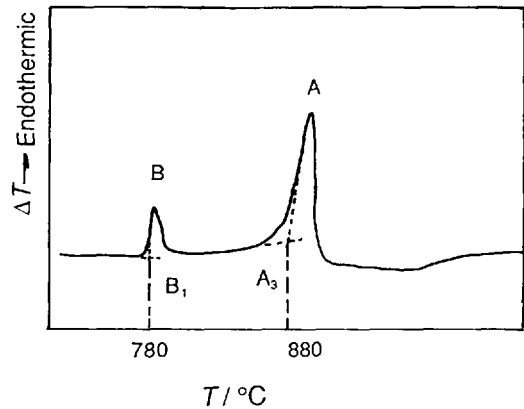


Figure 4.84 Phase transformation curve of Gd_3Co alloy [106]

3. Pure argon gas is passed through the furnace at 101.325 kPa (1 atm).
4. The temperatures of phase transformations are measured at a heating rate of 10 or -10 K min^{-1} .

Figure 4.84 shows the transformation temperatures (T_0) of Gd_3Co . The measured points are shown in the Gd-Co phase diagram (Figure 4.85). It should be noted that the phase transformation temperature of 780 K includes a

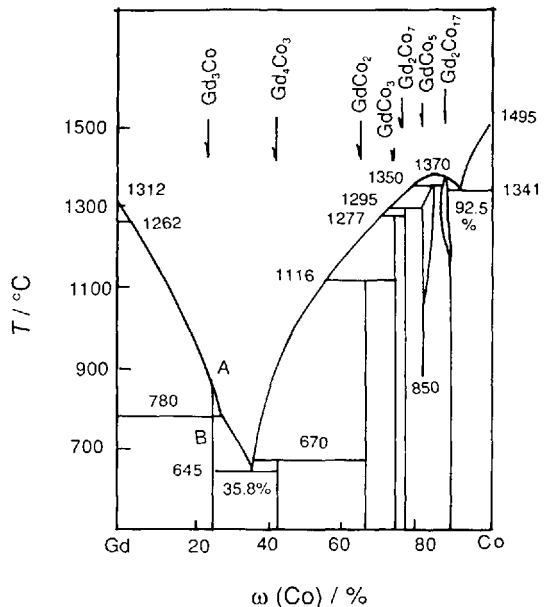


Figure 4.85 Binary Gd-Co diagram [106]

slight error, as explained earlier. In order to determine an accurate T_0 , M_i and A_i are measured through heating and cooling. Then T_0 is determined by using equation (4.62).

4.6.1.6 Mixing Enthalpy and Entropy of Metallic Liquid by Measurements and Calculation [108, 109]

The enthalpy H of a liquidus alloy consisting of A and B is not equal to the sum of H_A and H_B (enthalpies of elements A and B, respectively). During the formation of a liquid, mixing of different atoms leads to energy absorption or release (mixing enthalpy, H_{mix}). If it is assumed that the atom percentages of elements A and B are x_A and $1 - x_A$, H is expressed as:

$$H = H_{\text{mix}} + [x_A H_A + (1 - x_A) H_B] \quad (4.68)$$

H_A and H_B can be found in handbooks of thermodynamic data. H_{mix} is measured using a special DTA system where the solution element is melted in a crucible at a temperature higher than T_m . The solute element is added to the solution. The absorbed or released heat or H_{mix} are measured by DTA. After the measurement of H_{mix} , H is obtained by using equation (4.68). Figure 4.86 shows the measured and calculated H_{mix} [110].

The mixing entropy of a liquid can be calculated using the model of a regular solution:

$$S_{\text{mix}} = -k(x_A \ln x_A + x_B \ln x_B) \quad (4.69)$$

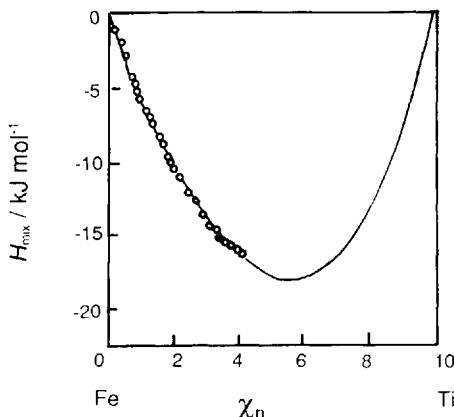


Figure 4.86 Measured H_{mix} points of Fe-Ti alloy [109]

where k is Boltzmann's constant. When the model of the regular solution cannot describe the thermodynamic behavior of the solution, there are many models of sub-regular solutions to treat the case. One of them is represented by the following equation with the assumption that the difference in atom sizes of two elements ($\phi_A \neq \phi_B$) changes

$$S_{\text{mix}} = -k[x_A \ln \phi_A + (1 - x_A) \ln \phi_B] \quad (4.70)$$

S_A and S_B values can be found by consulting relevant handbooks and using a calculation similar to equation (4.70), and then S is obtained. Finally, $G = H - TS$.

4.6.2 Determination of Kinetic Parameters for Phase Transformations of Metals and Alloys

4.6.2.1 Stable, Metastable and Unstable Phase Diagrams [111]

A stable phase diagram is a constitution diagram where all existing phases at any point (x, T) have the lowest $G(x, T)$. The kinetic characteristics of this diagram are that x and T change at an infinitely slow rate, or the time of phase transformation is subject to the condition of $\tau \rightarrow \infty$.

A metastable phase diagram is different from the stable type. The $G(x, T)$ function of the metastable phases is not located at a minimum position, but at a secondary minimum. Under the condition $\tau(T) > \tau_p(T)$ (the critical time), metastable phases transform to stable phases. A method to attain a metastable phase is that the stable phase in the (x_1, T_1) state under the condition $\tau(T) < \tau_p(T)$ changes to the (x_2, T_2) state (it is also allowed that only x or T changes). In order to obtain a metastable phase, the corresponding $\tau_p(T)$ must be realized technologically. When long-distance diffusion of atoms is required for crystallization of a liquid, amorphous alloys can be obtained by quenching the liquid under the condition of $\tau(T) < \tau_p(T)$. However, when the crystallization of a liquid is a polymorphous transformation, only a solid solution will be

formed. Therefore, amorphous alloys can be formed only in a phase zone where polymorphous crystallization cannot occur. This kind of metastable phase diagram is known as a polymorphous diagram. In the polymorphous diagram, x remains constant during a transition. Hence the degree of freedom of the phase diagram during a transformation is decreased. In other words, when a phase transformation occurs at any composition, there is a certain temperature where the Gibbs free enthalpies of the liquid and crystals are equal. As shown in Figure 4.87, the solid and liquid lines combine into one line (T_0 line). Between two T_0 lines there are the undercooled liquid ($T > T_k$) and glass ($T \leq T_k$), where T_k is the Kauzmann temperature.

Unstable phases cannot be thermodynamically and kinetically maintained. Any small change in x or T leads to a decrease in $G(x, T)$. The condition from a metastable phase to an unstable phase is known as the stability limit of phases. A nucleus of new phases is formed with $\sigma = 0$ and (T_0 line) $\tau_s = 0$ (τ_s is the induction time at the stability limit). Because $\tau_s \ll \tau_p$, the transformation must be a non-diffusion transformation (only

when $\tau > \tau_p$ does a diffusion transformation take place). When $T = T_k$ (stability limit), the difference in the entropies of two phases is $\Delta S(T) = S^l(T) - S^c(T) = 0$ where the metastable phase immediately transforms to another metastable or a stable phase. A diagram consisting of a $T_k(x)$ line is known as an unstable or isentropic diagram (see Figure 4.87). In Figure 4.87, the T_k line (isentropic temperature between undercooling liquid and crystal) is considered as the stability limit of the liquid. The stability limit of crystals is plotted as T_{sc} lines (isentropic temperature between overheating crystal and liquid). These isentropic lines show the existence of metastable phases. They are also helpful for estimating the GFA of alloys and for determining the temperature condition for a glass transition. Details can be found in the literature [103, 110, 111]. At T_k :

$$\Delta S(T_k) = T_m \int_{T_m}^{T_k} \Delta C_p(T)/T dT = 0 \quad (4.71)$$

where $\Delta C_p(T) = C_p^l(T) - C_p^c(T)$. T_k can also be obtained using equation (4.71). Details are given in Section 4.6.2.2.

4.6.2.2 Determination of Activation Energy for Phase Transformation [100]

In order to determine the activation energy, samples are measured at different heating rates (ϕ). To guarantee a correct temperature measurement for different ϕ s, factors affecting the results must be taken into consideration, i.e. ϕ in DSC varies between 0.01 and 500 K min⁻¹ (Pyris 1 DSC). However, if the mass of the specimens and crucibles is large (>100 g), the thermal conductivity of the specimen is not high when $\phi > 100$ K min⁻¹. Under this heating condition, the temperature of the specimen cannot reach the given temperature shown in DSC. Hence specimens for thermal analysis usually have a mass of <50 mg. To realize a large ϕ , it is suggested that an aluminum crucible (17 mg) is used. In order for the given and real temperature to coincide, temperature calibration should be carried out at the same ϕ as in the actual measurements. When $\phi < 1$ K min⁻¹, the temperature error is <0.5 K.

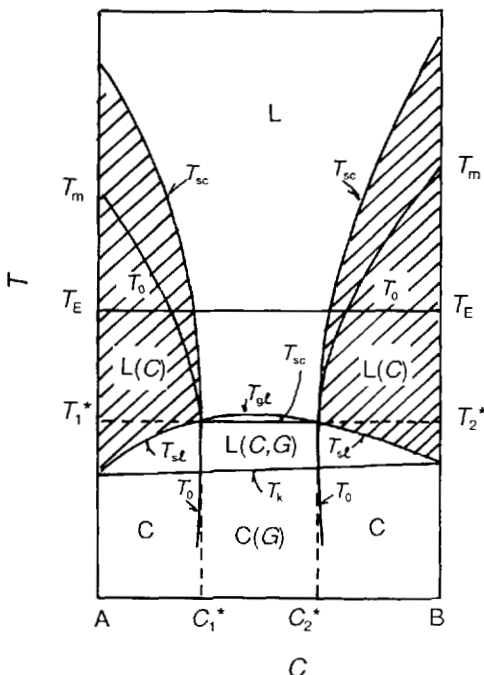


Figure 4.87 Binary polymorphous and isoentropic diagram

Activation energy is related to the order of phase transformation: a higher order of phase transformation gives a smaller activation energy, and a larger activation energy leads to a slow transformation rate. Therefore, the study of the activation energy for phase transformation can help in understanding the possibility of phase transformation and the stability of metastable phases. The activation energy of the crystallization of a liquid and glass (E_x), which is a first-order transformation, is measured as follows. The crystallization process can be described by the Johnson–Mehl–Avrami (JMA) model, the equation for which is

$$x(t) = 1 - \exp[-k'(t - t_0)^n] \quad (4.72)$$

where $x(t)$ as a function of time (t) is the transformation fraction, k' depends on T but is independent of t , t_0 is the induction time and n is the JMA exponent, which can describe the characteristics of transformation. For example, when the nucleus has the shape of a sphere with homogeneous bulk crystallization, $n = 4$. Usually n is 1–4. The parameter k' is defined as follows:

$$\ln k' = \ln k_0 - E_x/(kT_x) \quad (4.73)$$

where k_0 is a constant. In order to determine the JMA exponent n and E_x with equations (4.72) and (4.73), the following method is suggested:

1. A specimen of mass 5–10 mg is placed in the specimen vessel and a constant flow of argon gas is passed through the furnace to prevent oxidation of the specimen.
2. The specimen is heated to different temperatures near T_g with $\phi = 400 \text{ K min}^{-1}$. Then Q is measured.
3. Let $Q = H_x$. Kinetic software is used to calculate $x(t)$ and t_0 . From a plot of $\ln(t - t_0)$ against $\ln \ln[1/x(t)]$, the slope of the fitted straight line is obtained as n and the intercept of the line is $\ln k'$.
4. With the obtained $\ln k'$ at different T_x , a plot of $1/T_x$ against $\ln k$ is constructed and the slope of the line is $-E_x/k$.

The measured results for Ni–P alloy are shown in Figures 4.88 and 4.89 [100]. At first, transition is present only at the defect of amorphous alloys, such as surface ($n = 1.3$). Later, the bulk specimen

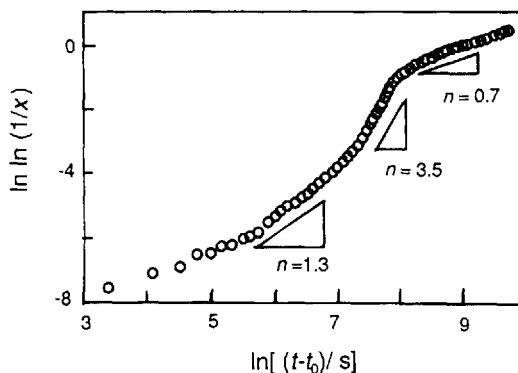


Figure 4.88 Measurement of Avrami exponent of Ni–P alloys [100]

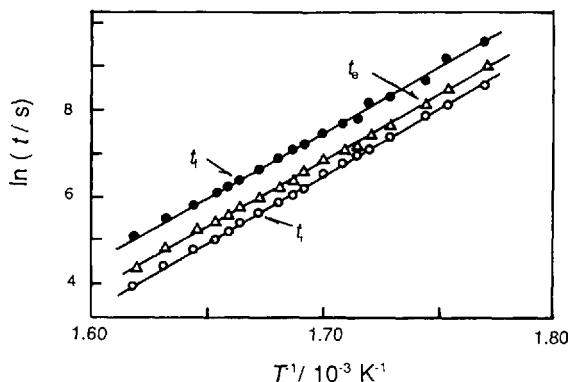


Figure 4.89 Determination of E_x for Ni–P alloy [100]

begins to transform ($n = 3.5$). Finally, growth of crystallites occurs ($n = 0.7$).

Melting of glass or a glass transition is a second-order transition, which is described by the Vogel–Fulcher law [103]:

$$\ln \tau = \ln \tau_0 - E_g/[k(T_g - T_k)] \quad (4.74)$$

The definition in equation (4.74) is the same as in equation (4.73). τ_0 is a constant. The measuring method is as follows:

1. A specimen of mass 5–10 mg is placed in the specimen holder and, a constant flow of argon gas is passed through the furnace to prevent oxidation of specimens.
2. The specimen is heated to $T_x + 100 \text{ K}$ with different ϕ s.
3. Let $\tau = (T_g - T_k)/\phi$ [103]. A plot is made of $\ln \tau$ against $1/(T_g - T)$. Through the change in T , a best fit with the smallest error is found. This T

is taken as T_k . The slope of the straight line is E_g/k .

Figure 4.90 shows the measured results for Pt-Ni-P alloy. From this method, the E_g obtained is of the order of 1 kJ mol^{-1} , which is two orders of magnitude smaller than E_x . From this result, it is obvious that a second-order transformation occurs much more easily than a first-order transformation.

4.6.2.3 Determination of Time-Temperature-Transformation Diagram (TTT Diagram), Continuous-temperature-Transformation Diagram (CTT Diagram) and Critical Cooling Rate

TTT and CTT diagrams describe the transformation fraction as a function of time. The starting and finishing times of the transformation (τ_i and τ_f) are the most important times. A TTT diagram is obtained by rapidly cooling the alloy to a certain temperature, then maintaining it for various time intervals. After the specimen has been quenched, the corresponding state of the alloy remains. By metallographic observations and X-ray diffraction, τ_i and τ_f are determined. For a CTT diagram, τ_i and τ_f are defined as the same as in a TTT diagram, but these values are measured during

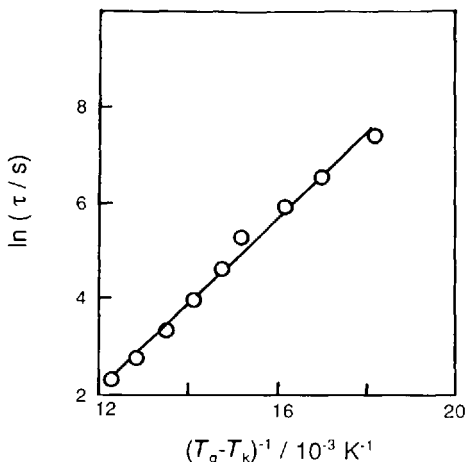


Figure 4.90 Plot of $\ln \tau$ against $1/(T_g - T_k)$ for Pt-Ni-P alloy

continuous cooling. A CTT diagram is more useful in technology, because it is similar to an actual industrial process. The critical cooling rate in a CTT diagram is very important and is expressed as $\phi_c = A/\tau_c$, where A is a constant and τ_c is the smallest τ_i at different T s. The condition to obtain a metastable phase is $\phi > \phi_c$.

For a glass transition, ϕ_c cannot be measured directly because usually $\phi_c = 10^6 \text{ K min}^{-1}$. Measurement of ϕ_c is carried out by measuring the $\tau_i(T)$ function for both the glass transition and crystallization near T_g . The measuring method is the same as in Section 4.6.2.2. The method of calculating $\tau_i(T)$ is by using equation (4.74), where T_x takes the place of T_g . Then $\tau_i(T)$ for the crystallization is obtained. Figure 14.91 shows a calculated CTT diagram for Zr-Al-Ni-Cu-Co alloy based on equation (4.74).

4.6.3 Determination of Specific Heats of Metals and Alloys

4.6.3.1 Measuring Methods for Specific Heats and Estimation of Measuring Error [101, 112]

C_p measurements are made by DSC. The standard method is the scanning method, which is performed as follows:

1. Argon gas is passed through the DSC furnace, and an empty pan is heated with $\phi = 40 \text{ K min}^{-1}$.
2. A specimen of mass 20–40 g with the shape

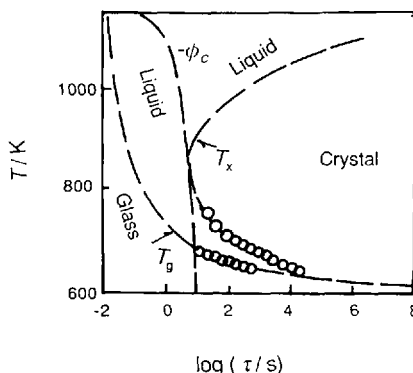


Figure 4.91 CTT diagram for Zr-Al-Ni-Cu-Co alloy [103]

- $\phi = 5.88 \text{ mm}$ and $d = 2 \text{ mm}$ is placed in the specimen holder and heated with $\phi = 40 \text{ K min}^{-1}$ with the same argon flow.
3. C_p values are obtained by the difference in heat flows between measurement runs with and without a specimen.
 4. The measured heat flow values are calibrated by comparison with measurements on a standard specimen (sapphire) with a similar mass to the specimen with $\phi = 40 \text{ K min}^{-1}$;
 5. To increase the measurement accuracy, the measuring error can be reduced by repeated measurements (according to the statistical theory, with N -fold measurements the measuring error is $N^{-1/2}$ of the original error) [112, 113].

Because C_p values are obtained by multiple measurements, repeatedly putting in and taking out specimens results in the crucible and specimen not being located in the same position each time, which in turn leads to errors. Hence calibration with a standard specimen may increase the possibility of errors arising (the measuring error of C_p is about 1%).

It should be noted that when the enthalpy is measured only once, measuring errors exist not only in the transformation temperature but also from the baseline. The enthalpy is obtained by integration of the measured area from the peak and a virtual baseline extending from the baseline. The error is small owing to this operation and is $<0.5\%$. If the enthalpy method is used to measure C_p , the measuring error decreases [113]. The enthalpy method is as follows:

1. A specimen of mass 20–40 mg with a shape $\phi = 5.8 \text{ mm}$ and $d = 2 \text{ mm}$ is placed in the specimen holder. Argon gas is passed through the DSC furnace to prevent the oxidation of the specimen.
2. The specimen is heated stepwise with $\phi = 0.1\text{--}10 \text{ K min}^{-1}$. After every 10 K heating step, a new quasi-balance state is established for the thermal arrest. Each individual measurement for one C_p value corresponds to an enthalpy measurement. The time for heating between two temperature steps is fixed in these measurements as 25% of the total. Thus an average ϕ is one quarter of the original ϕ .

3. With the same method an empty crucible is measured.
4. The measured curve with the empty crucible should be subtracted from the measured curve with the specimen. Then the area is integrated and divided by 10. The value obtained is the average C_p at the middle temperature of temperature range during heating.

A schematic diagram of the measurement is shown in Figure 4.92. An advantage of the enthalpy method is that relaxation of amorphous alloys does not influence the measured specific heat (C_p^s) because the relaxation arises not only during the heating, but also during the thermal arrest. Therefore, relaxation hardly changes C_p^s .

During the measurement of C_p , although argon gas is passed through the furnace, the oxidation must be carefully monitored. At higher temperature, trace oxidation will lead to trace heat release, and the temperature coefficient of C_p of metals and alloys decreases. Thus, when some alloys which are easily oxidized are measured, the specimen must be sealed. In addition, the mass of the specimen should be measured after the measurement. In our experience, if the mass increase is $<1\%$, the measured result is acceptable.

4.6.3.2 Determination of Specific Heats of Metastable Solids (Nanostructured Crystals, Amorphous Alloys, Superheated Crystals) [103, 104]

In order to measure C_p of metastable solids, it is

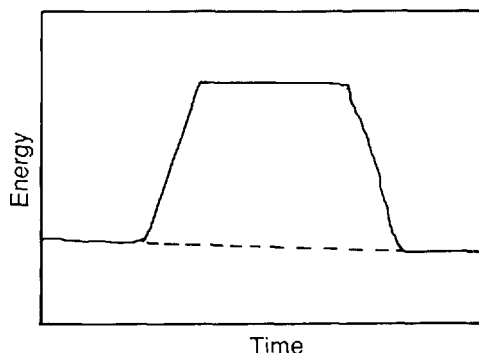


Figure 4.92 Schematic diagram of the enthalpy method

necessary to avoid transitions from the metastable phase to stable phases related to T and t . Using DSC with a standard ϕ , a characteristic temperature exists where this kind of transition arises. For nanostructure crystals, grains evidently begin growth at $0.4\text{--}0.6T_m$ and Figure 4.93 shows this case. In Figure 4.93, the C_p^n curve of Zr–Al–Ni–Cu–Co alloy changes the slope of the C_p function at 757 K showing this grain growth.

An amorphous alloy does not have a fixed thermodynamic state. When a liquid is rapidly cooled, a glass is formed. The glass obtained remains at a high energetic state of the liquid at T_g , and is known as quenched glass. When the glass is heated to a temperature lower than T_g , the as-quenched glass is relaxed and then has a lower energetic state. This glass is known as relaxed glass. If the relaxed glass is aged at a temperature lower than T_g , the longer the aging time, the lower is the energetic state of the glass. If C_p^g is measured with different ϕ s, this is the same as aging with different times. Hence the smaller is ϕ , the lower are the energetic state and C_p^g . Figure 4.93 shows the measured C_p^g values of Zr–Al–Ni–Cu–Co alloy with $\phi = 25, 50, 100, 200$ and 400 K min^{-1} , respectively. Therefore, the measured C_p^g depends on ϕ .

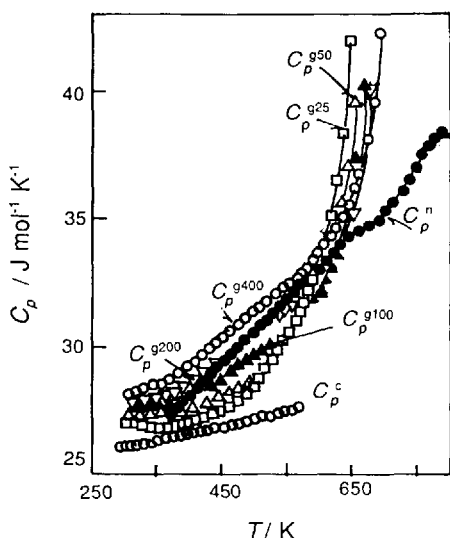


Figure 4.93 C_p^l , C_p^c and C_p^n for Zr–Al–Ni–Cu–Co alloy [103]

Crystals at $T > T_m$ are known as superheated crystals. To measure C_p^c , it is important to estimate the stability limit of crystals and melting must be avoided. Owing to σ , surfaces and interfaces of crystals have a higher energetic state and melt first at T_m . Atoms in the crystals remain in metastable states. Hence if surfaces are avoided, alloys can be superheated. In order to avoid the contribution of interfaces and surfaces, single crystals, such as plating metals, are selected. With these methods, a superheated crystal is obtained and its C_p^c can be measured.

4.6.3.3 Determination of Specific Heats of Undercooled Liquids (C_p^l)

Since liquids can easily react with crucibles, to measure C_p^l , it is necessary to use crucibles that do not undergo any reaction with the specimen. The measuring method is explained in Section 4.6.3.1. Usually $\phi < 0$ when $C_p^l(T > T_m)$ is measured because DSC can only measure up to 1000 K. If $\phi > 0$, the melting curve leads to the transition existing up to $T_m + 10\text{ K}$ or more, which decreases the measuring temperature range of C_p^l . When $T > 1000\text{ K}$, C_p^l of alloys is measured the relevant indirectly (C_p^l of elements can be found in relevant handbooks). One of the methods is to measure H_m at different temperatures (see Section 4.6.1.6). Then C_p^l is calculated with the following equations:

$$\Delta C_p(T_1) = [H_m^l(T_2) - H_m^l(T_1)] / (T_2 - T_1) \quad (4.75)$$

$$C_p^l(T_1) = C_p(T_1) + x_A C_{pA}^l(T_1) + x_B C_{pB}^l(T_1) \quad (4.76)$$

where ΔC_p is the difference between C_{pA}^l of the liquid and the mechanical mixture of elemental liquids and C_{pA}^l and C_{pB}^l are the C_p^l of liquids A and B, respectively.

A liquid at $T < T_m$ is called an undercooled liquid. The incubation time of metals and alloys is very short, hence C_p^l can only be measured near T_m . To extend the measuring temperature range or to increase undercooling, inhomogeneous nucleation must be avoided. This can be ensured as follows:

1. A crucible made of glass is used in order to increase the σ required for forming nuclei on the crucible wall.

2. The liquid is heated to a higher temperature to melt any crystallites.
3. The volume of liquid is decreased. When this is done, there are no nuclei in a drop of the liquid. This kind of small drop of liquid is obtained as follows: the liquid is stirred with argon gas, then an amorphous inorganic or organic emulsifier is added to the liquid. For 1 g of liquid, 5 ml of emulsifier is used to obtain drops of the liquid with a size of 5–30 μm . The disadvantage of this method is that the measuring accuracy of C_p^l is low owing to the presence of a large amount of emulsifier.

At T_g (about $0.5T_m$), C_p^l can be measured by heating glasses. For an alloy with a large GFA, the undercooled liquid can exist in the temperature range 20–30 K by a standard ϕ (such as 20 K min^{-1}). To increase the measuring temperature range of C_p^l near T_g , different ϕ s are used to get different T_g s. Since the undercooled liquid still exists at 20–30 K, the measuring temperature range is increased. Figure 4.94 shows the measured C_p^l results for Pt–Ni–P alloy near T_g and T_m .

4.6.4 Properties of Anti-oxidation of Metals and Alloys [106]

Thermogravimetric analysis (TGA) can be used to measure mass changes during heating and aging at a certain temperature. Thus TGA is used to study the corrosion resistance of metals and alloys. TGA can also compare the anti-oxidant ability of metals or alloys in different concentrations of various media. The measuring method is

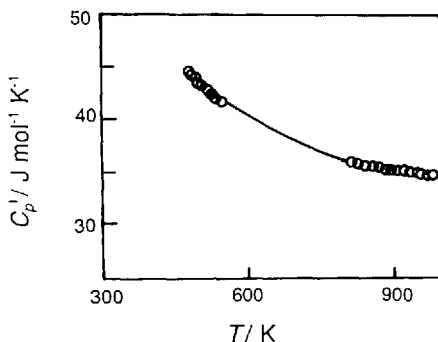


Figure 4.94 C_p^l values of Pt–Ni–P alloy [103]

as follows:

1. A specimen of mass 10 mg is heated to a certain temperature with $\phi = 500 \text{ K min}^{-1}$, and maintained at that temperature for various time intervals.
2. The furnace is evacuated to obtain a vacuum and purged, then supplied with different concentrations of a certain medium.
3. The mass increase is measured as a function of time.

Figure 4.95 shows an example of this method. The mass increase of Fe15Cr alloy at 900 °C with different volume fractions of H_2O was measured [106]. It is clear that the concentration of H_2O changes the corrosion resistance of Fe15Cr alloy.

4.6.5 Determination of Thermal Expansion Coefficients [106]

By using dynamic mechanical analysis (DMA), tensile, compression, bending and torsion tests can be carried out under static or dynamic conditions. Elastic moduli can also be obtained by DMA. With DMA, measurements of constant stress or constant strain can also be made. Thus thermal expansion coefficients, stress relaxation and creep can be investigated by DMA. Here we only give an example of the measurement of the thermal expansion coefficient. In Figure 4.96, the thermal expansion curves of Fe–Co–Si–B amorphous alloy are plotted. Curves 1 and 2 are the measured results for a relaxed glass and as-quenched glass,

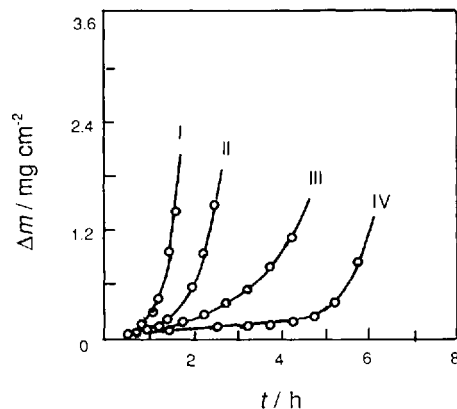


Figure 4.95 Mass increase of Fe15Cr alloy at 900 °C with different volume fraction of H_2O : I, 10; II, 6; III, 5; IV, 2%

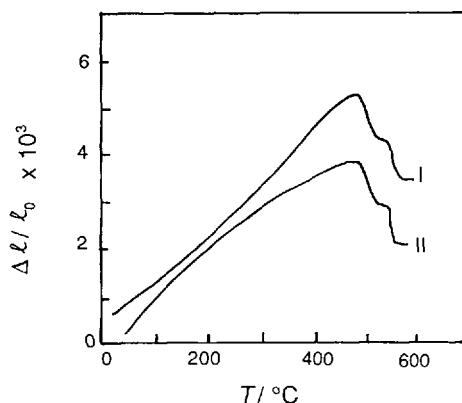


Figure 4.96 Thermal expansion curve of Fe-Co-Si-B alloy [106]. I, Relaxed glass; II, as quenched glass

respectively. Before crystallization, the linear expansion coefficient of the as-quenched glass is 8% smaller than that of the relaxed glass.

4.7 Miscellaneous

4.7.1 Cryobehavior of Suspended Single Cells by Low-temperature DSC

The understanding of the factors contributing to the cryoinjury of a suspended single cell is useful and helpful in cryopreservation of the cell. Low-temperature DSC is a powerful method for proving the thermodynamic basis of clinical cryopreservation. Standard DSC equipped with cooling accessories can be controlled from -150°C using liquid nitrogen and a cooling rate from 0.5 to $50^{\circ}\text{C min}^{-1}$. Various coolant suppliers are commercially available (see Chapter 2).

Figure 4.97 shows the DSC curve of McCoy's 5A medium supplemented with 10% AB serum. The sample was prepared as follows: Bone marrow and mononuclear cells, granulocytes and red cells were collected and washed. Fetal livers were removed from human fetuses from patients undergoing therapeutic abortion. The lower mononuclear cells were isolated using a Ficoll density separation gradient and washed for use. HL-60, CTLL2 and L929, three kinds of widely used cell lines, were cultured continuously. DMEM, IMDM, McCoy's 5A and

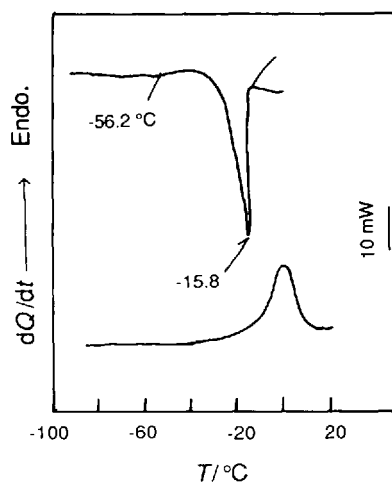


Figure 4.97 DSC curve of McCoy's 5A-AB serum solution. Sample mass, 3.9 mg; cooling rate, $5^{\circ}\text{C min}^{-1}$

RPM11640 were used as culture media and DMSO, glycerol and AB sera used as cryoprotective agents. Cell suspensions containing cryoprotective agents were placed in sealed aluminum pans. As shown in Figure 4.98, two exothermic peaks during cooling and one endothermic peak during thawing were observed.

Figure 4.98 was obtained from a system where a solution consisting of McCoy's medium with 10% AB serum was further supplemented with a final concentration of 10% of DMSO. It can be seen that the exothermic peak (-56.2°C and 12.3 Jg^{-1}) appearing in Figure 4.97 disappeared.

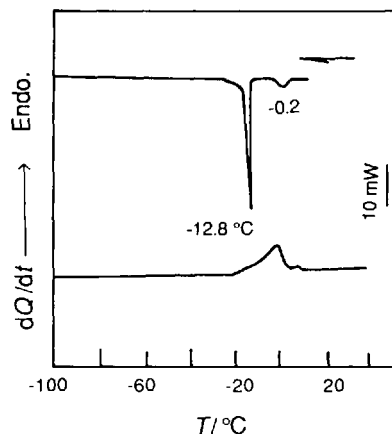


Figure 4.98 DSC curves of a cell-free system (10% AB serum-10% DMSO-80% McCoy's 5A medium. Sample mass, 3.9 mg; cooling rate, $5^{\circ}\text{C min}^{-1}$

In contrast, a new exothermic peak arose at -0.2°C . In the process of warming, two corresponding endothermic peaks emerged, one at -2.5°C (178 Jg^{-1}) and the other at 7.1°C (7.775 Jg^{-1}). Obviously, both of them lack the characteristics that the melting peak of pure water usually possesses as far as the temperature at which the melting occurs is concerned. It seems that the freezing system consisting of a cryoprotective agent will freeze or melt more or less as a mixture instead of as pure ice. The results of DSC measurements indicated that for definite cell species there exists a threshold of cell density in suspension. A cell density higher than the threshold may cause considerable delays for both exothermic and endothermic peaks. Medical cryobiologists should take this fact into consideration when programming the cryopreservation of high-density cell suspensions.

4.7.2 Thermal Analysis of Mixed Fat [114]

DSC can be used to determine mixed edible fat. This can be illustrated with the results obtained from a study of a mixture of lard and beef fat using DSC and the sealed sample pan technique.

Figure 4.99 shows the DSC melting curves for the mixed fat. It can be seen that the DSC curve I for pure lard exhibits a strong endothermic peak at about 30°C , and from curves II–IV for the mixed fat both the peak temperature and area decrease with increase in the proportion of beef fat in the samples. Finally, the peak almost disappears in the case of pure beef fat (curve V). Hence the content of beef fat (or other fat) in mixed fat can be evaluated from the peak heights on the DSC curves [114].

4.7.3 DSC Measurement of Edible Meat [115]

Edible meats contain a lot of protein and fat, and their quality can be estimated by a study on their melting behavior. Using high-precision DSC, tenderloin pork was measured.

Figure 4.100 shows the DSC curves for samples of raw meat and meat after being annealed for 20 min at 70°C . The exothermic

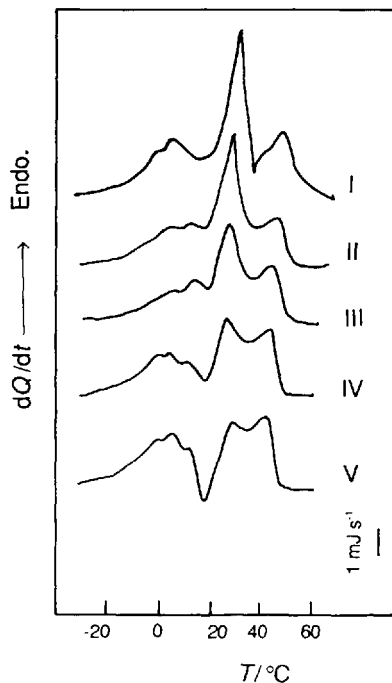


Figure 4.99 DSC curves for the melting of mixed fat. Sample mass, 40 mg; heating rate, $2^{\circ}\text{C min}^{-1}$; apparatus, Seiko SSC/560U DSC. Ratio of lard to beef fat: (I) 100 : 0; (II) 75 : 25; (III) 50 : 50; (IV) 25 : 75; (V) 0 : 100

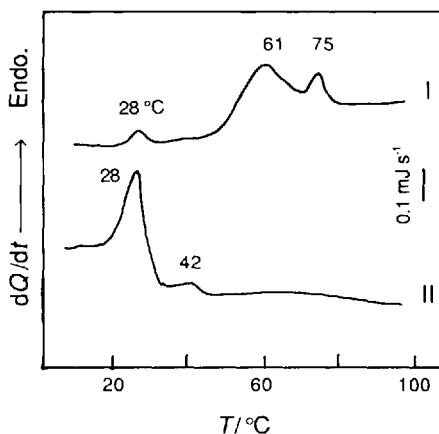


Figure 4.100 DSC curves for (I) raw pork sample and (II) pork after thermal treatment at 70°C for 20 min

peaks at about 28 and 42°C correspond to the melting of the fat in the samples. The endothermic peaks at about 60 and 75°C can be observed on curve I, but not on curve II, which is attributed to thermal denaturation of protein in the sample which was thermally treated.

The variation of DSC curves between samples with or without thermal treatment can aid in differentiating protein denaturation from fat melting, and consequently in identifying the contents of protein and fat.

4.7.4 Thermal Analysis of Silicone Rubber [116]

Since silicone rubber possesses many excellent properties, such as thermotolerance, electric insulation, chemical resistance, oil resistance and waterproofness, it can be used for making a great variety of machine elements and electrical components, and it is also widely used in various fields, such as household necessities, food processing and medicine production.

The characteristics of silicone rubber vary with both the kind and amount of additives used and the mixing and vulcanization conditions. Various thermal properties of silicone rubber can be inspected by means of thermal analysis.

Figure 4.101 shows the DSC curve for silicone rubber from -150°C to 0°C . The sample studied was rapidly cooled to below -150°C before the DSC run. As shown by the DSC curve, the glass transition at about -127°C , the exothermic cold crystallization peak at about -102°C and the endothermic melting peak at about -43°C of the sample can all be observed.

The thermotolerance of silicone rubber can be appraised with the help of TG-DTA. In the course of the decomposition of the sample, the

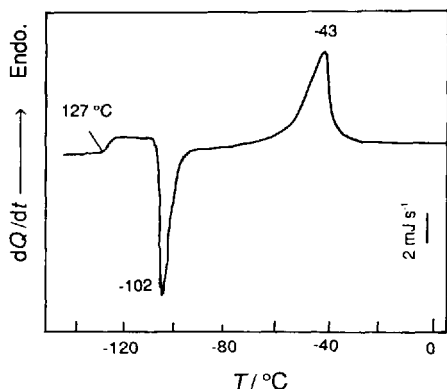


Figure 4.101 DSC curve for silicone rubber. Sample mass, 10 mg; heating rate, $10^{\circ}\text{C min}^{-1}$

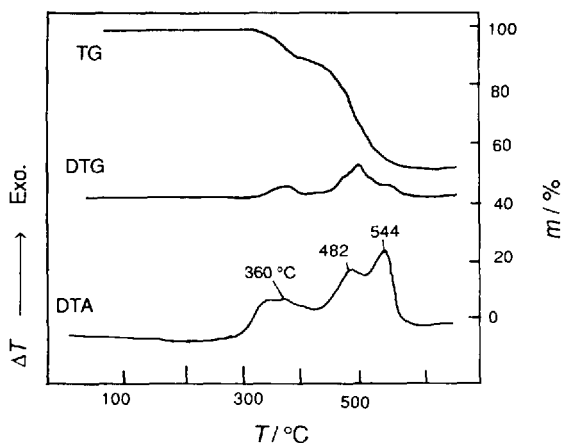


Figure 4.102 TG-DSC curves for thermal decomposition of silicone rubber. Sample mass, 15 mg; heating rate, $10^{\circ}\text{C min}^{-1}$; atmosphere, air; flow-rate, 200 ml min^{-1} .

exothermic peaks on the DTA curve and the mass loss which begins at approximately 300°C and reaches about 49% at 600°C can be observed (Figure 4.102).

4.8 References

- 1 Nakamura, S., Todoki, M., Nakamura, K., and Kanetsuna, H., *Thermochim. Acta*, 1989, **147**, 387.
- 2 Olabisi, O., Robeso, L. M., and Shaw, M. T., *Polymer-Polymer Miscibility*. New York, Academic Press, 1979.
- 3 Fox, T. G., and Flory, P. J., *J. Polym. Sci.*, 1954, **14**, 315.
- 4 Beevers, R. B., and White, E. G. T., *Trans. Faraday Soc.*, 1960, **56**, 744.
- 5 Thompson, E. V., *J. Polym. Sci., Part A-2*, 1966, **4**, 199.
- 6 Cowie, J. M. G., and Toprowski, P. J., *Eur. Polym. J.*, 1968, **4**, 621.
- 7 Cowie, J. M. G., and Bywater, S. J. J., *Polym. Sci. Part C*, 1970, **30**, 85.
- 8 Cowie, J. M. G., *Eur. Polym. J.*, 1973, **9**, 1041.
- 9 Hatakeyama, T., and Serizawa, M., *Polym. J.*, 1982, **14**, 51.
- 10 Struik, L. C. E., *Physical Aging in Amorphous Polymers and Other Materials*. Amsterdam, Elsevier, 1978.
- 11 Yoshida, H., and Kobayashi, Y., *J. Macromol. Sci.*, 1982, **B21**, 565.
- 12 Kasuga, K., Hatakeyama H., and Hatakeyama, T., *Mol. Cryst. Liq. Cryst.*, 1989, **27**, 168.
- 13 Ni, S., Liu, J. J., and Liu, W. Z., *Chin. J. Appl. Chem.*, 1989, **6**(2):15.

- 14 Liu, J. J., Liu, W. Z., and Zhou, H. R., *Chin. J. Appl. Chem.*, 1987, 4(2), 56.
- 15 Liu, J. J., Liu, W. Z., Zhou, H. R., and Yu, F. S., *Chin., J. Appl. Chem.*, 1987, 4(2), 56.
- 16 Nakamura, S., Todoki, M., Nakamura, K., and Kanetsuna, H., *Thermochim. Acta*, 1988, **136**, 163.
- 17 Hoffman, J. D., and Weeks, J. J., *J. Res. Natl. Bur. Stand. US*, 1962, **66**, 13.
- 18 Alfonso, G. C., Chiappa, V., Liu, J., et al., paper presented at a meeting of the Italian Association of Macromolecular Science and Technology, Ferrara, Italy, 1991.
- 19 Hoffman, J. D., *Soc. Plast. Eng. Trans.*, 1964, **4**, 315.
- 20 ASTM D3417-83.
- 21 Japanese Industrial Standard JIS K 7122-1987.
- 22 Monasse, B., and Handin, J. M., *Colloid Polym. Sci.*, 1985, **263**, 822.
- 23 Mandekern, L., *Chem. Rev.*, 1956, **56**, 903.
- 24 Baker, K. F., *Du Pont Thermal Analysis Technical Report*, No. TA-63.
- 25 Seiko Application Brief, TA. 9. Seiko.
- 26 Kamide, K., and Saito, M., *Fundamentals and Application of Thermal Analysis*. Tokyo, Realize, 1989, p. 70.
- 27 Liu, J., *Chin. J. Appl. Chem.*, 1993, **10**(1), 25.
- 28 Thomas, D. J., and Staveley, L. A. K., *J. Chem. Soc.*, 1952, 4569.
- 29 Marand, H., and Hoffman, J. D., *Macromolecules*, 1990, **23**, 3682.
- 30 Liu, J., *Chin. J. Appl. Chem.*, 1993, **10**(1), 25.
- 31 Alfonso, G. C., Chiappa, V., Liu, J., et al., *Eur. Polym. J.*, 1991, **27**, 795.
- 32 Day, M., Deslandes, Y., Roovers, J., et al., *Polymer*, 1991, **32**, 1258.
- 33 Hoffman, J. D., Davies, T., and Lauritzen, J. L., Jr, in Hannay, N. B. (Ed.), *Treatise in Solid State Chemistry*, Vol. 3. New York, Plenum Press, 1976, p. 570.
- 34 Liu, J., Tang, G., Qu, G., et al., *J. Appl. Polym. Sci.*, 1993, **47**, 2111.
- 35 Hoffman, J. D., Davies, T., and Lauritzen, J. L., Jr, in Hannay, N. B. (Ed.), *Treatise in Solid State Chemistry*, Vol. 3, New York, Plenum Press, 1976, p. 572.
- 36 TA Instruments, *Thermal Analysis Technical Report*, No. TA-123.
- 37 Seiko Technical Application Report, TA-7. Seiko.
- 38 Kawasaki, K., *Seiko Technical Application Report*, No. TA-26. Seiko.
- 39 *Application of Thermal Analysis to Polymers*. Shimadzu, 1991, p. 4.
- 40 Sorai, M., *Fundamentals and Application of Thermal Analysis*. Tokyo, Realize, 1989, p. 163.
- 41 Ohoki, K., and Ichimura, Y., *Seiko Technical Report*, No. TA-34. Seiko, 1986.
- 42 Sorai, M., *Fundamentals and Application of Thermal Analysis*. Tokyo, Realize Publisher, 1989, p. 163.
- 43 Chapoy, L. L., *Recent Advances in Liquid Crystalline Polymers*. London, Elsevier Applied Science, 1985.
- 44 Ciferri, A., Krigbaum, W. R., and Meyer, R. B., *Polymer Liquid Crystals*. New York, Academic Press, 1982.
- 45 Ciferri, A., *Liquid Crystallinity in Polymers: Principles and Fundamental Properties*. New York, VCH 1991.
- 46 Koide, N., *Fundamentals and Application of Thermal Analysis*. Tokyo, Realize, 1989, p. 165.
- 47 Ohta, M., *Shimadzu Hyoron*, 1986, **43**, 63.
- 48 Eibl, H., *Angew. Chem., Int. Ed. Engl.*, 1984, **23**, 257.
- 49 Blaine, R. L., *Du Pont Thermal Analysis Technical Literature, Application Brief*, No. TA-44. Wilmington, DE, Du Pont.
- 50 Houslay, M. D., and Stanley, K. K., *Dynamics of Biological Membranes*. Chichester, Wiley, 1984.
- 51 Kodama, M., Miyata, T., and Takaichi, Y., *Biochim. Biophys. Acta*, 1993, **1169**, 90.
- 52 Privalov, P. L., in *Advances in Protein Chemistry*, (C. B. Anfinsen, ed.). New York, Academic Press, 1979, Vol. 23, p. 169.
- 53 Privalov, P. L., and Khechinashvili, N. N., *J. Mol. Biol.*, 1974, **86**, 665.
- 54 Privalov, P. L., Plotnikov, V. V., and Filimonov, V. V., *J. Chem. Thermodyn.*, 1975, **4**, 41.
- 55 Kawasaki, K., *Seiko Technical Report*, No. 34. Seiko, 1986.
- 56 Fox, T. G., *Bull. Am. Phys. Soc.*, 1956, **1**, 123.
- 57 Gordon, M., and Taylor, J. S., *J. Appl. Chem.*, 1952, **2**, 495.
- 58 Guo, Q., *Makromol. Chem Rapid Commun.*, 1990, **11**, 279.
- 59 Utracki, L. A., *Polymer Alloys and Blends.*, New York, Oxford University Press, 1989.
- 60 Guo, Q., *Macromol. Chem. Rapid Commun.*, 1995, **16**, 785.
- 61 Zhong Z., and Guo, Q., *Polymer*, 1997, **38**, 279.
- 62 Guo, Q., Zheng, S., Li, J., and Mi, Y., *J. Polym. Sci. Polym. Chem. Ed.*, 1997, **35**, 211.
- 63 Fernandes, A. C., Barlow, J. W., and Paul, D. R., *J. Appl. Polym. Sci.*, 1984, **29**, 1971.
- 64 Vidotto G., Levy, D. L., and Kovacs, A. J., *Kolloid, Z. Z. Polym.*, 1969, **230**, 289.
- 65 Hoffman, J. D., *SPE. Trans.*, 1964, **4**, 315.
- 66 Nishi, T., and Wang, E. T., *Macromolecules*, 1975, **8**, 909; Stein, R. S., *J. Polym. Sci. Polym. Phys. Ed.*, 1981, **19**, 1281.
- 67 Morra, B. S., and Stein, R. S., *J. Polym. Sci. Polym. Phys. Ed.*, 1982, **20**, 2243.
- 68 Krevelen, D. W., *Properties of Polymers*, 2nd edn., Amsterdam, Elsevier, 1976.
- 69 Guo, Q., *Makromol. Chem.*, 1990, **191**, 2639.

- 70 Zheng, S. J., Huang, Y. H., Li Y., and Guo, Q., *J. Polym. Sci., Polym. Phys. Ed.*, 1997, **35**, (9), 1383.
- 71 McMaster, L. P., *Macromolecules*, 1973, **6**, 760.
- 72 Cong, G. M., Huang, Y. H., Macknight, W. J., and Karasz, F. E., *Macromolecules*, 1986, **19**, 2765.
- 73 Alfonso, G. C., Chiappa V., Liu, J., et al., *Eur. Polym. J.*, 1991, **27**, 795.
- 74 Pizzoli, M., Scandola, M., and Ceccorulli, G., *Macromolecules*, 1994, **27**, 4755.
- 75 Blaine, R. L., *Du Pont Thermal Analysis Technical Literature*, No. TA-36. Wilmington, DE, Du Pont, 1989.
- 76 Ichimura, Y., and Umehara, S., *Seiko Rep.*, 1985, No. 21.
- 77 Ichimura, Y., *Seiko Rep.*, 1985, No. 20.
- 78 Takahashi, T., Serizawa M., Okino T., and Kanetko, T., *Thermochim. Acta*, 1989, **147**, 387.
- 79 Ichimura, Y., and Umehara, S., *Seiko Rep.*, 1990, No. 51.
- 80 Ichimura, Y., and Nishimoto, U., *Seiko Rep.*, 1987 No. 47.
- 81 Gross, B., *Mathematical Structure of the Theories of Viscoelasticity*. Paris, Hermann, 1953.
- 82 Buche, F., *Physical Properties of Polymers*. New York, Wiley 1962.
- 83 Matsuoka, S., *Relaxation Phenomena in Polymers*. Munich, Hanzer, 1992.
- 84 Choi, K. Y., Lee, J. H., Lee, S. G., and Liu, J., *J. Polym. Eng. Sci.*, 1995, **35**, 1643.
- 85 Ni, S., Liu, J. J., and Liu, W. Z., *Chin. J. Appl. Chem.*, 1989, **6**(2), 15 (in Chinese).
- 86 Yano, S., and Hatakeyama, H., *Polymer*, 1988, **29**, 566.
- 87 Yano, S., Rigdahl, M., Kolseth, P., and de Ruvo, A., *Sven. Papperstidn.*, 1984, No. 18, R170.
- 88 Yano, S., Rigdahl, M., Kolseth, P., and de Ruvo, A., *Sven. Papperstidn.*, 1985, No. 3, R10.
- 89 Nakamura, K., Hatakeyama, T., and Hatakeyama, H., *Polymer*, 1983, **24**, 871.
- 90 Nakamura, K., Hatakeyama, T., and Hatakeyama, H., *Text. Res. J.*, 1981, **51**, 607.
- 91 Hatakeyama, T., Yoshida, H., and Hatakeyama, H., *Polymer*, 1987, **28**, 1282.
- 92 Hatakeyama, H., and Hatakeyama, T., *Thermochim. Acta*, in press.
- 93 Hatakeyama, T., Nakamura, K., and Hatakeyama, H., *Thermochim. Acta.*, 1988, **123**, 153.
- 94 Hatakeyama, T., and Hatakeyama, H., *ACS Sup. Ser.*, **489**, 329.
- 95 Koga, T. K., in *Fundamentals and Application of Thermal Analysis*, 2nd ed. Tokyo, Realize, 1982, p. 203.
- 96 Ichimura, Y., and Okubo, N., *Seiko Tehn. Rep.*, 1990, No. TA 52.
- 97 Uedaira, H., in Nishinari, K., and Yano, T. (Eds), *Science of Food Hydrocolloids*. Tokyo, Asakura, 1990, p. 7.
- 98 *Seiko Application Report*, 1983, No. 14.
- 99 *Seiko Application Report*, 1983, No. 16.
- 100 Lu, K., *Mater. Sci. Eng.*, 1996, **R16**, 161.
- 101 Jiang, Q., *J. Mater. Sci. Technol.*, 1995, **11**, 176.
- 102 Li, J. C., Nan, S. H., and Jiang, Q., *Acta Metall. Sin. (Engl. Lett.)*, 1996, **9**, 193.
- 103 Jiang, Q., Zhao, M., and Xu, X. Y., *Philos. Mag B*, 1997, **76**, 1.
- 104 Jiang, Q., Sui, Z. X., Li, J. C., and Xu, X. Y., *J. Mater. Sci. Technol*, 1997, **13**, 286.
- 105 Jiang, Q., Zhao M., and Li, J. C., *Acta Metall. Sin. (Engl. Lett.)*, 1995, **8**, 23.
- 106 Wei, X. L., in Liu, Z. H., and Hatakeyama, T., (Eds), *Handbook of Thermal Analysis*. Beijing, Chemical Industry Press, 1994, **96** (in Chinese).
- 107 Tomiska, J., Jiang, Q., and Luck, R., *Z. Metallkd.*, 1993, **84**, 755.
- 108 Jiang, Q., Xu, X. Y., Niu, H. J., and Lu, X. X., *J. Mater. Sci. Technol.*, 1996, **12**, 299.
- 109 Wang, H., Luck, R., and Predel, B., *Z. Metallkd.*, 1993, **84**, 662.
- 110 Jiang, Q., Xu, X. Y., and Li, J. C., *Acta Metall. Sin.*, 1997, **33**, 660.
- 111 Jiang, Q., Xu, X. Y., and Zhao, M., *Acta Metall Sin.*, 1997, **33**, 763.
- 112 Jiang, Q., Li, J. C., and Tong, J., *Mater. Sci. Eng.*, 1995, **A196**, 169.
- 113 Jiang, Q., Luck, R., and Predel, B., *Z. Metallkd.*, 1990, **81**, 9.
- 114 *Seiko Report*, 1979, No. TA 4.
- 115 Nishimoto, Y., *Seiko Report*, 1985, No. TA 33.
- 116 Ohkubo, N., *Seiko Report*, 1985, No. TA 18.

Application of TA to Chemical Reactions

5.1 Thermal Stability

5.1.1 Relative Thermal Stability of Polymeric Materials

The chemico-thermal stability of polymeric materials can be expressed by the mass loss at a particular temperature by thermogravimetry, since polymers are degraded by thermo-oxidative reactions. On the other hand, the thermal stability of the physical structure of materials is characterized by the softening temperature for

Table 5.1 Temperatures of 5% and 10% mass loss, residual mass at 700 °C and T_g values for heat-resistant polymers (for structures, see Table 5.2) [1]

Sample	Temperatures of mass loss/°C		Residual mass at 700 °C/%	T_g /°C
	5%	10%		
Upilex S	577	591	66.1	359
Kapton	553	566	59.8	428
Upilex R	550	562	65.4	303
Larc-TPI	530	547	64.8	256
Novax	517	537	60.1	399
Utem	490	500	53.3	216
PI-2080	484	521	63.1	342
PEEK	533	539	53.4	143
PSF	482	490	33.6	190
PESF	481	493	39.1	235
POD	474	485	46.5	—
PPX	464	469	9.0	70
U-polymer	451	462	28.8	190

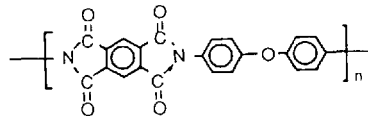
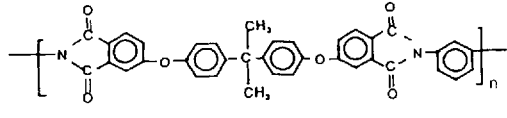
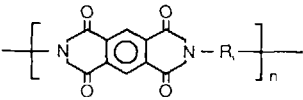
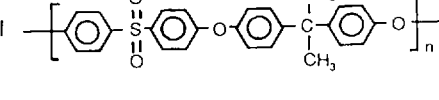
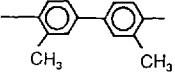
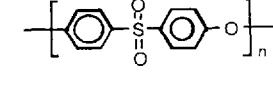
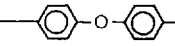
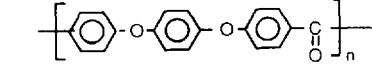
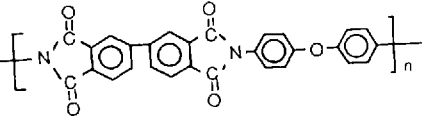
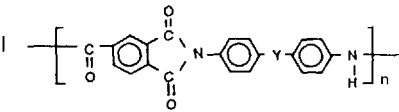
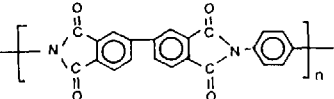
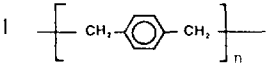
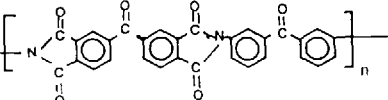
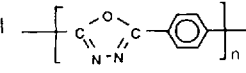
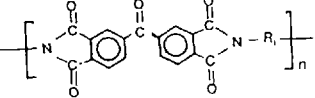
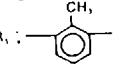
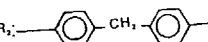
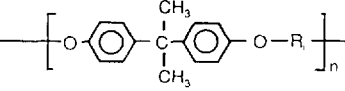

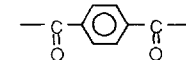
solid materials (such as the glass transition temperature, T_g , or melting temperature, T_m) by means of TMA, DMA or thermodilatometry. It is important to know the relative thermal stability in order to utilize polymeric materials in a conventional temperature range. Further, thermal stability is necessarily required in order to choose suitable synthetic and processing conditions.

For several typical heat-resistant polymers, the temperatures of 5% and 10% mass loss and residual mass at 700 °C obtained from TG curves, which were determined at a heating rate 5 °C min⁻¹ under an N₂ atmosphere, are given in Table 5.1. The T_g of each polymer is also given in Table 5.1. The structures of some heat-resistant polymers are given in Table 5.2.

5.1.2 Estimation of Thermal Index of Electrical Insulating Materials by the Toop Method

A test commonly used for estimating the lifetime of wire insulation is ANSI/AMTM procedure D-2307. Twisted pairs of insulated wire are aged in an oven for various time intervals (up to 50 days) at elevated temperatures (up to 240 °C) until voltage breakdown occurs. A series of such tests, performed at different oven temperatures, create a semi-logarithmic plot of lifetime versus the reciprocal of failure temperature. This procedure is useful but it is time consuming. For example, it takes many months for the

Table 5.2 Structures and T_g values of polyimides and other heat-resistant polymers

I 	VII 
II 	VIII 
R_1  (30%)	IX 
R_2  (70%)	X 
III 	XI 
IV 	XII 
V 	XIII 
VI  R_1  20 % R_2  80%	.IV  R_1  R_2 

completion of an experiment, particularly for highly stable materials. With the development of stable polymeric electrical insulation materials, the time needed for a full series of tests becomes enormous and it is impossible to carry out the tests. However, when the Toop method using the

data from a TG curve is introduced, the total time to evaluate a material is less than 1 day.

Toop [2] proposed an equation relating the mass-loss data obtained by both TG and aging in an oven concerning failure time, i.e. the mass loss at 5% was obtained either under dynamic

conditions or at constant temperature. In terms of kinetics, the failure time is estimated at the temperature T_f as shown in the following equation:

$$\ln t_f = (E/RT_f) + \ln[(E/\phi R)P(E/RT_c)] \quad (5.1)$$

where t_f (h) is the estimated time to failure at temperature T_f , assuming the mass-loss conversion is 5% in that time, E is the activation energy (J mol^{-1}), T_f is the failure temperature (K), R is the gas constant ($8.314 \text{ J mol}^{-1} \text{ K}^{-1}$), $P(E/RT_c)$ is a function of the kinetics of thermal analysis and T_c is the temperature of the TG curve for mass loss 5% at a heating rate ϕ ($^{\circ}\text{C min}^{-1}$).

When $20 < (E/RT_c) < 60$, the P function may be expressed by Doyle's approximate equation, and equation (5.1) can be rewritten as

$$T_f = (E/R) / [\ln t_f - \ln(E/\phi R) + 5.3305 + 1.052(E/RT_c)] \quad (5.2)$$

Usually the TG curve should be determined at a slow heating rate, and E was estimated for low conversion (say mass loss 5%) by using the Ozawa–Flynn–Wall method. If we assume $t_f = 20\,000$ h, T_f equals the thermal index of the material. With the use of higher temperatures, the shorter is the lifetime, as shown in Figure 5.1.

5.1.3 Estimation of Thermal Index of Electrical Insulating Materials by the TG-secant Method

The TG-secant method [3] is based on polyimide film as a standard of comparison assuming it has a thermal index of 240. From the TG curve of the sample, the index is calculated by the equation:

$$T_{20\,000}(^{\circ}\text{C}) = (A + B)/2K \quad (5.3)$$

where $T_{20\,000}$ ($^{\circ}\text{C}$) is the thermal index, that is, the temperature limitation for the long-term use (20 000 h) at the highest temperature A is the temperature at which a straight line drawn through the 50% and 20% mass-loss points intercepts the 0% mass-loss line, B is the temperature at which the curve intercepts the 50% mass-loss line and K is a factor obtained from a TG curve on polyimide film using equation (5.3). The purpose

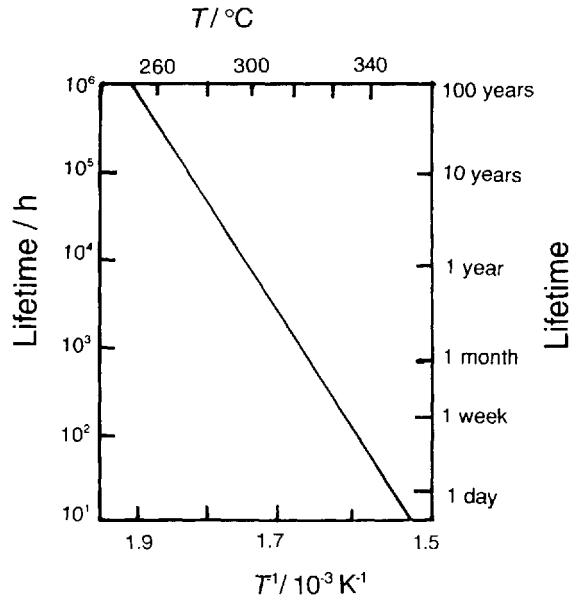


Figure 5.1 Temperature dependence of lifetime of insulating materials

of using K is twofold. First, it standardizes the instrument, thus putting all instruments on a comparative basis. Second, polyimide film is a good reference point because it has the highest thermal index of the most commonly used insulations.

For example, from TG curves of polyimide (PI) film (H film), determined using a sample mass of 10 mg and a heating rate of $5^{\circ}\text{C min}^{-1}$, in air, A and B were estimated to be 567 and 618°C , respectively. Using equation (5.3),

$$240^{\circ}\text{C} = (567^{\circ}\text{C} + 618^{\circ}\text{C})/2K \quad K = 2.47 \quad (5.4)$$

Under the same experimental conditions as mentioned above, from TG curves of a meltable polyimide, prepared from 3,3',4,4'-triphenyldioxytetracarboxylic acid and 4,4'-diaminodiphenyloxide, $A = 546^{\circ}\text{C}$, and $B = 603^{\circ}\text{C}$ were estimated. Then, using equation (5.3) and $K = 2.47$, $T_{20\,000} = 232^{\circ}\text{C}$ was obtained.

The TG-secant method is a valuable tool for shortening the development and evaluation time and selecting the material composition and technological conditions, although this method is not as accurate as routine oven-aging testing.

5.1.4 Determination of Oxidative Induction Time of Organic Materials

The useful lifetime of an organic product (e.g. polymers, lubricants) is often related to its resistance to oxidative decomposition, the so-called oxidative stability of the material [1, 4]. Oxidative degradation of polymers is an exothermic process and is detectable by differential scanning calorimetry (DSC). In order to determine oxidative stability by DSC, a small, unweighed sample is raised to an elevated temperature in an inert atmosphere. After reaching the desired temperature, the inert atmosphere of the sample is rapidly changed to an oxidizing atmosphere. The time to onset of the exothermic oxidation of the material is a measure of the oxidative stability of the product.

The experimental conditions for polyalkenes are sample size, 15 mg; temperature program, isothermal at 200 °C; inert gas, nitrogen; reactive gas, oxygen; gas flow-rate, 100 ml min⁻¹. The procedure is as follows:

1. One pellet of the resin sample is placed in an open (uncrimped) pan in the DSC sample holder at ambient temperature. An inert (nitrogen) gas purge is supplied to the sample holder.
2. The sample is equilibrated at the temperature of interest.
3. The purge gas is rapidly switched from the inert to the reactive gas (oxygen) and the recorder time base is started simultaneously.
4. The scan is continued until the oxidation exotherm is observed.

A typical DSC curve for polyethylene is shown in Fig. 5.2 [5].

The oxidative induction time (OIT) is determined from data recorded during the isothermal test. The elapsed time between time zero and the extrapolated onset of oxidation is recorded as a measure of oxidative stability. A dynamic heating method is also used. In this method, the sample is heated at a rate of 10 °C min⁻¹ from ambient temperature in an air or oxygen atmosphere. The temperature at the onset of oxidation is taken as a measure of oxidative stability. When

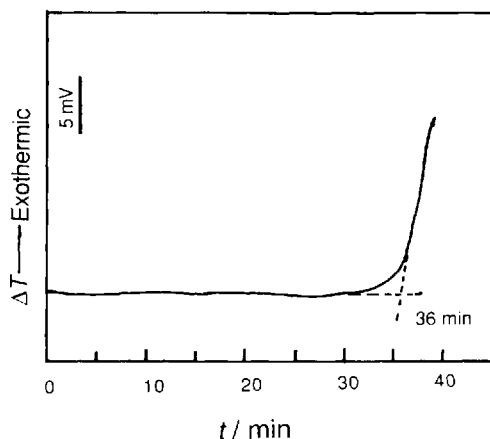


Figure 5.2 Determination of oxidative induction time of polyethylene. Sample mass, 21 mg; atmosphere, oxygen; temperature, maintained isothermally at 200 °C

an elevated partial pressure of the reactive gas is applied to the pressure cell, e.g. up to 7 MPa, the analysis time can be reduced in both of the above-mentioned model procedures for particularly stable products.

It is believed that copper or copper oxide is a catalyst for the oxidation of polyalkenes. For this reason, polymers to be used for coating copper wire should be run in copper or oxidized copper sample pans. Coating for aluminum wire should be run in aluminum pans. From an Arrhenius plot of the logarithm of oxidative induction time against reciprocal temperature, the oxidation energies were obtained as 110.9 kJ mol⁻¹ for an aluminum pan and 37.2 kJ mol⁻¹ for a copper pan [4–6].

Precision data from a round-robin test were obtained for polyethylene and polypropylene at 200 °C; the critical difference values of repeatability (between paired values) was 5.9 min for polyethylene and 6.9 min for polypropylene; the reproducibility (between averages of pairs) was 8.2 min for polyethylene and 14.1 min for polypropylene.

It is very important to control the temperature carefully. For example, when grease is measured, a difference of 1 °C at constant temperature leads to a 10% variation in the experimental results. Oxygen is a strong oxidant which accelerates combustion. Oil and grease should be eliminated from equipment when oxygen or

oxygen-containing materials are measured. The surfaces of the apparatus should be clean.

5.2. Cross-linking and Polymerization Reactions

5.2.1 The Contents, Construction, and Significance of Time–Temperature–Transformation (TTT) Isothermal Cure Diagram

The time–temperature–transformation (TTT) isothermal cure diagram, as shown in Figure 5.3, was suggested by Gillham [7]. Further work in this area has been carried out by the same group [8–10] and many other researchers.

The diagram generally shows the three critical temperatures in the course of the curing process: $T_{g,\infty}$ (T_g for completely cured thermoset), $_{gel}T_g$ (the temperature at which vitrification and gelation occur simultaneously) and $T_{g,0}$ (T_g for reactant); in addition to the various material states encountered during cure: liquid, sol/gel rubber, elastomer, gelled glass, ungelled glass and char. In the diagram, a full cure curve [10] (viz. $T_g = T_{g,\infty}$) divides the gelled glass region into two

areas: in the absence of degradation, the upper area represents the gelled glass state and the lower area the sol/gel (incompletely cured) glass state. In the liquid region there are a series of iso-viscosity curves showing the variation in viscosity, and sometimes phase separation curves (not shown in Figure 5.3) for a multi-component system (e.g. rubber-modified epoxy resin). In actual practise the TTT diagram usually shows only part of the above contents, i.e. the two most essential curves: the gelation curve and the sigmoid vitrification curve.

The procedure for constructing a TTT diagram is as follows:

1. Measure $T_{g,\infty}$ and $T_{g,0}$ of the sample using either torsional braid analysis (TBA) or dynamic thermomechanometry (DMA).
2. Perform several isothermal cure measurements at several pre-selected temperatures ranging from $T_{g,0}$ to $T_{g,\infty}$.
3. Read t_{gel} , the time to gel, and t_{vit} the time to vitrify, which can be defined as peak temperatures on the TBA or DMA isothermal curve.
4. On the coordinate system of T_{cure} (the cure temperature) versus $\log t$ (the cure time), draw the gelation curve and the vitrification curve.
5. Then draw a straight line parallel with the time axis from the intersection point of the above two curves with the temperature axis, obtaining an intersection point, i.e. $_{gel}T_g$.
6. Refer to the literature for constructing the iso-viscosity curves [8], the charring vitrification curve [9] and the full cure curve [10].

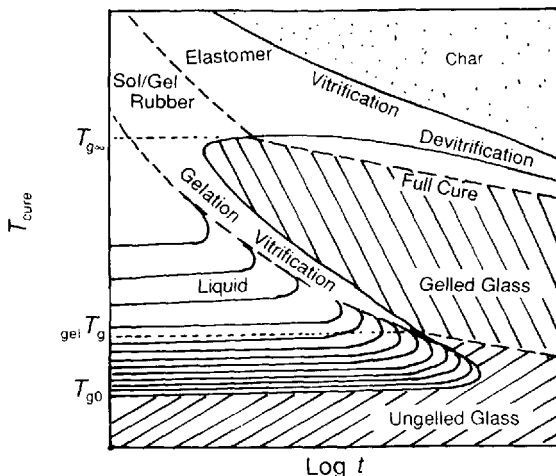


Figure 5.3 Time–temperature–transformation (III) isothermal cure diagram

The TTT diagram provides a clear graph for the purpose of understanding and comparing the curing process and the physical properties of the thermosets. The diagram shows the relationship between the various phase transition phenomena, such as gelation and vitrification, and the curing time or temperature during cure. Gelation is a process in which a network of infinite molecular weight is formed, thus showing viscoelastic behavior; vitrification begins to occur as the glass transition temperature, $T_{g'}$, increases and approaches the cure temperature, T_{cure} . The decrease in T_g due to degradation is called 'devitrification.' These transformations caused

by chemical reaction bring about vitrification in the system which is shown as the hatched area in Figure 5.3. In industrial applications, thermosets are often identified under three conditions or at three stages of cure: stages, A, B and C corresponding to ungelled glass, sol/gel glass and gelled glass, respectively.

The TTT diagram can be used to interpret the effect of the phase transformation on the physical properties of thermosets during curing. For example, polymer flow and growth of the disperse phase are inhibited by gelation. At the same time, chemical conversion is retarded by vitrification and the rupture lifetime under the loaded condition is reduced by the devitrification owing to thermal degradation. It is noteworthy that the application of the TTT diagram to rubber is more limited than to thermosets, as the diagram can be used for rubber only at temperatures higher than T_g . The ungelled glassy state is used commercially as molding materials, as it is processible like a solid ($T_{g,0} > \text{ambient temperature}$) before gelation or it can be cast like a liquid ($T_{g,0} < \text{ambient temperature}$). $_{gel}T_g$ serves to define the storage temperature for the unreacted resin, in other words, to avoid the critical gelation temperature. The state for a disperse system depends on the cure temperature, which can be defined by the competition between thermodynamics and kinetics. In order to obtain the best mechanical properties, it is suggested that the disperse system should first be allowed to cure under conditions of a certain temperature to reach a specified state and then the reaction is completed under conditions of higher temperature.

During gelation above $_{gel}T_g$ or vitrification below $_{gel}T_g$, the shrinking stress caused by curing develops along a rigid base accompanied with adhesive reaction, and both the tension stress in the resin and the inner stress on the base affect the properties of composite materials. If the curing reaction is terminated by vitrification, then the continuous isothermal cure at a T_{cure} below $T_{g\infty}$ leads to $T_g = T_{cure}$. In actual practise, however, T_g increases during the heating, and accordingly $T_g > T_{cure}$ is expected. In addition, although the vitrification occurs to a certain extent at $T_g = T_{cure}$, T_g at this stage corresponds to an intermediate state between rubbery and

glassy states. Hence, the reaction after vitrification can continue, resulting in $T_g > T_{cure}$. The achievable extent of the reaction in the glassy state is dependent on the effect of the glassy state on the reaction mechanism.

It is easy to reach full cure under the conditions of temperature higher than $T_{g\infty}$, but it is very slow at temperatures lower than $T_{g\infty}$. At high temperature, a non-curing chemical reaction brings about degradation, consequently leading to either a decrease in the degree of cross-linking or the formation of an elasticized substance, resulting in devitrification. Degradation can also lead to vitrification. Charring, for example, accelerates the increase in the degree of cross-linking or the vaporization of some plasticized substances of lower molecular weight. In the case of a high $T_{g\infty}$ system, curing and thermal degradation proceed competitively.

The finite viscosity in the flow state is under the control of the gelation (above $_{gel}T_g$) and vitrification (below $_{gel}T_g$). When gelation occurs, the weight-average molecular weight and the zero shear viscosity become infinite, and the viscosity near vitrification below $_{gel}T_g$ can be determined using the WLF equation.

The time in which a characteristic viscosity is achieved is often used as a practical method for measuring the gel time, t_{gel} . When the temperature is higher than $_{gel}T_g$, the apparent activation energy is obtained from the relationship between the time when a characteristic viscosity is attained and the temperature. The activation energy obtained is close to the true activation energy of the gelation reaction which brings about an increase in the characteristic viscosity.

The times to gelation and to vitrification can be calculated using a computer program by kinetically analyzing the degrees of conversion of gelation and vitrification, α_g and α_v , and the relationship between α_v and T_g . In the absence of thermal degradation, a sigmoid glass transition curve from T_{g0} to $T_{g\infty}$, obtained by an experiment on the epoxy resin system agreed well with the calculated results. At temperatures slightly higher than $T_{g,0}$, the vitrification time reaches a maximum value. This is caused by the fact that the decrease in viscosity and the increase in reaction rate constant occur simultaneously with

increase in temperature. In contrast, at temperatures slightly below $T_{\text{g,cool}}$ the time to vitrification shows a minimum. This can be attributed to the fact that the decrease in reaction rate constant and the increase in the concentration of the active reaction center occur simultaneously. The minimum and its corresponding temperature are useful in molding processes.

5.2.2 Curing and Glass Transition of Epoxy Resin

The determination of the curing heat and the glass transition temperature of thermosetting resins plays a very important role in understanding their properties [11]. Figure 5.4 presents the DSC curing curves of epoxy resin. The DSC curve recorded during the first heating run exhibits a deviation from the baseline at about 60 °C due to the glass transition and an exothermic peak from 120 to 245 °C attributable to the curing of the sample. The curve of the sample quenched before the second heating run exhibits a rise in the glass transition temperature and disappearance of the exothermic peak. This indicates that the curing of the sample was completed in the course of the first heating.

When the curing reaction is carried out in the presence of water, a sealed sample pan should be

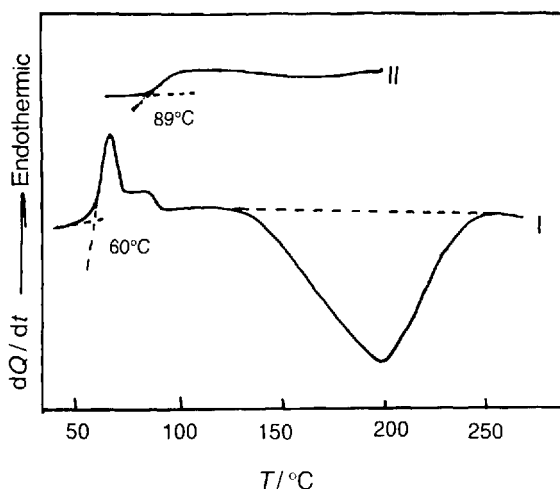


Figure 5.4 DSC curves for the curing of an epoxy resin. TA instrument, Seiko SSC/5605; sample mass, 10 mg; heating rate, 20 °C min⁻¹

used, since a resin like a phenolic is produced. When the vapor pressure exceeds the limit, the seal of the sample pan is broken and steam abruptly emanates from the sample pan. This can be detected by the abrupt deviation of the sample baseline in the endothermic direction. In order to protect the sample holder, the scan should be stopped immediately.

5.2.3 Thermal Analysis of Photopolymerization

Photopolymerization processes used to be difficult to measure quantitatively by conventional techniques such as dilatometry, UV spectrometry, IR spectrometry and gravimetry. Using a special TA apparatus one can determine the fractional conversion according to the measurement of the polymerization heat. The advantages of measuring the photochemical reaction heat are as follows: (1) photopolymerization analysis can be carried out on the system with the photosensitive resin produced from multi-component compounds; (2) film-shaped samples can be measured using a high-sensitivity apparatus; and (3) kinetic analysis of the polymerization heat can be performed directly.

For example, the photopolymerization heat for the benzoin methyl ether system (with 4–10 mmol of initiator for each mole of dodecane methylacrylate) was measured using a non-volatile sample pan. Typical data are given in Figure 5.5 [12]. The dotted line shows the enthalpy versus time and the solid line is the

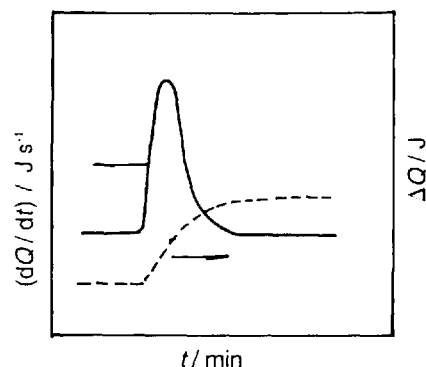


Figure 5.5 Photopolymerization heat for the benzoin methyl ether system.

derivative curve after a correction for the time lag of the heat response. If Q_0 represents the total polymerization heat, the fractional conversion from monomer to polymer, x , can be calculated using the equation

$$\alpha = \Delta Q / Q_0 \quad (5.5)$$

Figure 5.6 shows the DSC curves for a methacrylic acid sample radiated for 30, 60 and 90 s. It can be seen from the curves that an exothermic reaction occurs during irradiation and then the reaction slows gradually when the radiation stops, resulting in an exothermic curve due to the after-polymerization.

Both the degree of polymerization during radiation and after-polymerization after radiation can be calculated using the following equation:

$$\text{degree of polymerization} = \left\{ \int [q(t)dt] / Q_0 \right\} \times 100\% \quad (5.6)$$

where Q_0 is total polymerization heat obtained from the DSC curve; generally, $Q_0 = 55.2$ and $75.3 \text{ } \mu\text{kJ mol}^{-1}$ for monomeric methacrylic acid and acrylic acid, respectively, n being the number of functional groups in the molecule; $\int q(t)dt$ is the reaction heat at time t which is proportional to the amount polymerized.

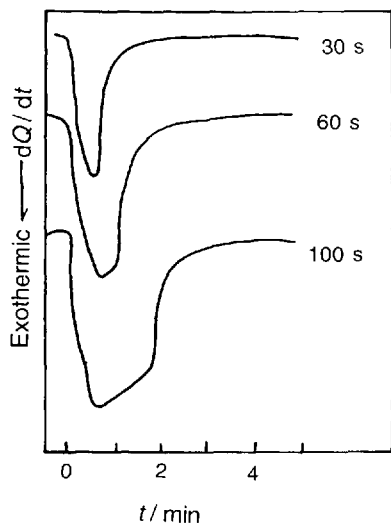


Figure 5.6 DSC curves for after-polymerization of methacrylic acid radiated for different times. Instrument, Seiko SSC 550 high-sensitivity calorimeter

The photopolymerization rate is dependent on the radiation wavelength and the ambient temperature and atmosphere. The properties of the polymer (e.g. glass transition temperature, T_g) is also dependent on the radiation conditions (e.g. radiation time). The optimum conditions for photochemical reaction can therefore be determined by taking the above factors into full account.

5.3 Evaluation of Catalysts in the Solid State

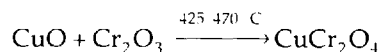
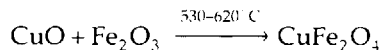
5.3.1 Evaluation of Catalysts in the Solid State by the DTA-EGD-GC On-line Coupled Simultaneous Technique

DTA-EGD-GC on-line coupled simultaneous technique and relevant equipment (see section 2.4) are effective tools for evaluating catalysts [14–17].

5.3.1.1 Spinel-type Catalyst

The spinel-type catalyst is a complex oxide that has attracted attention owing to its wide applications as a catalyst [18–19]. The basic state of Cu-Fe-O and Cu-Cr-O spinels is prepared by the coprecipitation method and is measured in air by the DTA-EGD coupled technique [20] (Figures 5.7 and 5.8).

The exotherms observed at 530–620 °C in Figure 5.7 and those at 425–470 °C in Figure 5.8 are attributed to solid–solid phase reactions. The reaction process is as follows:



The basic state of Cu-Cr-O is prepared by the complexing method using citric acid. The exotherms observed at 440–475 °C are slightly higher than those obtained by the coprecipitation method. The DTA-EGD curves,

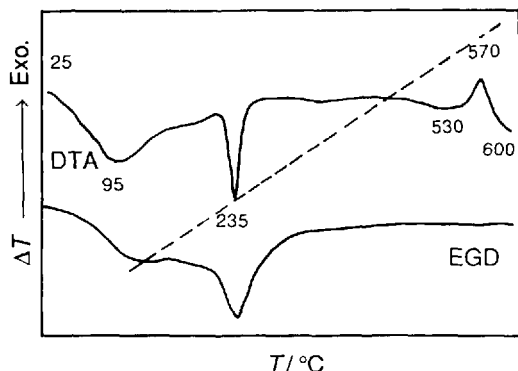


Figure 5.7 DTA-EGD curves for Cu-Fe-O spinel in the basic state[20]. The sample (Research Institute of Industrial Catalysis, ECUST, China) was prepared by the coprecipitation method. DTA: $\pm 100 \mu\text{V}$, $10^\circ\text{C min}^{-1}$; atmosphere, air at 20 ml min^{-1} ; sample mass, 7.88 mg; reference material empty crucible. EGD-TCD₁: bridge current, 100 mA; cell temperature, 115°C . Endotherm 95°C , desorption of water; $530\text{--}620^\circ\text{C}$, exotherms; see text

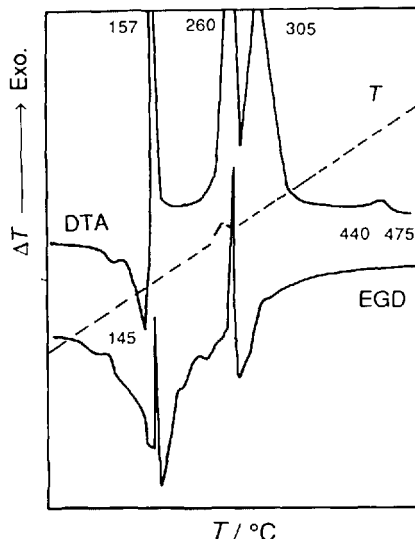


Figure 5.9 DTA-EGD curves for Cu-Cr-O spinel in the basic state[20]. The sample was prepared by the complexing method using citric acid. Sample mass, 2.18 mg; reference material empty crucible. Measuring conditions as in Figure 5.7. Three exotherms at 157 , 260 and 305°C ; thermal decomposition and oxidation. Owing to the decomposition reaction of nitrate and citric acid, CuO and Cr_2O_3 are formed

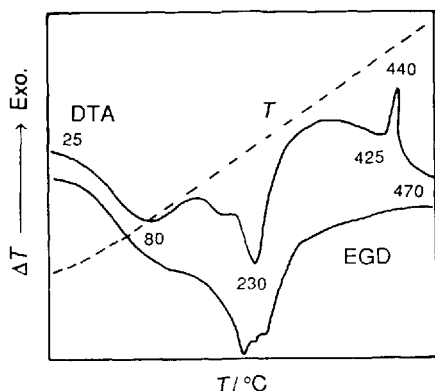
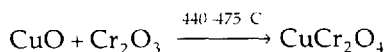


Figure 5.8 DTA-EGD curves for Cu-Cr-O spinel in the basic state [20]. Sample mass, 6.37 mg. Measuring conditions as for Figure 5.7

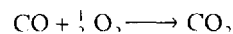
for the formation of CuCr_2O_4 spinel are shown in Figure 5.9.



The chemical structures of the above three reaction products were identified by X-ray diffractometry. Using a DTA-EGD coupled technique, the calcining temperature range of spinel formation can be confirmed.

5.3.1.2 Screening of Oxidative Activity of CuO Catalysts

In order to establish a method for the screening of the oxidative activity of catalysts, a DTA-GC coupled technique is applied to the oxidative activity of CuO(A) [20] and CuO(B) catalysts using a model reaction shown below:



CuO(A) catalyst was prepared by the thermal decomposition of $\text{Cu}(\text{NO}_3)_2 \cdot 3\text{H}_2\text{O}$ using a DTA furnace in air. CuO(B) catalyst was obtained commercially. The composition of the reaction gas (%) was $\text{CO-O}_2\text{-N}_2$ ($2.7:5.0:92.3$) and the flow-rate was 35 ml min^{-1} . About 2 mg of catalyst were placed in an aluminum crucible and an empty crucible was used as a reference. GC columns connected in series were packed with 401 organic support and SA molecular sieves. Argon was used as the carrier gas (the other experimental conditions are the same as in Figure 5.7).

During the programmed heating, in conjunction with a constant flow-rate of reaction gas over the catalyst, an exotherm was observed on

the DTA curve which was attributed to catalytic oxidation. After detecting the DTA exotherm, the reaction gas evolved was intercepted by a six-way sampling valve and analysed by GC at various reaction temperatures during the programmed cooling process. DTA-GC curves for the CuO(A) and CuO(B) catalysts are shown in Figures 5.10 and 5.11.

Figure 5.11 shows the initial temperature and the ΔT_{\max} temperature of the catalyst. The above two temperatures can be used as a measure of the relative oxidation activity of the catalyst under given experimental conditions. The gas chromatogram corresponds to the relationship between the oxidative activity and the selectivity of a catalyst as can be observed from the conversion of CO to CO₂. The curve of the CO conversion rate is obtained from the peak area of CO at various temperatures.

The exotherms of DTA for CuO(A) and CuO(B) are shown in Figure 5.12. The curves of the CO conversion rate for CuO(A) and CuO(B) on the gas chromatograms are shown in Figure 5.13. The CO conversion rate on the gas chromatogram increases with decreasing initial oxidation temperature and the $1/2\Delta T_{\max}$ temper-

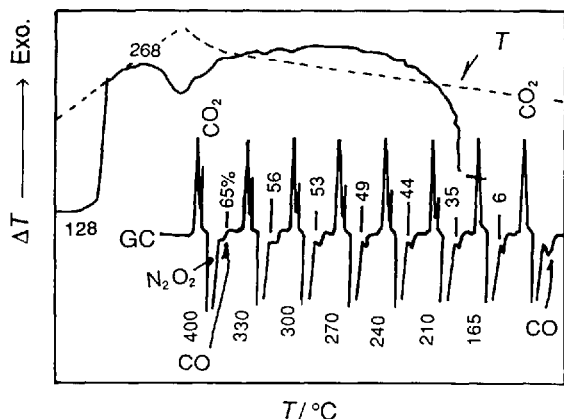


Figure 5.10 DTA-GC curves for screening the oxidation activity of CuO catalyst [18]. DTA: $\pm 250 \mu\text{V}$, $20^\circ\text{C min}^{-1}$; cooling rate, 5°C min^{-1} ; reference material: empty crucible; composition of reactive gases, CO-O₂-N₂ (2.7:5.92:3); flow-rate, 35 ml min^{-1} ; mass of CuO, 1.95 mg. GC-TCD₂; bridge current, 140 mA; cell temperature, 60°C ; GC columns in series containing 401 organic support and 5A molecular sieve; carrier gas, Ar at 20 ml min^{-1} . Model reaction screening oxidation activity of catalyst, $\text{CO} + \frac{1}{2}\text{O}_2 \rightarrow \text{CO}_2$ the conversion rate(%) of CO to CO₂ was obtained from the CO peak area on the GC trace

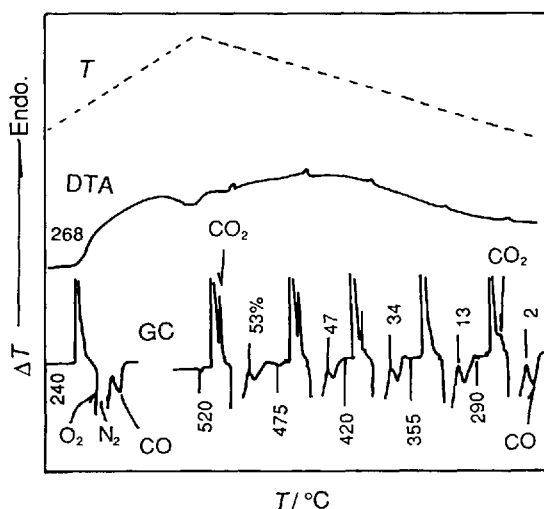


Figure 5.11 DTA-GC curves for screening the oxidation activity of CuO₂ catalyst [18]. Mass of CuO₂, 2.09 mg. The other measurement conditions as in Figure 5.10

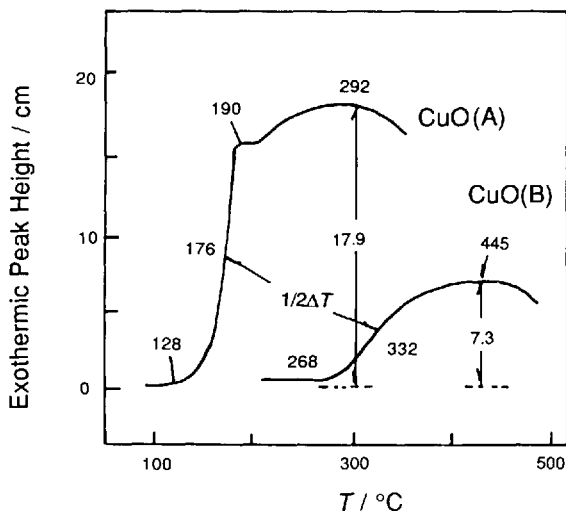


Figure 5.12 Exothermic DTA curves for CuO(A) and CuO(B)

ature of the DTA curves at various temperatures. This suggests that DTA curves can be used as an index of catalytic activity and selectivity.

5.3.1.3 Screening of Perovskite-type Catalysts Containing Rare Earths

The oxidative activity of Perovskite-type catalysts has been investigated using the DTA

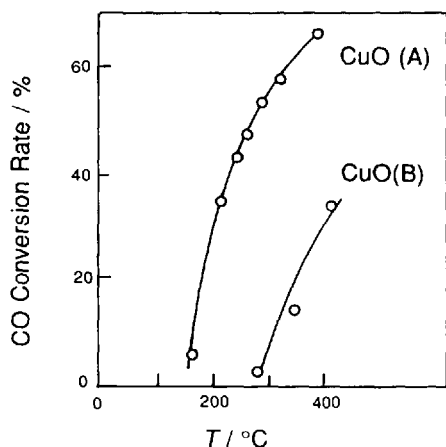


Figure 5.13 Curves of CO conversion rate on gas chromatograms of CuO(A) and CuO(B)

technique [21]. The DTA-GC coupled technique (isothermal method) can be applied to the screening of the oxidative activity of perovskite-type catalysts containing rare earths.

The complexing method with citric acid has been applied to the preparation of LaMnO_3 , LaCoO_3 and $\text{La}_{0.7}\text{Sr}_{0.3}\text{CoO}_3$, automobile exhaust catalysts [22,23]. Oxidation of CO is used as a model reaction for the oxidative activity of the above three types of catalysts [20]. The reaction gas at a constant flow-rate is introduced into the DTA system during programmed heating after the DTA exotherm has been detected. The DTA system is flushed with inert argon gas by a three-way valve in the process of programmed cooling. While the temperature decreases to a predetermined isothermal temperature of reaction, the reaction gas is introduced into the DTA system by three-way valves. The reaction gas evolved at the predetermined temperature is intercepted by a six-way sampling valve and analyzed by GC. Thus, DTA-GC curves are detected at this predetermined isothermal temperature (the measurement conditions are given in Figure 13.1). A repeated run is carried out according to the above method and a series of DTA-GC curves are obtained successively at the various predetermined isothermal temperatures. (Using the isothermal method, DTA-GC curves of the above catalysts are shown in Figures 13.1–13.3) The DTA exotherm and the curves of the CO con-

version rate on the gas chromatogram are shown in Figures 5.14 and 5.15, respectively.

The experimental results indicate that the order of the oxidation activities of the three perovskite-type catalysts containing rare earths is $\text{La}_{0.7}\text{Sr}_{0.3}\text{CoO}_3 > \text{LaCoO}_3 > \text{LaMnO}_3$. This order agrees well with the evaluation using a catalytic reactor [22,23].

5.3.1.4 Screening of Calcination Conditions of Multi-component Catalysts

Catalytic activity and selectivity are related not only to the chemical components, structure and preparation method of the catalyst, but also to the calcination conditions. The catalytic oxidation of dilute propylene to acrolein is a complex reaction. If the calcination conditions of a catalyst

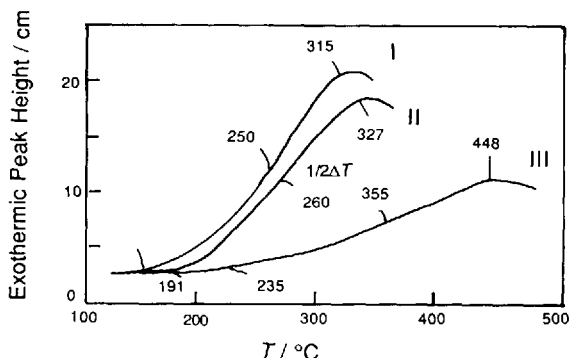


Figure 5.14 Exothermic curves of DTA for $\text{La}_{0.7}\text{Sr}_{0.3}\text{CoO}_3$ (I), LaCoO_3 (II) and LaMnO_3 (III)

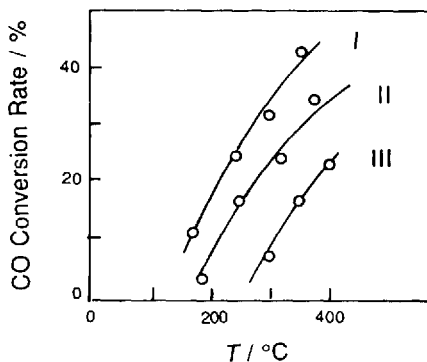


Figure 5.15 Curves of CO conversion rate for the gas chromatograms of $\text{La}_{0.7}\text{Sr}_{0.3}\text{CoO}_3$ (I), LaCoO_3 (II) and LaMnO_3 (III)

are formulated incorrectly, by-products are formed in the reaction products. On this account, the DTA exotherm does not always correspond to the conversion rate to the required product. For screening the activity and selectivity of a catalyst, it is necessary to analyze the gases evolved from the DTA system [24].

5.3.1.5 Screening of Activity of Supported Methanation Catalysts

Supported 4.0% Ni/Al₂O₃ (catalyst I), 4.0% Ni-2.3% La₂O₃/Al₂O₃ (catalyst II) and 4.0% Ni-2.3% La₂O₃-0.5% Pd/Al₂O₃ (catalyst III) methanation catalysts were prepared [25] and it was found that catalyst III has a synergistic effect on the methanation activity. DTA-GC was applied for the fast screening of the activity of these three methanation catalysts [26]. The composition of the reaction gas was CO-H₂-N₂ 4.6:15.4:80; the precise measurement conditions are shown in Figure 13.5. From the DTA-GC curves for catalysts I, II and III for the methanation reaction (see Figures 13.5-13.7), the DTA curves, conversion rate and density of CH₄ in the reaction gas are shown in Figures 5.16, 5.17 and 5.18, respectively.

The order of the activity and selectivity for the methanation catalysts is III >> II > I. Ni is the main activity component, the lanthanum oxide component increases the dispersity of metallic Ni

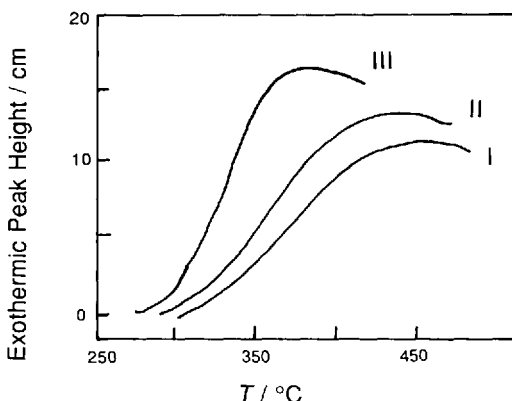


Figure 5.16 DTA exotherms for methanation catalysts I, II and III

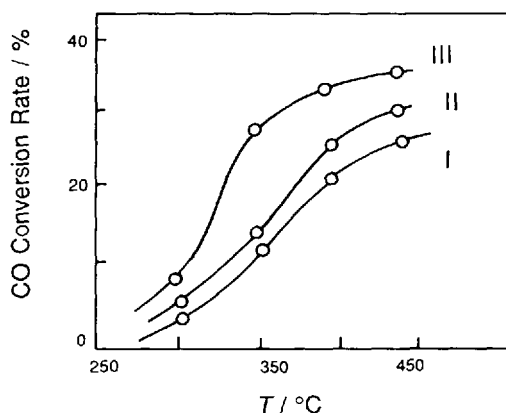


Figure 5.17 CO conversion rate curves for methanation catalysts I, II and III

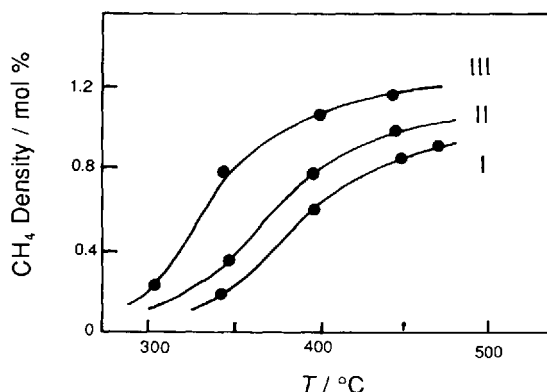


Figure 5.18 Density curves of CH₄ in reaction of methanation catalysts I, II and III

and Pd promotes hydrogen spillover, so that catalyst III shows the highest activity.

5.3.1.6 Examination of Poisoning Effect of SO₂ on Methanation Catalysts

The catalyst is thought to be poisoned by chemisorption or accumulated coke on the active center of the catalyst surface, and the activity of the catalyst is reduced. The poisoning effect of some sulfur compounds on nickel catalyst was investigated by the microbalance flowing state method [27]. The poisoning effects of pulsing SO₂ on catalysts I and III (see above) were examined by DTA-GC under isothermal temperature conditions [26]. The DTA-GC curves for the total

of service owing to the formation of an organic resin or membranous coke that covers the surface activity site of the catalyst. The accumulated resin and coke can be burned in air or oxygen to restore the catalyst activity. The burning temperature must be controlled in order to prevent sintering of the catalyst. The process of burning coke on ZSM-5A molecular sieve catalyst was examined using an aromatized reaction and DTA-GC. The DTA-GC curves for burned coke in air for the above catalyst are shown in Figure 5.20.

Owing to the burned coke, the exothermic reaction $\text{CO} + \frac{1}{2} \text{O}_2 \rightarrow \text{CO}_2$ occurs and variation of the peak height of CO_2 is observed on the GC trace. The first stage of the oxidative exothermic reaction of a micro-resin containing a large amount of hydrogen takes place at 310 °C on the DTA curve. The second stage is coke ignition; a large peak on the DTA curve is observed at about 520 °C, and at the same time, the CO_2 peak increases substantially on the gas chromatogram. When the coke is burned at 655 °C, the DTA exotherm decreases continuously to the baseline and the CO_2 peak on the GC trace disappears.

5.3.2 Evaluation of Metal Catalysts by Pressure DSC

Pressure differential scanning calorimetry (PDSC) provides a faster method for the evaluation of precious metal reduction catalysts. The efficient

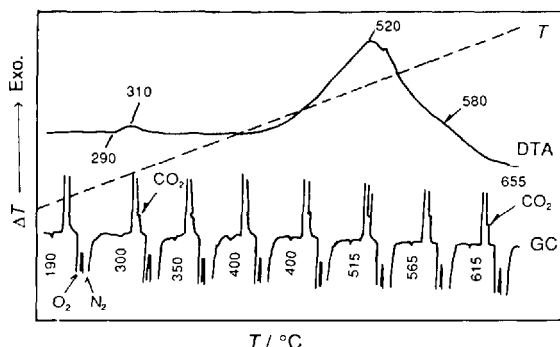


Figure 5.20 DTA–GC curves for burning coke on ZSM-5A molecular sieve catalyst. Sample provided by the Department of Organic Chemical Technology, ECUST, China. DTA: $\pm 100 \mu\text{V}$, $10^\circ\text{C min}^{-1}$; air flow-rate, 20 ml min^{-1} ; sample mass, 5.62 mg (containing 10% coke); reference material, empty crucible. GC–TCD₂: bridge current, 160 mA; cell temperature, 60°C ; carrier gas, Ar at 40 ml min^{-1} ; GC columns in series.

reduction of numerous organic compounds depends on the activity of the catalyst, such as platinum and palladium. These metals are normally deposited on inert, porous substrates, such as carbon and silica. Catalyst activities are generally evaluated by measuring both the volume of hydrogen adsorbed by the catalysts under pressure as an indication of the active sites available, and the volume of hydrogen consumed during the reduction of a test compound added to the catalyst. Chemisorption and catalytic reduction are both exothermic reactions, with the evolved products being directly related to the hydrogen consumed.

The presence of a higher concentration of the reactive-gas accelerates the reaction for rapid screening or comparison of materials. Using increased pressures of hydrogen, a PDSC reduction can be completed in 15 min or less. This kind of experiment was performed under hydrogen at 1379 kPa (200 psig). A 5 mg amount (nominal) of catalyst was placed in an open aluminum sample pan and loaded into the PDSC system at room temperature. The cell was closed, flushed several times with helium at 345 kPa (50 psig) and then pressurized to 1034 kPa (150 psig) before initiation of heating at $20^{\circ}\text{C min}^{-1}$. When the sample temperature reached 75°C , the purge gas was switched from helium to hydrogen at 1379 kPa [14].

Figure 5.21 shows a typical DSC curve obtained; an initial endothermic blip occurs when the gas is introduced, followed by a large exothermic peak due to the chemisorption reaction. The PdO/carbon catalyst shown in Figure 5.21 was measured six times and the average heat of reaction was $81.6 \pm 1.05 \text{ J g}^{-1}$ (1.25% rel.). A shoulder peak is observed on the exothermic peak at around 5 min, which is attributed to physical adsorption on the carbon. However, it was difficult to separate the heat of chemisorption and physical adsorption on the carbon from Figure 5.21.

An extension of this procedure can be used to evaluate mixed metal catalysts and to evaluate the catalyst activity by reduction of an organic substrate. The characteristics of various substrates are affected by differences in structure, surface area, pore size, pore volume, etc., which

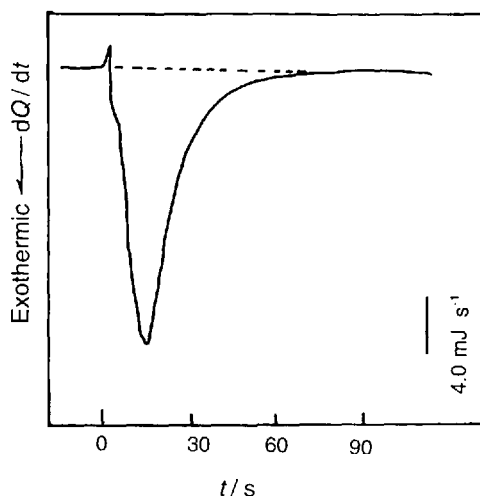


Figure 5.21 Determination of heat of catalyst reduction for a PdO/carbon catalyst by PDSC [28]

means that both the surface area of the catalyst metal and the distribution on the substrate affect the activity. It is noteworthy that the order of activity observed in chemical reductions using a series of commercial catalysts agrees well with the PDSC results. For example, Pd is generally more reactive than Pt, and a carbon substrate is more reactive than alumina.

5.4 TA of Wood

Wood is a major resource of organic compounds and has an important role in human life. TA is widely applied to investigate the chemical reactions of wood and wood components [29,30].

5.4.1 Thermal Decomposition of Cellulose by TG-DTA-FTIR

Cellulose is the most abundant polymer in wood. Figure 5.22 shows the thermal decomposition of natural cellulose powder (Arbocel, obtained from Miki Sangyo) observed by TG-DTA-FTIR. In order to avoid the effect of sorbed water, the sample was dried at 105°C for 2 h. The sample mass was 10.25 mg, the heating rate was $20^{\circ}\text{C min}^{-1}$ and the flow-rate of N_2 gas was 200 ml min^{-1} . For simultaneous measurement by TG-FTIR, temperature control of the interface

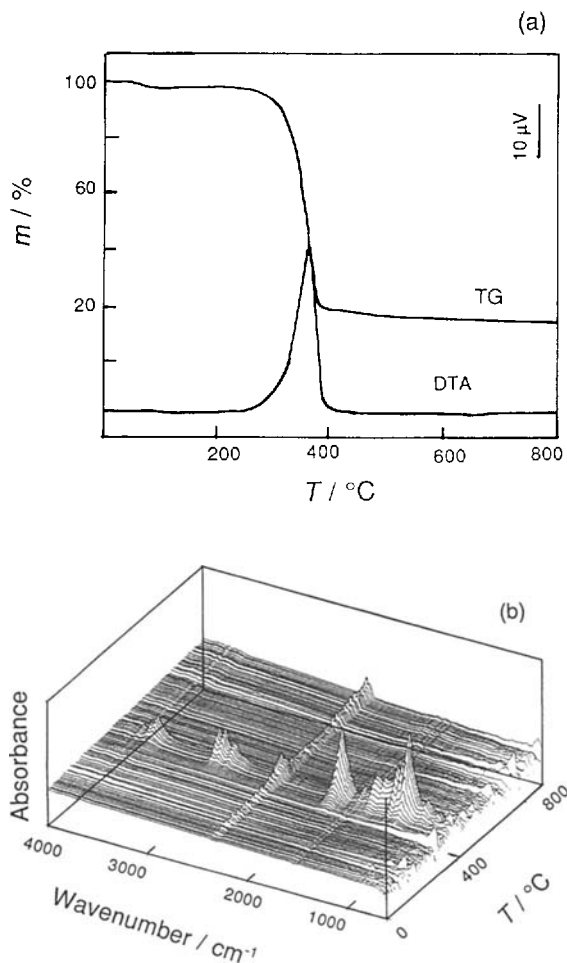


Figure 5.22 (a) TG-DTA curves and (b) three-dimensional diagram of IR absorption, temperature and wavenumber for cellulose powder

units connecting the TG instrument and IR spectrometer is most important. The connecting tube should be maintained at an appropriate temperature in order to avoid condensation of gas on the surface of the tube. In this experiment, the temperature was controlled at 270 ± 0.5 °C. Acquisition of FTIR data was carried out at 2 s intervals, with 10 acquisitions. The IR wavenumber resolution was 8 cm^{-1} .

As shown in Figure 5.22(a), thermal decomposition starts at 330 °C. The mass residue at 500 °C is 15%. Figure 5.22(b) shows the stacked FTIR spectra of the gases evolved from cellulose at various temperatures. The representative peaks

observed for the samples were as follows [wavenumber (assignment)]: 1126 cm^{-1} ($n\text{C}-\text{O}-$), 1260 cm^{-1} [$-\text{C}(=\text{O})-\text{O}-\text{C}-$], 1517 and 1617 cm^{-1} ($n\text{C}=\text{C}$), 1718 cm^{-1} ($n\text{C}=\text{O}$), 2345 cm^{-1} ($n\text{CO}_2$), 2980 cm^{-1} ($n\text{C}-\text{H}$) and 3700 cm^{-1} ($n\text{H}_2\text{O}$).

As shown in Figure 5.22(b), evolution of CO_2 gas is first observed in the initial stage of thermal degradation of cellulose in the temperature range from *ca* 200 to 350 °C. Other gases are evolved in the higher temperature region from *ca* 350 to 600 °C. Accordingly, we may conclude that CO_2 evolves in two stages. However, the evolution of other gases corresponding to 1260 cm^{-1} [$-\text{C}(=\text{O})-\text{O}-\text{C}-$], 1517 and 1617 cm^{-1} ($n\text{C}=\text{C}$), 1718 cm^{-1} ($n\text{C}=\text{O}$), 2345 cm^{-1} ($n\text{CO}_2$), 2980 cm^{-1} ($n\text{C}-\text{H}$) and 3700 cm^{-1} ($n\text{H}_2\text{O}$) is observed as almost a single-stage process at around 400 °C.

TG-DTA-FTIR curves of model cellulose compounds, such as glucose and sucrose, can be found in Ref. 32.

5.4.2 Thermal Decomposition of Lignin by TG-DTA-FTIR

Lignin is the second major component in wood. The core chemical structures of lignin are 4-hydroxyphenyl, guaiacyl and syringyl groups. The chemical structure of lignin varies depending on the wood species. Lignin is a slightly cross-linked amorphous polymer. The glass transition temperature of lignin is *ca* 130 °C [32–35].

TG-DTA and TG-FTIR data for softwood Kraft lignin (KL) are shown in Figure 5.23. KL is obtained as a by-product of Kraft pulping. As shown in Figure 5.23(a), KL starts to decompose at around 320 °C in an N_2 atmosphere and the mass residue is 55% at 500 °C. As shown in Figure 5.23(b), the prominent evolution of CO_2 gas is one of the major obvious characteristics of KL samples. KL shows the apparent evolution of compounds containing alkyl groups ($-\text{CH}-$, *ca* 1126 cm^{-1}). The evolution of CO_2 and compounds having $-\text{CH}-$ groups is due to degradation concerned with end-groups. Peaks at 1126 and 2890 cm^{-1} , which are assigned to $-\text{CH}-\text{O}-$ and $-\text{CH}-$, are also observed. The appearance of the above IR peaks

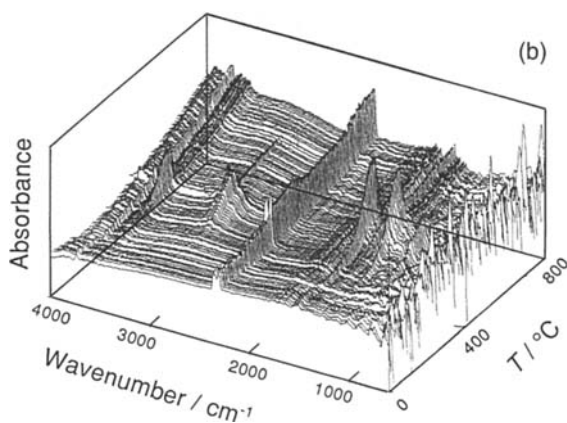
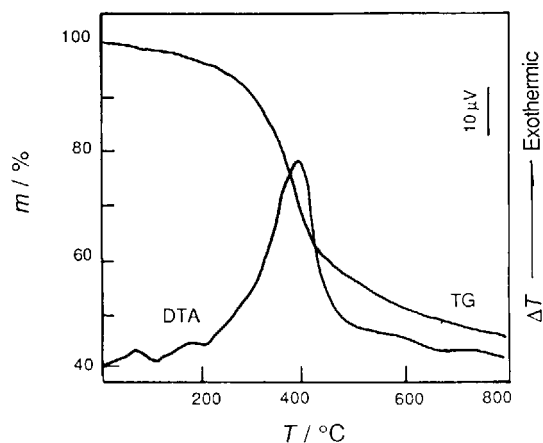


Figure 5.23 (a) TG-DTA curves and (b) three-dimensional diagram of IR absorption, temperature and wavenumber for Kraft lignin. Experimental conditions as in Section 5.4.1

suggests that the evolution of gases having $-\text{CH}=\text{CH}-$, $-\text{CH}-\text{O}-$ and $-\text{C}$ structures is a single-stage process. However, the gas evolution corresponding to $n\text{H}_2\text{O}$ seems to occur in stages and the most prominent gas evolution is observable at around 400 °C.

5.4.3 Thermal Decomposition of Wood by TG-DTA-FTIR

Lignocell (softwood powder supplied by Miki Sangyo) was used as a representative wood sample. Lignocell starts to decompose at 325 °C and the mass residue at 500 °C is 23% [Figure 5.24(a)]

Figure 5.24(b) shows the stacked FTIR spectra of the gases evolved from softwood at various temperatures. The evolution process of degrada-

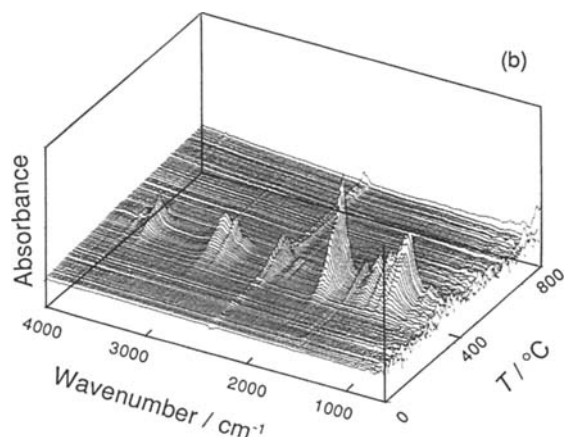
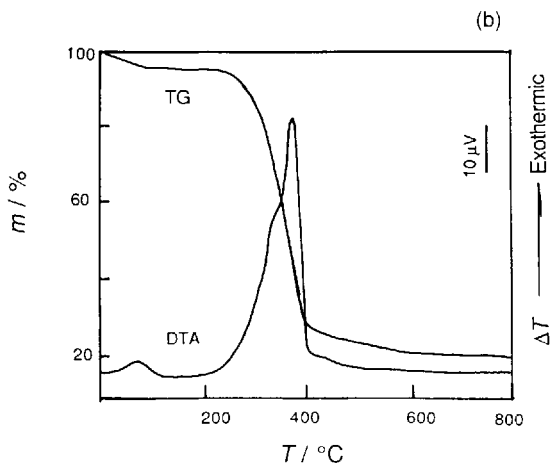


Figure 5.24 (a) TG-DTA curves and (b) three-dimensional diagram of IR absorption, temperature and wavenumber for softwood powder. Experimental conditions as in Section 5.4.1

tion gases from softwood seems to be between those for cellulose and lignin. However, the evolution of gases having $-\text{CH}=\text{CH}-$, $-\text{CH}-\text{O}-$ and $-\text{CH}$ structures is more prominent than CO_2 and $n\text{H}_2\text{O}$ at around 400 °C.

5.4.4 Acid Hydrolysis of Cellulose

DSC can be applied to study the acid hydrolysis reaction of cellulose [36,37]. In order to eliminate the effect of vaporization of water during heating on the DSC curve, it is necessary that acid-proof, high-pressure stainless-steel or high-pressure gold-plated containers should be employed. The experiment can be made according to the

following procedures:

1. Prepare an acid solution of known concentration.
2. Weigh about 2 mg of cellulose sample and the required quantity of acid solution in an acid-resistant, high-pressure container. For the sample shown in Figure 5.25 the mass ratio of sample to acid solution is 1 : 4–5.
3. Seal the sample container carefully using sealer and place it in the sample holder. Heat the sample at the predetermined heating rate, e.g. for Figure 5.25 the heating rate is $1.25^{\circ}\text{min}^{-1}$, and record the DSC curve.
4. A typical DSC curve for acid hydrolysis of cellulose appears as an exothermic peak as shown in Figure 5.25. If the DSC curve shifts to the endothermic side abruptly, it indicates that seal of the sample has been broken, which seriously harms the sample holder. It is strongly recommended to avoid breaking the seal.
5. Analyze the data obtained.

5.4.5 Oxidative Stability of Rosins

Rosin is a complex mixture, mainly consisting of various isomers of rosin acid. When exposed to air for a long period, rosins are easily discolored by oxidation. High-pressure DSC (HPDSC) can be used to determine oxidative stability of various rosins and rosin products. The measurement method is as follows:

1. Weigh 5–7 mg of rosin sample in a container. Note that the sample must be taken from the

interior of a piece of the rosin because surfaces exposed to air have usually been oxidized.

2. Place the sample container in the HPDSC system and fill with O_2 to a predetermined oxygen pressure. For Figure 5.26, the oxygen pressure is 3.79 MPa.
3. Heat the sample at a slow heating rate to a selected temperature (in Figure 5.26, it is 100°C). Maintain this temperature for a definite time, so as to oxidize the sample, and record the DSC curve.
4. Determine the time required for the oxidation exotherm. The times for the oxidation exotherms of pale wood rosin fines and gum rosin were determined to be 6 and 30 min, respectively [38].

5.4.6 Combustion Characteristics of Flame-retarded Wood

It is highly recommended to use TG-DSC in various atmospheres to measure the combustion characteristics of flame-retarded wood. The measurement procedure is as follows:

1. The chemical composition of wood is complex. Its main components consist of cellulose, hemicelluloses, lignin and extractives. The amount of each component varies with the tree species and tree part. For flame-retarded wood prepared by treating with a retardant, care should be taken in order to obtain homogeneous samples. Select a suitable amount of the sample from representative parts of the wood, then grind the sample

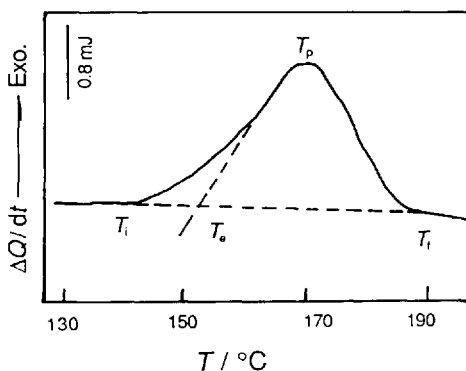


Figure 5.25 DSC curve for acid hydrolysis of cellulose T_i , 408.2 K; T_o , 426.6 K; T_p , 443.3 K; T_f , 463.7 K; ΔH , -842.7 J g^{-1}

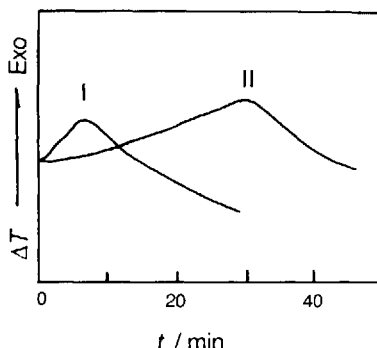


Figure 5.26 HPDSC curves for rosins at 3.49 MPa O_2 at 100°C [39]. I, Pale wood rosin fines; II, gum rosin

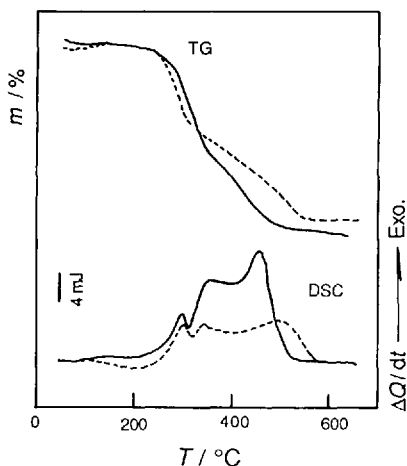


Figure 5.27 TG–DSC curves for flame-retarded wood in air. Solid line, fibreboard; dashed line, fibreboard treated with flame retardant

so as to pass through a 100-mesh sieve and mix it thoroughly.

2. Weigh a sample of about 2 mg. Place it in a simultaneous TG–DSC system, then choose appropriate test conditions. Figure 5.27 shows TG–DSC curves recorded in a static air atmosphere at a heating rate of $10\text{ }^{\circ}\text{C min}^{-1}$, with conditions of 10 mg for TG and 40 mJ s^{-1} for DSC. The same set of experiments should be conducted under the same conditions for the purpose of comparison.
3. Measure the sample under various atmosphere conditions, such as static air or O_2 flow.
4. Analyze the data.

The mass-loss fraction of wood treated with flame retardant is greater than that of untreated wood in the initial stage, but it subsequently becomes smaller. The wood with less mass loss in the second stage allows better flame retardancy. Furthermore, wood that has a small exothermic enthalpy and a higher final decomposition temperature on the DSC curve has better flame retardancy. The exothermic enthalpy (ΔH) and final decomposition temperature (T_f) of fibreboard without flame retardant were 7.66 kJ g^{-1} and $556.0\text{ }^{\circ}\text{C}$, respectively, whereas those of fibreboard treated with flame retardant were 5.49 kJ g^{-1} and $587.5\text{ }^{\circ}\text{C}$, respectively.

5.5. TA of Explosives and Coals

5.5.1 Monitoring the Instantaneous Change of Energy-stored Materials

The mass of an energy-stored material will change rapidly when it is heated to a given temperature. The heat released in the fast changing process can be described in detail with thermal analysis.

Figure 5.28 shows a thermogravimetric curve of an explosive. A 5 mg amount of sample was used in a dynamic air atmosphere (50 ml min^{-1}) at a heating rate of $2\text{ }^{\circ}\text{C min}^{-1}$. The TG curve shows that an instantaneous explosive reaction took place at $192\text{ }^{\circ}\text{C}$. The data between points A and B can be processed and the curve can be transformed as shown in Figure 5.29.

It can be seen that the mass of sample decreased abruptly from 76.74% to 13.74% from 50.77 to 50.90 min (curve 1). Curve 2 shows that the rate of mass loss varied from $798\%\text{ min}^{-1}$ ($13.29\%\text{ s}^{-1}$) to $1270\%\text{ min}^{-1}$ ($21.16\%\text{ s}^{-1}$), and decreased to $14\%\text{ min}^{-1}$ ($0.23\%\text{ s}^{-1}$). Owing to the large amount of heat released from the energy-stored explosive in such a short time, the temperature nearby rose from 193.5 to $210\text{ }^{\circ}\text{C}$, and a temperature pulse emerged (curve 3)

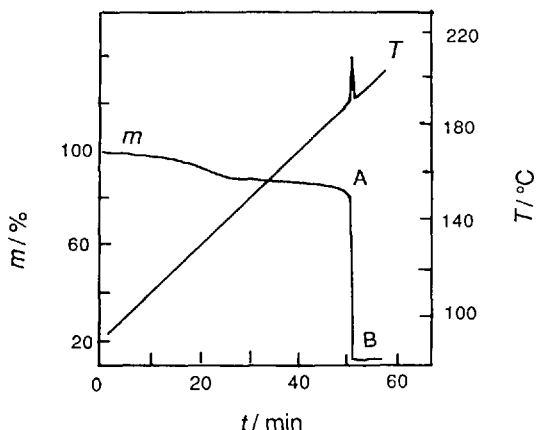


Figure 5.28 TG curve of an explosive

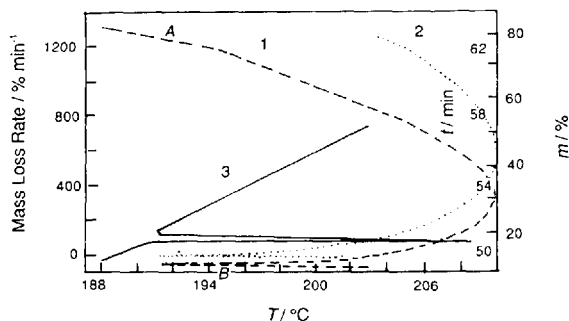


Figure 5.29 TG curve of the instantaneous process between points A and B in Figure 5.28

5.5.2 DSC Measurement of Self-reacting Substances

Self-reacting substances ignite or explode by themselves even in the absence of oxygen from air. Since these chemicals readily jeopardize personal safety, it is important to estimate the risks that they pose [39]. As DSC is a safe and simple method for the appraisal of these substances it has become of increasing interest.

Almost all self-reacting substances evolve large amounts of gas, so it is difficult to measure the evolved heat accurately without the use of special high-pressure-resistant sample containers. Three types of sealed pan, aluminum, silver or stainless steel, are recommended for this purpose. The pressure-resistant limits are 2.94 MPa for aluminum and 4.9 MPa for silver and stainless steel.

The DTA curves shown in Figure 5.30 were obtained using a stainless-steel sealed pan. The samples studied were benzoyl peroxide (BPO), 2,4-dinitrotoluene (2,4-DNT) and pentaerythritol tetranitrate (PETN).

The following method has been proposed for the appraisal of self-reacting substances. On the coordinate system of $0.7Q_{1/2}$ versus $T_s - 25^\circ\text{C}$, draw a straight line passing through the two points $(\log Q_{1/2}, T_s - 25^\circ\text{C})$ for 2,4-DNT and $(\log Q_{1/2}, T_s - 25^\circ\text{C})$ for BPO, where $Q_{1/2}$ is the amount of the heat evolved for 70% 2,4-DNT and 80% BPO, T_s is the temperature at which heat evolution begins and the subscripts indicate the sample studied. This line is called the PE function line which is used as a criterion: any substance with their

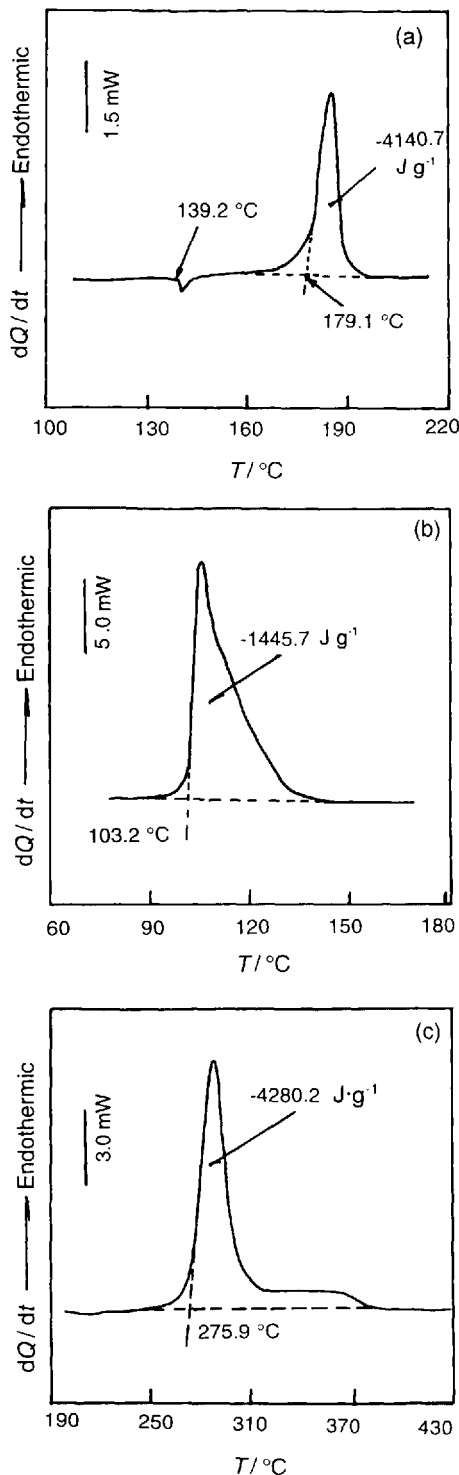


Figure 5.30 DSC curves for (a) PETN, (b) BPO and (c) 2,4-DNT. Heating rate, 2°C min^{-1} ; atmosphere, air; sample container, sealed stainless steel (15 μl)

respective point lying above or on the PE line is classified as a dangerous substance.

5.5.3 Proximate Analysis of Coal and Coke

In quality control, the proximate analysis of coal and coke is of importance. Thermogravimetry provides a convenient method for performing a proximate analysis, usually in 10–20 min. Proximate analysis covers the determination of moisture, volatile matter, fixed carbon and ash in coals and cokes and is used to establish the rank of coals, to determine the ratio of combustible to incombustible constituents, or to provide the basis for commercial trading and otherwise evaluating coal for various purposes. Hence it is important to both the suppliers and users of coal to have a rapid, accurate and reliable procedure for proximate analysis.

In order to obtain a complete proximate analysis in a single TG experiment, the system is programmed to hold initially at 200 °C in nitrogen, then to jump to 900 °C and hold there for a specified period of time in nitrogen before switching to oxygen. In the experiment considered here, 40–45 mg of sample were used and nitrogen and oxygen purge gases at 60 ml min⁻¹ were introduced at appropriate times [40]. Figure 5.31 shows the data obtained by the ASTM method.

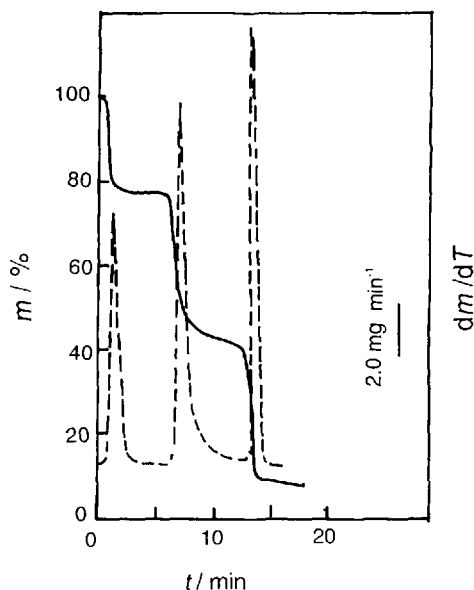


Figure 5.31 TG-DTG curve for coal [40]

(O₂) and a flow-rate of 50 ml min⁻¹ is maintained through the cell for 30 s at ambient temperature.

3. The cell is pressurized to 3447 kPa (500 psig) with O₂; the DSC curve is obtained in the temperature range 150–600 °C at a heating rate of 20 °C min⁻¹ as shown in Figure 5.32.

5.5.4 Determination of Heat Content of Coal

The heat content, or heat of combustion, is an important quality control parameter for coal. The heat of reaction of coal can be determined by differential scanning calorimetry (DSC). With DSC, one can directly determine the heat content of coal. Pressure DSC (PDSC) is particularly applicable to such determinations, since the increased pressure of the reactive gas permits the determination of the heat content of most coals in 20 min. The procedure is as follows [39]:

1. The sample (1.0–1.5 mg) is placed in a hermetically sealed aluminum sample pan with a pinhole in the lid and weighed.
2. The cell is closed and purged by pressurizing to 344.7 kPa (50 psig) with the reactive gas

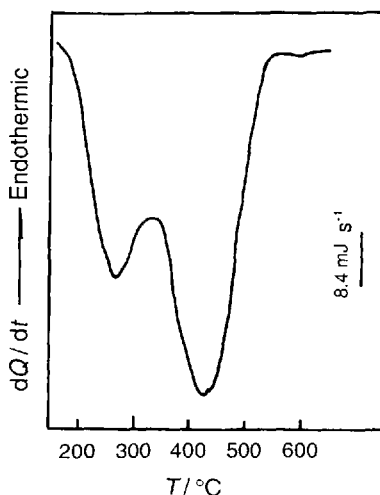


Figure 5.32 DSC curve for exothermic combustion for coal [41]

- The area under the combustion exotherm is measured and the heat of combustion is calculated.

The average deviation between the PDSC data and the ASTM adiabatic bomb calorimetric data on a series of coal samples is 1–3%.

5.6 Quantitative Analysis of Minerals and Determination of Coexistence of Minerals by TG

5.6.1 Quantitative Analysis of Minerals by Thermogravimetry[42]

When minerals are heated, dehydration, decomposition, oxidation and sublimation occur accompanied by a mass change. Based on the mass-loss of a particular component of a mineral, the content of that component in the sample can be determined.

Quantitative analysis of a sample by thermogravimetry is based on the following equation:

$$m = r_a / m_a \quad (5.7)$$

where m is the content of a substance in the sample, r_a is the mass loss of the substance and m_a is the mass fraction of the substance.

The DTA–TG curves for carbonate mineral are shown in Figure 5.33, which exhibits two endothermic peaks at 815 and at 955 °C with mass losses of 5.75 and 39.25%, respectively. From the results of thermal analysis, it can be estimated that the sample is composed of calcite and dolomite.

The dolomite [$\text{CaMg}(\text{CO}_3)_2$] decomposes in two steps. Decomposition starts at 750 °C and produces MgCO_3 and CaCO_3 ; MgCO_3 decomposes at the same time, exhibiting the first endothermic peak with a loss of 23.87% CO_2 in the range of 750–805 °C. The second peak observed in the range 860–940 °C shows evolution of CO_2 with a 23.87% mass loss. If both calcite and dolomite are formed in a sample, it is difficult to distinguish the endothermic peaks,

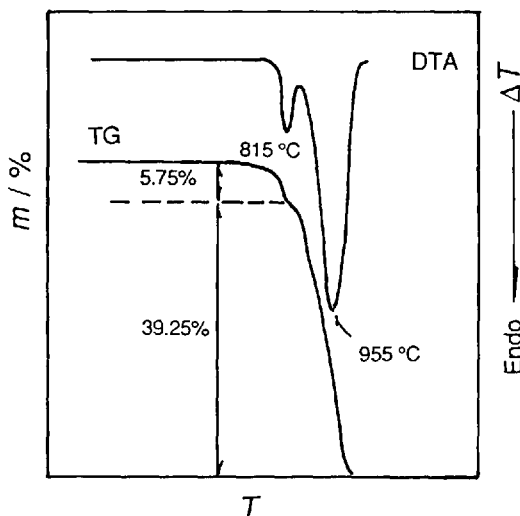


Figure 5.33 DTA–TG curves for carbonate mineral. Sample mass, 200 mg; heating rate, 20 °C min⁻¹; thermocouples, Pt–Pt₉₀/Rh₁₀; furnace atmosphere, static air

which are attributed to decomposition of CaCO_3 , from either calcite or dolomite.

By using equation (5.7), the contents of dolomite and calcite can be calculated to be $(5.75/23.87) \times 100\% = 24.10\%$ and $(29.25 - 5.75)/43.97 = 76.19\%$, respectively.

5.6.2 Determination of Composition of Minerals Showing Isomorphism

For minerals showing isomorphism, the content of a particular component changes with the composition. The contents of components in this kind of mineral can be determined based on the mass loss of the components. For example, the amounts of CO_2 evolved from carbonate differ with change in the isomorphous composition. Hence the composition and the amounts of the particular components can be estimated.

As shown in Figure 5.34, the DTA–TG curves of carbonate mineral show endothermic decomposition with a mass loss 41.25% at 650 °C and an exothermic mass gain at 710 °C due to oxidation. TG–DTA curves of carbonate mineral show a similar pattern to those of siderite. However, the temperature of the endothermic peak of siderite is observed at 600 °C and the mass loss is 37.99%. A higher peak temperature and larger mass loss

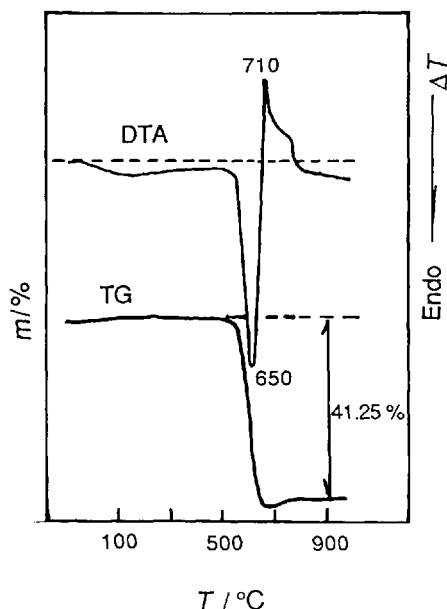


Figure 5.34 DTA-TG curves for magnesium siderite. Amount of sample, 200 mg; heating rate, $20^{\circ}\text{C min}^{-1}$

of the sample indicate that this sample is attributable to magnesium siderite ($[\text{Mg}_x\text{Fe}_{1-x}]\text{CO}_3$). The quantity of magnesium and iron may be expressed by the following equation:

$$\text{CO}_2/(\text{Mg}_x\text{Fe}_{1-x})\text{CO}_3 = M_{\text{CO}_2}$$

$$44.009/[24.305x + 55.85(1-x) + 60.008] = M_{\text{CO}_2} \quad (5.8)$$

$$x = 3.673039 - 1.395251/M_{\text{CO}_2}$$

where x is the amount of magnesium and M_{CO_2} is the mass loss of CO_2 in the sample. According to the mass loss of this carbonate, we can calculate

$$x = 3.673039 - 1.395251/0.4125 = 0.2906$$

The chemical formula is $(\text{Mg}_{0.29}\text{Fe}_{0.71})\text{CO}_3$ (sideroplestite).

5.7 Miscellaneous

5.7.1 Thermal Decomposition of Heat-conductive Oil

Although various kinds of DSC sample pan are

commercially available, a hermetically sealed pan was designed to investigate the thermal decomposition of oil. Figure 5.35 shows the cross-sectional profile of the sealed pan made of stainless steel.

Under an atmosphere of high-purity nitrogen, 2 ml of oil were pipetted with a syringe into the pan, which was covered, tightened and weighed immediately. The DSC measurement was carried in an N_2 atmosphere (50 ml min^{-1}) at a heating rate of $10^{\circ}\text{C min}^{-1}$. (The entire operation should be protected by high-purity N_2 to prevent oxidation of the oil.) The mass loss after the measurement was less than 0.1 mg, verifying the good sealed quality of the pan. Note that it is necessary to weigh the sample before and after DSC measurements in order to confirm whether leakage has occurred or not. The DSC curves of two heat-conductive oils are shown in Figure 5.35. An endothermic peak appeared between 320 and 380 $^{\circ}\text{C}$ on curve I. In contrast, the smooth curve II shows that the oil was still stable up to 380 $^{\circ}\text{C}$.

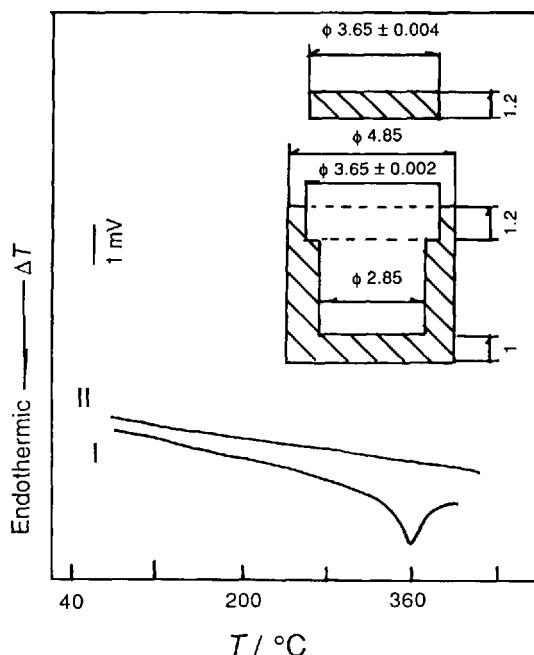


Figure 5.35 DSC curves for heat-conductive oils. A cross-section of the hermetically sealed DSC pan is also shown

5.7.2 Measurement of the Content of Carbon Black in Rubber[44]

5.7.2.1. Continuous Heating Method

As a reinforcing agent, carbon black improves the properties of rubber, such as tensile strength, tearing strength and abrasion resistance. The amount, the particle size and shape of the added carbon black affect the physical properties of rubber products. Taking several milligrams of the sample and a time of 20 min, the content of carbon black can be obtained using TG. The procedure is as follows:

1. Heat the rubber sample in a nitrogen atmosphere to about 600 °C, where the all organic compounds except the carbon black completely decompose.
2. Replace the N_2 with O_2 and allow the carbon black to burn off.
3. Determine the content of carbon black from the resulting mass loss curve as shown in Figure 5.36.

The content of carbon black in other polymeric materials can also be determined in the same way. This method gives a repeatability of about 2%.

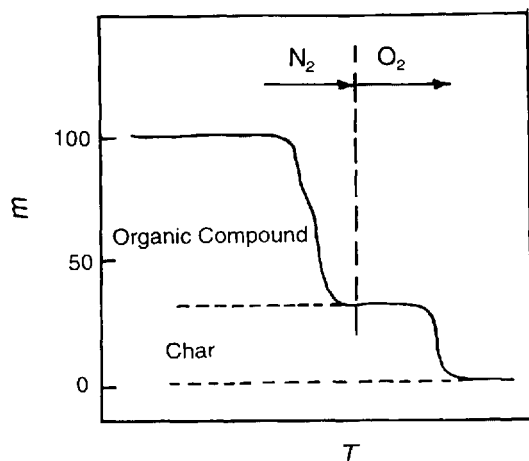


Figure 5.36 TG curve for rubber

5.7.2.2. Double Heating Method

The double heating method is suggested as an improvement of the continuous method. By the continuous method, the determined value for rubber is lower and that for carbon black is higher than the real values. Using the double heating method, it becomes possible to distinguish between mass losses due to oxidation of the polymeric residue after the first stage decomposition and those due to oxidation of the carbon black.

The double heating method is interpreted graphically in Figure 5.37. The procedure is follows:

1. Heat the sample from ambient temperature to 550 °C in an N_2 atmosphere at a heating rate of $50\text{ }^{\circ}\text{C min}^{-1}$.
2. Cool the sample to 350 °C at a cooling rate of $30\text{ }^{\circ}\text{C min}^{-1}$.
3. At this time, replace the N_2 atmosphere with air and heat the sample to 700 °C at a heating rate of $2.5\text{ }^{\circ}\text{C min}^{-1}$.
4. Obtain the content of the carbon black obtained from the resulting TG curve by taking into account the mass loss due to the oxidation of the polymeric residue. The entire above run will take approximately 2.5 h.

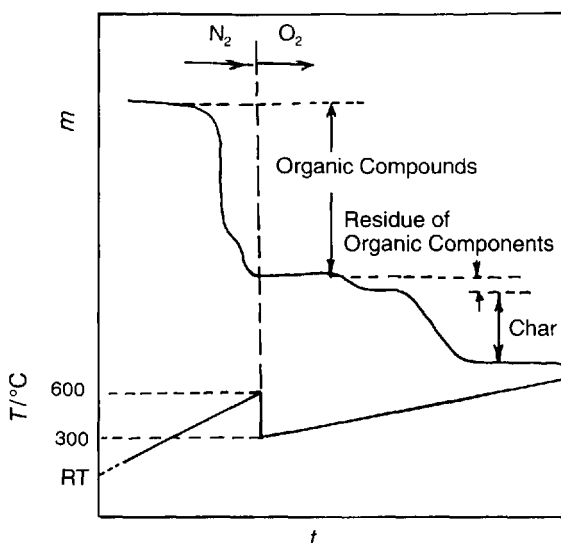


Figure 5.37 Scheme of the double heating method

If it is difficult to determine the initial mass loss of the carbon black on the TG curve, the lowest valley point of DTG curve can be used. The average deviation of the resulting value obtained using this method from the added amount of carbon black is approximately 3%.

5.7.3 Measurement of Oxidization of Oils and Fats

Oils or fats and oil/fat-based foods are readily denatured during a long storage period, because the oil or fat absorbs oxygen from air and is then oxidized. An appraisal of the stability of oils or fats can be made according to its initial oxidation time t_i at ambient temperature, which can easily be calculated using thermogravimetry [45].

The procedures are as follows:

1. Heat the sample to a pre-selected temperature T in an N_2 atmosphere and maintain the sample at T .
2. Replace N_2 with an oxygen atmosphere and simultaneously begin to measure time.
3. The time when a mass gain starts to show on the isothermal TG curve due to the oxidation of the sample corresponds to the initial oxidation time, t_i .
4. Repeat a series of such isothermal TG runs at various pre-selected temperatures and finally obtain a set of t_i and T values.
5. The results will show that the higher is T , the less is t_i . The relationship between $1/T$ and $\ln t_i$ obeys the Arrhenius equation. Accordingly, the initial oxidation time t_i at ambient temperature can be obtained by extrapolating the plot of $1/T$ versus $\ln t_i$. The slope of the line gives the activation energy, ΔE .

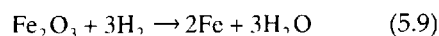
Table 5.3 shows a set of experimental data for bean oil using the above method, from which $\Delta E = 88.7 \text{ kJ mol}^{-1}$ is obtained.

Table 5.3 Oxidation temperature, T , and the initial mass gain time, t_i , of bean oil

$T/^\circ\text{C}$	$(1/T) \times 10^3$	t_i/min	$\ln t_i$
160	2.309	3.9	1.361
150	2.364	7.2	1.974
140	2.421	13.0	2.565
131	2.475	23.8	3.170

5.7.4 Measurement of Reaction of Metals with Gases

The conditions under which metallic materials are used are very complex. In particular, understanding the reactions of metals with various kinds of gases at high temperature is of great importance in estimating the service duration and the thermal stability of the metallic materials. The reactions of metals with gases are gas--solid reactions [46] and TG can be used to measure the variation in the mass of the metal with temperature and to perform kinetic analysis of the amount reacted. Tests of this kind of reaction can even be carried out in an atmosphere of corrosive gases such as SO_2 or NH_3 . Figure 5.38 shows an example of a metal--gas reaction, the reduction reaction of iron(III) oxide with hydrogen, which proceeds according to equation (5.9).



The experimental conditions were as follows: hydrogen flow-rate of 30 ml min^{-1} ; heating rate, $10^\circ\text{C min}^{-1}$; and sample (Fe_2O_3) mass, of 23.6 mg. The final mass loss is 30.1%, indicating that the iron(III) oxide is almost completely reduced. Similarly, the mass gain of iron in air can also be determined.

5.7.5 Determination of the Degree of Conversion of Gypsum to Plaster of Paris by DSC

Plaster of Paris (calcium sulfate hemihydrate) is produced by the partial dehydration of gypsum

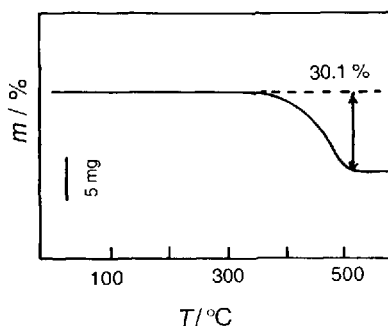
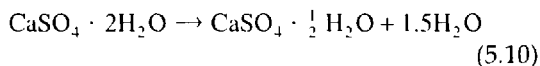


Figure 5.38 TG curve for the reduction reaction of iron(III) oxide

(calcium sulfate dihydrate) as follows:



This reaction under similar conditions can go one step further to anhydrous calcium sulfate, hence the calcination temperature must be carefully controlled for complete conversion to the hemihydrate.

The determination of the quantitative conversion of gypsum to plaster of Paris is therefore very important to the manufacturers of this product. Since plaster of Paris tends to absorb moisture and revert to gypsum readily, it is also necessary to monitor the gypsum content of plaster of Paris during storage. Quantitative measurements of the amount of gypsum are based on the heat of reaction of gypsum to plaster of Paris by DSC. The purity of crude gypsum may also be rapidly and accurately determined by this procedure.

The experimental procedure is as follows [48]:

1. Place an accurately weighed sample (2~5 mg) into a gold sealed-type DSC pan and hermetically crimp on the lid.
2. Place the sample in the DSC sample holder with an empty gold pan with lid for reference. Aluminum pans cannot be used owing to interference from the reaction between water and aluminum.
3. Set the temperature program over the range 70–220 °C at 5 °C min⁻¹. The reaction endotherm can be observed from 138 °C as shown in Figure 5.39.
4. Calculate the enthalpy of the reaction endotherm by a suitable technique (e.g. area can be measured by planimetry, cutting and weighing, etc.).
5. When the heat of the reaction has been obtained, determine the mass fraction of gypsum as follows:

mass fraction of gypsum

$$= [(\Delta H \text{ of sample})/(\Delta H \text{ of 100\% pure gypsum})] \times 100\% \quad (5.11)$$

The value of ΔH for pure gypsum can be determined from the standard material to be 122.2 J/g.

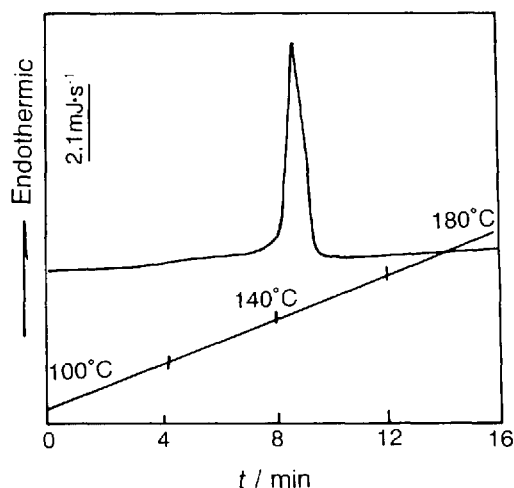


Figure 5.39 DSC curve for conversion of gypsum to plaster of Paris. Sample size, 3.44 mg; atmosphere, nitrogen [47]

5.8 References

- 1 Mita, T., *Recent Advances in Heat-Resistant Polymers*. General Technical Centre Publication, No. 8, p. 117.
- 2 Toop, D. J., *IEEE Trans. Electr. Insul.*, 1971, E-1-6, 2.
- 3 DiCerbo, P. M., *Insul./Circuits*, 1975, (2), 21.
- 4 ASTM D3895-80. Philadelphia, PA, American Society for Testing and Materials, 1980.
- 5 Blaine, R. L., *Du Pont Thermal Analysis Technical Report*, No. TA-40. Wilmington, DE, Du Pont, 1989.
- 6 Doyle, C. D., *J. Appl. Polym. Sci.*, 1961, 5, 285.
- 7 Gillham, J. K., *Soc. Plast. Eng. (Proc. Annu. Tech. Conf.)*, 1980, 38, 268.
- 8 Erms, J. B., Gillham, J. K., and Small, R., *Polym. Chem. Reprint*, 1981, 22, 123.
- 9 Chan, J. B., Nae, H. N., and Gillham, J. K., *J. Appl. Polym. Sci.*, 1984, 29, 3307.
- 10 Peng, X., and Gillham, J. K., *J. Appl. Polym. Sci.*, 1985, 30, 4685.
- 11 *Seiko Report*, 1981, No. TA 8.
- 12 Ikeda, M., and Teramoto, Y., *Seiko Report*, 1987, No. TA 42.
- 13 Ikeda, M., and Teramoto, Y., *Seiko Report*, 1987, No. TA 44.
- 14 Cai Gencai, *J. East China Inst. Chem. Technol.*, 1981, 1, 115.
- 15 Cai Gencai, *J. East China Inst. of Chem. Technol.*, 1982, 1, 87.
- 16 Cai Gencai, *Chem. Technology Pet.*, 1981, 7, 468.
- 17 Cai Gencai, *Analytical Apparatus*, 1982, 4, 10.
- 18 Papadatos, K., and Shelstad, K. A., *J. Catal.*, 1973, 28, 116.

- 19 Wang Ren, Jin Xing Mei and Wu Shanling, *Chem. Technol. Pet.*, 1982, **12**, 769.
- 20 Cai Gencai, *J. East China Inst. Chem. Technol.*, 1963, **4**, 579.
- 21 Johnson Jr, D. W., and Gallagher P. K., *Thermochim. Acta*, 1973, **7**, 303.
- 22 Wang Ren, Go Yanghao and Lu Hongye, *J. Fuel Chem. Technol.*, 1982, **10**, 20
- 23 Wang Ren, and Go Yanghao, *J. Fuel Chem. Technol.*, 1982, **10**, 193
- 24 Cai Gencai and Zhu Xiaolin, *J. East China Inst. Chem. Technol.*, 1987, **13**, 437
- 25 Wang Ren, Xue Qixin and Wu Shanliang, *J. Fuel Chem. Technol.*, 1983, **11**, 1.
- 26 Cai Gencai, *J. Fuel Chem. Technol.*, 1989, **13**, 357
- 27 Feng Yangjie, *J. East China Inst. Chem. Technol.*, 1982, **4**, 419
- 28 TA Instruments, *Thermal Analysis Technical Literature*, TA-136.
- 29 Nguyen, T., Zavarin, E., and Barrall II, E. M., *J. Macromol. Sci. Rev. Macromol Chem*, 1981, **C20**, 1
- 30 Nguyen, T., Zavarin, E., and Barrall II, E. M., *J. Macromol. Sci. Rev. Macromol Chem*, 1981, **C21**, 1
- 31 Nakamura, K., Nishimura, Y., Zetterlund, P., Hatakeyama, T., and Hatakeyama H., *Thermochim. Acta*, 1996, **282/283**, 433.
- 32 Hatakeyama, H., Kubota, K., Nakano, J., *Cellulose Chem. Technol.*, 1971, **6**, 521
- 33 Hatakeyama, H., Nakamura, K., and Hatakeyama, T., *Pulp Paper Mag. Can.*, 1978, **6**, 624.
- 34 Hatakeyama, T., Nakamura, K., and Hatakeyama, H., *Polymer*, 1982, **23**, 1801.
- 35 Hatakeyama, T., Hirose, S., and Hatakeyama, H., *Makromol. Chem.*, 1983, **184**, 1265.
- 36 Kunihiisa, K. S., and Ogawa, H., *J. Thermal Anal.*, 1985, **30**, 49.
- 37 Kunihiisa K. S., and Ogawa, H., *Thermochim. Acta*, 1988, **123**, 255
- 38 Minn, J., *Thermochim. Acta*, 1985, **91**, 87.
- 39 Fujimoto, K., *Seiko Technical Report*, TA No. 48, 1988.
- 40 TA Instruments, *Thermal Analysis Technical Literature*, No. TA 129.
- 41 Hassel, R. L., *Du Pont Thermal Analysis Technical Literature*, No TA-55. Wilmington, DE, Du Pont.
- 42 Huang Kelong, *Geochemistry*, 1979, (4), 331 (in Chinese).
- 43 Huang Kelong. *Geochemistry*, 1982, (3), 310 (in Chinese).
- 44 Shimadzu Application News, CA 160-054, Thermal Analysis 34; Shimadzu J., 1987, **44**, 65.
- 45 Ohta, M., Shimadzu J., 1986, **43**, 59.
- 46 Ohta, M., Shimadzu Application News, TA Applications on Metals.
- 47 Gill, P. S., *Du Pont Thermal Analysis Technical Literature*, No. TA-38. Wilmington, DE, Du Pont.

TA Measurement of Physical Characterization Parameters for Substances

6.1 Thermodynamic Parameters

6.1.1 Determination of Heat Capacity by DSC

6.1.1.1 Scanning Method

The heat capacity of a substance can be measured from the sample mass and difference in heat flow rate of DSC curves, which are determined by programmed constant temperature, rising temperature and constant temperature procedures, using sapphire as a standard reference material [1].

The following procedure is recommended for heat capacity measurement. The heat capacity measurement of polystyrene is described as an example.

First a blank experiment is carried out following steps 1–8:

1. Choose a pair of aluminum sample containers having similar masses (the mass difference should be less than 0.01 mg).
2. Set the apparatus at an initial temperature of 330 K (T_i) and an end temperature of 395 K (T_e).
3. Maintain T_i for 1 min and obtain the straight line I, as shown in Figure 6.1.
4. Scan at a heating rate of 5 or 10 K min⁻¹ and obtain curve II, as shown in Figure 6.1.
5. Maintain at T_e for 1 min and obtain the straight line III, as shown in Figure 6.1.
6. Adjust the slope controller of the apparatus in order that line I meets line III on the same line, as shown in Figure 6.1.
7. If step 6 is not attained, adjust again until this condition is satisfied.
8. Once the above conditions have been satisfied, they should be maintained.

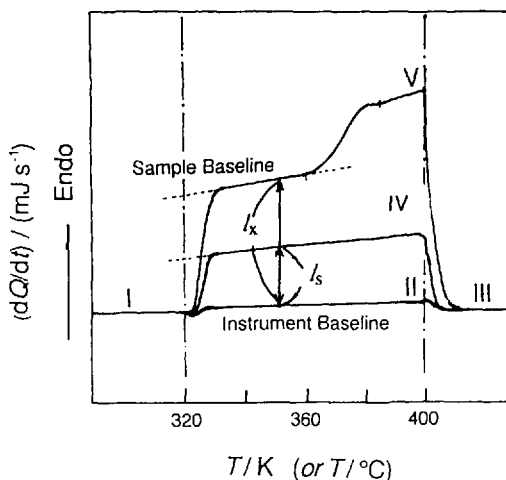


Figure 6.1 Heat capacity measurement of polystyrene

Next, the standard material and the sample are measured.

9. Weigh 10–30 mg of the synthetic Al_2O_3 (standard sapphire) with a precision of 0.01 mg.
10. Scan (curve IV).
11. Weigh the sample (approximately 10 mg) with a precision of 0.01 mg.
12. In order to eliminate the thermal history of the sample, heat it at a rate of 20 K min^{-1} to 395 K and maintain this temperature for 10 min. Then cool the sample at a rate of 10 K min^{-1} to 335 K and maintain for 10 min. This procedure is the same as that used in the glass transition measurement.
13. Measure the sample under the same conditions as in step 10 (curve V).
14. If the three curves II, IV and V are not in accordance at T_i and T_e , adjust the apparatus and repeat the procedure again.

Recent computer software includes sapphire heat capacity data. On this account, it is not necessary to measure the standard material.

Calculation is performed as follows:

15. Calculate C_p using the following equation:

$$C_{px} = (l_x/l_s)(M_s/M_x)C_{ps} \quad (6.1)$$

where C_{px} is the heat capacity of the sample, C_{ps} is that of the standard material, M_x is the mass of the sample and M_s is that of the standard and l_x and l_s are shown in Figure 6.1.

16. When the calculation is performed, C_p data obtained from T_i to $T_i + 10$ should be omitted.

Using the computer software, calculation steps 15 and 16 are carried out automatically. In order to obtain reliable data, the sample should be flat and the surface of the sample should be in close contact with the aluminium container. The measurement error can be reduced by eliminating the thermal history of the sample before the measurement (step 12) and ensuring that the baselines I and II are stable and constant. In this way, a precision of 0.1% was achieved.

6.1.1.2 Enthalpy Method

As shown in Figure 6.2, the enthalpy of the area between the sample and reference material (the

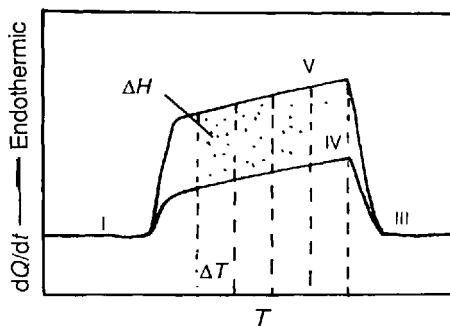


Figure 6.2 Schematic DSC curves to measure C_p by the enthalpy method

hatched area in the figure) is obtained by adjusting the sample and reference baseline to isothermal states. When T_i and T_e are small, C_p is obtained by $C_p = \Delta H / \Delta T$. In practice, data are accumulated by computer; for example, when one point data is stored each 12 s, C_p can be calculated for each 1 K at a heating rate of 5°C min^{-1} . The C_p values of sapphire samples of different mass were measured from 350 to 750 K [2,3]. The C_p values agreed to within a $\pm 1\%$ with those obtained by adiabatic calorimetry.

The difference between the C_p values obtained by the scanning method and those obtained by the enthalpy method has not been fully investigated. The C_p values obtained by DSC agree to within $\pm 1.0\%$ with those obtained by adiabatic calorimetry, when the sample is carefully measured.

6.1.2 Measurement of Linear Expansion Coefficient by TMA

Using TMA apparatus, the expansion or contraction of a sample can be detected by the deformation detection device. As shown in Figure 6.3, the probe makes contact with the sample and the probe moves upwards or downwards accompanied by sample deformation. The coefficient of linear thermal expansion, β , can then be calculated using the equation

$$\beta = (\Delta L / L_0)(T_2 - T_1)^{-1} \quad (6.2)$$

where ΔL is the variation in dimension from temperature T_2 to T_1 ($^\circ\text{C}$) caused by the expansion of the sample (μm) and L_0 is the initial length of the sample (μm).

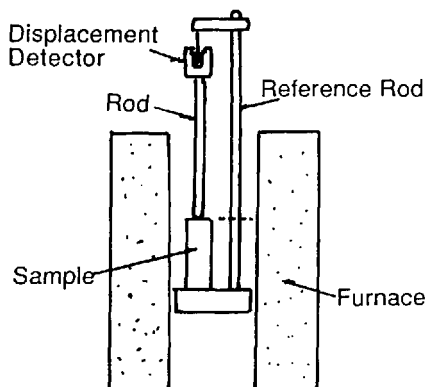


Figure 6.3 Schematic diagram of the TMA apparatus

If measurements are made using a TMA as shown in Figure 6.2, two types of correction have to be taken into account:

1. Reference correction: as shown in Figure 6.3, the thermal expansions of the probe and the portion of the sample holder are mutually cancelled, but the lower part of the sample holder must be compensated.
2. Blank correction: since there is a temperature distribution in the system, a slight difference in the thermal expansion between the sample part and the reference part may exist which should also be corrected-using a blank experiment.

Therefore, ΔL should be

$$\Delta L = \Delta l_s + \Delta l_b + L_0 \beta_t (T_2 - T_1)^{-1} \quad (6.3)$$

where Δl_s is the measured value by TMA for the sample from T_2 to T_1 (μm), Δl_b is the value measured by TMA for the probe from T_2 to T_1 (μm) (also the value of the blank experiment) and β_t is the coefficient of linear expansion of the reference material, e.g. for quartz $\beta_t = 5.5 \times 10^{-7}$. The coefficient of linear expansion is as follows:

$$\beta = (\Delta l_s + \Delta l_b) [L_0 (T_2 - T_1)]^{-1} + \beta_t \quad (6.4)$$

When the sample is measured using a differential-type TMA, it is not necessary to make corrections [4]. The volumetric thermal expansion coefficient, α , cannot be measured by TMA. Generally, the expansion coefficient of solids is small; $\alpha = 3\beta$ is currently used. However, for samples whose Poisson's constant is not 1.0, α

is difficult to estimate. Dilatometry has been used, but this method is not as widely used as before because mercury is used as a purging liquid [5]. The thermal expansion coefficients of various materials are shown in Figure 6.4 [6]. Reference materials for thermal expansion coefficients are shown in the Appendix.

6.1.3 Determination of Thermal Conductivity

Heat conduction occurs when a temperature gradient exists in matter. Heat conduction is an energy transport process. For steady-state conditions of unidirectional heat flow in an isotropic matter, the Fourier-Biot equation holds:

$$q = -\lambda(\partial T/\partial x) \quad (6.5)$$

where q is the heat flux (W m^{-2}), $\partial T/\partial x$ is the temperature gradient (K m^{-1}) and λ is the

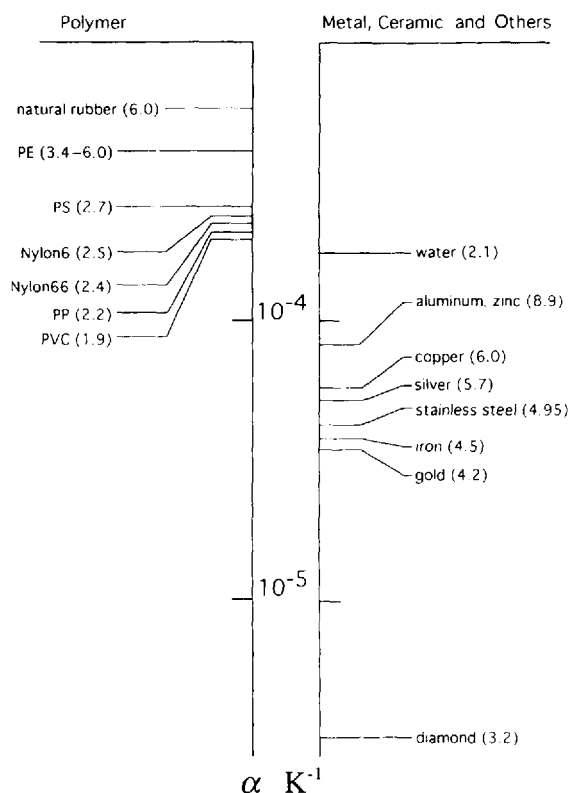


Figure 6.4 Thermal expansions coefficient of various materials

thermal conductivity ($\text{W m}^{-1} \text{K}^{-1}$). The minus sign in equation 6.5 indicates opposite directions of the heat flux and temperature gradient. Thermal conductivity is a physical property of materials with its capability of heat energy transportation. Heat conduction of matter is carried out by heat conduction carriers, including molecules, electrons, photons and phonons (lattice waves). Thermal conductivity can be expressed as

$$\lambda = \sum_i (1/3) C_i v_i l_i \quad (6.6)$$

where C_i , v_i and l_i are the specific heat, velocity of motion and average free length of the i th carrier, respectively. Thermal conductivity is affected by many factors, such as composition, structure, pressure and temperature. The above factors make it difficult to obtain thermal conductivities accurately by theoretical prediction. Generally, thermal conductivity is obtained by experimental measurements.

The methods for measuring thermal conductivity can be divided into two groups, the steady-state and non-steady-state methods. By means of the definition of thermal conductivity (equation 6.6) in steady-state methods, a unidirectional heat flow should be built up in the sample and the heat energy through the sample and the temperature difference at two or more points must be measured to obtain the thermal conductivity. Depending on the values of the thermal conductivity of different materials, the longitudinal method (including the plate method and bar method), the radial method, globe method, ellipse method, direct electrical heating method and comparative method, etc., can be selected. As an example, with the plate method which is available for low thermal conductivity refractories, plastics and some ceramics, the thermal conductivity can be calculated by

$$\lambda = (Q \Delta L) / (A \Delta T) \quad (6.7)$$

where Q is the unidirectional heat energy which passes through the sample in unit time, A is the sample area in the heat flow direction, ΔL is the thickness of the plate sample and ΔT is the temperature difference between the two plate surfaces.

Non-steady-state methods can be used to measure thermal conductivity according to

$$\lambda = \alpha C_p \rho \quad (6.8)$$

where α is the thermal diffusivity ($\text{m}^2 \text{s}^{-1}$ or $\text{cm}^2 \text{s}^{-1}$), C_p is the specific heat ($\text{kJ kg}^{-1} \text{K}^{-1}$ or $\text{J g}^{-1} \text{K}^{-1}$) and ρ is the density (kg m^{-3} or g cm^{-3}).

The thermal conductivities of various materials differ widely, as shown below (see Ref. 7 and Appendix, Table X):

Typical metals:	50–415	$\text{W m}^{-1} \text{K}^{-1}$
Typical alloys:	12–120	$\text{W m}^{-1} \text{K}^{-1}$
Non-metallic liquids:	0.17–0.7	$\text{W m}^{-1} \text{K}^{-1}$
Refractory materials:	0.03–0.17	$\text{W m}^{-1} \text{K}^{-1}$
Gases at normal pressures:	0.007–0.17	$\text{W m}^{-1} \text{K}^{-1}$

6.1.4 Determination of Thermal Diffusivity

The standard heat conduction equation is

$$\rho C_p (\partial T / \partial t) = \nabla \lambda \Delta t \quad (6.9)$$

where ρ is the density (kg m^{-3} or g cm^{-3}), C_p the specific heat ($\text{kJ kg}^{-1} \text{K}^{-1}$ or $\text{J g}^{-1} \text{K}^{-1}$) and λ the thermal conductivity ($\text{W m}^{-1} \text{K}^{-1}$ or $\text{W cm}^{-1} \text{K}^{-1}$). The thermal conductivity λ does not change with position for homogeneous materials, so equation 6.9 can be rewritten as

$$\partial T / \partial t = (\lambda / \rho C_p) (\partial^2 T / \partial x^2) = \alpha (\partial^2 T / \partial x^2) \quad (6.10)$$

where α is the thermal diffusivity ($\text{m}^2 \text{s}^{-2}$ or $\text{cm}^2 \text{s}^{-1}$). The thermal diffusivity α indicates a capability to effect the temperature homogenization in materials during non-steady-state heat flow. In DTA and DSC experiments, different sample masses and heating rates may result in different analysis data and the main reason for this may be the thermal diffusivity of the sample and container. The thermal diffusivity of typical substances is shown in Figure 6.5 [6]. The thermal diffusivity of elements can be found elsewhere [8].

Generally, thermal diffusivity measurement has many advantages, such as small sample size, short measuring period and wide temperature range. On this account, it is an important method for obtaining thermal conductivity data. There

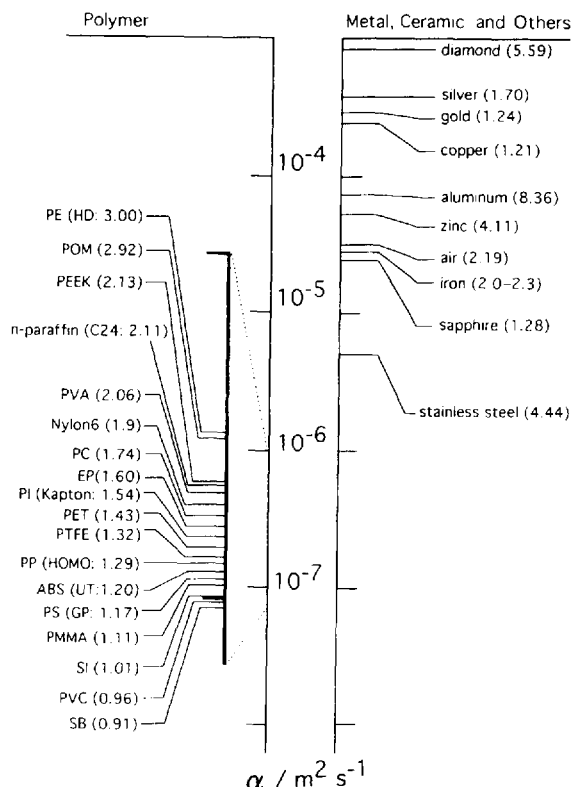


Figure 6.5 Thermal diffusivity of typical substances at room temperature

are two kinds of methods according to the heat source, i.e. the pulse heat source method and the periodic heat source method. The laser pulse method is one of the most well known and widely applied methods. In this methods (Figure 6.6), the front surface of a small disk sample is irradiated by a uniform pulse laser and the temperature rise curve of the back face of the sample can be used to measure thermal diffusivity. The equation is [9]:

$$\alpha = (W_{1/2}/\pi^2)(L^2/t_{1/2}) \quad (6.11)$$

where $W_{1/2}$ is a constant ($W_{1/2}=1.37$), L is the thickness of the sample and $t_{1/2}$ is the time required for the back face to attain half its maximum rise temperature. Various assumptions, such as heat loss, uniform thermal pulse, homogeneous sample and short pulse duration, must be satisfied to measure thermal diffusivity. If these conditions cannot be satisfied, revision

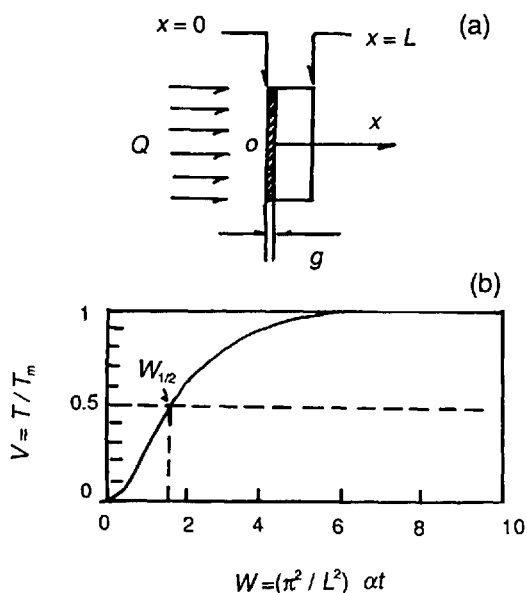


Figure 6.6 Thermal measurement by laser pulse method. (a) Laser pulse on the sample. (b) Temperature response of back face of sample

should be considered. The Cowen method [10] and the Clerk and Taylor method [11] can usually be used to revise the original data obtained from equation (6.11).

6.2 Purity Determination

DSC provides a rapid, accurate and precise method for determining absolute purity. A small amount of sample (milligrams) is required and it is not necessary to use a high-purity standard of the compound for an accurate purity determination. The calorimetric purity method is accepted by the US Pharmacopeia/National Formulary [12] as a reference test method.

The purity is determined by analyzing the shape of the melting DSC curve of a sample. The higher the concentration of an impurity in a given sample, the lower is the melting point and the broader the melting range. Determination of the purity of a substance by DSC is based on the Van't Hoff equation modified as follows:

$$T_s = T_0 - [(RT_0^2\chi)/\Delta H_f](1/F) \quad (6.12)$$

where T_s is the sample temperature (K), T_0 the melting point (K) of the pure sample, R the gas

constant ($8.314 \text{ J mol}^{-1} \text{ K}^{-1}$), χ the mole fraction of the impurity, H_f the heat of fusion (J mol^{-1}) of the pure major component and F the area fraction of the DSC melting curve at T_s . A plot of T_s versus $1/F$ will give a line of slope $-[(RT_s^2\chi)/\Delta H_f]$. H_f can be obtained directly from the DSC curve or from the literature. The mole fraction of impurity is then calculated.

The test and calculation procedure is as follows:

1. Determination of the DTA or DTA-TG curve of an unknown sample. Estimate the initial temperature of melting T_i and confirm whether or not sublimation (or vaporization) is observed. DSC may also be used for determining T_i .
2. Determination of DSC curve for samples. Weigh the sample (1–3 mg) with a precision of $\pm 0.01 \text{ mg}$. The DSC sensitivity should be high, e.g. 4.184 mJ s^{-1} (full-scale). The atmosphere is nitrogen (flow rate 50 ml min^{-1}). A slow heating rate (e.g. $0.5^\circ \text{C min}^{-1}$) and a small sample mass are employed in order to ensure equilibrium conditions. The sample temperature is programmed slowly from several degrees below the nominal melting point until melting is completed. When a chart recorder is used, a chart speed of 1200 mm h^{-1} is recommended. If sublimation takes place during the melting, use sealed-type sample vessels.
3. Temperature and enthalpy calibration of DSC curve. Calibration is carried out using the DSC curve determined under the same conditions as in step 2 for high-purity indium (purity $>99.99\%$), and the leading slope of the indium is used to determine the instantaneous sample temperature during melting taking into account the heat-resistance correction and the heat of fusion of indium (28.41 J g^{-1}) used to calibrate the enthalpy of the DSC curve (mJ cm^{-2}).
4. Construct a T_s versus $1/F$ plot. The linear range of this plot usually is $0.1 < F < 0.5$. Calculate the slope of the corrected line and employ equation (6.12) to calculate the mole fraction of impurity.

A typical DSC melting curve and a plot of the sample temperature T_s versus the reciprocal area

fraction $1/F$ for 4,4'-dichlorodiphenyl sulfone recrystallized three times from ethanol are shown in Figures 6.7 and 6.8, respectively.

Note the following two points. (1) Determine the temperature (T_s) at which each fraction has melted and transpose a line of the same slope as the leading edge of the indium curve through point E to the baseline G. Point G is the temperature at which fraction ADE has melted. (2) In actual practice, the plot (Figure 6.8) is not a straight line, but is concave upwards owing to the presence of undetected pre-melting. In order

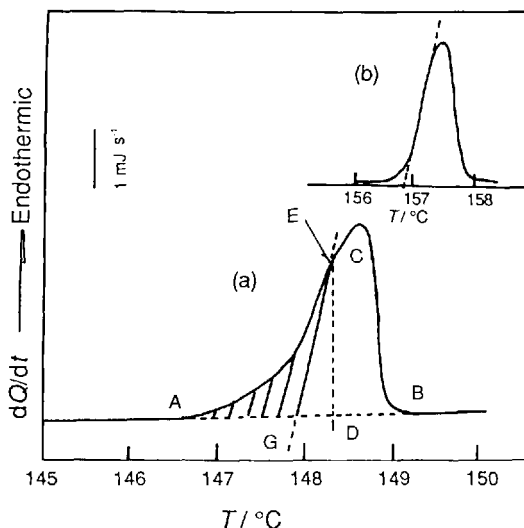


Figure 6.7 Curves for 4,4'-dichlorodiphenyl sulfone and indium

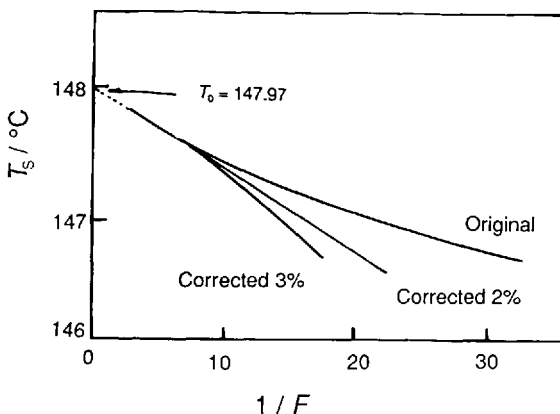


Figure 6.8 Plot of T_s vs $1/F$ for 4,4'-dichlorodiphenyl sulfone

to correct this curvature, an empirical quantity is added to both each partial and full area and T_s versus $1/F$ is replotted until a straight line is produced (as assumed by the Van't Hoff equation). Excessive correction results in a line which is concave downwards.

From the experimental data for 4,4'-dichlorodiphenyl sulfone, $T_0 = 147.97^\circ\text{C}$, $\Delta H_f = 2.43 \text{ kJ mol}^{-1}$ and slope $= 0.0583 \text{ K}$, then

$$\chi = [0.0583 (\text{K}) \times 24.3 (\text{kJ mol}^{-1})] / [8.314 (\text{J mol}^{-1} \text{K}^{-1}) \times (147.97 + 273.15)^2 (\text{K}^2)] = 0.00096$$

The purity is $1 - x = 0.99904$, that is, 99.90 mol%.

The DSC method for calculating absolute purity is not universally applicable to all materials; only samples of high purity can be analyzed. The generally accepted limit and standard deviation of purity are 98 mol% and 0.04%, respectively.

This method is based on the assumption that the pure major component exists in the solid state as a single phase (i.e. the absence of solid-solution formulation as it would be undetected). It also assumes that decomposition does not occur at or below melting as the decomposition products would act as internally generated impurities and give erroneously low results.

6.3 Thermoporosimetry

Thermoporosimetry is based on the calorimetric measurement of solid-liquid transformations (e.g. pure water) in porous materials. This can be the pores in the skin of a membrane. The temperature at which water in the pores freezes (the extent of undercooling) depends on the pore size. Each pore (pore size) has its own freezing temperature. For cylindrical pores with water in the pores, the following equation can be derived for freezing [14]:

$$r_p = (-64.57/\Delta T) + 0.57 \quad (6.13)$$

where r_p is the pore radius (nm) and ΔT the extent of undercooling (K). From equation 6.13 it can be seen that the pore radius becomes smaller when the extent of undercooling increases. Figure 6.9 is a schematic diagram of the freezing

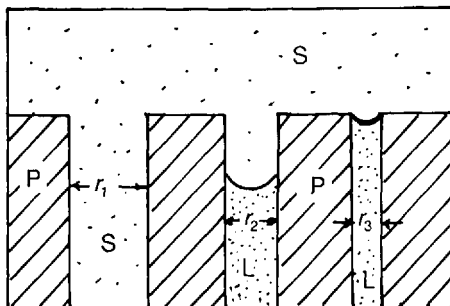


Figure 6.9 Schematic diagram of the extent of undercooling in relation to the pore diameter. L, liquid (water); S, solid (ice); P, porous membrane; r , pore radius ($r_1 > r_2 > r_3$)

of a liquid (water) in a porous medium as a function of the pore size.

The temperature has been decreased so far that all the water in the pore r_1 has become ice. In pore r_2 water just starts to freeze whereas in pore r_3 all the water is still liquid. As the temperature is lowered further, the water in pore r_3 will also freeze. The heat effect of the liquid-solid transition ('freezing') is measured by DSC.

From calorimetric data and equation 6.13, the pore size and its distribution can be obtained. The pore size distribution of a ceramic membrane determined by DSC is in good agreement with data obtained by the gas adsorption-desorption method.

6.4 References

- 1 Hatakeyama, T., and Kanetusna, H., *Thermochim. Acta*, 1989, **146**, 311.
- 2 Kaminoto, M., in Japan Society of Thermal Analysis and Calorimetry (Ed.), *Fundamentals and Applications of Thermal Analysis*, 3rd edn. Tokyo, Realize, 1994, p. 56.
- 3 Takahashi, Y., Sakamoto, R., and Kaminoto, M., *Int. J. Thermophys.*, 1988, **9**, 1081.
- 4 Mizutani, T., in Japan Society of Thermal Analysis and Calorimetry (Ed.), *Fundamentals and Applications of Thermal Analysis*, 3rd edn. Tokyo, Realize, 1994, p. 20.
- 5 Hatakeyama, T., and Quinn, F. X., *Thermal Analysis; Fundamentals and Applications to Polymer Science*. Chichester, Wiley, 1994, p. 120.
- 6 Hashimoto, T., in *Data Handbook of Thermal Diffusivity, Heat Capacity and Thermal Conductivity of Polymers*. Tokyo, Youtes, 1997.
- 7 Yu Changmin, *Heat Conduction*. Beijing, High Education Press, 1983, p. 2 (in Chinese);

- Translated from M. N. Ozisik, *Heat Conduction*, 1980.
- 8 Touloukian, Y. S., Powell, R. W., Ho, C. Y., and Nicolau, M. C., *Thermophysical Properties of Matter*, New York, Plenum Press, 1974, vol. 10, p. 6.
- 9 Parker, W. J., Jenkins, R. J., Butler, C. P., and Abbott, G. L., *J. Appl. Phys.*, 1961, **32**, 1679.
- 10 Cowen, R. D., *J. Appl Phys.*, 1963, **34**, 926.
- 11 Clerk, L. M., and Taylor, R. E., *J. Appl. Phys.*, 1974, **46**, 714.
- 12 *United States Pharmacopeia/National Formulary*.
- 13 Liu Zhenhai, *Chem. Res. Appl.* 1990, **2** (2), 4 (in Chinese).
- 14 Brun, M., Lallemand, A., Qccinson, J. F., and Fyraud, C., *Thermochim Acta*, 1977, **21**, 59.

Part II

Thermal Analysis Curves

This page intentionally left blank

Thermal Analysis Curves of Polymers

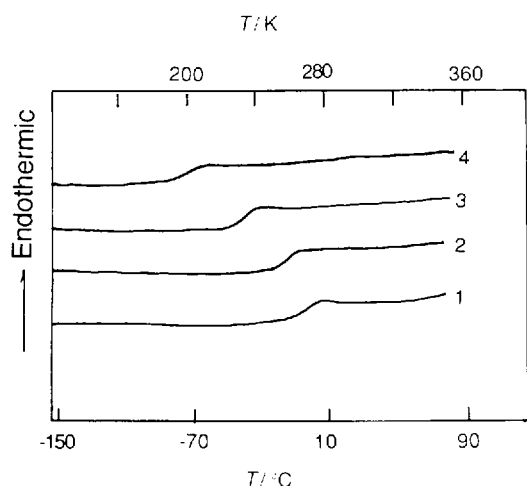


Figure 7.1 Glass transition of amorphous styrene oligomers with a butyl group at both ends, $\text{Bu}[\text{CH}(\text{C}_n\text{H}_5)\text{CH}_2]_n\text{Bu}$: 1, $n = 5$; 2, $n = 4$; 3, $n = 3$; 4, $n = 2$ [1]

Samples

Mixtures of styrene oligomers were fractionated using a gel permeation chromatograph.

Measurements

Perkin-Elmer DSC II; heating rate $10^\circ\text{C min}^{-1}$; sample mass 5 mg; atmosphere He gas.

Results

Glass transition temperature increases linearly with increasing chain length.

Sample

Polystyrene ($M_w = 1.30 \times 10^5$) from Formosa Chemical and Fibre Co. (Taipei). The samples were sealed between KBr discs (6 mm) by hydraulic pressing.

Measurements

FTIR-IDSC, Mettler FP84 (Switzerland); FTIR; Jasco Micro FTIR-200 (Japan); heating rate 5 or $10^\circ\text{C min}^{-1}$. KBr discs were placed in the DSC

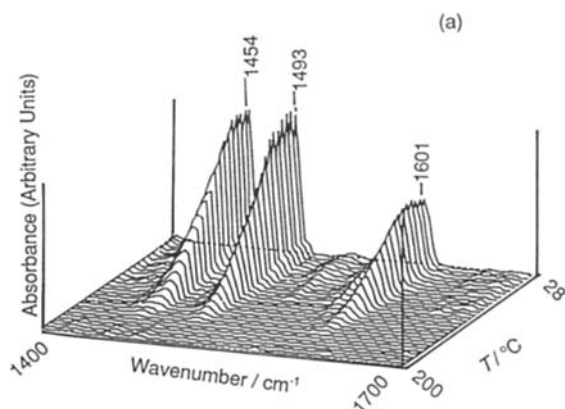


Figure 7.2 Glass transition temperature of polystyrene measured with an FTIR-DSC combined system. (a) Three-dimensional plots of IR spectra of polystyrene

(continued)

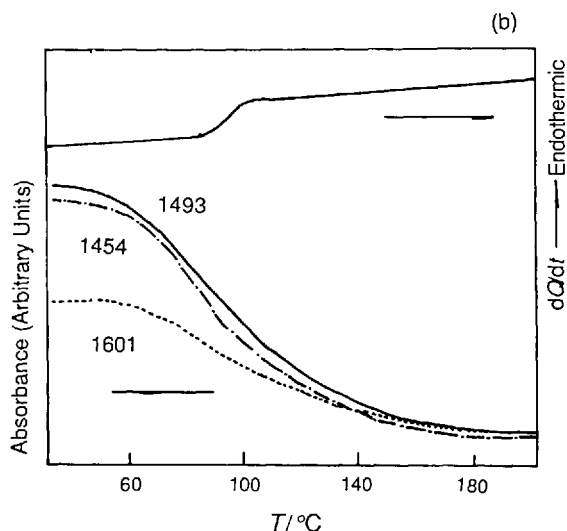


Figure 7.2 Glass transition temperature of polystyrene measured with an FTIR-DSC combined system. (b) DSC heating curve and absorbance of the specified bands as a function of temperature [2]

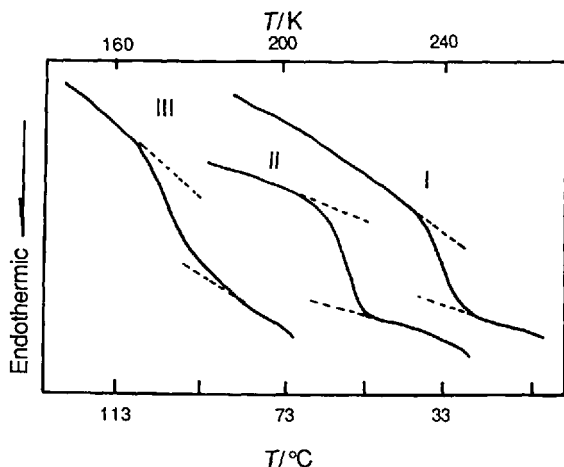


Figure 7.3 Glass transition temperature of various synthetic elastomers [3]

microscopy cell. The temperature of the DSC microscopy cell was controlled with a Mettler FT80HT processor.

Results

Variation of sensitive band corresponding to conformational change agrees well with DSC data. At the glass transition temperature, the freedom of the molecular chain increases and intramolecular rotation and/or main-chain motion is enhanced.

Samples

I, Neoprene; II, butyl rubber; III, *cis*-polybutadiene.

Measurements

Setaram Model 101 DSC; Al crucible; heating rate $5^{\circ}\text{C min}^{-1}$; sensitivity $100\text{ }\mu\text{V full-scale}$.

Results

Glass transition temperature T_{mg} determined by middle-point method: neoprene -37°C , butyl rubber -61°C , *cis*-polybutadiene -104°C .

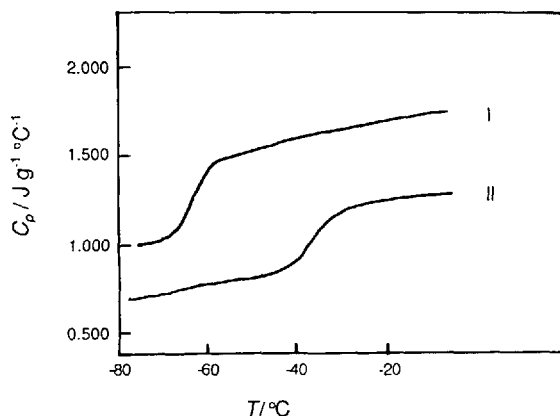


Figure 7.4 Specific heat capacity of elastomers [3]

Samples

I, natural rubber; II, polychloroprene.

Measurements

Setaram model 111 DSC; sample mass, natural rubber 156.7 mg, polychloroprene 230.8 mg; Al crucible; heating rate $5^{\circ}\text{C min}^{-1}$; sensitivity $50 \mu\text{V full-scale}$.

Results

The mean values of the specific heat before and after the glass transition (in $\text{J g}^{-1}^{\circ}\text{C}^{-1}$) are given in Table 7.1.

Table 7.1

	Before T_g	After T_g
Natural rubber	1.004	1.506
Polychloroprene	0.795	1.255

The variations of the specific heats of natural rubber and polychloroprene due to the glass transition are 0.502 and $0.460 \text{ J g}^{-1}^{\circ}\text{C}^{-1}$, respectively.

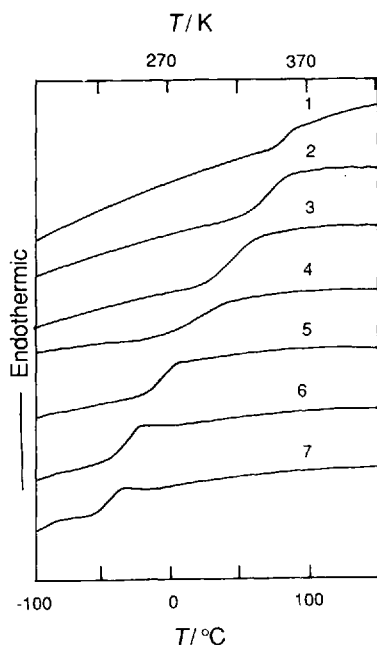


Figure 7.5 Glass transitions of copolymers of (trimethylsilyl)methyl methacrylate (TMSMMA) and *n*-butyl acrylate (*n*-BA) having high permselectivity [4]. TMSMMA-*n*-BA composition: 1, TMSMMA; 2, 90:10; 3, 70:30; 4, 50:50; 5, 30:70; 6, 10:90; 7, *n*-BA

Samples

Samples were prepared by radical polymerization.

Measurements

Perkin-Elmer DSC 7; sample mass 10 mg; heating rate $20^{\circ}\text{C min}^{-1}$.

Results

Glass transition temperatures of the copolymers decreased with increasing *n*-BA content, which gave the high segmental mobility. Copolymer membranes showed high permselectivity for chlorinated hydrocarbons.

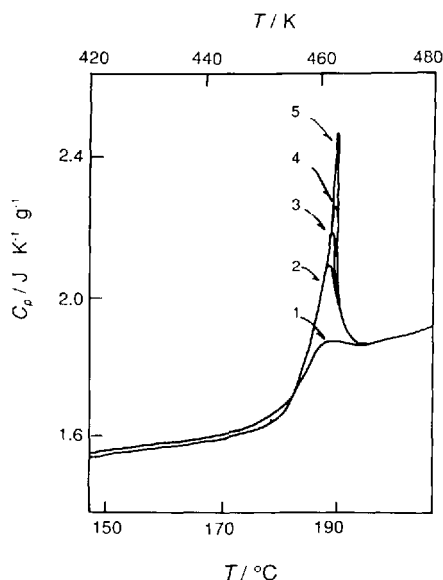
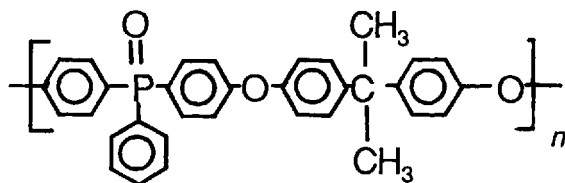


Figure 7.6 Enthalpy relaxation of engineering plastics [5]. Annealing temperature: 175 °C, annealing time: 1, 0; 2, 20; 3, 40; 4, 75; 5, 393 min

Sample



The samples were heated to a temperature higher than $T_g + 50$ °C, quenched to 27 °C and then reheated at 10 °C min⁻¹.

Measurements

Perkin-Elmer DSC 7; sample mass 3 mg; heating rate 20 °C min⁻¹; Al sample vessel; atmosphere N₂.

Results

The activation energy of enthalpy relaxation was calculated as $E_a = 250$ kJ mol⁻¹. It was suggested that the internal rotation of the main chain is related to the enthalpy relaxation of the amorphous chains.

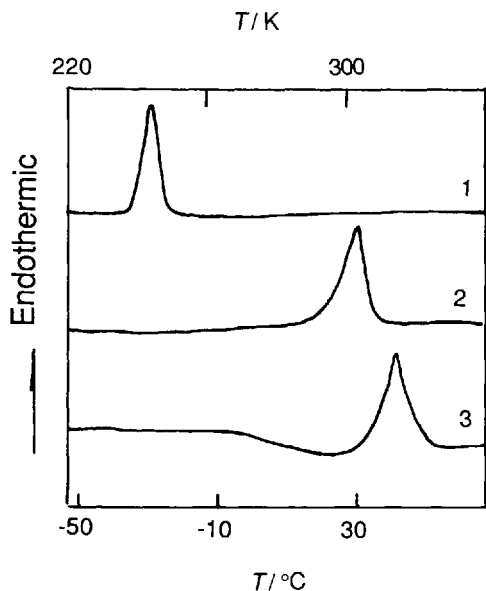


Figure 7.7 Melting DSC curves of crystalline styrene monomers with different end groups and dimer [1]. 1, PhCH=CH₂; 2, Bu¹(Ph)CHCH₂ Bu¹; 3, Bu¹(Ph)(CHCH₂)₂ Bu¹

Samples

Styrene monomers were purified by vacuum distillation. Dimer was fractionated using gel permeation chromatography (purity 99%; 1% impurity was monomer and trimer).

Measurements

Perkin-Elmer DSC 2, heating rate 10 °C min⁻¹, sample mass 5 mg, atmosphere He gas.

Results

The melting temperature of monomer depends on relative molecular mass. A broad endotherm observed at around 25 °C is attributed to pre-melt crystallization.

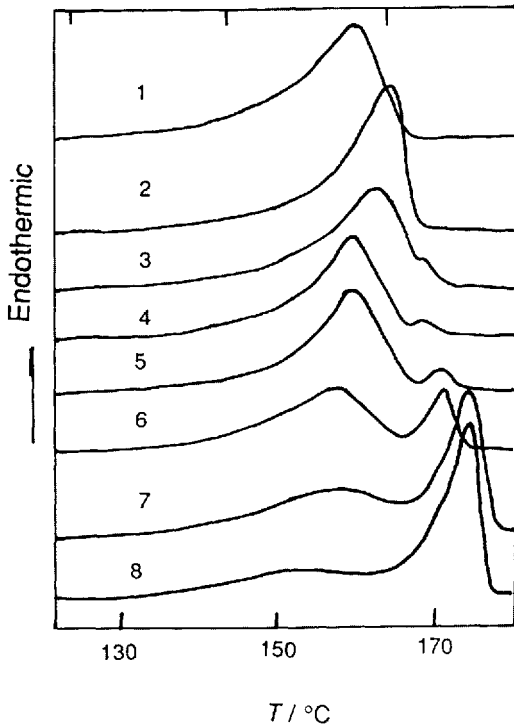


Figure 7.8 Melting DSC curves of polypropylene (PP) annealed at 163 °C for various times [6]. 1, Original; 2, 20 s; 3, 1 min; 4, 2 min; 5, 5 min; 6, 15 min; 7, 45 min; 8, 150 min

Sample

Commercial PP was extracted with boiling *n*-heptane. Relative molecular mass ($M_w = 1.93 \times 10^5$) was calculated from $[\eta] = 1.86$ (at 135 °C, decalin). PP films with 0.1 mm thickness were annealed at 163 °C for various periods of time and quenched in dry-ice-ethanol.

Measurements

Perkin-Elmer DSC 1; sample mass 10 mg; heating rate 5 °C min⁻¹.

Results

The low-temperature side peak is attributed to melting of the crystallites of original film or melting of crystallites formed during the cooling process. The high-temperature side peak is attributed to melting of crystallites formed by annealing. The equilibrium melting temperature is 186.5 °C.

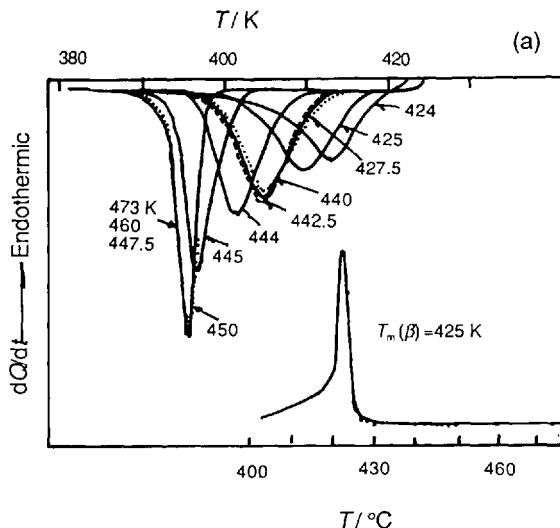


Figure 7.9 (continued)

Sample

Polypropylene with nucleating agent.

Measurements

Perkin-Elmer DSC 2. The original samples were first fused at 473 K for 5 min to erase the effect of thermal and mechanical history, followed by complete crystallization under isothermal conditions at 401 K for 30 min. The samples were then fused again by heating them to different temperatures (T_i). Finally, the crystallization curves were recorded by cooling the samples to 383 K at a rate of 10 K min⁻¹.

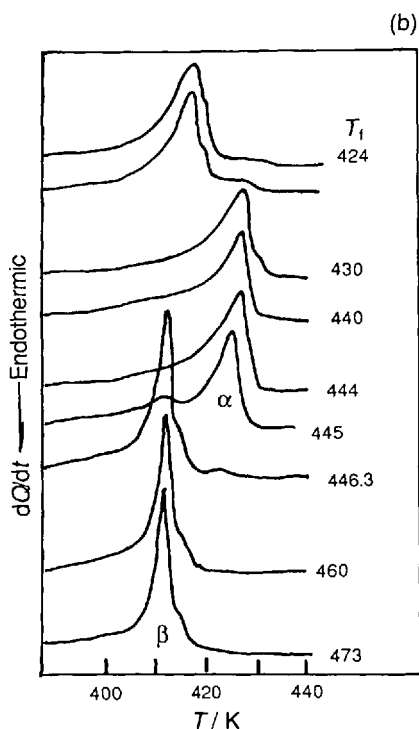


Figure 7.9 Crystallization and melting DSC curves of polypropylene. (a) Cooling curves from different final temperatures T_f [7] (reference melting curve of initial sample). (b) Heating curves of (a)

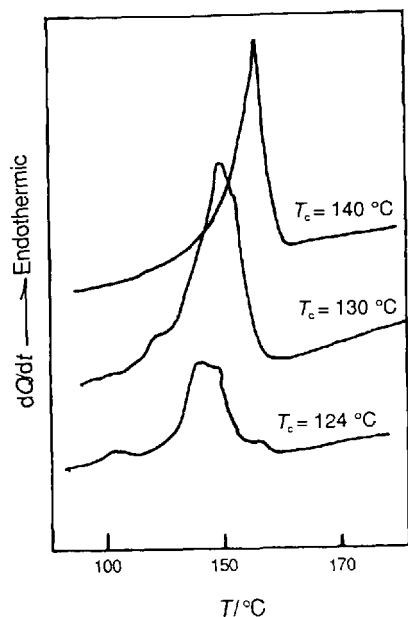


Figure 7.10 Melting DSC curves of polypropylene grafted anhydride samples crystallized at various temperatures [8]. I, 125 °C; II, 130 °C; III, 140 °C

Results

The melting DSC curves reflected the effect of the final fusion temperature on the polymorphic composition (β -, α -crystal forms) of the sample.

Samples

Polypropylene grafted maleic anhydride was prepared as reported [8]. Grafting ratio = mass fraction 10.2% (estimated by FTIR); MFR = 6 g/10 min (ASTM D 1238).

Measurements

Perkin-Elmer DSC 7; sample mass *ca* 0.5 mg; heating rate 20 °C min⁻¹; N₂ atmosphere.

Results

The melting temperature of grafted PP crystal decreased with decreasing crystallization temperature.

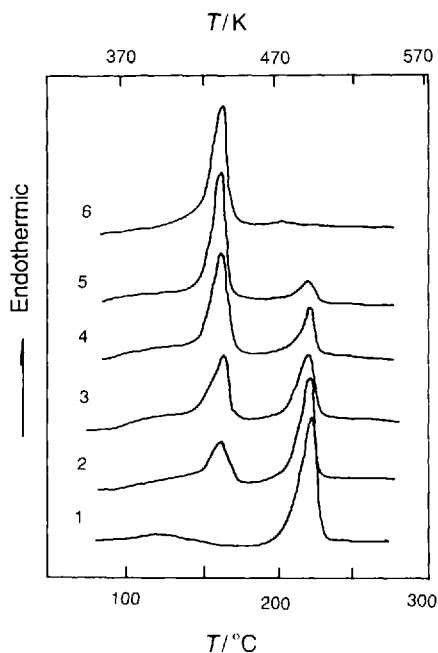


Figure 7.11 DSC curves of undrawn polypropylene (PP)-polyamide 6 (PA6) blend fibres [9]. 1, PA6. PP:PA6:compatibilizer mass ratio 2, 20:80:10; 3, 40:60:10; 4, 60:40:10; 5, 80:20:10; 6, PP

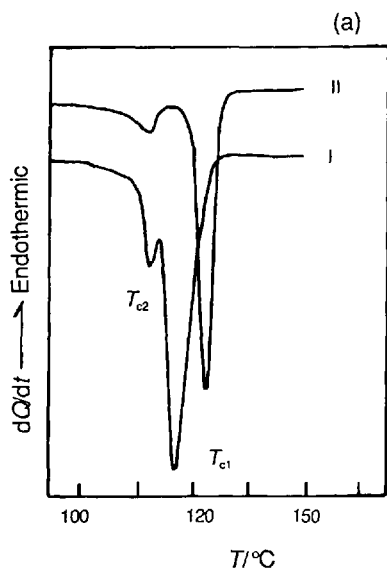


Figure 7.12 Continued

Samples

PP: MFR = 2.7 g/10 min; $M_w = 3.30 \times 10^5$; $M_w/M_n = 5.5-6.5$. PA6: MFR = 3.0 g/10 min; $M_w = 7.10 \times 10^4$; $M_w/M_n = 5.5-6.5$. PP and PA6 were mixed by adding a compatibilizer (maleic anhydride modified PP) using a biaxial extruder at 260 °C, flow rate 150 g min⁻¹.

Measurements

Seiko DSC 200, heating rate 10 °C min⁻¹; sample mass ca 2 mg; N₂ atmosphere.

Results

Two peaks corresponding to each component were observed.

Samples

PP 1330 was obtained from Beijing Yanshan Petrochemical (China); MFR = 1.5 g/10 min; density = 0.905 g cm⁻³. PP 1330 and wollastonite were mixed using a Brabender at 180 °C.

Measurements

Perkin Elmer DSC 7; sample mass 8–12 mg; cooling rate 10 °C min⁻¹.

Results

Two exothermic peaks, T_{c1} and T_{c2} are attributed to the crystallization of polyethylene and polypropylene sequences. The high-temperature crystallization peak shifts to the high-temperature side when wollastonite is added to PP 1330. Sample I shows two melting peaks, T_{m1} and T_{m3} .

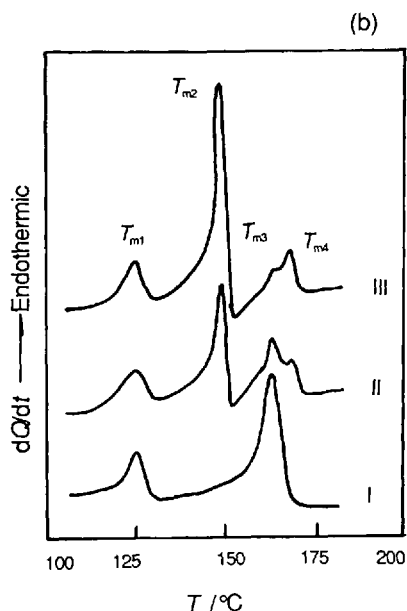


Figure 7.12 (a) Cooling and (b) heating DSC curves of polypropylene 1330 (PP) and PP-wollastonite composites [10]. I, PP 1330 (PP containing 22% mass fraction of ethylene); II, volume ratio of PP 1330 to wollastonite = 96.8 : 3.2; III, 91.2 : 8.8

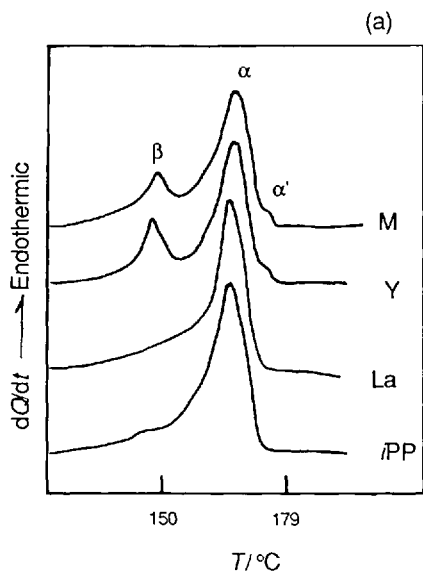


Figure 7.13 DSC curves of isotactic polypropylene (*i*PP) filled with La_2O_3 (L), Y_2O_3 (Y) and mixed rare earth oxide (M) [11]. (a) Heating curves

(continued)

attributed to the melting of crystallites of polyethylene and polypropylene sequences. Two new peaks, T_{m2} and T_{m4} , observed with samples II and II correspond to the fusion of α' - and β -forms of PP.

Samples

*i*PP 1300 was obtained from Yanshan Petrochemical (Beijing, China). *i*PP and each of the three rare earth oxides were mixed using a Brabender at 190 °C. The original *i*PP was prepared following the same procedure.

Measurements

Perkin-Elmer DSC 7; heating rate 10 °C min⁻¹; N₂ atmosphere.

Results

Three crystal forms (β , α and α') are observed. The amount of β -form crystals in *i*PP and La is small.

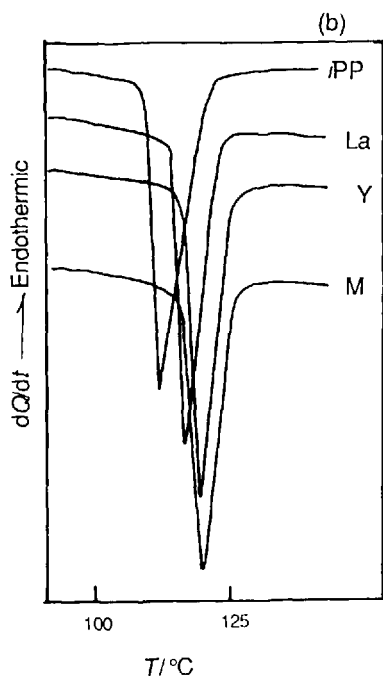


Figure 7.13 DSC curves of isotactic polypropylene (iPP) filled with La_2O_3 (L), Y_2O_3 (Y) and mixed rare earth oxide (M) [11]. (b) Cooling curves

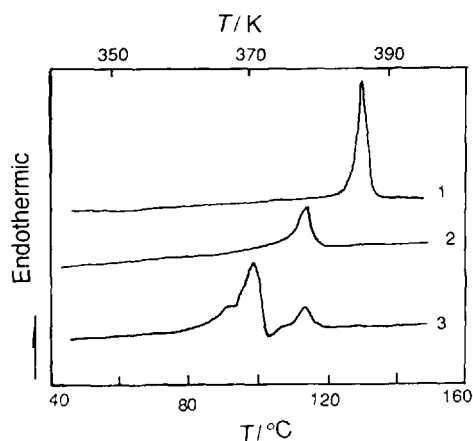


Figure 7.14 Melting DSC curves of isotactic poly(butene-1) (iPB-1) having various crystalline forms [12, 13]. 1, Sample cast from xylene; 2, melt crystallized sample; 3, sample held for 24 h after cooling from the melt to room temperature

Sample

iPB - 1; $M_w = 7800$.

Measurements

Rigaku 8230D; heating rate 6°C min^{-1} .

Results

Three different crystalline forms were observed. Sample 1, crystalline form I; sample 2, crystalline form II; sample 3, crystalline form III.

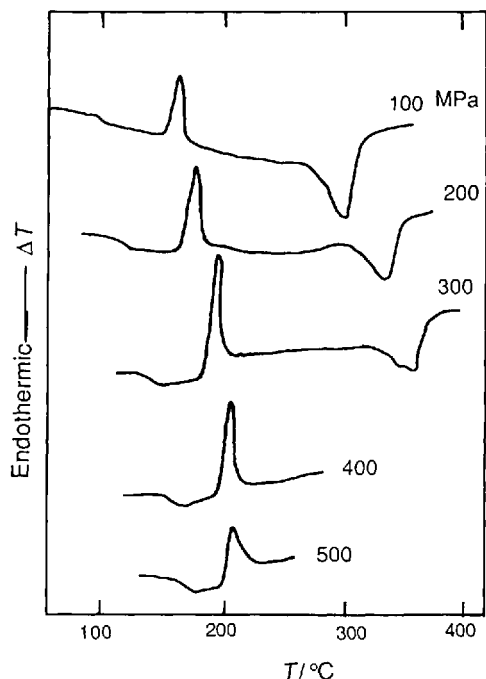


Figure 7.15 High-pressure DTA curves of poly(ethylene terephthalate)(PET) [14]

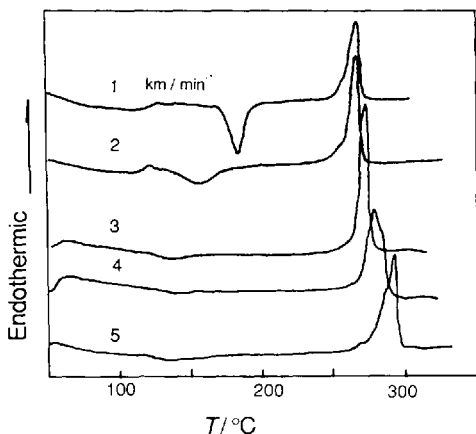


Figure 7.16 DSC curves of as-spun yarn of poly(ethylene 2,6-naphthalenedicarboxylate) (PEN) [16]. Numerals indicate the spinning speed in km min^{-1}

Sample

Teijin Tetron PET ($M_v = 40\,000$) pellets.

Measurements

Custom high-pressure DTA was used [15]. Sample mass 8–10 mg; heating rate $10\text{ }^\circ\text{C min}^{-1}$.

Results

Glass transition, cold crystallization and melting temperatures increased with increasing pressure. In the high-pressure region, melting was not observed owing to limitations of the laboratory made apparatus.

Sample

A Teijin PEN pellet was used. Spinning conditions were as follows: melting temperature, $335\text{ }^\circ\text{C}$; number of nozzle holes, 24; diameter of nozzle, 0.4 mm; flow-rate, 41 g min^{-1} . The intrinsic viscosity $[\eta]$ after spinning was 0.6 ($M_n \approx 2.1 \times 10^5$).

Measurements

Rigaku DSC; heating rate $10\text{ }^\circ\text{C min}^{-1}$; N_2 atmosphere.

Results

The cold crystallization temperature shifts to the low-temperature side with increasing spinning speed. In contrast, the melting peak temperature shifts to the high-temperature side with increasing spinning speed.

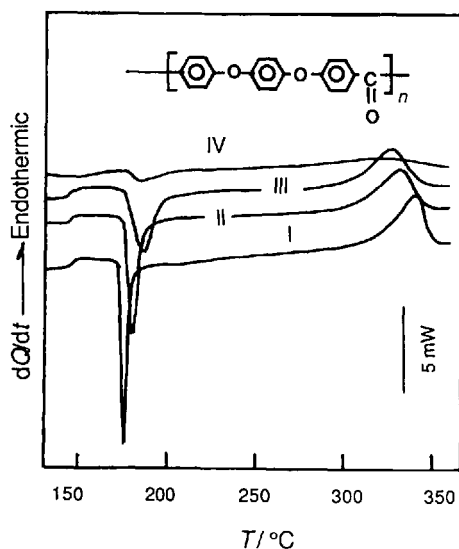


Figure 7.17 DSC curves for poly(ether ether ketone) (PEEK) samples annealed at 400 °C for various times [17]. I, 5 min in N₂; II, 120 min in N₂; III, 30 min in air; IV, 120 min in air

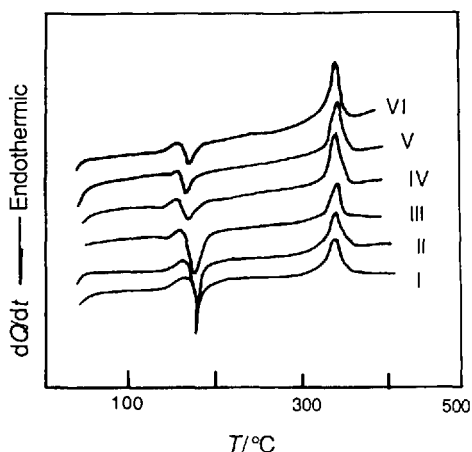


Figure 7.18 DSC curves of poly(ether ether ketone) (PEEK) stretched fibres with various draw ratios [18]

Sample

PEEK (ICI Victrex PEEK 450G; crystallinity 27%). Samples were quenched in liquid N₂.

Measurements

Du Pont Model 1090 thermal analyzer; sample mass 7 ± 0.001 mg; Al vessel; heating rate 10 °C min⁻¹; atmosphere air or nitrogen; flow-rate 50 ml min⁻¹.

Results

T_g 145 °C, exothermic peak of crystallization 175 °C, endothermic peak of melting of crystalline PEEK 340 °C. The crystallizable part decreases with increasing hold time.

Sample

PEEK (ICI Victrex PEEK 450G) (the structure is shown in Figure 7.17). Draw ratio: I, 10.6; II, 32.6; III, 57.7; IV, 520; V, 760; VI, 1140.

Measurements

Du Pont Model 9900 differential scanning calorimeter; heating rate 20 °C min⁻¹.

Results

At low draw ratios, the fibers are largely amorphous and exhibit a significant crystallization exotherm at the cold crystallization temperature.

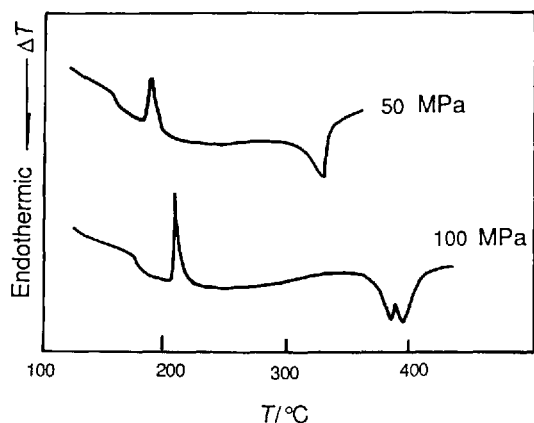


Figure 7.19 DTA curves for quenched PEEK sample under different pressures [14]

Sample

Poly(ether ether ketone) (ICI Victrex PEEK 450G), (the structure is shown in Figure 7.17). The PEEK samples were prepared by heating the pellets at *ca* 400 °C in an evacuated oven and then quenching them in liquid nitrogen (*ca* 5 min). The samples were dried at room temperature.

Measurements

Custom DTA [18]. Sample mass 8–10 mg; heating rate 10 °C min⁻¹.

Results

The glass transition temperatures, the subsequent cold crystallization temperatures and melting temperatures increase with increasing pressure. Melting under 100 MPa pressure produced double endothermic peaks. The double peaks suggest melting of the PEEK crystal formed during the cold crystallization and fusion of the reorganized crystal at high temperature.

Sample

PPS (Ryton GR-02) was obtained from Phillips Petroleum. Samples were dried in a vacuum oven at 70 °C for 20 h and spun from a nozzle, the temperature of which was controlled at 300 °C, into air. Fiber of 158 denier was obtained at a winding rate of 500 m min⁻¹.

Measurements

Perkin-Elmer DSC II; sample mass 3–6 mg; scanning rate 20 °C min⁻¹.

Results

PPS fibre was amorphous immediately after spinning. Enthalpy relaxation occurs easily.

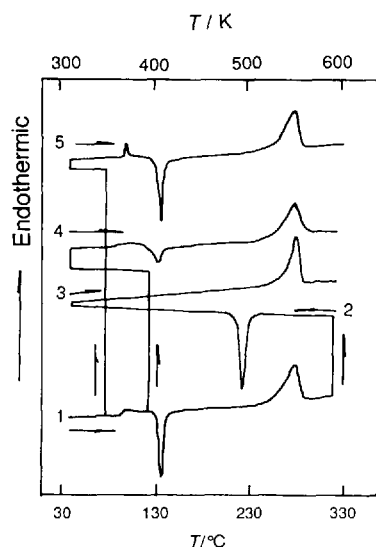


Figure 7.20 DSC curves for poly(*p*-phenylene sulfide) (PPS) fibers [19]. 1, Heating curve of as-spun fiber; 2, cooling curve; 3, heating curve of the sample cooled from the molten state at 20 °C min⁻¹; 4, heating curve of the sample quenched from a temperature between the glass transition temperature and the cold crystallization temperature; 5, heating curve of the sample cooled from the glassy state

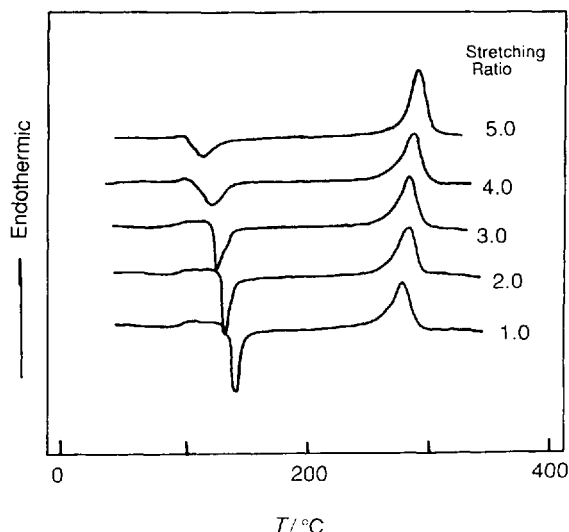


Figure 7.21 DSC curves for quenched and stretched poly(phenylene sulfide) (PPS) films [20]. Numerals indicate the stretching ratio

Sample

Toray; film thickness 110 μm . The stretching of films was carried out manually in a silicone oil bath at 90 $^{\circ}\text{C}$.

Measurements

Shimadzu TA-50WS DSC; heating rate 20 $^{\circ}\text{C min}^{-1}$; sample mass $5.00 \pm 0.003 \text{ mg}$.

Results

Cold crystallization shifts to the low-temperature side and glass transition is hardly observed with increasing stretching ratio. The mobile amorphous phase decreases as the stretching ratio increases.

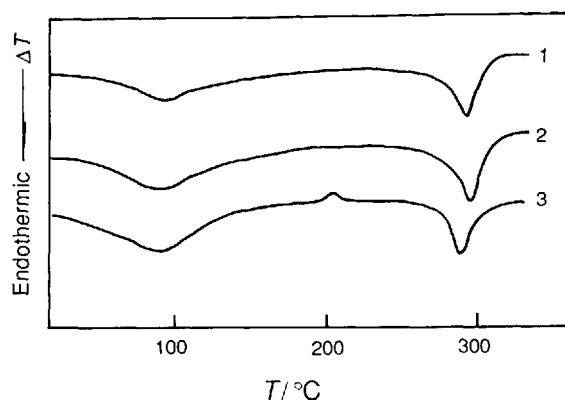


Figure 7.22 DTA curves for silk fibroin films. 1, α -form; 2, β -form; 3, random coil

Samples

Silk fibroin solution was obtained from the posterior part of the middle division of the silk gland in full-grown larvae (1 day before spinning) of *Bombyx mori*. The sericin was removed by washing with deionized water [21–23].

Measurements

Rigaku DTA; heating rate 10 $^{\circ}\text{C min}^{-1}$; reference material α -alumina.

Results

The broad endotherm at ca 100 $^{\circ}\text{C}$ is attributed to water vaporization. The exotherm observed at 218 $^{\circ}\text{C}$ on curve 3 is attributed to the transformation from random coil chains to β -form crystal. The endotherm at ca 290–346 $^{\circ}\text{C}$ is due to thermal decomposition.

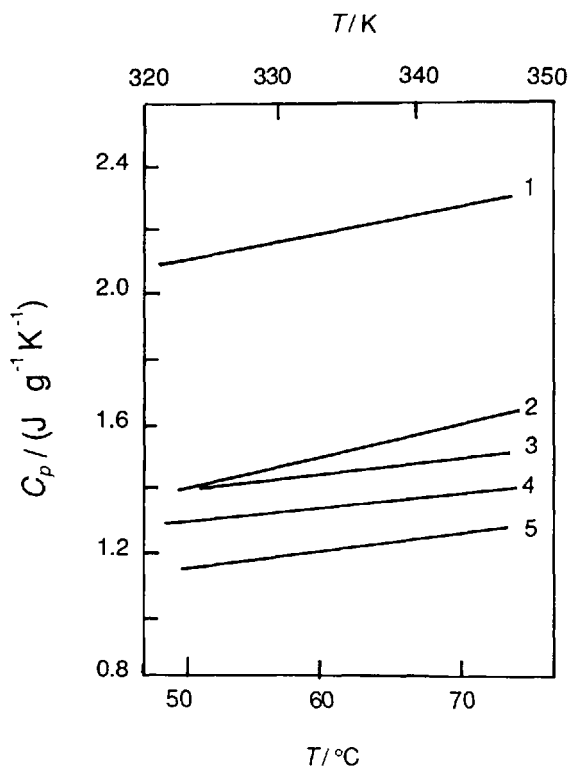


Figure 7.23 Heat capacities of cellulose and related compounds [24]. 1, Amorphous D-glucose; 2, amorphous cellulose; 3, α -D-glucose; 4, cellobiose; 5, cellulose I

Samples

Amorphous D-glucose was prepared by quenching from molten D-glucose and amorphous cellulose was prepared by saponification of cellulose triacetate film using 1% sodium ethylate dissolved in anhydrous ethanol. α -D-glucose and cellobiose were obtained commercially. Cellulose I is natural cellulose.

Measurements

Perkin-Elmer DSC 2; heating rate $10^{\circ}\text{C min}^{-1}$; sample mass 3 mg, atmosphere N_2 .

Results

No transition was observed. Linear relationships between heat capacity and crystallinity were obtained.

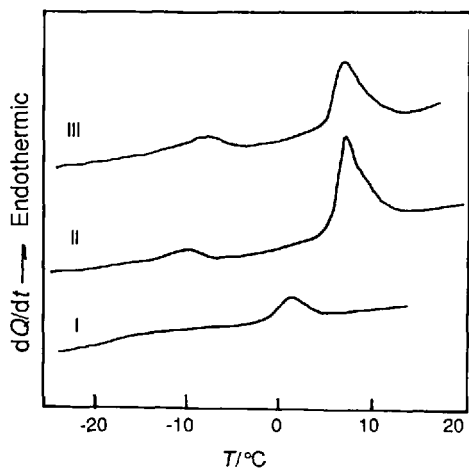


Figure 7.24 DSC curves for polystyrene (PS)-carbon disulfide (CS_2) gels at various gelation times [25]. I, 10 min; II, 20; III, 30

Sample

Atactic polystyrene from Wako Pure Chemical Industries, $M_w = 2.1 \times 10^5$; $M_w/M_n = 1.7$; gelation temperature -10°C ; mass concentration of polymer 30 g l^{-1} .

Measurements

Seiko DSC 560 and DSC 100; Heating rate $20^{\circ}\text{C min}^{-1}$.

Results

The low-temperature side peak is attributed to the gel-sol transition and the high-temperature side peak to melting of coaggregated crystallites in the sol.

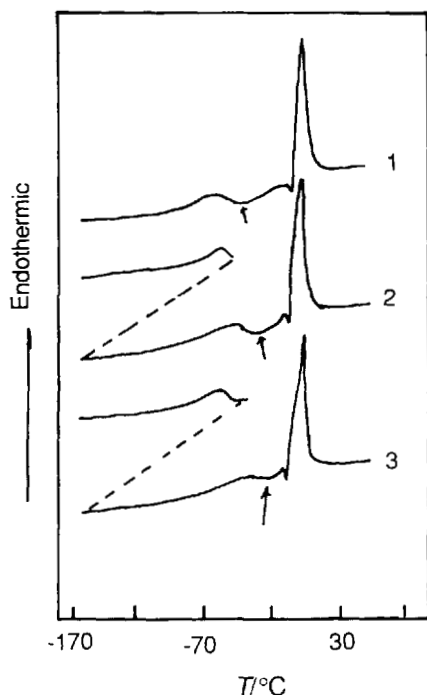


Figure 7.25 Heating DSC curves for hyaluronic acid (HA) hydrogel with different thermal histories [26, 27]. Water content (W_c) 0.86 g g^{-1} . $W_c = (\text{grams of water})/(\text{gram of dry sample})$. 1, Original sample cooled at $10^\circ\text{C min}^{-1}$; 2, heated to -60°C and immediately cooled; 3, heated to -50°C and immediately cooled. Dashed line, quenching

Samples

HA obtained from Wako Pure Chemical industries; 2.2 Na per repeating unit.

Measurements

A Seiko Denshi DSC 200 was connected to an SSC 5000TA system; sample mass (water + HA) $\approx 10 \text{ mg}$; scanning rate $10^\circ\text{C min}^{-1}$.

Results

The cold crystallization peak decreased on heat treatment. By changing the thermal history, HA gels with various states of water can be prepared.

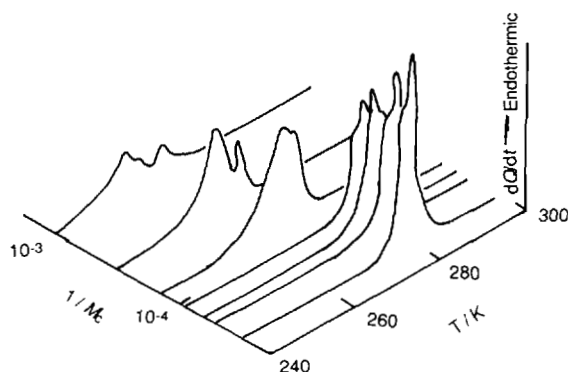


Figure 7.26 Melting DSC curves for water in poly(vinyl alcohol) (PVA) gel having various cross-linking densities ($1/M_c$) [28]

Sample

PVA (degree of polymerization 2000) powder was dissolved in distilled water (mass fraction 7%) after dialysis. The PVA solution was irradiated with ^{60}Co γ -rays at a dose rate of $0.170\text{--}1.071 \text{ Mrad h}^{-1}$ for 7–18 h. The cross-linking density was calculated using Flory's equation.

Measurements

Perkin-Elmer DSC-II; sample mass 3–4 mg; heating rate $10^\circ\text{C min}^{-1}$.

Results

The melting peak shifts to the low temperature side with increasing cross-linking density.

Sample

Viscose rayon.

Measurements

Perkin-Elmer 2; heating rate $10^{\circ}\text{C min}^{-1}$; sample mass 5 mg; sealed-type aluminum sample vessel.

Results

Non-freezing water is observed for the sample with $W_c = 0.21 \text{ g g}^{-1}$. On the crystallization curves, freezing bound water is observed at a temperature lower than the melting temperature of free water (Nos 2 and 3). The melting peak of freezing bound water merges into that of free water (Nos 6 and 7).

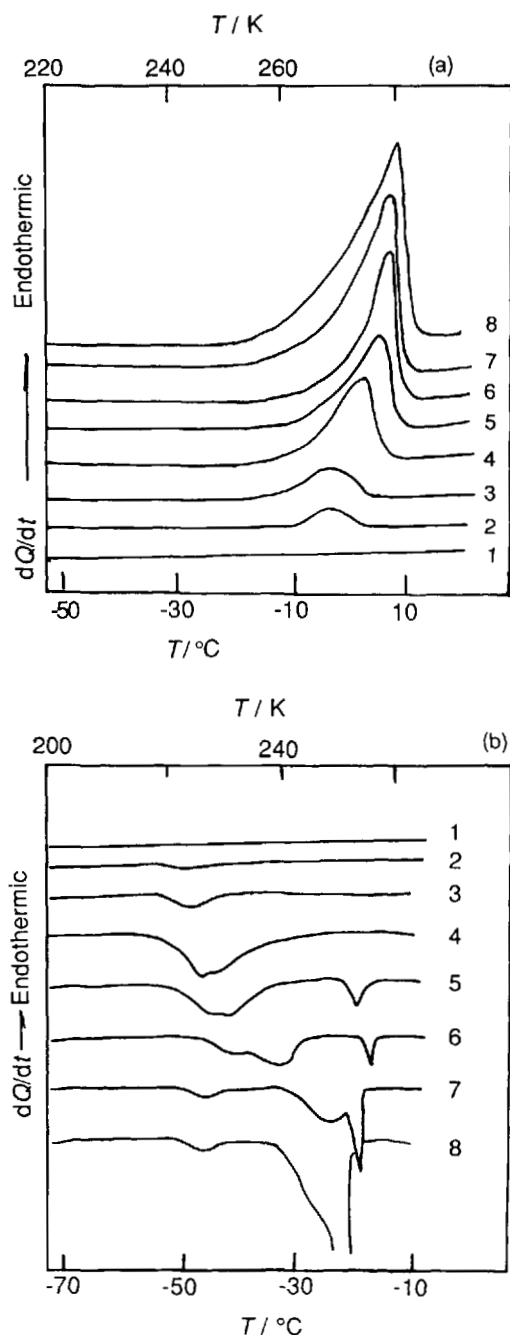


Figure 7.27 DSC curves for various amounts of water adsorbed on regenerated cellulose [29, 30]. (a) Heating curve; (b) cooling curve. Numerals indicate the water content (W_c); $W_c = (\text{grams of water})/(\text{gram of dry sample})$: 1, 0.21; 2, 0.27; 3, 0.38; 4, 0.42; 5, 0.45; 6, 0.46; 7, 0.51; 8, 0.60 g g^{-1}

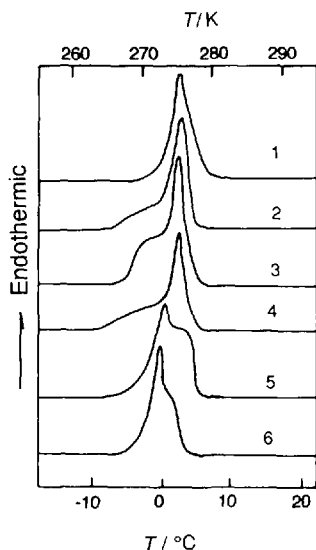


Figure 7.28 Melting DSC curves for water trapped in various kinds of cellulose [29]. Water content (grams of water/gram of sample) = 1.0 g g^{-1} . 1, Kapok; 2, linen; 3, wood cellulose; 4, jute; 5, rayon; 6, polynosic; 7, cotton

Sample

Samples were purified by extracting contaminants with toluene, carbon tetrachloride and *n*-hexane successively using a Soxhlet extractor.

Measurements

Perkin-Elmer 1B DSC; heating rate 8°C min^{-1} ; sample mass 5 mg; sealed-type aluminum sample vessel.

Results

Results are given in Table 7.2.

Table 7.2

Sample	Degree of crystallinity/% (from X-ray analysis)	Bound water content/ g g^{-1}	M_{ba}^a
Linen	69	0.11	3.3
Cotton	54	0.16	3.2
Cotton lint	52	0.30	3.8
Wood cellulose	44	0.23	3.6
Jute	36	0.24	3.4
Kapok	33	0.23	3.1
Polynosic rayon	46	0.21	3.5
Cupra rayon	43	0.22	3.5
Viscose rayon	42	0.23	3.7

^a Number of bound water molecules per OH group in the amorphous region of cellulose.

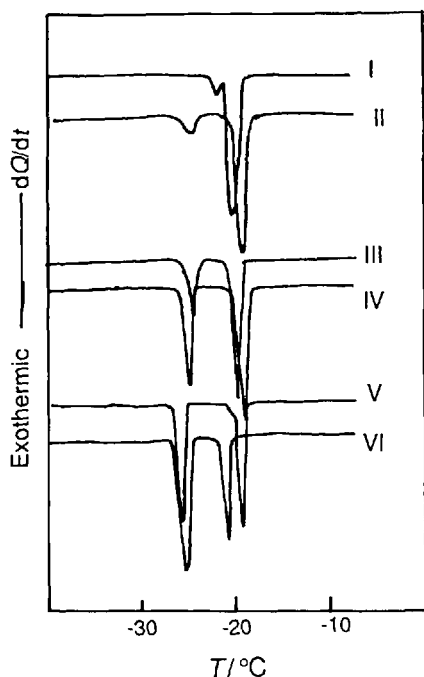


Figure 7.29 Cooling DSC curves for xanthan gum-water systems (mass concentration 2 g l^{-1}) as a function of annealing time at 365 K [31]. I, 5; II, 10; III, 15; IV, 30; V, 60; VI, 90 min

Sample

Mitsubishi Chemical. Hermitically sealed solutions were placed in an oven pre-heated at 313 K for 24 h.

Measurements

Perkin-Elmer 2C DSC; heating rate $10^\circ\text{C min}^{-1}$; sample mass 4–5 mg.

Results

Structural change of water was observed with increasing number of junction zones of polysaccharide hydrogel.

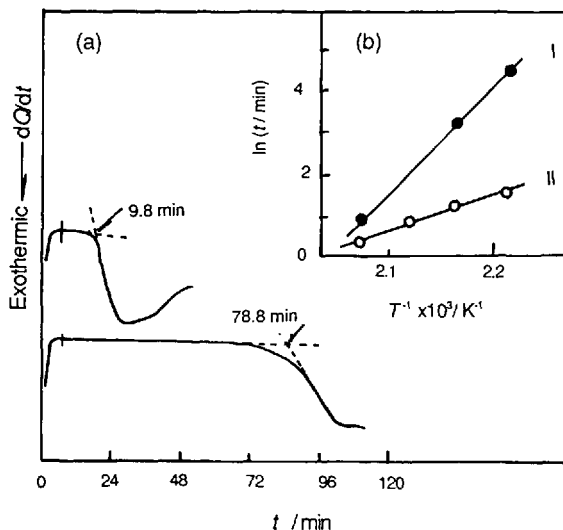


Figure 7.30 Induction time of oxidation determined by (a) DSC and (b) Arrhenius plot for polyethylene [32]

Sample

Polyethylene.

Measurements

Sample mass 5.050 mg; Al and Cu crucibles; heating rate $99.9^\circ\text{C min}^{-1}$; holding temperature 190°C , atmosphere N_2/O_2 ; gas flow-rate 50 ml min^{-1} . The sample was heated rapidly to 190°C and maintained there, then the atmosphere was changed from nitrogen to oxygen.

Results

The DSC curve shows an exothermic peak due to absorption of oxygen after a certain induction time. The induction time obviously decreases for the Cu crucible, showing distinct catalytic oxidation. From Arrhenius plots constructed from data for induction times at different temperatures. The activation energies of oxidation for polyethylene were obtained as $110.9 \text{ kJ mol}^{-1}$ for the Al crucible and 37.2 kJ mol^{-1} for the Cu crucible.

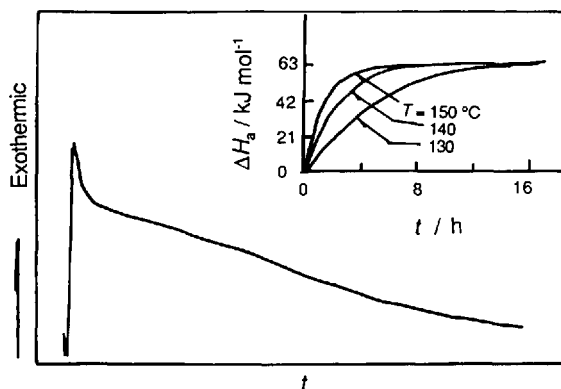


Figure 7.31 DSC curve for polymerization of styrene-butadiene system [3]

Sample

Styrene +7% butadiene.

Measurements

Setaram Model 111 DSC; sample mass 106.6 mg; sensitivity 100 μV full-scale; sealed-type Al crucible. The crucible with the sample and an identical empty crucible were introduced directly into the DSC at 130, 140 or 150 $^{\circ}\text{C}$.

Results

The polymerization proceeds during the first 10 min. The rate of polymerization increases with increase in temperature; the duration of polymerization is 20 h at 130 $^{\circ}\text{C}$, 14 h at 140 $^{\circ}\text{C}$ and 9 h at 150 $^{\circ}\text{C}$. The heat of polymerization for styrene is 62.8 kJ mol^{-1} .

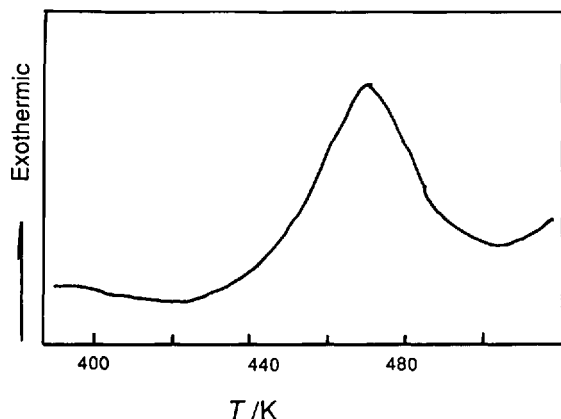


Figure 7.32 Determination of vulcanization enthalpy of polyisoprene-sulfur mixture [3]

Sample

Fine powdered rubber +2% sulfur.

Measurements

Setaram Model 111 DSC; sample mass 94.2 mg; closed stainless-steel crucible; atmosphere Ar; heating rate 5 $^{\circ}\text{C min}^{-1}$; sensitivity 100 μV full-scale.

Results

The vulcanization reaction occurs from 145 to 240 $^{\circ}\text{C}$, with an exothermic effect. The reaction heat of the sample is 13.8 J g^{-1} .

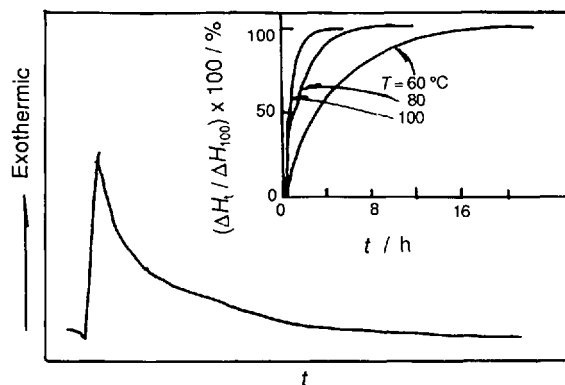


Figure 7.33 Determination of heat of polymerization of polyurethane (polyol + polyisocyanate) [3]

Samples

Polyisocyanate, polyol.

Measurements

Setaram C80 heat flow calorimeter; sample mass, polyisocyanate 264 mg, polyol 292 mg; crucible, mixing cell with metallic membrane; isothermal at 80°C , sensitivity $1\mu\text{V}$. Initially, the two reagents are isolated by a membrane and stabilized in the calorimeter at 80°C . The membrane is cut, and mixing is effected by manual rotation of the stirrer.

Results

After mixing the two components, polymerization begins rapidly. The duration of the reaction is dependent of temperature: 20 h at 60°C , 10 h at 80°C and 5 h at 100°C . The heat of polymerization of polyisocyanate is 334.7 J g^{-1} . The curve obtained permits the relationship between the conversion degree of monomers to polymers (%) and time to be established.

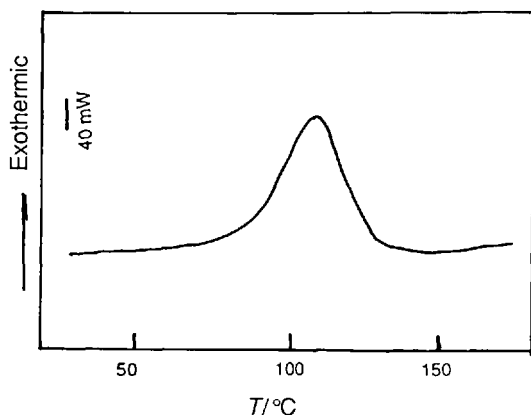


Figure 7.34 Determination of heat of reaction of epoxy resin curing [33]

Samples

Epoxy resin + hardener.

Measurements

Setaram C80 calorimeter; sample mass 3.895 g (use larger amounts of samples to ensure good homogeneity between resin and hardener); standard vessel (a glass tube is introduced into the vessel in order to make the cleaning of the vessel easier); heating rate $0.5^\circ\text{C min}^{-1}$.

Results

The reticulation of the epoxy resin under study occurs between 50 and 150°C . The heat of the curing reaction obtained by integration of the exothermic effect is 142.7 J g^{-1} .

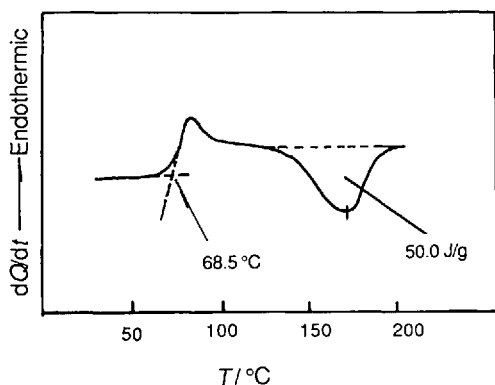


Figure 7.35 DSC determination of heat of polycondensation of phenolic resin [32]

Sample

Phenolic resin.

Measurements

Sample 3.440 mg; heating rate $10^\circ\text{C min}^{-1}$; measurement temperature range from ambient to 250°C . For the determination of the heat of polycondensation it is necessary to use a hermetically sealed sample vessel, preventing vaporization of water.

Results

In the temperature range $104.6\text{--}199.3^\circ\text{C}$ the exothermal effect of polycondensation was observed to be 50.047 J g^{-1} ; peak temperature, 168.5°C .

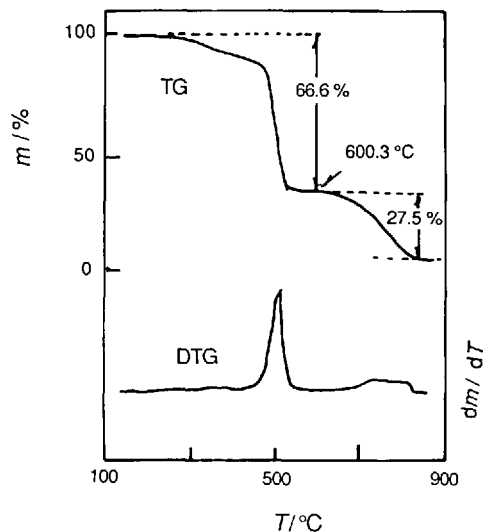


Figure 7.36 TG curve for butadiene-styrene rubber containing carbon black [32]

Sample

Butadiene-styrene rubber.

Measurements

Sample mass 16.120 mg; heating rate $20^\circ\text{C min}^{-1}$; measurement temperature range from ambient to 900°C .

Results

After thermal decomposition of rubber under an N_2 atmosphere, the atmosphere was changed from N_2 to O_2 at 600°C and the carbon black content was determined to be 27.5% from its combustion mass loss.

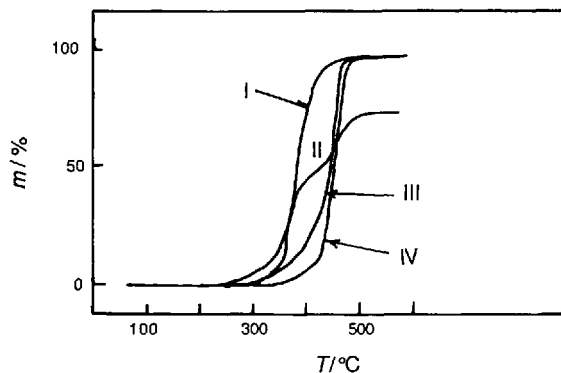


Figure 7.37 Determination of thermal stability of various elastomers by TG [3]

Samples

I, Natural rubber; II, polychloroprene (neoprene); III, butyl rubber; IV, *cis*-polybutadiene.

Measurements

Setaram G70 thermoanalyzer; sample mass 24.7 mg; crucible silica; atmosphere He; heating rate 10 °C min⁻¹; sensitivity 25 mg (full-scale).

Results

cis-Polybutadiene is the most resistant to temperature (beginning to decompose at 300 °C), followed by butyl rubber (290 °C), natural rubber (215 °C) and neoprene (207 °C). Neoprene has a lower rate of decomposition than natural rubber.

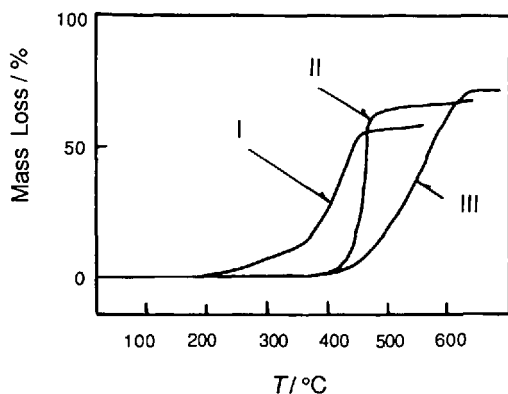


Figure 7.38 Determination of thermal stability of elastomers by TG [3]

Samples

I, Nitrile elastomer (Perbunan); II, fluorinated elastomer (Viton); III, silicone elastomer.

Measurements

Setaram G70 thermoanalyzer; sample mass 24.7 mg; crucible silica; sensitivity 25 mg (full-scale).

Results

Perbunan is the least stable of the three elastomers, beginning to decompose at 200 °C (mass loss 54%). Viton and silicone elastomers start to decompose at similar temperatures, 375 and 345 °C, respectively. However, the rate of decomposition is much slower for the silicone elastomer than for Viton.

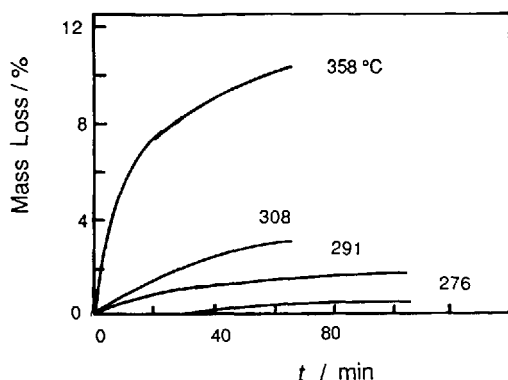


Figure 7.39 Thermal stability of polybutadiene determined by TG [3]

Sample

cis-Polybutadiene.

Measurements

Setaram G70 thermoanalyzer; sample mass 24.5 mg; crucible silica; atmosphere He; isothermal at 276, 291, 308 and 358 °C; sensitivity 25 mg (full-scale).

Results

The mass-loss rate increases considerably with increase in temperature. The mass losses at different temperatures at 20 and 60 min are given in Table 7.3.

Table 7.3

Temperature/°C	Mass loss/%	
	20 min	60 min
276	—	0.38
291	0.85	1.40
308	1.38	2.85
358	7.15	9.76

The experimental data allow the calculation of the kinetics of decomposition and extrapolation for longer periods.

Samples

Cotton, flame-retardant cotton.

Measurements

Sample mass cotton 2.500 mg and flame-retardant cotton 2.600 mg; heating rate 10 °C min⁻¹; flow-rate of air 30 ml min⁻¹; measurement temperature range from ambient to 500 °C.

Results

The oxidative decomposition was retarded and the residual amount increased during the treatment.

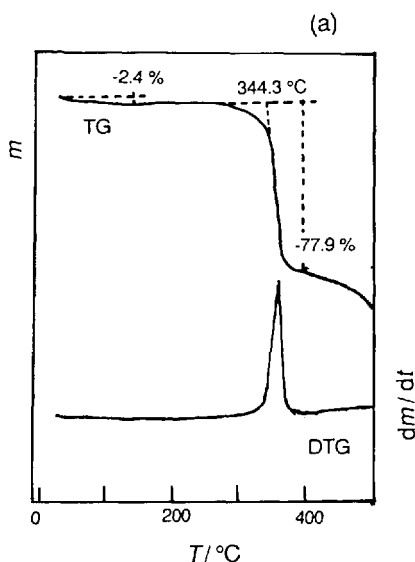


Figure 7.40 (a) TG curves for cotton

(continued)

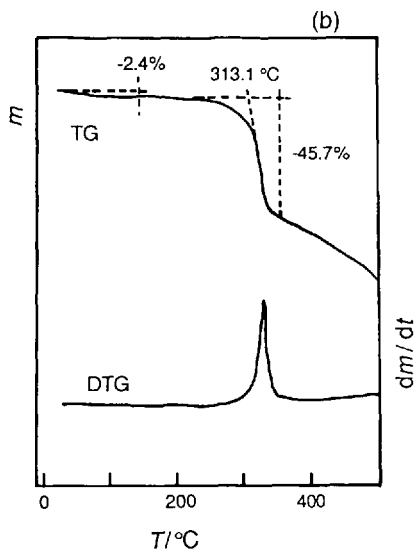


Figure 7.40 (b) TG curves for flame-retardant cotton [32]

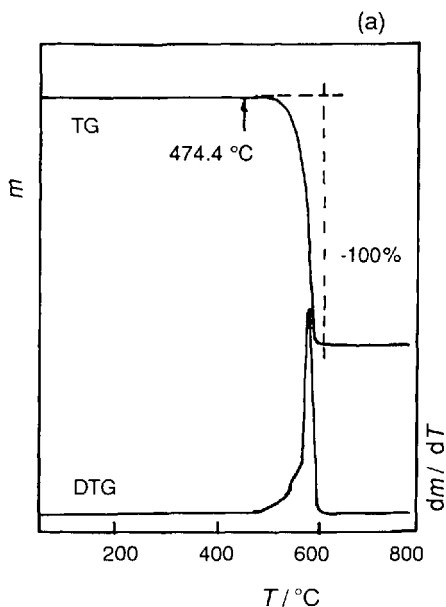


Figure 7.41 (a) TG curves for polytetrafluoroethylene in air

(continued)

Sample

Polytetrafluoroethylene (Teflon).

Measurements

Sample mass (a) 24.470 and (b) 21.260 mg; heating rate $10\text{ }^{\circ}\text{C min}^{-1}$; flow-rate of atmosphere (a) 40 and (b) 30 ml min^{-1} ; measurement temperature range from ambient to $800\text{ }^{\circ}\text{C}$.

Results

For temperatures of thermooxidation, decomposition and thermal decomposition, see Figure 7.41.

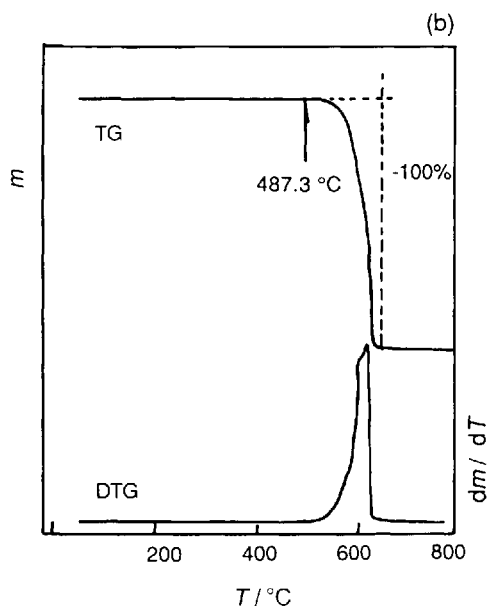


Figure 7.41 (b) TG curves for polytetrafluoroethylene in argon [32]

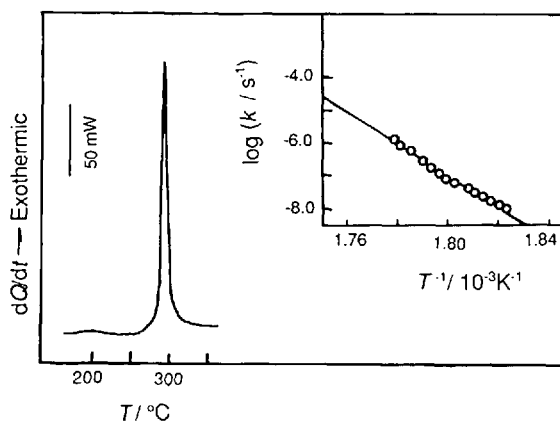


Figure 7.42 Thermal decomposition of polyacrylonitrile [34]

Sample

Polyacrylonitrile.

Measurements

Setaram DSC 111; sample mass 20.47 mg; heating rate 10 K min^{-1} ; atmosphere argon; sealed stainless steel vessel (nickel O-ring).

Results

Polyacrylonitrile decomposition begins at $260 ^\circ\text{C}$ and passes through a maximum $297 ^\circ\text{C}$. From the DSC curve, the kinetic parameters are calculated to be reaction order = 0.9 and $E_a = 410 \text{ kJ mol}^{-1}$.

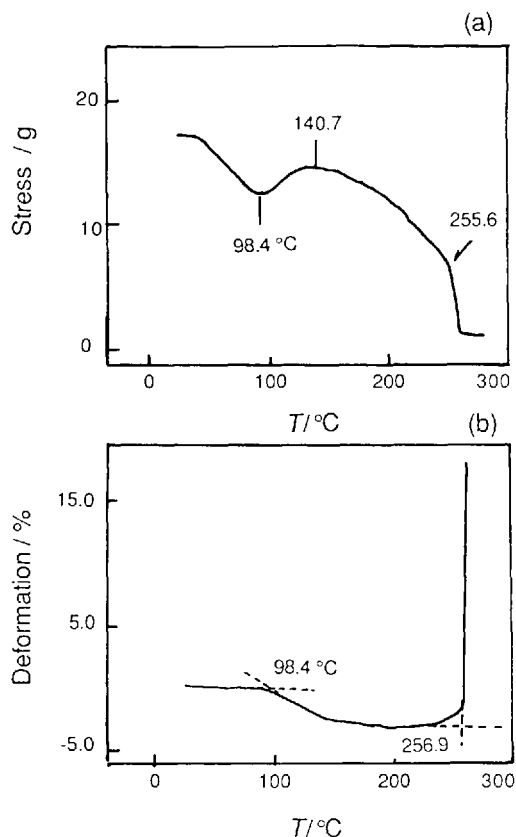


Figure 7.43 TMA curve for poly(ethylene terephthalate) (PET) fiber. (a) Thermal stress curve and (b) thermomechanical curve [32]

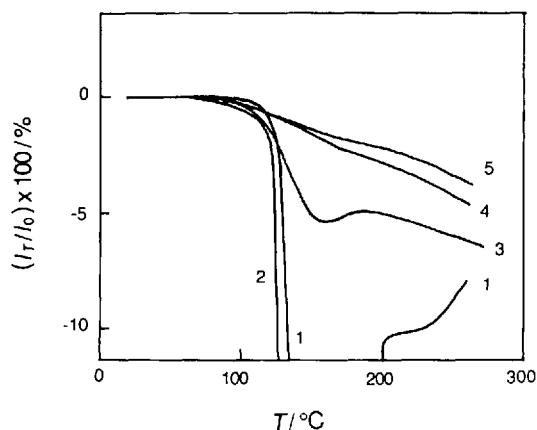


Figure 7.44 TMA curves for poly(ethylene-6-naphthalenedicarboxylate) (PEN) fibers spun at high speed [16]. Numerals on curves are spinning speeds (see the table below)

Sample

Poly(ethylene terephthalate) fiber.

Measurements

Sample size 15.250 mm; heating rate $10^{\circ}\text{C min}^{-1}$; measurement temperature range from ambient to 300°C .

Results

The fiber started to shrink from 98°C , and accordingly the stress increased; it melted at *ca* 257°C .

Sample

A Teijin PEN pellet was used. Spinning conditions were as follows: melting temperature, 335°C ; numbers of nozzle holes, 24; diameter of nozzle, 0.4 mm; flow-rate, 41 g min^{-1} ; spinning speed and drawing conditions as in Table 7.4. The intrinsic viscosity $[\eta]$ after spinning was 0.6 ($M_n \approx 2.1 \times 10^5$).

Measurements

Rigaku thermomechanical analyzer; Heating rate $10^{\circ}\text{C min}^{-1}$; atmosphere N_2 .

Results

Fibers stretched at a high draw ratio shrink at the glass transition temperature.

Table 7.4

Spinning speed/ km min ⁻¹	Draw ratio			Total
	1st step (155 °C)	2nd step (190 °C)	3rd step (220 °C)	
1	3.01			2.95–3.13
2	1.50			1.47–1.64
3	1.10	1.00–1.2	0.98	1.08–1.28
4	1.07			1.05–1.13
5	1.02			1.00–1.04

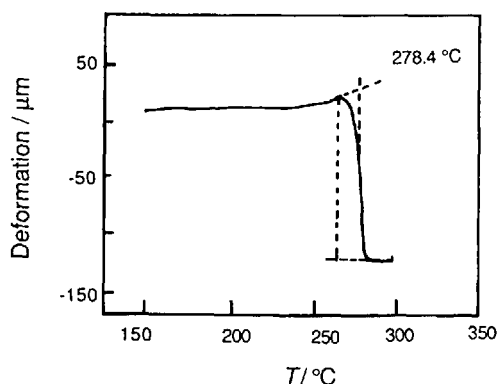


Figure 7.45 TMA curve for poly(phenylene sulfide) [35]

Sample

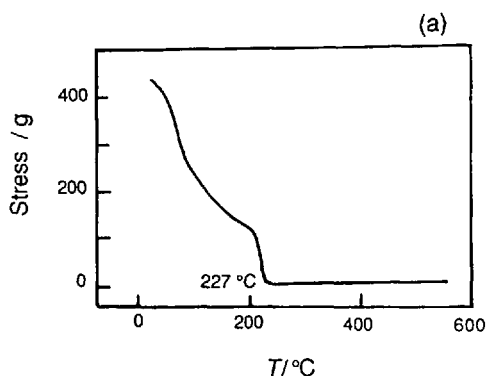
Poly(phenylene sulfide) (PPS).

Measurements

Sample size 0.130 mm; load 50 g; heating rate 5 °C min⁻¹; measurement temperature range from ambient to 300 °C.

Results

For the melting temperature of PPS, see Figure 7.45.

Figure 7.46 (a) TMA curves for a polyimide in nitrogen
(continued)*Sample*

Polyimide.

Measurements

Sample size 15.250 mm; loading model, makes sample elongation 1% at a draw rate of 0.05 mm min⁻¹; heating rate 5 °C min⁻¹; measurement temperature range from ambient to 600 °C.

Results

When the sample was heated at 1% elongation to

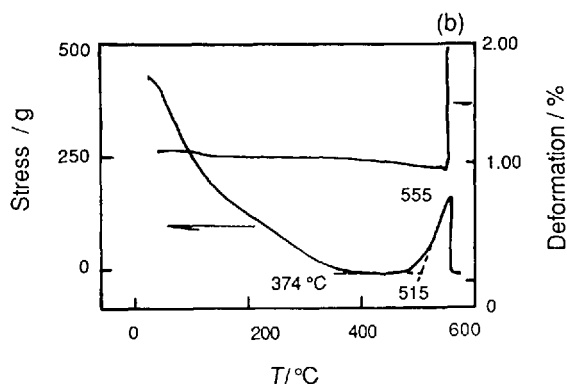


Figure 7.46 (b) TMA curves for a polyimide in air [35]

600 °C in nitrogen, the stress decreased to zero at 227 °C. In air, the stress decreased to 1.08 g at 374 °C, then increased again at 515 °C owing to a cross-linking reaction, and the sample broke at 560 °C.

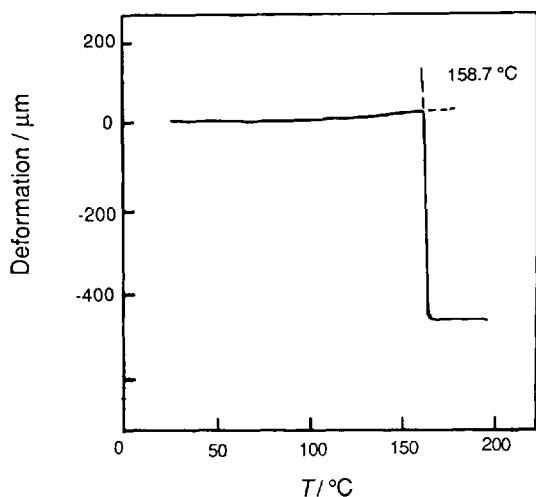


Figure 7.47 TMA curve for polyoxymethylene [35]

Sample

Polyoxymethylene (POM).

Measurements

Sample size 0.468 mm; load 50 g; heating rate 5 °C min⁻¹; measurement temperature range of ambient to 300 °C.

Results

Melting of POM leads to penetration. A needle with a length of 1 mm is suitable only for measurements of samples with thickness <1 mm (for samples with thickness > 1 mm, see the JIS K 7206 determination method for Vicat softening temperature).

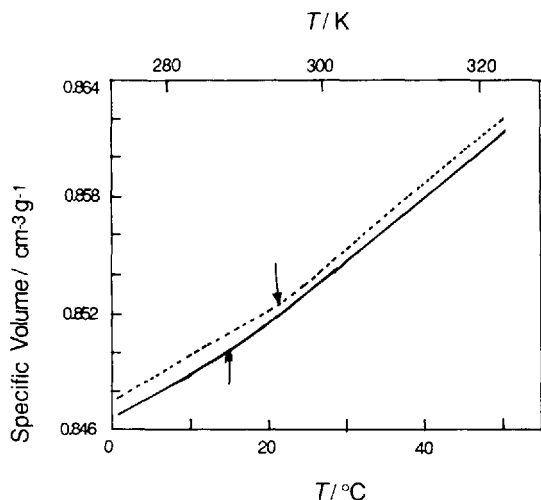


Figure 7.48 Specific volume of water-sorbing cellophane (water content 1.2 g g^{-1}) as a function of temperature measured with a laboratory-assembled capillary-type dilatometer [36]. Solid line, heating; dashed line, cooling

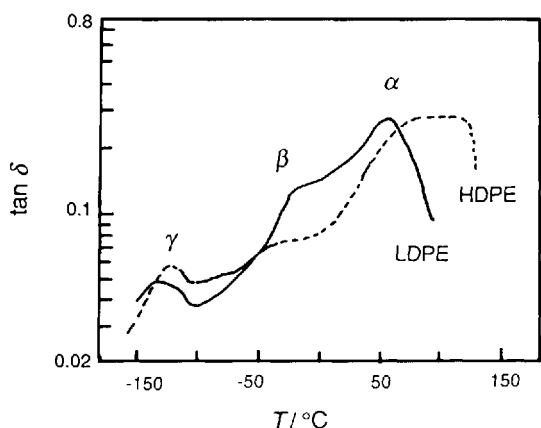


Figure 7.49 Temperature- $\tan \delta$ curve for low-density polyethylene (LDPE) and high-density polyethylene (HDPE) [37]

Sample

Cellophane film with thickness 20 mm, birefringence index $D_n = 8.6 \times 10^{-4}$.

Measurements

Laboratory-assembled capillary-type dilatometer; heating rate $0.5 \text{ }^\circ\text{C min}^{-1}$; silicon oil was used as a filling solvent.

Results

The inflection point observed at 15°C on the heating curve and at 21°C on the cooling curve is attributed to breakage of weak hydrogen bonds.

Samples

LDPE (Mirason 68) and HDPE (HiZex 5000F). Samples were molded at 150°C for LDPE, and 180°C for HDPE and then cooled to ambient temperature.

Measurements

Seiko SDM 5500 rheometer; DMS Model 100 viscoelastometer; sample size LDPE 20.00 mm (length) \times 12.05 mm (width) \times 1.7 mm (thickness), HDPE 20.00 mm (length) \times 6.45 mm (width) \times 2.22 mm (thickness); heating rate 1 K min^{-1} ; atmosphere N_2 ; measurement temperature range for LDPE from -150 to 90°C and for HDPE from -150 to 130°C ; deformation mode bending; measurement frequency 0.5, 1, 2, 5 and 10 Hz (data given here were measured at a frequency of 1 Hz).

Results

Temperatures of $\tan \delta$ peaks and activation energies of the corresponding transitions are given in Table 7.5.

Table 7.5

Loss peak	LDPE		HDPE		Molecular implication
	Temperature/°C	Activation energy/ kJ mol ⁻¹	Peak Temperature/°C	Activation energy/ kJ mol ⁻¹	
α	54	145	102	—	Melting of crystallites
β	-19	—	-32	—	glass transition of amorphous region
γ	-124	69	-121	129	Local relaxation of amorphous region and relaxation of defects in crystals

DSC data (heating rate 10 K min⁻¹) are as follows: LDPE, $T_m = 106.2$ °C and $\Delta H_m = 139.6$ J g⁻¹; HDPE, $T_m = 132.1$ °C and $\Delta H_m = 219.4$ J g⁻¹;

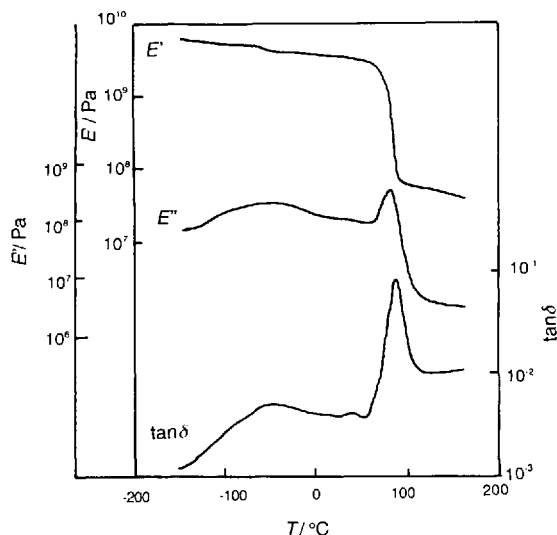


Figure 7.50 DMA curves for poly(vinyl chloride) [38]

Sample

Poly(vinyl chloride). The sample was molded at 190 °C, and then cooled to ambient temperature.

Measurements

Seiko Model 100 DMS rheometer; sample size 20.00 × 12.00 × 1.20 mm; heating rate 2 K min⁻¹; atmosphere N₂; measurement temperature range from -150 to 160 °C; deformation bending; measurement frequency 0.5, 1, 2, 5 and 10 Hz (data given here were measured at a frequency of 1 Hz).

Results

Temperatures of tan δ peaks and activation energies of the corresponding transitions are given in Table 7.6.

Table 7.6

Loss peak	Temperature/°C	E_a / kJ mol ⁻¹	Molecular implication
α	86.5	804	Glass transition
β	-39.0	101	Local mode relaxation

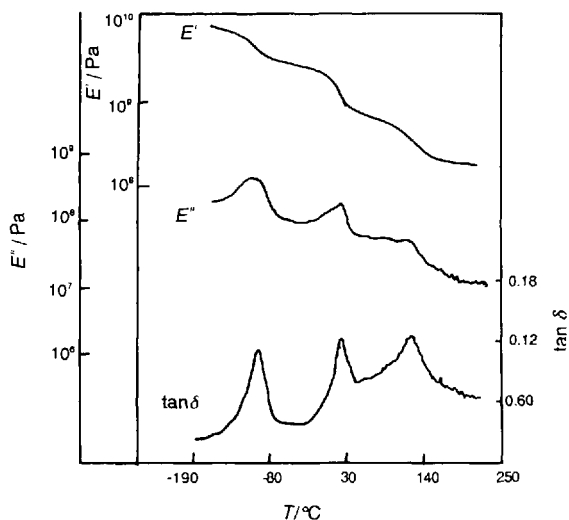


Figure 7.51 DMA curves for polytetrafluoroethylene [39]

Sample

Polytetrafluoroethylene (Teflon).

Measurements

Seiko Model SDM 5500 rheometer; Model DMS 100 viscoelastometer; sample size 20.00 mm (length) \times 12.10 mm (width) \times 0.93 mm (thickness); heating rate 2 K min⁻¹; atmosphere nitrogen; measurement temperature range from -165 to 220 °C. deformation mode bending; measurement frequency 0.5, 1, 2, 5 and 10 Hz (data given here were measured at a frequency of 1 Hz).

Results

Temperatures of tan δ peak and activation energies of the corresponding transitions are given in Table 7.7.

Table 7.7

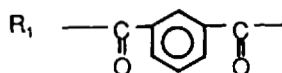
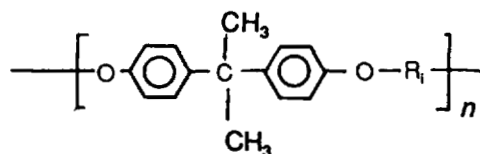
Loss peak	Temperature/°C	E_a /kJ mol ⁻¹	Molecular implication
α	123	347	Main-chain motion in amorphous region
β	21	286	Crystal crystal transition
γ	-99	93	Local-mode relaxation

DSC data (heating rate 10 K min⁻¹) are as follows: $T_{c1} = 22.3$ °C; $T_{c2} = 31.1$ °C; $H_c = 7.2$ J g⁻¹; $T_m = 330.7$ °C; $H_m = 37.4$ J g⁻¹.

Part II

Sample

Polyarylate (U-polymer):



The sample was molded at 250 °C, cooled rapidly in ice-water and dried under vacuum at ambient temperature.

Measurements

Seiko Model SDM 5500 rheometer; Model DMS 100 viscoelastometer; sample size 8.00 mm (length) × 10.10 mm (width) × 0.7 mm (thickness); heating rate 2 K min⁻¹; atmosphere nitrogen; deformation mode bending; measurement frequency 1, 2, 5 and 10 HE (data given here were measured at a frequency of 1 Hz).

Results

Temperatures of $\tan \delta$ peak and activation energies of the corresponding transitions are given in Table 7.8.

Table 7.8

Loss peak	Temperature/°C	E_a /kJ mol ⁻¹	Molecular implication
α	189	581	Glass transition
β	95	—	
γ	-77	79	

DSC data (heating rate 10 K min⁻¹) are as follows: $T_g = 182.6$ °C; $C_p = 0.175$ J °C⁻¹ g⁻¹.

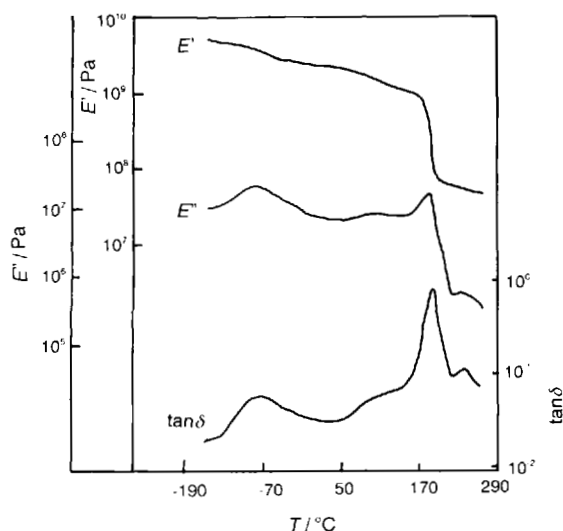


Figure 7.52 DMA curves for polyarylate [40]

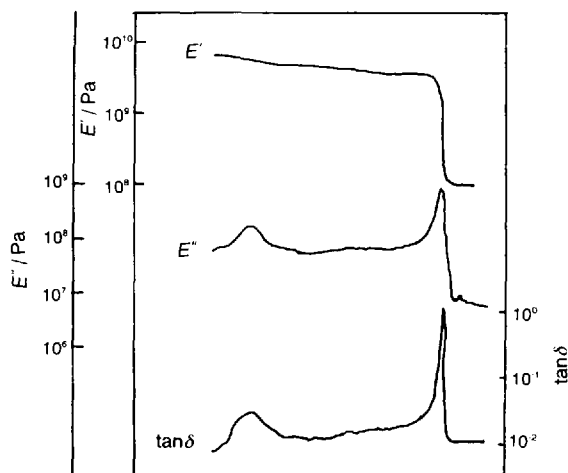
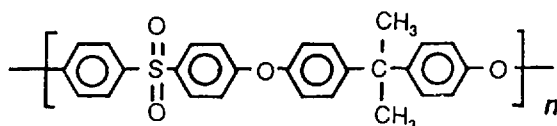


Figure 7.53 DMA curves for polysulfone [41]

Sample

Polysulfone:



Samples were molded at 250 °C, cooled rapidly in ice–water and dried under vacuum at ambient temperature for 1 week.

Measurements

Seiko Model SDM 5500 rheometer; Model DMS 100 viscoelastometer; sample size 20.00 mm (length) × 10.00 mm (width) × 1.310 mm (thickness); heating rate 2 K min⁻¹; atmosphere nitrogen; measurement temperature range from –165 to 250 °C; deformation mode bending, measurement frequency 0.5, 1, 2, 5 and 10 Hz (data given here were measured at a frequency of 1 Hz).

Results

Temperatures of tan δ peak and activation energies of the corresponding transitions are given in Table 7.9.

Table 7.9

Loss peak	Temperature/°C	E_a /kJ mol ⁻¹	Molecular implication
α	187	732	Glass transition
β	75	—	
γ	–111	44	

DSC data (heating rate 10 K min⁻¹) are as follows: $T_g = 183.7$ °C; $\Delta C_p = 0.230$ J °C⁻¹ g⁻¹.

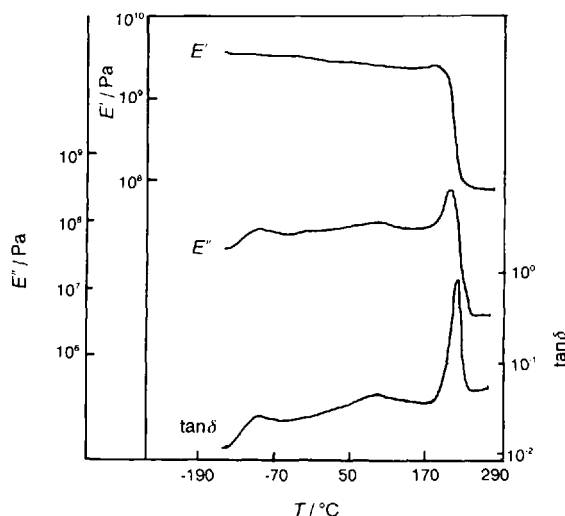
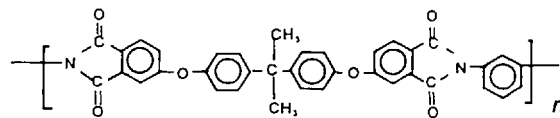


Figure 7.54 DMA curves for poly(ether imide) [42]

Sample

Poly(ether imide) (ULTEM):



Samples were molded at 280 °C, cooled rapidly in water and dried at ambient temperature for 1 week.

Measurements

Seiko Model SDM 5500 rheometer; Model DMS 100 viscoelastometer; sample size 20.00 mm (length) × 10.00 mm (width) × 1.24 mm (thickness); heating rate 2 K min⁻¹; atmosphere nitrogen; measurement temperature range from -165 to 270 °C; deformation mode bending; measurement frequency 1, 2, 5 and 10 Hz (data given here were measured at a frequency of 1 Hz).

Results

Temperatures of tan δ peak and activation energies of the corresponding transitions are given in Table 7.10.

Table 7.10

Loss peak	Temperature/°C	E_a /kJ mol ⁻¹	Molecular implication
α	214	777	Glass transition
β	90	95	
γ	-98	44	

DSC data (heating rate 10 K min⁻¹) are as follows: $T_g = 212.9$ °C; $C_p = 0.259$ J °C⁻¹ g⁻¹.

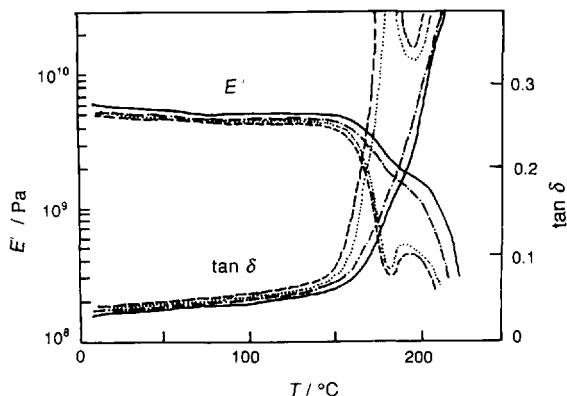


Figure 7.55 Temperature dependence of E' and $\tan \delta$ for silk fibroin films [21, 22]. —, α -form; ---, β -form; ·····, random coil; ---, regenerated fibroin

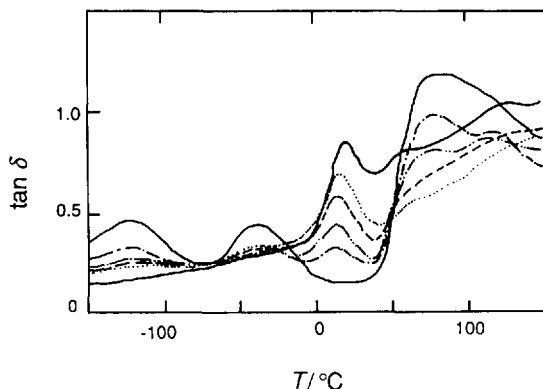


Figure 7.56 Temperature dependence of loss $\tan \delta$ for polypropylene (PP)-polyamide 6 (PA6) blend fibers [9]. 1, —, PA6; 2, ---, PP-PA6-compatible, 20:80:10; 3, -·-·-, 40:60:10; 4, ---, 60:40:10; 5, ·····, 80:20:10; 6, —, PP

Samples

Silk fibroin solution was obtained from the posterior part of the middle division of the silk gland in full-grown larvae (1 day before spinning) of *Bombyx mori*. The sericin was removed by washing with deionized water [21, 22].

Measurements

Toyo Sokki, Vibron II; frequency 110 Hz, heating rate 3°C min^{-1} .

Results

The decrease in E' at $ca\ 150^\circ\text{C}$ is attributed to the molecular motion of the amorphous region of Elbroin. Thermal decomposition took place at the same time.

Samples

PP, MFR 2.7 g/10 min, $M_w = 3.30 \times 10^5$, $M_w/M_n = 5.5-6.5$; PA6, MFR 3.0 g/10 min, $M_w 7.80 \times 10^4$; $M_w/M_n = 5.5-6.5$. PP and PA6 were mixed by adding a compatibilizer (maleic anhydride modified PP) using a biaxial extruder at 260°C , flow-rate 150 g min^{-1} .

Measurements

Toyo-Baldwin Vibron DDV-II; frequency 110 Hz; heating rate 2°C min^{-1} .

Results

The $\tan \delta$ peak at $ca\ -125^\circ\text{C}$ is attributed to rotation of the methylene group (γ relaxation), the peak at -39°C is due to a small amount of water trapped by the polyamide and the peak at $60-75^\circ\text{C}$ represents molecular motion of the polyamide due to breakage of hydrogen bonds (α relaxation).

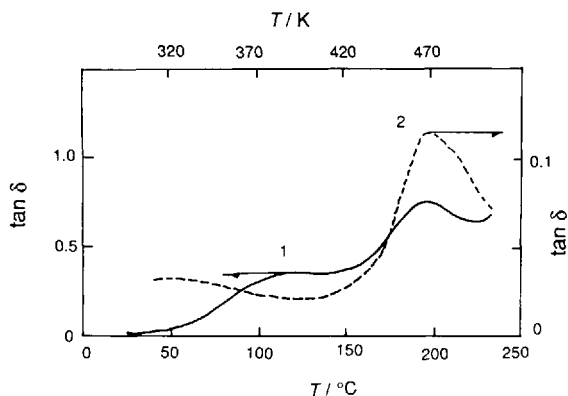


Figure 7.57 Temperature dependence of $\tan \delta$ curves for sericin-poly(vinyl alcohol) (PVA) blend films [43]

Samples

Silk sericin was extracted from *Bombyx mori* in hot water. A 5 g per 100 ml aqueous solution of PVA ($M_w = 91\,000$) was mixed with sericin in various ratios. Films with 0.05 mm thickness were prepared on a glass plate.

Measurements

Toyo-Baldwin Rheovibron DDV-II; heating rate $1\text{ }^\circ\text{C min}^{-1}$; frequency 110 Hz; sample size 2 mm (width) \times 30 mm (length) \times 0.05 mm (thickness).

Results

A microphase-separated structure was found in the blend films. The PVA-sericin complex seems to be observed at the interfacial region between two phases.

Samples

PECH: M_w 2000; hydroxyl content $16.72 \times 10^{-4} \text{ mol g}^{-1}$; C1 content 30%. Polyaryl polyisocyanate (PAPI): mass fraction of NCO 31%; density 1.24 g cm^{-3} . PMMA-MMA solution [containing 1.0% mole fraction of ethylene glycol dimethacrylate (EGDMA) and 0.5% mole fraction of benzoyl peroxide (BPO)]. PAPI and PMMA were mixed into PECH. After vacuum treatment, it was poured into a mold and cured for 2 days at $50\text{ }^\circ\text{C}$, 1 day at $90\text{ }^\circ\text{C}$ and 1 day at $120\text{ }^\circ\text{C}$.

Measurements

Metravib MAK-04 viscoelastometer (France); heating rate $3\text{ }^\circ\text{C min}^{-1}$; frequency 29.3 Hz; measurement temperature range from -70 to $180\text{ }^\circ\text{C}$; liquid N_2 ; sample size 18 mm (length) \times 10 mm (width) \times 2 mm (thickness).

Results

The main peak on the $\tan \delta$ curve is attributed to main-chain motion (T_g). The results indicate that the PECH-PMMA IPNs are completely compatible. The temperature of the T_g peak increases with increasing PMMA content.

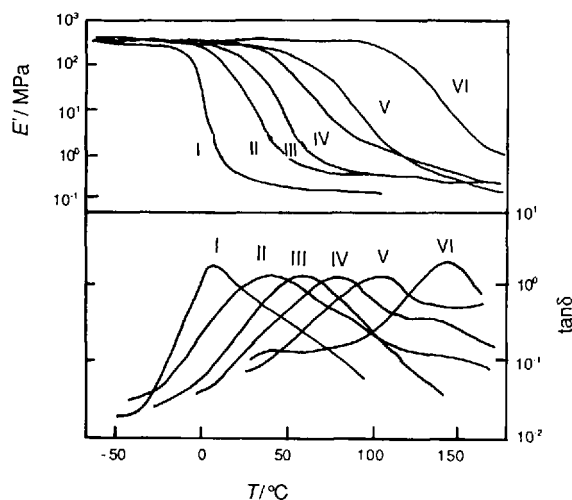


Figure 7.58 DMA curves for polyepichlorohydrin (PECH)-poly(methyl methacrylate) (PMMA) interpenetrating polymer networks (IPNs) with different compositions [44]. PECH:PMMA mass ratio: I, 100:0; II, 75:25; III, 65:35; IV, 50:50; V, 35:65; VI, 0:100

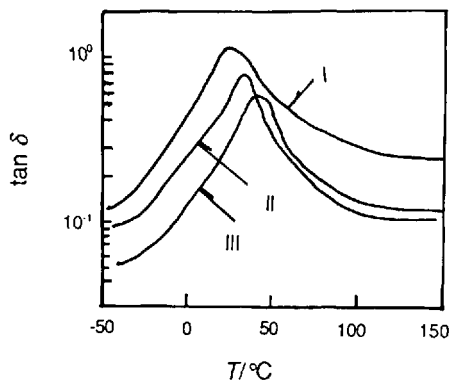


Figure 7.59 DMA curves for polyepichlorohydrin (PECH)-castor oil (CO) blends [45]. PECH : CO mass ratio: I, 100 : 0; II, 50 : 50; iii, 0 : 100

Samples

PECH: M_w 1400; hydroxyl content $16.72 \times 10^{-4} \text{ mol g}^{-1}$; Cl content 30%. CO: M_w 932; hydroxyl content $32.15 \times 10^{-4} \text{ mol g}^{-1}$. PECH and CO were mixed in proportions as indicated. After vacuum treatment, it was poured into a mold. The PECH-CO blends were cured for 48 h at 100°C .

Measurements

Metravib MAK-04 viscoelastometer (France); heating rate 3°C min^{-1} ; frequency 50 Hz; measurement temperature range from -50 to 150°C ; liquid N_2 ; sample size: 18 mm (length) \times 10 mm (width) \times 2 mm (thickness).

Results

The $\tan \delta$ peak of PECH decreases and the glass transition temperature (T_g) of PECH increases with increasing CO content.

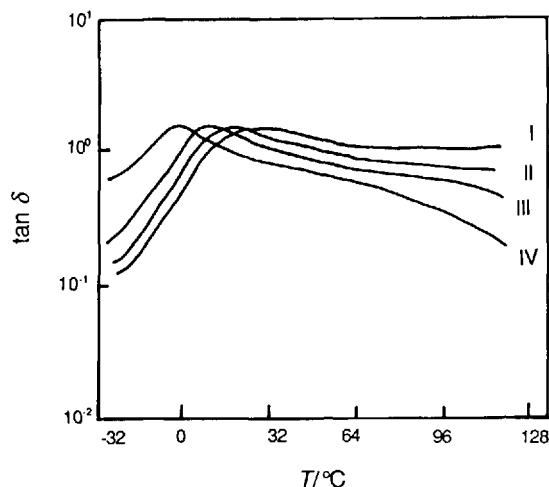


Figure 7.60 Effect of testing frequencies on DMA data for polyepichlorohydrin (PECH)-polyurethane (PU) [46]. Frequency: I, 500; II, 300; III, 50; IV, 5 Hz

Samples

PECH: $M_w = 1200$; hydroxyl content $16.67 \times 10^{-4} \text{ mol g}^{-1}$; Cl content 32.5%; viscosity (25°C) 10.5 Pa s . Polyaryl polyisocyanate (PAPI): NCO content 31%; density 1.24 g cm^{-3} . PECH and PAPI were mixed and poured into a mold after vacuum treatment and then cured at 100 – 120°C .

Measurements

Metravib MAK-04 viscoelastometer (France); heating rate 3°C min^{-1} ; frequency: 5, 50, 300 and 500 Hz; measurement temperature range from -20 to 120°C ; liquid N_2 ; sample size $18 \times 10 \times 2 \text{ mm}$.

Results

The T_g of PU(PECH) increases with increasing frequency; $\tan \delta$ increases in the high-temperature region with increasing frequency.

Sample

PP 1330 containing a 22% mass fraction of ethylene was obtained from Yanshan Petrochemical (Beijing, China); MFR = 1.5 g/10 min, density = 0.905 g cm⁻³. PP 1330 and wollastonite were prepared in a Brabender at 180 °C. The volume fraction of wollastonite was 17.7%.

Measurements

Toyco-Baldwin Rheovibron DDV-II-EA dynamic viscoelastometer; frequency 3.5 Hz; heating rate 3.0 °C min⁻¹; sample size 30.0 × 4.0 × 0.3 mm.

Results

The sharp decreases in E' at *ca* 175 and 125 °C are attributable to the melting of the crystalline phase of the PP and PE sequences, respectively. $\tan \delta$ shows three relaxation peaks, α , β and γ , from the high-temperature to the low-temperature side. Relaxation peaks α and β are attributable to the melting of the crystalline phase of the PP and PE sequences, respectively. Relaxation γ is attributable to main-chain motion of the PP sequence. The $\tan \delta$ values from -70 to 50 °C of composites are lower than those of pure PP.

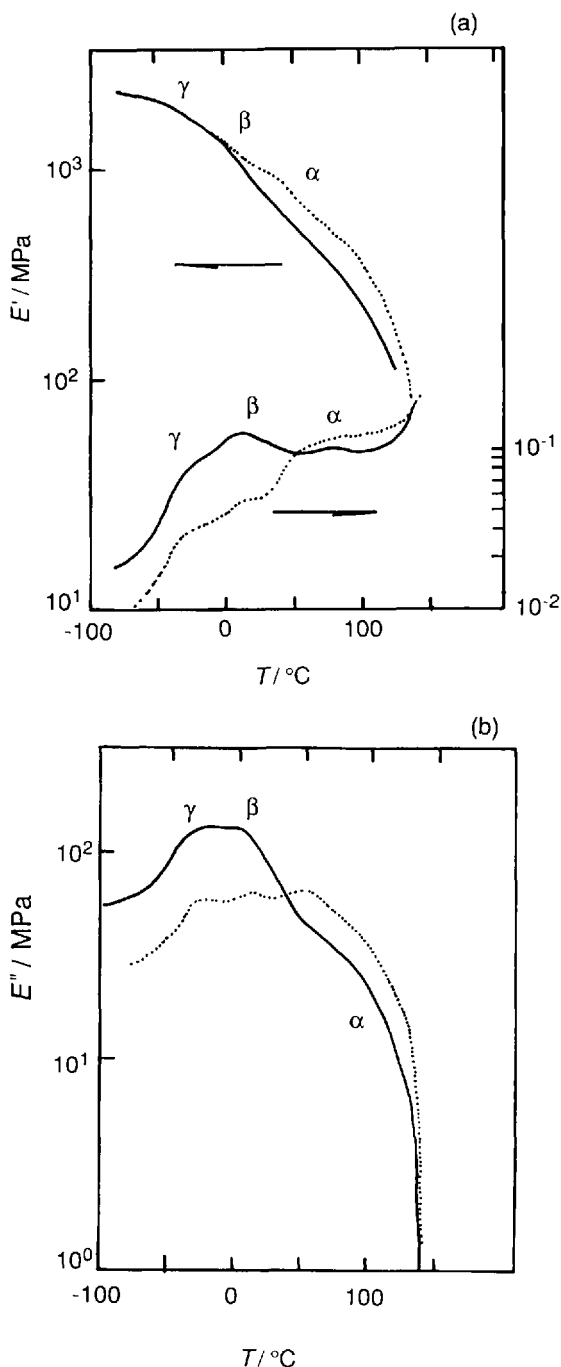


Figure 7.61 (a) Storage modulus E' and $\tan \delta$ vs. temperature and (b) loss modulus E'' vs. temperature curves for polypropylene and its composite containing wollastonite [47]. —, PP 1330; ·····, composite

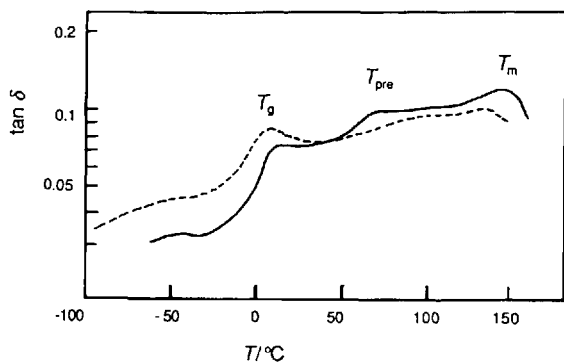


Figure 7.62 Tan δ curves for iPP and iPP filled with Y_2O_3 (Y) [48]. —, Y; ---, iPP

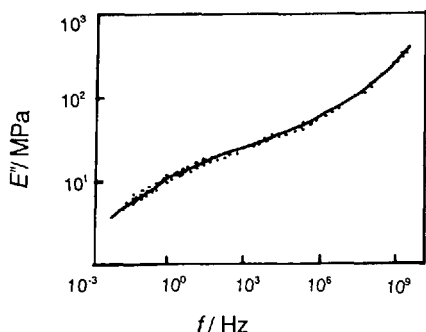


Figure 7.63 Master curves (E') for Ln-BR/SBR (20:80) blends ($T_{ref} = 15.5^\circ C$)

Samples

iPP 1300 was obtained from Yanshan Petrochemical (Beijing, China). iPP and rare earth oxides were mixed using a Brabender at $190^\circ C$. The original iPP was prepared following the same procedure.

Measurements

Toyo-Baldwin Rheovibron DDV-II-EA dynamic viscoelastometer; frequency 3.5 Hz; heating rate $3.0^\circ C \text{ min}^{-1}$; sample size $40 \times 4 \times 0.3 \text{ mm}$.

Results

Tan δ peaks of Y are observed at higher temperatures than for iPP. This is due to the fact that the amount of the β -form crystal of iPP in Y is much higher than that of iPP.

Samples

Poly(cis-1,4-butadiene) rubber polymerized with rare earth catalyst system (Ln-BR): $ML^{100^\circ C} = 40.0$; $[\eta] = 3.2 \text{ dl g}^{-1}$; cis-1,4 content 97.7%; trans-1,4 content 1.4%. Styrene butadiene (SBR): $ML^{100^\circ C} = 45.5$; cis-1,4 content 9.0%; trans-1,4 content 76%. Ln-BR and SBR were mixed and compressed for 1015 min using a plate vulcanizer at $100^\circ C$ and 10 MPa, then cooled to room temperature.

Measurements

Metravib MAK-04 viscoelastometer (France); heating rate $3^\circ C \text{ min}^{-1}$; frequency 7.8, 11.0, 18.8 and 35.0 Hz; measuring temperature range from -50 to $100^\circ C$; liquid N_2 ; sample size 20 mm (length) \times 10.40 mm (width) \times 2.18 mm (thickness). A WLF computer program was used to treat the data.

Results

When $T_{ref} = 25.5^\circ C$, $C_1 = 7.28$ and $C_2 = 134.91$. E' changed from 1×10^6 to $1 \times 10^9 \text{ Pa}$ corresponding to frequencies from 0.1×10^{-2} to $1 \times 10^{10} \text{ Hz}$.

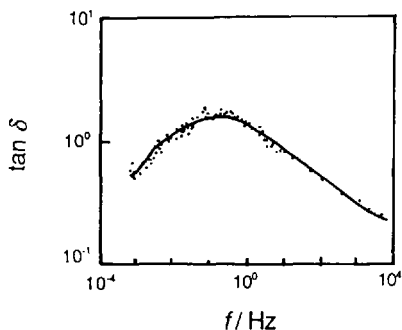


Figure 7.64 Master curves ($\tan \delta$) for polyepichlorohydrin (PECH)-Styrene (St) + methyl methacrylate (MMA) + butyl methacrylate (BMA) blends ($T_{\text{ref}} = 21^\circ\text{C}$)

Samples

PECH: $M_w = 1346$; hydroxyl content $13.46 \times 10^{-4} \text{ mol g}^{-1}$; C1 content 30%. PECH, St, MMA and BMA were mixed. After vacuum treatment, the mixtures were poured into a mold and cured for 24 h at 20°C and for 2 h at 80°C .

Measurements

Metravib MAK-04 viscoelastometer (France); heating rate 3°C min^{-1} ; frequency 7.8, 15.6, 31.2 and 62.5 Hz ; measuring temperature range from 0 to 68°C ; sample size 20 mm (length) \times 11 mm (width) \times 1.96 mm (thickness). A WLF computer program was used to treat the data.

Results

When $T_{\text{ref}} = 21^\circ\text{C}$, $C_1 = 33.06$ and $C_2 = 403.38$. $\tan \delta$ changed from 0.2 to 2.0 corresponding to frequencies from 1×10^{-4} to $1 \times 10^4 \text{ Hz}$.

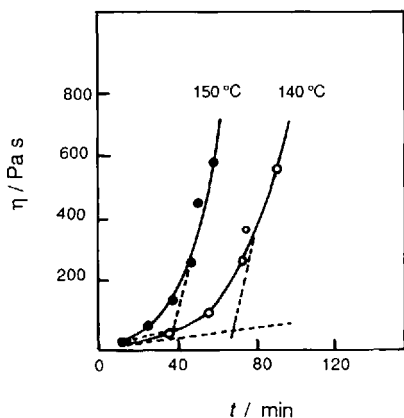


Figure 7.65 Viscosity change of epoxy resin (EP)-phenol formaldehydes (PF) at 140 and 150°C

Samples

EP: $M_w = 700$; density 2.0 g cm^{-3} . PF: density 1.460 g cm^{-3} . EP and PF were mixed in the mass ratio 10 : 3. The samples (5 g) were poured into a mold after vacuum treatment.

Measurements

Metravib MAK-04 viscoelastometer (France); frequency 7.8 Hz; viscosity test every 10 minutes; temperature 140 and 150°C .

Results

The sample was cured for *ca* 69 min at 140°C and for *ca* 38 min at 150°C .

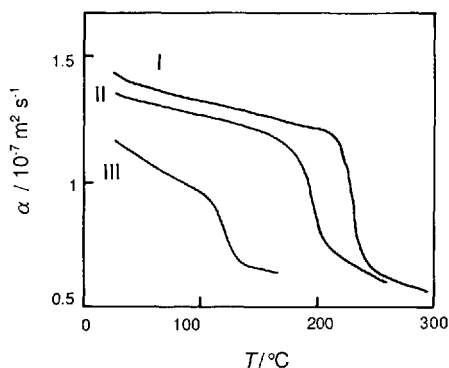


Figure 7.66 Thermal diffusivities of amorphous engineering plastics. I, Poly(ether imide) (PEI); II, poly(aryl ether sulfone) (PSF); III, poly(styrene-co-acrylonitrile) (SAN)

Samples

PEI, PSF and SAN are cooled at a rate of $2^{\circ}\text{C min}^{-1}$ from the molten state to room temperature.

Measurements

Apparatus, see 2.3.4; heating rate $1^{\circ}\text{C min}^{-1}$.

Results

A drastic decrease in diffusivity was observed at the glass transition temperature of the polymers.

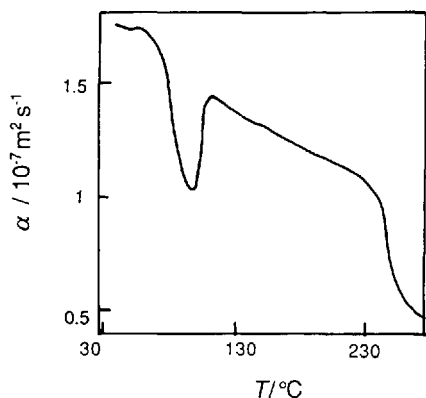


Figure 7.67 Thermal diffusivities of amorphous poly(ethylene terephthalate) (PET)

Samples

PET was quenched from the molten state.

Measurements

Apparatus, see 2.3.5; heating rate $1^{\circ}\text{C min}^{-1}$.

Results

The variations of α observed at 90, 110 and 260°C correspond to the glass transition, cold crystallization and melting of PET, respectively.

7.1 Appendix: Transition Maps of Representative Polymers

These maps show the relationship between the reciprocal temperature of molecular relaxation and frequency for representative polymers (reproduced by permission of Baihu-kan Publisher, Tokyo).

Each relaxation is designated from the high-temperature to the low-temperature side by α , β , γ , δ , etc. The following are added when relaxation mechanism is known: c, crystalline relaxation; gr, grain boundary relaxation; p, main-chain motion; l, local mode relaxation; s, side-chain motion; Me, relaxation due to the methyl group; Ph, relaxation due to the phenyl group; d, relaxation due to defects in the crystalline region; w, relaxation in the presence of water or other small molecules; and pa, metastable crystalline state (or intermediate region between amorphous and crystalline states).

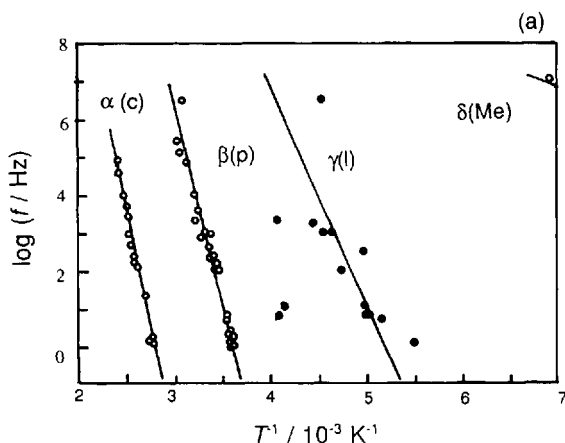


Figure 7.A1 (a) Polypropylene (high-temperature region)

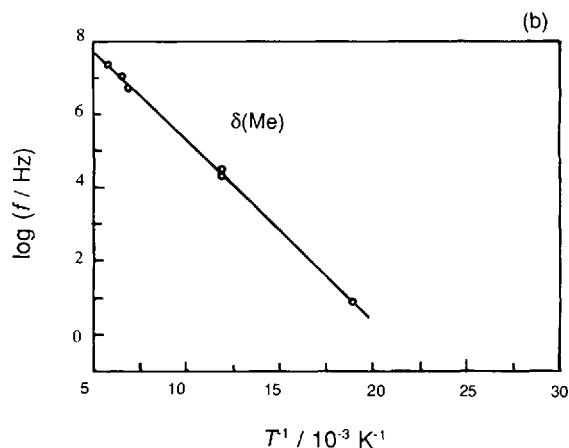


Figure 7.A1 (b) Polypropylene (low-temperature region)

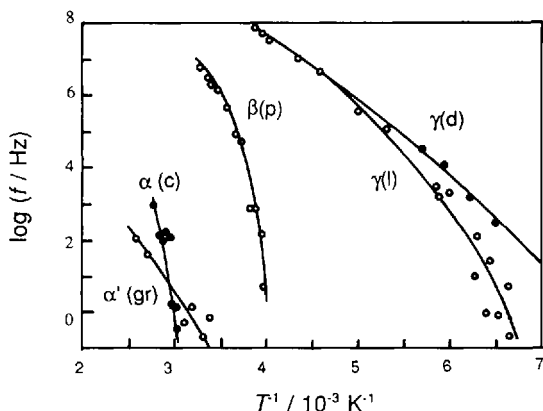


Figure 7.A2 Polyethylene

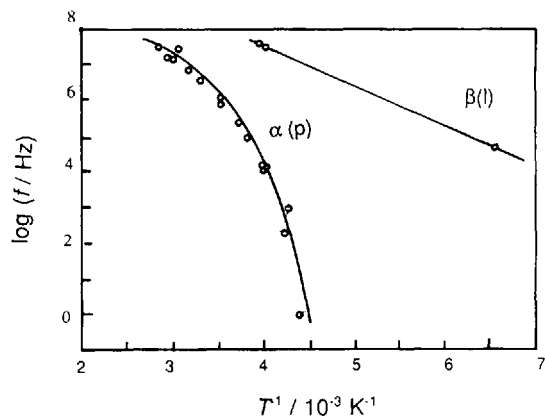


Figure 7.A3 Polyisobutylene

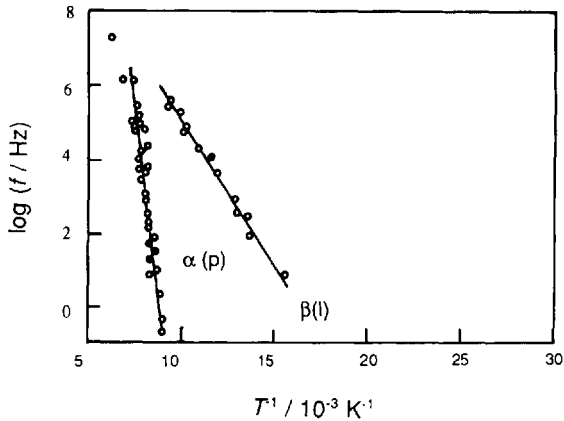


Figure 7.A4 Poly(vinyl chloride)

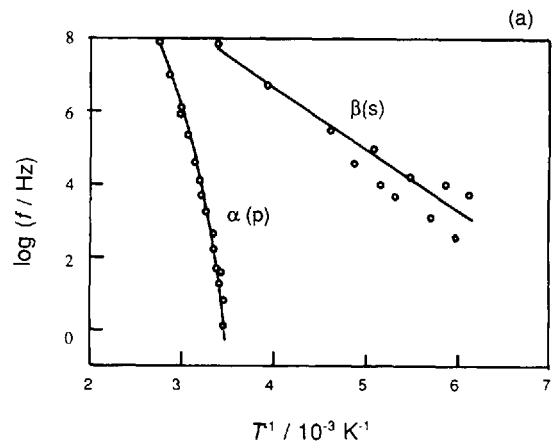


Figure 7.A6 (a) Poly(methyl acrylate) (high temperature region)

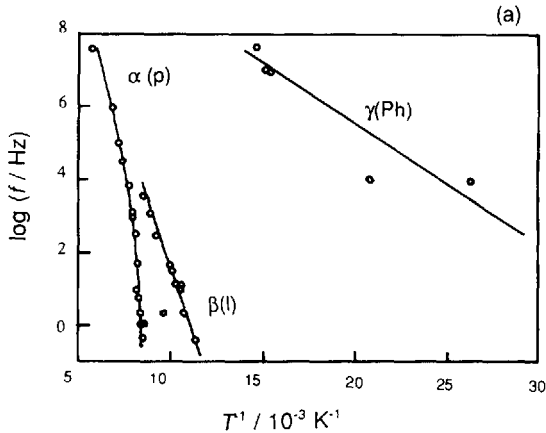


Figure 7.A5 (a) Polystyrene (high-temperature region)

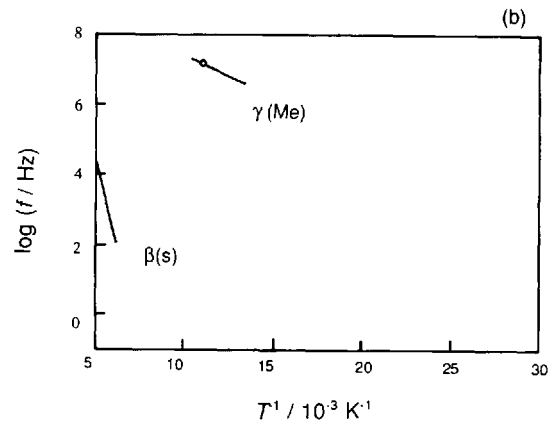


Figure 7.A6 (b) Poly(methyl acrylate) (low-temperature region)

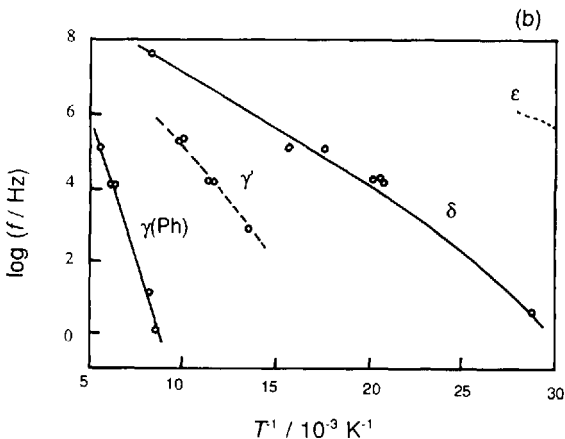


Figure 7.A5 (b) Polystyrene (low-temperature region)

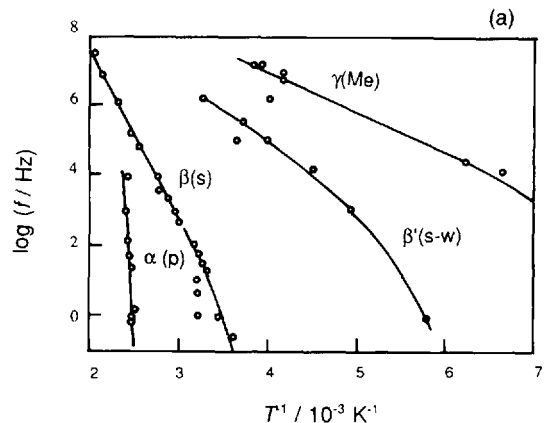


Figure 7.A7 (a) Poly(methyl methacrylate) (high-temperature region)

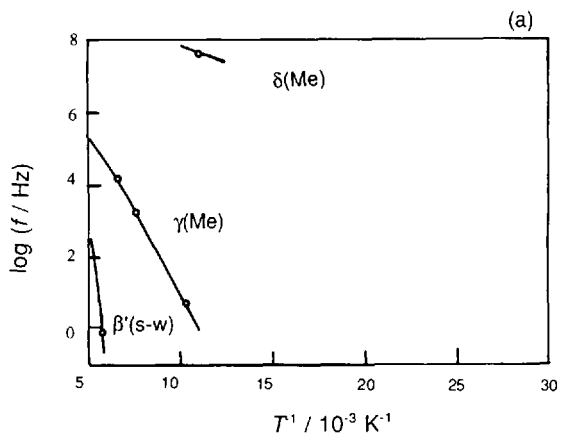


Figure 7.A7 (b) Poly(methyl methacrylate) (low-temperature region)

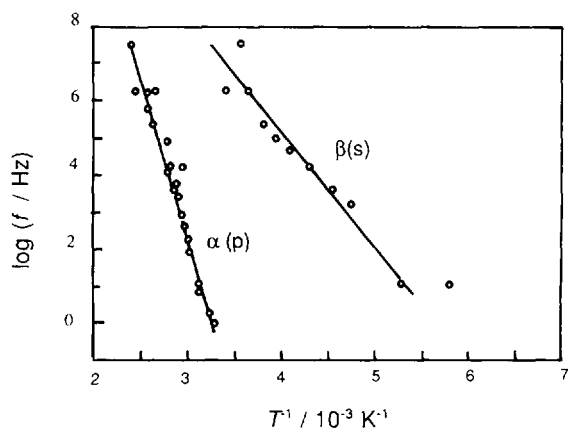


Figure 7.A9 Poly(vinyl acetate)

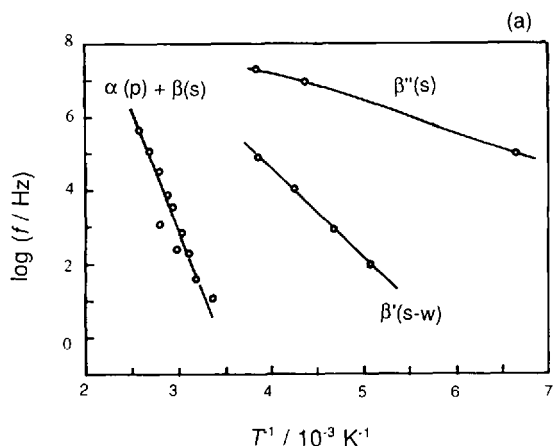


Figure 7.A8 (a) Poly(*n*-butyl acrylate) (high-temperature region)

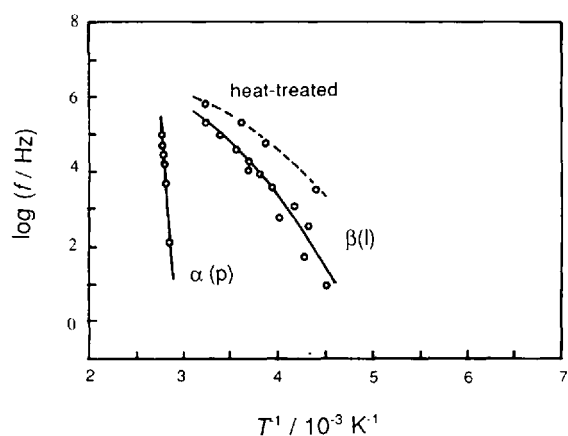


Figure 7.A10 Poly(vinyl alcohol)

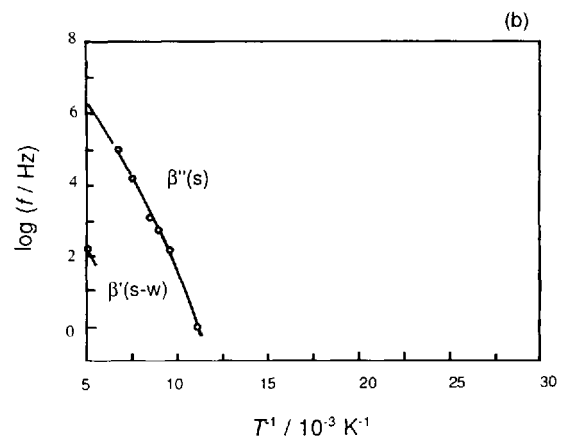


Figure 7.A8 (b) Poly(*n*-butyl acrylate) (low-temperature region)

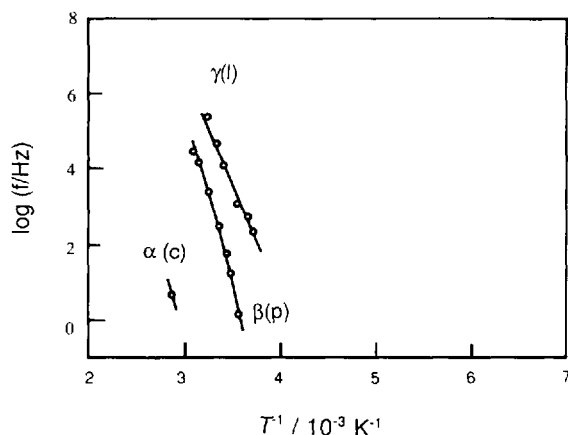


Figure 7.A11 Poly(vinylidene chloride)

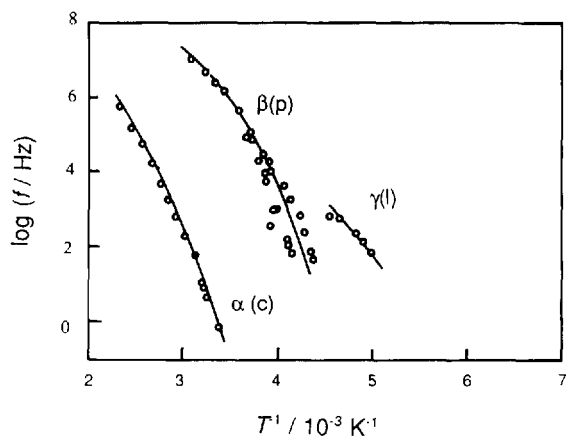


Figure 7.A12 Poly(vinylidene fluoride)

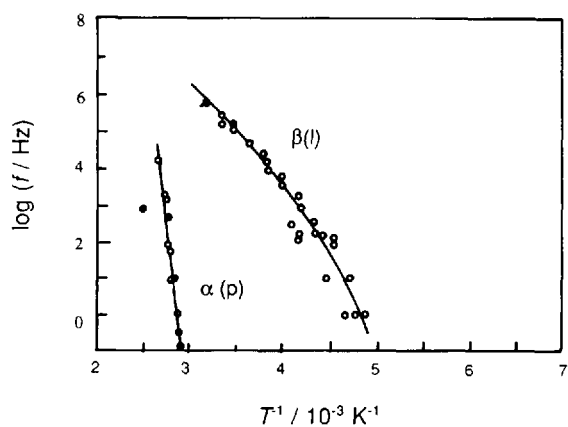


Figure 7.A15 Poly(ethylene terephthalate)

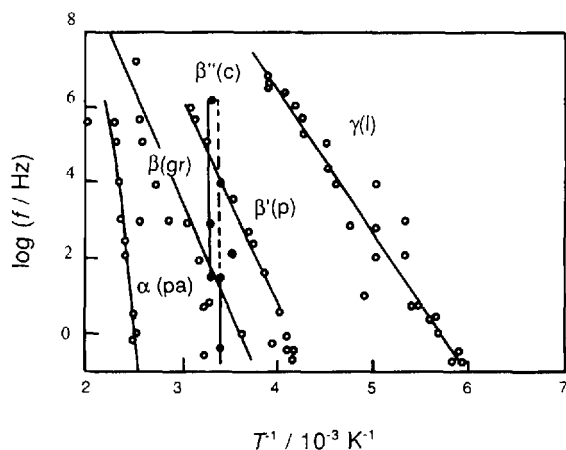


Figure 7.A13 Polytetrafluoroethylene

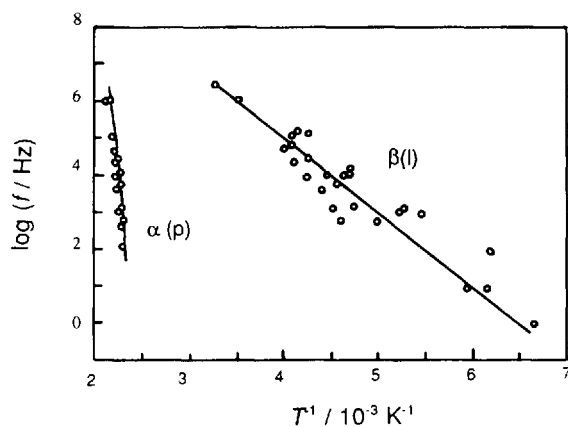


Figure 7.A16 Poly(bisphenol-A carbonate)

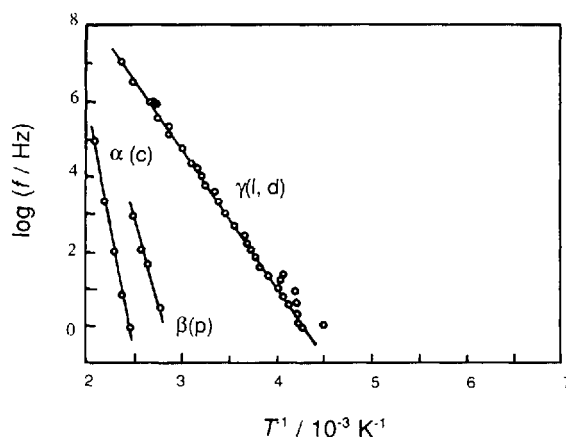


Figure 7.A14 Polytrifluorochloroethylene

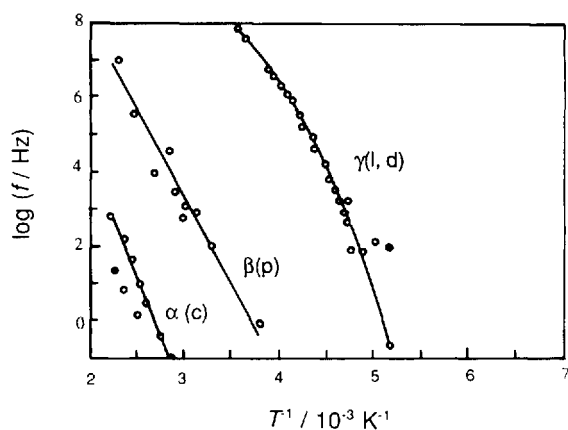


Figure 7.A17 Polyoxymethylene

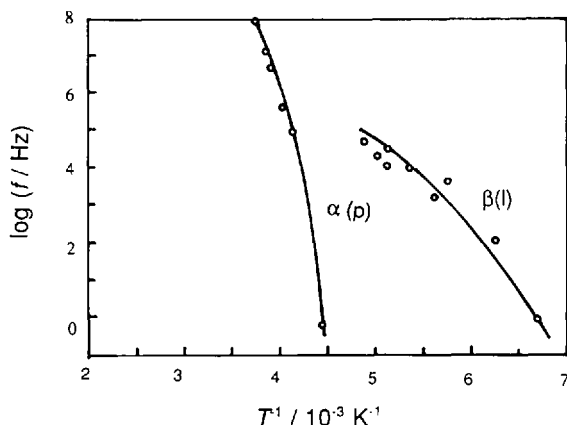


Figure 7.A18 Poly(ethylene oxide)

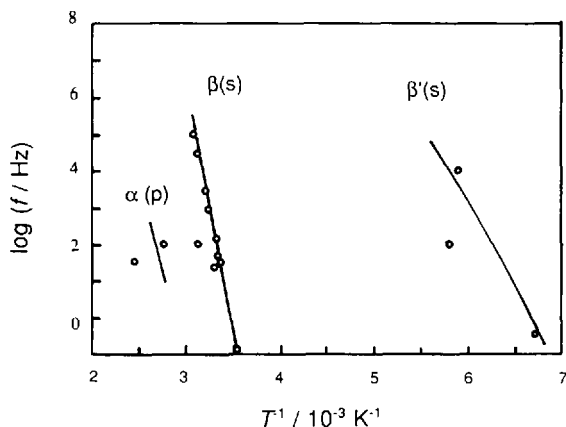
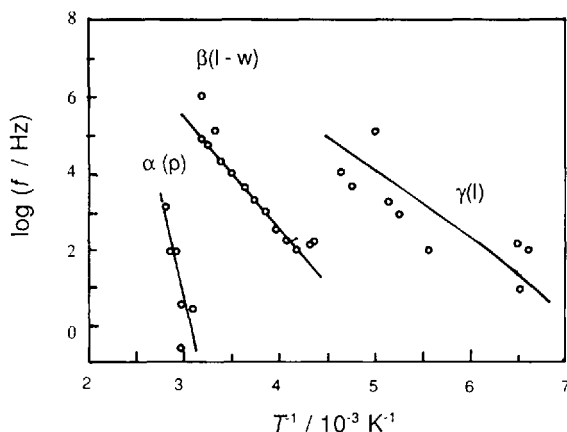
Figure 7.A21 Poly(γ -benzyl-L-glutamate)

Figure 7.A19 Nylon 6

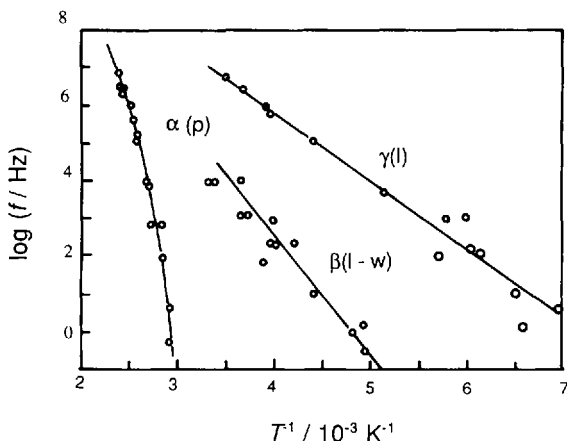


Figure 7.A20 Nylon 66

7.2 References

1. Hatakeyama, T., and Serizawa, M., *Polym. J.*, 1982, **14**, 51.
2. Lin Shan-Yan, Liao Chao-Ming and Liang Run-Chu, *Polym. J.*, 1955, **27**, 201.
3. *Setaram Applications, File 1: Elastomers.*
4. Nakagawa, T., and Kanemasa, A., *Sen-i Gakkaishi*, 1995, **51**, 123.
5. Hirose, S., Yoshida, H., Hatakeyama, T., and Hatakeyama, H., in Glasser, W., and Hatakeyama, H. (Eds), *Viscoelasticity of Biomaterials*, ACS Symposium Series, Vol. 489. Washington, DC, American Chemical Society, 1992, p. 385.
6. Kamide, K., *Koubunshi Kagaku*, 1968, **25**, 532 (J).
7. Varga, J., Schulek-Toth, F., and Ille, A., *Colloid Polym. Sci.*, 1991, **269**, 655.
8. Liu Jingjiang, *Chin. J. Appl. Chem.*, 1993, **10** (1), 27 (in Chinese).
9. Takahashi, T., Konda, A., and Shimizu, Y., *Sen-i Gakkaishi*, 1995, **51**, 354 (in Japanese).
10. Liu Jingjiang, Wei Xiufen and Guo Qipeng, *J. Appl. Polym. Sci.*, 1990, **4**, 2831.
11. Liu Jingjian, Tang Gongben and Zhau Huarong, *Chin. J. Appl. Chem.*, 1993, **10**(3), 22.
12. Nakafuku, C., and Miyaki, T., *Polymer*, 1983, **24**, 141.
13. Nakafuku, C., *Rep. Prog. Polym. Phys. Jpn.*, 1995, **38**, 249.
14. Maeda, Y., *Polym. Commun.*, 1991, **32**, 279.
15. Maeda, Y., *Thermochim. Acta*, 1990, **163**, 211.
16. Nagi, A., Murase, Y., Kuroda, T., Matsui, M., Mitsuishi, Y., and Miyamoto, T., *Sen-i Gakkaishi*, 1995, **51**, 470.
17. Day, M., Suprunchuk, T., Cooney, J. D., and Wiles, D. M., *J. Appl. Polym. Sci.*, 1988, **36**, 1097.

- 18 Song, S. S., White, J. L., and Cakmak, M., *Sen-i Gakkaishi*, 1989, **45**, 243.
- 19 Ejiri, K., Yamaoto, S., and Hatakeyama, T., *Sen-i Gakkaishi*, 1989, **45**, 55 (in Japanese).
- 20 Jimbo, T., Asai, S., and Sumita, M., *Sen-i Gakkaishi*, 1995, **51**, 517 (in English).
- 21 Magoshi, J., *J. Soc. Rheol. Jpn.*, 1973, **1** (1), 22 (in Japanese).
- 22 Magoshi, J., and Nakamura, S., *J. Appl. Polym. Sci.*, 1975, **19**, 1013.
- 23 Magoshi, J., Magoshi, Y., and Nakamura, S., *Appl. Polym. Symp.*, 1985, **41**, 187.
- 24 Hatakeyama, T., and Hatakeyama, H., in Kennedy, J. F., Philipps, G. O., Wedlock, D. J., and Williams, P. A. (Eds), *Cellulose and its Derivatives*. Chichester, Ellis Horwood, 1985, p. 87.
- 25 Xie Xu-Ming, Tanioka, A., and Miyasaka, K., *Polymer*, 1991, **32**, 1248.
- 26 Yoshida, H., Hatakeyama, T., and Hatakeyama, H., in Glasser, W., and Hatakeyama, H. (Eds), *Viscoelasticity of Biomaterials*, ACS Symposium Series, Vol. 489. Washington, DC, American Chemical Society, 1992, p. 385.
- 27 Yoshida, H., Hatakeyama, T., Nakamura, K., and Hatakeyama, H., *Kobunshi Ronbunshu*, 1989, **46**, 597 (in Japanese).
- 28 Hatakeyama, T., Yamauchi, A., and Hatakeyama, H., *Eur. Polym. J.*, 1984, **20**, 61.
- 29 Nakamura, K., Hatakeyama, T., and Hatakeyama, H., *Text. Res. J.*, 1981, **51**, 607.
- 30 Hatakeyama, T., Ikeda, Y., and Hatakeyama, H., *Macromol. Chem.*, 1987, **188**, 1875.
- 31 Quinn, F. X., Hatakeyama, T., Takahashi, M., and Hatakeyama, H., *Polymer*, 1994, **35**, 1248.
- 32 Shimadzu, *Stand-Alone Thermal Analysis Instruments*. Data Series of Novel Application.
- 33 Setaram File 6: C80 Calorimeter, Vessels and Application.
- 34 Setaram Application, File 3: Thermic Hazards Evaluation.
- 35 Shimadzu. *Stand-Alone Thermal Analysis Instruments*. Data Series of TMA-50 Application.
- 36 Yano, S., Hatakeyama, T., and Hatakeyama, H., *Rep. Prog. Polym. Phys. Jpn.*, 1987, **15**, 271.
- 37 Seiko Application Brief, 1989, SDM No. 5.
- 38 Seiko Application Brief, 1990, SDM No. 8.
- 39 Seiko Application Brief, 1989, SDM No. 4.
- 40 Seiko Application Brief, 1989, SDM No. 2.
- 41 Seiko Application Brief, 1989, SDM No. 3.
- 42 Seiko Application Brief, 1989, SDM No. 1.
- 43 Ichikawa, H., Nagura, M., and Tsuchiy, Y., *Sen-i Gakkaishi*, 1987, **43**, 283.
- 44 Chen Baoquan, Han Xiaozu and Guo Fengchun, *Yingyong Huaxue*, 1995, **12**(4), 66 (in Chinese).
- 45 Guo Fengchun, Han Xiaozu and Zhang Qingyu, *Juanzhi Gongye*, 1992, (3), 13 (in Chinese).
- 46 Guo Fengchun, Han Xiaozu and Wei Xuerong, *Gaofenzi Cailiao Kexue yu Gongcheng*, 1988, **10**(5), 74 (in Chinese).
- 47 Liu Jingjiang, Wei Xiufen and Guo Qipeng, *Appl. Polym. Sci.*, 1990, **4**, 2831.
- 48 Liu Jingjian, Tang Gongben and Zhau Huarong, *Chin. J. Appl. Chem.*, 1993, **10**(3), 22 (in Chinese).

Thermal Analysis Curves of Foods and Food Additives

8.1 Thermal Analysis Curves of Foods

Samples

Sodium-type gellan gum.

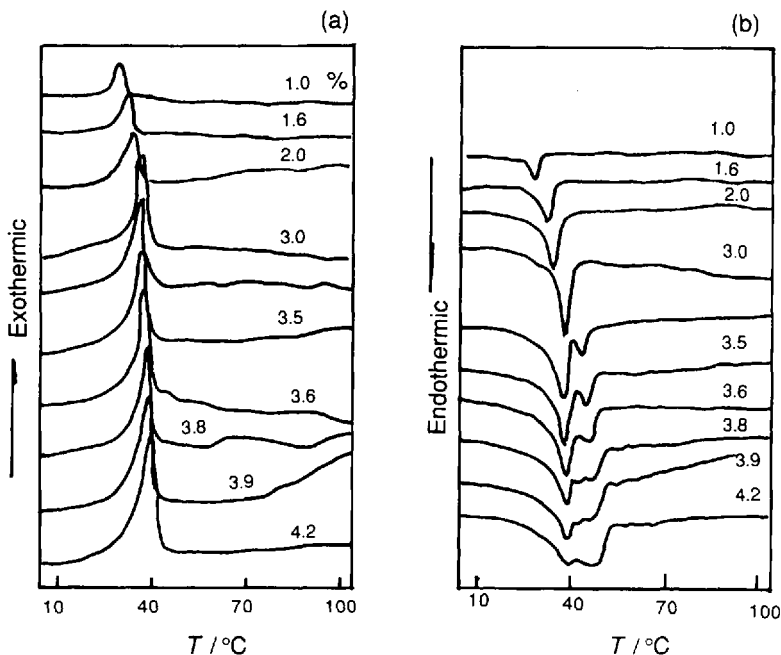


Figure 8.1 (a) Cooling and (b) heating DSC curves for sodium-type gellan gum solutions of various concentrations [1]. Numerals indicate polymer concentration

Measurements

Setaram micro DSC-III calorimeter; cooling and heating rate $0.5^{\circ}\text{C min}^{-1}$; sample mass *ca* 900 mg; N_2 atmosphere.

Results

The exothermic peak on the cooling DSC curves shifted to the higher temperature side with increasing polymer concentration. The endothermic peak on the heating DSC curves shifted to the higher temperature side and split into multiple peaks with increasing polymer concentration.

Samples

1% sodium-type gellan gum solutions containing CaCl_2 at various concentrations.

Measurements

Setaram micro DSC-III calorimeter; cooling and heating rate $0.5^{\circ}\text{C min}^{-1}$; sample mass *ca* 900 mg; N_2 atmosphere.

Results

The exothermic peak on the cooling DSC curves shifted to the higher temperature side with increasing concentration of added CaCl_2 . The endothermic peak on the heating DSC curves shifted to the higher temperature side and then split into multiple peaks with increasing concentration of added CaCl_2 .

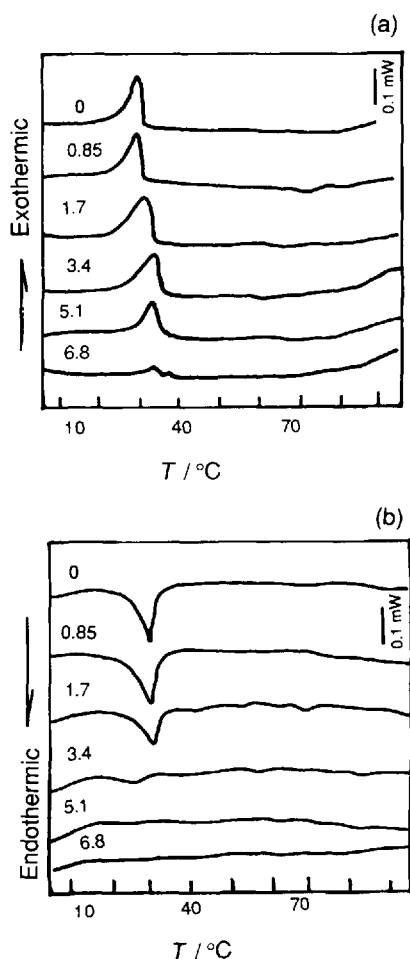


Figure 8.2 (a) Cooling (b) and heating DSC curves for 1% sodium-type gellan gum solutions containing CaCl_2 at various concentrations [2]. Numerals indicate the concentration of CaCl_2 in mmol l^{-1}

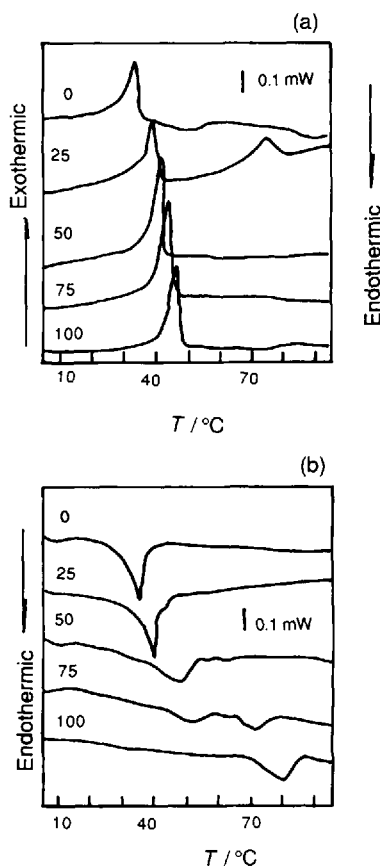


Figure 8.3 (a) Cooling (b) and heating DSC curves for 1% sodium-type gellan gum solutions containing NaCl at various concentrations [2]. Numerals indicate the concentration of NaCl in mmol l^{-1}

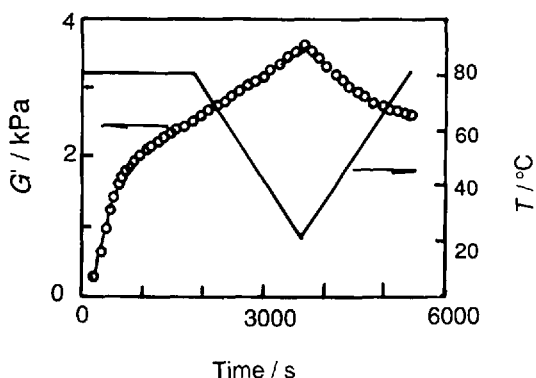


Figure 8.4 Gelation process of 15% mass fraction β -conglycinin dispersion at pH 7.6. [3]

Samples

2.0% sodium-type gellan gum solutions containing NaCl at various concentrations.

Measurements

Setaram micro DSC-III calorimeter; cooling and heating rate $0.5\text{ }^{\circ}\text{C min}^{-1}$; sample mass *ca* 900 mg; N_2 atmosphere.

Results

The exothermic peak on the cooling DSC curves shifted to the higher temperature side with increasing concentration of added NaCl_2 . The endothermic peak on the heating DSC curves shifted to the higher temperature side and then split into multiple peaks with increasing concentration of added NaCl.

Samples

Soybean (Enrei) β -conglycinin.

Measurements

CSL-500 rheometer (Carri-Med, Surrey, UK). The storage shear modulus G' was observed at 1 Hz and 5% strain. The solution was heated at $80\text{ }^{\circ}\text{C}$ for 30 min, cooled to $20\text{ }^{\circ}\text{C}$ at $2\text{ }^{\circ}\text{C min}^{-1}$, and then heated to $80\text{ }^{\circ}\text{C}$ at the same rate.

Results

G' increased during the 30 min at $80\text{ }^{\circ}\text{C}$, and continued to increase with decreasing temperature from 80 to $20\text{ }^{\circ}\text{C}$. Then G' decreased with increasing temperature from 20 to $80\text{ }^{\circ}\text{C}$.

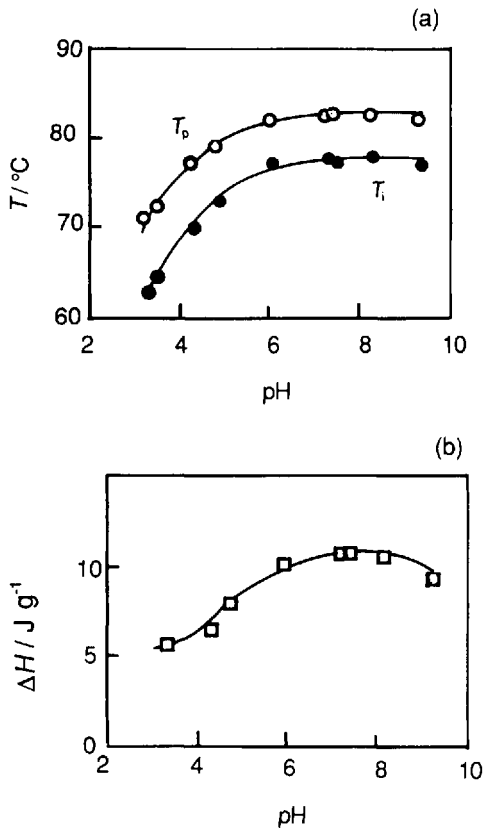


Figure 8.5 (a) Initial temperature (T_i) and endothermic peak temperature (T_p) and (b) enthalpy of denaturation (ΔH) of 15% mass fraction β -conglycinin dispersions as a function of pH [4]

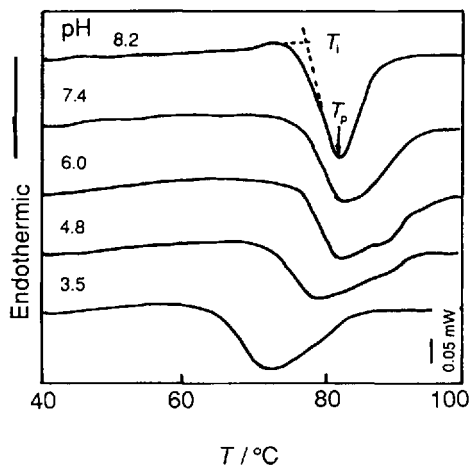


Figure 8.6 Heating DSC curves of 15% mass fraction β -conglycinin dispersions in the presence of 2.5% NaCl at different pH values [4]

Samples

Soybean (Enrei) β -conglycinin dispersion in 2.5% NaCl.

Measurements

Seiko DSC 120; heating rate 2°C min^{-1} ; sample mass *ca* 45 mg.

Results

Both T_i and T_p shifted to the higher temperature side with increasing pH up to pH 7 and then levelled off. ΔH showed a maximum at pH 7.

Samples

Soybean (Enrei) β -conglycinin.

Measurements

Seiko DSC 120; heating rate 2°C min^{-1} ; sample mass *ca* 45 mg

Results

Both T_i and T_p shifted to higher temperatures with increasing pH up to pH 7 and then levelled off. ΔH showed a maximum at pH 7.

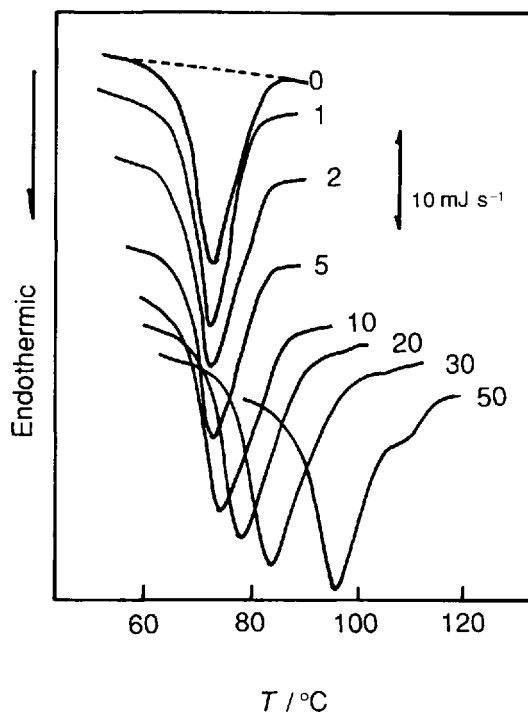


Figure 8.7 Heating DSC curves for 33% mass fraction sweet potato starch in sucrose solution of different concentrations [5]. Numbers beside each curve represent mass function of sucrose (%)

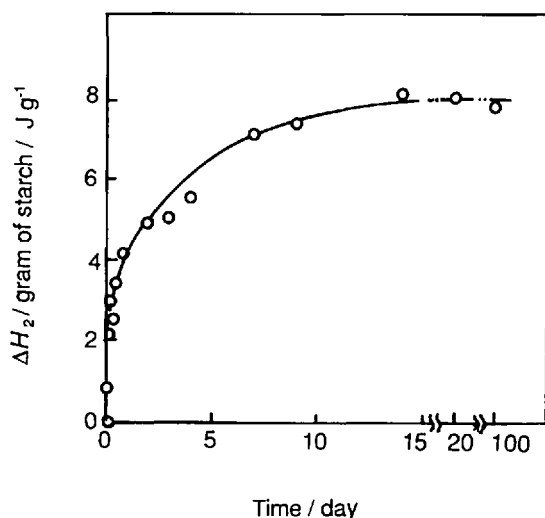


Figure 8.8 Regelatinization heat ΔH_2 for 33% mass fraction sweet potato starch as a function of storage time [5]

Sample

33% mass fraction sweet potato starch aqueous dispersion.

Measurements

Seiko DSC 580 with DSC 10 module; heating rate $1\text{ }^{\circ}\text{C min}^{-1}$; sample mass *ca* 45 mg.

Results

The endothermic peak temperature accompanying the gelatinization of starch was $72.4\text{ }^{\circ}\text{C}$ in the absence of sucrose. This temperature shifted to the higher temperature side with increasing concentration of added sucrose.

Samples

33 mass fraction sweet potato starch dispersion.

Measurements

Seiko DSC 580 with DSC 10 module. The temperature was raised from room temperature to $130\text{ }^{\circ}\text{C}$ at $1\text{ }^{\circ}\text{C min}^{-1}$ and then the pan was immediately quenched from 130 to $5\text{ }^{\circ}\text{C}$ and stored at $5\text{ }^{\circ}\text{C}$ for various periods. Regelatinization curves were observed by heating at $1\text{ }^{\circ}\text{C min}^{-1}$ from $5\text{ }^{\circ}\text{C}$. Sample mass *ca* 45 mg.

Results

ΔH_2 increased rapidly at the beginning of storage and then levelled off after 14 days.

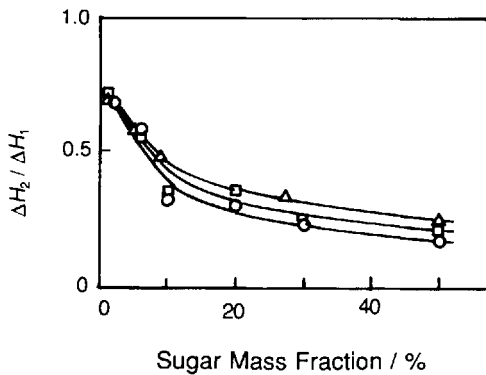


Figure 8.9 Retrogradation ratio ($\Delta H_2/\Delta H_1$) for mass fraction 33% sweet potato starch suspension as a function of sugar concentration [5]. Δ , sucrose; \square , glucose; \circ , fructose

Samples

33% (w/w) sweet potato starch aqueous dispersions with various sugar concentrations.

Measurements

Seiko DSC 580 with DSC 10 module; heating rate 1°C min^{-1} in both the first and second runs; sample mass *ca* 45 mg. The ratio of the heat required for regelatinization (ΔH_2) after storage for 14 days at 5°C to the heat required for the gelatinization (ΔH_1) is defined as retrogradation ratio.

Results

The retrogradation was retarded by the addition of sugar, and sucrose was found to retard the retrogradation most effectively among three types of sugar.

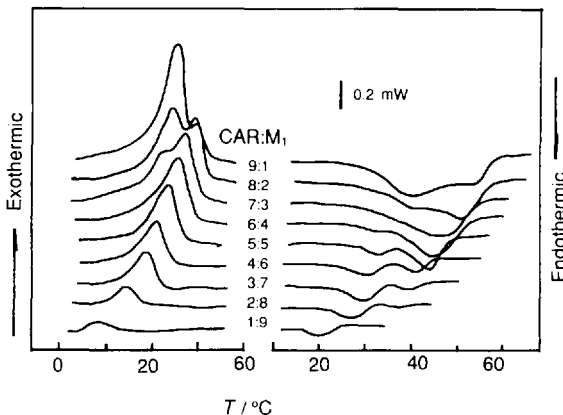


Figure 8.10 Cooling (left) and heating (right) DSC curves for 1.5% mass fraction mixtures of κ -carrageenan (CAR) and konjac glucomannan (KGM) [6]. Numbers beside each DSC curve represent the ratio of CAR to KGM

Samples

Powders of CAR and KGM were mixed in various ratios and dispersed in water.

Measurements

Setaram micro DSC-III; sample mass *ca* 300 mg; reference water. The temperature was raised to 80°C and maintained there for 30 min, then cooled to 0°C at 1°C min^{-1} and kept at 0°C for 30 min, and finally heated at 1°C min^{-1} .

Results

Exothermic and endothermic peak temperatures shifted to the higher temperature side with increasing content of CAR, and both peaks split into double peaks above a certain CAR content.

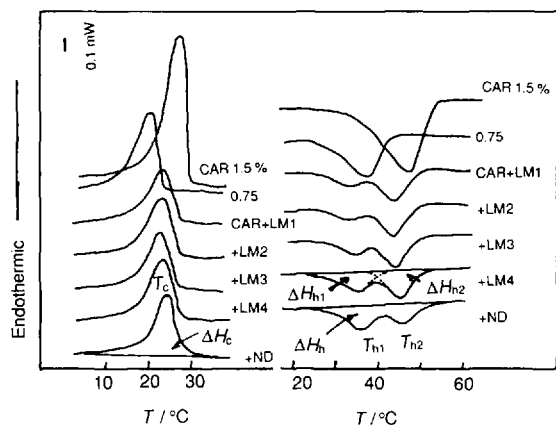


Figure 8.11 Cooling (left) and heating (right) DSC curves for κ -carrageenan (CAR) and konjac glucomannan (KGM) mixtures [6]

Samples

Powders of CAR and KGM were mixed (1:1). The mass fraction of total polysaccharide was 1.5%. Five fractions of KGM with different relative molecular mass were used.

Measurements

Setaram micro DSC-III; sample mass *ca* 300 mg; reference water. The temperature was raised to 80 °C and maintained there for 30 min, then cooled to 0 °C at 1 °C /min⁻¹ and kept at 0 °C for 30 min, and finally heated at 1 °C min⁻¹.

Results

The lower temperature endothermic enthalpy on the heating DSC curves for mixtures increased with increasing relative molecular mass of KGM.

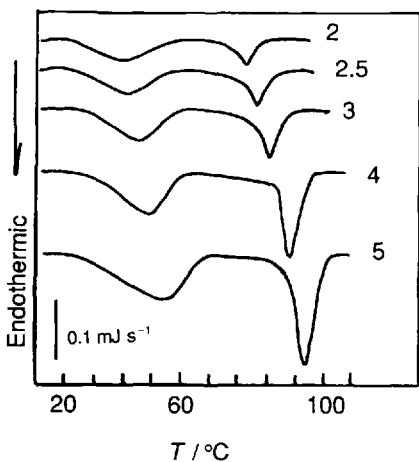


Figure 8.12 Heating DSC curves for mixed gels of gellan and κ -carrageenan [7]. Numbers beside each curve represent total polysaccharide concentration in % mass fraction

Samples

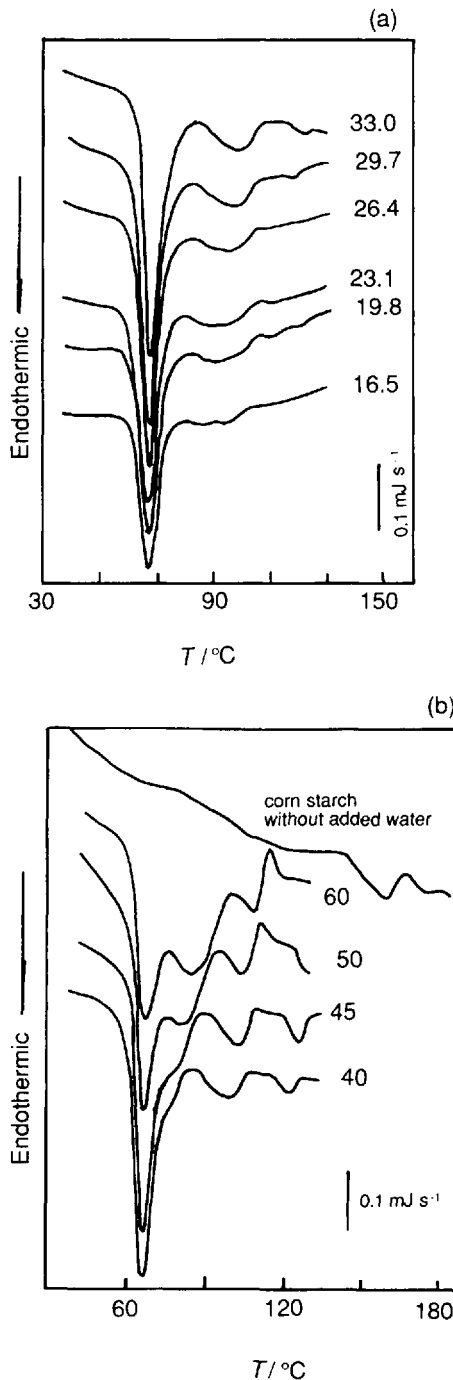
Mixed gels of gellan and κ -carrageenan. Mixing ratio 3:1.

Measurements

Seiko DSC SSC 500U; sample mass *ca* 45 mg; reference water; heating rate 2 °C min⁻¹.

Results

Two separated endothermic peaks were observed. Each peak shifted to the higher temperature side with increasing concentration of total polysaccharide.



Samples

CS dispersions.

Measurements

Rigaku DSC PTC10D; sample mass *ca* 60 mg; reference water; heating rate 1 °C min⁻¹. Numbers indicate concentration in %.

Results

The endothermic peak temperature of 66–67 °C was independent of the CS concentration (mass fraction 16.5–60%). The height of the main endothermic peak increased steeply with increasing CS concentration (mass fraction 16.5–40%). However, in CS containing <55% water, the height of the main endothermic peak decreased steeply with increasing CS concentration (40–60%). The second peak area increased and the second peak temperature shifted to the higher temperature side. Powders of CS alone (without added water, moisture content 12.5%) showed a small endothermic peak at about 150 °C.

Figure 8.13 Heating DSC curves for corn starch (CS) dispersions of various concentrations [8]. Mass fraction: (a) 16.5–33 and (b) 40–60%

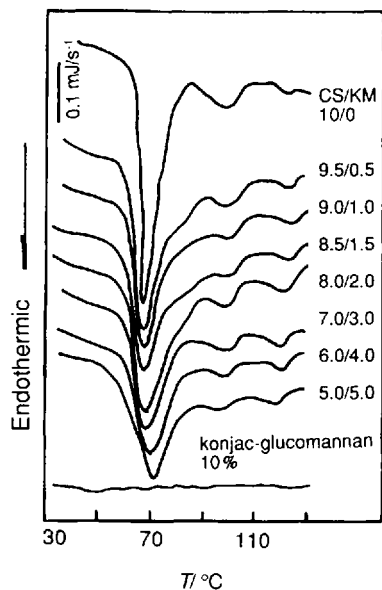


Figure 8.14 Heating DSC curves for corn starch (CS) plus water (10/0) and CS-konjac glucomannan (KMG)-water mixtures [8]. The mass fraction of total polysaccharide was 33% except for the lowest curve for KGM plus water

Samples

CS plus water (10/0) and CS-KGM-water mixtures.

Measurements

Rigaku DSC PTC10D; sample mass *ca* 60 mg; reference water; heating rate $1\text{ }^{\circ}\text{C min}^{-1}$.

Results

The endothermic peak temperature accompanying the gelatinization shifted slightly to the higher temperature side with increasing KGM concentration.

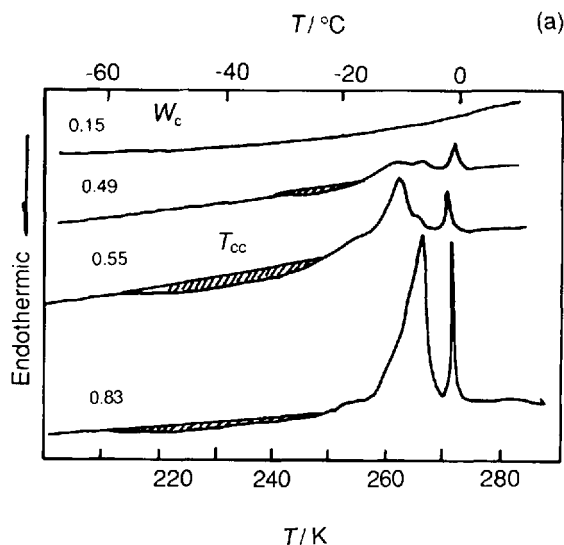


Figure 8.15 Heating DSC curves for water-Acacia senegal systems. [9]. W_c , mass fraction of water; T_{cc} cold crystallization

(continued)

Samples

Powder of *Acacia senegal* (produced in Sudan) plus water.

Measurements

Perkin-Elmer DSC II equipped with cooling apparatus. The temperature was lowered from 303 to 150 K at 10 K min^{-1} and then raised to 303 K at the same rate; sample mass 0.1–3 mg.

Results

Water content is defined as $W_c = W_f + W_{fb} + W_{nf}$, where W_c is water content, W_{nf} non-freezing water, W_{fb} freezing-bound water and W_f free water. At $W_c = 0.15$ there is no observable transition. At $W_c = 0.49$ there are two distinct transitions at 263.7 and 267.4 K. Several metastable states of water can be distinguished by the multi-peak nature of the DSC curves with increasing

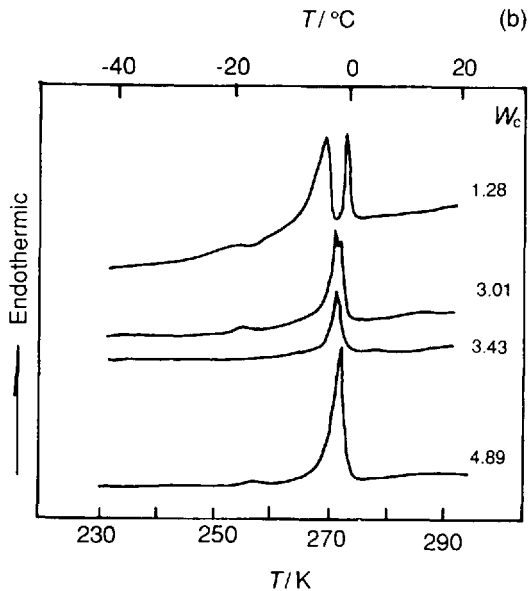


Figure 8.15 Heating DSC curves for water-*Acacia senegal* systems. [9]. W_c , mass fraction of water; T_{cc} cold crystallization

water content. As W_c is increased even further, the transition at 255 K becomes more distinguishable than at W_c 1.28, with the main freezing-bound transition moving closer to that of W_i at 273 K. When W_c reaches 3.43, the transitions due to W_{b1} and W_i are no longer separable and at $W_c = 4.89$ only the W_i transition due to free water is observable.

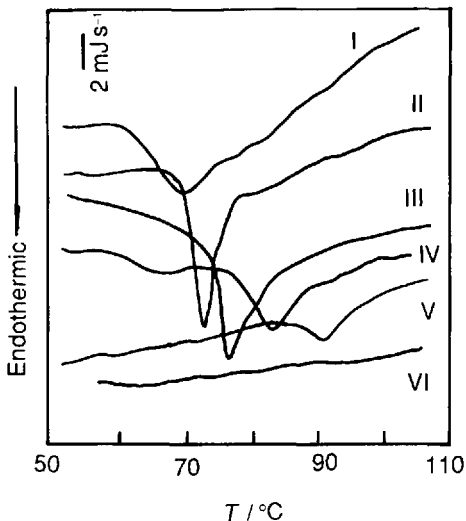


Figure 8.16 Heating DSC curves of cotyledon cells after thermal pretreatment at various temperatures [10]

Samples

Cotyledon cells of Adzuki beans (*Vigna angularis*). Pretreatment temperature: I, control; II, 60; III, 65, IV, 70; V, 80; VI, 90 °C.

Measurements

Seiko DSC-10; heating rate 1 °C min⁻¹; sample mass 55 mg; reference, water.

Results

The endothermic peak temperature shifted to the higher temperature side with increasing temperature of thermal pretreatment. Pretreatment at 60 and 65 °C caused a sharpening of the peak. The endothermic enthalpy for gelatinization decreased with a further increase in the pretreatment temperature.

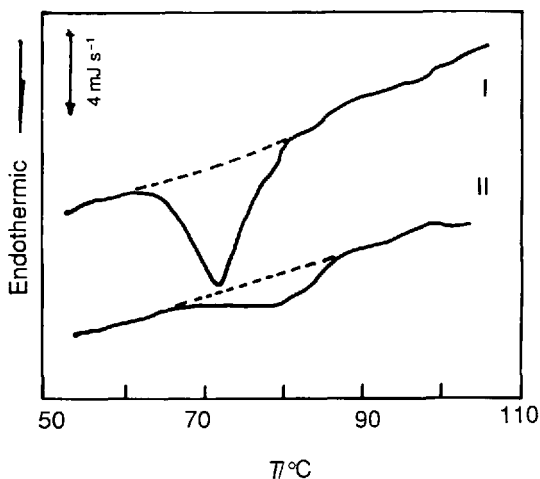


Figure 8.17 Heating DSC curves of mixtures of isolated starches and adzuki protein [11]

Samples

I, 4.15 mg of isolated starches and 1.83 mg of adzuki protein with 37.12 mg of water; II, 1.70 mg of adzuki protein with 46.23 mg of water.

Measurements

Seiko DSC-10; heating rate $1^{\circ}\text{C min}^{-1}$; sample mass 55 mg; reference, water.

Results

Adzuki protein showed a broad endothermic peak at 79°C (curve II). The effect of protein on the gelatinization of starch was not significant because a heating DSC curve of the mixture of starch and protein with the same mixing ratio as in adzuki beans, i.e. 40% protein (curve I), showed a similar endothermic peak to that of isolated starch alone (not shown), and the enthalpy per gram of starch did not change on addition of protein.

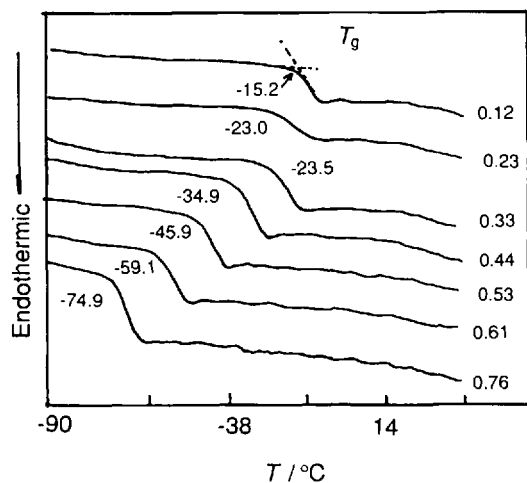


Figure 8.18 Heating DSC curves of grape previously equilibrated at different water activities at 25°C [12]. Numbers beside each curve represent the water activity

Samples

Grape (*Vitis vinifera*) of the Azal white wine-making cultivar, washed and dried with paper cloth. Moisture equilibration was carried out over saturated salt solutions (a_w 0.12–0.90) for 15 days at room temperature.

Measurements

Shimadzu DSC-50 fitted with an LTC-50 cooling unit; reference, empty aluminum pan; carrier gas, helium at a flow-rate of 30 ml min^{-1} ; samples cooled by liquid nitrogen and scanned at $5^{\circ}\text{C min}^{-1}$ from -120 to 100°C ; sample mass 6–8 mg.

Results

The glass transition temperature shifted to lower temperatures with increasing moisture content.

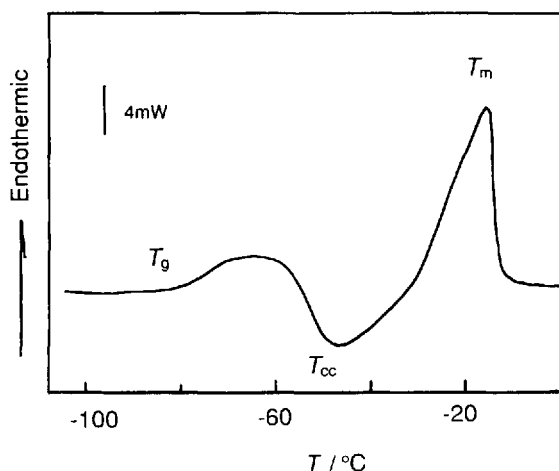


Figure 8.19 Heating DSC curves of 65% sucrose solution after rapid uncontrolled cooling ($>50^{\circ}\text{C min}^{-1}$) [13]

Sample

Sucrose.

Measurements

Perkin-Elmer DSC 7 equipped with a liquid nitrogen controlled cooling accessory; heating rate $5^{\circ}\text{C min}^{-1}$. Sample mass *ca* 10 mg.

Results

Glass transition (T_g), cold crystallization (T_{cc}) and devitrification and ice melting (T_m) were observed.

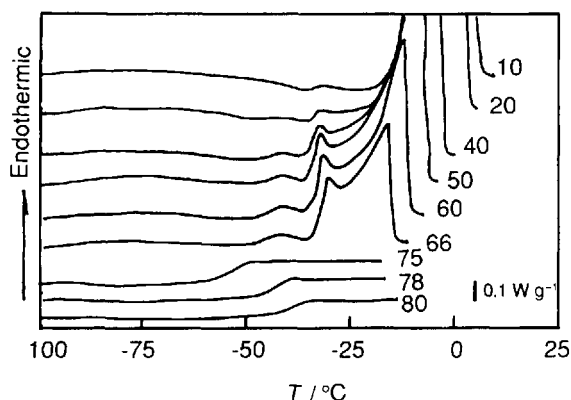


Figure 8.20 Heating DSC curves of 10–80% sucrose solution which had been annealed at -30°C for 30 min [13]

Sample

Sucrose.

Measurements

Perkin-Elmer DSC 7 equipped with a liquid nitrogen controlled cooling accessory; heating rate $5^{\circ}\text{C min}^{-1}$; sample mass *ca* 10 mg.

Results

Only a simple glass transition is observed from the vitrified samples (i.e. $>66\%$ sucrose) which did not form any ice. In contrast, for the other samples, which did form ice, the initial glass transition is followed by a larger second transition which precedes the ice-melting peak.

8.2 Thermal Analysis Curves of Food Additives

The thermal behavior of food additives is an important characteristic, which is related to scientific processing, storage and safe usage of foods. After food additives have been heated, various physical and chemical changes may occur, such as crystalline transition, sublimation, melting, dehydration and decomposition. In this section, DSC curves of over 20 samples are listed. The majority of samples chosen conform to standards of the

People's Republic of China for food additives [GB (Guo Biao, Chinese National Standard)].

DSC curves were measured under the following conditions: Shimadzu DSC-50; heating rate $10^{\circ}\text{C min}^{-1}$; dynamic nitrogen atmosphere (purity $>99.99\%$); flow-rate 20 ml min^{-1} ; open Pt crucible ($3\text{ mm} \times 5\text{ mm}$ diameter); reference crucible empty. Before using the DSC-50, the temperature was calibrated with In, Sn and Al. The significance of each peak on the measured curve is explained. In order to analyze the curve, some data relating closely to the samples are quoted from the literature, such as melting point (m.p.) boiling point (b.p.), decomposition temperature (T_d) and crystalline transition temperature (T_s). Owing to the limited space available, the experimental conditions are not given when they are the same as in the previous case.

Sample

Benzoic acid ($\text{C}_7\text{H}_6\text{O}_2$, $M_r = 122.12$; calorificity standard in calorimetry, B class).

Measurements

Sample mass 1.284 mg.

Results

Peak 1 (melting), T_c 395.25 K (122.10°C), T_p 397.10 K (123.95°C); peak 2 (vaporization), T_i 405.35 K (132.20°C), T_p 431.58 K (158.43°C), T_f 444.17 K (171.02°C). There is a sloping deviation from the baseline towards the endotherm at the about 80°C .

Reference data

White fluorescent crystal-like scales or needles: m.p. 122.4°C [14]; b.p. 249.2°C (101.3 kPa) [14], 234°C (66.6 kPa), 186°C (13.3 kPa), 133°C (1.33 kPa) [15]; sublimation at about 100°C ; m.p. (used in foods) $121\text{--}123^{\circ}\text{C}$ (GB 1901-80, content $>99.5\%$), $121.5\text{--}123.5^{\circ}\text{C}$ [FAO/WHO (1977), content $>99.5\%$], solidifying point $121\text{--}123^{\circ}\text{C}$ (FCC (1981)), content $99.5\%\text{--}100.5\%$ [14]; decomposition at 370°C according to Scheme 8.1 [16]:

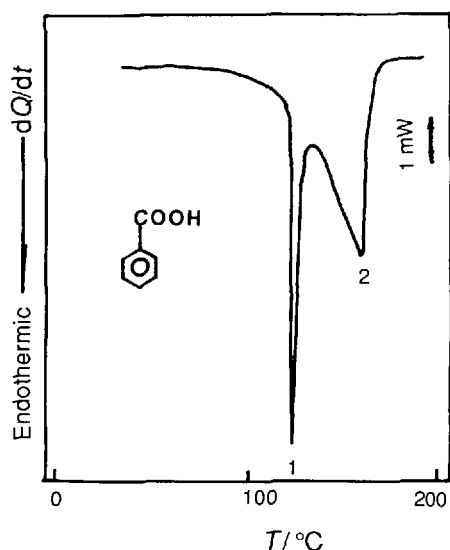
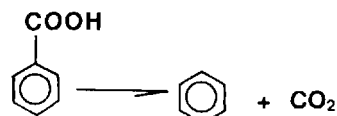


Figure 8.21 DSC curve of benzoic acid

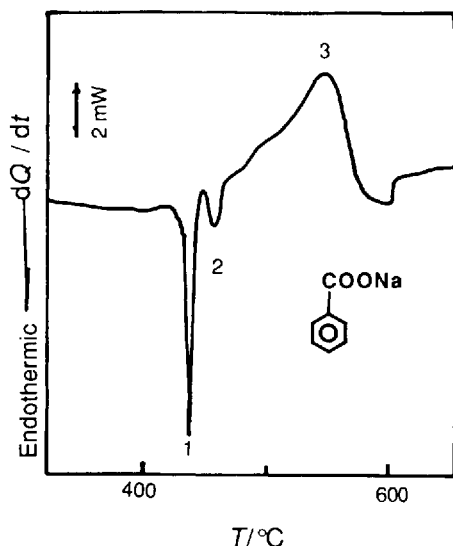


Figure 8.22 DSC curve of sodium benzoate

Sample

Sodium benzoate ($C_7H_5NaO_2$, $M_r = 144.11$), obtained commercially (GB 1902-80).

Measurements

Sample mass 2.226 mg.

Results

Peak 1, T_i 695.12 K (421.97 °C), T_c 705.73 K (432.58), T_p 710.66 K (437.51 °C); Peak 2, T_i 720.45 K (447.30 °C), T_c 723.59 K (450.44 °C), T_p 729.62 K (456.47 °C); Peak 3, T_p 819.72 K (546.57 °C), T_i 866.08 K (592.93 °C). Invisible endothermic process at 398.63 °C.

Reference data

Measured under the following conditions: atmosphere air; heating rate 3 °C min^{-1} . The endothermic process is rather complex; splitting carbon may be burned (residue: Na_2CO_3).

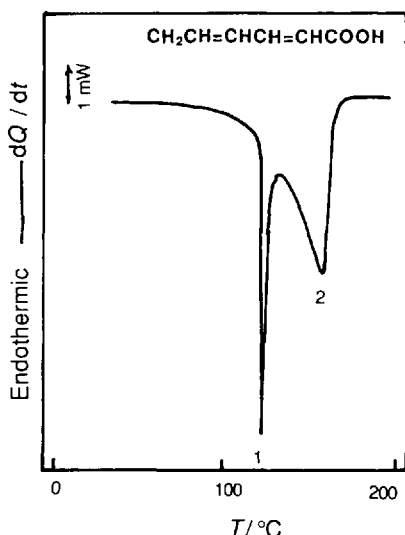


Figure 8.23 DSC curve of sorbic acid

Sample

Sorbic acid ($C_6H_8O_2$, $M_r = 112.13$), Nantong Acetic Acid Chemical Plant (GB 1905-80, purity >98.5%, m.p. 132–135 °C).

Measurements

Sample mass 2.041 mg.

Results

Peak 1 (melting), T_c 407.65 K (134.50 °C), T_p 409.18 K (136.03 °C); peak 2 (vaporization), T_i 418.38 K (145.23 °C), T_p 435.53 K (162.38 °C), T_f 447.63 K (174.48 °C).

Reference data

Colorless or white crystalline powder like needles; m.p. 407.7 K (134.5 °C); b.p. 501 K (228 °C) (decomposition) [17].

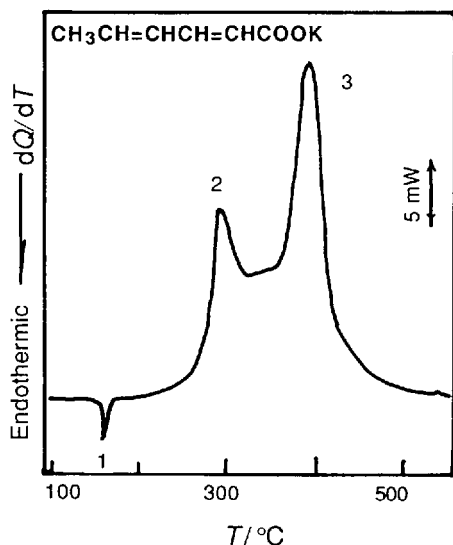


Figure 8.24 DSC curve of potassium sorbate

Sample

Potassium sorbate ($C_6H_7O_2K$, $M_r = 150.22$), Nantong Acetic Acid Chemical plant (GB 13736-92), content 98.0–102.0%.

Measurements

Sample mass 1.700 mg.

Results

Peak 1, T_i 423.22 K (150.07 °C), T_e 430.10 K (156.95 °C), T_p 434.18 K (161.03 °C), T_f 448.86 K (175.71 °C); peak 2 (decomposition), T_i 448.86 K (175.71 °C), T_e 541.07 K (267.9 °C), T_p 566.66 K (293.51 °C); peak 3, T_i 602.06 K (328.91 °C), T_p 665.75 K (392.60 °C), T_f 766.58 K (493.43 °C).

Reference data

Colorless to white crystal scales or crystalline powder, m.p. 270 °C (decomposition) [18]. When measured in static air, it decomposes exothermically after melting, products K_2CO_3 and carbon [19].

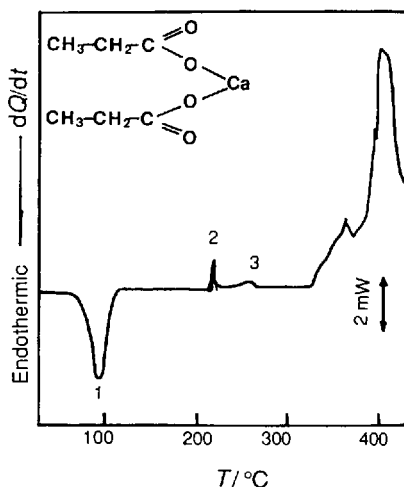


Figure 8.25 DSC curve of calcium propionate

Sample

Calcium propionate ($C_6H_{10}O_4Ca$, $M_r = 186.22$), obtained commercially (Guilin, Guangxi) (GB 6225-86, content >99.0%, dry basis).

Measurements

Sample mass 1.862 mg.

Results

Peak 1 (dehydration), T_i 333.02 K (59.87 °C), T_e 348.42 K (75.27 °C), T_p 369.58 K (96.43 °C); Peak 2, T_i 484.00 K (210.85 °C), T_p 501.00 K (227.85 °C); Peak 3, T_i 510.76 K (237.61 °C), T_p 528.84 K (255.69 °C). It decomposes sharply with an exotherm at 328.08 °C.

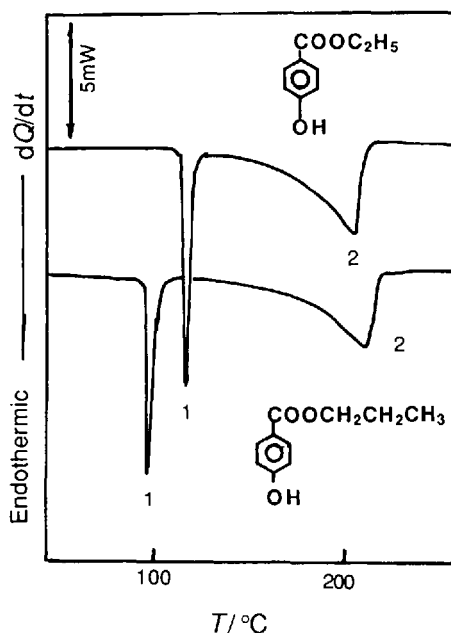


Figure 8.26 DSC curves of ethyl *p*-hydroxybenzoate and propyl *p*-hydroxybenzoate in nitrogen

Samples

Ethyl *p*-hydroxybenzoate ($C_9H_{10}O_3$, $M_r = 166.18$); propyl *p*-hydroxybenzoate ($C_{10}H_{12}O_3$, $M_r = 180.21$); chemically pure reagent, recrystallization, m.p. range (1) 0.5 and (2) 1.0 °C.

Measurements

Sample mass, (1) 1.850 and (2) 1.520 mg.

Results

Characteristic temperatures of peak 1 (melting) and peak 2 (vaporization) are given in Table 8.1.

Reference data

Chinese standards of foods: sample 1, m.p. 115–118 °C (GB 8850-88, purity >99.0 °C, dry basis; sample 2, m.p. 95–98 °C (GB 8851-88, purity >99.0%, dry basis) [20]. Sample 1, m.p. 116–118 °C, b.p. 297–298 °C (decomposition); Sample 2, m.p. 96–97 °C [21].

Table 8.1

No.	Peak 1			Peak 2		
	T_i/K	T_c/K	T_p/K	T_i/K	T_p/K	T_f/K
1	385.66	388.37	390.10	395.13	479.80	492.51
2	362.33	368.89	370.54	383.92	486.61	498.08

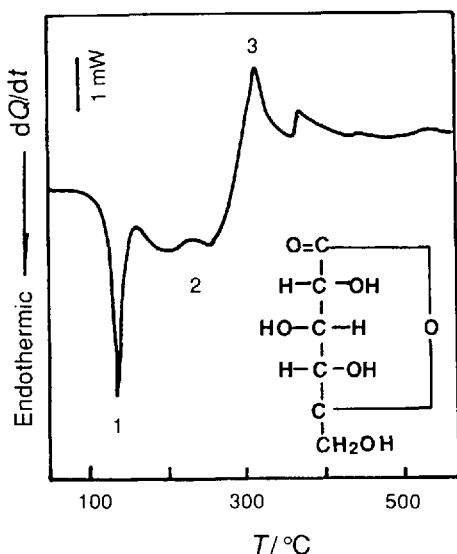


Figure 8.27 DSC curve of glucono-delta-lactone

Sample

Glucono-delta-lactone ($C_6H_{10}O_6$, $M_r = 178.14$), obtained commercially (GB 7657-87, content 99.0%).

Measurements

Sample mass 2.009 mg.

Results

Peak 1 (melting), T_p 358.67 K (85.52 °C), T_e 395.11 K (121.96 °C), T_p 411.44 K (138.29 °C); Peak 3 (apparently decomposing), T_i 529.93 (256.78 °C), T_p 583.65 K (310.50 °C); Peak 2 (endotherm) with several shoulder peaks, between peaks 1 and peak 3, remains at 0.183 mg, until 600 °C, then mass loss 90.89%.

Reference data

Colorless crystals; m.p. 150–152 °C (decomposition) [22] or m.p. 155 °C, (decomposition) [23].

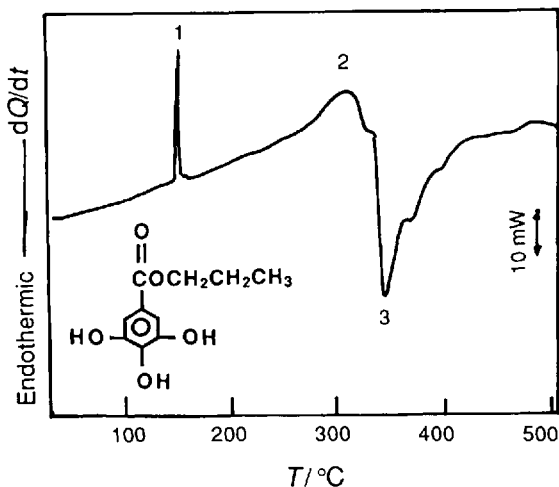


Figure 8.28 DSC curve of propyl gallate

Sample

Propyl gallate ($C_{10}H_{12}O_5$, $M_r = 212.21$), synthesized in our laboratories, recrystallized once.

Measurements

Perkin-Elmer 7 Series DSC; atmosphere dynamic air; flow-rate 40 ml min⁻¹; heating rate 20 °C min⁻¹; crucible material Pt; sample mass 1.400 mg.

Results

Peak 1 (melting), T_i 416 K (143 °C), T_e 421.10 K (147.95 °C), T_p 422.57 K (149.42 °C); peak 2 (vaporization and decomposition), T_i 513 K (240 °C), T_p 575.24 K (302.09 °C); peak 3 with several shoulder peaks, main decomposition peak (decomposing and oxidizing), T_p 615.4 K (342.2 °C).

Reference data

White to fawn yellow crystalline powder; m.p. 150 °C [24]. It begins to decompose after heating for 1 h at 227 °C [25]. Standard m.p. (Chinese food grade) 146–150 °C [GB 3263-82, content 98–102% ($C_{10}H_{12}O_5$)].

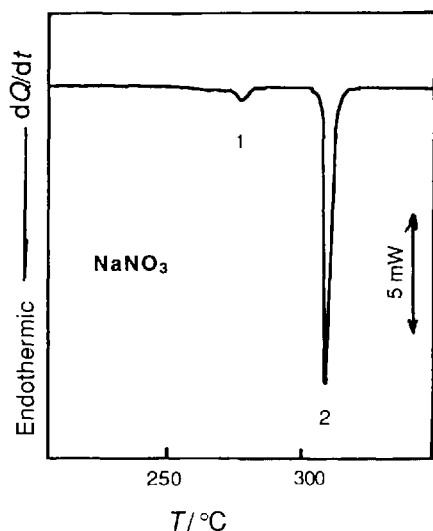


Figure 8.29 DSC curve of sodium nitrate

Sample

Sodium nitrate (NaNO_3 , $M_r = 84.993$), obtained commercially (chemically pure reagent).

Measurements

Sample mass 1.495 mg.

Results

Peak 1 (α - β transition), T_p 549.94 K (276.79 °C); peak 2 (melting), T_i 570.61 K (297.46 °C), T_c 578.56 K (305.41 °C), T_p 581.76 K (308.61 °C), T_i 587.03 K (313.88 °C).

Reference data

T_m 276.1 °C; ΔH_f 3–39 kJ mol⁻¹; m.p. 306.1 °C; ΔH_f 14.60 kJ mol⁻¹; T_d 380 °C; products Na_2O and NO_2 [26].

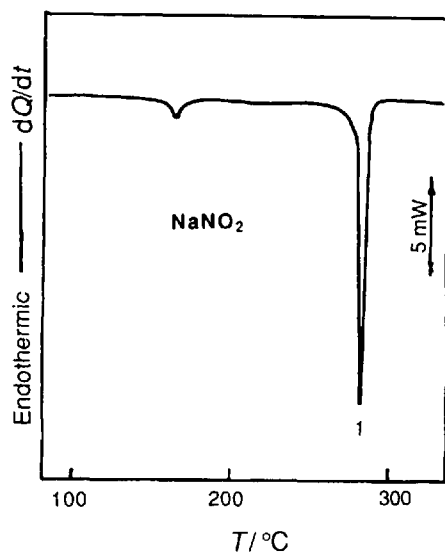


Figure 8.30 DSC curve of sodium nitrite

Sample

Sodium nitrite (NaNO_2 , $M_r = 69.00$), obtained commercially (GB 1907-84, content >99.0%, dry basis).

Measurements

Sample mass 2.629 mg.

Results

Peak 1 (crystal transition), T_i 428.92 K (155.77 °C), T_c 434.17 K (161.02 °C), T_p 439.77 K (166.22 °C). peak 2 (melting), T_i 538.10 K (264.95 °C), T_c 553.14 K (279.99 °C), T_p 556.44 K (283.29 °C).

Reference data

M.p. 276.9 °C; b.p. 320 °C (decomposition) [27]; decomposition products N_2 , O_2 and NO , final product Na_2O .

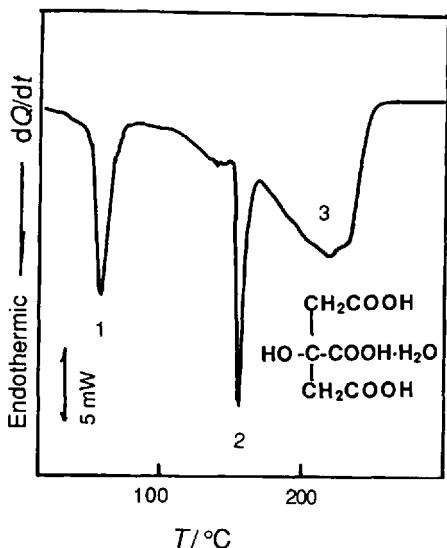


Figure 8.31 DSC curve of citric acid

Sample

Citric acid ($C_6H_8O_7 \cdot H_2O$, $M_r = 210.14$), obtained commercially (GB1987-86, content 99.5%, calculated as $C_6H_8O_7 \cdot H_2O$).

Measurements

Sample mass 5.492 mg.

Results

Peak 1 (hydration), T_i 309.32 K (36.17 °C), T_e 322.99 K (49.84 °C), T_p 329.83 K (56.68 °C); peak 2 (melting), T_i 421.42 K (148.27 °C), T_e 424.97 K (151.82 °C), T_p 428.12 K (154.97 °C); peak 3, T_i 442.08 K (168.93 °C), T_p 487.26 K (214.11 °C), T_f 526.81 K (253.66 °C).

Reference data

Hydration at 70–75 °C; the exact m.p. of citric acid without water is 153 °C [28].

Sample

Fumaric acid ($C_4H_4O_4$, $M_r = 116.07$), Suzhou Synthetic Chemical Plant (Enterprise standards: Q/320500HC005-92, content 99.3%).

Measurements

Sample mass 1.810 mg.

Results

Peak 1, T_i 416.96 K (143.81 °C), T_e 488.97 K (215.82 °C), T_p 520.92 K (247.77 °C); peak 2, T_i 534.46 K (261.31 °C), T_e 554.72 K (281.57 °C), T_p 562.65 K (289.50 °C), T_f 633.16 K (360.01 °C); peak 3, T_i 699.47 K (426.32 °C), T_p 725.57 K (452.42 °C), T_f 739.16 K (466.01 °C).

Reference data

Sublimation above 200 °C in open container; dehydration to maleic dialdehyde at 230 °C; m.p. (in sealed tube) 30–320 °C (or 286–287 or 282–284 °C) [29]; b.p. 290 °C (decomposition) [30].

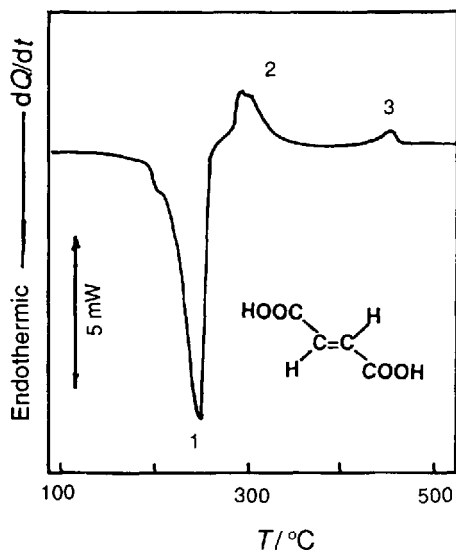


Figure 8.32 DSC curve of fumaric acid

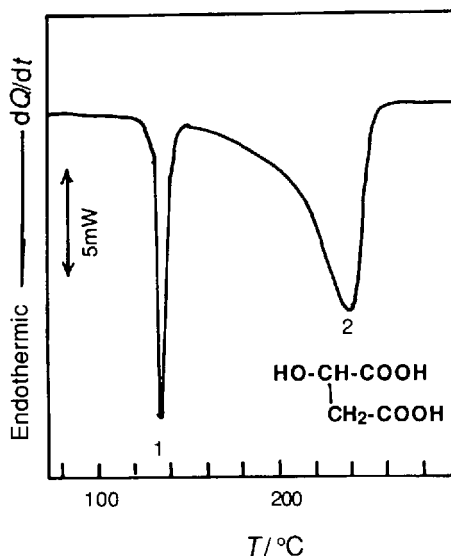


Figure 8.33 DSC curve of malic acid

Sample

Malic acid ($C_4H_6O_5$, $M_r = 134.09$), obtained commercially (lot number DL-960403).

Measurements

Sample mass 2.171 mg.

Results

Peak 1 (melting), T_i 384.56 K (111.41 °C), T_e 403.85 K (130.70 °C), T_p 406.96 K (133.81 °C); peak 2 (vaporization and decomposition), T_i 420.26 K (147.11 °C), T_p 511.50 K (238.35 °C), T_f 530.90 K (257.75 °C).

Reference data

Colourless to white crystalline powder; m.p. 128 °C; b.p. 150 °C; T_d 180 °C [31].

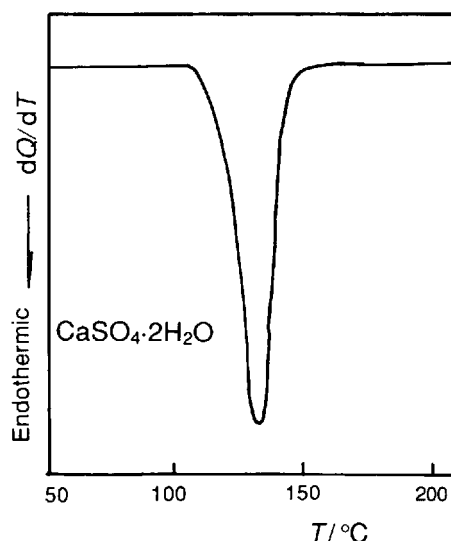


Figure 8.34 DSC curve of calcium sulfate

Sample

Calcium sulfate ($CaSO_4 \cdot 2H_2O$, $M_r = 172.18$), obtained commercially (chemically pure reagent).

Measurements

Sample mass 1.151 mg.

Results

Peak (dehydration), T_i 377.62 K (104.47 °C), T_e 389.15 K (116.00 °C), T_p 406.30 K (133.15 °C), T_f 427.69 K (154.54 °C). TG measurement results (Shimadzu TGA-50, flow-rate of N_2 20 ml min⁻¹, sample mass 2.616 mg): range of dehydration temperature 110.66–158.25 °C; $\alpha = 20.543\%$.

Reference data

When heated to 100 °C, $CaSO_4 \cdot 2H_2O$ lost $1\frac{1}{2}$ H_2O to give $CaSO_4 \cdot \frac{1}{2} H_2O$ [32], then it lost the remaining H_2O at 163 °C [33]. M.p. ($CaSO_4$) 1360 °C [34].

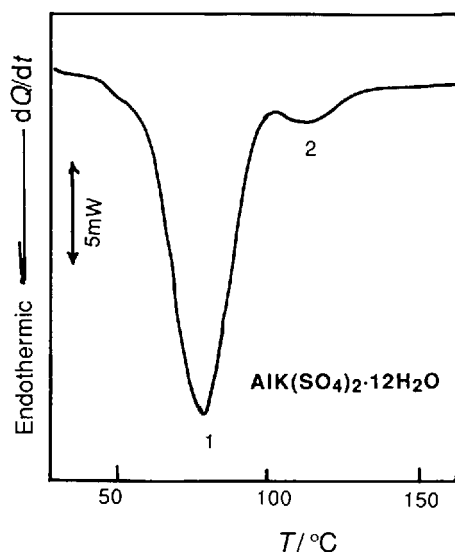


Figure 8.35 DSC curve of aluminum potassium sulfate

Sample

Aluminum potassium sulfate $[\text{AlK}(\text{SO}_4)_2 \cdot 12\text{H}_2\text{O}]$, $M_r = 474.39$, Anhui Lujiang Alum Mine [GB 1895-80, $\text{AlK}(\text{SO}_4)_2$ content $>99.0\%$, dry basis).

Measurements

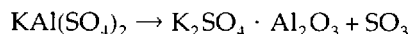
Sample mass 2.455 mg.

Results

Peak 1, T_i 311.37 K (38.22 °C), T_c 332.47 K (59.32 °C), T_p 351.68 K (78.53 °C); peak 2, T_i 374.81 K (101.66 °C), T_p 384.65 K (111.50 °C), T_f 407.88 K (134.73 °C). TG measurement results (Shimadzu TGA-50, $\beta = 10^\circ\text{C min}^{-1}$, sample mass 1.412 mg, static air); α_1 (the first mass loss) = 32.841%, α_2 (the second mass loss) = 12.448% (to 300 °C). DTG gives two peaks; sample contracts after losing water.

Reference data

Measured under the following conditions: static air, heating rate $10^\circ\text{C/min}^{-1}$, sample mass 666.0 mg. Peak (dehydration on DTA curve), T_i 343 °K (70 °C), T_f 653 K (380 °C). Sulfur removal by decomposition (endotherm) from about 760 °C to 950 °C. The reaction is as follows [35]:



There is a loss of 9 mol of crystal water at 92.5 °C and a further loss of 3 mol of crystal water at 200 °C, leading to a white powder after loss of water.

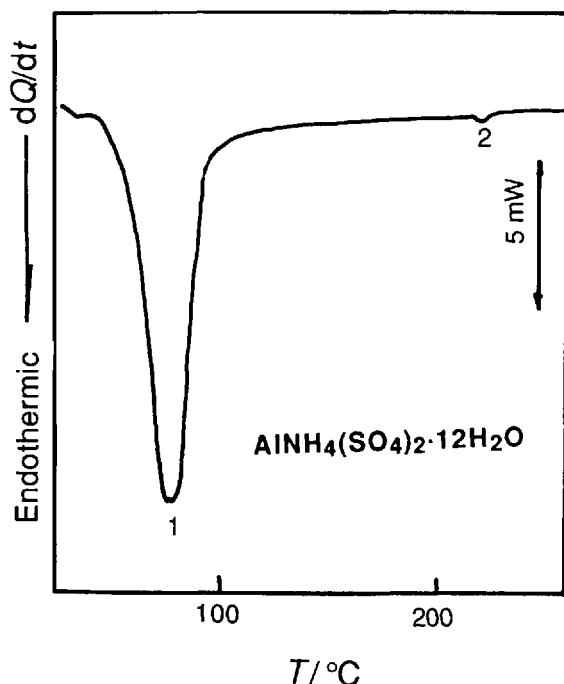


Figure 8.36 DSC curve of aluminum ammonium sulfate

Sample

Aluminum ammonium sulfate $[\text{AlNH}_4(\text{SO}_4)_2 \cdot 12\text{H}_2\text{O}]$, $M_r = 453.33$, Anhui Lujiang Alum Mine [GB 1896-80, $\text{AlNH}_4(\text{SO}_4)_2$ content >99.0%, dry basis].

Measurements

Sample mass 1.835 mg.

Results

Peak 1, T_i 312.43 K (39.28 °C), T_c 330.51 K (57.36 °C), T_p 350.09 K (76.94 °C); peak 2, T_i 488.25 K (215.10 °C), T_p 492.16 K (219.01 °C). TG measurement results (Shimadzu TGA-50, sample mass 1.547 mg, heating rate $10^\circ\text{C min}^{-1}$, static air); $\alpha = 38.276\%$ (to 126.87 °C), $\alpha = 47.219\%$ (to 300 °C).

Reference data

M.p. 93.5 °C; loss of 10 mol of water on heating to 120 °C with the formation of an anhydrous compound; decomposition at about 280 °C [36].

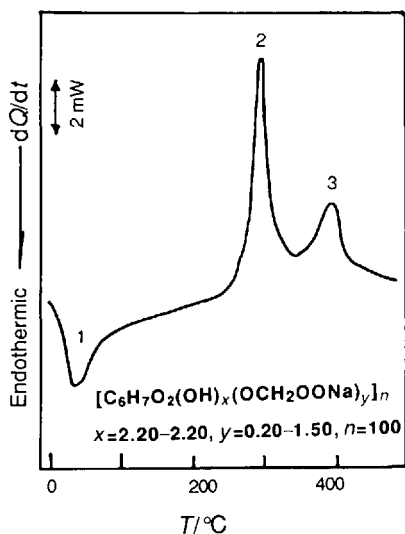


Figure 8.37 DSC curve of sodium carboxymethylcellulose (CMC-Na)

Sample

Sodium carboxymethylcellulose, $[\text{C}_6\text{H}_7\text{O}_2(\text{OH})_x(\text{OCH}_2\text{OONa})_y]_n$, $x = 1.50\text{--}2.80$, $y = 0.20\text{--}1.50$, $n = 100$, Xi'an Hui'an Fine Chemical Industry, (GB1904-89, model FH6).

Measurements

Sample mass 1.521 mg.

Results

Peak 1 (dehydration), T_p 313.87 K (40.72 °C); peak 2 (decomposition), T_i 526.60 K (253.45 °C), T_c 549.05 K (275.90 °C), T_p 574 K (301.60 °C); peak 3, T_i 622.35 K (349.20 °C), T_p 671.96 K (398.81 °C), T_f 710 K (437 °C).

Reference data

Turns brown at 226–228 °C; carbonized at 252–253 °C [37].

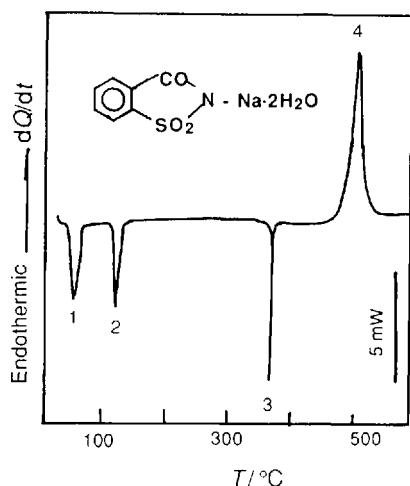


Figure 8.38 DSC curve of sodium saccharin

Sample

Sodium saccharin ($C_7H_4O_3NSNa \cdot 2H_2O$, $M_r = 241.21$), obtained commercially (GB 4578-84, content >99.0%, dry basis).

Measurements

Sample mass 1.213 mg.

Results

Peak 1 (dehydration), T_i 308.31 K (35.16 °C), T_e 316.76 K (43.61 °C), T_p 328.51 K (55.36 °C); peak 2 (dehydration), T_i 382.07 K (108.92 °C), T_e 386.48 K (113.33 °C), T_p 394.17 K (121.02 °C); peak 3 (melting), T_i 629.22 K (356.07 °C), T_e 636.71 K (363.56 °C), T_p 638.78 K (365.63 °C); peak 4 (decomposition), T_i 704.07 K (430.92 °C), T_e 755.80 K (482.65 °C), T_p 776.18 K (503.03 °C). TG measurement results (Shimadzu TGA-50, sample mass 2.916 mg, static air): α_1 (the first mass loss) = 8.996% (36.60–95.00 °C), α_2 (the second mass loss) = 5.451% (96.62–300.94 °C), α_3 (the third mass loss) = 29.976% (302.89–559.70 °C). When measured under conditions of static air, LCT model thermal analyzer (Beijing Optical Instrument Factory), sample mass 3.9 mg, and heating rate 10 °C min^{-1} the sample was first oxidized and decomposed (exotherm), then reached the melting point and formed an obvious exothermic peak; the size can affect the oxidation and decomposition before melting.

Reference data

White prism-like crystals; m.p. 226–231 °C [38].

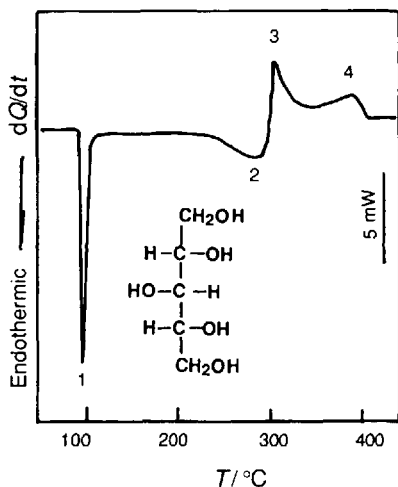


Figure 8.39 DSC curve of xylitol

Sample

Xylitol ($C_5H_{12}O_5$, $M_r = 152.15$), Hebei Baoding Second Chemical Plant (enterprise standard Q/ZHJ 08.04-94, content >99.5%).

Measurements

Sample mass 1.841 mg.

Results

Peak 1 (melting), T_i 363.76 K (90.61 °C), T_e 365.20 K (92.05 °C), T_p 367.64 K (94.49 °C); T_i 382.84 K (109.59 °C); peak 2 (vaporization and decomposition), T_i 481.63 K (208.48 °C), T_p 563.27 K (290.12 °C); peak 3 (decomposition), T_i 563.27 K (290.12 °C), T_p 577.10 K (303.95 °); peak 4 (further decomposition).

Reference data

White crystals or crystalline powder, melting range 92–96 °C [39].

Sample

Glycerin monostearate ($C_{21}H_{42}O_4$, $M_r = 358.56$), Shanghai Yan'an Grease Chemical Plant (GB 1986-89, solidifying point >54.0 °C).

Measurements

Sample mass 1.980 mg.

Results

Peak 1 (melting), T_i 313.15 K (40 °C), T_e 327.13 K (53.98 °C), T_p 330.04 K (56.89 °C), T_i 348.04 K (74.89 °C); peak 2 (exotherm), from 245.82 °C, T_p 561.03 K (287.88 °C).

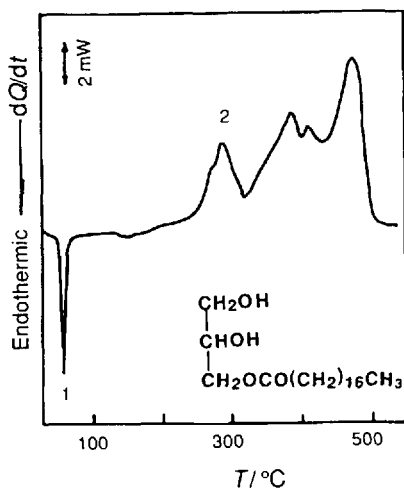


Figure 8.40 DSC curve of glycerin monostearate

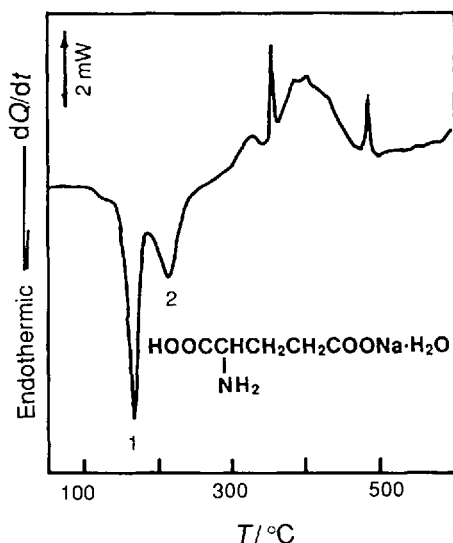


Figure 8.41 DSC curve of sodium glutamate

Sample

Sodium glutamate ($\text{C}_5\text{H}_8\text{O}_4\text{NNa}\cdot\text{H}_2\text{O}$, levorotatory, $M_r = 187.13$), Shenyang Gourmet Powder Factory (GB8967-88, content >99.0%).

Measurements

Sample mass 2.120 mg.

Results

Peak 1 (dehydration), T_i 411.81 K (138.66 °C), T_p 438.71 K (165.56 °C); peak 2 (dehydration in molecule and decomposition), T_i 456.09 K (182.94 °C), T_p 483.59 K (210.44 °C), T_f 516.66 K (243.51 °C). Decomposition exothermically from 252 to 600 °C; residue 1.022 mg.

Reference data

Dehydration at 120 °C. Sodium pyroglutamate was formed at 155–160 °C [40].

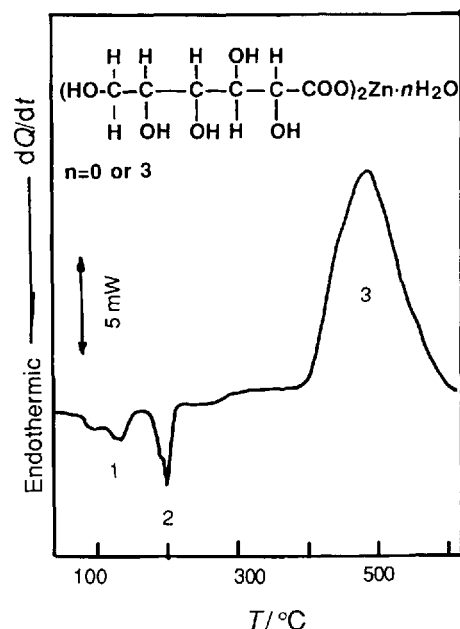


Figure 8.42 DSC curve of zinc gluconate

Sample

Zinc gluconate ($\text{C}_{12}\text{H}_{22}\text{O}_{14}\text{Zn}\cdot n\text{H}_2\text{O}$, $M_r = 455.68$ $n = 0$ or 3 [41]), synthesized in our laboratories.

Measurements

Sample mass 1.683 mg.

Results

Peak 1 (dehydration), T_i 340.27 K (67.12 °C), T_f 421 K (148 °C); peak 2 (melting and decomposition), T_i 421 K (148 °C), T_p 466.14 K (192.99 °C), T_f 484.94 K (211.789 °C), baseline tending to exotherm from about 162 °C; peak 3 (decomposition), T_i 642.25 K (369.10 °C), T_e 671.39 K (398.24 °C), T_p 752.91 K (479.76 °C), residue 0.341 mg at 600.43 °C.

Reference data

Zinc gluconate (food grade): content 97.0%–102.0% ($C_{12}H_{22}O_{14}Zn$), moisture content <11.6% (GB8820-88) [42]. Measured under the following conditions: static air, LCT model thermal analyzer (Beijing Optical Instrument Factory), heating rate $10^{\circ}C\ min^{-1}$, using DTA and EGD; results [43]:

1. $C_{12}H_{22}O_{14}Zn \cdot nH_2O \xrightarrow{103\ 150^{\circ}C} C_{12}H_{22}O_{14}Zn + nH_2O$
2. $C_{12}H_{22}O_{14}Zn \xrightarrow{159\ 211^{\circ}C} CO + CO_2 + H_2O + C + \text{organic residue} + ZnCO_3$
3. Oxidative decomposition and carbon burning at 211–566 $^{\circ}C$, final product ZnO .
4. The actual content of water is related to the technological process and affected the shape of the dehydration peak.

8.3 References

- 1 Miyoshi, E., Takaya, T., and Nishinari, K., *Thermochim. Acta*, 1996, **267**, 269.
- 2 Miyoshi, E., Takaya, T., and Nishinari, K., *Food Hydrocolloids*, 1994, **8**, 529.
- 3 Nagano, T., Mori, H., and Nishinari, K., *J. Agric. Food Chem.*, 1994, **42**, 1415.
- 4 Nagano, T., Mori, H., and Nishinari, K., *Biopolymers*, 1994, **34**, 293.
- 5 Kohyama, K. and Nishinari, K., *J. Agric. Food Chem.*, 1991, **39**, 1406.
- 6 Kohyama, K., Sano, Y., and Nishinari, K., *Food Hydrocolloids*, 1996, **10**, 229.
- 7 Nishinari, K., Watase, M., Rinaudo, M., and Milas, M., *Food Hydrocolloids*, 1996, **10**, 277.
- 8 Yoshimura, M., Takaya, T., and Nishinari, K., *J. Agric. Food Chem.*, 1996, **44**, 2970.
- 9 Phillips, G. O., Takigami, S., and Takigami, M., *Food Hydrocolloids*, 1996, **10**, 11.
- 10 Fujimura, T., and Kugimiya, M., *Nippon Shokuhin Kogyo Gakkaishi*, 1994, **41**, 206.
- 11 Fujimura, T., and Kugimiya, M., *Nippon Shokuhin Kogyo Gakkaishi*, 1993, **40**, 702.
- 12 Sa, M. M., and Sereno, A. M., *Thermochim. Acta*, 1994, **246**, 285.
- 13 Ablett, S., Izzard, M. J., and Lillford, P. J., *J. Chem. Soc., Faraday Trans.*, 1992, **88**, 789.
- 14 Ling Guanting, Wang Yiyun and Tang Shuchao, *Handbook of Food Additives*. Beijing, Chemical Industry Press, 1989, Vol. 1, p. 287 (in Chinese).
- 15 Heilbron, I., et al. (translated by Nature Science Noun Copy Editor Group of the Chinese Academy of Sciences), *Dictionary of Organic Compounds (I)*. Beijing, Science Press, 1964, p. 386.
- 16 Wang Jian, et al., *Chemical Industry Dictionary*, 2nd edn. Beijing, Chemical Industry Press, 1979, p. 321 (in Chinese).
- 17 Heilbron, I., et al. (translated by Nature Science Noun Copy Editor Group of Chinese Academy of Sciences), *Dictionary of Organic Compounds (II)*. Science Press, Beijing, 1964, p. 545.
- 18 Teaching and Research Section of Food Industry in Tianjin Institute of Light Industry, *Food Additives*. Beijing, Light Industry Press, 1993, p. 20.
- 19 Liptay, G., (Weng Zuqi, transl.) *Atlas of Thermoanalytical Curves*. Jiangsu, Jiangyin Changjing Instrument Factory, 1978, p. 133.
- 20 Jin Shijun, *Food Additives—Current Situation, Production, Performance and Application*. Shanghai, East China Institute of Chemical Industry, 1992, p. 314.
- 21 Zhang Sigui, et al., *Technical Handbook of Fine Organic Chemicals*. Beijing, Science Press, 1992, pp. 999 and 1524.
- 22 Zhang Sigui, et al. *Technical Handbook of Fine Organic Chemicals (II)*. Beijing, Science Press, 1992, p. 1070.
- 23 Duan Mugan et al., *Dictionary of Chemistry, Chemical Engineering and Medicines*. Taizhong, Humanities Press, 1985, p. 3372.
- 24 Zhang Sigui, et al., *Technical Handbook of Fine Organic Chemicals*, Beijing, Science Press, 1992, p. 1523.
- 25 Ma Tongjiang and Yang Guanfeng, *New Handbook of Food Additives*. Beijing, Countryside Readings Press, 1989, p. 66.
- 26 Pan Gongpei, *Handbook of Pyrotechnic Material*, Nanjing, East China Institute of Technology, 1983, p. 379.
- 27 Ma Tongjiang and Yang Guanfeng, *New Handbook of Food Additives*, Countryside Readings Press, Beijing, 1989, p. 84.
- 28 Heilbron, I., et al., (translated by Nature Science Noun Copy Editor Group of Chinese Academy of Sciences), *Dictionary of Organic Compounds (I)*. Beijing, Science Press, 1964, p. 902.
- 29 Heilbron, I., et al., (translated by Nature Science Noun Copy Editor Group of Chinese Academy of Sciences), *Dictionary of Organic Compounds (II)*. Beijing, Science Press, 1964, p. 870.
- 30 Ling Guanting, Wang Yiyun and Tang Shuchao, *Handbook of Food Additives (I)*. Beijing, Chemical Industry Press, 1989, p. 260.
- 31 Ling Guanting, Wang Yiyun and Tang Shuchao, *Handbook of Food Additives*, Vol. 1, Beijing, Chemical Industry Press, 1989, p. 190.
- 32 Fan Jishan, et al., *Practical Food Additives*. Tianjin, Tianjin Science and Technology Press, 1993, p. 41.

- 33 Chemical Engineering Department, Tianjin Chemical Engineering Research Institute, *Handbook of Chemicals (Inorganic Chemicals)*. Beijing, Chemical Industry Press, 1982, p. 421.
- 34 Duan Mugan, et al., *Dictionary of Chemistry, Chemical Engineering and Medicine*. Taizhong, Humanities Press, 1985, p. 2715.
- 35 Liptay, G. (Weng Zhuqi, transl.), *Thermoanalysis Atlas*. Jiangsu, Jiangyin Changjing Instrument Plant, 1978, p. 55.
- 36 Chemical Engineering Department, Tianjin Chemical Engineering Research Institute, *Handbook of Chemicals (Inorganic Chemicals)*. Beijing, Chemical Industry Press, 1982, p. 472.
- 37 Ma Tongjiang and Yang Guanfeng, *New Handbook of Food Additives*. Beijing, Countryside Readings Press, 1989, p. 251.
- 38 Zhang Sigui, et al., *Technical Handbook of Fine Organic Chemicals (II)*. Beijing, Science Press, 1992, p. 1575.
- 39 Fan Jishan, et al., *Practical Food Additives*. Tianjin, Tianjin, Science and Technology Press, 1993, p. 71.
- 40 Ma Jongjiang and Yang Guanfeng, *New Handbook of Food Additives*. Beijing, Countryside Readings Press, 1989, p. 153.
- 41 Ling Guanting, Wang Yiyun and Tang Shuchao, *Handbook of Food Additives (I)*. Beijing, Chemical Industry Press, 1989, p. 39.
- 42 Fan Jishan, et al., *Practical Food Additives*, Tianjin, Tianjin Science and Technology Press, 1993, p. 282.
- 43 Chai Zhengqian, Xi Yuyie, Hu Jianping and Hu Xiaowen, *Thermal Analysis Studies on Zinc Gluconate*, Nanjing, Jiangsu Chemical Industry, 1992, Vol. 3, p. 51.

Thermal Analysis Curves of Plant Materials

This chapter covers the thermal analysis curves of plant materials and their components, such as cellulose, wood, bark and wheat straw.

Sample

Cotton cellulose, 200–300 mesh, Japan Toyo Roshi Kaisha.

Measurements

Rigaku Thermal Analysis Station TAS-100; sample mass *ca* 2 mg; heating rate $10^{\circ}\text{C min}^{-1}$; furnace atmosphere I, N_2 and II, air; flow-rate 20 ml min^{-1} .

Results

Results are given in Table 9.1.

Table 9.1

Sample No.	First stage		Second stage	
	Temperature range $^{\circ}\text{C}$	Mass loss %	Temperature range $^{\circ}\text{C}$	Mass loss %
I	269.4–408.1	84.9	408.1–600.2	8.5
II	263.6–371.3	81.1	371.3–513.7	13.6

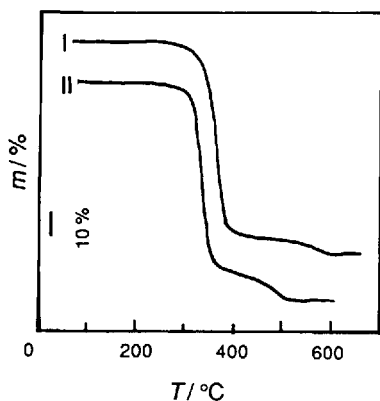


Figure 9.1 TG curves of cotton cellulose in various atmospheres

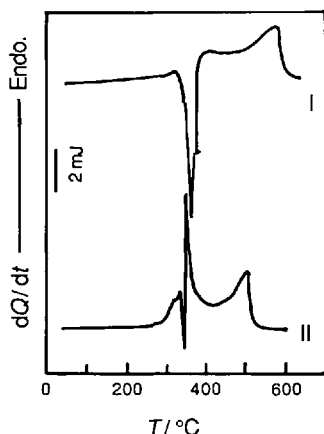


Figure 9.2 DSC curves of cotton cellulose in various atmospheres

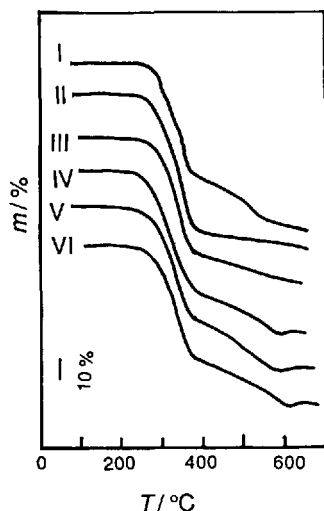


Figure 9.3 TG curves of wood in a dynamic N_2 atmosphere. I, Larch; II, birch; III, metasequoia; IV, diversiform-leaved poplar; V, spruce; VI, shash pine

Sample

As for Figure 9.1.

Measurements

As for Figure 9.1.

Results

Results are given in Table 9.2.

Table 9.2

Sample No.	Initial decomposition temperature/°C
I	326.8
II	273.6

Sample

Wood samples were collected from different parts of the tree. After air-drying each sample was ground to pass a 40–60 mesh sieve and mixed homogeneously.

Measurements

Rigaku Thermal Analysis Station TAS-100; sample mass *ca* 2 mg; heating rate $10\text{ }^{\circ}\text{C min}^{-1}$; furnace atmosphere N_2 ; flow-rate 20 ml min^{-1} .

Results

Wood is a natural organic material consisting primarily of cellulose, hemicelluloses, lignin and various extractives. The amount and nature of each component vary considerably with tree species and tree parts. TG results are given in Table 9.3.

Table 9.3

Sample No.	First stage		Second stage	
	Temperature range °C	Mass loss %	Temperature range °C	Mass loss %
I	238.8–385.7	61.4	385.7–629.5	27.6
II	237.2–396.2	71.7	396.2–646.9	9.2
III	225.6–390.2	61.4	390.2–646.5	16.0
IV	225.4–379.3	61.7	379.3–590.9	23.3
V	235.0–384.5	59.0	384.5–572.8	26.9
VI	226.1–378.9	58.5	378.9–617.8	26.4

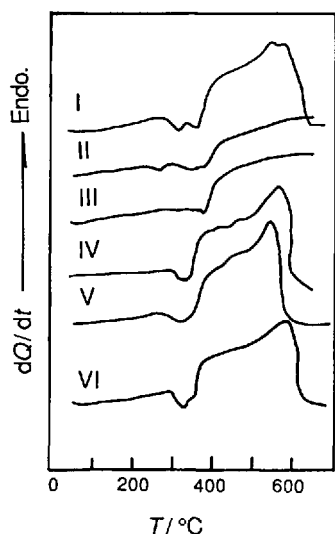


Figure 9.4 DSC curves of wood in a dynamic N_2 atmosphere. I–VI as for Figure 9.3

Samples

As for Figure 9.3.

Measurements

As for Figure 9.3.

Results

Results are given in Table 9.4.

Table 9.4

Sample No.	Initial decomposition temperature/ $^{\circ}C$
I	271.3
II	244.1
III	282.3
IV	196.0
V	296.3
VI	235.5

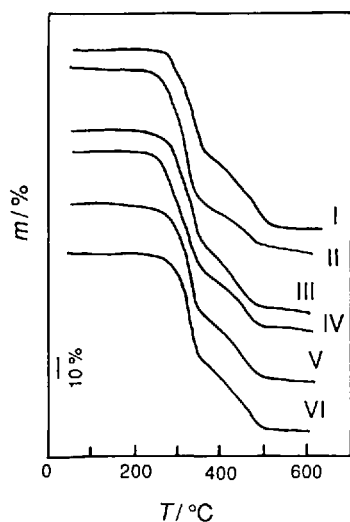


Figure 9.5 TG curves of wood in static air. I–VI as in Figure 9.3

Samples

As for Figure 9.3.

Measurements

As for Figure 9.3, except that the furnace atmosphere was static air.

Results

Results are given in Table 9.5.

Table 9.5

Sample No.	First stage		Second stage	
	Temperature range $^{\circ}C$	Mass loss %	Temperature range $^{\circ}C$	Mass loss %
I	244.2–366.1	53.6	366.1–528.8	35.5
II	232.0–350.5	66.0	350.5–497.4	22.1
III	225.9–356.6	57.1	356.6–483.9	32.4
IV	223.2–354.2	58.8	354.2–496.0	30.8
V	236.4–357.2	54.4	357.2–491.7	32.3
VI	222.9–355.2	54.6	355.2–502.9	34.4

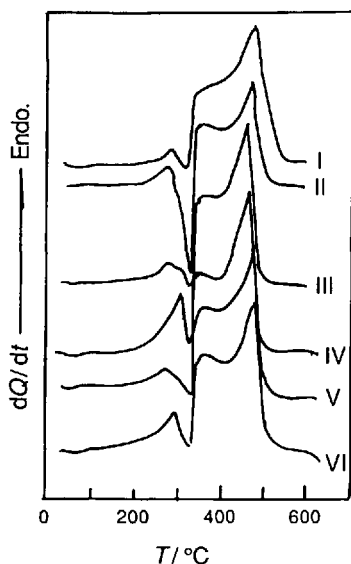


Figure 9.6 DSC curves of wood in static air. I–VI as in Figure 9.3

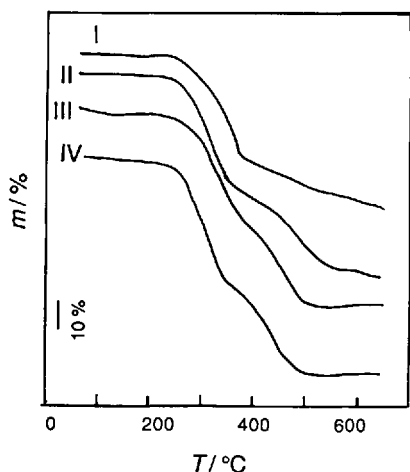


Figure 9.7 TG curves of bark and its components in different atmospheres. I, Thumb bark, dynamic N_2 ; II, holocellulose from thumb bark, dynamic N_2 ; III, thumb bark, static air; IV, holocellulose from thumb bark, static air

Samples

As for Figure 9.3.

Measurements

As for Figure 9.3, except that the furnace atmosphere was static air.

Results

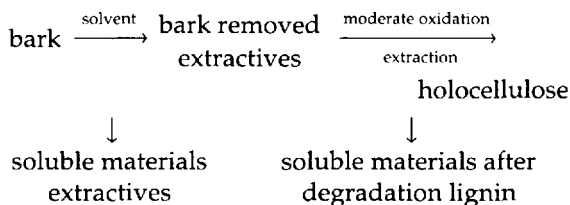
Results are given in Table 9.6.

Table 9.6

Sample No.	Initial decomposition temperature/°C
I	236.1
II	207.1
III	216.6
IV	184.1
V	198.8
VI	176.0

Samples

Bark samples were collected from different parts of the tree. After air-drying, each sample was ground to pass a 40–60 mesh sieve and mixed homogeneously. Samples were prepared as follows:



Measurements

Rigaku Thermal Analysis Station TAS-100; sample mass *ca* 2 mg; heating rate $10\text{ }^{\circ}\text{C min}^{-1}$; furnace atmosphere N_2 or air; flow-rate 20 ml min^{-1} .

Results

Chemical components of bark, which can also be divided into cellulose, hemicelluloses, lignin and extractives, are similar to those of wood. The content of each component of bark is very different from that of the components of wood. Bark contains large amounts of phenolic acids, lignin, extractives, ash and more cork fat, but much less cellulose and hemicellulose compared with wood. TG results are given in Table 9.7.

Table 9.7

Sample No.	First stage		Second stage	
	Temperature range °C	Mass loss %	Temperature range °C	Mass loss %
I	228.3–387.7	43.4	387.7–647.5	19.2
II	218.5–369.6	47.9	369.6–629.7	34.3
III	224.8–376.3	44.7	376.3–506.1	33.3
IV	209.3–366.3	52.1	366.3–501.9	32.9

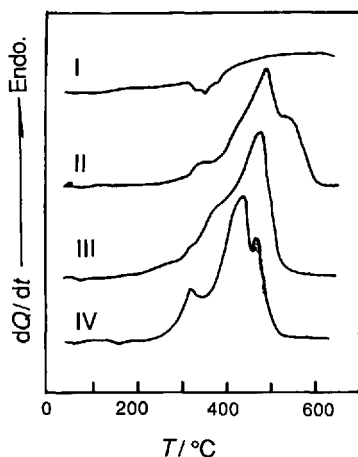


Figure 9.8 DSC curves of bark and its components in different atmospheres. I–IV as in Figure 9.7

Samples

As for Figure 9.7.

Measurements

As for Figure 9.7.

Results

Results are given in Table 9.8.

Table 9.8

Sample No.	Initial decomposition temperature/°C
I	315.5
II	293.4
III	206.0
IV	228.0

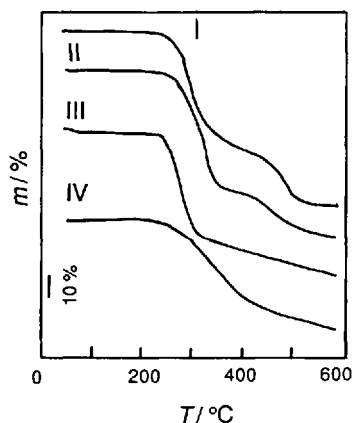
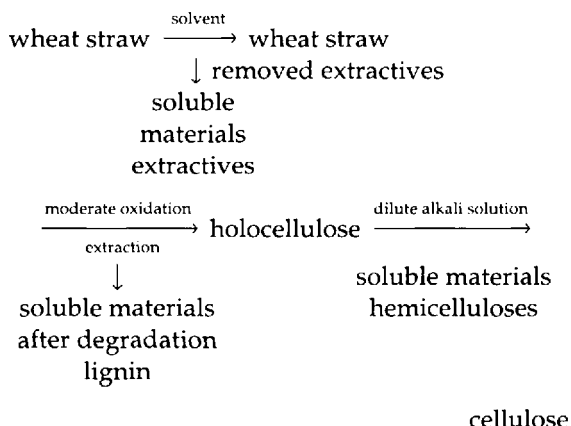


Figure 9.9 TG curves of wheat straw and its components in a dynamic N_2 atmosphere. I, wheat straw; II, wheat straw holocellulose; III, wheat straw hemicellulose; IV, wheat straw lignin

Samples

Samples were prepared as follows:



Measurements

Rigaku Thermal Analysis Station TAS-100; sample mass *ca* 2 mg; heating rate $10\text{ }^{\circ}\text{C min}^{-1}$; furnace atmosphere N_2 ; flow-rate 20 ml min^{-1} .

Results

Chemical components of wheat straw can be divided into cellulose, hemicellulose, lignin and extractives. The content and structure of each component for wheat straw are very different to those for wood. TG results are given in Table 9.9.

Table 9.9

Sample No.	First stage		Second stage	
	Temperature range $^{\circ}\text{C}$	Mass loss %	Temperature range $^{\circ}\text{C}$	Mass loss %
I	219.7–352.4	51.7	352.4–527.8	31.6
II	227.3–362.9	57.5	362.9–556.6	24.7
III	210.7–310.1	51.6	310.1–598.0	20.5
IV	209.3–412.0	40.6	412.0–597.8	15.3

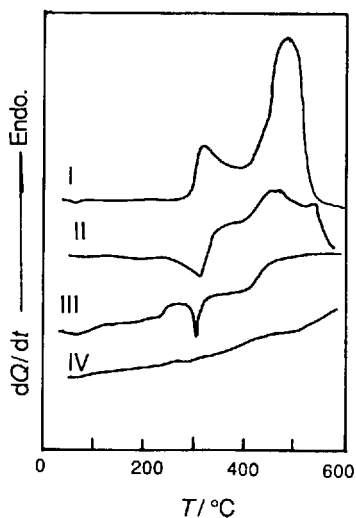


Figure 9.10 DSC curves of wheat straw and its components in a dynamic N_2 atmosphere. I–IV as in Figure 9.9

Samples

As for Figure 9.9.

Measurements

As for Figure 9.9.

Results

Results are given in Table 9.10.

Table 9.10

Sample No.	Initial decomposition temperature °C
I	262.0
II	245.2
III	225.6
IV	197.7

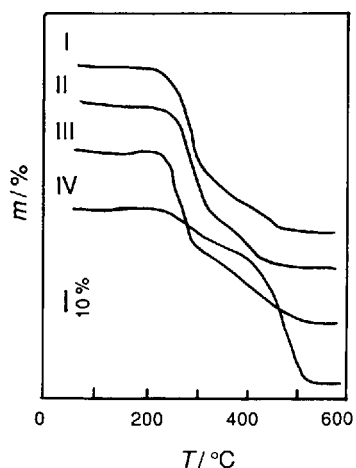


Figure 9.11 TG curves of wheat straw and its components in static air. I–IV as in Figure 9.9

Samples

As for Figure 9.9

Measurements

As for Figure 9.9, except that the furnace atmosphere was static air.

Results

Results are given in Table 9.11.

Table 9.11

Sample No.	First stage		Second stage	
	Temperature range °C	Mass loss %	Temperature range °C	Mass loss %
I	213.2–329.9	54.9	329.9–475.2	26.3
II	213.0–331.6	53.8	331.6–468.8	26.5
III	213.3–298.4	46.1	298.4–491.2	36.5
IV	204.3–333.5	17.2	333.5–528.9	68.8

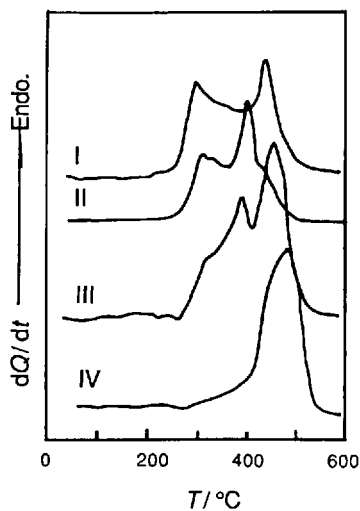


Figure 9.12 DSC curves of wheat straw and its components in static air. I–IV as in Figure 9.9

Samples

As for Figure 9.9.

Measurements

As for Figure 9.9, except that the furnace atmosphere was static air.

Results

Results are given in Table 9.12.

Table 9.12

Sample No.	Initial decomposition temperature/°C
I	204.7
II	220.8
III	211.6
IV	203.2

Thermal Analysis Curves of Minerals

Thermal analysis is widely used in the investigation of minerals, e.g. for identification, quantitative analysis and studies of isomorphism, water existence, etc. [1–7]. In this chapter, more than 400 TA curves of minerals are collected in 138 figures which are derived from data obtained at the author's laboratory. Furthermore, data are cited from Ref. [3].

Measurement conditions were as follows: Apparatus, LCT-2B thermal analyzer (Beijing Optical Instrument Factory); sample mass, 10 mg (unless indicated otherwise); reference material, Al_2O_3 (10 mg); heating rate, $20^\circ\text{C min}^{-1}$; atmosphere, static air; thermocouple Pt–Pt/Rh; cru-

cible, Pt or ceramic. Data in Ref. 3 were obtained using an LCT-2 thermal analyzer (Beijing Optical Instrument Factory).

10.1 Thermal Analysis Curves of Natural Elements

The major thermal properties of natural elements are characterized by melting. Polymorphic transformations and oxidation are also observed by heating process.

Sample

Sulfur, S.

Experimental conditions

Amount of sample 100 mg + 20 mg Al_2O_3 ; reference material 150 mg annealed Al_2O_3 ; thermocouples Pt–Pt₉₀/Rh₁₀; ϕ 0.1–0.3 mm; heating rate $10^\circ\text{C min}^{-1}$; furnace atmosphere air.

Results

96°C endotherm, structural transformation from orthorhombic to monoclinic form; 130°C endotherm, melting (melting point of sulfur: 119°C [2]); 380°C exotherm, sulfur oxidizes to SO_2 .

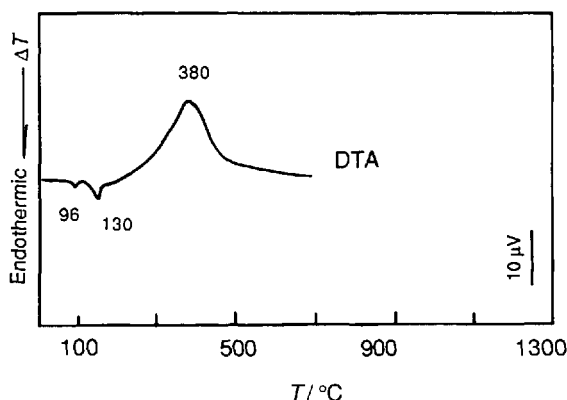


Figure 10.1 DTA curves of sulfur [3]

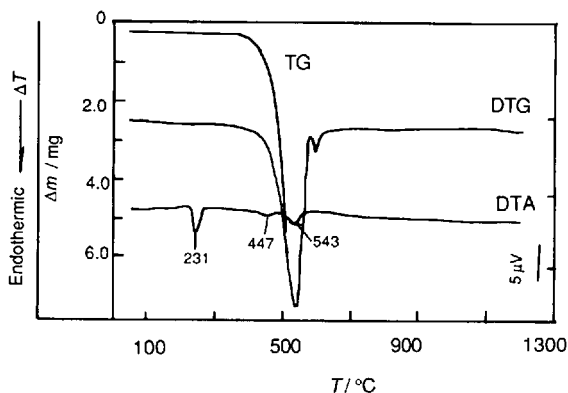


Figure 10.2 DTA-TG-DTG curves of selenium [3]

Sample

Selenium, Se.

Experimental conditions

Amount of sample 10 mg; reference material 10 mg; heating rate $10^{\circ}\text{C min}^{-1}$; furnace atmosphere air.

Results

231 °C endotherm, melting (melting point of selenium: 217 °C [2]); 447 °C endotherm, evaporation of molten selenium accompanied by a mass loss.

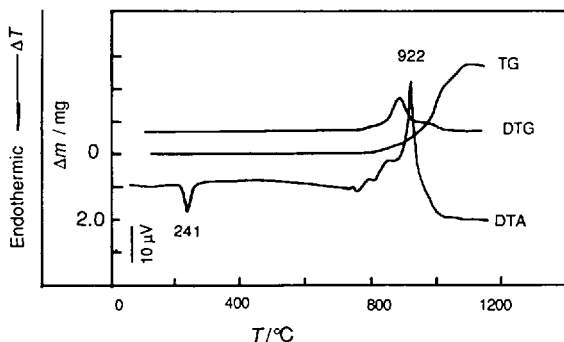


Figure 10.3 DTA-TG-DTG curve of tin

Sample

Tin, Sn.

Results

241 °C endotherm, melting of tin (melting point of tin: 231.91 °C [2]); 922 °C exotherm, oxidation of tin, generates SnO_2 accompanied by a mass increase.

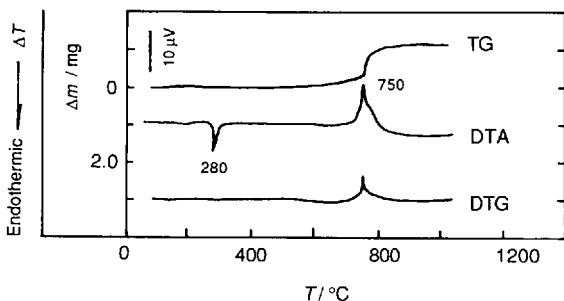


Figure 10.4 DTA-TG-DTG curve of bismuth

Sample

Bismuth, Bi.

Results:

280 °C endotherm, melting (melting point of bismuth: 273.1 °C [2]); 750 °C exotherm, molten bismuth oxidizes to Bi_2O_3 .

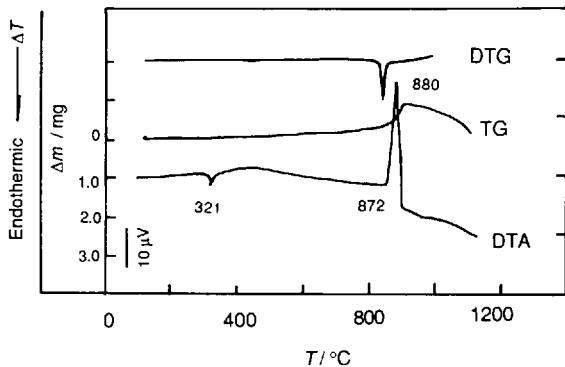


Figure 10.5 DTA-TG-DTG curve of lead

Sample

Lead, Pb.

Results

321 °C endotherm, melting of lead (melting point of lead: 327.3 °C [2]); 872 °C exotherm, oxidation generating PbO, accompanied by a mass increase.

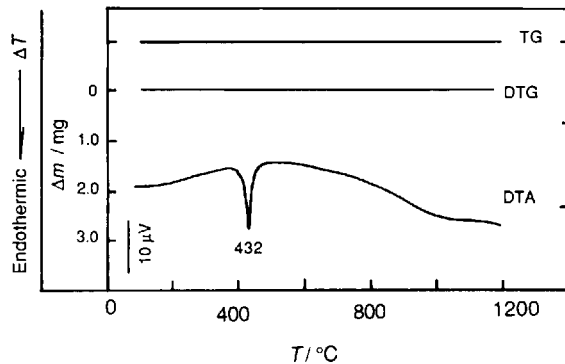


Figure 10.6 DTA-TG-DTG curve of zinc

Sample

Zinc, Zn.

Results

432 °C endotherm, melting (melting point of zinc: 419.4 °C [2]).

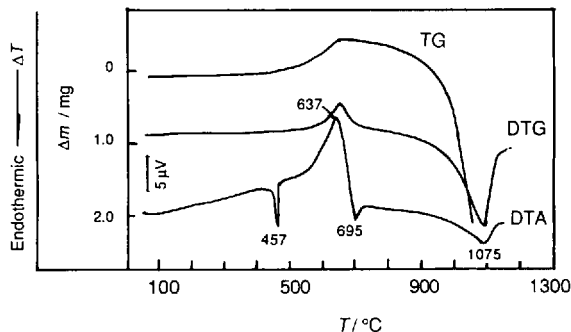


Figure 10.7 DTA-TG-DTG curve of tellurium [3]

Sample

Tellurium, Te.

Results

457 °C endotherm, melting of tellurium (melting point of tellurium: 449.5 °C [2]); 637 °C exotherm, molten tellurium oxidizes to TeO₂; 695 °C endotherm, melting of TeO₂. At temperatures higher than 800 °C, molten tellurium evaporates accompanied by a mass loss.

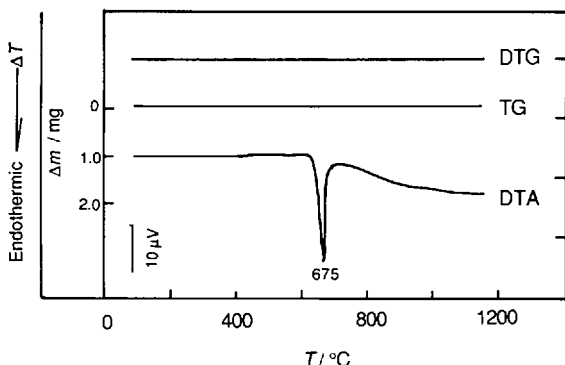


Figure 10.8 DTA-TG-DTG curve of aluminum

Sample

Aluminum, Al.

Results

675 °C endotherm, melting of aluminum (melting point of aluminum: 660.1 °C [2]).

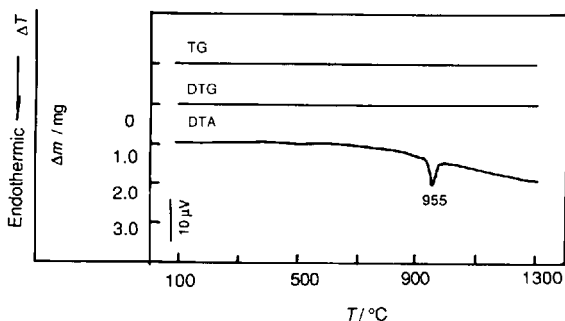


Figure 10.9 DTA-TG-DTG curve of silver

Sample

Silver, Ag.

Results

955 °C endotherm, melting of silver (melting point of silver: 960.8 °C [2]).

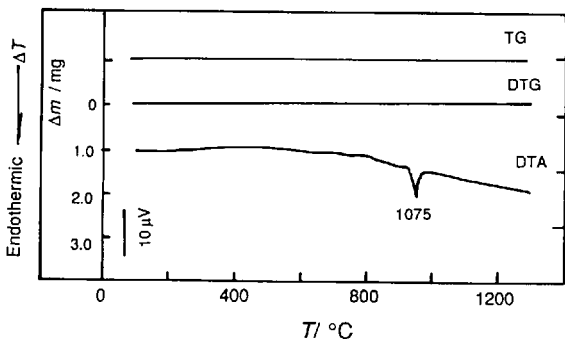


Figure 10.10 DTA-TG-DTG curve of copper

Sample

Copper, Cu.

Results

1075 °C endotherm, melting of copper (melting point of copper: 1083 °C [2]).

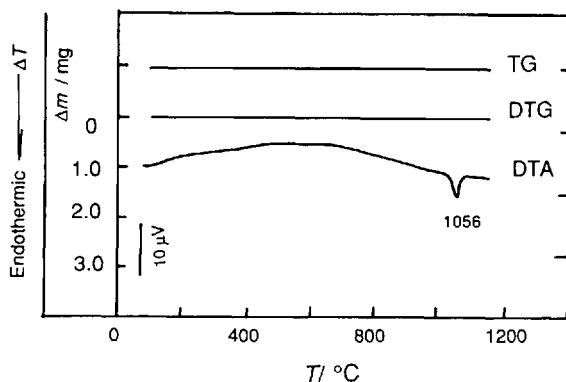


Figure 10.11 DTA-TG-DTG curve of gold

Sample

Gold, Au.

Results

1056 °C endotherm, melting of gold (melting point of gold: 1063.0 °C [2]).

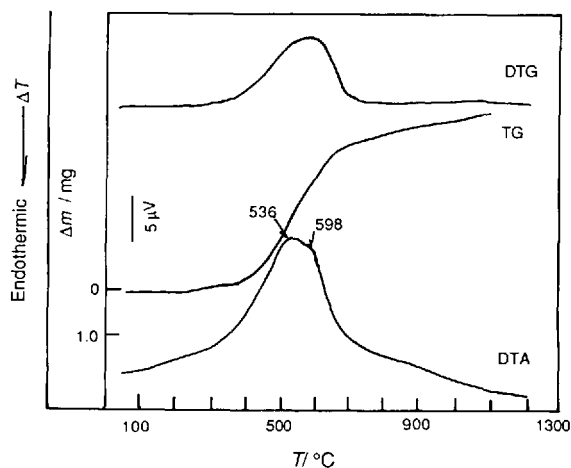


Figure 10.12 DTA-TG-DTG curve of iron [3]

Sample

Iron, Fe.

Results

536 and 598 °C exotherms, iron oxidizes to Fe_3O_4 and Fe_2O_3 .

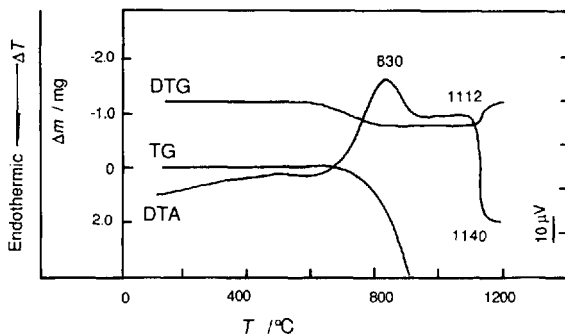


Figure 10.13 DTA-TG-DTG curve of graphite

Sample

Graphite (clay-like), C.

Results

830 °C exotherm, oxidation of graphite starts at 600 °C and generates CO_2 accompanied by a mass loss.

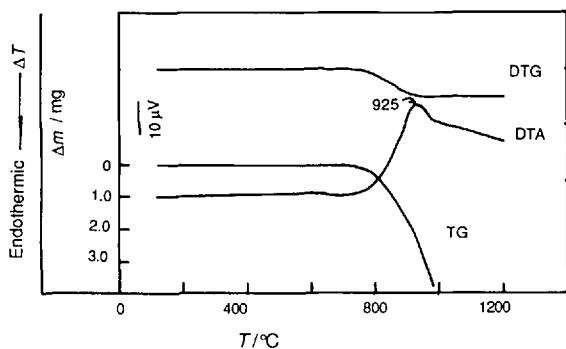


Figure 10.14 DTA-TG-DTG curve of graphite

Sample

Graphite (flakes), C.

Results

925 °C exotherm, oxidation of graphite starts at 800 °C and generation of CO_2 is observed as a mass loss.

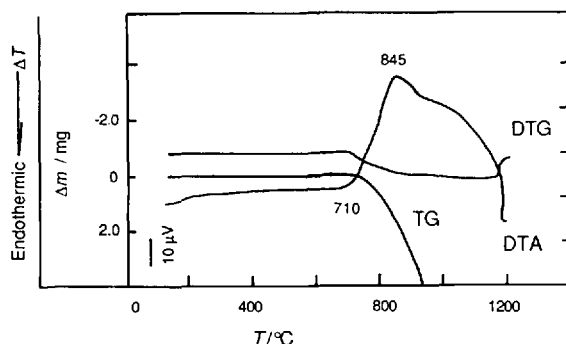


Figure 10.15 DTA-TG-DTG curve of diamond

Sample

Diamond (synthetic), C.

Results

845 °C exotherm, oxidation of diamond starts at 710 °C and generation of CO_2 is observed as a mass loss.

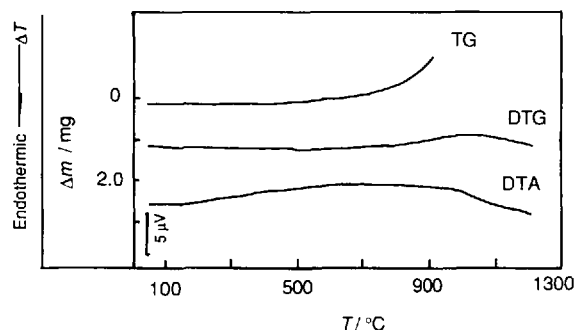


Figure 10.16 DTA-TG-DTG curve of nickel [3]

Sample

Nickel, Ni.

Results

Nickel starts to oxidize at 700 °C and is gradually transformed into NiO and Ni_2O_3 accompanied by mass increase. Melting point of nickel, 1453 °C [2]; melting point of NiO , 1984 °C [4].

10.2 Thermal Analysis Curves of Halide Minerals

The thermal properties of halides are characterized by melting and dehydration of the water present at a particular stage during heating.

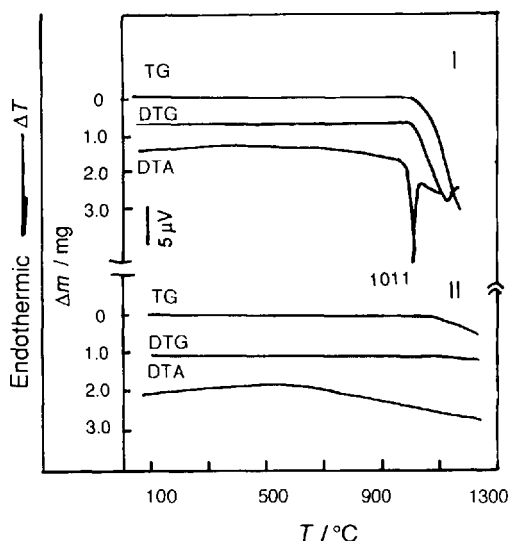


Figure 10.17 DTA-TG-DTG curves of (I) villaumite and (II) fluorite [3]

Samples

I, Villaumite, NaF (Na 54.76%, F 45.24%); II, fluorite, CaF_2 (Ca 51.1%, F 48.9%).

Results

I. Villaumite—1011 °C endotherm, melting of villaumite; after melting evaporation starts (melting point of villaumite: 993 °C [4]).

II. Fluorite—DTA curve shows no changes upto 1200 °C (melting point of fluorite: 1360 °C [2]).

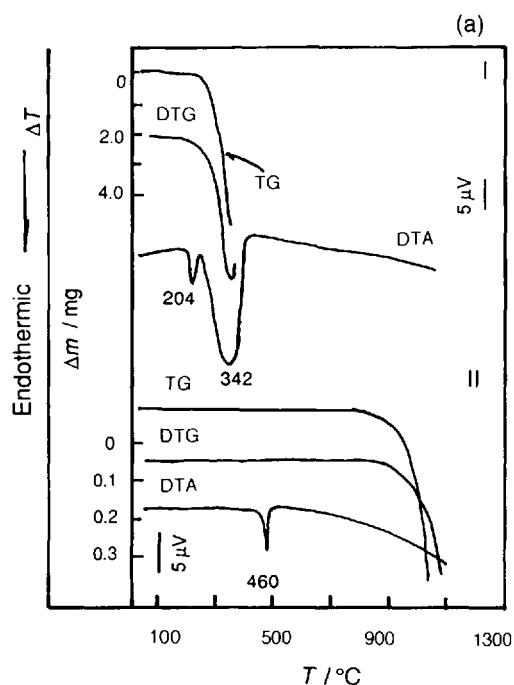


Figure 10.18 (a) DTA-TG-DTG curves of (I) ammoniac and (II) chloragryrite

(continued)

Samples

I, Ammoniac, NH_4Cl ; II, chloragryrite, AgCl ; III, sylvite, KCl ; IV, halite, NaCl .

Results

I. Ammoniac—204 °C endotherm, ammoniac melts; 342 °C endotherm, molten ammoniac evaporates accompanied by a mass loss.

II. Chloragryrite—460 °C endotherm, melting of chloragryrite (melting point of chloragryrite: 436 °C [5]); molten chloragryrite evaporates at a temperature higher than 900 °C.

III. Sylvite—779 °C endotherm, melting of sylvite (melting point of sylvite: 775 °C [3]). Immediately after melting, sylvite evaporates.

IV. Halite—804 °C endotherm, halite melts (melting point of halite: 804 °C [4]), after melting, halite evaporates.

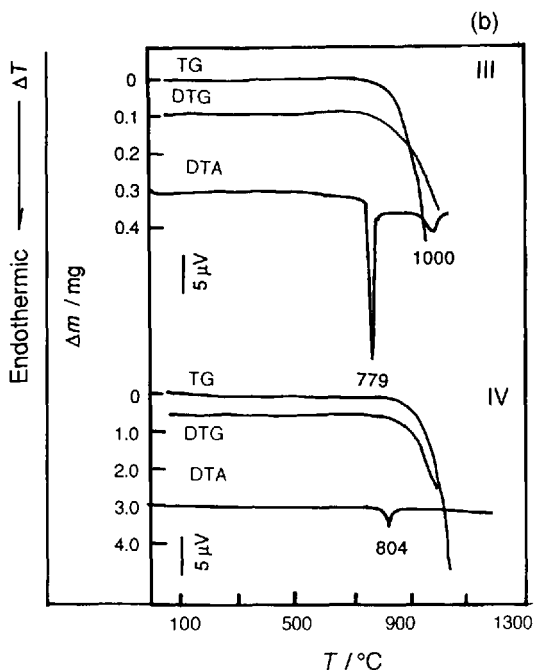


Figure 10.18 (b) DTA-TG-DTG curves of (III) sylvite and (IV) halite [3]

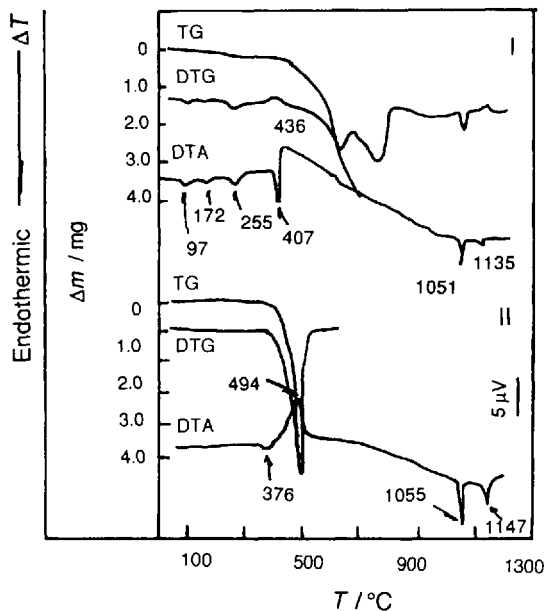


Figure 10.19 DTA-TG-DTG curves of (I) nantokite and (II) marshite [3]

Samples

I, Nantokite CuCl (Cu 64.19%, Cl 35.81%); II, marshite, CuI (Cu 33.37%, I 66.63%).

Results

I. Nantokite—97, 172 and 255 °C endotherms, polymorphic transformation; 407 °C endotherm, nantokite decomposes and evolves Cl_2 accompanied by a mass loss; 436 °C exotherm, Cu oxidizes to CuO ; 1051 °C endotherm, CuO changes to Cu_2O accompanied by a mass loss; 1135 °C endotherm, partial Cu_2O oxidation to CuO .

II. Marshite—376 °C endotherm, marshite undergoes a polymorphic transformation; 494 °C exotherm, marshite decomposes to Cu and I, copper oxidizes to CuO and iodine sublimes accompanied by a mass loss; 1055 °C endotherm, CuO changes to Cu_2O ; 1147 °C endotherm, partial Cu_2O oxidation to CuO .

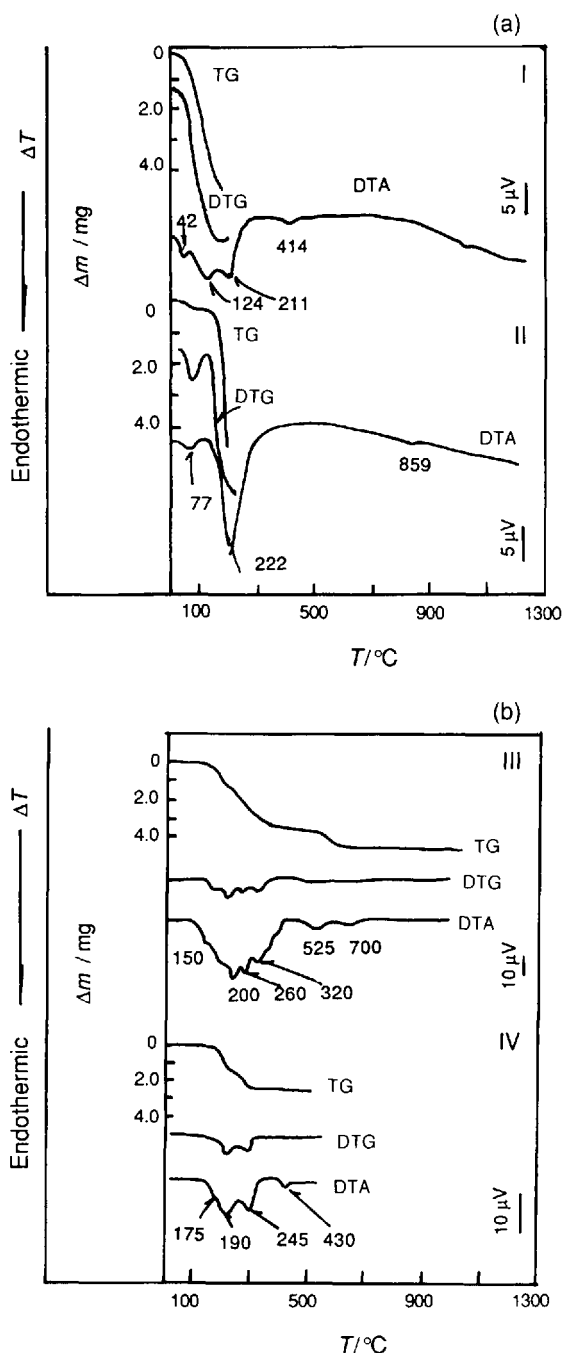


Figure 10.20 DTA-TG-DTG curves of (a) (I) hydromolysite and (II) chloraluminite and (b) (III) bischafite and (IV) carnalite [3]

Samples

I, Hydromolysite, $\text{FeCl}_3 \cdot 6\text{H}_2\text{O}$; II, chloraluminite, $\text{AlCl}_3 \cdot 6\text{H}_2\text{O}$ (Al 11.17%, Cl 44.06%, H_2O 44.77%); III, bischofite, $\text{MgCl}_2 \cdot 6\text{H}_2\text{O}$ (Mg 11.96%, Cl 34.87%, H_2O 53.11%); IV, carnalite, $\text{MgKCl}_3 \cdot 6\text{H}_2\text{O}$ (K 14.1%, Mg 8.7%, Cl 38.3%, H_2O 38.9%).

Results

I. Hydromolysite—42 °C endotherm, polymorphic transformation; 124 °C endotherm, hydromolysite dehydrates; 211 °C endotherm, FeCl_3 decomposes to iron and chlorine and iron oxidizes to Fe_2O_3 .

II. Chloraluminite—77 and 222 °C endotherms, chloraluminite dehydrates and decomposes and forms Al_2O_3 ; 859 °C exotherm, Al_2O_3 polymorphic transformation from α -corundum to γ -corundum.

III. Bischofite—150, 200, 260 and 320 °C endotherms, bischofite releases 4 mol of H_2O per mole of sample; at the stages of the 525 and 700 °C endotherms, bischofite releases 2 mol H_2O per mole of sample and is transformed to MgCl_2 .

IV. Carnalite—175, 190 and 245 °C endotherms, carnalite dehydrates; 430 °C endotherm, MgKCl_3 melts.

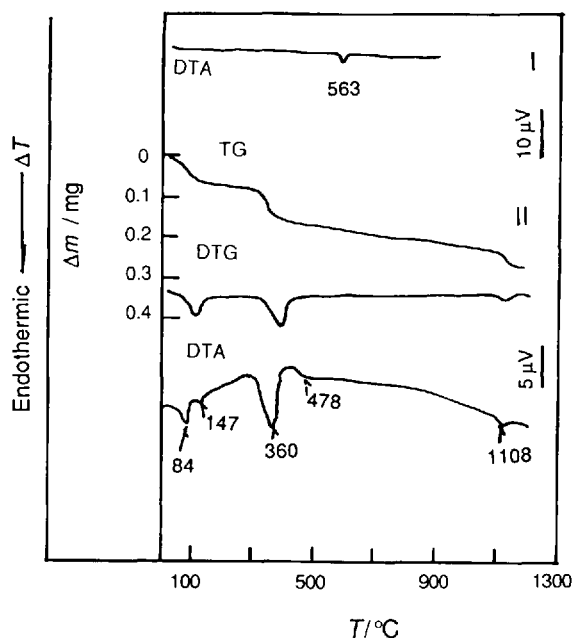


Figure 10.21 DTA-TG-DTG curves of (I) cryolite [2] and (II) prosopite [3]

Samples

I, Cryolite, Na_3AlF_6 (Na 32.8%, Al 12.8%, F 54.4%); II, prosopite, $\text{CaAl}_2(\text{F},\text{OH})_8$.

Results

I. *Cryolite*—563.7 °C endotherm, cryolite transforms from monocline to cubic.

II. *Prosopite*—84 and 147 °C endotherms, prosopite decomposes to CaF_2 and $\text{Al}(\text{OH})_3$; 360 °C endotherm, $\text{Al}(\text{OH})_3$ dehydrates and forms to $\text{AlO}(\text{OH})$; 478 °C endotherm, $\text{AlO}(\text{OH})$ is transformed to Al_2O_3 ; 1108 °C endotherm, CaF_2 melts.

10.3 Thermal Analysis Curves of Sulfide Minerals

Sulfide minerals show oxidation and decomposition by releasing SO_2 accompanied by a mass loss during heating. The decomposition and oxidation reactions take place at temperatures from 300 to 800 °C. Sulfide of many elements is transformed into complex oxides, some of which are volatilized at low temperature whereas others melt at high temperature. Some Sulfide is polymorphically transformed before oxidation and decomposition.

Samples

I, Pyrite, FeS_2 (Fe 46.55%, S 53.45%); II, hauerite, MnS_2 (Mn 46.14%, S 53.84%); III, tungstenite, WS_2 (W 74.16%, S 25.84%); IV, molybdenite, MoS_2 (Mo 59.94%, S 40.06%).

Results

I. *Pyrite*—311 °C exotherm, polymorphic transformation; 498 °C exotherm, oxidation and decomposition; Fe_2O_3 is obtained by liberation of SO_2 accompanied by a mass loss; 637 °C

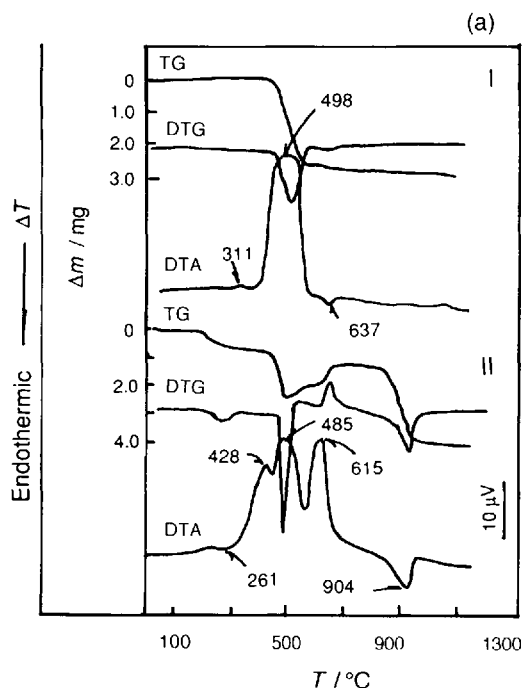


Figure 10.22 (a) DTA-TG-DTG curves of (I) pyrite and (II) hauerite

(continued)

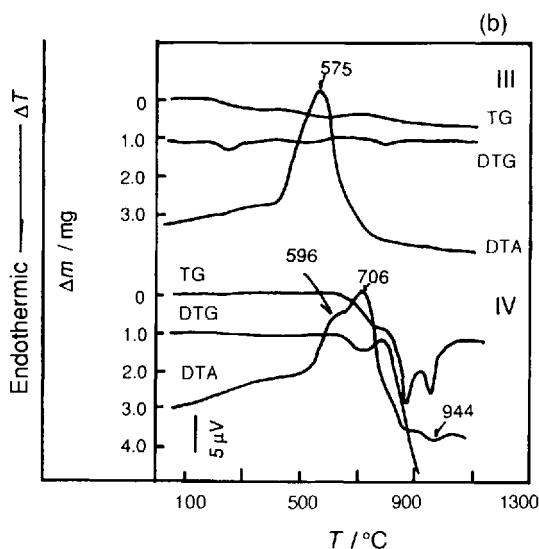


Figure 10.22 (b) DTA-TG-DTG curves of (III) tungstenite and (IV) molybdenite [3]

endotherm, Fe_2O_3 changes to Fe_3O_4 accompanied by a mass loss.

II. Hauerite—261 °C endotherm, partial decomposition of hauerite; 428 and 485 °C exotherms, hauerite decomposes and oxidizes. MnS is obtained by liberation of SO_2 accompanied by a mass loss; 615 °C exotherm, MnS oxidizes and is transformed to MnSO_4 accompanied by mass increase; 904 °C endotherm, MnSO_4 decomposes and is transformed to Mn_3O_4 by liberation of SO_3 accompanied by a mass loss.

III. Tungstenite—575 °C exotherm, tungstenite oxidizes and decomposes; WO_3 is formed with loss of SO_2 .

IV. Molybdenite—596 °C exotherm, molybdenite starts oxidation and decomposition; 706 °C exotherm, molybdenite oxidizes to MoO_3 and SO_2 is released; 800 °C MoO_3 melts and evaporates.

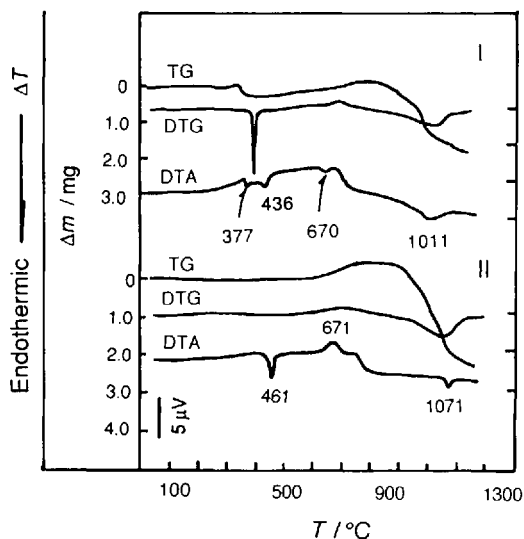


Figure 10.23 DTA-TG-DTG curves of (I) krennerite and (II) calaverite[3]

Samples

I, Krennerite, AuTe_2 (Au 43.59%, Te 56.43%); II, calaverite, AuTe_2 .

Results

I. Krennerite—377 °C endotherm, krennerite starts to decompose; 436 °C endotherm, krennerite decomposes and Te melts; at temperatures higher than 500 °C the tellurium oxidizes and is transformed to TeO_2 ; SO_2 is released accompanied by a mass loss; 670 °C endotherm, TeO_2 melts, then TeO_2 evaporates; 1011 °C endotherm, gold melts.

II. Calaverite—461 °C endotherm, calaverite decomposes and is transformed to Au and Te; 671 °C exotherm, tellurium oxidizes and is transformed to TeO_2 ; at a temperature higher than 800 °C, TeO_2 sublimates; 1071 °C endotherm, gold melts.

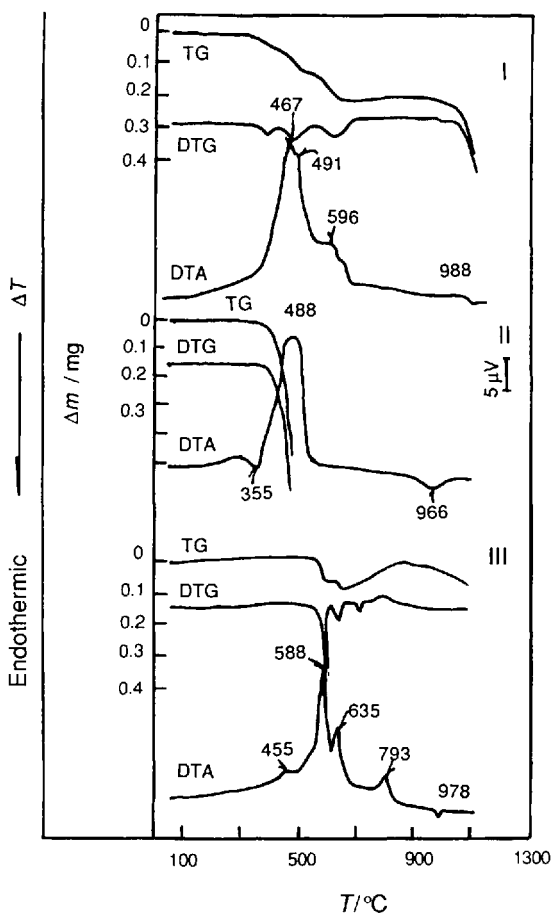


Figure 10.24 DTA-TG-DTG curves of (I) stibnite, (II) orpiment and (III) bismuthinite [3]

Samples

I, Stibnite, Sb_2S_3 (Sb 71.38%, S 28.62%); II, orpiment, As_2S_3 (As 60.91%, S 39.09%); III, bismuthinite, Bi_2S_3 (Bi 81.30%, S 18.70%).

Results

I. Stibnite—467 and 491 °C exotherms, stibnite oxidizes and decomposes; Sb_2O_3 and $\text{Sb}^{\text{III}}\text{Sb}^{\text{V}}\text{O}_4$ are formed by releasing SO_2 ; 596 °C exotherm, Sb_2O_3 changes to $\text{Sb}^{\text{III}}\text{Sb}^{\text{V}}\text{O}_4$.

II. Orpiment—355 °C endotherm, orpiment melts; 488 °C exotherm, molten orpiment oxidizes, is transformed to As_2O_3 and SO_2 is released accompanied by a mass loss.

III. Bismuthinite—455 °C exotherm, partial oxidation of bismuthinite; 588 °C exotherm, Bi_2S_3 changes to Bi_4S_5 , Bi_2O_3 and Bi and releases SO_2 accompanied by a mass loss; 793 °C exotherm, Bi and Bi_4S_5 oxidize and are transformed to Bi_2O_3 accompanied by a mass increase; 978 °C endotherm, Bi_2O_3 melts.

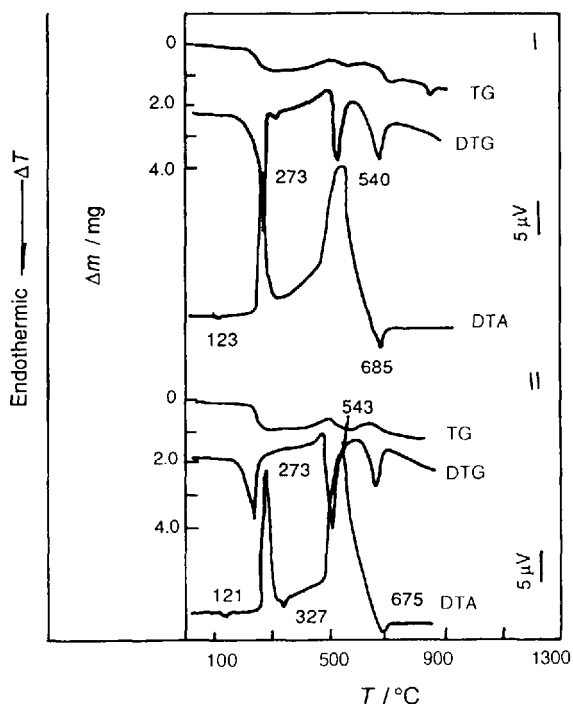


Figure 10.25 DTA-TG-DTG curves of (I) hexagonal pyrrhotite and (II) monoclinic pyrrhotite [3]

Samples

I, Hexagonal pyrrhotite, Fe_{1-x}S ; II, monoclinic pyrrhotite.

Results

121–123 °C endotherm, pyrrhotite undergoes a polymorphic transformation; 273 °C exotherm, partial decomposition of pyrrhotite, sulfur oxidizes and SO_2 is released, although the constitution shows no change; 327 °C endotherm, monoclinic pyrrhotite changes to hexagonal pyrrhotite; 540–543 °C exotherm, pyrrhotite oxidizes and decomposes and changes to $\text{Fe}_2(\text{SO}_4)_3$ and Fe_2O_3 ; SO_2 is released accompanied by a mass loss; 675–685 °C endotherm, $\text{Fe}_2(\text{SO}_4)_3$ decomposes, Fe_2O_3 is formed and SO_3 is released accompanied by a mass loss.

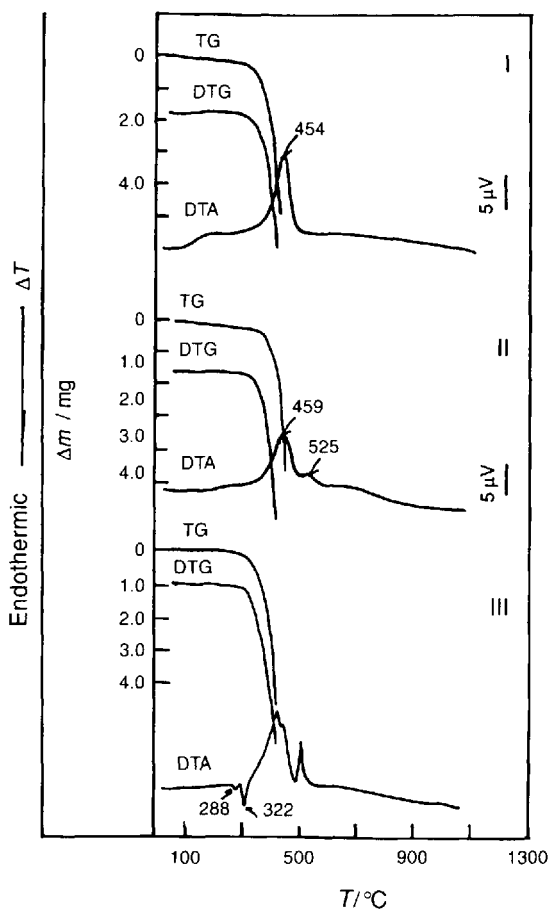


Figure 10.26 DTA-TG-DTG curves of (I) metacinnabar, (II) cinnabar and (III) realgar [3]

Samples

I, Metacinnabar, HgS (Hg 86.22%, S 13.78%); II, cinnabar, HgS ; III, realgar, AsS (As 70.1%, S 29.9%).

Results

I, II. Metacinnabar and cinnabar—454–459 °C exotherm, HgS decomposes, oxidizes and is transformed to Hg and SO_2 , Hg sublimes and SO_2 is evolved.

III. Realgar—288 °C endotherm, realgar undergoes a polymorphic transformation; 322 °C endotherm, realgar melts; 436 and 498 °C exotherms, molten realgar decomposes and oxidizes and is transformed to As_2O_3 and SO_2 .

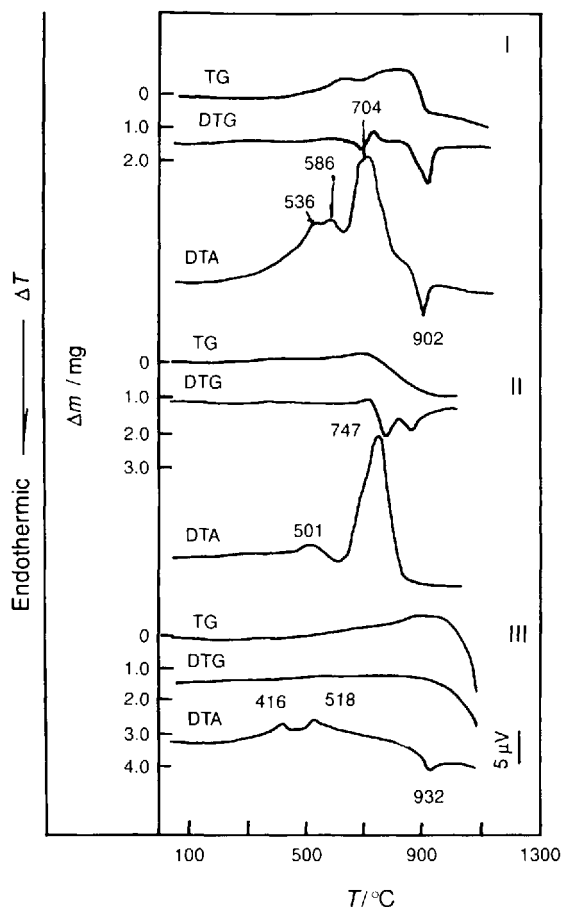


Figure 10.27 DTA-TG-DTG curves of (I) alabandite, (II) sphalerite and (III) galena [3]

Samples

I, Alabandite, MnS (Mn 63.14%, S 36.86%); II, sphalerite, ZnS (Zn 67.10%, S 32.90%); III, galena, PbS , (Pb 86.60%, S 13.40%).

Results

I. Alabandite—536 °C exotherm, alabandite starts to oxidize, 586 °C exotherm, partial oxidation of alabandite and transformation to hausmannite; 704 °C exotherm, alabandite and hausmannite oxidize and are transformed to Mn_2O_3 ; 902 °C endotherm, Mn_2O_3 becomes Mn_3O_4 .

II. Sphalerite—501 °C exotherm, sphalerite starts to oxidize; 747 °C exotherm, sphalerite oxidizes and decomposes; it is transformed to ZnO and SO_2 is released accompanied by a mass loss.

III. Galena—416 and 518 °C exotherms, galena starts to oxidize; 932 °C endotherm, Pb_3SO_6 melts, following which it evaporates.

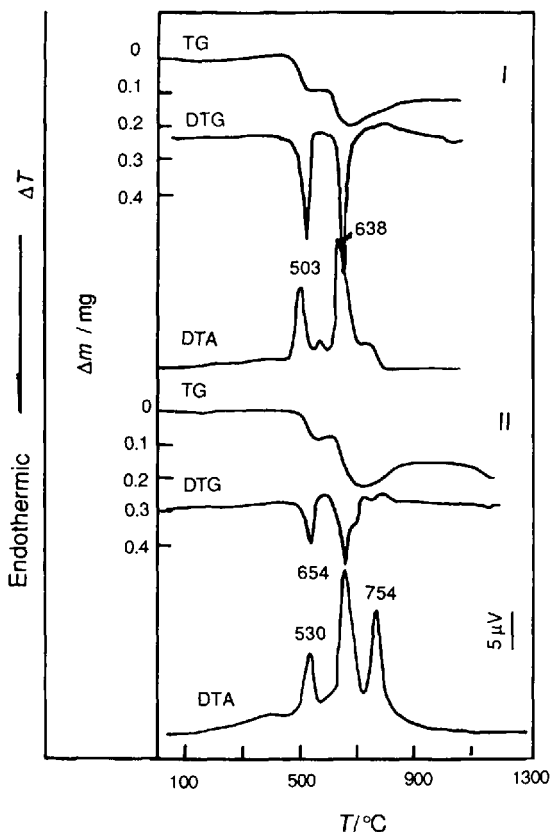


Figure 10.28 DTA-TG-DTG curves of (I) nickeline and (II) maucherite [3]

Samples

I, Nickeline, NiAs (Ni 43.92%, As 56.08%); II, maucherite, $\text{Ni}_{11}\text{As}_8$ (Ni 51.85%, As 48.15%).

Results

I. Nickeline—503 °C exotherm, nickeline oxidizes and decomposes, being transformed to Ni_5As_2 and As_2O_3 ; the As_2O_3 evaporates; 638 °C exotherm, Ni_5As_2 oxidizes and is transformed to $\text{Ni}_6(\text{AsO}_4)_2\text{O}_3$, NiO , and As_2O_3 ; the As_2O_3 evaporates.

II. Maucherite—530 °C exotherm, partial decomposition and oxidation of maucherite, and transformation to As_2O_3 ; the As_2O_3 evaporates; 654 °C exotherm, maucherite oxidizes and decomposes and is transformed to NiO , Ni_5As_2 and As_2O_3 ; the As_2O_3 evaporates; 754 °C exotherm, Ni_5As_2 oxidizes and is transformed to $\text{Ni}_6(\text{As}_5\text{O}_4)_2\text{O}_3$ and As_2O_3 ; the As_2O_3 evaporates.

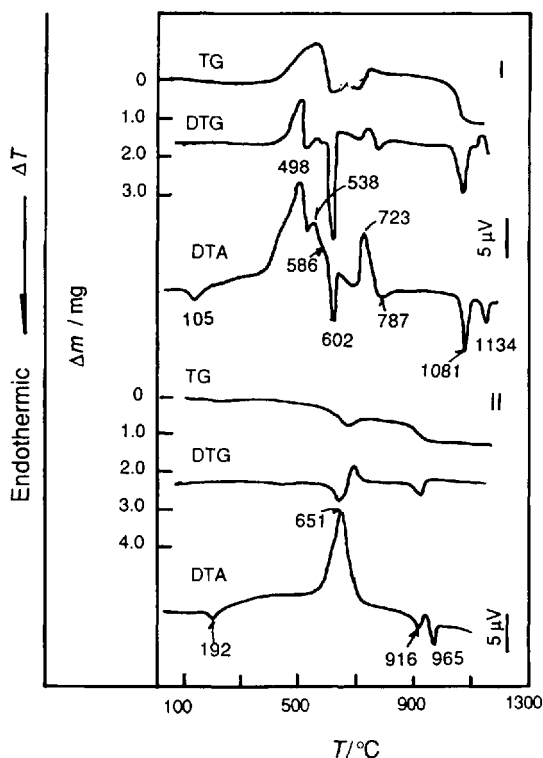


Figure 10.29 DTA-TG-DTG curves of (I) chalcocite and (II) acanthite [3]

Samples

I, Chalcocite, Cu_2S (Cu 79.74%, S 20.3%); II, acanthite, Ag_2S (Ag 87.06%, S 12.94%).

Results

I. Chalcocite—105 °C endotherm, chalcocite is transformed from $\alpha\text{-Cu}_2\text{O}$ to $\beta\text{-Cu}_2\text{O}$; 498, 538 and 586 °C exotherms, chalcocite oxidizes and is transformed to CuSO_4 accompanied by a mass increase; 602 °C endotherm, CuSO_4 decomposes to Cu_2O and SO_3 is released accompanied by a mass loss.; 723 °C exotherm, Cu_2O oxidizes to CuO accompanied by a mass increase; 787 °C endotherm, CuO is partially reduced to Cu_2O ; 1081 °C endotherm, CuO is partially reduced to Cu_2O ; 1134 °C endotherm, partial Cu_2O oxidation to CuO .

II. Acanthite—192 °C endotherm, acanthite undergoes a polymorphic transformation; 651 °C exotherm, acanthite oxidizes and is transformed to Ag_2SO_4 and SO_2 is released; 916 °C endotherm, Ag_2SO_4 decomposes to silver and SO_3 is released accompanied by a mass loss; 965 °C endotherm, silver melts (melting point of silver: 960 °C [2]).

Samples

I, Coloradoite, HgTe (Hg 61.14%, Te 38.86%); II, sylvanite, AgAuTe_4 (Ag 13.22%, Au 24.19%, Te 62.59%).

Results

I. Coloradoite—449 °C endotherm, coloradoite decomposes and is transformed to mercury and tellurium; mercury volatilizes and tellurium melts; 601 °C exotherm, tellurium oxidizes and is transformed to TeO_2 ; 656 °C endotherm, TeO_2 melts; 986 °C endotherm, TeO_2 evaporates.

II. Sylvanite—337 °C endotherm, sylvanite decomposes; 436 °C endotherm, tellurium melts, oxidation starts at 500 °C and it is transformed to TeO_2 ; 608 °C endotherm, TeO_2 melts; 983 °C endotherm, silver melts and TeO_2 evaporates.

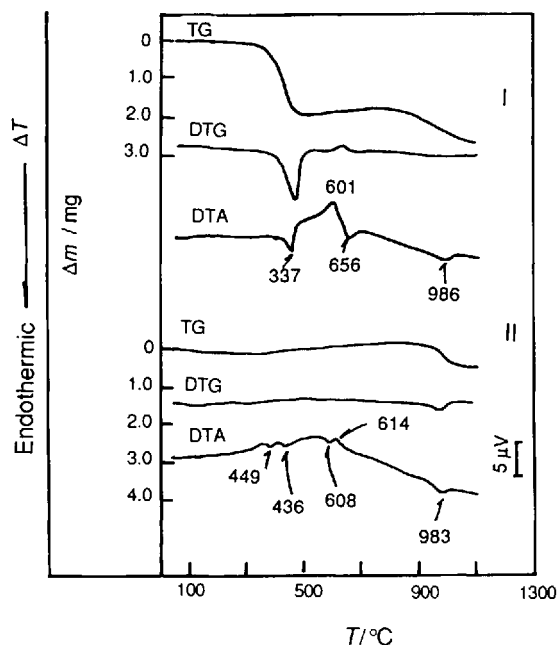


Figure 10.30 DTA-TG-DTG curves of (I) coloradoite and (II) sylvanite [3]

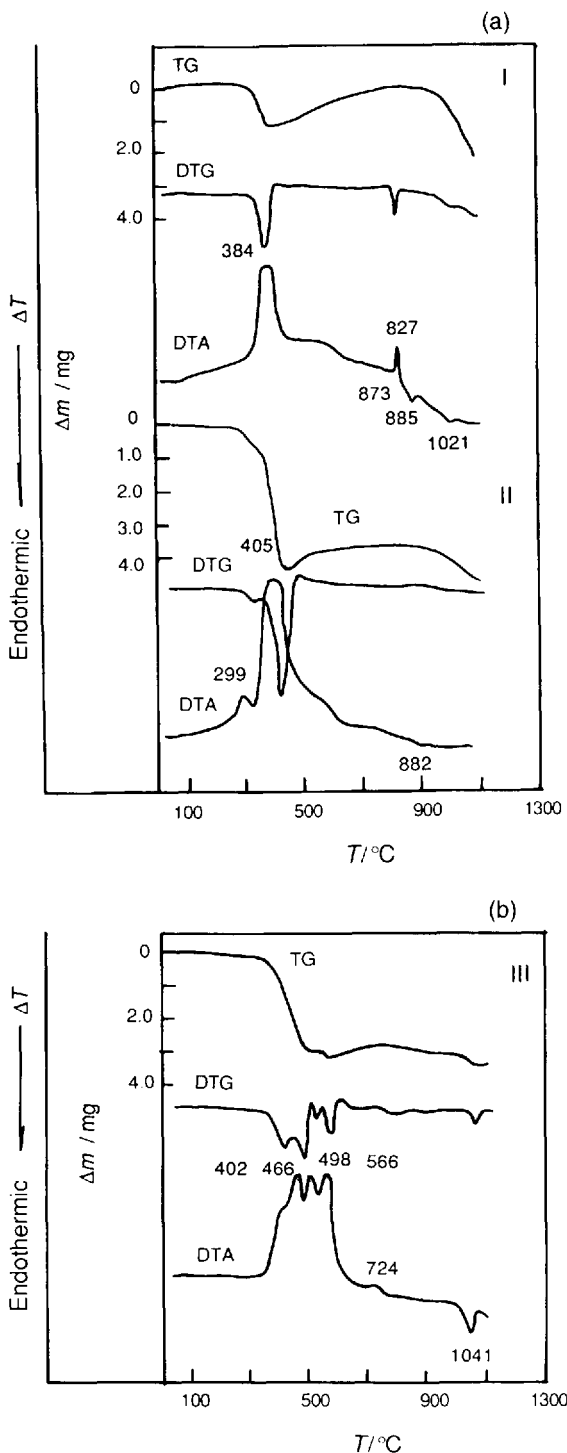


Figure 10.31 DTA-TG-DTG curves of (a) (I) jordanite and (II) sartorite and (b) (III) enargite [3]

Samples

I, Jordanite, $\text{Pb}_{14}(\text{As}, \text{Sb})_6 \text{S}_{23}$; II, sartorite, PbAs_2S_4 (Pb 42.70%, As 30.87%, S 26.43%); III, enargite, Cu_3AsS_4 (Cu 48.42%, As 19.02%, S 32.56%).

Results

I. Jordanite—384 °C exotherm, jordanite oxidizes and decomposes to PbS , PbSO_4 and As_2O_3 , releasing SO_2 ; PbS then partially oxidizes to PbSO_4 ; 827 °C exotherm, PbS oxidizes to PbSO_4 ; PbSO_4 partially becomes $\text{Pb}_3(\text{SO}_4)_2$ and releases SO_2 ; 873 °C endotherm, PbSO_4 melts; 885 °C endotherm, $\text{Pb}_3(\text{SO}_4)_2$ melts; 1021 °C endotherm, $\text{Pb}_3(\text{SO}_4)_2$ evaporates.

II. Sartorite—299 °C exotherm, sartorite decomposes and oxidizes; PbS , PbSO_4 and AsS are formed and SO_2 is released accompanied by a mass loss; 405 °C exotherm, PbS and AsS oxidize to PbSO_4 and As_2O_3 ; the As_2O_3 is released; 882 °C endotherm, PbSO_4 melts.

III. Enargite—402 °C exotherm, enargite decomposes and oxidizes; $\text{Cu}_{12}\text{As}_4\text{S}_{13}$ and $\text{Cu}_6\text{Cu}^{\text{II}}\text{S}_4$ are formed; As_2O_3 is released; 466 °C exotherm, $\text{Cu}_{12}\text{As}_4\text{S}_{13}$ oxidizes to CuSO_4 ; at the same time, As_2O_3 and SO_2 are released; 498 °C exotherm, Cu_6CuS_4 oxidizes and decomposes; CuSO_4 is formed and SO_2 is released; 566 °C exotherm, CuSO_4 partially decomposes to CuO and releases SO_3 ; 724 °C exotherm, remainder of CuSO_4 decomposes to CuO and SO_3 is released; 1041 °C endotherm, CuO reduces to Cu_2O .

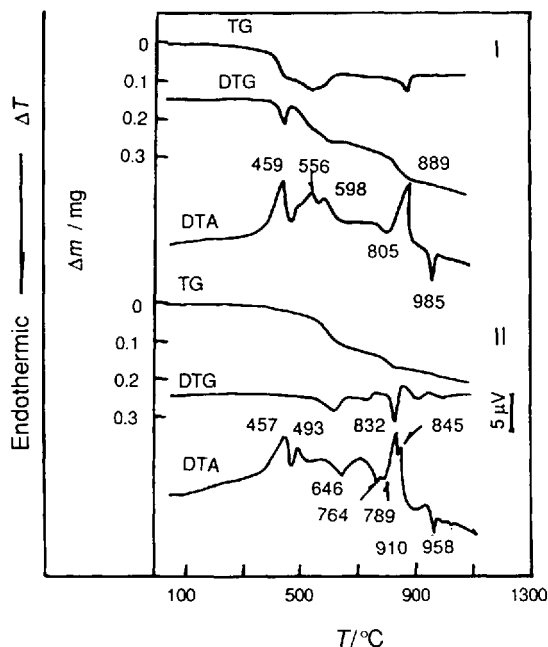


Figure 10.32 DTA-TG-DTG curves of (I) proustite and (II) pyrargyrite [3]

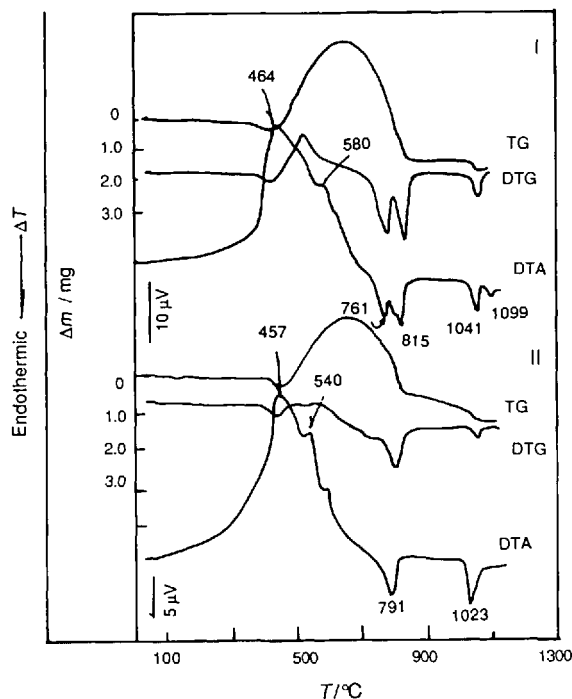


Figure 10.33 DTA-TG-DTG curves of (I) chalcopyrite and (II) bornite [3]

Samples

I, Proustite, Ag_3AsS_3 (Ag 65.42%, As 15.15%, S 19.44%); II, pyrargyrite, AgSbS_3 (Ag 59.76%, Sb 22.48%, S 17.76%).

Results

I. Proustite—459 °C exotherm, proustite oxidizes and decomposes; Ag_2S and Ag_7AsS_6 are formed and SO_2 is released; 556 °C exotherm, Ag_7AsS_6 partially oxidizes to Ag_2S and releases As_2O_3 accompanied by a mass loss; 598 °C exotherm, remainder of Ag_7AsS_6 oxidizes to Ag_2S and releases As_2O_3 ; 889 °C exotherm, Ag_2S oxidizes and decomposes; it is transformed to Ag and releases SO_2 ; 985 °C endotherm, silver melts.

II. Pyrargyrite—457 °C exotherm, pyrargyrite partially decomposes and oxidizes; It is transformed to $\text{Sb}^{\text{III}}\text{Sb}^{\text{V}}\text{O}_4$ and Ag_2S and releases SO_2 ; 493 °C exotherm, remainder of pyrargyrite decomposes and oxidizes; 646 °C endotherm, Ag_2S partially decomposes to Ag and $\text{Sb}^{\text{III}}\text{Sb}^{\text{V}}\text{O}_4$ and is transformed to Sb_2O_5 ; 764 and 789 °C endotherms, Sb_2O_5 partially becomes Sb_2O_3 ; 832 and 845 °C exotherms, Ag_2S decomposes to Ag and SO_2 is released; 910 °C endotherm, Sb_2O_3 melts; 958 °C endotherm, Ag melts.

Samples

I, Chalcopyrite, CuFeS_2 (Cu 34.56%, Fe 30.52%, S 34.92%); II, bornite, Cu_5FeS_4 (Cu 63.33%, Fe 11.10%, S 25.55%).

Results

I. Chalcopyrite—464 and 580 °C exotherms, chalcopyrite oxidizes, CuSO_4 and $\text{Fe}_2(\text{SO}_4)_3$ are formed, accompanied by a mass increase; 761 °C endotherm, $\text{Fe}_2(\text{SO}_4)_3$ and some CuSO_4 decompose to CuO and Fe_2O_3 ; SO_2 is released accompanied by a mass loss; 815 °C endotherm,

(continued)

remainder of CuSO_4 decomposes to CuO and SO_2 is released accompanied by a mass loss; 1041 °C endotherm, CuO is reduced to Cu_2O ; 1099 °C endotherm, Cu_2O partially oxidizes to CuO .

II. Bornite—457 °C exotherm, bornite oxidizes and is transformed to Cu_2O and Fe_2O_3 ; it releases SO_2 accompanied by a mass loss; 540 °C exotherm, Cu_2S oxidizes and is transformed to CuSO_4 accompanied by a mass increase; 791 °C endotherm, CuSO_4 decomposes to CuO and SO_3 is released accompanied by a mass loss; 1032 °C endotherm, CuO reduces to Cu_2O accompanied by a mass loss.

Samples

I, Plagionite, $\text{Pb}_5\text{Sb}_8\text{S}_{17}$ (Pb 40.75%, Sb 37.78%, 21.47%); II, semseyite, $\text{Pb}_9\text{Sb}_8\text{S}_{21}$.

Results

I. Plagionite—456 and 598 °C exotherms, plagionite oxidizes and PbSO_4 and $\text{Pb}_3(\text{SbO}_4)_2$ are formed; it releases SO_2 accompanied by a mass loss; 877 °C endotherm, PbSO_4 melts; 960 °C endotherm, $\text{Pb}_3(\text{SbO}_4)_2$ becomes $\text{Pb}(\text{SbO}_3)_2$.

II. Semseyite—421 °C exotherm, semseyite decomposes and oxidizes; it is transformed to PbS and Sb_2O_3 and releases SO_2 ; 493 °C exotherm, PbS partially oxidizes to PbSO_4 ; 601 °C exotherm, remainder of PbS oxidizes to PbSO_4 ; 721 °C exotherm, Sb_2O_3 and some PbSO_4 are transformed to $\text{Pb}(\text{Sb}_2\text{O}_3)_2$ and SO_3 is released; 876 °C endotherm, PbSO_4 melts.

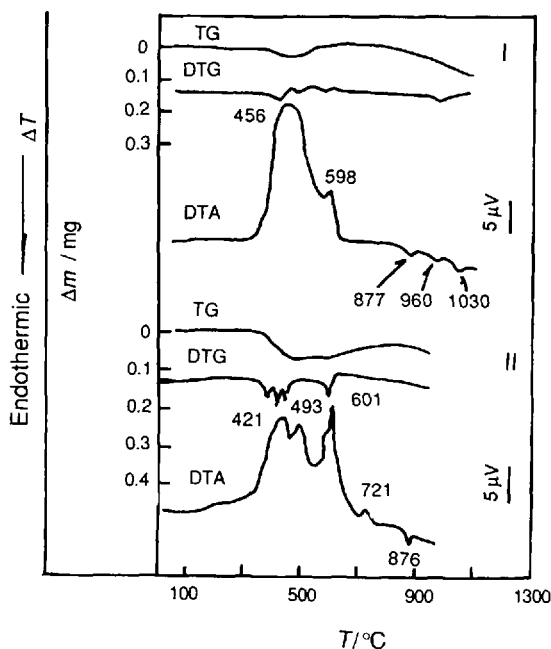


Figure 10.34 DTA-TG-DTG curves of (I) plagionite and (II) semseyite [3]

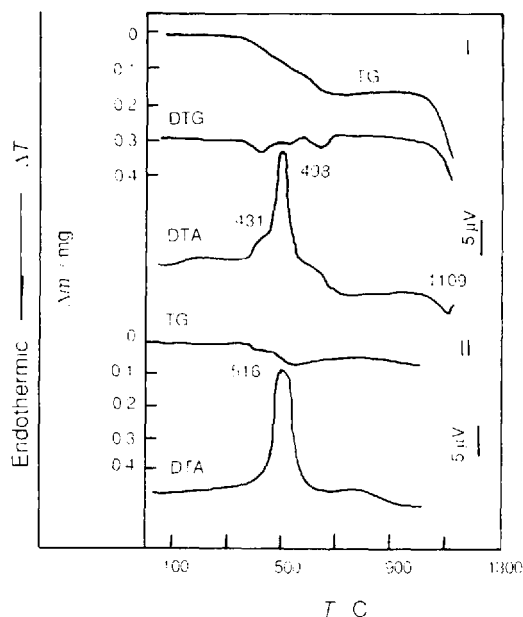


Figure 10.35 DTA-TG-DTG curves of (I) livingstonite and (II) berthierite [3]

Samples

I, Livingstonite, $\text{HgSb}_4\text{S}_2\text{S}_6$ (Hg 21.25%, Sb 51.59%, S 27.16%); II, berthierite, $\text{FeS} \cdot \text{Sb}_2\text{S}_3$ (Fe 13.21%, Sb 56.55%, S 30.24%).

Results

I. Livingstonite—431 °C exotherm, livingstonite decomposes to HgS_2 and Sb_2O_3 , HgS_2 oxidizes, Hg and SO_2 are formed, Hg evaporates and releases SO_2 ; 498 °C exotherm, Sb_2S_3 oxidizes to Sb_2S_3 and releases SO_2 ; 1109 °C endotherm, Sb_2O_3 volatilizes.

II. Berthierite—516 °C exotherm, berthierite decomposes to FeS and Sb_2S_3 ; FeS oxidizes to Fe_2O_3 and releases SO_2 ; Sb_2S_3 oxidizes to Sb_2O_3 and releases SO_2 .

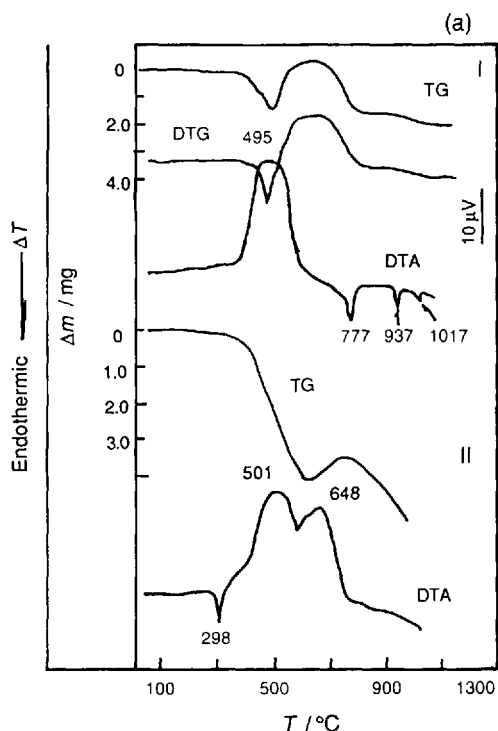


Figure 10.36 (a) DTA-TG-DTG curves of (I) tennantite and (II) lorandite

(continued)

Samples

I, Tennantite, $\text{Cu}_{12}\text{As}_4\text{S}_{13}$ (Cu 51.57%, As 20.26%, S 28.17%); II, lorandite, TiAsS_2 (Ti 59.46%, As 21.87%, S 18.67%); III, arsenopyrite, FeAsS (Fe 34.40%, As 46.01%, S 19.69%).

Results

I. Tennantite—495 °C exotherm, tennantite starts to decompose at 320 °C and is transformed to Cu_2S , CuS and As_2S_3 , then As_2S_3 oxidizes to As_2O_3 and volatilizes; Cu_2S and CuS oxidize to CuSO_4 at 500 °C; 777 °C endotherm, CuSO_4 decomposes to CuO and releases SO_3 ; 937 °C endotherm, Sb_2O_3 (Sb is isomorphic with As) volatilizes accompanied by a mass loss; 1017 °C endotherm, CuO reduces to Cu_2O .

II. Lorandite—298 °C endotherm, lorandite decomposes to Ti_2S and As_2S_3 ; 501 °C exotherm, As_2S_3 oxidizes and releases As_2O_3 and SO_2 accompanied by a mass loss; 648 °C exotherm, Ti_2S oxidizes and Ti_2O_3 is formed; at a temperature higher than 750 °C, Ti_2O_3 volatilizes.

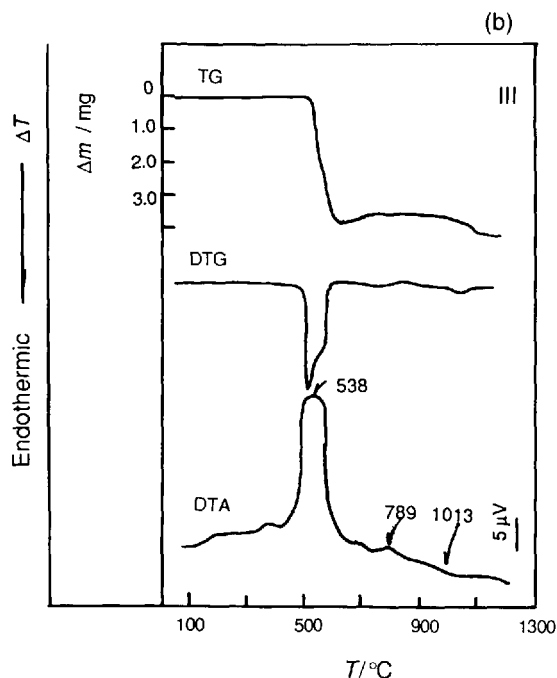


Figure 10.36 (b) DTA-TG-DTG curves of (III) arsenopyrite [3]

III. *Arsenopyrite*—538 °C exotherm, arsenopyrite oxidizes and is transformed to γ -Fe₂O₃; it releases As₂O₃ and SO₂; 789 °C exotherm, γ -Fe₂O₃ changes to α -Fe₂O₃.

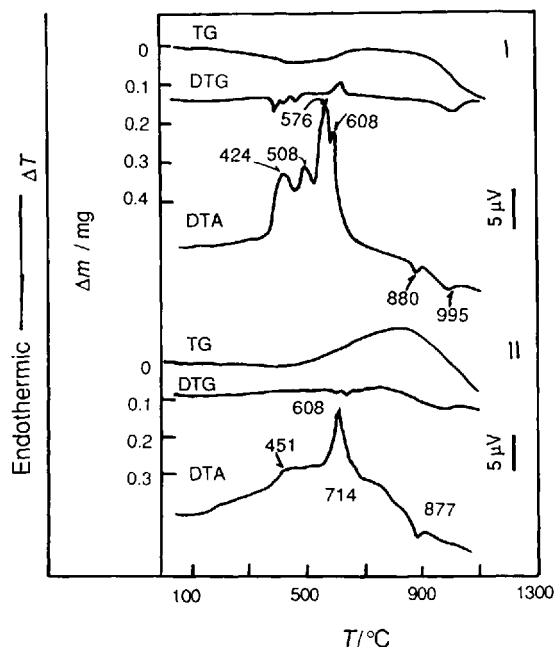


Figure 10.37 DTA-TG-DTG curves of (I) boulangerite and (II) galenobismutite [3]

Samples

I, *Boulangerite*, Pb₅Sb₄S₁₁ (Pb 55.42%, Sb 25.69%, S 18.89%); II, *galenobismutite*, PbBi₂S₄ (Pb 27.50%, Bi 55.48%, S 17.02%).

Results

I. *Boulangerite*—424 °C exotherm, boulangerite partially decomposes and oxidizes; it is transformed to PbS and Sb₂O₃ and releases SO₂; 508 °C exotherm, remainder of boulangerite decomposes and oxidizes; it is transformed to PbS and Sb₂O₃ and releases SO₂; 576 °C exotherm, PbS partially oxidizes to PbSO₄; 608 °C exotherm, remainder of PbS oxidizes to PbSO₄; 880 °C endotherm, PbSO₄ melts; 995 °C endotherm, PbSO₄ and Sb₂O₃ volatilize.

II. *Galenobismutite*—451, 608 and 714 °C exotherms, galenobismutite decomposes and oxidizes; it is transformed to PbSO₄ and Bi₂O₃; 877 °C endotherm, PbSO₄ melts, then molten PbSO₄ volatilizes.

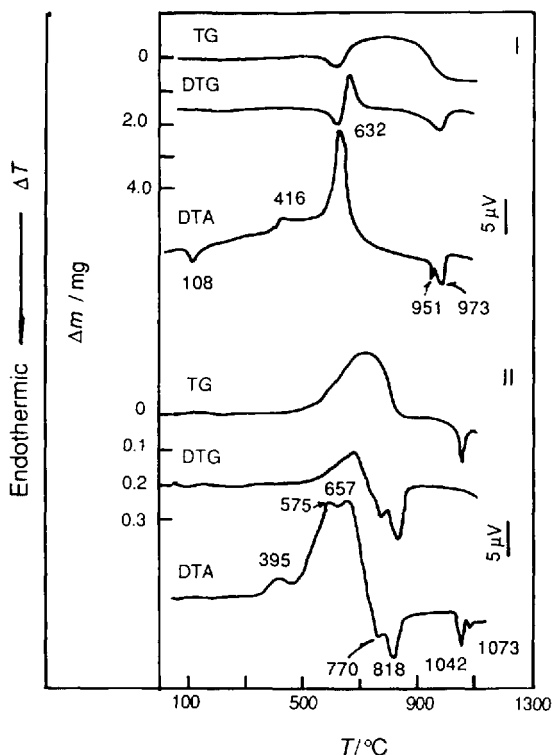


Figure 10.38 DTA-TG-DTG curves of (I) stromeyerite and (II) stannite [3]

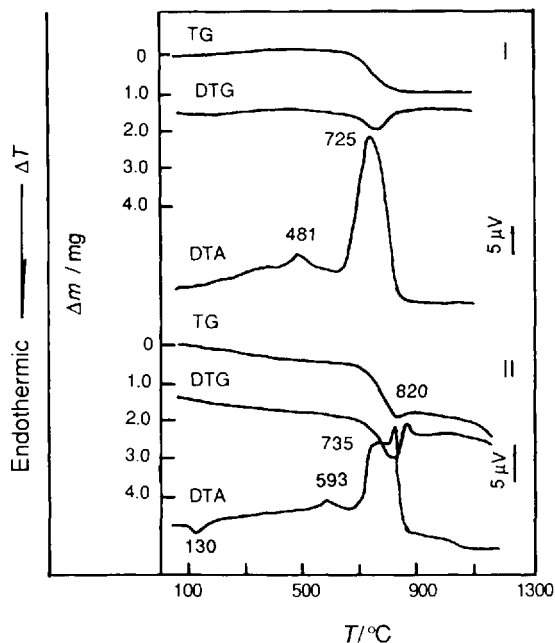


Figure 10.39 DTA-TG-DTG curves of (I) teallite and (II) cobaltite [3]

Samples

I, Stromeyerite, AgCuS (Ag 53.01%, Cu 31.24%, S 15.75%); II, stannite, $\text{Cu}_2\text{FeSnS}_4$ (Cu 29.58%, Fe 12.99%, Sn 27.61%, S 29.82%).

Results

I. Stromeyerite—108 °C endotherm, stromeyerite undergoes a polymorphic transformation; 416 °C exotherm, stromeyerite decomposes to Ag_2S and Cu_2S ; 632 °C exotherm, Ag_2S decomposes and oxidizes; it is transformed to Ag and SO_2 is released; Cu_2S oxidizes to CuSO_4 ; 951 °C endotherm, CuSO_4 decomposes and is transformed to CuO and SO_3 is released; 973 °C endotherm, Ag melts.

II. Stannite—395 °C exotherm, stannite undergoes a polymorphic transformation; 575 and 657 °C exotherms, stannite decomposes and oxidizes; it is transformed to SnO , CuSO_4 and $\text{Fe}_2(\text{SO}_4)_3$ and releases SO_2 ; 770 °C endotherm, CuSO_4 decomposes; it is transformed to CuO and releases SO_3 ; 818 °C endotherm, $\text{Fe}_2(\text{SO}_4)_3$ decomposes; it is transformed to Fe_2O_3 and releases SO_3 ; 1042 °C endotherm, CuO reduces to Cu_2O ; 1073 °C endotherm, Cu_2O partially oxidizes to CuO .

Samples

I, Teallite, PbSnS_2 (Pb 53.05%, Sn 30.51%, S 16.44%); II, cobaltite, CoAsS (Co 35.41%, As 45.26%, S 19.33%).

Results

I. Teallite—481 °C exotherm, teallite undergoes a polymorphic transformation; 725 °C exotherm, teallite decomposes and oxidizes; it is transformed to PbSO_4 and SnO_2 , and releases SO_2 .

II. Cobaltite—130 °C endotherm, cobaltite undergoes a polymorphic transformation; 583 °C exotherm, cobaltite undergoes a polymorphic transformation; 735 °C exotherm, cobaltite decomposes and oxidizes; CoAs is formed and SO_2 is released; 820 °C exotherm, CoAs oxidizes to $\text{Co}_3\text{As}_2\text{O}_8$ and As_2O_3 ; As_2O_3 volatilizes.

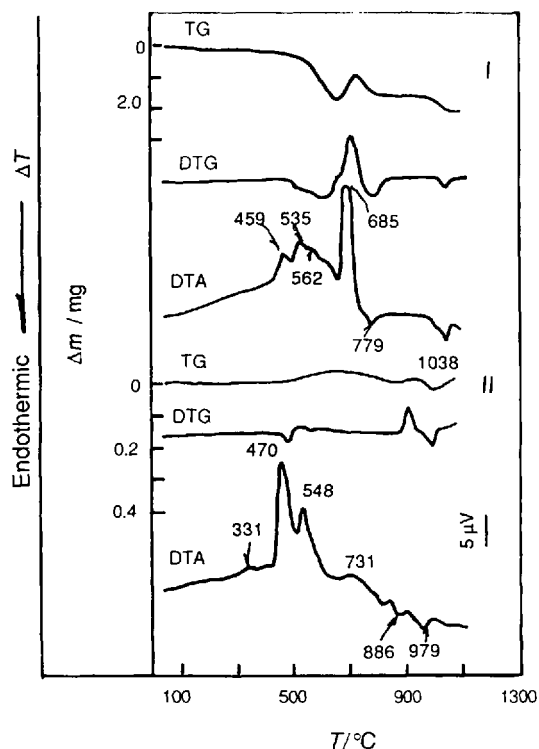


Figure 10.40 DTA-TG-DTG curves of (I) tetrahedrite and (II) jamesonite [3]

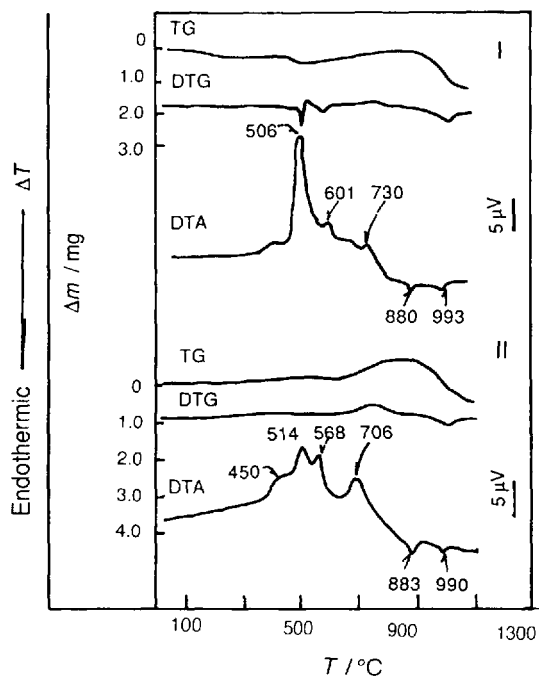


Figure 10.41 DTA-TG-DTG curves of (I) cylindrite and (II) franckeite [3]

Samples

I, Tetrahedrite, $\text{Cu}_{12}\text{Sb}_4\text{S}_{13}$ (Cu 45.77%, Sb 29.225%, S 25.01%); II, jamesonite, $\text{Pb}_4\text{FeSb}_6\text{S}_{14}$ (Pb 40.16%, Fe 2.71%, Sb 35.39%, S 21.74%).

Results

I. Tetrahedrite—459, 535 and 562 °C exotherms, tetrahedrite decomposes and oxidizes; it is transformed to CuS and CuSb_2O_6 and releases SO_2 ; 685 °C exotherm, CuS oxidizes and is transformed to CuSO_4 . 779 °C endotherm, CuSO_4 decomposes; it is transformed to CuO and SO_3 is released; 1038 °C endotherm, CuO reduces to Cu_2O .

II. Jamesonite—331 °C exotherm, jamesonite undergoes a polymorphic transformation; 470 °C exotherm, jamesonite decomposes and oxidizes; $\text{Fe}_2(\text{SO}_4)_3$, PbS and Sb_2S_3 are formed; 548 °C exotherm, PbS oxidizes to PbSO_4 ; 731 °C exotherm, PbSO_4 and Sb_2S_3 are transformed to $\text{Pb}_3(\text{SbO}_4)_2$ and Sb_2O_3 and SO_3 is released; 886 °C endotherm, $\text{Pb}_3(\text{SbO}_4)_2$ decomposes and is transformed to $\text{Pb}_3(\text{SbO}_3)_2$ and $\text{PbO} \cdot \text{Pb}(\text{SbO}_3)_2$; 979 °C endotherm.

Samples

I, Cylindrite, $\text{Pb}_3\text{Sb}_2\text{Sn}_4\text{S}_{14}$ (Pb 34.75%, Sb 13.62%, Sn 26.54%, S 25.09%); II, franckeite, $\text{Pb}_5\text{Sb}_2\text{Sn}_3\text{S}_{14}$ (Pb 49.71%, Sb 11.69%, Sn 17.09%, S 21.51%).

Results

I. Cylindrite—506 °C exotherm, cylindrite decomposes and oxidizes; SnO_2 , PbS and Sb_2S_3 are formed and SO_2 is released; 601 °C exotherm, PbS partially oxidizes to PbSO_4 ; 730 °C exotherm, some PbS and Sb_2S_3 are transformed to $\text{PbO} \cdot \text{Pb}(\text{SbO}_3)_2$; 880 °C endotherm, PbSO_4 melts; 993 °C endotherm, molten PbSO_4 evaporates.

II. Franckeite—450 °C exotherm, franckeite decomposes and oxidizes; SnO_2 , PbS and Sb_2S_3 are formed and SO_2 is released; 514 °C exotherm, PbS partially oxidizes to PbSO_4 ; 568 °C exotherm, remainder of PbS oxidizes to PbSO_4 ; 706 °C exotherm, PbSO_4 and Sb_2S_3 are transformed to $\text{PbO} \cdot \text{Pb}(\text{SbO}_3)_2$; 883 °C endotherm, PbSO_4 melts; 990 °C endotherm, molten PbSO_4 evaporates.

10.4 Thermal Analysis Curves of Oxide Minerals

The thermal properties of oxide minerals are characterized by structure transformation, melting, dehydration and valence-state changes during heating.

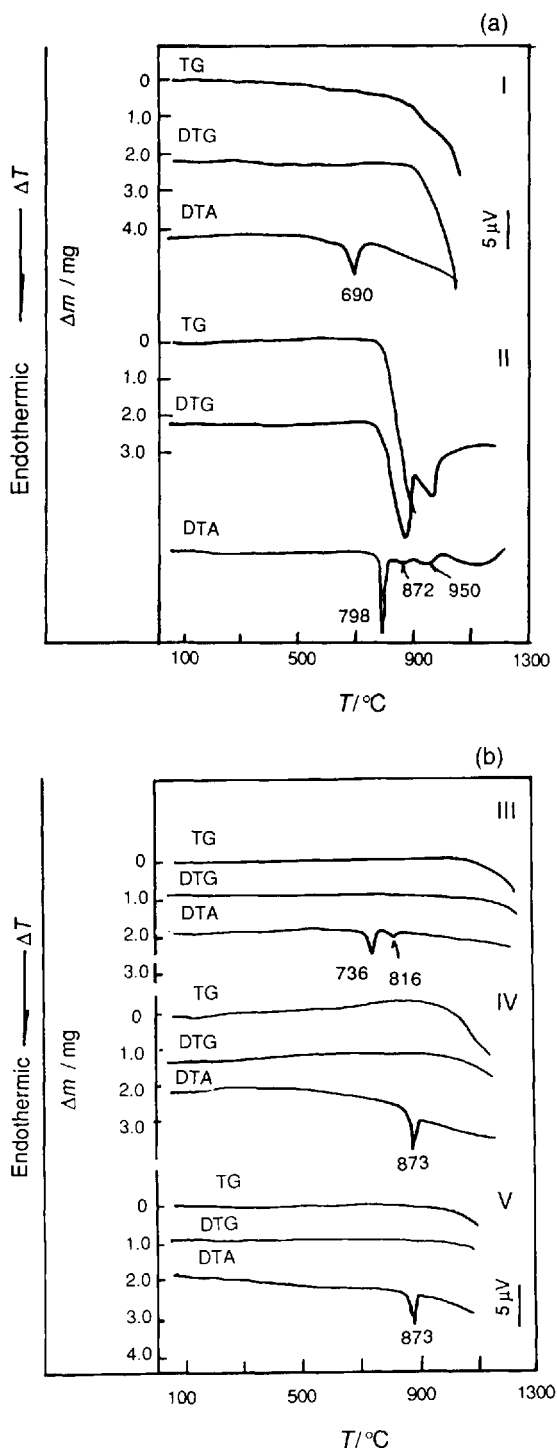


Figure 10.42 DTA-TG-DTG curves of (a) (I) paratellurite and (II) molybdate and (b) (III) bismite, (IV) litharge and (V) massicot [3]

Samples

I, Paratellurite, TeO_2 (Te 79.94%, O 20.06%); II, molybdate, MoO_3 (Mo 66.66%, O 33.34%); III, bismite, Bi_2O_3 (Bi 89.68%, O 10.32%); IV, litharge, $\alpha\text{-PbO}$ (Pb 92.83%, O 7.17%); V, massicot, $\beta\text{-PbO}$ (Pb 92.83%, O 7.17%).

Results

I. Paratellurite—690 °C endotherm, paratellurite melts; at a temperature higher than 850 °C, it evaporates.

II. Molybdate—798 °C endotherm, molybdate melts, then it evaporates.

III. Bismite—738 °C endotherm, bismite undergoes a polymorphic transformation; 816 °C endotherm, bismite melts; at a temperature higher than 1050 °C, it evaporates.

IV. Litharge—At a temperature higher than 300 °C, litharge transforms to massicot.

V. Massicot—873 °C endotherm, massicot melts; at a temperature higher than 950 °C, it evaporates.

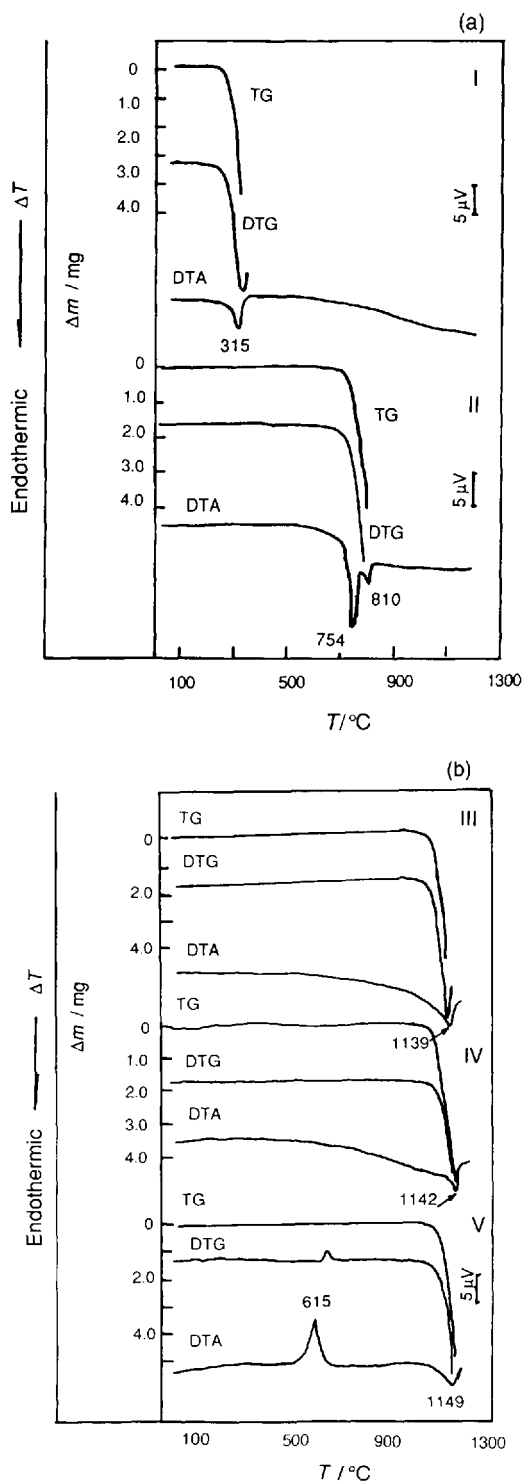


Figure 10.43 DTA-TG-DTG curves of (a) (I) arsenolite and (II) avicennite and (b) (III) cervantite, (IV) stibiconite and (V) valentinite [3]

Samples

I, Arsenolite, As_2O_3 (As 75.74%, O 24.26%); II, avicennite, Tl_2O_3 (Tl 89.49%, O 10.51%); III, cervantite, $\text{Sb}^{\text{III}}\text{Sb}^{\text{V}}\text{O}_4$ (Sb 79.19%, O 20.81%); IV, stibiconite, $\text{Sb}^{\text{III}}\text{Sb}^{\text{V}}\text{O}_6(\text{OH})$; V, valentinite, Sb_2O_3 (Sb 83.54%, O 16.46%).

Results

I. *Arsenolite*—315 $^\circ\text{C}$ endotherm, arsenolite sublimes.

II. *Avicennite*—754 $^\circ\text{C}$ endotherm, avicennite sublimes.

III. *Cervantite*—1139 $^\circ\text{C}$ endotherm, cervantite sublimes.

IV. *Stibiconite*—1142 $^\circ\text{C}$ endotherm, stibiconite dehydrates and sublimes.

V. *Valentinite*—615 $^\circ\text{C}$ exotherm, valentinite oxidizes to $\text{Sb}^{\text{III}}\text{Sb}^{\text{V}}\text{O}_4$; 1149 $^\circ\text{C}$ endotherm, $\text{Sb}^{\text{III}}\text{Sb}^{\text{V}}\text{O}_4$ sublimes.

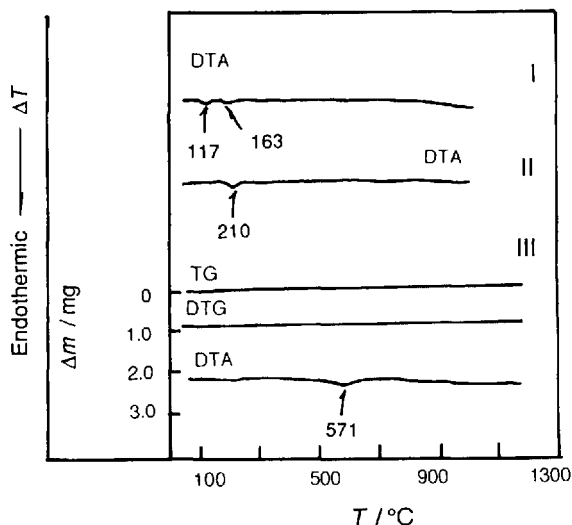


Figure 10.44 DTA-TG-DTG curves of (I) tridymite, (II) cristobalite and (III) coesite [6]

Samples

I, Tridymite, SiO_2 ; II, cristobalite, SiO_2 ; III, coesite, SiO_2 .

Results

I. Tridymite—117 °C endotherm, tridymite undergoes a polymorphic transformation; 163 °C endotherm, tridymite undergoes a polymorphic transformation.

II. Cristobalite—200–270 °C endotherm, α -cristobalite transforms to β -cristobalite.

III. Coesite—571 °C endotherm, coesite undergoes a structural transformation.

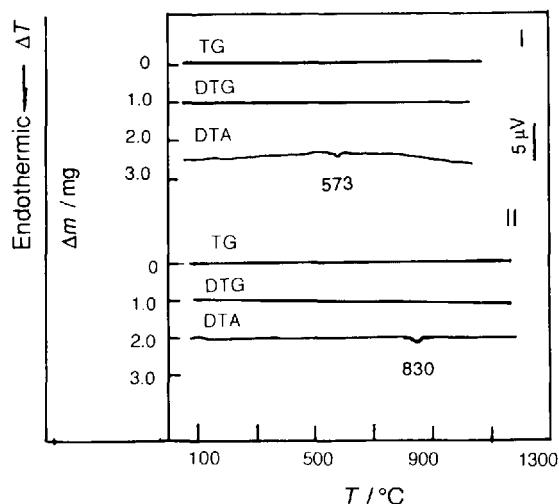


Figure 10.45 DTA-TG-DTG curves of (I) quartz and (II) hematite

Samples

I, Quartz, SiO_2 ; II, hematite, Fe_2O_3 (Fe 69.94%, O 30.06%).

Results

I. Quartz—573 °C endotherm, quartz undergoes a polymorphic transformation from α - SiO_2 to β - SiO_2 .

II. Hematite—830 °C endotherm, hematite undergoes a polymorphic transformation from α - Fe_2O_3 to γ - Fe_2O_3 .

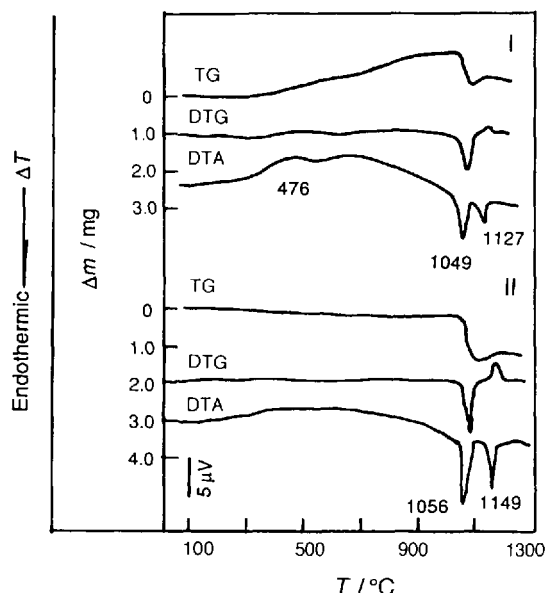


Figure 10.46 DTA-TG-DTG curves of (I) cuprite and (II) tenorite

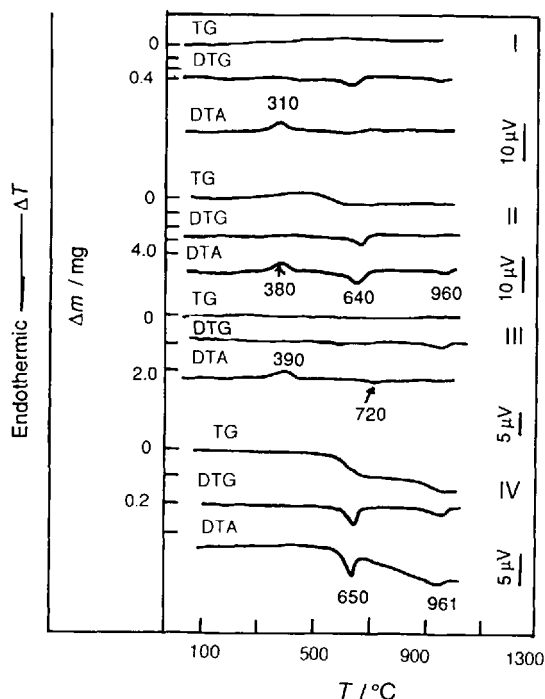


Figure 10.47 DTA-TG-DTG curves of (I) wuestite [6], (II) manganosite[6], (III) magnetite and (IV) pyrolusite

Samples

I, Cuprite, Cu_2O (Cu 88.8%, O 11.2%); II, tenorite, CuO (Cu 79.89%, O 20.11%).

Results

476 °C exotherm, cuprite oxidizes to tenorite; 1049 and 1056 °C endotherms, tenorite reduces to Cu_2O ; 1127 and 1149 °C endotherms, Cu_2O partially oxidizes to CuO .

Samples

I, Wuestite, FeO (Fe 77.73%, O 22.27%); II, manganosite, MnO (Mn 77.44%, O 22.56%), III, magnetite, $\text{Fe}^{\text{II}}\text{Fe}^{\text{III}}_2\text{O}_4$ (Fe 31.04%, O 68.96%); IV, pyrolusite, MnO_2 (Mn 63.19%, O 36.81%).

Results

I. Wuestite—310 °C exotherm, wuestite oxidizes to hematite.

II. Manganosite—380 °C exotherm, manganosite oxidizes to MnO_2 accompanied by a mass increase; 640 °C endotherm, MnO_2 is transformed to $\beta\text{-Mn}_2\text{O}_3$ accompanied by a mass loss; 960 °C exotherm, $\beta\text{-Mn}_2\text{O}_3$ becomes Mn_3O_4 accompanied by a mass loss.

III. Magnetite—390 °C exotherm, magnetite oxidizes to hematite accompanied by a mass increase; 720 °C endotherm, hematite is transformed to $\gamma\text{-Fe}_2\text{O}_3$.

IV. Pyrolusite—650 °C endotherm, pyrolusite becomes Mn_2O_3 accompanied by a mass loss; 961 °C exotherm, Mn_2O_3 is transformed to Mn_3O_4 accompanied by a mass loss.

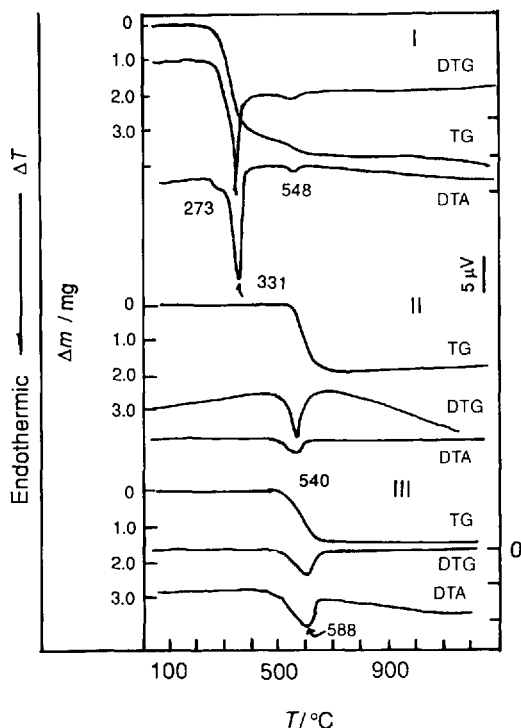


Figure 10.48 DTA-TG-DTG curves of (I) gibbsite [3], (II) boehmite and (III) diaspore [3]

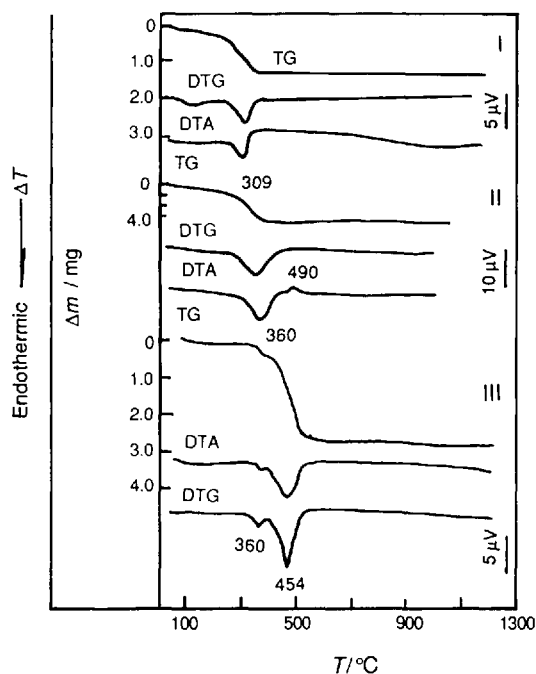


Figure 10.49 DTA-TG-DTG curves of (I) goethite [3], (II) lepidocrocite and (III) brycite [6]

Samples

I, Gibbsite, $\text{Al}(\text{OH})_3$ (Al_2O_3 65.4%, H_2O 34.6%);
 II, boehmite, $\text{AlO}(\text{OH})$ (Al_2O_3 84.98%, H_2O 15.02%);
 III, diaspore, AlOOH (Al_2O_3 84.98%, H_2O 15.02%).

Results

I. *Gibbsite*—273, 331 °C endotherms, gibbsite is transformed to boehmite.

II. *Boehmite*—540–548 °C endotherm, boehmite is transformed to Al_2O_3 .

III. *Diaspore*—588 °C endotherm, diaspore is transformed to Al_2O_3 .

Samples

I, Goethite, $\alpha\text{-FeO}(\text{HO})$ (Fe 62.9%, O 27%, H_2O 10.1%);
 II, lepidocrocite, $\gamma\text{-FeO}(\text{OH})$ (Fe_2O_3 89.9%, H_2O 10.1%);
 III, brycite, $\text{Mg}(\text{OH})_2$ (MgO 69.12%, H_2O 30.88%).

Results

I. *Goethite*—309 °C endotherm, goethite is transformed to $\alpha\text{-Fe}_2\text{O}_3$ (hematite).

II. *Lepidocrocite*—360 °C endotherm, lepidocrocite is transformed to $\gamma\text{-Fe}_2\text{O}_3$; 490 °C exotherm, $\gamma\text{-Fe}_2\text{O}_3$ becomes $\alpha\text{-Fe}_2\text{O}_3$.

III. *Brycite*—360 °C endotherm, brycite undergoes dehydration and is transformed to $\text{Mg}_8\text{O}_5(\text{OH})_6$; 455 °C endotherm, $\text{Mg}_8\text{O}_5(\text{OH})_6$ dehydrates and is transformed to MgO .

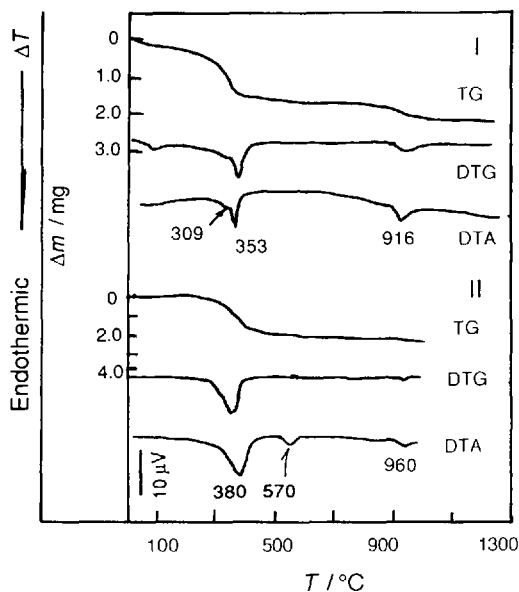


Figure 10.50 DTA-TG-DTG curves of (I) heterogenite [3] and (II) manganite [6]

Samples

I, Heterogenite, $\text{CoO}(\text{OH})$ (Co_2O_3 90.20%, H_2O 9.80%); II, manganite, $\text{Mn} \cdot \text{MnO}_2(\text{OH})_2$ (MnO 40.4%, MnO_2 49.4%, H_2O 10.2%).

Results

I. Heterogenite—309 and 353 °C endotherms, heterogenite is transformed to Co_3O_4 ; 916 °C endotherm, Co_3O_4 is transformed to CoO .

II. Manganite—380 °C endotherm, manganite is transformed to $\text{MnO} \cdot \text{MnO}_2$; 570 °C endotherm, $\text{Mn} \cdot \text{MnO}_2$ becomes $\beta\text{-Mn}_2\text{O}_3$; 960 °C endotherm, $\beta\text{-Mn}_2\text{O}_3$ becomes Mn_3O_4 .

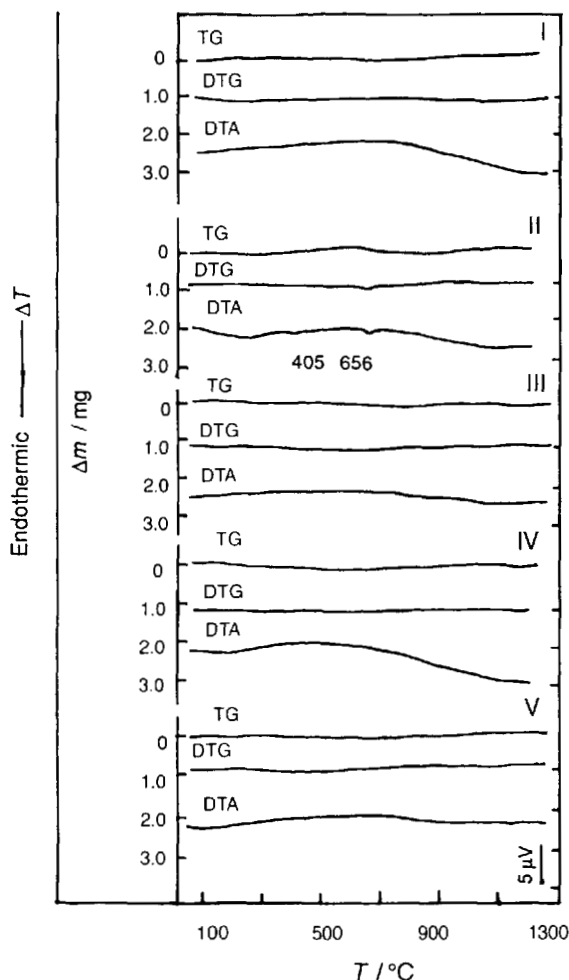


Figure 10.51 DTA-TG-DTG curves of (I) bunsenite, (II) lime, (III) periclase, (IV) zincite and (V) bromellite [3]

Samples

I, Bunsenite, NiO (Ni 78.58%, O 21.42%); II, lime, CaO (Ca 71.44%, O 28.56%); III, periclase, MgO (Mg 60.32%, O 39.68%); IV, zincite, ZnO (Zn 80.34%, O 19.66%); V, bromellite, BeO (Be 36.05%, O 63.95%).

Results

From 20 to 1200 °C bunsenite, lime, periclase, zincite and bromellite show no thermal events. Any thermal effects shown by lime are due to the decomposition of impurities.

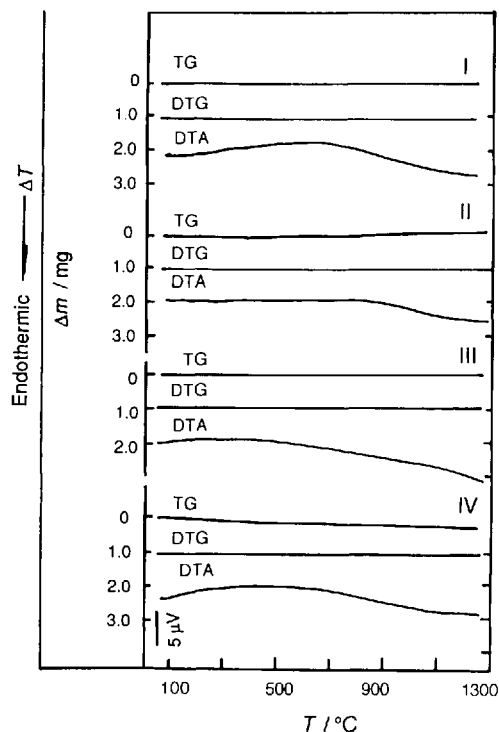


Figure 10.52 DTA-TG-DTG curves of (I) eskolaite, (II) cerianite, (III) thorianite and (IV) baddeleyite [3]

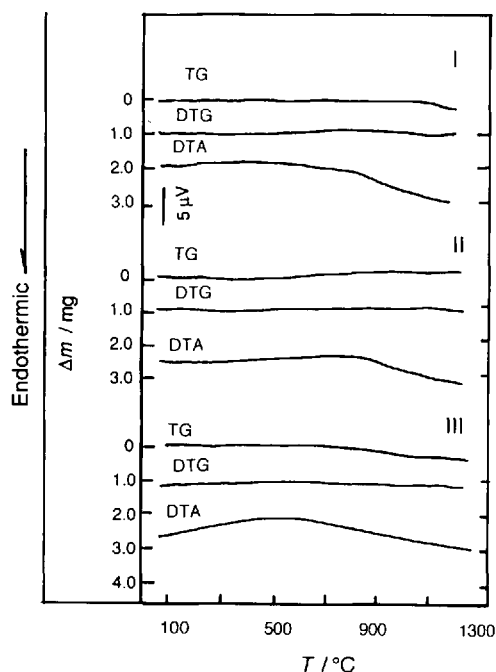


Figure 10.53 DTA-TG-DTG curves of (I) anatase, (II) rutile and (III) cassiterite [3]

Samples

I, Eskolaite, Cr_2O_3 (Cr 68.43%, O 31.57%); II, cerianite, CeO_2 (Ce 81.47%, O 18.53%); III, thorianite, ThO_2 (Th 87.88%, O 12.12%); IV, baddeleyite, ZrO_2 (Zr 74.1%, O 25.9%).

Results

From 20 to 1300 °C eskolaite, cerianite, thorianite and baddeleyite show no thermal events.

Samples

I, Anatase, TiO_2 (Ti 60%, O 40%); II, rutile, TiO_2 (Ti 60%, O 40%); III, cassiterite, SnO_2 (Sn 78.8%, O 21.2%).

Results

Thermal effects of anatase are due to the decomposition of impurities. At 1200 °C anatase becomes rutile. From 20 to 1200 °C rutile and cassiterite show no thermal events.

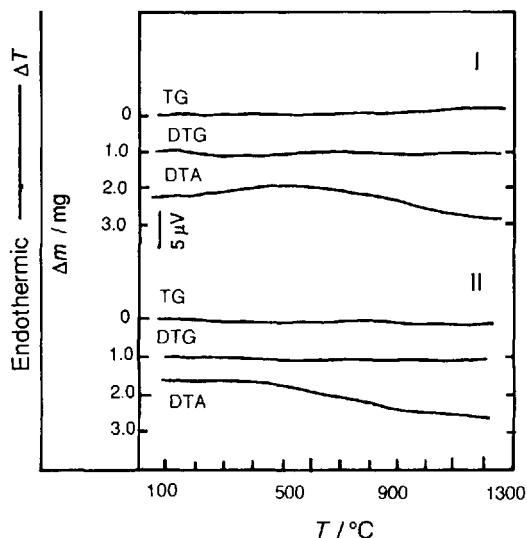


Figure 10.54 DTA-TG-DTG curves of (I) manganotantalite and (II) bismutotantalite [3]

Samples

I, Manganotantalite, MnTa_2O_6 ; II, bismutotantalite, BiTaO_4 (Bi_2O_3 51.33%, Ta_2O_5 48.67%).

Results

From 20 to 1300 °C manganotantalite and bismutotantalite show no thermal events.

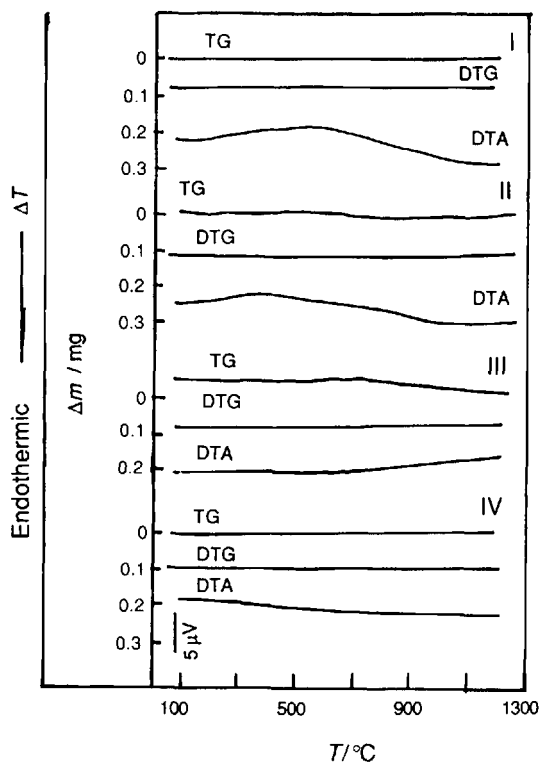


Figure 10.55 DTA-TG-DTG curves of (I) franklinite, (II) gahnite, (III) spinel and (IV) chrysoberyl [3]

Samples

I, Franklinite, ZnFe_2O_4 (ZnO 33.76%, Fe_2O_3 66.24%); II, gahnite, ZnAl_2O_4 (ZnO 44.3%, Al_2O_3 55.7%); III, spinel, MgAl_2O_4 (MgO 28.2%, Al_2O_3 71.8%); IV, chrysoberyl, BeAl_2O_4 (BeO 7.09%, Al_2O_3 92.90%).

Results

From 20 to 1200 °C franklinite, gahnite, spinel and chrysoberyl show no thermal events.

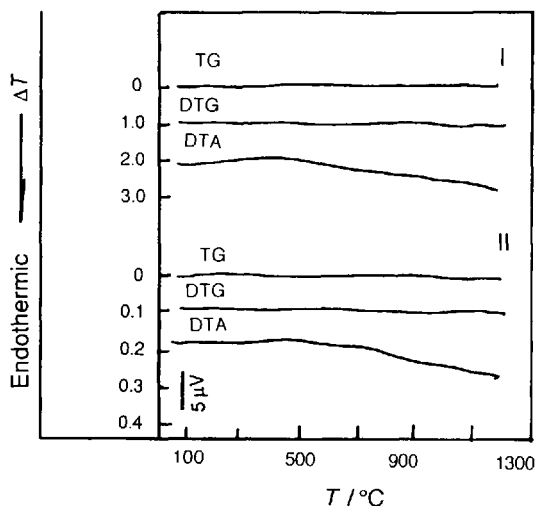


Figure 10.56 DTA-TG-DTG curves of (I) pyrochlore and (II) vavlamoffite [3]

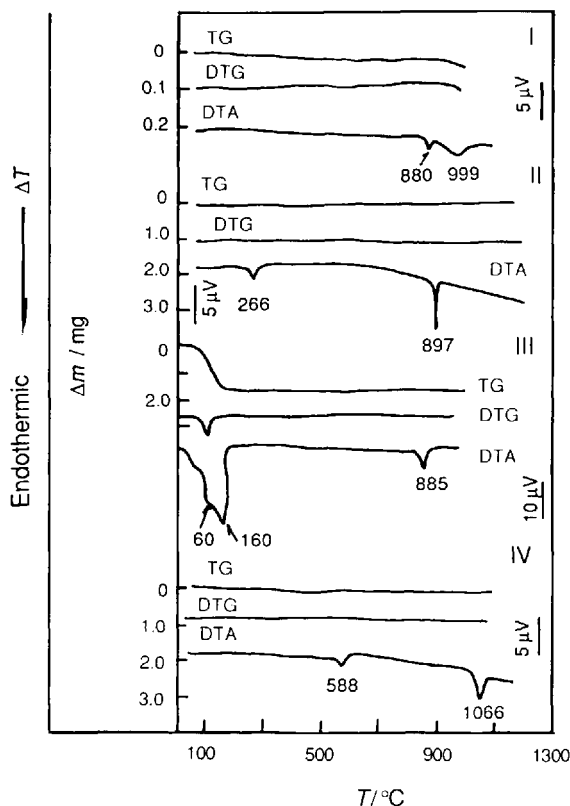


Figure 10.57 DTA-TG-DTG curves of (I) anglesite [3], (II) thenardite [3], (III) mirabilite [2] and (IV) arkanite [3]

Samples

I, Pyrochlore, $(\text{Ca}, \text{Nb})_2\text{Nb}_2\text{O}_6(\text{OH}, \text{F})$; II, vavlamoffite, $(\text{Sn}, \text{Fe})(\text{O}, \text{OH})_2$.

Results

From 20 to 1200 °C pyrochlore and vavlamoffite show no thermal events.

10.5 Thermal Analysis Curves of Sulfate Minerals

Sulfate minerals can be categorized into the following: sulfate with free water, with crystalline water, with constitution water and with both crystalline and constitution water. Sulfate with free water exhibits structure transformation and melting. Sulfate partially decomposes and releases SO_3 on heating. Sulfate with crystalline water dehydrates at low temperature and the dehydrated substance shows structure transformation, melting and decomposition with release of SO_3 . Sulfate with constitution water releases water at temperatures higher than 400 °C in one or two stages and decomposes. Sulfate with both crystalline and constitution water releases crystalline water at low temperature and then releases constitution water at temperatures higher than 300 °C; some of the dehydrated substances release SO_3 in one or two stages.

Samples:

I, Anglesite, PbSO_4 (PbO 73.6%, SO_3 26.4%); II, thenardite, Na_2SO_4 (Na_2O 43.7%, SO_3 56.3%); III, miabilite, $\text{Na}_2\text{SO}_4 \cdot 10\text{H}_2\text{O}$ (Na_2 19.24%, SO_3 24.85%, H_2O 55.91%); IV, arkanite, K_2SO_4 .

Results

I. Anglesite—880 °C endotherm, anglesite melts; 999 °C endotherm, molten anglesite decomposes; PbO is formed and SO_3 is released.

(continued)

II. Thenardite—266 °C endotherm, thenardite undergoes a polymorphic transformation; 897 °C endotherm, thenardite melts.

III. Mirabilite—60 °C endotherm, mirabilite is a solution in crystalline water, 160 °C endotherm, mirabilite releases water of crystallization; 885 °C endotherm, Na_2SO_4 melts.

IV. Arkanite—588 °C endotherm, arkanite undergoes a polymorphic transformation; 1066 °C endotherm, arkanite melts.

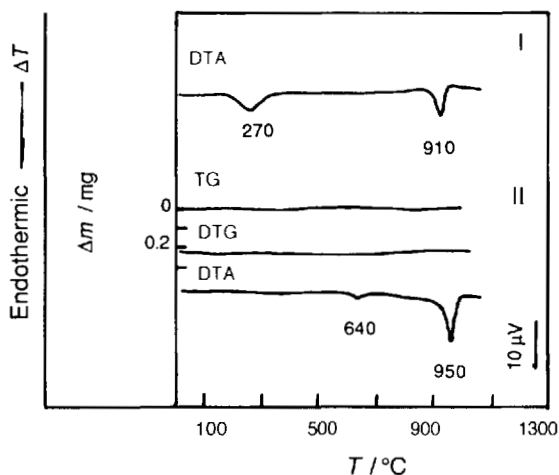


Figure 10.58 DTA-TG-DTG curves of (I) glauberite and (II) langbeinite [6]

Samples

I, Glauberite, $\text{Na}_2\text{Ca}(\text{SO}_4)_2$ (Na_2O 22.28%, CaO 20.16%, SO_3 57.56%); II, langbeinite, $\text{K}_2\text{Mg}_2(\text{SO}_4)_3$ (K_2O 22.70%, MgO 19.43%, SO_3 57.87%).

Results

I. Glauberite—270 °C endotherm, thenardite present in glauberite undergoes a polymorphic transformation; 910 °C endotherm, glauberite melts.

II. Langbeinite—640 °C endotherm, langbeinite undergoes a polymorphic transformation; 950 °C endotherm, langbeinite melts.

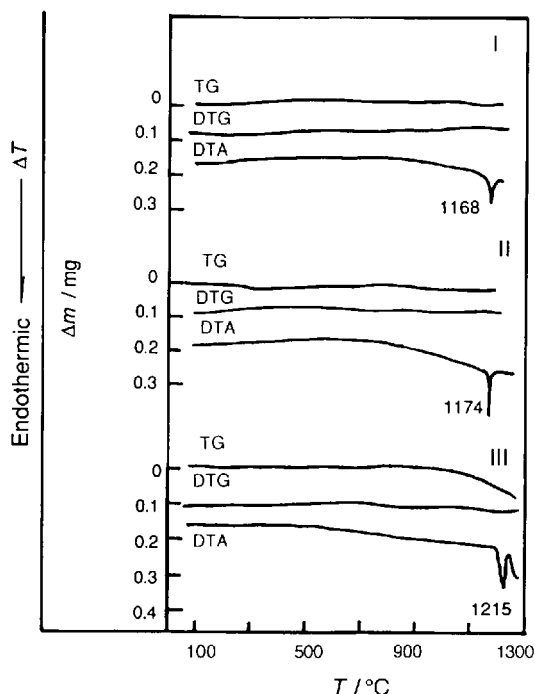


Figure 10.59 DTA-TG-DTG curves of (I) barite, (II) celestine and (III) anhydrite [3]

Samples

I, Barite, BaSO_4 (Ba 65.7%, SO_3 34.3%); II, celestine, SrSO_4 (SrO 56.41%, SO_3 43.59%); III, anhydrite: CaSO_4 (CaO 41.2%, SO_3 58.8%).

Results

I. Barite—1168 °C endotherm, barite undergoes a polymorphic transformation.

II. Celestine—1174 °C endotherm, celestine undergoes a polymorphic transformation.

III. Anhydrite—1215 °C endotherm, anhydrite undergoes a polymorphic transformation.

Samples

I, Melantherite, $\text{FeSO}_4 \cdot 7\text{H}_2\text{O}$ (FeO 25.84%, SO_3 28.80%, H_2O 45.36%); II, morenosite, $\text{NiSO}_4 \cdot 7\text{H}_2\text{O}$ (NiO 26.59%, SO_3 28.51%, H_2O 44.90%); III, goslarite, $\text{ZnSO}_4 \cdot 7\text{H}_2\text{O}$ (ZnO 28.29%, SO_3 27.83%, H_2O 43.84%); IV, epsomite, $\text{MgSO}_4 \cdot 7\text{H}_2\text{O}$ (MgO 16.3 %, SO_3 32.5%, H_2O 51.2%).

Results

I. Melantherite—160 °C endotherm, melantherite releases 6 mol H_2O ; 240 °C endotherm, melantherite releases one water molecule and Fe^{2+} oxidizes to Fe^{3+} ; it is transformed to $\text{Fe}_2\text{O}(\text{SO}_4)_2$; 660 °C endotherm, $\text{Fe}_2\text{O}(\text{SO}_4)_2$ decomposes to $\text{Fe}_2\text{O}(\text{SO}_4)_3$ and Fe_2O_3 and SO_3 is released; 760 °C endotherm, $\text{Fe}_2\text{O}(\text{SO}_4)_2$ decomposes, to Fe_2O_3 and releases SO_3 .

II. Morenosite—200 °C endotherm, 1 mol morenosite releases 6 mol H_2O ; 430 °C endotherm, morenosite releases one water mole-

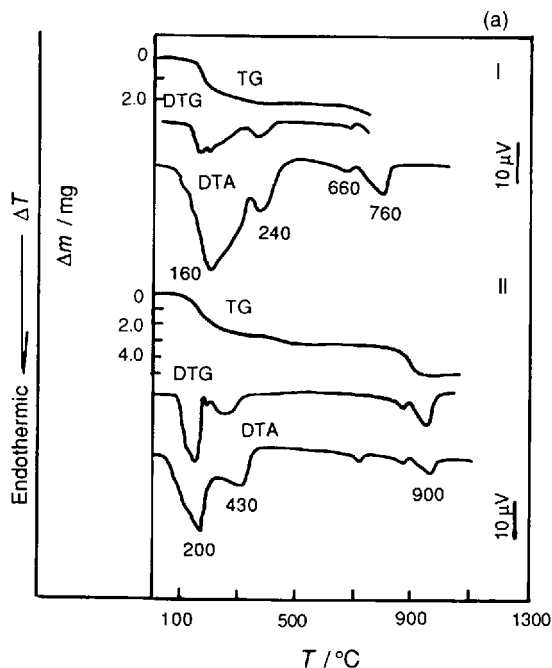


Figure 10.60 (a) DTA-TG-DTG curves of (I) melantherite [6] and (II) morenosite [6]

(continued)

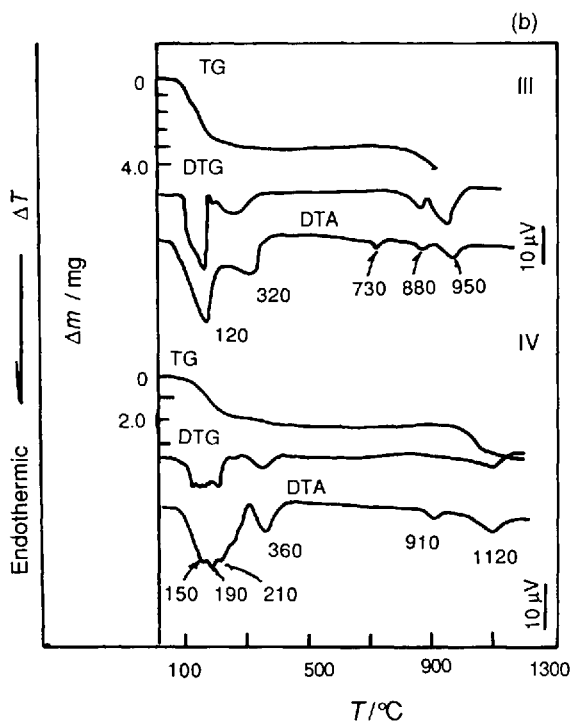


Figure 10.60 (b) DTA-TG-DTG curves of (III) goslarite and (IV) epsomite [6]

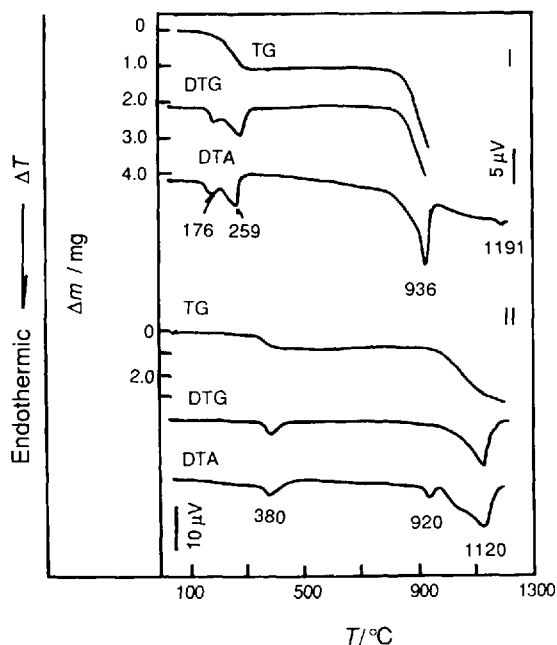


Figure 10.61 DTA-TG-DTG curves of (I) szmikite [3] and (II) kieserite [6]

cule; 900 °C endotherm, NiSO_4 decomposes to NiO and releases SO_3 .

III. Goslarite—120 °C endotherm, 1 mol goslarite releases 5 mol H_2O ; 320 °C endotherm, goslarite releases two water molecules; 730 °C endotherm, ZnSO_4 melts; 880 °C endotherm, ZnSO_4 partially decomposes and releases SO_3 ; 950 °C endotherm, remainder of ZnSO_4 decomposes to ZnO and releases SO_3 .

IV. Epsomite—150, 190 and 210 °C endotherms, 1 mol epsomite releases 6 mol H_2O in these stages; 360 °C endotherm, epsomite releases 1 mol H_2O to give MgSO_4 ; 910 °C endotherm, MgSO_4 melts; 1120 °C endotherm, MgSO_4 decomposes to MgO and releases SO_3 .

Samples

I, Szmikite, $\text{MnSO}_4 \cdot \text{H}_2\text{O}$ (MnO 41.97%, SO_3 47.37%, H_2O 10.66%); II, kieserite, $\text{MgSO}_4 \cdot \text{H}_2\text{O}$ (MgO 29.13%, SO_3 57.85%, H_2O 13.02%).

Results

I. Szmikite—176 °C endotherm, 1 mol szmikite releases 0.5 mol H_2O ; 259 °C endotherm, szmikite releases 0.5 mol H_2O and is transformed to MnSO_4 ; 936 °C endotherm, MnSO_4 decomposes and oxidizes; it is transformed to Mn_3O_4 and releases SO_3 ; 1191 °C endotherm, $\beta\text{-Mn}_3\text{O}_4$ is transformed to $\gamma\text{-Mn}_3\text{O}_4$.

II. Kieserite—380 °C endotherm, kieserite releases water; 920 °C endotherm, MgSO_4 melts; 1120 °C endotherm, molten MgSO_4 decomposes to MgO and SO_3 is released.

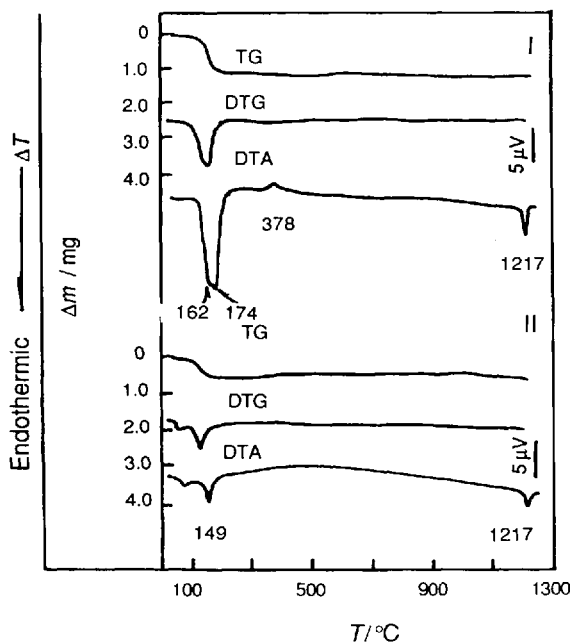


Figure 10.62 DTA-TG-DTG curves of (I) gypsum and (II) bassanite [3]

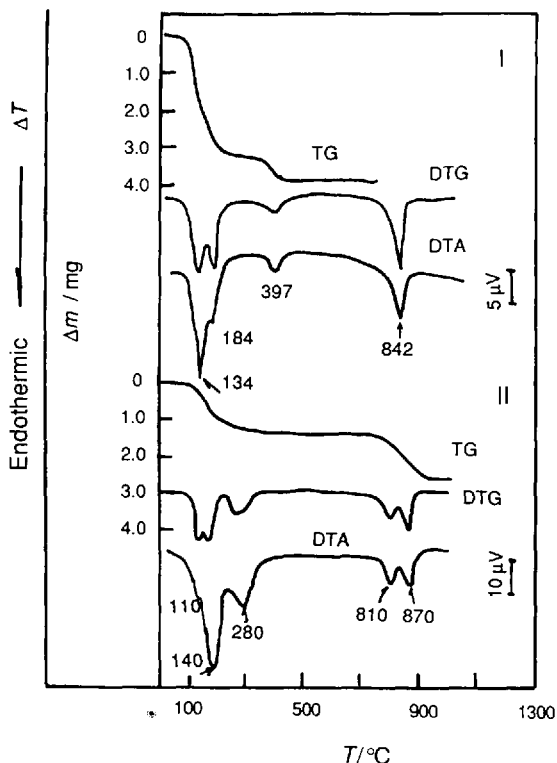


Figure 10.63 DTA-TG-DTG curves of (I) retgersite [3] and (II) chalcantite [6]

Samples

I, Gypsum, $\text{CaSO}_4 \cdot 2\text{H}_2\text{O}$ (CaO 32.5%, SO_3 46.6%, H_2O 20.9%); II, bassanite, $\text{CaSO}_4 \cdot 0.5\text{H}_2\text{O}$ (CaO 38.64%, SO_3 55.16%, H_2O 6.20%).

Results

I. Gypsum—162 and 174 °C endotherms, gypsum dehydrates in stages; 378 °C exotherm, CaSO_4 crystallizes and forms anhydrite; 1217 °C endotherm, anhydrite undergoes a polymorphic transformation.

II. Bassanite—149 °C endotherm, bassanite dehydrates; 1217 °C endotherm, CaSO_4 undergoes a polymorphic transformation.

Samples

I, Retgersite, $\text{NiSO}_4 \cdot 6\text{H}_2\text{O}$ (NiO 28.42%, SO_3 30.46%, H_2O 41.12%); II, chalcantite, $\text{CuSO}_4 \cdot 5\text{H}_2\text{O}$ (CuO 31.80%, SO_3 32.10%, H_2O 36.10%).

Results

I. Retgersite—134 °C endotherm, 1 mol retgersite releases 4 mol H_2O ; 184 °C endotherm, 1 mol retgersite releases 1 mol H_2O ; 397 °C endotherm, 1 mol retgersite releases 1 mol H_2O and is transformed to NiSO_4 ; 842 °C endotherm, NiSO_4 decomposes to NiO and releases SO_3 .

II. Chalcantite—110 °C endotherm, 1 mol chalcantite releases 2 mol H_2O ; 140 °C endotherm, 1 mol chalcantite releases 1 mol H_2O ; 280 °C endotherm, 1 mol chalcantite releases 1 mol H_2O and is transformed to CuSO_4 ; 810 °C endotherm, CuSO_4 decomposes to $\text{Cu}_2\text{O}(\text{SO}_4)$ and releases SO_3 ; 870 °C endotherm, $\text{Cu}_2\text{O}(\text{SO}_4)$ decomposes to CuO and SO_3 is released.

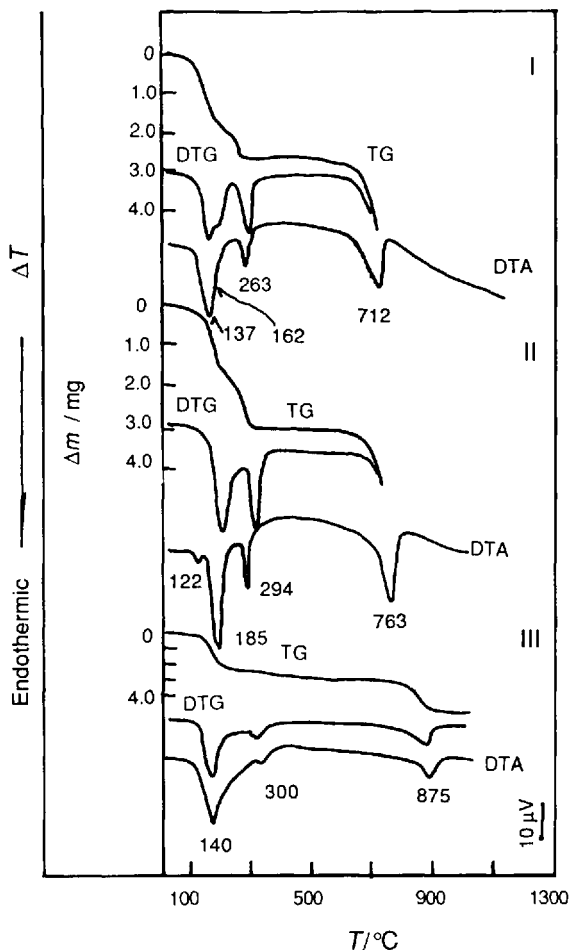


Figure 10.64 DTA-TG-DTG curves of (I) quenstedtite [3], (II) coquimbite [3] and (III) alunogen [6]

Samples

I, Quenstedtite, $\text{Fe}_2(\text{SO}_4)_3 \cdot 10\text{H}_2\text{O}$ (Fe_2O_3 27.53%, SO_3 41.41%, H_2O 31.06%); II, coquimbite, $\text{Fe}_2(\text{SO}_4)_3 \cdot 9\text{H}_2\text{O}$ (Fe_2O_3 28.41%, SO_3 42.74%, H_2O 28.85%); III, alunogen, $\text{Al}_2(\text{SO}_4)_3 \cdot 18\text{H}_2\text{O}$ (Al_2O_3 15.30%, SO_3 36.04%, H_2O 48.66%).

Results

I. Quenstedtite—137 °C endotherm, 1 mol quenstedtite releases 6 mol H_2O ; 162 °C endotherm, 1 mol quenstedtite releases 2 mol H_2O ; 263 °C endotherm, 1 mol quenstedtite releases 2 mol H_2O and gives $\text{Fe}_2(\text{SO}_4)_3$; 712 °C endotherm, $\text{Fe}_2(\text{SO}_4)_3$ decomposes to Fe_2O_3 and releases SO_3 .

II. Coquimbite—122 °C endotherm, 1 mol coquimbite releases 1 mol H_2O ; 185 °C endotherm, 1 mol coquimbite releases 6 mol H_2O ; 294 °C endotherm, 1 mol coquimbite releases 2 mol H_2O and is transformed to $\text{Fe}_2(\text{SO}_4)_3$; 763 °C endotherm, $\text{Fe}_2(\text{SO}_4)_3$ decomposes to Fe_2O_3 and SO_3 is released.

III. Alunogen—140 °C endotherm, 1 mol alunogen releases 15 mol H_2O ; 300 °C endotherm, 1 mol alunogen releases 3 mol H_2O and is transformed to $\text{Al}_2(\text{SO}_4)_3$; 875 °C endotherm, $\text{Al}_2(\text{SO}_4)_3$ decomposes to Al_2O_3 and releases SO_3 .

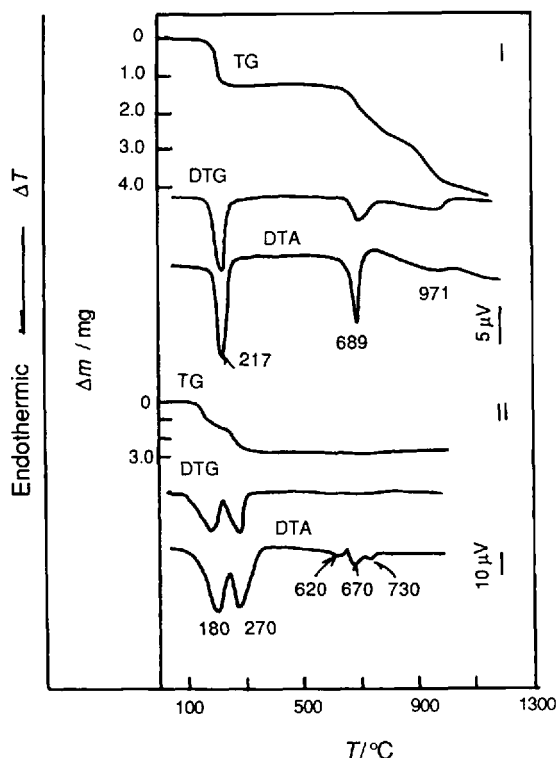


Figure 10.65 DTA-TG-DTG curves of (I) ferrinatrinite [3] and (II) astrakanite [6]

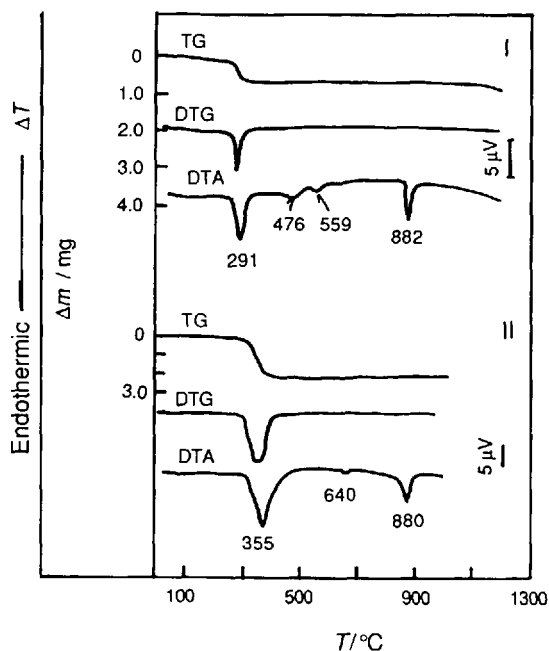


Figure 10.66 DTA-TG-DTG curves of (I) syngenite [3] and (II) polyhalite [6]

Samples

I, Ferrinatrinite, $\text{Na}_3\text{Fe}(\text{SO}_4)_3 \cdot 3\text{H}_2\text{O}$ (Na_2O 19.91%, Fe_2O_3 17.10%, SO_3 51.42%, H_2O 11.57%); II, astrakanite, $\text{Na}_2\text{Mg}(\text{SO}_4)_2 \cdot 4\text{H}_2\text{O}$ (Na_2O 18.53%, MgO 12.06%, SO_3 47.87%, H_2O 21.5%).

Results

I. Ferrinatrinite—217 °C endotherm, ferrinatrinite dehydrates; 689 °C endotherm, $\text{Na}_3\text{Fe}(\text{SO}_4)_3$ decomposes with release of SO_3 ; 971 °C endotherm, $\text{NaFeO}(\text{SO}_4)$ decomposes to $\text{Na}_2\text{OFe}_2\text{O}_3$ and releases SO_3 , followed by transformation to Na_2SO_4 and $\text{NaFeO}(\text{SO}_4)$.

II. Astrakanite—180 °C endotherm, 1 mol astrakanite releases 2 mol H_2O ; 270 °C endotherm, 1 mol astrakanite releases 2 mol H_2O and is transformed to Na_2MgSO_4 ; 620 °C endotherm, $\text{Na}_2\text{Mg}(\text{SO}_4)_2$ undergoes a polymorphic transformation; 670 °C endotherm, $\text{Na}_2\text{Mg}(\text{SO}_4)$ decomposes and $\text{Na}_2\text{SO}_4 \cdot 3\text{MgSO}_4$ and Na_2SO_4 are formed; 730 °C endotherm, impurity melts.

Samples

I, Syngenite, $\text{K}_2\text{Ca}(\text{SO}_4)_2 \cdot \text{H}_2\text{O}$ (K_2O 28.68 %, CaO 17.08%, SO_3 48.750%, H_2O 5.49%); II, polyhalite, $\text{K}_2\text{MgCa}_2(\text{SO}_4)_4 \cdot 2\text{H}_2\text{O}$ (K_2O 15.6%, CaO 18.6%, MgO 6.7%, SO_3 53.1%, H_2O 6.0%).

Results

I. Syngenite—291 °C endotherm, syngenite dehydrates; 476 °C endotherm, $\text{K}_2\text{Ca}(\text{SO}_4)_2$ decomposes and is transformed to K_2SO_4 and $\text{K}_2\text{Ca}(\text{SO}_4)$; 559 °C endotherm, K_2SO_4 undergoes a polymorphic transformation; 882 °C endotherm, K_2SO_4 and $\text{K}_2\text{MgCa}_2(\text{SO}_4)_4$ melt.

II. Polyhalite—355 °C endotherm, polyhalite releases water of crystallization; 640 °C endotherm, $\text{K}_2\text{MgCa}_2(\text{SO}_4)_4$ undergoes a polymorphic transformation; 880 °C endotherm, $\text{K}_2\text{MgCa}_2(\text{SO}_4)_4$ melts.

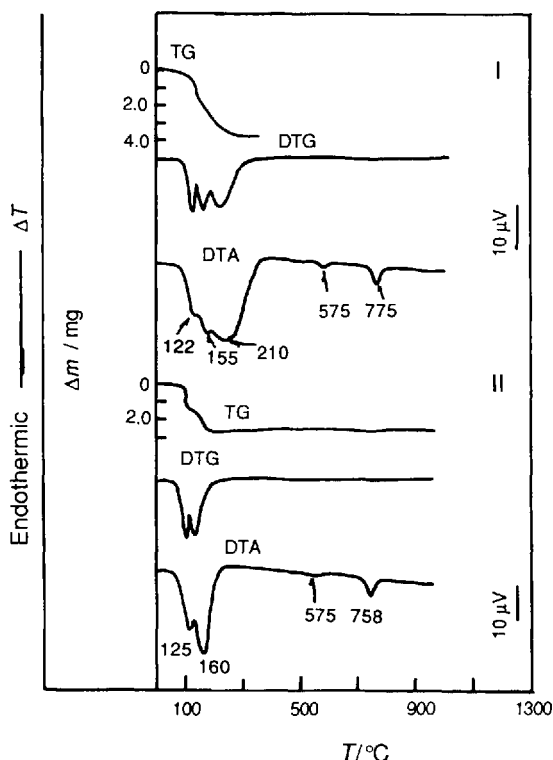


Figure 10.67 DTA-TG-DTG curves of (I) schonite and (II) leonite [6]

Sample

I, Schonite, $K_2Mg(SO_4)_2 \cdot 6H_2O$ (K_2O 23.39%, Mg 10.01%, SO_3 39.76%, H_2O 26.84%); II, leonite, $K_2Mg(SO_4)_2 \cdot 4H_2O$ (K_2O 25.69%, Mg 10.99%, SO_3 43.67%, H_2O 19.65%).

Results

I. Schonite—122 °C endotherm, 1 mol schonite releases 2 mol H_2O ; 155 °C endotherm, 1 mol schonite releases 2 mol H_2O and is transformed to $K_2Mg(SO_4)_2$.

II. Leonite—125 °C endotherm, 1 mol leonite releases 2 mol H_2O ; 160 °C endotherm, 1 mol leonite releases 2 mol H_2O and is transformed to $K_2Mg(SO_4)_2$; 575 °C endotherm, $K_2Mg(SO_4)_2$ undergoes a polymorphic transformation; 758 °C and 775 °C endotherms, $K_2Mg(SO_4)_2$ melts.

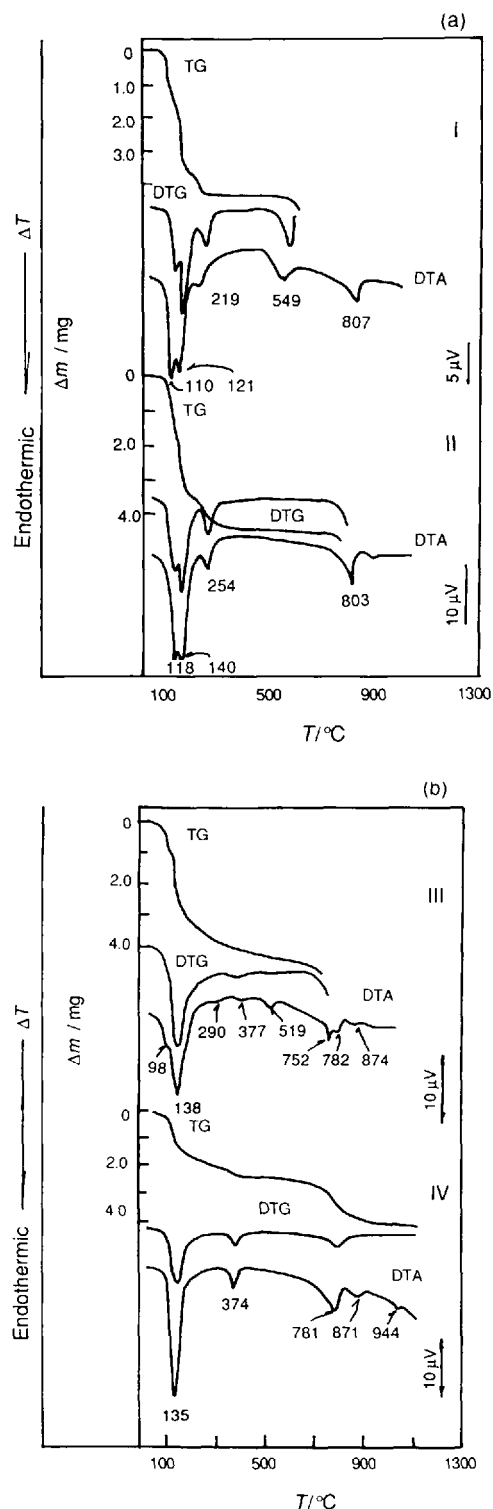


Figure 10.68 DTA-TG-DTG curves of (a) (I) tschermigite and (II) alum and (b) (III) pickeringite and (IV) halotrichite

Samples

I, Tschermigite, $(\text{NH}_4)\text{Al}(\text{SO}_4)_2 \cdot 12\text{H}_2\text{O}$ (NH_3 3.76%, Al_2O_3 11.25%, SO_3 35.32%, H_2O 49.67%); II, alum, $\text{KAl}(\text{SO}_4)_2 \cdot 12\text{H}_2\text{O}$ (K_2O 9.9%, Al_2O_3 10.8%, SO_3 33.8%, H_2O 45.5%); III, pickeringite, $\text{MgAl}_2(\text{SO}_4)_4 \cdot 22\text{H}_2\text{O}$ (MgO 4.69%, Al_2O_3 11.87%, SO_3 37.29%, H_2O 46.15%); IV, halotrichite, $\text{Fe}^{\text{II}}\text{Al}_2(\text{SO}_4)_4 \cdot 22\text{H}_2\text{O}$ (FeO 8.07%, Al_2O_3 11.45%, SO_3 35.97%, H_2O 44.51%).

Results

I. Tschermigite—110 and 121 °C endotherms, 1 mol tschermigite releases 10 mol crystalline water; 219 °C endotherm, 1 mol tschermigite releases 2 mol crystalline water and is transformed to $(\text{NH}_4)\text{Al}(\text{SO}_4)_2$; 549 °C endotherm, $(\text{NH}_4)(\text{AlSO}_4)_2$ decomposes to $\text{Al}_2(\text{SO}_4)_3$ and releases SO_3 , NH_3 and H_2O ; 807 °C endotherm, $\text{Al}_2(\text{SO}_4)_3$ decomposes to Al_2O_3 and releases SO_3 .

II. Alum—118 and 140 °C endotherms, 1 mol alum releases 10 mol H_2O ; 254 °C endotherm; 1 mol alum releases 2 mol H_2O and is transformed to $\text{KAl}(\text{SO}_4)_2$; 803 °C endotherm, $\text{KAl}(\text{SO}_4)_2$ decomposes to Al_2O_3 and K_2SO_4 and releases SO_3 .

III. Pickeringite—98, 138, 290 and 377 °C endotherms, pickeringite releases water of crystallization in stages; 519 °C endotherm, $\text{MgAl}_2(\text{SO}_4)_4$ decomposes to $\text{Al}_2(\text{SO}_4)_3$ and MgSO_4 ; 752, 782 and 874 °C endotherms, MgSO_4 and $\text{Al}_2(\text{SO}_4)_3$ react and MgAl_2O_4 is formed with release of SO_3 .

IV. Halotrichite—135 °C endotherm, 1 mol halotrichite releases 20 mol crystalline H_2O ; 374 °C endotherm, 1 mol halotrichite releases 2 mol crystalline H_2O ; 781 and 871 °C endotherms, $\text{Fe}^{\text{II}}\text{Al}_2(\text{SO}_4)_4$ decomposes to FeAl_2O_4 and releases SO_3 .

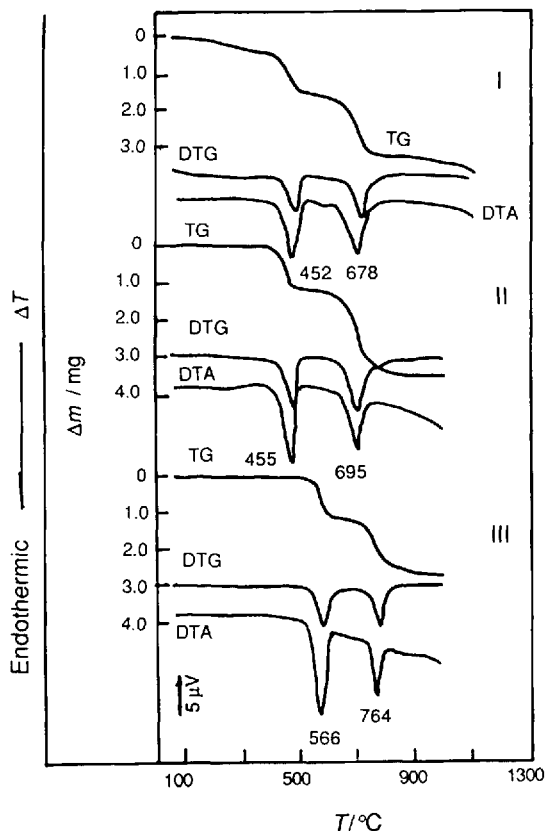


Figure 10.69 DTA-TG-DTG curves of (I) natrojarosite, (II) jarosite and (III) alunite [3]

Samples

I, Natrojarosite, $\text{NaFe}^{\text{III}}(\text{SO}_4)_2(\text{OH})_6$ (Na_2O 6.40%, Fe_2O_3 49.42%, SO_3 33.04%, H_2O 11.14%); II, jarosite, $\text{KFe}^{\text{III}}(\text{SO}_4)_2(\text{OH})_6$ (K_2O 9.4%, Fe_2O_3 47.9%, SO_3 31.9%, H_2O 10.8%); III, alunite, $\text{KAl}(\text{SO}_4)_2(\text{OH})_6$ (K_2O 11.4%, Al_2O_3 37.0%, SO_3 38.6%, H_2O 13.0%).

Results

I. Natrojarosite—452 °C endotherm, natrojarosite releases constitution water and is transformed to $\text{NaFe}^{\text{III}}\text{O}_3(\text{SO}_4)_2$; 678 °C endotherm, $\text{NaFe}^{\text{III}}\text{O}_3(\text{SO}_4)_2$ decomposes. It is transformed to Fe_2O_3 and $\text{NaFeO}(\text{SO}_4)$ and releases SO_3 .

II. Jarosite—455 °C endotherm, jarosite releases constitution water and decomposes to $\text{K}_2\text{SO}_4 \cdot \text{Fe}_2(\text{SO}_4)_3$ and Fe_2O_3 ; 695 °C endotherm, $\text{K}_2\text{SO}_4 \cdot \text{Fe}_2(\text{SO}_4)_3$ decomposes to $\text{Fe}_2\text{O}_3 \cdot \text{K}_2\text{SO}_4$ and releases SO_3 .

III. Alunite—566 °C endotherm, alunite releases constitution water and is transformed to $\text{KAl}_3\text{O}_3(\text{SO}_4)_2$; 764 °C endotherm, $\text{KAl}_3\text{O}_3(\text{SO}_4)_2$ decomposes to $\text{K}_2\text{O} \cdot \text{Al}_2\text{O}_3$ and releases SO_3 .

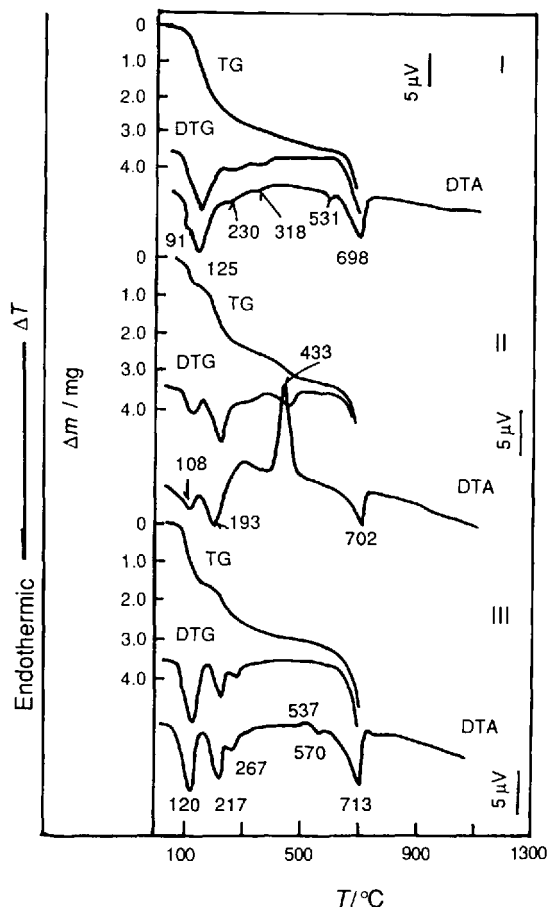


Figure 10.70 DTA-TG-DTG curves of (I) fibroferrite, (II) butlerite and (III) hohmannite [3]

Samples

I, Fibroferrite, $\text{Fe}^{\text{III}}(\text{SO}_4)(\text{OH}) \cdot 5\text{H}_2\text{O}$ (Fe_2O_3 30.83%, SO_3 30.91%, H_2O 38.26%); II, butlerite, $\text{Fe}^{\text{III}}(\text{SO}_4)(\text{OH}) \cdot 2\text{H}_2\text{O}$ (Fe_2O_3 38.96%, SO_3 39.06%, H_2O 21.98%); III, hohmannite, $\text{Fe}_2^{\text{III}}2(\text{SO}_4)_2(\text{OH})_2 \cdot 7\text{H}_2\text{O}$ (Fe_2O_3 34.42%, SO_3 34.51%, H_2O 31.07%).

Results

I. Fibroferrite—91, 125, 230 and 318 °C endotherms, fibroferrite releases water of crystallization in stages; 531 °C endotherm, fibroferrite releases constitution water and is transformed to $\text{Fe}_2^{\text{III}}\text{O}(\text{SO}_4)_2$; 698 °C endotherm, $\text{Fe}_2^{\text{III}}\text{O}(\text{SO}_4)_2$ decomposes to Fe_2O_3 and releases SO_3 .

II. Butlerite—108 and 193 °C endotherms, butlerite releases crystalline water; 433 °C exotherm, butlerite releases constitution water, is transformed to Fe_2O_3 and $\text{Fe}_2(\text{SO}_4)_3$ and releases SO_3 ; 702 °C endotherm, $\text{Fe}_2(\text{SO}_4)_3$ decomposes to Fe_2O_3 and releases SO_3 .

III. Hohmannite—120, 217 and 267 °C endotherms, hohmannite releases crystalline water, 537 °C exotherm, hohmannite releases constitution water, is transformed to Fe_2O_3 and $\text{Fe}_2(\text{SO}_4)_3$ and releases SO_3 ; 713 °C endotherm, $\text{Fe}_2(\text{SO}_4)_3$ decomposes to Fe_2O_3 and releases SO_3 .

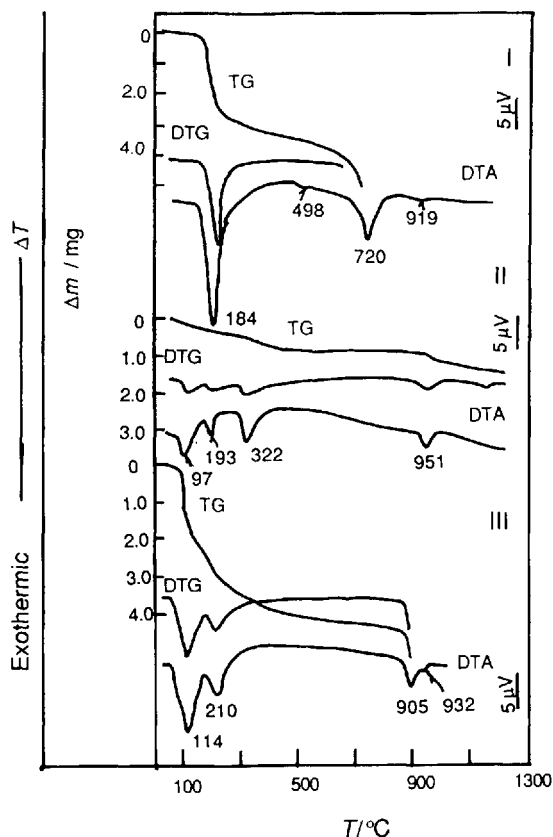


Figure 10.71 DTA-TG-DTG curves of (I) rostitite, (II) basaluminite and (III) aluminite [3]

Sample

I, Rostite, $\text{Al}(\text{SO}_4)(\text{OH}) \cdot 5\text{H}_2\text{O}$ (Al_2O_3 22.15%, SO_3 34.79%, H_2O 43.06%); II, basaluminite, $\text{Al}_4(\text{SO}_4)(\text{OH})_{10} \cdot 5\text{H}_2\text{O}$ (Al_2O_3 43.94%, SO_3 17.25%, H_2O 38.81%); III, aluminite, $\text{Al}_2(\text{SO}_4)(\text{OH})_4 \cdot 5\text{H}_2\text{O}$ (Al_2O_3 29.63%, SO_3 23.26%, H_2O 47.11%).

Results

I. Rostite—184 °C endotherm, rostitite releases water of crystallization; 498 °C endotherm, rostitite releases constitution water and is transformed to $\text{Al}_2\text{O}(\text{SO}_4)_2$; 720 °C endotherm, $\text{Al}_2\text{O}(\text{SO}_4)_2$ decomposes to Al_2O_3 and releases SO_3 .

II. Basaluminite—97 and 193 °C endotherms, basaluminite releases crystalline water; 322 °C endotherm, basaluminite releases constitution water and is transformed to $\text{Al}_4\text{O}_5(\text{SO}_4)$; 951 °C endotherm, $\text{Al}_4\text{O}_5(\text{SO}_4)$ decomposes to Al_2O_3 and releases SO_3 .

III. Aluminite—114 and 210 °C endotherms, aluminite releases water of crystallization and constitution; it is transformed to $\text{Al}_2\text{O}_2(\text{SO}_4)$; 905 °C endotherm, $\text{Al}_2\text{O}_2(\text{SO}_4)$ decomposes to Al_2O_3 and releases SO_3 .

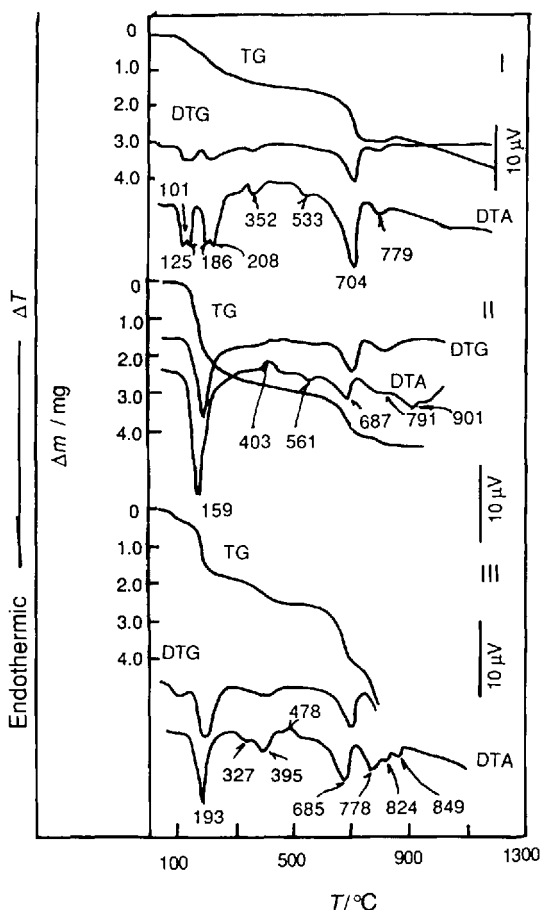


Figure 10.72 DTA-TG-DTG curves of (I) zincocapiapite, (II) zincobotryogen and (III) chaidamuite [3]

Samples

I, Zincocapiapite, $\text{ZnFe}^{\text{III}}(\text{SO}_4)_6(\text{OH})_2 \cdot 18\text{H}_2\text{O}$ (ZnO 6.65%, Fe_2O_3 26.11%, SO_3 39.26%, H_2O 27.89%); II, zincobotryogen, $\text{ZnFe}^{\text{III}}(\text{SO}_4)_2(\text{OH}) \cdot 7\text{H}_2\text{O}$ (ZnO 17.82%, Fe_2O_3 17.49%, SO_3 35.08%, H_2O 29.61%); III, chaidamuite, $\text{ZnFe}^{\text{III}}(\text{SO}_4)_2(\text{OH}) \cdot 4\text{H}_2\text{O}$ (ZnO 20.22%, Fe_2O_3 19.84%, SO_3 39.78%, H_2O 20.15%).

Results

I. Zincocapiapite—101, 125, 186 and 208 °C endotherms, zincocapiapite releases crystalline water in stages; 352 and 533 °C endotherms, zincocapiapite releases constitution water and is transformed to ZnSO_4 and $\text{Fe}_4^{\text{III}}\text{O}(\text{SO}_4)_5$; 704 °C endotherm, $\text{Fe}_4^{\text{III}}\text{O}(\text{SO}_4)_5$ decomposes to Fe_2O_3 and releases SO_3 ; 779 °C endotherm, ZnSO_4 decomposes to ZnO and releases SO_3 .

II. Zincobotryogen—159 °C endotherm, zincobotryogen releases crystalline water, 403 °C exotherm, impurity oxidizes; 561 °C endotherm, zincobotryogen releases water and decomposes; it is transformed to ZnSO_4 and $\text{Fe}_2^{\text{III}}\text{O}(\text{SO}_4)_2$; 687 °C endotherm, $\text{Fe}_2\text{O}(\text{SO}_4)$ decomposes to Fe_2O_3 and releases SO_3 ; 791 °C endotherm, ZnSO_4 decomposes to ZnO and releases SO_3 .

III. Chaidamuite—193 °C endotherm, chaidamuite releases water of crystallization; 327 and 395 °C endotherms, chaidamuite releases constitution water and is transformed to ZnSO_4 and $\text{Fe}_2\text{O}(\text{SO}_4)_3$; 478 °C exotherm, the dehydrated substance recrystallizes; 685 °C endotherm, $\text{Fe}_2\text{O}(\text{SO}_4)$ decomposes to Fe_2O_3 and releases SO_3 ; 778 °C endotherm, ZnSO_4 decomposes to ZnO and releases SO_3 .

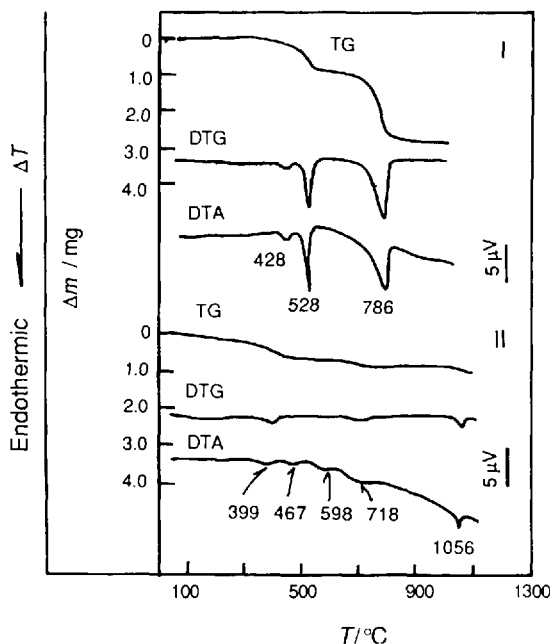


Figure 10.73 DTA-TG-DTG curves of (I) antlerite and (II) poznyakite [3]

Samples

I, Antlerite, $\text{Cu}_3(\text{SO}_4)(\text{OH})_4$ (CuO 67.27%, SO_3 22.57%, H_2O 10.16%); II, poznyakite, $\text{Cu}_4(\text{SO}_4)(\text{OH})_6 \cdot \text{H}_2\text{O}$ (CuO 67.65, SO_3 17.02%, H_2O 15.32%).

Results

I. Antlerite—428 and 528 °C endotherms, antlerite releases constitution water in stages and is transformed to $2\text{CuO} \cdot \text{CuSO}_4$; 786 °C endotherm, $2\text{CuO} \cdot \text{CuSO}_4$ decomposes to CuO and SO_3 .

II. Poznyakite—Poznyakite releases crystalline water at a temperature lower than 300 °C; 399 and 467 °C endotherms, poznyakite releases constitution water in stages and is transformed to $\text{Cu}_4\text{O}_3(\text{SO}_4)$; 598 °C endotherm, $\text{Cu}_4\text{O}_3(\text{SO}_4)$ decomposes to CuSO_4 and CuO; 718 °C endotherm, CuSO_4 decomposes to CuO and releases SO_3 ; 1056 °C endotherm, CuO is transformed to Cu_2O .

10.6 Thermal Analysis Curves of Carbonate Minerals

Carbonate minerals decompose by releasing H_2O and CO_2 . Crystalline water in carbonates is released at low temperature and constitution water is released at high temperature. Minerals with variable valence elements change valence state by heating. Alkali metal carbonates melt by heating, but do not decompose.

Sample

Witherite, BaCO_3 (BaO 77.70%, CO_2 22.30%).

Results

810 °C endotherm, witherite undergoes a polymorphic transformation; 910 °C endotherm, witherite is transformed to another polymorphic structure.

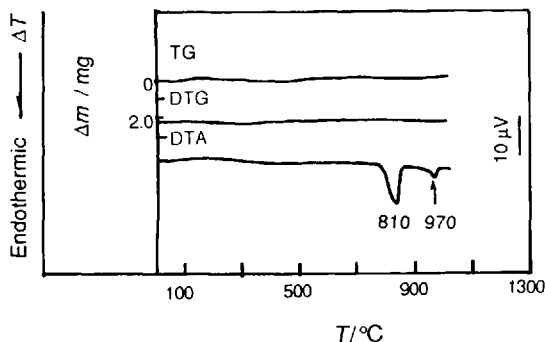


Figure 10.74 DTA-TG-DTG curves of witherite [6]

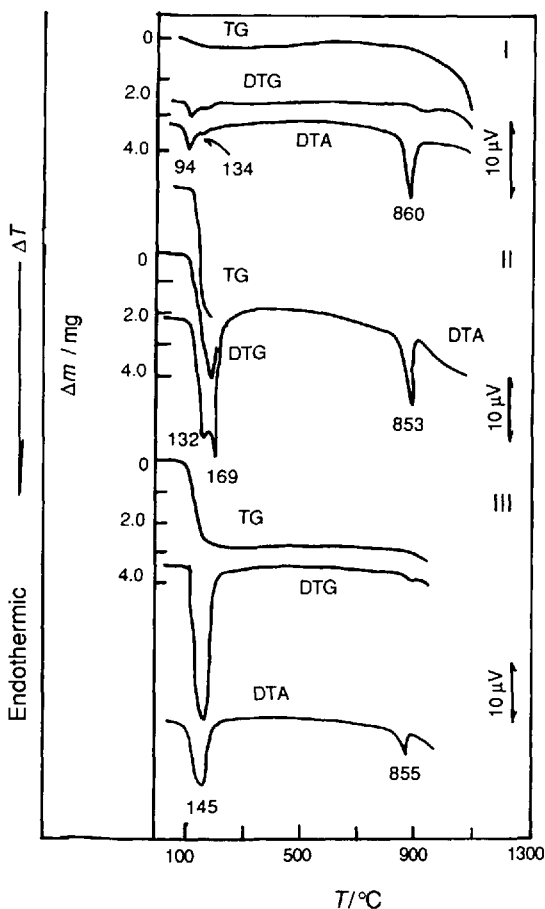


Figure 10.75 DTA-TG-DTG curves of (I) thermonatrite, (II) nahcolite and (III) trona [3]

Samples

I, Thermonatrite, $\text{NaCO}_3 \cdot \text{H}_2\text{O}$ (Na_2O 50.03%, CO_2 35.45%, H_2O 14.52%); II, nahcolite, NaHCO_3 (Na_2O 36.90%, CO_2 52.38%, H_2O 10.72%); III, trona, $\text{Na}_3\text{H}(\text{CO}_3)_2 \cdot 2\text{H}_2\text{O}$ (Na_2O 41.14%, CO_2 38.94%, H_2O 19.92%).

Results

94 and 134 °C endotherms, thermonatrite releases crystalline water in stages and forms Na_2CO_3 ; 132 and 169 °C endotherms, nahcolite decomposes; Na_2CO_3 is formed and releases CO_2 and H_2O ; 145 °C endotherm, trona decomposes; it is transformed to Na_2CO_3 and releases CO_2 and H_2O . 853–860 °C endotherms for all three samples, Na_2CO_3 melts.

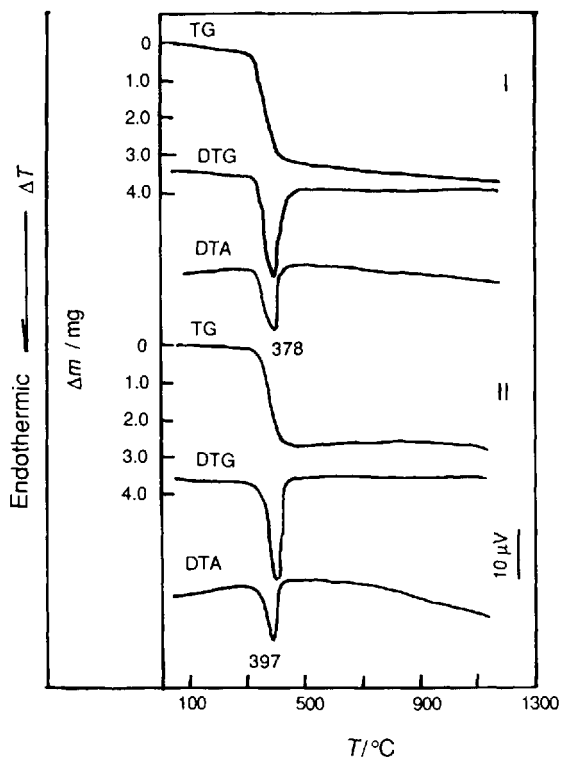


Figure 10.76 DTA-TG-DTG curves of (I) spherocobaltite and (II) otavite [6]

Sample

I, Spherocobaltite, CoCO_3 (CoO 62.9%, CO_2 37.1%); II, otavite, CdCO_3 (CdO 75.2%, CO_2 24.8%).

Results

I. *Spherocobaltite*—378 °C endotherm, spherocobaltite decomposes to CoO and releases CO_2 .

II. *Otavite*—397 °C endotherm, otavite decomposes to CdO and releases CO_2 .

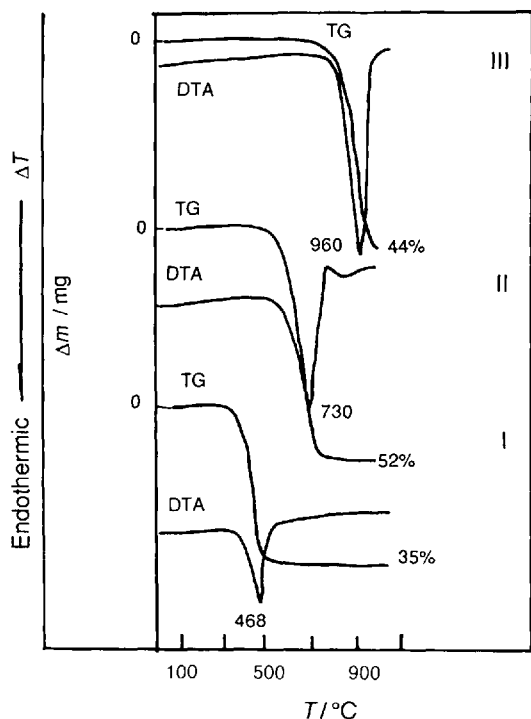


Figure 10.77 DTA-TG curves of (I) smithsonite, (II) magnesite and (III) calcite

Sample

I, Smithsonite, ZnCO_3 (ZnO 64.90%, CO_2 35.10%); II, magnesite, MgCO_3 (MgO 47.81%, CO_2 52.19%); III, calcite, CaCO_3 (CaO 56.03%, CO_2 43.97%).

Experimental conditions

Amount of sample, 50 mg.

Results

I. *Smithsonite*—468 °C endotherm, smithsonite decomposes to ZnO and CO_2 is released.

II. *Magnesite*—730 °C endotherm, magnesite decomposes to MgO and releases CO_2 .

III. *Calcite*—960 °C endotherm, calcite decomposes to CaO and releases CO_2 .

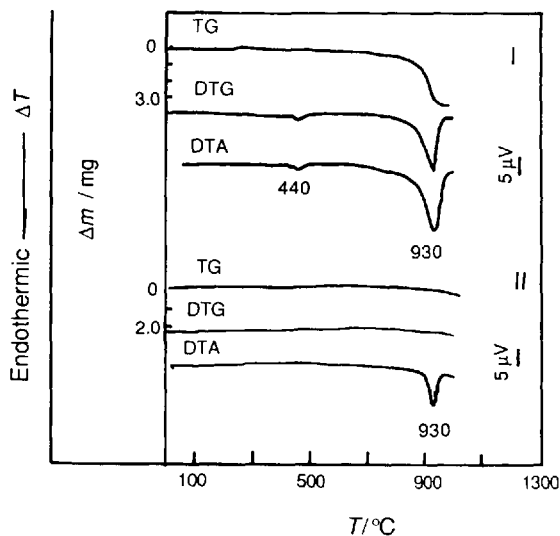


Figure 10.78 DTA-TG-DTG curves of (I) aragonite and (II) strontianite [6]

Samples

I, Aragonite, CaCO_3 (CaO 56.03%, CO_2 43.97%); II, strontianite, SrCO_3 (SrO 70.09%, CO_2 29.81%).

Results

440 °C endotherm, aragonite is transformed to calcite; 930 °C endotherm, calcite decomposes to CaO and releases CO_2 ; 930 °C endotherm, strontianite undergoes a polymorphic transformation.

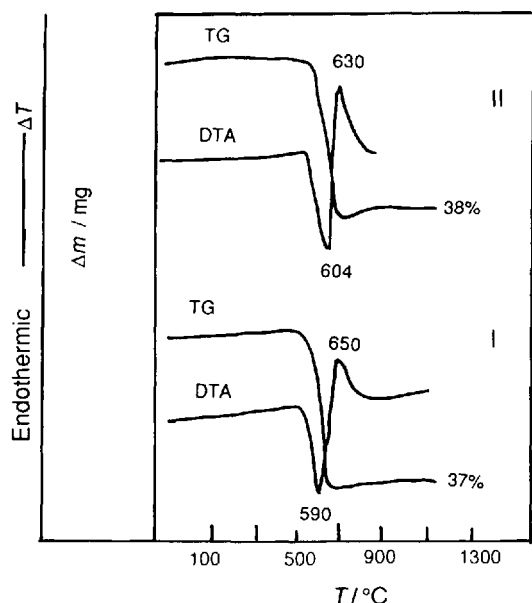


Figure 10.79 DTA-TG curves of (I) siderite and (II) rhodochrosite

Sample

I, Siderite, FeCO_3 (FeO 62.01%, CO_2 37.99%); II, rhodochrosite, MnCO_3 (MnO 61.71%, CO_2 38.29%).

Experimental conditions

Amount of sample, 50 mg.

Results

I. Siderite—590 °C endotherm, siderite decomposes to FeO and releases CO_2 ; 650 °C exotherm, FeO oxidizes to Fe_3O_4 .

II. Rhodochrosite—604 °C endotherm, rhodochrosite decomposes to MnO and releases CO_2 ; 630 °C exotherm, MnO oxidizes to Mn_3O_4 .

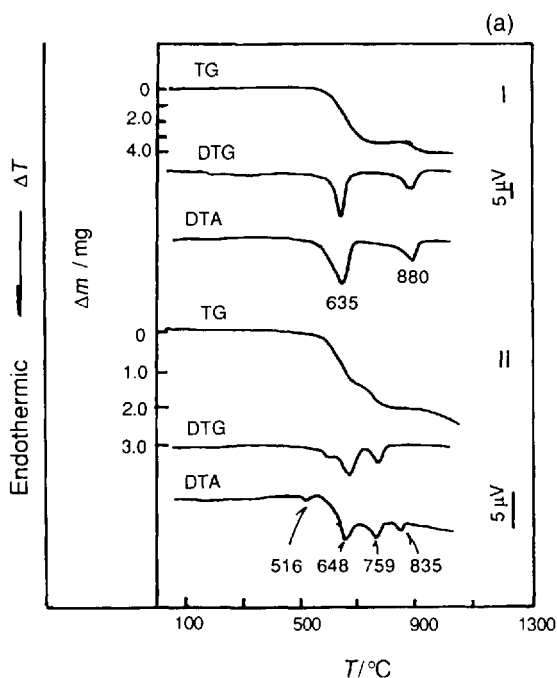


Figure 10.80 (a) DTA-TG-DTG curves of (I) huntite [6] and (II) norsethite [3]

(continued)

Samples

I, Huntite, $\text{CaMg}_3(\text{CO}_3)_4$ (CaO 15.89%, MgO 34.25%, CO_2 49.86%); II, norsethite, $\text{BaMg}(\text{CO}_3)_2$ (BaO 54.44%, MgO 14.31%, CO_2 31.25%); III, dolomite, $\text{CaMg}(\text{CO}_3)_2$ (CaO 30.41%, MgO 21.86%, CO_2 47.33%); IV, barytocalcite, $\text{BaCa}(\text{CO}_3)_2$ (BaO 51.56%, CaO 18.85%, CO_2 29.59%).

Experimental conditions

Amount of sample III, 200 mg.

Results

I. Huntite—635 °C endotherm, huntite decomposes to MgO and CaCO_3 and releases CO_2 ; 880 °C endotherm, CaCO_3 decomposes to CaO and releases CO_2 .

II. Norsethite—516 °C endotherm, norsethite undergoes a polymorphic transformation; 648 °C endotherm, norsethite decomposes to MgO and $\text{BaO} \cdot \text{BaCO}_3$ and releases CO_2 ; 759 °C

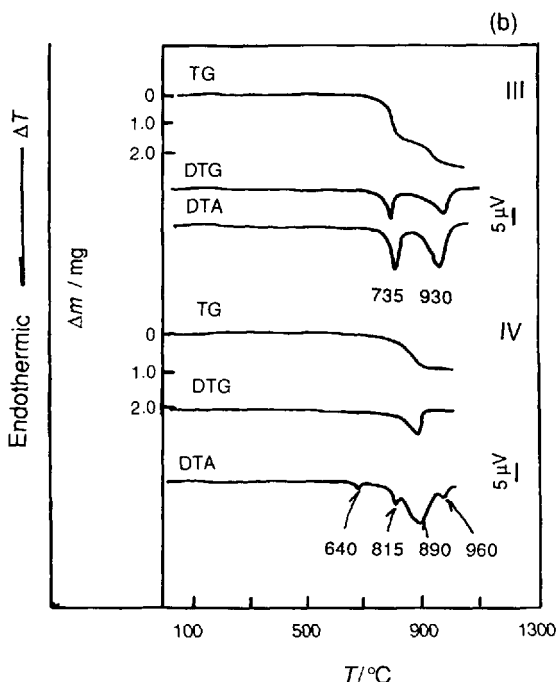


Figure 10.80 (b) DTA-TG-DTG curves of (III) dolomite and (IV) barytocalcite [6]

endotherm, $\text{BaO} \cdot \text{BaCO}_3$ decomposes to BaO and releases CO_2 ; 835 °C endotherm, MgO undergoes a polymorphic transformation.

III. Dolomite—735 °C endotherm, dolomite to MgO and CaCO_3 and releases CO_2 ; 930 °C endotherm, CaCO_3 decompose to CaO and releases CO_2 .

IV. Barytocalcite—640 °C endotherm, barytocalcite undergoes a polymorphic transformation; 815 °C endotherm, barytocalcite decomposes to CaO and BaCO_3 and releases CO_2 ; 890 °C endotherm, BaCO_3 (witherite) undergoes a polymorphic transformation; 960 °C endotherm, witherite transforms to another polymorphic crystalline structure.

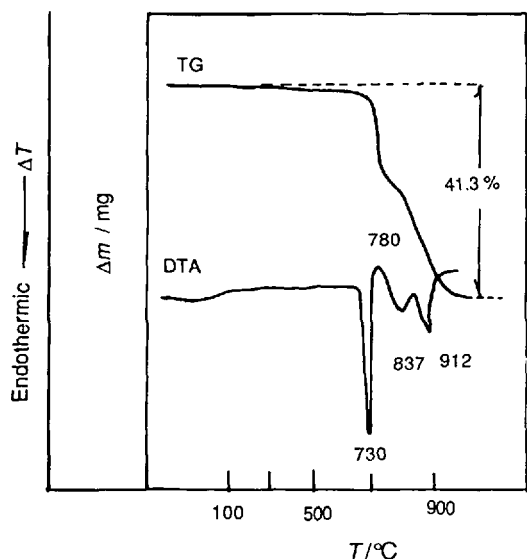


Figure 10.81 DTA-TG curves of ankerite

Samples

Ankerite, $\text{Ca}(\text{Mg,Fe})(\text{CO}_3)_2$.

Experimental conditions

Amount of sample, 200 mg.

Results

730 °C endotherm, FeCO_3 of ankerite decomposes; it is transformed to FeO and releases CO_2 ; 780 °C exotherm, FeO oxidizes and is transformed to Fe_2O_3 ; 837 °C endotherm, MgCO_3 of ankerite decomposes; it is transformed to MgO and releases CO_2 ; 912 °C endotherm, CaCO_3 of ankerite decomposes; it is transformed to CaO and releases CO_2 .

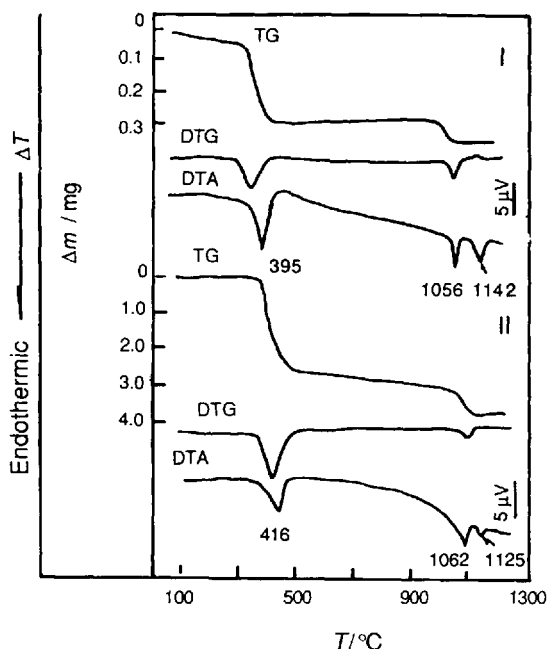


Figure 10.82 DTA-TG-DTG curves of (I) malachite and (II) azurite

Samples

I, Malachite, $\text{Cu}_2(\text{CO}_3)(\text{OH})_2$ (CuO 71.95%, CO_2 19.90%, H_2O 8.15%); II, azurite, $\text{Cu}_3(\text{CO}_3)_2(\text{OH})_2$ (CuO 69.24%, CO_2 25.54%, H_2O 5.22%).

Experimental conditions

Amount of sample, 50 mg.

Results

395 °C endotherm, malachite to CuO and releases CO_2 and H_2O ; 416 °C endotherm, azurite decomposes to CuO and releases CO_2 and H_2O ; 1056–1062 °C endotherm, CuO becomes Cu_2O ; 1125 and 1142 °C endotherms, Cu_2O partially oxidizes to CuO.

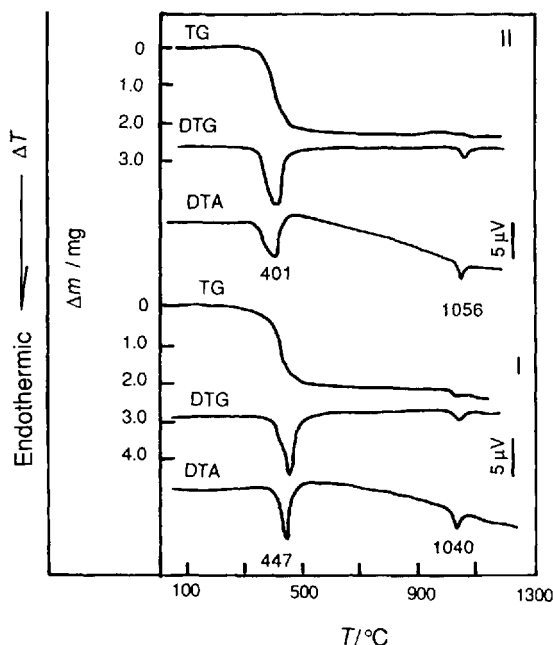


Figure 10.83 DTA-TG-DTG curves of (I) rosasite and (II) aurichalcite [3]

Samples

I, Rosasite, $\text{ZnCu}(\text{CO}_3)(\text{OH})_2$ (ZnO 36.50%, CuO 35.68%, CO_2 19.74%, H_2O 8.08%); II, aurichalcite, $\text{Zn}_3\text{Cu}_2(\text{CO}_3)_2(\text{OH})_6$ (ZnO 44.77%, CuO 29.18%, CO_2 16.14%, H_2O 9.91%).

Results

447 °C endotherm, rosasite decomposes and is transformed to ZnO and CuO and releases CO_2 and H_2O ; 401 °C endotherm, aurichalcite decomposes to ZnO and CuO and releases CO_2 and H_2O ; 1056 °C endotherm, CuO is transformed to Cu_2O .

Samples

I, Pyroaurite, $\text{Mg}_6\text{Fe}_2^{III}(\text{CO}_3)(\text{OH})_{16} \cdot 4\text{H}_2\text{O}$ (MgO 36.55%, Fe_2O_3 24.13%, CO_2 6.65%, H_2O 32.67%);
 II, hydrotalcite, $\text{Mg}_6\text{Al}_2(\text{CO}_3)(\text{OH})_{16} \cdot 4\text{H}_2\text{O}$ (MgO 40.04%, Al_2O_3 16.88%, CO_2 7.29%, H_2O 35.79%); III, stichite, $\text{Mg}_6\text{Cr}_2(\text{CO}_3)(\text{OH})_{16} \cdot 4\text{H}_2\text{O}$;
 IV, sjogrenite, $\text{Mg}_6\text{Fe}_2(\text{CO}_3)(\text{OH})_{16} \cdot 4\text{H}_2\text{O}$.

Results

I. Pyroaurite—242 °C endotherm, pyroaurite releases crystalline water; 449 °C endotherm, $\text{Mg}_6\text{Fe}_2(\text{CO}_3)(\text{OH})_{16}$ decomposes to MgO and MgFe_2O_4 and releases CO_2 and H_2O .

II. Hydrotalcite—242 °C endotherm, hydrotalcite releases water of crystallization; 333 °C endotherm, $\text{Mg}_6\text{Al}_2(\text{CO}_3)(\text{OH})_{16}$ decomposes to $\text{Mg}_6\text{Al}_2\text{O}(\text{OH})_{16}$ and releases CO_2 ; 469 °C endotherm, $\text{Mg}_6\text{Al}_2\text{O}(\text{OH})_{16}$ decomposes to MgAl_2O_4 and MgO and releases H_2O .

III. Stichite—254 °C endotherm, stichite releases crystalline water; 365 °C endotherm, $\text{Mg}_6\text{Cr}_2(\text{CO}_3)(\text{O})_{16}$ decomposes to $\text{Mg}_6\text{Cr}_2\text{O}(\text{OH})_{16}$ and releases CO_2 ; 473 °C endotherm, $\text{Mg}_6\text{Cr}_2\text{O}(\text{OH})_{16}$ decomposes to MgCr_2O_4 and MgO and releases H_2O .

IV. Sjogrenite—255 °C endotherm, sjogrenite releases crystalline water, 345 °C endotherm, $\text{Mg}_6\text{Fe}_2(\text{CO}_3)(\text{OH})_{16}$ decomposes to $\text{Mg}_6\text{Fe}_2\text{O}(\text{OH})_{16}$ and releases CO_2 ; 489 °C endotherm, $\text{Mg}_6\text{Fe}_2\text{O}(\text{OH})_{16}$ decomposes to MgFe_2O_4 and MgO and releases H_2O .

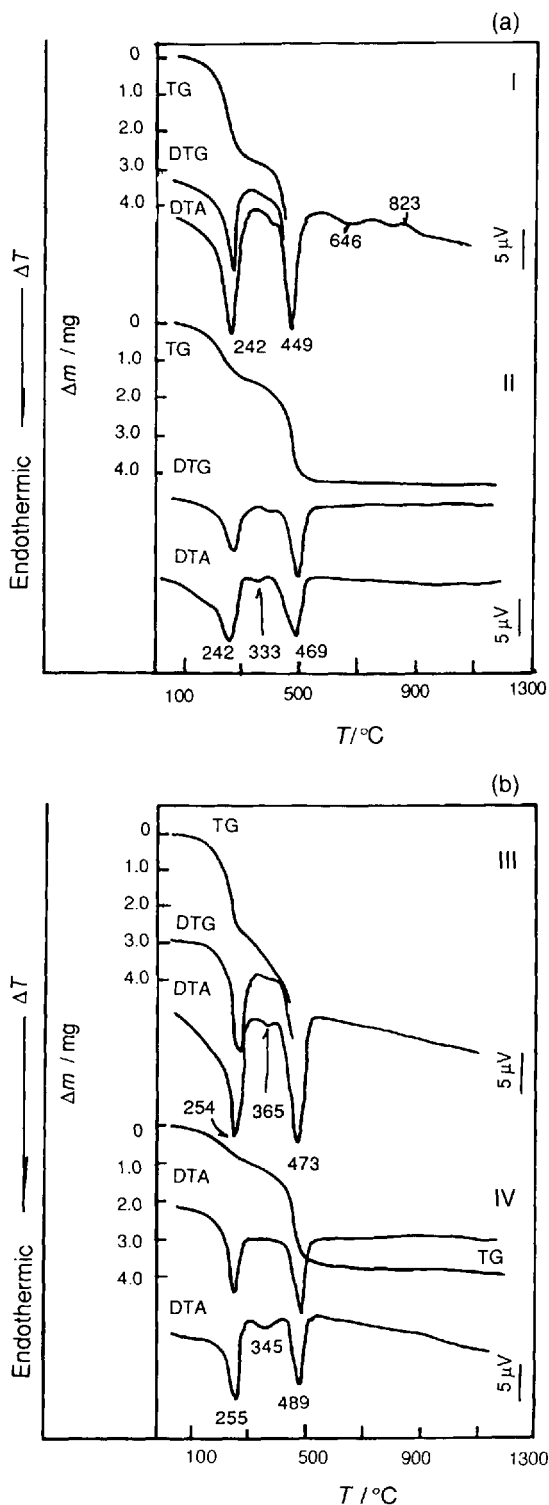


Figure 10.84 DTA-TG-DTG curves of (a) (I) pyroaurite and (II) hydrotalcite and (b) (III) stichite and (IV) sjogrenite [3]

10.7 Thermal Analysis Curves of Borate Minerals

Borate minerals lose crystalline water at a temperature lower than 250 °C and constitution water at a temperature higher than 250 °C, then they recrystallize and subsequently melt at high temperatures.

Samples

I, Sassolite: H_3BO_3 (B_2O_3 56.30%, H_2O 43.70%); II, vonsenite, $\text{Fe}_2^{\text{III}}\text{Fe}^{\text{II}}\text{BO}_5$ (FeO 38.52%, Fe_2O_3 42.81%, B_2O_3 18.67%); III, suanite, $\text{Mg}_2\text{B}_2\text{O}_5$ (MgO 53.66%, B_2O_3 46.34%).

Results

I. Sassolite—170 °C endotherm, sassolite melts; 196 °C endotherm, molten sassolite decomposes to B_2O_3 and releases H_2O .

II. Vonsenite—759 °C exotherm, vonsenite decomposes and oxidizes; Fe_2O_3 and FeBO_3 are formed; 980 °C endotherm, FeBO_3 melts.

III. Suanite—1280 °C endotherm, suanite melts.

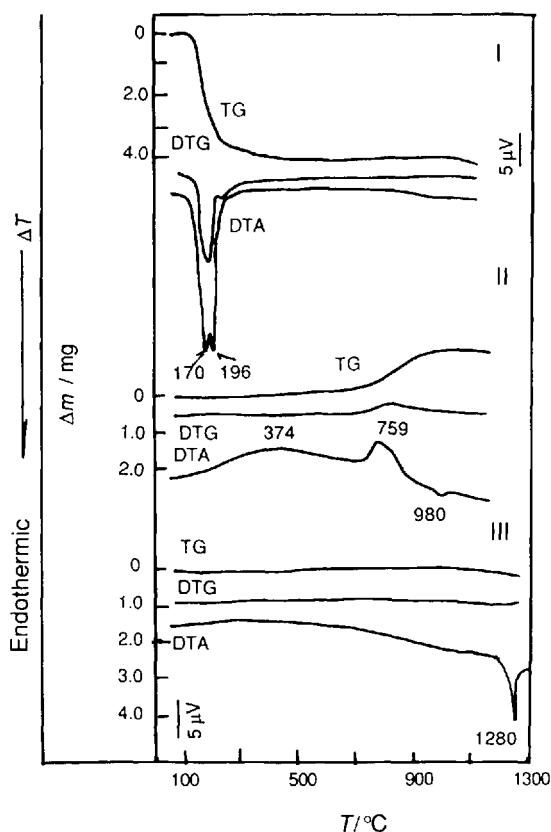


Figure 10.85 DTA-TG-DTG curves of (I) sassolite, (II) vonsenite and (III) suanite [3]

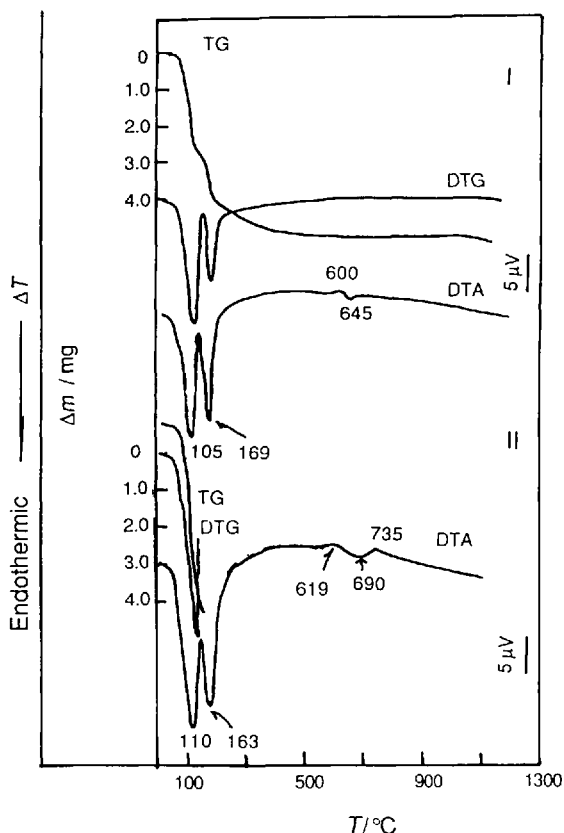


Figure 10.86 DTA-TG-DTG curves of (I) tincalconite and (II) borax [3]

Samples

I, Tincalconite, $\text{Na}_2\text{B}_4\text{O}_5(\text{OH})_4 \cdot 3\text{H}_2\text{O}$ (Na_2O 21.29%, B_2O_3 47.80%, H_2O 30.91%) II, Borax, $\text{Na}_2\text{B}_4\text{O}_5(\text{OH})_4 \cdot 8\text{H}_2\text{O}$ (Na_2O 16.26%, B_2O_3 36.51%, H_2O 47.23%).

Results

105 °C endotherm, tincalconite releases crystalline water; 169 °C endotherm, tincalconite releases constitution water and forms $\text{Na}_2\text{B}_4\text{O}_7$; 110 °C endotherm, borax releases crystalline water; 163 °C endotherm, borax releases constitution water and is transformed to $\text{Na}_2\text{B}_4\text{O}_7$; 645 and 690 °C endotherms, $\text{Na}_2\text{B}_4\text{O}_7$ melts.

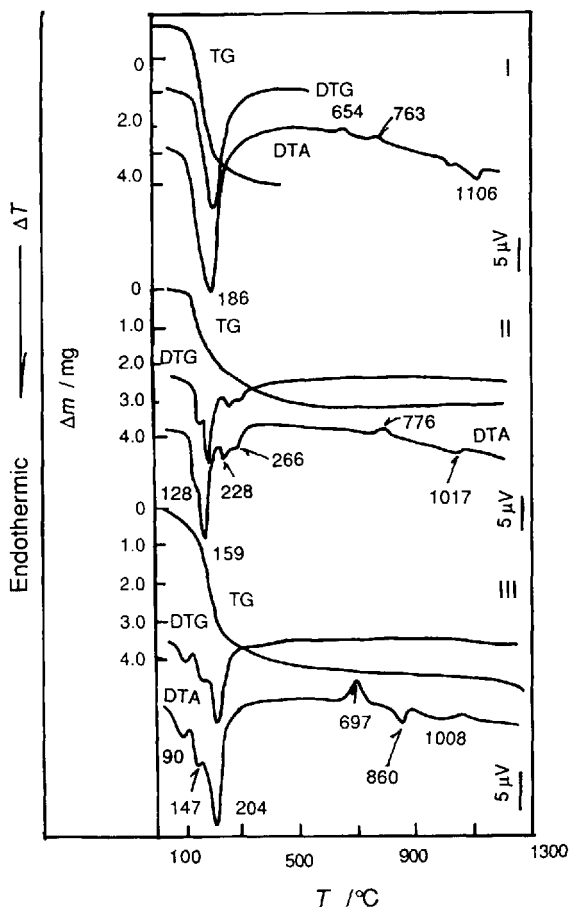


Figure 10.87 DTA-TG-DTG curves of (I) inderite, (II) inyoite and (III) ulexite [3]

Samples

I, Inderite, $\text{Mg}(\text{H}_2\text{O})_5[\text{B}_2\text{BO}_3(\text{OH})_5]$ (MgO 14.41%, B_2O_3 37.32%, H_2O 48.27%); II, inyoite, $\text{Ca}(\text{H}_2\text{O})_4[\text{B}_2\text{BO}_3(\text{OH})_5]$ (CaO 20.20%, B_2O_3 37.62%, H_2O 42.18%); III, ulexite, $\text{NaCa}[\text{B}_5\text{O}_7(\text{OH})_4] \cdot 6\text{H}_2\text{O}$ (Na_2O 7.65%, CaO 13.85%, B_2O_3 42.95%, H_2O 35.55%).

Results

I. Inderite—186 °C endotherm, inderite dehydrates; 763 °C exotherm, the dehydrated substance recrystallizes; 1106 °C endotherm, borates melt.

II. Inyoite—128, 159, 228 and 266 °C endotherms, inyoite dehydrates in stages; 776 °C exotherm, borates recrystallize; 1017 °C endotherm, borates melt.

III. Ulexite—90, 147 and 204 °C endotherms, ulexite dehydrates; 697 °C exotherm, borates recrystallize and are transformed to CaB_2O_4 and NaB_3O_5 ; 860 °C endotherm, NaB_3O_5 melts; 1008 °C endotherm, CaB_2O_4 melts.

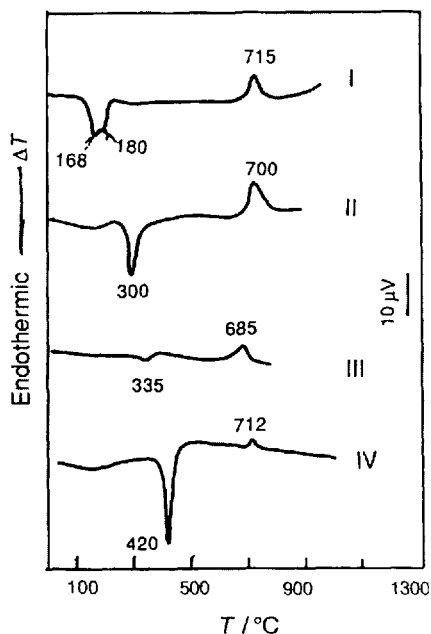


Figure 10.88 DTA curves of (I) pentahydroborite, (II) aksaite, (III) korzhinskite and (IV) colemanite [7]

Samples

I, Pentahydroborite, $\text{Ca}(\text{H}_2\text{O})_5[\text{B}(\text{OH})_4]_2$; II, aksaite, $\text{Mg}(\text{H}_2\text{O})_3[\text{BB}_2\text{O}_4(\text{OH})_2]_2$ (Mg 11.88%, B_2O_3 61.57%, H_2O 26.55%); III, korzhinskite, $\text{CaB}_2\text{O}_3(\text{OH})_2$; IV, colemanite, $\text{CaB}_3\text{O}_3(\text{OH})_5$ (CaO 27.28%, B_2O_3 50.81%, H_2O 21.91%).

Results

I. Pentahydroborite—168 and 180 °C endotherms, pentahydroborite releases crystalline water and is transformed to CaB_2O_4 ; 715 °C exotherm, CaB_2O_4 recrystallizes.

II. Aksaite—300 °C endotherm, aksaite dehydrates and is transformed to $\text{MgB}_6\text{O}_{10}$; 700 °C exotherm, $\text{MgB}_6\text{O}_{10}$ recrystallizes.

III. Korzhinskite—335 °C endotherm, korzhinskite dehydrates and is transformed to $\text{Ca}_2\text{B}_2\text{O}_4$; 685 °C exotherm, CaB_2O_4 recrystallizes.

IV. Colemanite—420 °C endotherm, colemanite dehydrates and is transformed to $\text{CaB}_6\text{O}_{10}$; 712 °C exotherm, $\text{CaB}_6\text{O}_{10}$ crystallizes.

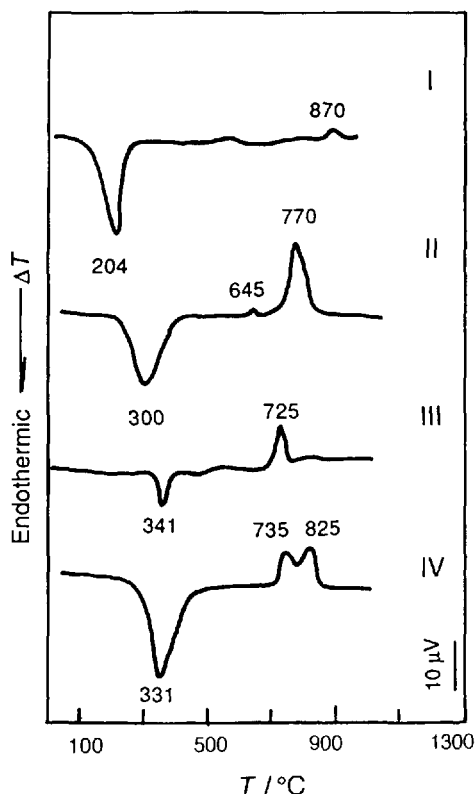


Figure 10.89 DTA curves of (I) inderborite, (II) lueneburgite, (III) uralborite and (IV) pinnoite [7]

Samples

I, Inderborite, $\text{CaMg}(\text{H}_2\text{O})_6[\text{B}_2\text{BO}_3(\text{OH})_5]_2$; II, lueneburgite, $\text{Mg}_3(\text{H}_2\text{O})_4[[\text{PO}_4]_2[\text{B}_2\text{O}(\text{OH})_4]]$; III, uralborite $\text{Ca}[\text{B}_2\text{O}_2(\text{OH})_4]$; IV, pinnoite, $\text{Mg}[\text{B}_2\text{O}(\text{OH})_6]$ (MgO 24.58%, B_2O_3 42.46%, H_2O 32.96%).

Results

I. Inderborite—204 °C endotherm, inderborite dehydrates and is transformed to $\text{CaMgB}_6\text{O}_{11}$; 870 °C exotherm, $\text{CaMgB}_6\text{O}_{11}$ recrystallizes.

II. Lueneburgite—300 °C endotherm, lueneburgite dehydrates and is transformed to phosphate and borate; 645 °C exotherm, phosphate crystallizes; 770 °C exotherm, borate crystallizes.

III. Uralborite—341 °C endotherm, uralborite releases constitution water and is transformed to CaB_2O_4 ; 725 °C exotherm, CaB_2O_4 crystallizes.

IV. Pinnoite—331 °C endotherm, pinnoite releases water of constitution and is transformed to MgB_2O_4 ; 735 °C exotherm, MgB_2O_4 crystallizes.

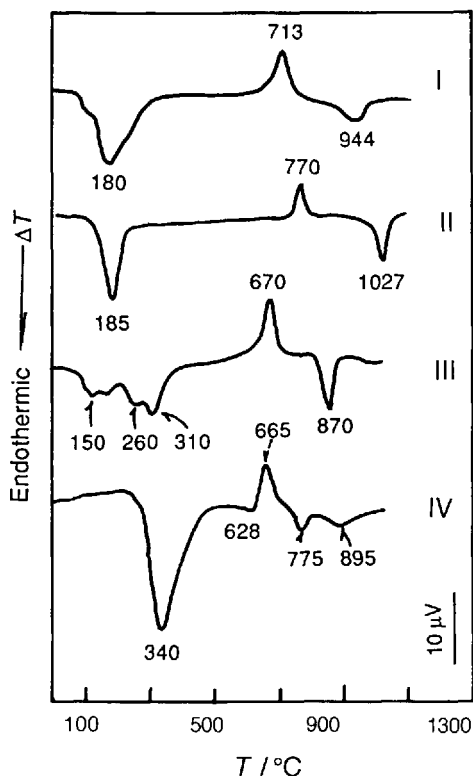


Figure 10.90 DTA curves of (I) hungchaoite, (II) kurnakovite, (III) probertite and (IV) kaliborite [7]

Sample

I, Hungchaoite, $\text{Mg}(\text{H}_2\text{O})_2[\text{B}_2\text{B}_2\text{O}_5(\text{OH})_4](\text{MgO}$ 11.81%, B_2O_3 40.77%, H_2O 47.42%); II, kurnakovite, $\text{Mg}(\text{H}_2\text{O})_5[\text{B}_2\text{B}_3(\text{OH})_5]$ (MgO 14.41%, B_2O_3 37.32%, H_2O 48.27%); III, probertite, $\text{NaCa}(\text{H}_2\text{O})_3[\text{B}_3\text{B}_2\text{O}_7(\text{OH})_4]$ (Na_2O 8.83%, CaO 15.98%, B_2O_3 49.56%, H_2O 25.63%); IV, kaliborite, $\text{KHMg}_2(\text{H}_2\text{O})_4[\text{B}_3\text{B}_3\text{O}_8(\text{OH})_5]_2$ (K_2O 7.00%, MgO 11.98%, B_2O_3 56.92%, H_2O 24.10%).

Results

I. Hungchaoite—180 °C endotherm, hungchaoite dehydrates and is transformed to MgB_4O_7 ; 713 °C exotherm, MgB_4O_7 crystallizes; 944 °C endotherm, MgB_4O_7 melts.

II. Kurnakovite—185 °C endotherm, kurnakovite is transformed to $\text{Mg}_2\text{B}_6\text{O}_{11}$; 770 °C exotherm, $\text{Mg}_2\text{B}_6\text{O}_{11}$ crystallizes; 1027 °C endotherm, $\text{Mg}_2\text{B}_6\text{O}_{11}$ melts.

III. Probertite—150, 260 and 310 °C endotherms, probertite dehydrates in stages and is transformed to NaCaB_5O_9 ; 670 °C exotherm, NaCaB_5O_9 crystallizes; 870 °C endotherm, NaCaB_5O_9 melts.

IV. Kaliborite—340 °C endotherm, kaliborite dehydrates; 628 °C endotherm, the dehydrated substance decomposes and is transformed to $\text{K}_2\text{B}_4\text{O}_7$, $\text{Mg}_2\text{B}_6\text{O}_{11}$ and B_2O_3 ; 665 °C exotherm, borates crystallize; 775 °C endotherm, $\text{K}_2\text{B}_4\text{O}_7$ melts; 895 °C endotherm, $\text{Mg}_2\text{B}_6\text{O}_{11}$ melts.

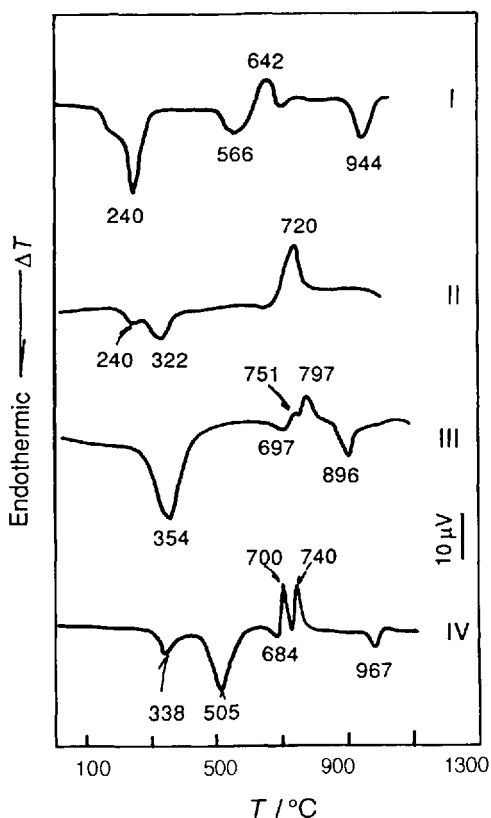


Figure 10.91 DTA curves of (I) carbaborite, (II) nifontovite, (III) hydroboracite and (IV) priceite [7]

Samples

I, Carbaborite, $\text{MgCa}_2[\text{HCO}_3]_2[\text{B}(\text{OH})_4]_2 \cdot (\text{OH})_2 \cdot 2\text{H}_2\text{O}$ (MgO 8.8%, CaO 24.2%, B_2O_3 15.7%, CO_2 19.4%, H_2O 31.9%); II, nifontovite, $\text{Ca}[\text{B}_2\text{O}(\text{OH})_6]$; III, hydroboracite, $\text{CaMg}(\text{H}_2\text{O})_3 \cdot [\text{B}_2\text{BO}_4(\text{OH})_3]_2$ (CaO 13.57%, MgO 9.75%, B_2O_3 50.53%, H_2O 26.15%); IV, priceite, $\text{Ca}_2(\text{H}_2\text{O}) \cdot [\text{B}_4\text{BO}_7(\text{OH})_5]$ (CaO 32.15%, B_2O_3 48.44%, H_2O 19.41%).

Results

I. Carbaborite—240 °C endotherm, carbaborite dehydrates; 566 °C endotherm, the dehydrated substance decomposes and releases CO_2 ; 642 °C exotherm, borate crystallizes; 944 °C endotherm, borate melts.

II. Nifontovite—240 and 322 °C endotherms, nifontovite releases crystalline water and is transformed to CaB_2O_4 ; 720 °C exotherm, CaB_2O_4 crystallizes.

III. Hydroboracite—354 °C endotherm, hydroboracite releases H_2O ; 697 °C endotherm, borates decompose and are transformed to MgB_2O_4 and CaB_4O_7 ; 751 °C exotherm, MgB_2O_4 crystallizes; 797 °C exotherm, CaB_4O_7 crystallizes; 896 °C endotherm, borates melt.

IV. Priceite—338 °C endotherm, priceite releases crystalline water, 505 °C endotherm, priceite releases constitution water; 684 °C endotherm, the dehydrated substance decomposes and is transformed to CaB_2O_4 and CaB_4O_7 ; 700 °C exotherm, CaB_2O_4 crystallizes; 740 °C exotherm, CaB_4O_7 crystallizes; 967 °C endotherm, borates melt.

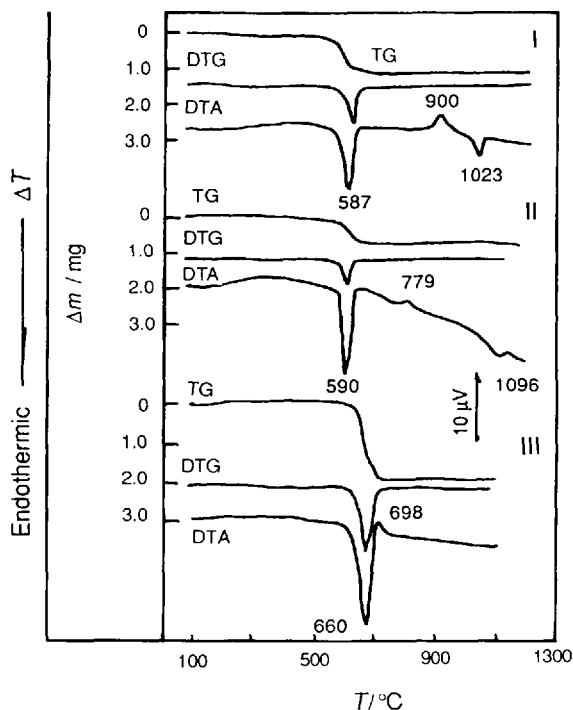


Figure 10.92 DTA-TG-DTG curves of (I) howlite, (II) preobrazhenskite and (III) szaibelyite [3]

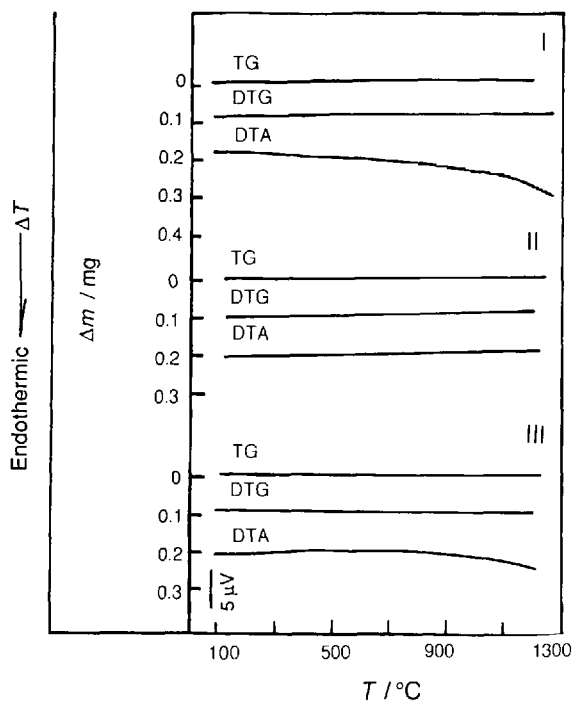


Figure 10.93 DTA-TG-DTG curves of (I) beryllonite, (II) xenotime and (III) cheralite [3]

Samples

I, Howlite, $\text{Ca}_2[\text{B}_4\text{SiO}_9(\text{OH})_5]$; II, preobrazhenskite, $\text{Mg}_3(\text{H}_2\text{O})[\text{B}_3\text{B}_2\text{O}_7(\text{OH})_4]_2$; III, szaibelyite, $\text{Mg}_2[\text{B}_2\text{O}_4(\text{OH})](\text{OH})$ (MgO 47.92%, B_2O_3 41.38%, H_2O 10.70%).

Results

I. Howlite—587 °C endotherm, howlite releases constitution water; 900 °C exotherm, the dehydrated substance crystallizes and is transformed to CaSi_2O_4 , CaB_2O_4 and CaB_4O_7 ; 1023 °C endotherm, borates melt.

II. Preobrazhenskite—590 °C endotherm, preobrazhenskite releases constitution water, 779 °C exotherm, borate crystallizes; 1096 °C endotherm, borates melt.

III. Szaibelyite—660 °C endotherm, szaibelyite releases constitution water and is transformed to $\text{Mg}_2\text{B}_2\text{O}_5$; 698 °C exotherm, $\text{Mg}_2\text{B}_2\text{O}_5$ crystallizes.

10.8 Thermal Analysis Curves of Phosphate Minerals

Phosphate minerals undergo structure transformation, dehydration and decomposition. The decomposed substances recrystallize.

Samples

I, Beryllonite, $\text{Na}[\text{Be}(\text{PO}_4)]$ (Na_2O 24.41%, BeO 19.70%, P_2O_5 55.89%); II, xenotime, $\text{Y}[\text{PO}_4]$ (Y_2O_3 61.40%, P_2O_5 38.60%); III, cheralite, $(\text{Ca}, \text{Ce}, \text{Th})[(\text{P}, \text{Si})\text{O}_4]$.

Results

From 20 to 1200 °C beryllonite, xenotime and cheralite show no thermal events.

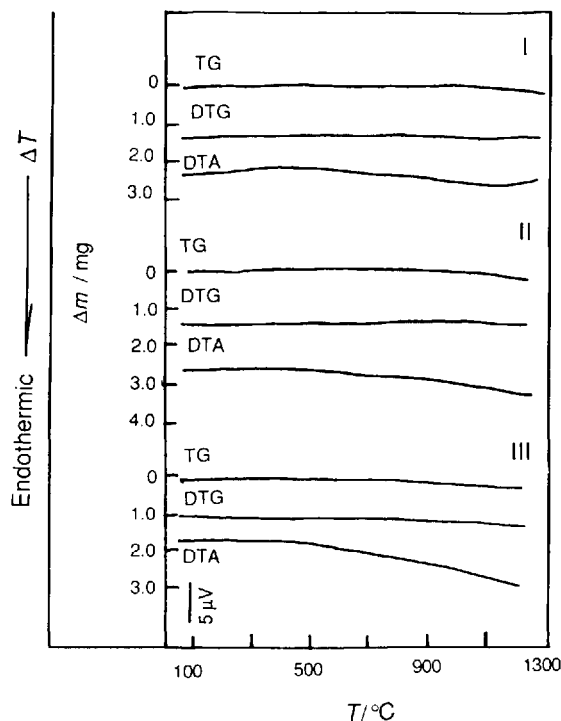


Figure 10.94 DTA-TG-DTG curves of (I) hydroxyapatite, (II) carbonate-hydroxyapatite and (III) britholite [3]

Samples

I, Hydroxyapatite, $\text{Ca}_2\text{Ca}_3[\text{PO}_4]_3(\text{OH})$ (CaO 55.82%, P_2O_5 42.39%, H_2O 1.79%); II, carbonate-hydroxyapatite, $\text{Ca}_2\text{Ca}_3[(\text{PO}_4)[\text{CO}_3]]_3(\text{OH})$; III, britholite, $\text{Ca}_2\text{Ce}_3[(\text{Si,P})\text{O}_4]_3(\text{F,OH})$.

Results

From 20 to 1200 °C hydroxyapatite carbonate-hydroxyapatite and britholite show no thermal events.

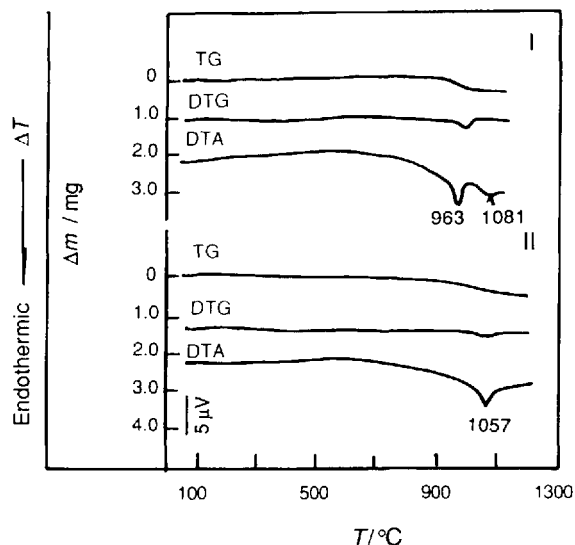


Figure 10.95 DTA-TG-DTG curves of (I) zwieselite and (II) triplite [3]

Samples

I, Zwieselite, $(\text{Fe}^{\text{II}}\text{Mn})_2[\text{PO}_4]\text{F}$ ($\text{Fe} > \text{Mn}$); II, triplite, $(\text{Mn,Fe})_2[\text{PO}_4]\text{F}$ ($\text{Mn} > \text{Fe}$).

Results

I. *Zwieselite*—963 °C endotherm, zwieselite decomposes to Fe_2O_3 and $\text{FeMn}_2[\text{PO}_4]_2$ and releases P_2O_5 and F; 1081 °C endotherm.

II. *Triplite*—1057 °C endotherm, triplite decomposes to Mn_3O_4 and $\text{MnFe}_2[\text{P}_4]_2$ and releases P_2O_5 and F.

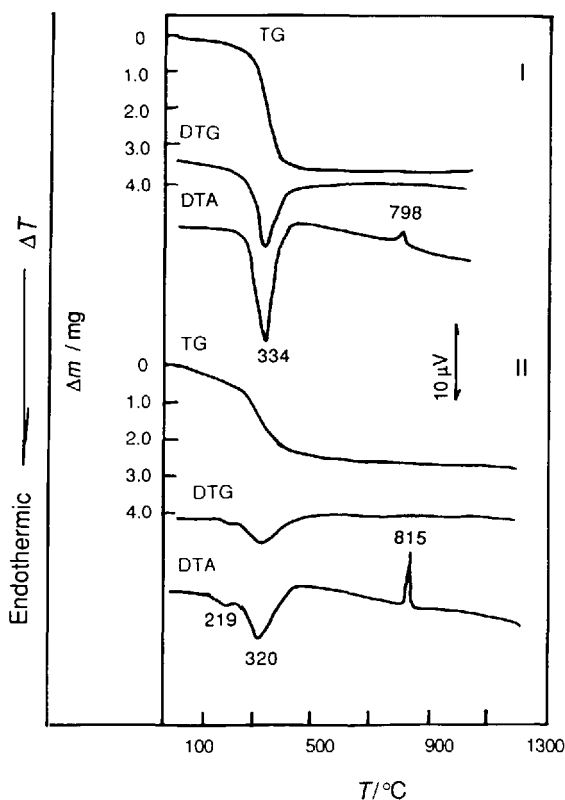


Figure 10.96 DTA-TG-DTG curves of (I) turquoise and (II) faustite [3]

Samples

I, Turquoise, $\text{CuAl}_6(\text{H}_2\text{O})_4[\text{PO}_4]_4(\text{OH})_8$ (CuO 9.78%, Al_2O_3 37.60%, P_2O_5 34.90%, H_2O 17.72%); II, faustite, $\text{ZnAl}_6(\text{H}_2\text{O})_4[\text{PO}_4]_4(\text{OH})_8$ (ZnO 9.99%, Al_2O_3 37.52%, P_2O_5 34.81%, H_2O 17.68%).

Results

I. Turquoise—334 °C endotherm, turquoise dehydrates; 798 °C exotherm, the dehydrated substance crystallizes; it is transformed to $\text{Al}[\text{PO}_4]$ and CuAl_2O_4 .

II. Faustite—219 and 320 °C endotherms, faustite dehydrates; 815 °C exotherm, the dehydrated substance crystallizes $\text{Al}[\text{PO}_4]$ and ZnAl_2O_4 is formed.

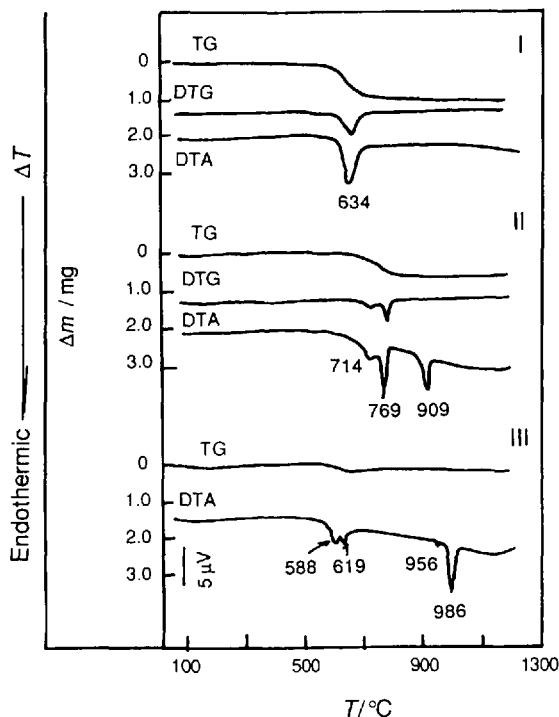


Figure 10.97 DTA-TG-DTG curves of (I) brazilianite, (II) montebrasite and (III) tarbuttite [3]

Samples

I, Brazilianite, $\text{NaAl}_3[\text{PO}_4]_2(\text{OH})_4$ (Na_2O 8.56%, Al_2O_3 42.25%, P_2O_5 39.23%, H_2O 9.96%), II, montebrasite, $\text{LiAl}[\text{PO}_4](\text{OH})$ (Li_2O 10.24%, Al_2O_3 34.94%, P_2O_5 48.65%, H_2O 6.17%); III, tarbuttite, $\text{Zn}_2[\text{PO}_4](\text{OH})$ (ZnO 67.05%, P_2O_5 29.24%, H_2O 3.71%).

Results

I. Brazilianite—634 °C endotherm, brazilianite releases constitution water and is transformed to $\text{Al}[\text{PO}_4]$.

II. Montebrasite—714 and 769 °C endotherms, montebrasite releases water of constitution; 909 °C endotherm, the dehydrated substance decomposes and is transformed to $\text{Al}[\text{PO}_4]$.

III. Tarbuttite—588 °C endotherm, tarbuttite releases constitution water; 619 °C endotherm, the dehydrated substance is transformed to $\alpha\text{-Zn}_3[\text{PO}_4]_2$; 956 °C endotherm, $\alpha\text{-Zn}_3[\text{PO}_4]_2$ converts to $\beta\text{-Zn}_3[\text{PO}_4]_2$; 986 °C endotherm, $\beta\text{-Zn}_3[\text{PO}_4]_2$ converts to $\gamma\text{-Zn}_3[\text{PO}_4]_2$.

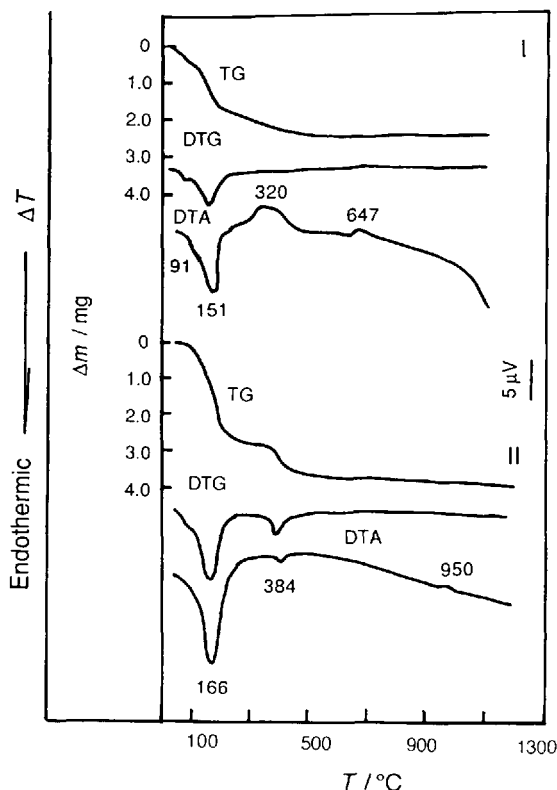


Figure 10.98 DTA-TG-DTG curves of (I) vivianite and (II) evansite [3]

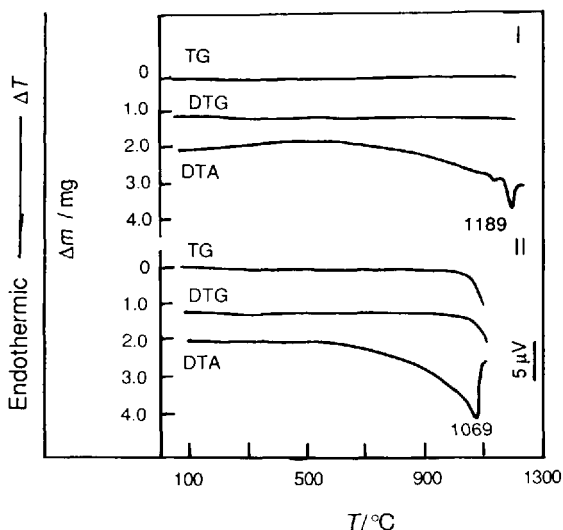


Figure 10.99 DTA-TG-DTG curves of (I) berzelite and (II) mimetite [3]

Samples

I, Vivianite $(\text{Fe}^{\text{II}}_{3-x}\text{Fe}^{\text{III}}_x)(\text{H}_2\text{O})_{8-x}[\text{PO}_4]_2(\text{OH})_x$ (FeO 43.0%, P_2O_5 28.3%, H_2O 28.7%); II, evansite, $\text{Al}_3[\text{PO}_4](\text{OH})_6 \cdot 6\text{H}_2\text{O}$ (Al_2O_3 39.62%, P_2O_5 18.38%, H_2O 42.00%).

Results

I. *Vivianite*—91 °C and 151 °C endotherms, vivianite releases crystalline water, 320 °C exotherm, vivianite releases water of constitution and Fe^{2+} oxidizes to Fe^{3+} ; 647 °C exotherm, phosphate crystallizes and is transformed to FePO_4 .

II. *Evansite*—166 °C endotherm, evansite releases crystalline water; 384 °C endotherm, evansite releases constitution water and $\text{Al}_3\text{O}_3\text{PO}_4$ is formed; 950 °C exotherm, $\text{Al}_3\text{O}_3\text{PO}_4$ decomposes, crystallizes and is transformed to AlPO_4 and Al_2O_3 .

10.9 Thermal Analysis Curves of Arsenide Minerals

Arsenide minerals undergo polymorphic transformation, melting, dehydration and recrystallization of the dehydrated and decomposed substances.

Samples

I, Berzelite, $\text{NaCa}_2(\text{MgMn})_2[\text{AsO}_4]_3$; II, mimetite, $\text{Pb}_2\text{Pb}_3[\text{AsO}_4]_3\text{Cl}$.

Results

I. *Berzelite*—1189 °C endotherm, berzelite melts.

II. *Mimetite*—1069 °C endotherm, mimetite melts and subsequently evaporates.

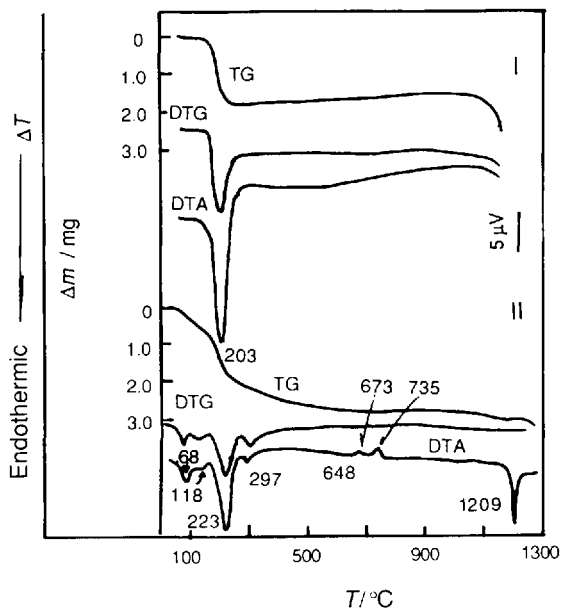


Figure 10.100 DTA-TG-DTG curves of (I) mansfieldite and (II) hoernesite [3]

Samples

I, Mansfieldite, $\text{Al}(\text{H}_2\text{O})_2[\text{AsO}_4]$; II, hoernesite, $\text{Mg}_3(\text{H}_2\text{O})_8[\text{AsO}_4]_2$ (MgO 24.44%, As_2O_3 46.44%, H_2O 29.12%).

Results

I. Mansfieldite—203 °C endotherm, mansfieldite releases water of crystallization. At a temperature higher than 1050 °C, AlAsO_4 sublimes.

II. Hoernesite—68, 118, 223 °C and 297 °C endotherms, hoernesite releases crystalline water and is transformed to $\text{Mg}_3(\text{AsO}_4)_2$; 673 °C exotherm, $\text{Mg}_3(\text{AsO}_4)_2$ recrystallizes; 735 °C exotherm, $\text{Mg}_3(\text{AsO}_4)_2$ undergoes a polymorphic transformation; 1209 °C endotherm, $\text{Mg}_3(\text{AsO}_4)_2$ melts.

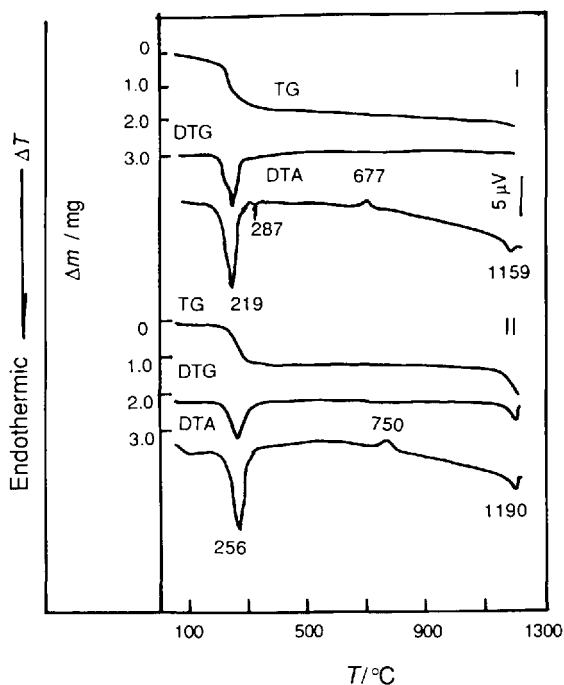


Figure 10.101 DTA-TG-DTG curves of (I) erythrite and (II) cabrerite [3]

Samples

I, Erythrite $\text{Co}_3(\text{H}_2\text{O})_8[\text{AsO}_4]_2$ (CoO 37.45%, As_2O_3 38.39%, H_2O 24.07%); II, cabrerite, $(\text{Ni,Mg})_3(\text{H}_2\text{O})_8[\text{AsO}_4]_2$.

Results

I. Erythrite—219 and 287 °C endotherms, erythrite releases crystalline water and is transformed to $\text{Co}_3(\text{AsO}_4)_2$; 677 °C exotherm, $\text{Co}_3(\text{AsO}_4)_2$ recrystallizes; 1159 °C endotherm, $\text{Co}_3(\text{AsO}_4)_2$ melts.

II. Cabrerite—256 °C endotherm, cabrerite releases crystalline water and $(\text{Ni,Mg})_3(\text{AsO}_4)_2$ is formed; 750 °C exotherm, $(\text{Ni,Mg})_3(\text{AsO}_4)_2$ recrystallizes; 1190 °C endotherm, $(\text{Ni,Mg})_3(\text{AsO}_4)_2$ decomposes and is transformed to $\text{Ni}_6\text{O}_3(\text{AsO}_4)$ and NiMgO_2 .

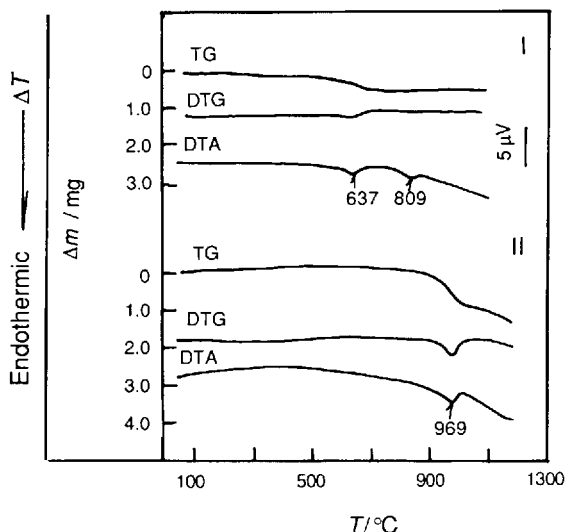


Figure 10.102 DTA-TG-DTG curves of (I) mottramite and (II) vanadinite [3]

Samples

I, Mottramite, $\text{PbCu}[\text{VO}_4]\text{OH}$ (PbO 55.43%, CuO 19.75%, V_2O_5 22.58%, H_2O 2.24%); II, vanadinite, $\text{Pb}_5[\text{VO}_4]_3\text{Cl}$ (PbO 78.80%, V_2O_5 19.26%, Cl 2.50%).

Results

I. *Mottramite*—637 °C endotherm, mottramite releases crystalline water; 809 °C endotherm, the dehydrated substance decomposes.

II. *Vanadinite*—969 °C endotherm, vanadinite decomposes to $\beta\text{-Pb}_3(\text{VO}_4)_2$ and PbO and releases Cl_2 ; PbO volatilizes.

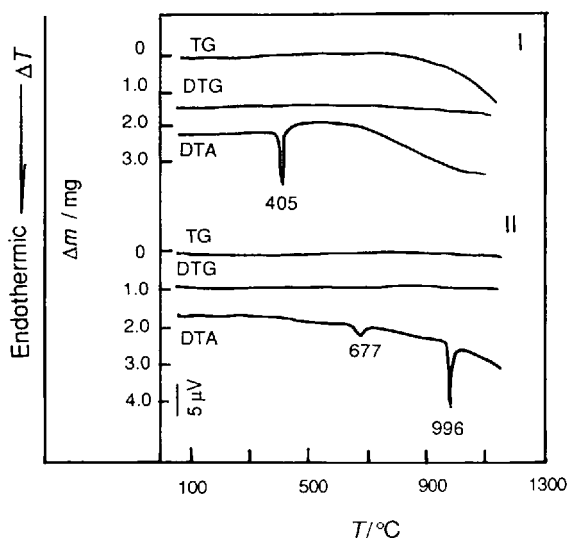


Figure 10.103 DTA-TG-DTG curves of (I) lopezite and (II) tarapacaite [3]

Samples

I, Lopezite, $\text{K}_2[\text{Cr}_2\text{O}_7]$ (K_2O 32.02%, CrO_3 67.98%); II, tarapacaite, $\text{K}_2[\text{CrO}_4]$ (K_2O 48.51%, CrO_3 41.49%).

Results

I. *Lopezite*—405 °C endotherm, lopezite melts.

II. *Tarapacaite*—677 °C endotherm, tarapacaite undergoes a polymorphic transformation; 996 °C endotherm, tarapacaite melts.

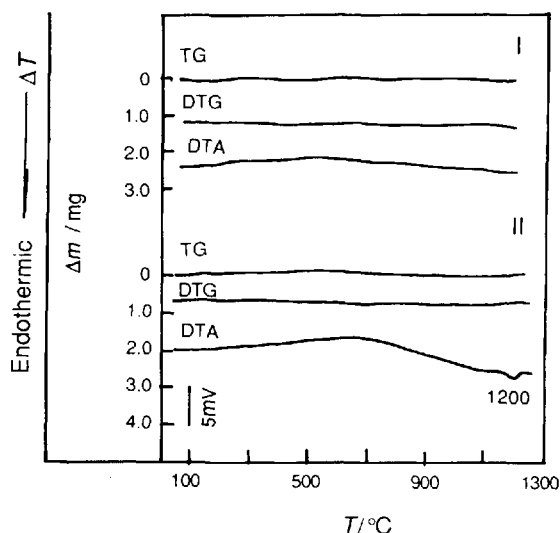


Figure 10.104 DTA-TG-DTG curves of (I) scheelite and (II) wolframite [3]

Samples

I, Scheelite, $\text{Ca}[\text{WO}_4]$ (CaO 19.4%, WO_3 80.6%);
II, wolframite, $(\text{Mn,Fe})\text{WO}_4$.

Results

From 20 to 1200 °C, scheelite shows no thermal events; 1200 °C endotherm, impurity in wolframite oxidizes.

10.10 Thermal Analysis Curves of Silicate Minerals

Silicate minerals undergo dehydration, decomposition, polymorphic transformation, recrystallization of the dehydrated substances, melting and valence-state change of variable-valence elements.

Samples

I, Forsterite, Mg_2SiO_4 (MgO 57.29%, SiO_2 42.71%); II, fayalite, Fe_2SiO_4 (FeO 70.51%, SiO_2 29.49%); III, tephroite, Mn_2SiO_4 (MnO 70.25%, SiO_2 29.75%).

Results

I. Forsterite—Shows no thermal events up to 1300 °C.

II. Fayalite—865 °C exotherm, fayalite decomposes and Fe^{2+} oxidizes to Fe^{3+} accompanied by a mass increase; 1321 °C exotherm, the decomposed and oxidized substance converts to hematite and cristobalite.

III. Tephroite—From 700 °C, Mn oxidizes, accompanied by a mass increase.

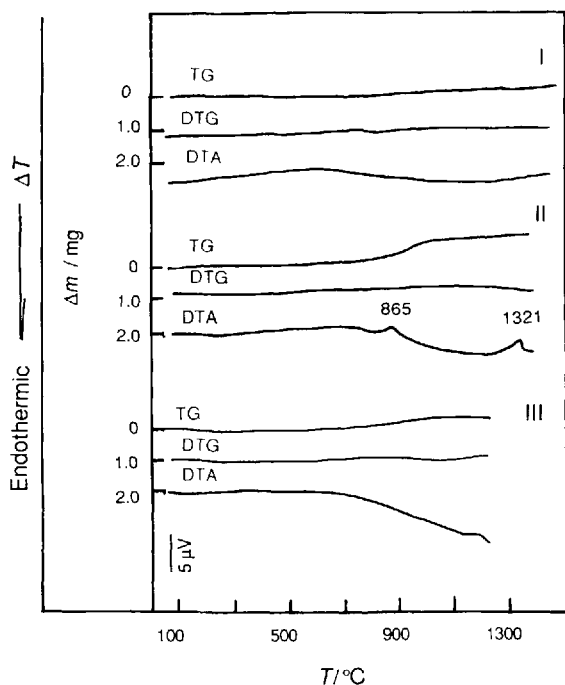


Figure 10.105 DTA-TG-DTG curves of (I) forsterite, (II) fayalite [3] and (III) tephroite [3]

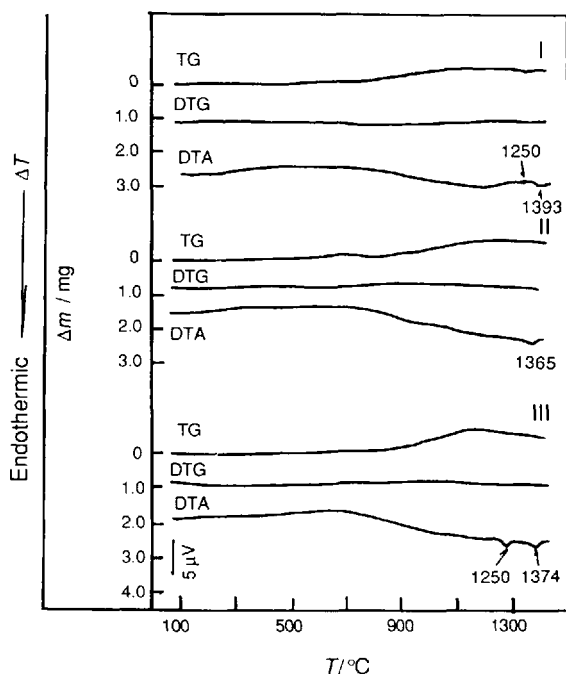


Figure 10.106 DTA-TG-DTG curves of (I) chrysolite, (II) hortonlite and (III) ferrohortonlite [3]

Samples

I, Chrysolite, $(\text{Mg}_{0.75}\text{Fe}_{0.25})_2\text{SiO}_4$; II, hortonlite, $(\text{Mg},\text{Fe})_2\text{SiO}_4$; III, ferrohortonlite, $(\text{Mg}_{0.25}\text{Fe}_{0.75})_2\text{SiO}_4$.

Experimental conditions

Amount of sample, 9.5 g.

Results

I. Chrysolite—1250 °C endotherm, part of chrysolite decomposes to hematite and enstatite $[(\text{Mg}_{0.9}\text{Fe}_{0.1})_2\text{Si}_2\text{O}_6]$; 1393 °C endotherm, part of chrysolite decomposes to magnesioferrite $(\text{MgFe}_2\text{O}_4)$, fayalite and enstatite; at a temperature higher than 800 °C, the Fe^{2+} oxidizes accompanied by a mass increase.

II. Hortonlite—At a temperature higher than 800 °C, Fe^{2+} oxidizes to Fe^{3+} accompanied by a mass increase; 1230 °C endotherm, hortonlite decomposes to hematite, cristobalite and forsterite; 1365 °C endotherm, magnesioferrite and enstatite are formed.

III. Ferrohortonlite—At a temperature higher than 800 °C, Fe^{2+} oxidizes to Fe^{3+} accompanied by an mass increase; 1250 °C endotherm, oxidized ferrohortonlite decomposes to magnesioferrite, cristobalite and hematite; 1374 °C endotherm, oxidized ferrohortonlite decomposes to magnesioferrite and cristobalite.

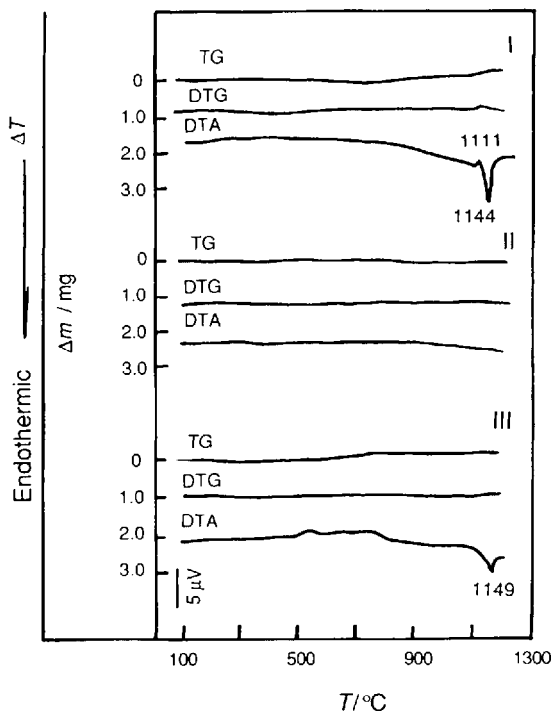


Figure 10.107 TDA-TG-DTG curves of (I) hedenbergite, (II) diopside and (III) johannsenite [3]

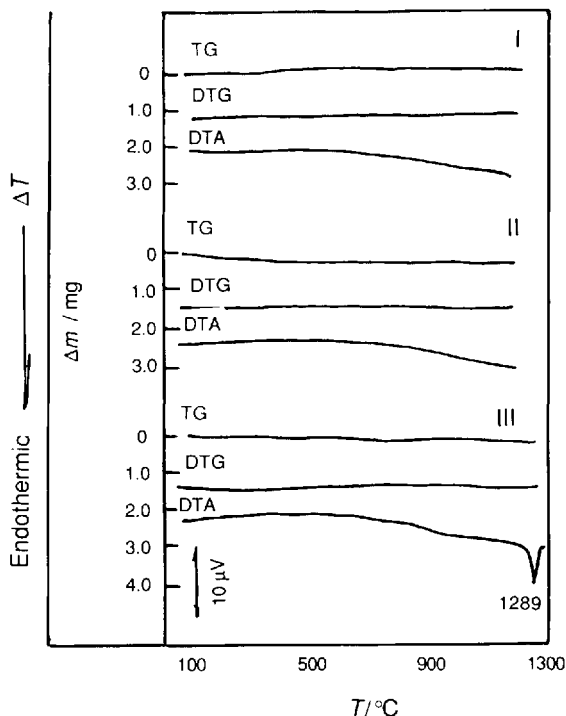


Figure 10.108 DTA-TG-DTG curves of (I) clinoenstatite, (II) omphacite and (III) fassaite

Samples

I, Hedenbergite, $\text{Ca}(\text{Mg}_{0-0.25}\text{Fe}_{0.75-1})[\text{Si}_2\text{O}_6]$; II, diopside, $\text{Ca}(\text{Mg}_{1-0.75}\text{Fe}_{0-0.25})[\text{Si}_2\text{O}_6]$; III, Johannsenite, $\text{CaMn}[\text{Si}_2\text{O}_6]$.

Results

I. *Hedenbergite*—1111 °C exotherm, Fe^{2+} oxidizes to Fe^{3+} ; 1144 °C endotherm, oxidized hedenbergite decomposes.

II. *Diopside*—Shows no thermal events up to 1200 °C.

III. *Johannsenite*—1149 °C endotherm, johannsenite decomposes and is transformed to amorphous material.

Samples

I, Clinoenstatite, $\text{Mg}_2\text{Si}_2\text{O}_6$; II, omphacite, $(\text{Ca},\text{Na})(\text{Mg},\text{Fe}^{\text{II}},\text{Fe}^{\text{III}},\text{Al})[\text{Si}_2\text{O}_6]$; III, fassaite, $\text{Ca}(\text{Mg},\text{Fe}^{\text{II}},\text{Al})(\text{Si},\text{Al})_2\text{O}_6$.

Results

I. *Clinoenstatite*—Shows no thermal events from 20 to 1200 °C.

II. *Omphacite*—Shows no thermal events from 20 to 1200 °C.

III. *Fassaite*—1289 °C endotherm, fassaite decomposes.

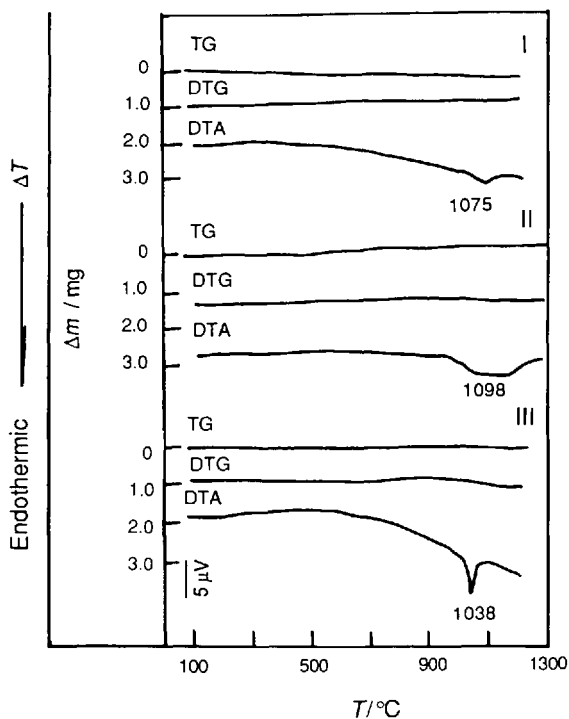


Figure 10.109 DTA-TG-DTG curves of (I) spodumene, (II) jadeite and (III) aegirine [3]

Samples

I, Spodumene, $\text{LiAl}[\text{Si}_2\text{O}_6]$ (Li_2O 8.07%, Al_2O_3 27.44%, SiO_2 64.49%); II, jadeite, $\text{NaAl}[\text{Si}_2\text{O}_6]$ (Na_2O 15.4%, Al_2O_3 25.2%, SiO_2 59.4%); III, aegirine, $\text{NaFe}^{\text{III}}[\text{Si}_2\text{O}_6]$ (Na_2O 13.4%, Fe_2O_3 34.6%, SiO_2 52.0%).

Results

I. *Spodumene*—1075 °C endotherm, spodumene undergoes a polymorphic transformation.

II. *Jadeite*—1098 °C endotherm, jadeite decomposes and is transformed to amorphous material.

III. *Aegirine*—1038 °C endotherm, aegirine decomposes.

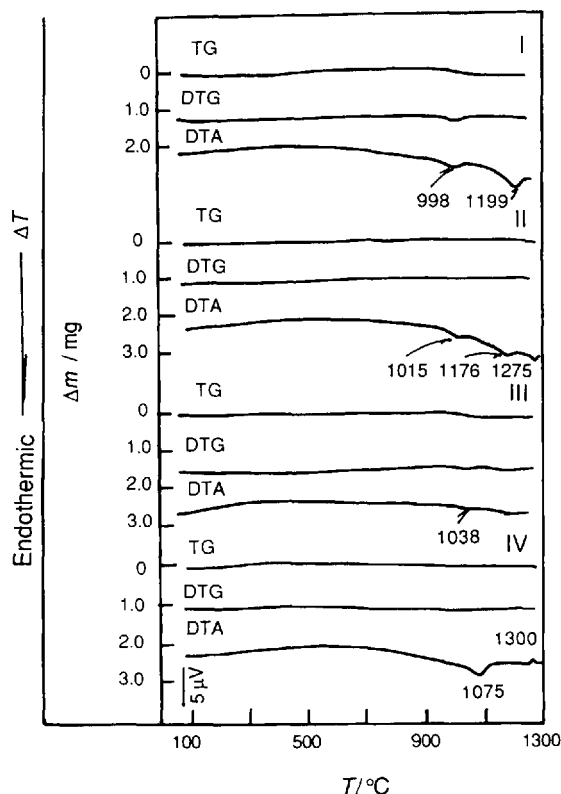


Figure 10.110 DTA-TG-DTG curves of (I) holmquistite, (II) glaucophane, (III) anthophyllite and (IV) riebeckite [3]

Samples

I, Holmquistite, $\text{Li}_2(\text{MgXFe}^{\text{II}})_3\text{Al}_2\text{Si}_8\text{O}_{22}(\text{OH})_2$;
 II, glaucophane, $\text{Na}(\text{Mg},\text{Fe}^{\text{II}})_3\text{Al}_2\text{Si}_8\text{O}_{22}(\text{OH})_2$;
 III, anthophyllite, $(\text{Mg},\text{Fe}^{\text{II}})_7[\text{Si}_8\text{O}_{22}](\text{OH})_2$; IV,
 riebeckite, $\text{Na}_2(\text{Fe}^{\text{II}},\text{Mg})_3\text{Fe}_2^{\text{III}}\text{Si}_8\text{O}_{22}(\text{OH})_2$.

Results

I. Holmquistite—998 °C endotherm, holmquistite releases constitution water, 1199 °C endotherm, the crystal lattice of the dehydrated holmquistite is broken.

II. Glaucophane—1015 °C endotherm, glaucophane releases constitution water and decomposes; subsequently it is transformed to magnesioferrite; 1176 °C endotherm, the substance decomposes again; 1275 °C endotherm, the substance melts.

III. Anthophyllite—1038 °C endotherm, anthophyllite releases constitution water and is transformed to enstatite and cristobalite.

IV. Riebeckite—1075 °C endotherm, riebeckite releases constitution water, decomposes and is transformed to magnetite; 1300 °C exotherm, magnetite oxidizes to hermatite.

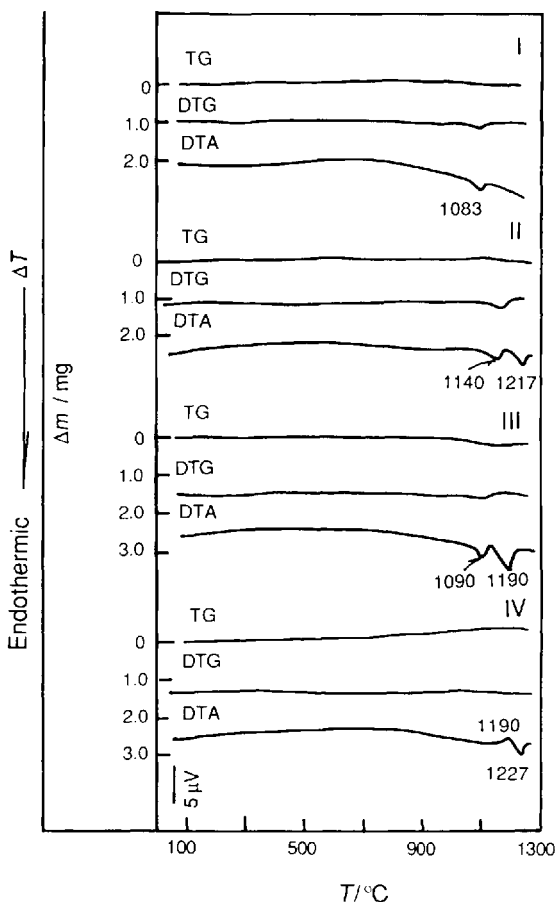


Figure 10.111 DTA-TG-DTG curves of (I) hastingsite, (II) pargasite, (III) tremolite and (IV) grunerite [3]

Samples

I, Hastingsite, $\text{NaCa}_2(\text{Fe}^{\text{II}}, \text{Mg})_4\text{Fe}^{\text{III}}[\text{Si}_6\text{Al}_2\text{O}_{22}](\text{OH})_2$; II, pargasite, $\text{NaCa}_2(\text{Mg}, \text{Fe}^{\text{II}})_4\text{Al}[\text{Si}_6\text{Al}_2\text{O}_{22}](\text{OH})_2$; III, tremolite, $\text{Ca}_2(\text{Mg}, \text{Fe}^{\text{II}})_5[\text{Si}_8\text{O}_{22}](\text{OH})_2$; IV, grunerite, $(\text{Fe}^{\text{II}} 1-0.7, \text{Mg} 0-0.3)_7[\text{Si}_8\text{O}_{22}](\text{OH})_2$.

Results

I. Hastingsite—1083 °C endotherm, hastingsite releases constitution water and the crystal lattice breaks; it is transformed to augite.

II. Pargasite—1140 °C endotherm, pargasite releases constitution water and the crystal lattice breaks; 1217 °C endotherm, the dehydrated material is transformed to fassaite.

III. Tremolite—1090 °C endotherm, tremolite releases constitution water and the crystal lattice breaks; 1190 °C endotherm, the dehydrated material forms cristobalite, diopside and ensatite.

IV. Grunerite—1190 °C exotherm, grunerite decomposes and oxidizes; hematite and cristobalite are formed; 1227 °C endotherm, magnesioferrite and cristobalite are formed.

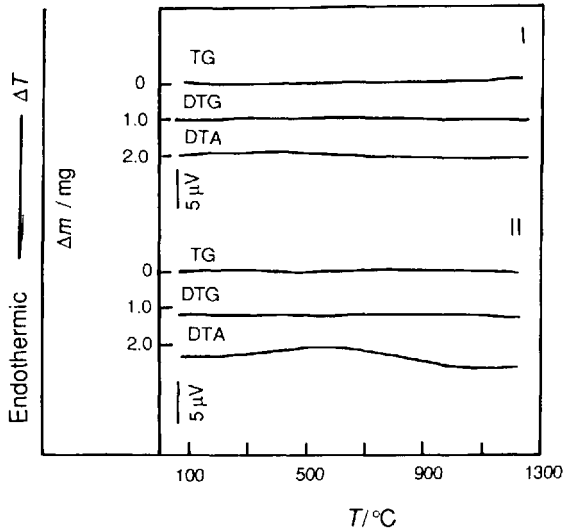


Figure 10.112 DTA-TG-DTG curves of (I) anorthite and (II) albite [3]

Samples

I, Anorthite, $\text{Ca}[\text{Al}_2\text{Si}_2\text{O}_8]$; II, albite, $\text{Na}[\text{AlSi}_3\text{O}_8]$.

Results

Anorthite and albite show no thermal events from 20 to 1200 °C.

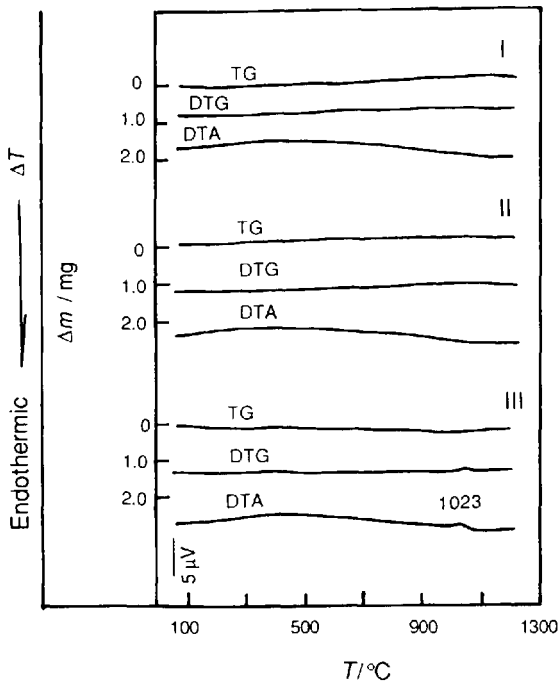


Figure 10.113 DTA-TG-DTG curves of (I) orthoclase, (II) sanidine and (III) adularia [3]

Samples

I, Orthoclase, $\text{K}[\text{AlSi}_3\text{O}_8]$ (K_2O 16.9%, Al_2O_3 18.4%, SiO_2 64.7%); II, sanidine, $\text{K}[\text{AlSi}_3\text{O}_8]$; III, adularia, $\text{K}[\text{AlSi}_3\text{O}_8]$.

Results

Orthoclase, sanidine and adularia show no thermal events from 20 to 1200 °C; 1023 °C exotherm for adularia, impurity oxidizes.

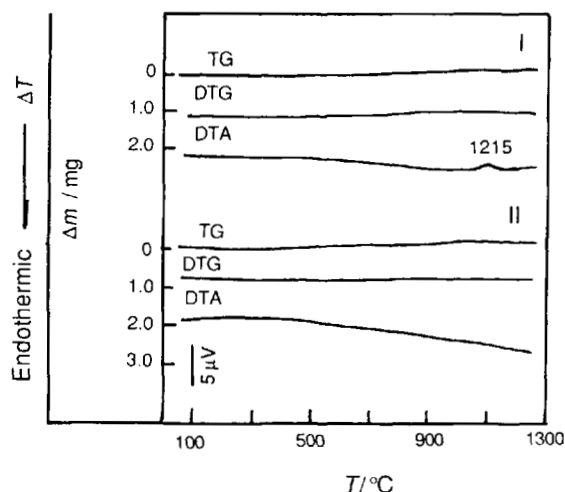


Figure 10.114 DTA-TG-DTG curves of (I) petalite and (II) leucite [3]

Samples

I, Petalite, $\text{Li}[\text{AlSi}_4\text{O}_{10}]$ (Li_2O 4.9%, Al_2O_3 16.7%, SiO_2 78.4%); II, leucite, $\text{K}[\text{AlSi}_2\text{O}_6]$ (K_2O 21.58%, Al_2O_3 23.4%, SiO_2 55.02%).

Results

I. *Petalite*—1215 °C exotherm, petalite decomposes and forms spodumene and cristobalite.

II. *Leucite*—Shows no thermal events from 20 to 1300 °C.

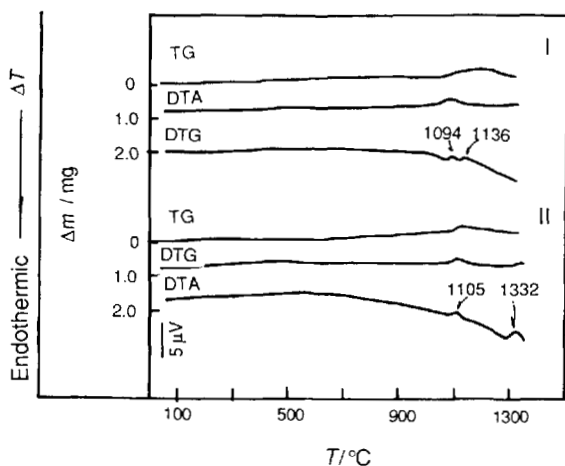


Figure 10.115 DTA-TG-DTG curves of (I) spessartine and (II) almandine [3]

Samples

I, Spessartine, $\text{Mn}_3\text{Al}_2[\text{Si}_4\text{O}_{13}]$; II, almandine, $\text{Fe}_3^{\text{II}}\text{Al}_2[\text{Si}_4\text{O}_{13}]$.

Results

I. *Spessartine*:—1094 °C exotherm, spessartine oxidizes and decomposes and forms galaxite, hausmannite and cristobalite; 1136 °C exotherm, the substance undergoes a polymorphic transformation.

II. *Almandine*—1105 °C exotherm, almandine decomposes and oxidizes; it is converted to cristobalite, $\text{MgFe}^{\text{III}}\text{AlO}_4$ and Fe_2O_3 ; 1332 °C exotherm, Fe_3O_4 converts to Fe_2O_3 .

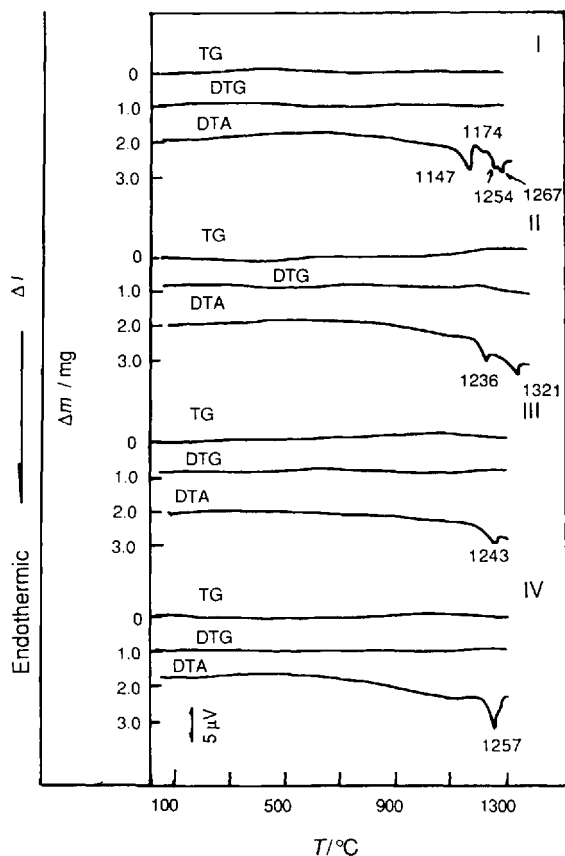


Figure 10.116 DTA-TG-DTG curves of (I) grossular, (II) pyrope, (III) uvarovite and (IV) andradite [3]

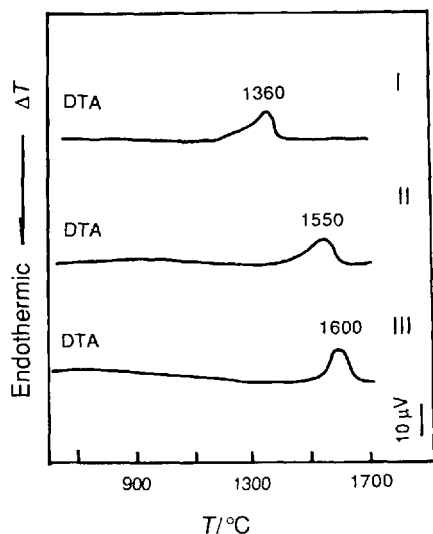


Figure 10.117 DTA curves of (I) kyanite, (II) andalusite and (III) sillimanite [6]

Samples

I, Grossular, $\text{Ca}_3\text{Al}_2[\text{SiO}_4]_3$; II, pyrope, $\text{Mg}_3\text{Al}_2[\text{SiO}_4]_3$; III, uvarovite, $\text{Ca}_3\text{Cr}_2^{III}[\text{SiO}_4]_3$; IV, andradite, $\text{Ca}_3\text{Fe}_2^{III}[\text{SiO}_4]_3$.

Results

I. Grossular—1147 °C endotherm, grossular decomposes; 1174 °C exotherm, the decomposed substance recrystallizes; 1254 and 1267 °C endotherms, the decomposed substance melts.

II. Pyrope—1236 °C endotherm, pyrope decomposes and forms forsterite, magnesiospinel and cristobalite; 1321 °C endotherms, forsterite and cristobalite transform to enstatite.

III. Uvarovite—1243 °C endotherm, uvarovite decomposes and forms chromite and an amorphous substance.

IV. Andradite—1257 °C endotherm, andradite converts to $\text{Ca}(\text{Fe},\text{Al})_2\text{SiO}_6$ and $\text{Ca}_2\text{Si}_2\text{O}_6$.

Samples

I, Kyanite, $\text{Al}_2[\text{SiO}_4]\text{O}$ (SiO_2 36.8%, Al_2O_3 63.2%); II, andalusite, $\text{Al}_2\text{Al}[\text{SiO}_4]\text{O}$; III, sillimanite, $\text{Al}[\text{AlSiO}_5]$ (Al_2O_3 62.93%, SiO_2 37.07%).

Results

Kyanite and andalusite convert to mullite and crysotor pellets at 1360 and 1550 °C, respectively and sillimanite at 1600 °C.

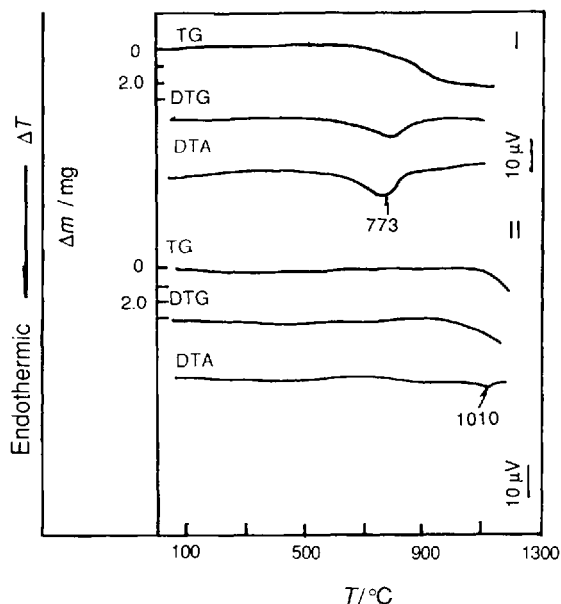


Figure 10.118 DTA-TG-DTG curves of (I) pyrophyllite [6] and (II) talc

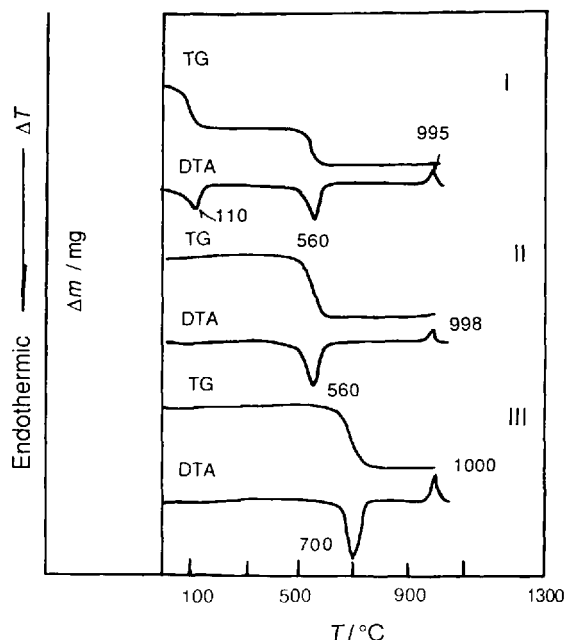


Figure 10.119 DTA-TG curves of (I) halloysite, (II) kaolinite and (III) dickite

Samples

I, Pyrophyllite, $\text{Al}_2[\text{Si}_4\text{O}_{10}](\text{OH})_2$ (Al_2O_3 28.3%, SiO_2 66.7%, H_2O 5.0%); II, talc, $\text{Mg}_3[\text{Si}_4\text{O}_{10}](\text{OH})_2$ (MgO 31.72%, SiO_2 63.12%, H_2O 4.76%).

Results

I. *Pyrophyllite*—773 °C endotherm, pyrophyllite loses constitution water and the crystal lattice breaks; sillimanite and quartz are formed.

II. *Talc*—1010 °C endotherm, talc dehydrates and the crystal lattice breaks; enstatite and quartz are formed.

Samples

I, Halloysite, $\text{Al}_4(\text{H}_2\text{O})_4[\text{Si}_4\text{O}_{10}](\text{OH})_8$ (Al_2O_3 34.66%, SiO_2 40.85%, H_2O 24.49%); II, kaolinite, $\text{Al}_4[\text{Si}_4\text{O}_{10}](\text{OH})_8$ (Al_2O_3 39.4%, SiO_2 46.55%, H_2O 13.96%); III, dickite $\text{Al}_4[\text{Si}_4\text{O}_{10}](\text{OH})_8$.

Experimental conditions

Amount of sample, 200 mg.

Results

I. *Halloysite*—110 °C endotherm, halloysite releases crystalline water and metahalloysite is formed; 560 °C endotherm, metahalloysite releases constitution water and the crystal lattice breaks; 995 °C exotherm, the dehydrated substance crystallizes to $\gamma\text{-Al}_2\text{O}_3$ and quartz.

II. *Kaolinite*—560 °C endotherm, kaolinite releases constitution water and the crystal lattice breaks; 998 °C exotherm, the dehydrated substance crystallizes to mullite and cristobalite.

III. *Dickite*—700 °C endotherm, dickite releases constitution water and the crystal lattice breaks; 1000 °C exotherm, the dehydrated substance recrystallizes to mullite and quartz.

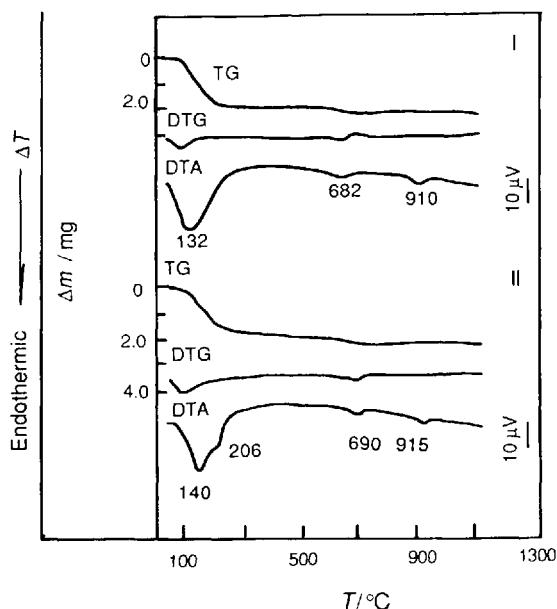


Figure 10.120 DTA-TG-DTG curves of montmorillonite: (I) Na montmorillonite; (II) Ca montmorillonite

Sample

Montmorillonite, $(\text{Na,Ca})_{0.33}(\text{Al,Mg})_2[\text{Si}_4\text{O}_{10}](\text{OH})_2 \cdot n\text{H}_2\text{O}$.

Results

I. Na-montmorillonite—132 °C endotherm, montmorillonite releases water layer by layer; 682 °C endotherm, montmorillonite releases constitution water and the crystal lattice breaks; 910 °C endotherm, the dehydrated substance recrystallizes and is transformed to enstatite and quartz.

II. Ca-montmorillonite—140 and 206 °C endotherms, montmorillonite releases water layer by layer; 690 °C endotherm, montmorillonite releases constitution water and the crystal lattice breaks; 915 °C endotherm, the dehydrated substance recrystallizes and is transformed to cordierite, enstatite and quartz.

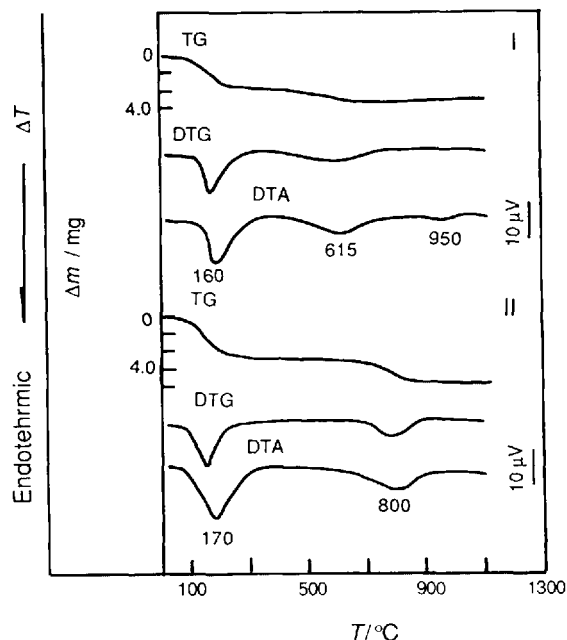


Figure 10.121 DTA-TG-DTG curves of (I) glauconite and (II) saponite [6]

Samples

I, Glauconite, $\text{K}_{1-x}(\text{Al,Fe})_2[\text{Al}_{1-x}\text{Si}_{3-x}\text{O}_{10}](\text{OH})_2$;
II, saponite, $\text{Na}_x(\text{H}_2\text{O})_4[\text{Mg}_2[\text{Al}_x\text{Si}_{4-x}\text{O}_{10}](\text{OH})_2]$.

Results

I. Glauconite—160 °C endotherm, glauconite releases hygroscopic water; 615 °C endotherm, glauconite releases constitution water and the crystal lattice breaks; 950 °C endotherm, the dehydrated substance recrystallizes.

II. Saponite—170 °C endotherm, saponite releases water layer by layer; 800 °C endotherm, saponite releases constitution water.

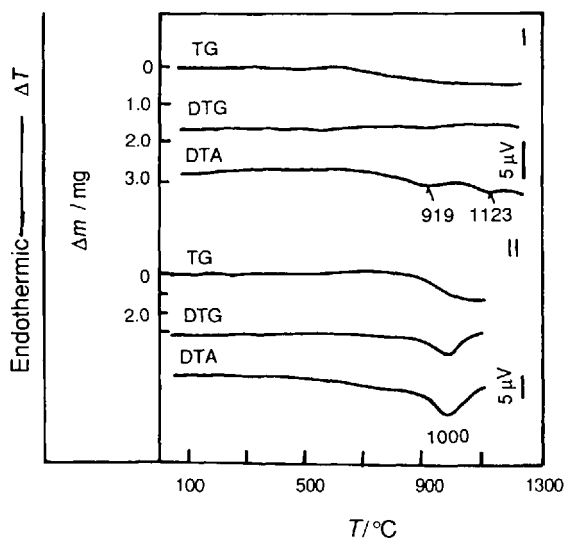


Figure 10.122 DTA-TG-DTG curves of (I) muscovite [3] and (II) biotite [2]

Samples

I, Muscovite, $KAl_2[(Al, Si_3)O_{10}](OH)_2$ (K_2O 11.8%, Al_2O_3 38.5%, SiO_2 45.2%, H_2O 4.5%); II, biotite, $K(Mg, Fe, Al)_{2-3}[(Al, Si_3)O_{10}](OH)_2$.

Results

I. Muscovite—919 $^\circ C$ endotherm, muscovite releases constitution water and the crystal lattice breaks; 1123 $^\circ C$ endotherm, the dehydrate crystallizes giving leucite, γ -corundum and spinel.

II. Biotite—1000 $^\circ C$ endotherm, biotite releases constitution water and the crystal lattice breaks.

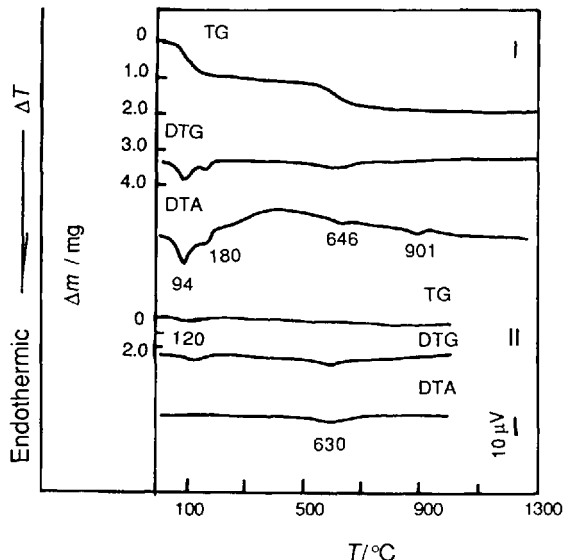


Figure 10.123 DTA-TG-DTG curves of (I) hydrobiotite [3] and (II) hydromuscovite [6]

Samples

I, Hydrobiotite; II, hydromuscovite.

Results

I. Hydrobiotite—94 and 180 $^\circ C$ endotherms, hydrobiotite releases water layer by layer; 646 $^\circ C$ endotherm, hydrobiotite releases constitution water; 901 $^\circ C$ endotherm, the dehydrated substance decomposes.

II. Hydromuscovite—120 $^\circ C$ endotherm, hydromuscovite releases water layer by layer, 630 $^\circ C$ endotherm, hydromuscovite releases water of constitution and the crystal lattice breaks.

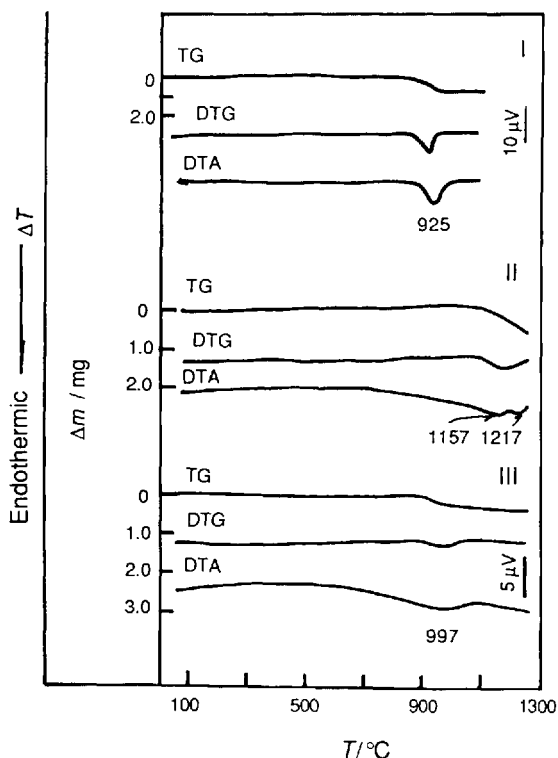


Figure 10.124 DTA-TG-DTG curves of (I) margarite [6], (II) phlogopite [3] and (III) paragonite [3]

Samples

I, Margarite, $\text{CaAl}_2(\text{Al}_2\text{Si}_2\text{O}_{10}(\text{OH})_2)$; II, phlogopite, $\text{KMg}_3(\text{AlSi}_3\text{O}_{10}(\text{OH})_2)$; III, paragonite, $\text{NaAl}_2(\text{AlSi}_3\text{O}_{10}(\text{OH})_2)$.

Results

I. Margarite—925 °C endotherm, margarite releases constitution water and the crystal lattice breaks.

II. Phlogopite—1157 and 1217 °C endotherms, phlogopite releases water of constitution and is transformed to forsterite (Mg_2SiO_4), leucite (KAlSi_2O_6) and MgO .

III. Paragonite—997 °C endotherm, paragonite releases constitution water and is transformed to albite ($\text{NaAlSi}_3\text{O}_8$) and Al_2O_3 .

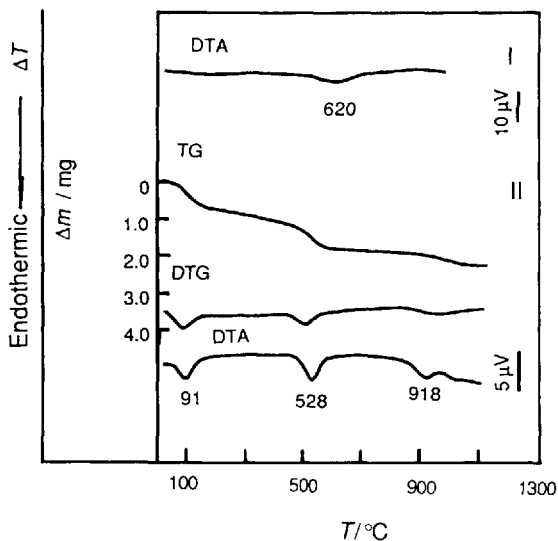


Figure 10.125 DTA-TG-DTG curves of (I) sericite [6] and (II) illite [3]

Samples

I, Sericite; II, illite, $\text{K}_{1-x}(\text{H}_2\text{O})_x\text{Al}_2[\text{AlSi}_3\text{O}_{10}(\text{OH})_{2-x}(\text{H}_2\text{O})_x]$

Results

I. Sericite—620 °C endotherm, sericite releases water of constitution and the crystal lattice breaks.

II. Illite—91 °C endotherm, illite releases water.

of between the layers; 528 °C endotherm, illite releases constitution water and the crystal lattice breaks; 918 °C endotherm, illite releases the remainder of the constitution water and decomposes; it is transformed to spinel, mullite, etc.

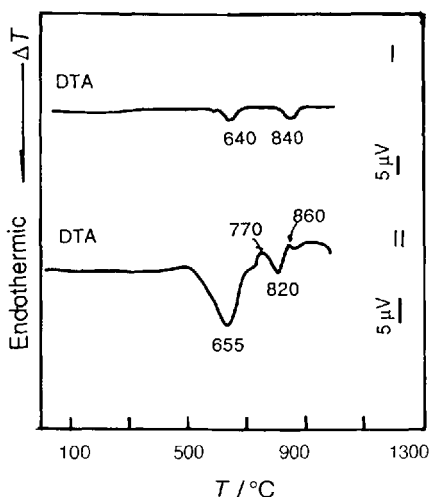


Figure 10.126 DTA curves of (I) sheridanite and (II) ripidolite [6]

Samples

I, Sheridanite, $\text{Mg}_3(\text{OH})\{\text{Al}_3[(\text{Si},\text{Al})_4\text{O}_{10}](\text{OH})_2\}$;
 II, ripidolite, $(\text{Mg},\text{Fe},\text{Al})_3(\text{OH})_6[(\text{Mg},\text{Fe},\text{Al})_3[(\text{Si},\text{Al})_4\text{O}_{10}](\text{OH})_2]$.

Results

I. Sheridanite—640 °C endotherm, sheridanite releases water of octahedron between the layers; 840 °C endotherm, sheridanite releases water of octahedron between the tetrahedra.

II. Ripidolite—655 °C endotherm, ripidolite releases water of octahedron between the layers; 770 °C exotherm, Fe^{2+} of ripidolite oxidizes to Fe^{3+} ; 820 °C endotherm, ripidolite releases water of octahedron between the tetrahedra; 860 °C exotherm, the dehydrated substance crystallizes; it is transformed to spinel $[(\text{Mg},\text{Fe})\text{Al}_2\text{O}_4]$ and enstatite $(\text{Mg}_2\text{Si}_2\text{O}_6)$.

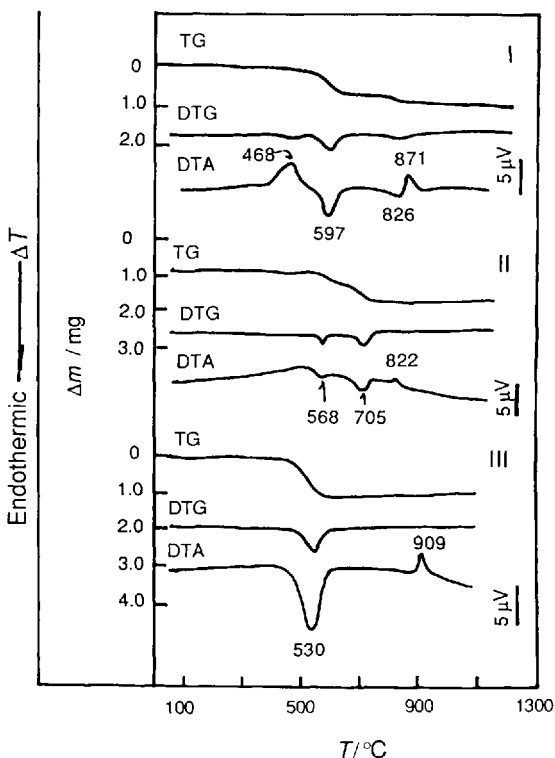


Figure 10.127 DTA-TG-DTG curves of (I) clinochlore, (II) nimite and (III) cookeite [3]

Samples

I, Clinochlore, $(\text{Mg},\text{Fe},\text{Al})_3(\text{OH})_6(\text{Mg},\text{Fe}^{\text{II}},\text{Al})_3[(\text{Si},\text{Al})_4\text{O}_{10}](\text{OH})_2$; II, nimite, $(\text{N},\text{Al})_3(\text{OH})_6[(\text{Ni},\text{Al})_3[\text{AlSi}_3\text{O}_{10}](\text{OH})_2]$; III, cookeite: $\text{LiAl}_2(\text{OH})_6\text{Al}_2[\text{AlSi}_3\text{O}_{10}](\text{OH})_2$.

Results

I. Clinochlore—468 °C exotherm, Fe^{2+} of clinochlore oxidizes; 597 °C endotherm, clinochlore releases water of octahedron between the layers; 826 °C endotherm, clinochlore releases water between octahedron and tetrahedra; 871 °C exotherm, the structure of the dehydrated substance is reorganized and is transformed to MgAl_2O_4 , MgO , SiO_2 , etc.

II. Nimite—568 °C endotherm, nimite releases water of octahedron between the layers; 705 °C endotherm, nimite releases water of octahedron between the tetrahedra; 822 °C exotherm, the dehydrated substance crystallizes; it is transformed to liebenbergite $(\text{Ni}_2[\text{Si}_4\text{O}])$, etc.

III. Cookeite—530 °C endotherm, cookeite
 (continued)

releases crystalline water and the crystal lattice breaks; 909 °C exotherm, the dehydrated substance crystallizes and is transformed to mullite, Li_2O , SiO_2 , etc.

Samples

I, α -Chrysotile, $\text{Mg}_6[\text{Si}_4\text{O}_{10}](\text{OH})_8$ (MgO 43%, SiO_2 44.1%, H_2O 12.9%); II, β -chrysotile, $\text{Mg}_6[\text{Si}_4\text{O}_{10}](\text{OH})_8$; III, α -antigorite, $\text{Mg}_6[\text{Si}_4\text{O}_{10}](\text{OH})_8$; IV, β -antigorite, $\text{Mg}_6[\text{Si}_4\text{O}_{10}](\text{OH})_8$.

Results

I. α -Chrysotile—710 °C endotherm, α -chrysotile releases constitution water and the crystal lattice breaks; 850 °C exotherm, the dehydrated substance recrystallizes; it is transformed to forsterite and $\text{Mg}_2\text{Si}_2\text{O}_6$ (amorphous).

II. β -Chrysotile—730 °C endotherm, β -chrysotile releases constitution water.

III. α -Antigorite—760 °C endotherm, α -antigorite releases constitution water and the crystal lattice breaks; 820 °C exotherm, the dehydrated substance recrystallizes and is transformed to forsterite (Mg_2SiO_4) and Mg_2SiO_6 (amorphous).

IV. β -Antigorite—770 °C endotherm, β -antigorite releases constitution water.

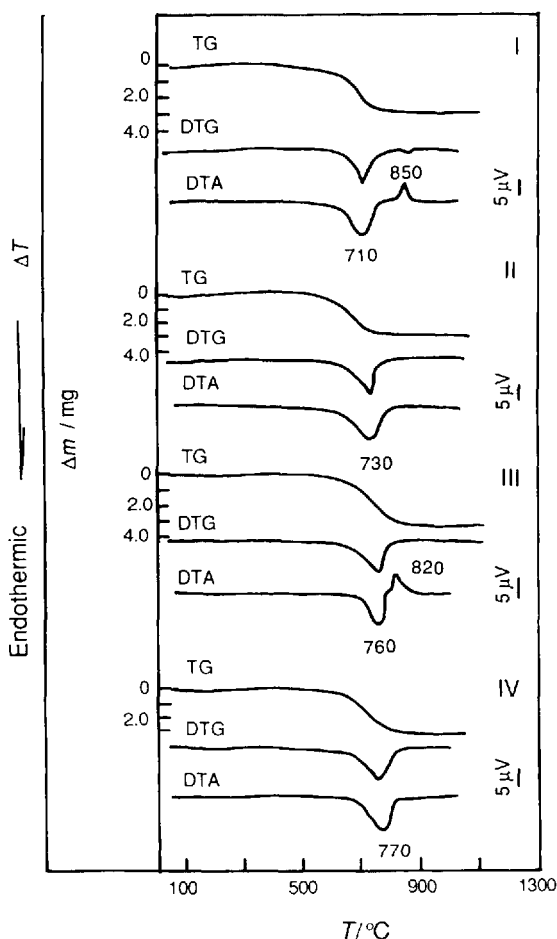


Figure 10.128 DTA-TG-DTG curves of (I) α -chrysotile, (II) β -chrysotile, (III) α -antigorite and (IV) β -antigorite [6]

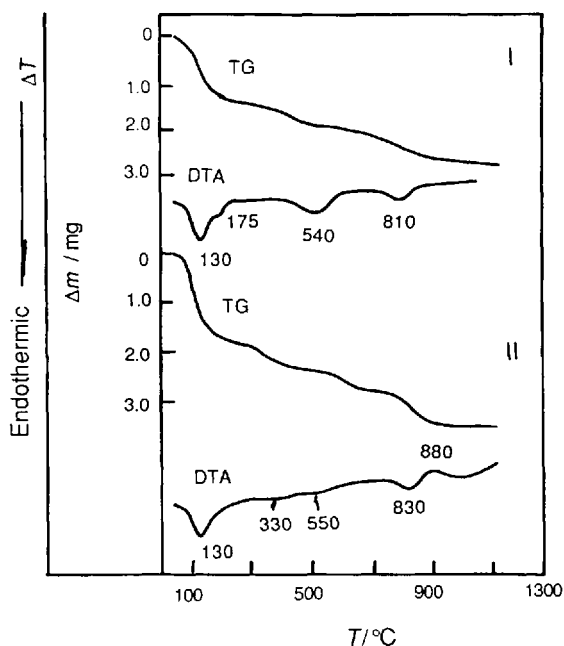


Figure 10.129 DTA-TG curves of (I) vermiculite and (II) sepiolite

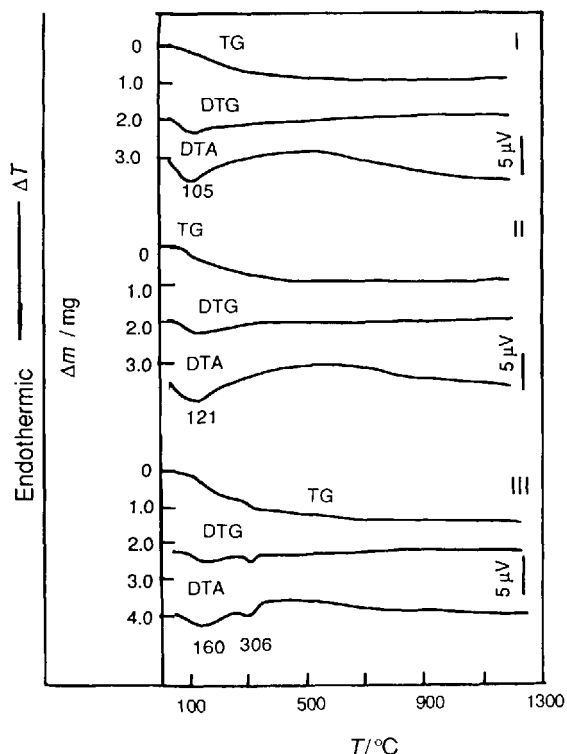


Figure 10.130 DTA-TG-DTG curves of (I) clinoptilolite, (II) mordenite and (III) heulandite [3]

Samples

I, Vermiculite, $(\text{Mg}, \text{Fe}^{\text{III}}, \text{Al})_3(\text{Al}, \text{Si})_4\text{O}_{10}(\text{OH})_2 \cdot n\text{H}_2\text{O}$; II, sepiolite, $\text{Mg}_8(\text{H}_2\text{O})_4[\text{Si}_6\text{O}_{15}]_2(\text{OH})_4 \cdot 8\text{H}_2\text{O}$.

Results

I. Vermiculite—130, 175 and 540 °C endotherms, vermiculite releases water between the layers in stages; 810 °C endotherm, vermiculite releases constitution water and the crystal lattice breaks; at a temperature higher than 850 °C, the dehydrated material crystallizes and is transformed to enstatite, Al_2O_3 , etc.

II. Sepiolite—130 °C endotherm, sepiolite releases zeolitic water; 330 and 550 °C endotherms, sepiolite releases water of integration; 830 °C endotherm, sepiolite releases constitution water and the crystal lattice breaks; 880 °C exotherm, the dehydrated material crystallizes and is transformed to enstatite and SiO_2 .

Samples

I, Clinoptilolite, $(\text{Na}, \text{K}, \text{Ca})_{2-3}[\text{Al}_3(\text{Al}, \text{Si})_2\text{Si}_{13}\text{O}_{36}] \cdot 12\text{H}_2\text{O}$; II, mordenite, $\text{Na}_2\text{Ca}[\text{AlSi}_5\text{O}_{12}]_4 \cdot 12\text{H}_2\text{O}$; III, heulandite, $(\text{Ca}, \text{Na}_2)(\text{Al}_2\text{Si}_7\text{O}_{18}) \cdot 6\text{H}_2\text{O}$.

Results

I. Clinoptilolite—105 °C endotherm, clinoptilolite releases zeolitic water.

II. Mordenite—121 °C endotherm, mordenite releases zeolitic water.

III. Heulandite—160 and 306 °C endotherms, heulandite releases zeolitic water.

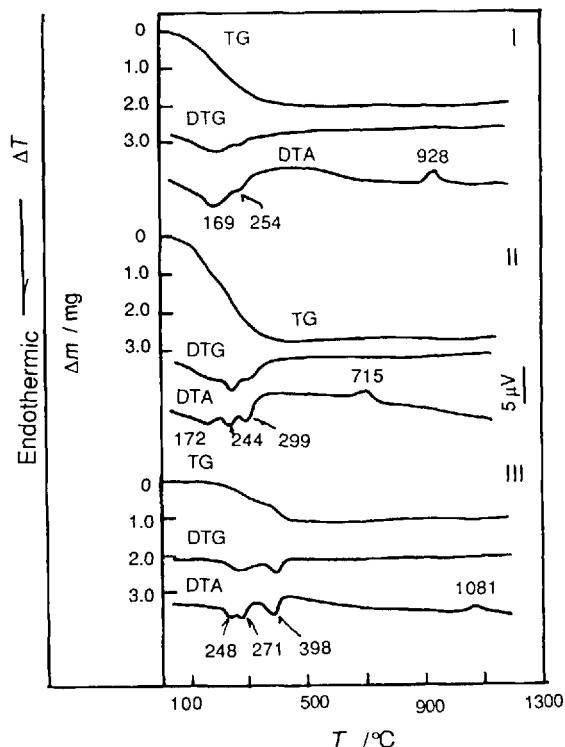


Figure 10.131 DTA-TG-DTG curves of (I) chabazite, (II) harmotome and (III) scolecite [3]

Samples

I, Chabazite, $(\text{Ca}, \text{Na}_2)[\text{Al}, \text{Si}_2\text{O}_6]_2 \cdot 6\text{H}_2\text{O}$; II, harmotome, $\text{Ba}[\text{AlSi}_3\text{O}_8]_2 \cdot 6\text{H}_2\text{O}$; III, scolecite, $\text{Ca}[\text{Al}_2\text{Si}_3\text{O}_{10}] \cdot 3\text{H}_2\text{O}$ (CaO 14.3%, Al_2O_3 26.0%, SiO_2 45.9%, H_2O 13.8%).

Results

I. Chabazite—169 and 254 °C endotherms, chabazite releases zeolitic water; 928 °C exotherm, the crystal lattice breaks and amorphous material is formed.

II. Harmotome—172, 244 and 299 °C endotherms, harmotome releases zeolitic water, 715 °C exotherm, the dehydrated substance crystallizes and is transformed to celsian.

III. Scolecite—248, 271 and 398 °C endotherms, scolecite releases zeolitic water; 1081 °C exotherm, the dehydrated substance crystallizes and is transformed to anorthite.

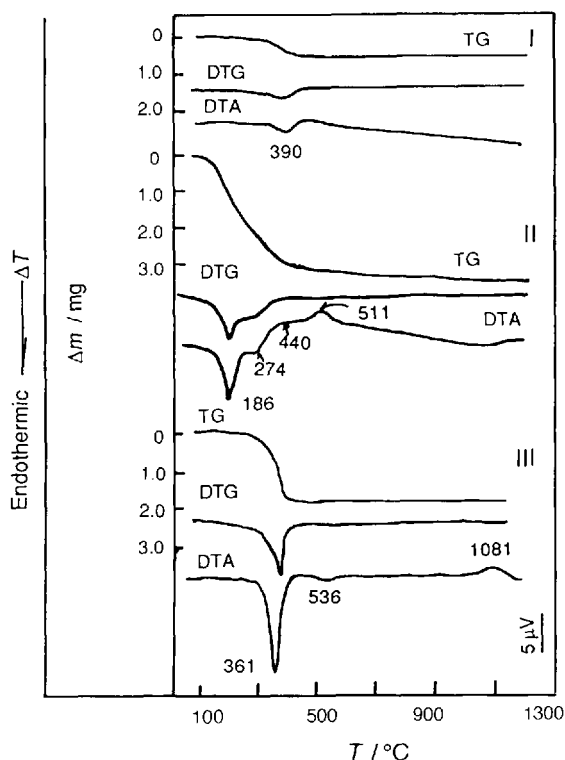


Figure 10.132 DTA-TG-DTG curves of (I) analcime, (II) stilbite and (III) natrolite [3]

Samples

I, Analcime, $\text{Na}_2[\text{AlSi}_2\text{O}_6]_2 \cdot 2\text{H}_2\text{O}$ (Na_2O 14.09%, Al_2O_3 23.20%, SiO_2 54.54%, H_2O 8.17%); II, stilbite, $(\text{Ca}, \text{Na}_2, \text{K}_2) [\text{Al}_2\text{Si}_7\text{O}_{18}] \cdot 7\text{H}_2\text{O}$; III, natrolite, $\text{Na}_2[\text{Al}_2\text{Si}_3\text{O}_{10}] \cdot 2\text{H}_2\text{O}$ (Na_2O 16.3%, Al_2O_3 26.8%, SiO_2 47.4%, H_2O 9.5%).

Results

I. *Analcime*—390 °C endotherm, analcime releases zeolitic water.

II. *Stilbite*—186 and 274 °C endotherms, stilbite releases zeolitic water; 511 °C exotherm, the crystal lattice breaks and amorphous material is formed.

III. *Natrolite*—361 °C endotherm, natrolite releases zeolitic water; 536 °C endotherm, the dehydrated substance is transformed to metanatlite ($\text{Na}_2\text{Al}_2\text{Si}_3\text{O}_{10}$); 1081 °C exotherm, metanatlite is transformed to nepheline.

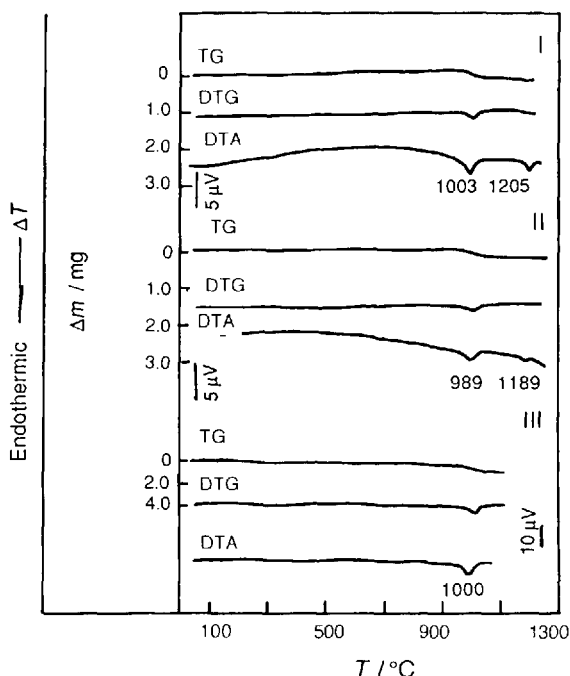


Figure 10.133 DTA-TG-DTG curves of (I) epidote [3], (II) piemontite [3] and (III) zoisite [6]

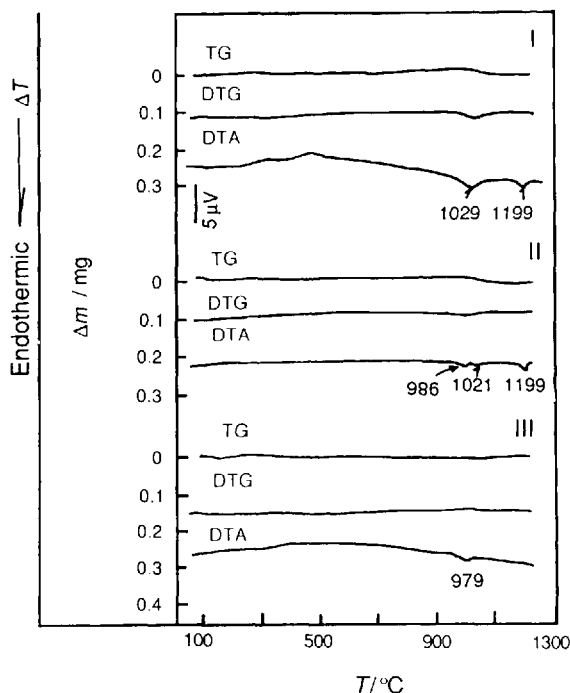


Figure 10.134 DTA-TG-DTG curves of (I) clinoziosite, (II) mukhinite and (III) allanite [3]

Samples

I, Epidote, $\text{Ca}_2\text{FeAl}_2[\text{Si}_2\text{O}_7][\text{SiO}_4]\text{O}(\text{OH})$; II, piemontite, $\text{Ca}_2\text{Mn}^{\text{III}}\text{Al}_2[\text{Si}_2\text{O}_7][\text{SiO}_4]\text{O}(\text{OH})$; III, zoisite, $\text{Ca}_2\text{Al}_3[\text{Si}_2\text{O}_7][\text{SiO}_4]\text{O}(\text{OH})$.

Results

I. Epidote—1003 °C endotherm, epidote releases constitution water; 1205 °C endotherm, the dehydrated substance is transformed to anorthite, etc.

II. Piemontite—989 °C endotherm, piemontite releases constitution water; 1189 °C endotherm, the dehydrated substance is transformed to anorthite.

III. Zoisite—1000 °C endotherm, zoisite releases constitution water and anorthite is formed.

Samples

I, Clinoziosite, $\text{Ca}_2\text{AlAl}_2[\text{Si}_2\text{O}_7][\text{SiO}_4]\text{O}(\text{OH})$ (CaO 24.6%, Al_2O_3 33.9%, SiO_2 39.5%, H_2O 2%); II, mukhinite, $\text{Ca}_2\text{Al}_2\text{V}[\text{Si}_2\text{O}_7][\text{SiO}_4]\text{O}(\text{OH})$; III, Allanite, $(\text{Ca}, \text{Mn}, \text{Ce}, \text{La}, \text{Y}, \text{Th})_2(\text{Fe}^{\text{II}}, \text{Fe}^{\text{III}}, \text{Ti})(\text{Al}, \text{Fe})_2[\text{Si}_2\text{O}_7][\text{SiO}_4]\text{O}(\text{OH})$.

Results

I. Clinoziosite—1029 °C endotherm, clinoziosite releases constitution water; 1199 °C endotherm, the dehydrated substance is transformed to grossular and anorthite.

II. Mukhinite—986 and 1021 °C endotherms, mukhinite releases constitution water; 1199 °C endotherm, the dehydrated substance is transformed to anorthite, goldmanite and SiO_2 .

III. Allanite—979 °C endotherm, allanite releases constitution water and decomposes; it is transformed to cerianite and silicates.

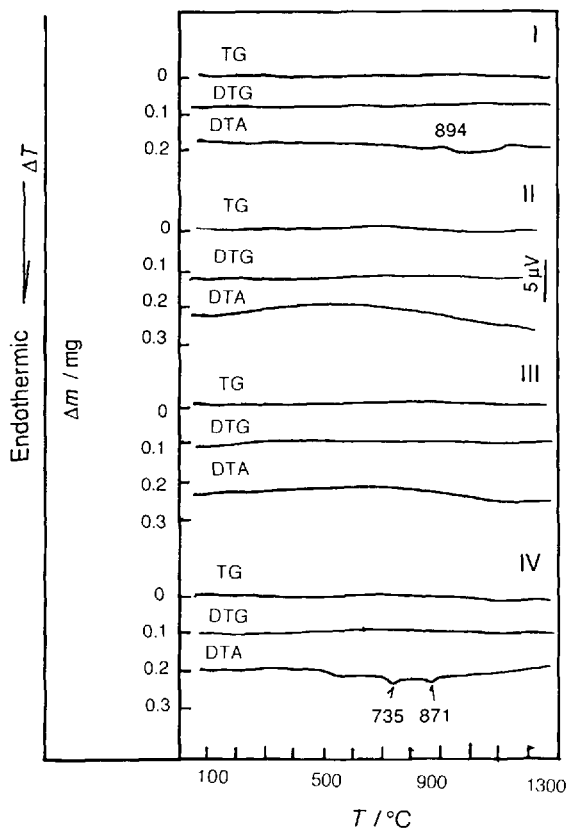


Figure 10.135 DTA-TG-DTG curves of (I) thorite, (II) zircon, (III) willemite and (IV) eulytite [3]

Samples

I, Thorite, $\text{Th}[\text{SiO}_4]$ (ThO_2 81.5%, SiO_2 18.5%); II, zircon, $\text{Zr}[\text{SiO}_4]$ (ZrO_2 67.1%, SiO_2 32.9%); III, willemite, $\text{Zn}_2[\text{SiO}_4]$ (ZnO 73.0%, SiO_2 27.0%); IV, eulytite, $\text{Bi}_4[\text{SiO}_4]_3$ (BiO 80.91%, SiO_2 19.08%).

Results

I. Thorite—894 °C exotherm, thorite decomposes and is transformed to ThO_2 and SiO_2 .

II. Zircon—From 20 to 1200 °C, zircon shows no thermal events.

III. Willemite—From 20 to 1300 °C, willemite shows no thermal events.

IV. Eulytite—735 °C endotherm, eulytite undergoes a polymorphic transformation; 871 °C endotherm, eulytite is transformed to another polymorphic crystalline structure.

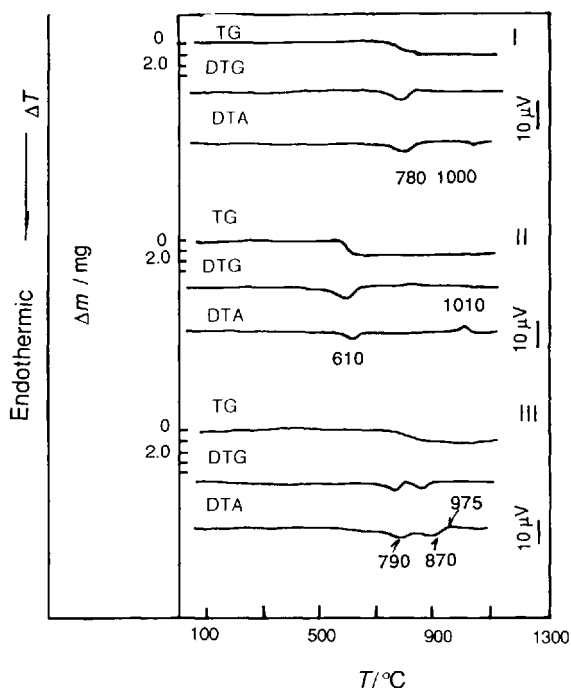


Figure 10.136 DTA-TG-DTG curves of (I) pectolite, (II) anauxite and (III) prehnite [6]

Samples

I, Pectolite, $\text{NaCa}_2[\text{Si}_3\text{O}_8(\text{OH})]$; II, anauxite, $\text{Al}_2\text{Si}_3\text{O}_7(\text{OH})_4$; III, prehnite, $\text{Ca}_2\text{Al}_2\text{Si}_3\text{O}_{10}(\text{OH})_2$ (CaO 27.16%, Al_2O_3 24.78%, SiO_2 43.69%, H_2O 4.37%).

Results

I. Pectolite—780 °C endotherm, pectolite releases constitution water; 1000 °C endotherm, the dehydrated substance melts.

II. Anauxite—610 °C endotherm, anauxite releases constitution water; 1010 °C exotherm, the dehydrated substance undergoes structural reorganization.

III. Prehnite—790 °C endotherm, 1 mol prehnite releases 0.5 mol constitution water; 870 °C endotherm, 1 mol prehnite releases another 0.5 mol constitution water; 975 °C exotherm, the dehydrated substance crystallizes and is transformed to anortite and wollastonite.

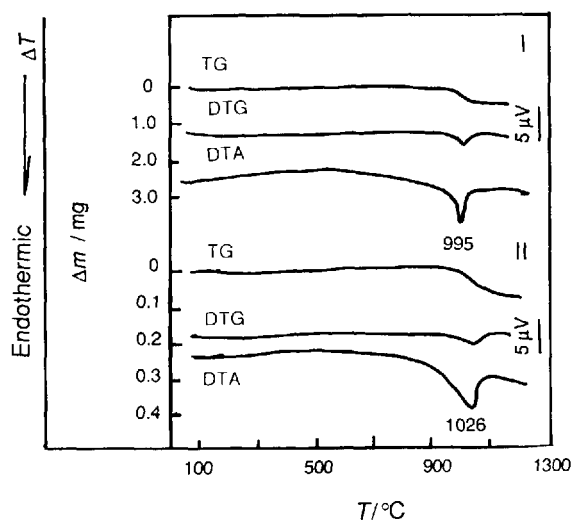


Figure 10.137 DTA-TG-DTG curves of (I) elbaite and (II) dravite [3]

Samples

I, Elbaite, $\text{NaLiAl}_2\text{Al}_6[\text{Si}_6\text{O}_{18}][\text{BO}_3]_3(\text{OH})_4$; II, dravite, $\text{NaMg}_3\text{Al}_6[\text{Si}_6\text{O}_{18}][\text{BO}_3]_3(\text{OH})_4$.

Results

I. Elbaite—995 °C endotherm, elbaite releases constitution water.

II. Dravite—1026 °C endotherm, dravite releases constitution water.

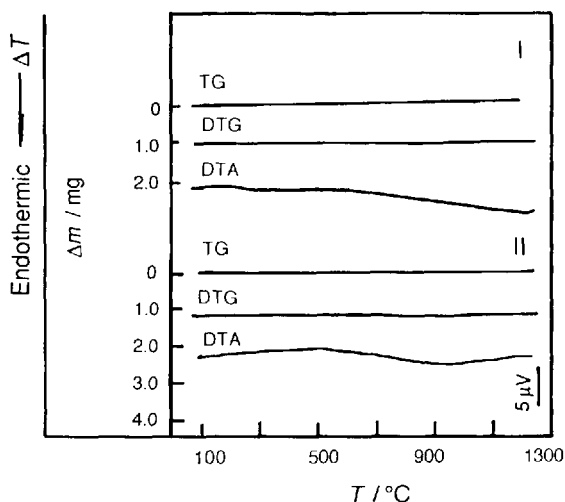


Figure 10.138 DTA-TG-DTG curves of (I) topaz and (II) nosean [3]

Samples

I, Topaz, $\text{Al}_2[\text{SiO}_4](\text{F},\text{OH})_2(\text{Al}_2\text{O}_3, 55.4\%, \text{SiO}_2, 32.6\%, \text{F } 22.0\%)$; II, nosean, $\text{Na}_8[\text{AlSiO}_4]_6[\text{sO}_4]$.

Results

From 20 to 1200 °C, topaz and nosean show no thermal events.

10.11 References

- 1 Werner, S. K., *Differential Thermal Analysis: Applications and Results in Mineralogy*. Berlin, Springer, 1974.
- 2 Dai Anbang and Shen Menghang, *Periodic Table of Elements*. Shanghai, Shanghai Science and Technology Press, 1981.
- 3 Chen Guoxi, Zhang Yueming, et al., *Handbook of Thermal Analysis and X-Ray Diffraction Curves of Minerals*. Chengdu, Sichuan Science and Technology Press, 1989.
- 4 *A Manual of Chinese Chemicals*, Beijing, Chinese Goods and Materials Press, 1992.
- 5 Blazek, A., *Thermal Analysis*. New York, Van Nostrand Reinhold, 1973.
- 6 Todor, D. N., *Thermal Analysis of Minerals*. Kent, Abacus Press, 1976.
- 7 Xie Xiande, Zheng Mianping and Liu Laibao, *Borate Minerals*, Beijing, Science Press, 1965.

Thermal Analysis Curves of Energetic Materials

Energetic materials exist in a substable state under normal conditions. In order to estimate their properties and potential danger, it is important to establish their thermal characteristics and thermal behavior. The thermal analysis curve is one of the important bases for obtaining information in this field.

In this chapter, about 70 thermal analysis curves for 60 samples are presented. Most of these curves were measured by the author with an LCT thermal analyzer equipped with a laboratory-made 4.1 model thermal analyzer (constructed at the Beijing Optical Instrument Factory) and a Shimadzu DSC-50 instrument. Other curves were obtained from the literature.

The conditions for the measurements with the LCT model were as follows: micro sample holder with a PtRh10-Pt thermocouple and quartz sheath; normal sample mass 2–3 mg; heating rate $10^{\circ}\text{C min}^{-1}$; DTA sensitivity $\pm 25 \mu\text{V}$ (total deflection); TG range 10 mg (total deflection); temperature measurement range 10 mV; paper speed of recorder 4 mm min^{-1} ; platinum crucible (diameter 5 mm, height 3 mm, open type); reference crucible empty; and temperature of the free end of thermocouples for temperature measurement was 0°C . A TWT-464 electronic potentiometric recorder made by the Shanghai Second Automatic Instrument and Meter Factory was used for recording data. KNO_3 , In, KClO_4 etc., were used to calibrate the temperatures, and a

mixture of SiO_2 and K_2SO_4 (4 : 1 mass ratio) was used for checking the resolution power. TG curves measured by simultaneous TG-DTA were used mainly to elucidate the mass-loss process. Sometimes the characteristic temperatures on some TG curves were used to help analyze the DTA curves.

The conditions for measurements using the Shimadzu DSC-50 instrument were as follows: sample mass about 1.0 mg; heating rate $10^{\circ}\text{C min}^{-1}$; nitrogen atmosphere (purity 99.99%); flow-rate 20 ml min^{-1} ; platinum crucible (diameter 5 mm, height 3 mm). In, Sn, Zn, Al, KClO_4 , etc., were used as standard samples for temperature calibration.

A Mettler II thermal analyzer was used in the work by Krien cited throughout this chapter. Other measurement conditions were as follows: heating rate $6^{\circ}\text{C min}^{-1}$; DTA sensitivity $\pm 100 \text{ mV}$ (total deflection); PtRh-Pt thermocouples used to measure the temperature, range $2 \mu\text{V}$ (full-scale); aluminum crucible, open; reference material $\alpha\text{-Al}_2\text{O}_3$; dynamic dry air, flow-rate $ca 97 \text{ ml min}^{-1}$ (5.8 l h^{-1}).

For the DTA or DSC curve of each sample, as far as possible the initial temperature (T_i), the extrapolated onset temperature (T_o) and the peak temperature (T_p) under the experimental conditions are given. For some samples the ignition temperature (T_{ig}) and slope temperature (T_{sl} , the temperature at the point where the steepest slope

appears to begin to move towards the exothermic peak) are also given. In the reference data, some physical and chemical properties of the samples and their configurational isomers which are intimately related to thermal analysis are listed as fully as possible, e.g. melting point (m.p.), boiling point at a pressure of 101.1 kPa (b.p.), decomposition temperature (T_d), crystalline transition temperature (T_s) and the percentage mass loss (α). The author thought it necessary to explain the thermal analysis curves obtained in order to understand the properties of

configurational isomers. On the DTA and DSC curves, some peaks are the result of comprehensive heat effects, and it is therefore impossible to show every process relating to these peaks. For peaks of this kind, only a qualitative description can be given regarding the comprehensive heat effects.

In the figures presented in this chapter, in order to save space, conditions of measurement which are the same as given above are not repeated.

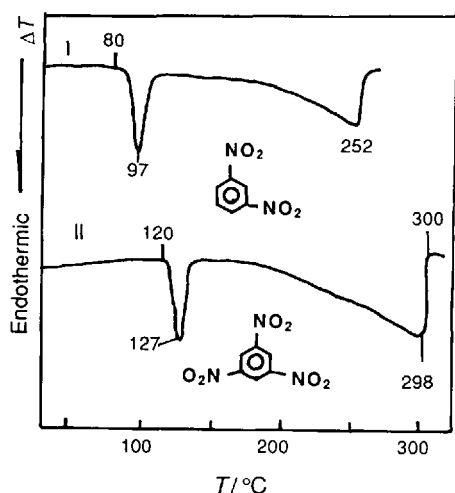


Figure 11.1 DTA curves of nitrobenzene in dynamic air. Reproduced by permission of Dr G. Krien from Refs 1 and 2

Samples

1, 1,3-Dinitrobenzene (1,3-DNB; *m*-DNB); 2, 1,3,5-trinitrobenzene (1,3,5-TNB).

Measurements

Sample mass: 1, 22.68 mg; 2, 19.15 mg.

Results

1. Melting peak T_i 353 K (80 °C), T_e 363 K (90 °C), T_p 370 K (97 °C); vaporization peak T_p 525 K (252 °C); T_i (for mass loss on TG curve, simultaneous TG-DTA) 388 K (115 °C). 2. Melting peak T_i 393 K (120 °C), T_e 395 K (122 °C), T_p 400 K (127 °C); vaporization peak T_p 571 K (298 °C); T_i (for mass loss on TG curve, simultaneous TG-DTA) 423 K (150 °C).

(continued)

Reference data

1. M.p. 363 K (80 °C) [1]; b.p. 564 K (291 °C) [1], 576 K (303 °C) [3]; T_d 548 K (275 °C) [1]. 2. M.p. 395.7 K (122.5 °C) [2], 394.4 K (121.2 °C) [4]; b.p. 623 K (350 °C) [2]; T_d 505 K (232 °C) [2]; 120 °C, 12 h, α 1.2%[1].

Others

Data measured under the following conditions: static air, CDR-I model DSC (Shanghai Balance Instrument Factory), 10 °C min⁻¹, sample mass *ca.* 1 mg, pressure-resistant sealed crucible made of soft stainless steel. 1. Melting peak T_p 365 K (92 °C); decomposition peak T_p 711 K (438 °C). 2. Melting peak T_p 398 K (125 °C); decomposition peak T_p 685 K (412 °C) [5].

M.p. and b.p. of structural isomers—1,2-dinitrobenzene, m.p. 391 K (118 °C) [3], 390.1 K (116.9 °C) [1]; b.p. 592 K (319 °C) [3]. 1,4-Dinitrobenzene, m.p. 445 K (172 °C) [3], 447 K (174 °C) [6], 446.7 K (173.5 °C) [1]; b.p. 582 K (309 °C) [3], 572 K (299 °C) [6]. 1,2,4-Trinitrobenzene, m.p. 335 K (62 °C) [3]. 1,2,3-Trinitrobenzene, m.p. 400.7 K (127.5 °C) [3].

Sample

2,4,6-Trinitro-*m*-xylene (TNX).

Measurements

Sample mass, 28.81 mg.

Results

Melting peak T_i 443 K (170 °C), T_e 456 K (183 °C), T_p 461 K (188 °C); vaporization peak T_p 563 K (290 °C); T_i (for mass-loss on TG curve, simultaneous TG-DTA) 408 K (135 °C).

Reference data

M.p. 456 K (183 °C) [1], 451–453 K (178–180 °C) [8]; 80 °C, 48 h α 0.035% [8]. Decomposition exothermic peak (measured in dynamic nitrogen using a hermetically sealed pressure-resistant soft stainless-steel crucible, Shimadzu DSC-20, 1–3 mg, 10 °C min⁻¹) T_i 581 K (308 °C) T_p 616 K (343 °C). ΔH 642 kJ mol⁻¹[9].

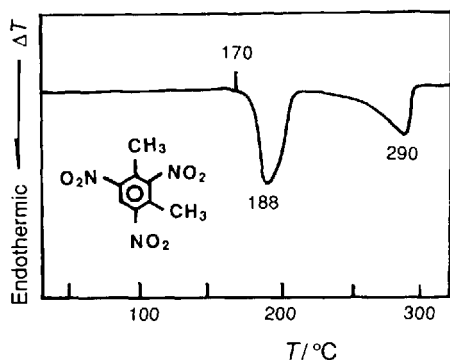


Figure 11.2 DTA curve of trinitro-*m*-xylene in dynamic air. Reproduced by permission of Dr G. Krien from Ref. 7

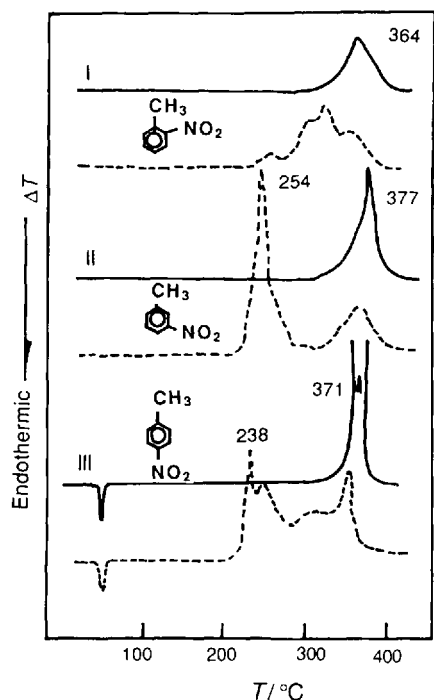


Figure 11.3 DTA curves of nitrotoluene in nitrogen (solid line) and oxygen (dotted line) under a gauge pressure of 2.9 MPa. Reproduced by permission of the *Journal of the Japanese Explosives Society* from Ref. 10

Samples

1, *o*-Nitrotoluene (*o*-MNT); 2, *m*-nitrotoluene (*m*-MNT); 3, *p*-nitrotoluene (*p*-MNT).

Measurements

Sample mass, 5 mg apparatus, Rigakudenki R-1 high-pressure DTA; crucible, hermetically sealed aluminum crucible with a pinhole in the center of the cover (diameter 5 mm, height 2.5 mm); heating rate, 10 °C min⁻¹.

Results

1. Decomposition peak (in nitrogen) T_p 637 K (364 min⁻¹). 2, Decomposition peak (in nitrogen) T_p 650 K (377 min⁻¹); first decomposition peak (in oxygen) T_p 527 K (254 min⁻¹). 3, Decomposition peak (in nitrogen) T_p 644 K (371 °C); first decomposition peak (in oxygen) 511 K (238 °C). The endothermic peak of 3 is a melting peak.

Reference data

1, M.p. 262.7 K (110.5 °C), (α unstable form) 269.1 K (-4.1 °C) (β , stable form); b.p. 494.9 K (221.7 °C). 2, M.p. 289.3 K (16.1 °C); b.p. 505.8 K (232.6 °C). 3, M.p. 324.80 K (51.65 °C) [11]; b.p. 511.4 K (238.2 °C) [11]. Data for decomposition peaks in helium at a gauge pressure of 4.9 MPa are given in Table 11.1

Table 11.1

Sample	T_i K (t/°C) ^a	T_p /K (t/°C)
<i>o</i> -MNT	593(320)	637(364)
<i>m</i> -MNT	599(326)	650(377)
<i>p</i> -MNT	603(330)	644(371)

^a T_i is the temperature at the 45° intersection point (tangent to the leading edge of the peak with the extrapolated baseline. T_i is slightly higher than T_i [12].

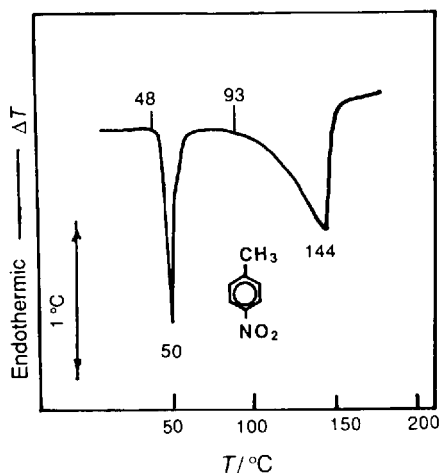


Figure 11.4 DTA curve of *p*-nitrotoluene in static air

Sample

p-Nitrotoluene (*p*-MNT) (chromatographically pure).

Measurements

Sample mass, 3.1 mg; apparatus, LCT; sensitivity (total deflection), $\pm 50 \mu\text{V}$; paper speed, 2 mm min^{-1} .

Results

Melting peak T_i 321 K (48 °C), T_e 322 K (49 °C); T_p 323 K (50 °C); vaporization peak T_i 366 K (93 °C), T_e 386 K (113 °C), T_p 417 K (144 °C).

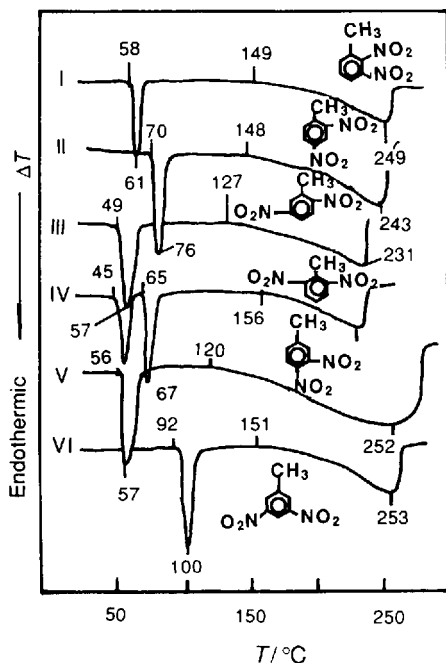


Figure 11.5 DTA curves of dinitrotoluene in dynamic air. Reproduced by permission of Dr G. Krien from Ref. 13

Samples

1, 2,3-Dinitrotoluene (2,3-DNT); 2, 2,4-dinitrotoluene (2,4-DNT); 3, 2,5-dinitrotoluene (2,5-DNT); 4, 2,6-dinitrotoluene (2,6-DNT); 5, 3,4-dinitrotoluene (3,4-DNT); 6, 3,5-dinitrotoluene (3,5-DNT).

Measurements

Sample mass: 1, 13.58 mg; 2, 22.61 mg; 3, 13.73 mg; 4, 16.29 mg; 5, 25.01 mg; 6, 21.40 mg.

Results

The melting, vaporization and mass-loss temperatures are given in Table 11.2.

Crystalline transition peak for sample 4, T_i 318 K (45 °C), T_p 329 K (56 °C).

Reference data

Melting, boiling and decomposition temperatures are given in Table 11.3.

In Table 11.4 data [10] were obtained by DTA in helium at a gauge pressure of 4.9 MPa; other conditions were as in Figure 11.3.

(continued)

Table 11.2

Sample No.	Melting peak		Vaporization peak		Mass-loss curve (simultaneous TG-DTA)	
	T_i/K (t/°C)	T_e/K (t/°C)	T_p/K (t/°C)	T_i/K (t/°C)	T_p/K (t/°C)	T_i/K (t/°C)
1	331(58)	333(60)	334(61)	422(149)	522(249)	379(106)
2	343(70)	347(74)	349(76)	421(148)	516(243)	363(90)
3	322(49)	326(53)	330(57)	400(127)	504(231)	383(110)
4	338(65)	339(66)	340(67)	429(156)	500(227)	363(90)
5	329(56)		330(57)	393(120)	525(252)	393(120)
6	365(92)	368(95)	373(100)	424(151)	526(253)	383(110)

Table 11.3

Sample No.	M.p./K	B.p./K	T_d/K
1	332.7 ^a ; 336 ^b	592 ^b	578 ^b
2	343.7 ^a ; 344 ^b	593 ^a ; 577 ^b	435 ^a ; 563 ^b
3	323.7 ^a ; 325.7 ^b	575 ^b	582 ^b
4	321 ^a (γ); 338.7 ^a (β)	558 ^a ; 563 ^b	580 ^b
5	332.7 ^a ; 333 ^b	606 ^b	584 ^b
6	366a; 364 ^b	588 ^a ; 589 ^b	607 ^b

^aRef. 13.^bRef. 14

Table 11.4

Sample No.	T_i^*/K (t/°C)	T_p/K (t/°C)
1	578(305)	627(354)
2	563(290)	595(322)
3	582(309)	522(349)
4	580(307)	616(343)
5	584(311)	608(335)
6	607(334)	642(369)

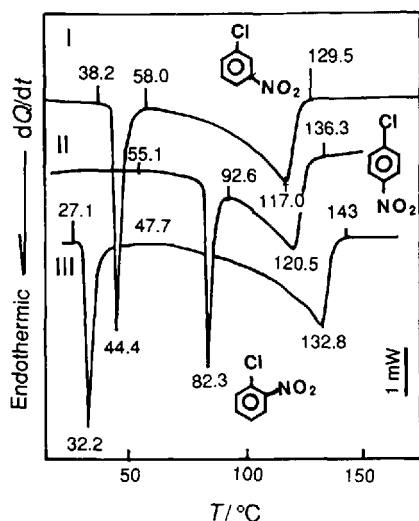


Figure 11.6 DSC curves of nitrochlorobenzene in dynamic nitrogen

Samples

1, *m*-Nitrochlorobenzene; 2, *p*-nitrochlorobenzene; 3, *o*-nitrochlorobenzene.

Measurements

Sample mass: 1, 0.972 mg; 2, 0.842 mg; 3, 0.680 mg. Apparatus, Shimadzu DSC-50.

Results

The characteristic temperatures of melting and vaporization peaks are given in Table 11.5

Reference data

1. M.p. 319 K (46 °C) [15]; b.p. 508 K (235 °C) [18]. 2. M.p. 356 K (83 °C) [15]; b.p. 515 K (242 °C) [15]. 3. M.p. 305.7 K (32.5 °C) [1]; b.p. 518 K (245 °C) [15].

Others

There are six configurational isomers for dinitro derivatives of chlorobenzene (DNCB). M.p. (of partial DNCB) [16]: 2,4-DNCB 326.6 K (53.4 °C) (α , stable form), 316 K (43 °C) (β), 300 K (27 °C) (γ); 2,6-DNCB (two kinds of crystal forms) 365 K (92 °C), 313 K (40 °C); 3,4-DNCB (three kinds of crystal forms) 309.5 K (36.3 °C), 310.3 K (37.19 °C), 301 K (28 °C).

Table 11.5

Sample No.	Melting peak			Vaporization peak	
	T_i /K (t_i /°C)	T_e /K (t_e /°C)	T_p /K (t_p /°C)	T_i /K (t_i /°C)	T_p /K (t_p /°C)
1	311.32(38.17)	316.21(43.06)	317.50(44.35)	331.10(57.95)	390.13(116.98)
2	328.25(55.10)	355.43(82.28)	356.38(83.23)	365.76(92.61)	393.60(120.45)
3	300.22(27.07)	303.90(30.75)	305.39(32.24)	320.85(47.70)	405.90(132.75)

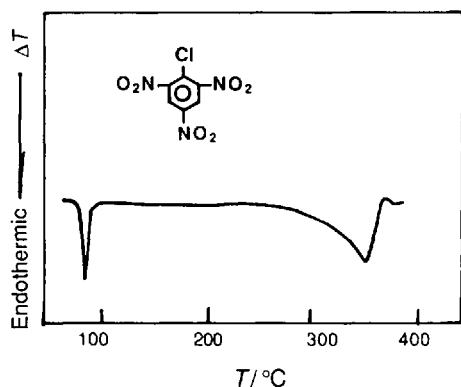


Figure 11.7 DTA curve of 2,4,6-trinitrochlorobenzene in static air. Reprinted by permission of the *Journal of the Japanese Explosives Society* from Ref. 17

Sample

2,4,6-Trinitrochlorobenzene (TNCB); picryl chloride.

Measurements

Sample mass, 5 mg; apparatus, Rigakudenki R-1 high-pressure DTA; heating rate, $10\text{ }^{\circ}\text{C min}^{-1}$; crucible aluminum (diameter 5 mm, height 2.5 mm), sealed type with a pinhole in the center of the cover.

Results

TNCB melts at *ca* $80\text{ }^{\circ}\text{C}$. Peak of comprehensive heat effect of vaporization and decomposition appears at *ca* $220\text{ }^{\circ}\text{C}$; T_p *ca* 623 K ($350\text{ }^{\circ}\text{C}$).

Reference data

M.p. 355.7 K ($82.5\text{ }^{\circ}\text{C}$) [18], 354.7–356 K ($81.5\text{--}83\text{ }^{\circ}\text{C}$) [19], 358 K ($85\text{ }^{\circ}\text{C}$) [12]; solidification point 356 K ($83\text{ }^{\circ}\text{C}$) [20]. 2,4,5-Trinitrochlorobenzene, m.p. 389 K ($116\text{ }^{\circ}\text{C}$) [18].

Sample

m-Nitroaniline.

Measurements

Sample mass, 0.980 mg; apparatus, Shimadzu DSC-50.

Results

Melting peak T_i 361.13 K ($87.98\text{ }^{\circ}\text{C}$), T_c 385.29 K ($112.14\text{ }^{\circ}\text{C}$), T_p 406.45 K ($133.30\text{ }^{\circ}\text{C}$); vaporization peak T_i 398.69 K ($125.54\text{ }^{\circ}\text{C}$), T_p 464.96 K ($191.81\text{ }^{\circ}\text{C}$), T_i 475.55 K ($202.40\text{ }^{\circ}\text{C}$).

Reference data

M.p. 387 K ($114\text{ }^{\circ}\text{C}$) [21].

Others

M.p. of configurational isomers: *o*-nitroaniline 344.7 K ($71.5\text{ }^{\circ}\text{C}$); *p*-nitroaniline 421 K ($148\text{ }^{\circ}\text{C}$) [22].

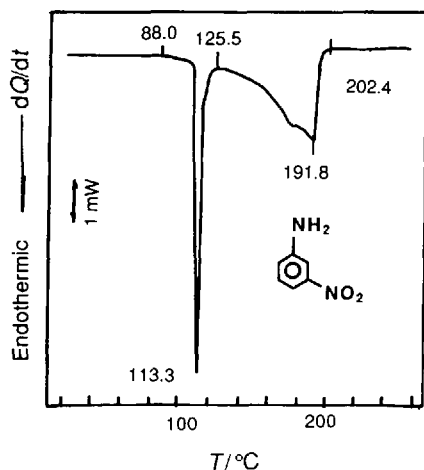


Figure 11.8 DSC curve of *m*-nitroaniline in dynamic nitrogen

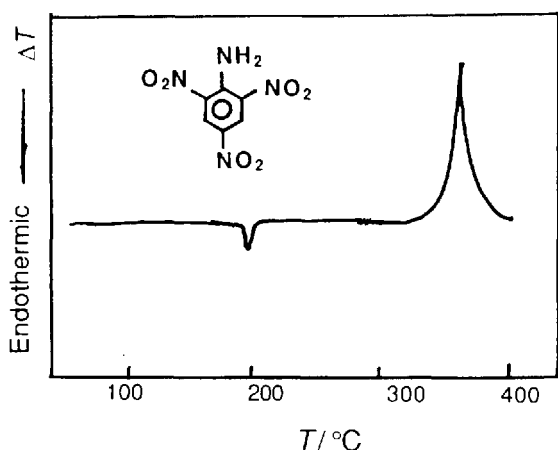


Figure 11.9 DTA curve of 2,4,6-trinitroaniline in helium at a gauge pressure of 4.9 MPa. Reproduced by permission of the Japanese Explosives Society from Ref. 12

Sample

2,4,6-Trinitroaniline; picrylamine.

Measurements

Sample mass, 5 mg; other conditions as in Figure 11.7.

Results

Melting peak T_p ca 464 K (ca 191 °C); decomposition peak T_i ca 597 K (ca 324 °C), T_p ca 633 K (ca 360 °C).

Reference data

M.p. 463 K (190 °C), T_d 533 K (260 °C); DTA curve in dynamic air (flow-rate 5.8 l h⁻¹, sample mass 40.43 mg, heating rate 6 °C min⁻¹): melting peak T_c ca. 463 K (ca. 190 °C), T_p ca. 468 K (ca 195 °C); decomposition peak T_i 533 K (260 °C), T_p 593 K (320 °C) [23]; b.p. (obtained by extrapolation) 663 K (390 °C) [24].

Others

In oxygen under a gauge pressure of 1.96 MPa, T_i of the decomposition peak increases by 50 °C compared with that in helium under the same pressure.

Sample

2,4,6-Trinitrobenzoic acid.

Measurements

Sample mass 0.736 mg; apparatus Shimadzu DSC-50.

Results

Melting peak (simultaneous decomposition) T_i 430.25 K (157.10 °C), T_c 493.20 K (220.05 °C), T_{p1} 502.16 K (229.01 °C), T_{p2} 505.80 K (232.65 °C), T_{p3} 508.46 K (235.31 °C).

Reference data

M.p. 501 K (228 °C) (simultaneous decomposition) [25], 501.9 K (228.7 °C) [12], T_d 493 K (220 °C) [25].

(continued)

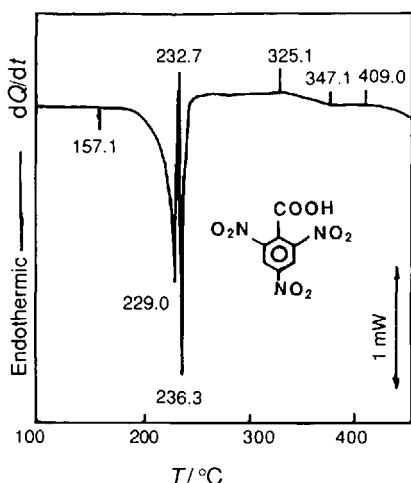


Figure 11.10 DSC curve of 2,4,6-trinitrobenzoic acid in dynamic nitrogen

Others

In dynamic air, $6\text{ }^{\circ}\text{C min}^{-1}$, sample mass 37.77 mg, simultaneous DTA-TG, the results [25] are that mass loss begins at $150\text{ }^{\circ}\text{C}$, there is rapid decomposition during the melting process and the temperature at the equilibrium point is about $200\text{ }^{\circ}\text{C}$.

In helium at a pressure of 4.9 MPa, $10\text{ }^{\circ}\text{C min}^{-1}$, sample mass 5 mg, the results of DTA [12] are that melting (endothermic peak) occurs at about $220\text{ }^{\circ}\text{C}$ and a decarboxylation reaction occurs simultaneously; after melting the reaction changes into a violent exothermic reaction (exothermic peak). Trinitrobenzene (TNB) forms by a decarboxylation reaction and it decomposes at about $400\text{ }^{\circ}\text{C}$.

Samples

I, 2,3,4-Trinitrotoluene; II, 2,3,5-trinitrotoluene; III, 2,3,6-trinitrotoluene; IV, 2,4,5-trinitrotoluene; V, 2,4,6-trinitrotoluene (α -TNT); VI, 3,4,5-trinitrotoluene.

Measurements

Sample mass: I, 23.28 mg; II, 18.82 mg; III, 27.04 mg; IV, 21.06 mg; V, 20.57 mg; VI, 16.99 mg.

Results

The melting, vaporization and mass-loss temperatures are given in Table 11.6.

When the temperature rises to the decomposition temperature in the later stages of vaporization, the sample decomposes at the same time and the curve of a comprehensive heat effect is obtained.

Reference data

Melting, boiling and decomposition temperatures are given in Table 11.7

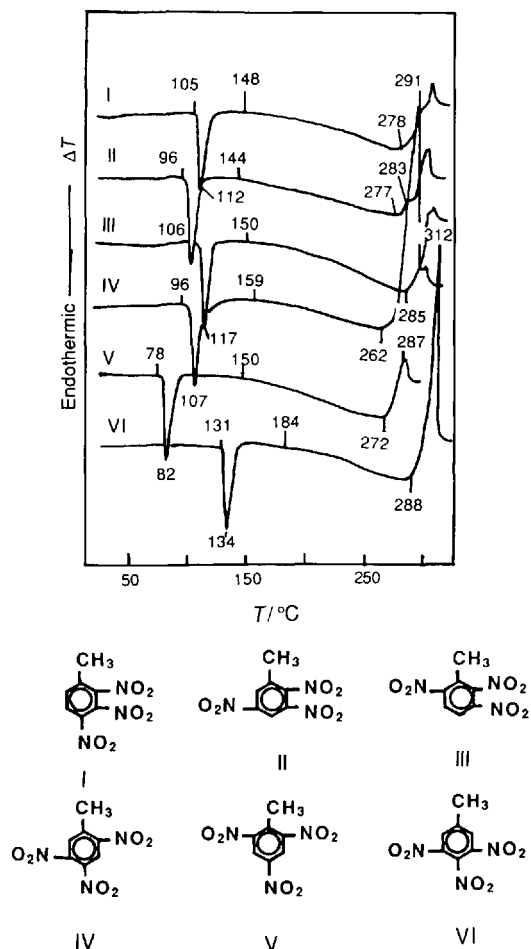


Figure 11.11 DSC curves of trinitrotoluene in dynamic air. Reproduced by permission of Dr. G. Krien from Ref. 26

Table 11.6

Sample No.	Melting peak			Vaporization peak T_i/K ($t/^{\circ}C$)	Mass-loss curve (simultaneous TG-DTA) T_i/K ($t/^{\circ}C$)
	T_i/K ($t/^{\circ}C$)	T_e/K ($t/^{\circ}C$)	T_p/K ($t/^{\circ}C$)		
I	378(105)	383(110)	385(112)	421(148)	421(148)
II	369(96)	373(100)	375(102)	417(144)	417(144)
III	379(106)	381(108)	390(117)	423(150)	397(124)
IV	369(96)	373(100)	380(107)	432(159)	419(146)
V	351(78)	353(80)	355(82)	423(150)	423(150)
VI	404(131)	405(132)	507(134)	457(184)	429(156)

Table 11.7

Sample No.	M.p./K	B.p./K	T_d/K
I	385 ^a	563–583 ^a (exp.)	555 ^a
II	370 ^a ; 370.7 ^b	606–610 ^a (exp.)	556 ^a
III	384 ^a ; 381 ^a	600–608 ^a (exp.)	553 ^a
IV	377 ^a	561–566 ^a (exp.)	535 ^a
V	54 ^a ; 354.1 ^c	611 ^d ; 618 ^a	523 ^a
VI	405 ^a ; 410.7 ^b	578–591 ^a (exp.)	561 ^a

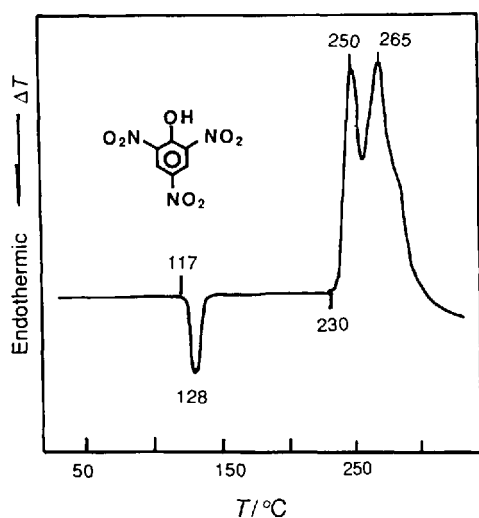
^a Ref. 26.^b Ref. 27.^c Ref. 28.^d Ref. 29.

Figure 11.12 DTA curve of trinitrophenol in dynamic air. Reproduced by permission of Dr G. Krien from Ref. 30

Sample

2,4,6-Trinitrophenol; picric acid (PA).

Measurement

Sample mass, 45.27 mg.

Results

Melting peak T_i 390 K (117 °C), T_e 394 K (121 °C) T_p 401 K (128 °C); decomposition peak T_i 503 K (230 °C), T_e 510 K (237 °C), T_{p1} 523 K (250 °C), T_{p2} 538 K (265 °C).

Reference data

M.p. 395 K (122 °C) [30], 395.7 K [31]; T_d 429 K (156 °C) [20], 471 K (198 °C) [30], 433 K (160 °C) [30].

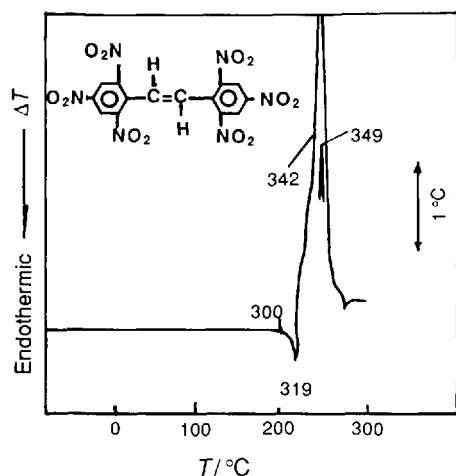


Figure 11.13 DTA curve of hexanitrostilbene (type I) in static air

Sample

2,2',4,4',6,6'-Hexanitrostilbene (HNS) (fine light-yellow crystal); synthesized in the laboratory.

Measurements

Sample mass, 3.0 mg; apparatus, LCT; DTA sensitivity (total deflection), $\pm 50 \mu\text{V}$.

Results

Melting peak (with decomposition) T_i 573 K (300 °C), T_p (heat balance point of melting and decomposition) 592 K (319 °C); decomposition peak T_{si} 615 K (342 °C), T_p 622 K (349 °C).

Reference data

M.p. 588–589 K (315–316 °C) [32], 586 K (313 °C) [33], 591 K (318 °C) (decomposition) [34]; T_d 563 K (290 °C) [34]. HNS-II (yellow needle-like crystals), m.p. 591 K (318 °C) [32].

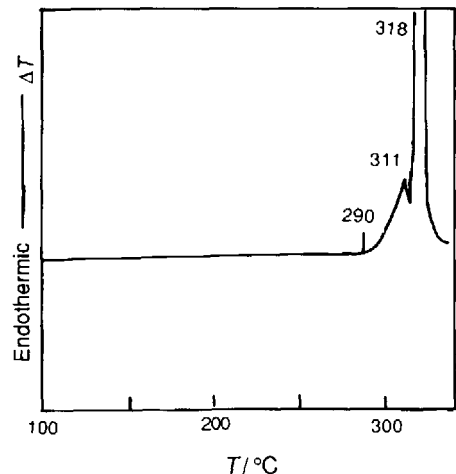


Figure 11.14 DTA curve of hexanitrostilbene in dynamic air. Reproduced by permission of Dr G. Krien from Ref. 3

Sample

2,2',4,4',6,6'-Hexanitrostilbene (HNS).

Measurements

Sample mass, 10.33 mg.

Results

Decomposition peak with a melting shoulder peak, T_{i1} 563 K (290 °C), T_{p1} (heat balance point of decomposition and melting) 584 K (311 °C), T_{i2} (heat balance point of melting and decomposition) *ca* 587 K (*ca* 314 °C), T_{p2} (ignition) 591 K (318 °C); T_i (for mass loss on TG curve, simultaneous TG-DTA) *ca* 498 K (*ca* 225 °C).

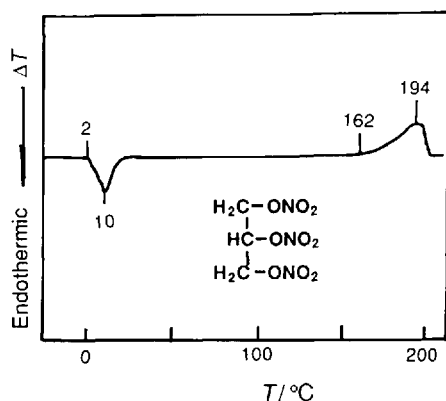


Figure 11.15 DTA curve of nitroglycerine in dynamic air. Reproduced by permission of Dr G. Krien from Ref. 36

Sample

Glycerine trinitrate; nitroglycerine (NG).

Measurements

Sample mass, 12.68 mg; heating rate, 4 °C min⁻¹.

Results

Melting peak of unstable form (clinorhomboidal system) T_i 275 K (2 °C), T_p 283 K (10 °C); decomposition peak T_i 435 K (162 °C), T_p 467 K (194 °C). T_i (for mass loss on TG curve, simultaneous TG-DTA) 385 K (112 °C).

Reference data

M.p. 286.4 K (13.2 °C) (stable form, orthorhombic system), 275.4 K (2.2 °C) (unstable form) [36]; b.p. 453 K (180 °C) (6.7 kPa), 398 K (125 °C) (0.27 kPa) [37].

Others

Stability [37]: (nitroglycerine begins to decompose at 223 K (50 °C), to decompose more rapidly at 333–343 K (60–70 °C), to decompose very quickly at 408 K (135 °C), 'boils' at 418 K (145 °C) and detonates at 488–491 K (215–218 °C).

In a nitrogen atmosphere at different pressures (high-pressure DTA, sample mass 5.0 mg, 5 °C min⁻¹), data obtained are as follows: when the pressure is >7.8 MPa, nitroglycerine ignites, whereas at normal pressure there is only a vaporization endothermic peak (T_p ca 463 K (ca 190 °C) [38]; when the pressure is 13 MPa (sample mass 3.5 mg), T_p increases with increase in heating rate; when the heating rate is 30 °C min⁻¹ nitroglycerine deflagrates [39].

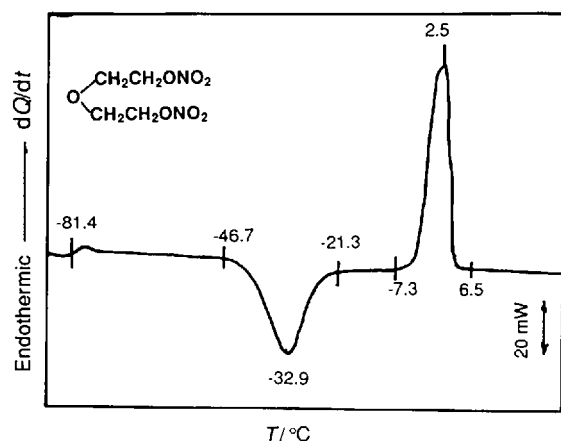


Figure 11.16 DSC curve of diethylene glycol dinitrate in dynamic air. Reproduced by permission of Tian Linxiang

Sample

Diethylene glycol dinitrate (DEGDN; DEGN).

Measurements

Sample mass, 25.50 mg; apparatus, Perkin-Elmer DSC-7; crucible, aluminum (with lid); heating rate, $10^{\circ}\text{C min}^{-1}$; atmosphere, nitrogen; flow-rate, 30 ml min^{-1} ; reference crucible empty (with lid).

Results

Glass transition T_g 191.73 K (-81.422°C); crystallization peak T_i 226.48 K (-46.667°C), T_e ca 225 K (-48°C), T_p 240.25 K (-32.905°C), T_i 251.82 K (-21.334°C); melting peak T_i 265.82 K (-7.334°C), T_e ca 269 K (ca 4°C), T_p 275.65 K (2.499°C), T_i 279.68 K (6.533°C).

Reference data

M.p. 275 K (2°C); (stable form), 262.3 K (-10.9°C) (unstable form); b.p. 433 K (160°C) (decomposition) [40].

Others

In dynamic air, sample mass 14.39 mg, $4^{\circ}\text{C min}^{-1}$, DTA shows melting peak T_i 263 K (-10 min^{-1}); decomposition exothermic peak T_i 443 K (170 min^{-1}); T_i (for mass loss on TG curve, simultaneous TG-DTA) 368 K (95°C [41].

Samples

Pentaerythritol tetranitrate (PETN).

Measurements

Sample mass, 2.00 mg; apparatus, Perkin-Elmer DSC-7; heating rate, $10^{\circ}\text{C min}^{-1}$; atmosphere, argon; flow-rate, 45 ml min^{-1} .

Results

Melting peak T_i ; 393.2 K (120.0 min^{-1} , T_e 412.7 K (139.5°C), T_p 414.4 K (141.2°C); decomposition peak T_i 429.5 K (156.3°C), T_p 470.4 K (197.2°C).

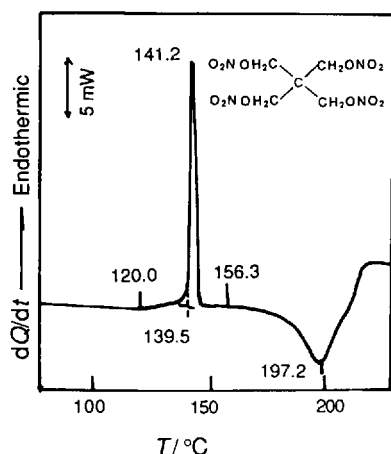


Figure 11.17 DSC curve of pentaerythritol tetranitrate in dynamic argon

(continued)

Reference data

M.p. 414–415 K (141–142 °C) [42], 414.5 K (141.3 °C) [43]; T_d 436 K [43], 443 K [43].

Others

Data for thermal decomposition obtained by simultaneous TG–FTIR: NO_2 , is first produced and then gases such as H_2O , CH_2O , CO_2 , NO , NO_2 , HCN and N_2 are obtained [44].

Sample

Di(nitroethyl) nitramine; diethanolnitramine dinitrate (DINA).

Measurements

Sample mass, 3.0 mg; apparatus, LCT.

Results

Melting peak T_i 321 K (48 °C), T_e 324 K (51 °C), T_p 325 K (52 °C); decomposition peak T_i 426 K (153 °C), T_e 458 K (185 °C), T_p 475 K (202 °C).

Reference data

M.p. 322.7–324.7 K (49.5–51.5 °C) [45], 322–324 K (49–51 °C) [46], 324.5 K (51.3 °C) [47]; T_d 433 K (160 °C) [45], 453 K (180 °C) (vigorous decomposition) [45]; 60 °C, 60 h, α 0.7% [45].

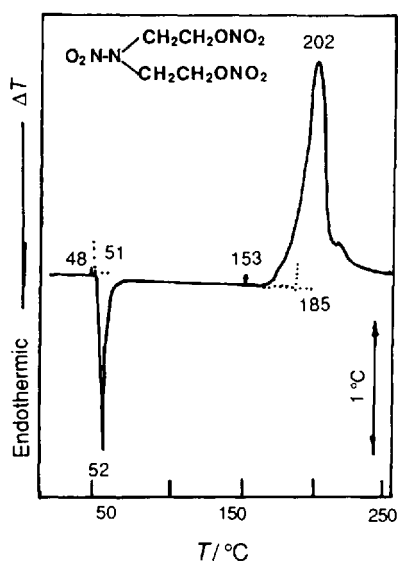


Figure 11.18 DTA curve of diethanolnitramine dinitrate in static air

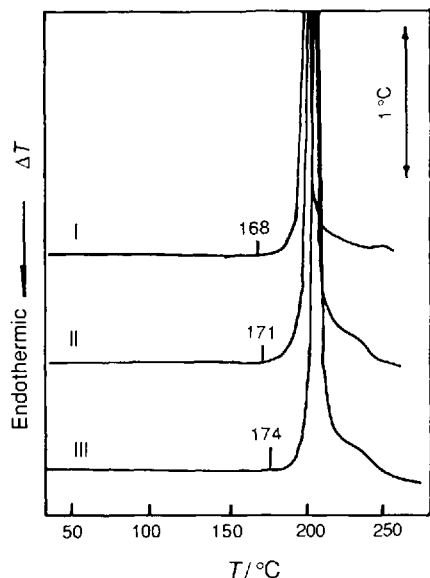


Figure 11.19 DTA curves of nitrocellulose in static air

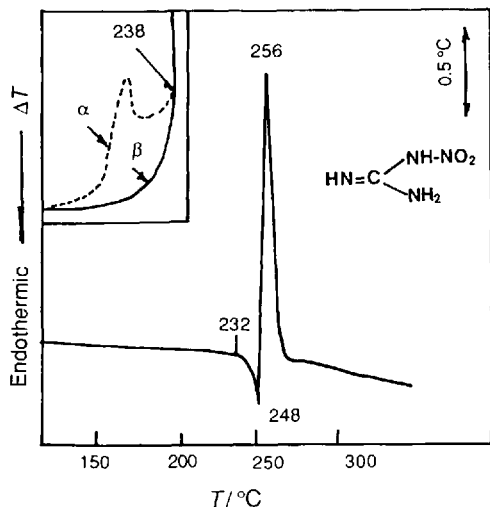


Figure 11.20 DTA curve of nitroguanidine in static air. The inset shows the partial DTA curves of α - and β -nitroguanidine [50]; sample mass ca 200 mg, heating rate $5\text{ }^{\circ}\text{C min}^{-1}$, dynamic air, flow-rate 5.8 l h^{-1} .)

Samples

1, Pyrocellulose; 2, nitrocellulose; 3, nitrocellulose. Specification of industrial products (degree of nitration; the gas volume in ml of NO evolved on decomposition of 1 g of nitrocellulose converted to $0\text{ }^{\circ}\text{C}$ and 101 kPa): 200–203.2 ml g^{-1} ; 2, 190–198 ml g^{-1} ; 3, 188–193.5 ml g^{-1}

Measurements

Sample mass, 2.0 mg for each; apparatus, LCT.

Results

1, Decomposition peak T_i 441 K ($168\text{ }^{\circ}\text{C}$), T_{ig} 470 K ($197\text{ }^{\circ}\text{C}$); 2, decomposition peak T_i 444 K ($171\text{ }^{\circ}\text{C}$), T_{ig} 473 K ($200\text{ }^{\circ}\text{C}$); 3, decomposition peak T_i 447 K ($174\text{ }^{\circ}\text{C}$), T_{ig} 475 K ($202\text{ }^{\circ}\text{C}$).

Reference data [49]

Ignition of nitrocellulose and pyrocellulose takes place at a constant temperature of $175\text{ }^{\circ}\text{C}$ for 4 min or $170\text{ }^{\circ}\text{C}$ for 10 min. The initial reaction of thermal decomposition is nearly a first-order reaction and denitration and cleavage of the glycosidic linkage take place simultaneously. The decomposition products contain NO, NO_2 , N_2 , CO_2 , H_2O , HN_3 , HNO_2 , and solid residues.

Sample

Nitroguanidine (NG).

Measurements

Sample mass, 2.0 mg; apparatus, LCT.

Results

Melting peak (with decomposition) T_i 505 K ($232\text{ }^{\circ}\text{C}$), T_p (heat balance point of melting and decomposition) 521 K ($248\text{ }^{\circ}\text{C}$); decomposition peak T_p 529 K ($256\text{ }^{\circ}\text{C}$). The inset shows that the initial exothermic point of β -NG ($205\text{ }^{\circ}\text{C}$) is $18\text{ }^{\circ}\text{C}$ higher than that of α -NG, but their ignition temperatures are the same ($238\text{ }^{\circ}\text{C}$).

(continued)

Reference data

M.p. 505 K (232 °C) (simultaneous decomposition) [51]; 100 °C, 24 h, α 0.08%; 100 °C, 48 h, α 0.11%; 150 °C, 55 min, α 1% [52].

Others

β -Nitroguanidine is crystalline, its structure is $\text{O}_2\text{N}-\text{N}=\text{C}(\text{NH}_2)_2$; α is the stablest form [51]. Rapid decomposition in the liquid phase [53].

Sample

Tetryl; 2,4,6-trinitrophenylmethylnitramine; *N*-methyl-*N*,2,4,6-tetranitroaniline

Measurements

Sample mass, 2.0 mg; apparatus, LCT.

Results

Melting peak T_i 395 K (122 °C), T_c 402 K (129 °C), T_p 403 K (130 °C); decomposition peak T_i 448 K (175 °C, T_c 470 K (197 °C), T_p 481 K (208 °C).

Reference data

M.p. 403 K (130 °C) [54], 402.7 K (129.5 °C) [56], 404 K (131 °C) [55]; T_d 443–447 K (170–174 °C) [55], 435 (162 °C) [55], 433 K (160 °C) [55]. 100 °C, 48 h, α 0.09% [54].

Others

In dynamic air (5.8 l h^{-1}), sample mass 22.42 mg heating rate 6°C min^{-1} , the data obtained by using DTA are as follows [55]: melting peak T_i 128 °C; decomposition peak T_i 156 °C; T_g 175 °C.

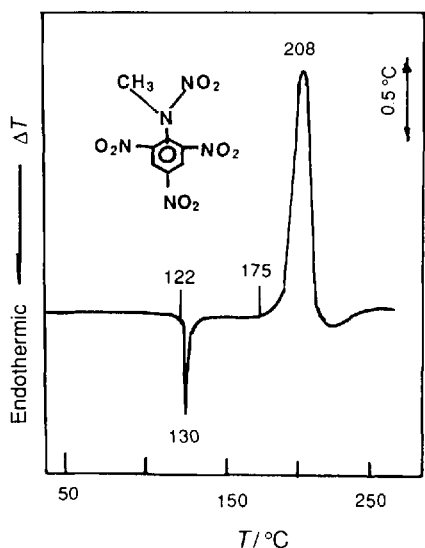


Figure 11.21 DTA curve of tetryl in static air

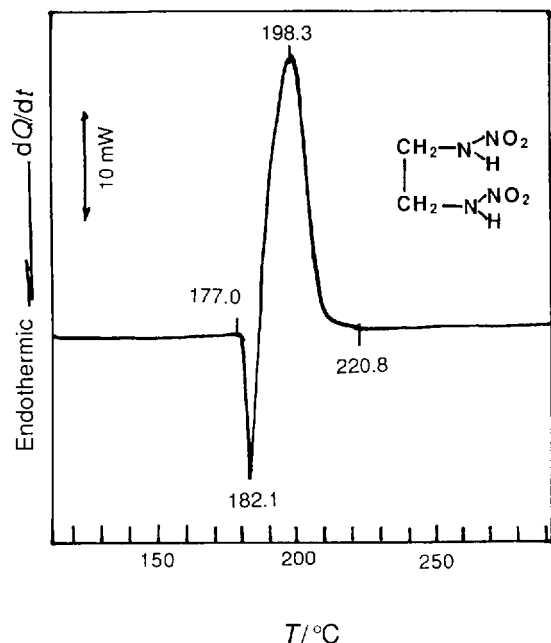


Figure 11.22 DSC curve of ethylenedinitramine in dynamic nitrogen

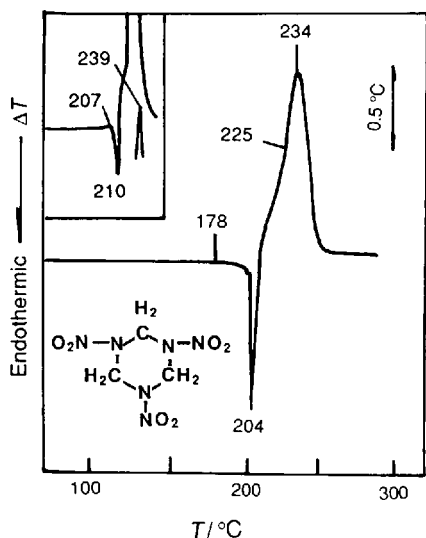


Figure 11.23 DTA curve of hexogen in static air. The inset is a partial DTA curve of RDX (industrial product) in static air. [60] The conditions of measurements were as follows: sample mass, 16 mg (170 mg α - Al_2O_3 placed below the sample); reference material, α - Al_2O_3 (ca 190 mg); heating rate, 5°C min^{-1} ; NiCr–NiSi thermocouples; DTA sensitivity (total deflection), $\pm 250 \mu\text{V}$; paper speed, 120 mm h^{-1} ; platinum crucible; apparatus, simultaneous TG–DTA (Model 4.1, Beijing Optical Instrument Factory)

Sample

Ethylenedinitramine (EDNA).

Measurements

Sample mass, 1.692 mg; apparatus, Shimadzu DSC-50.

Results

Melting peak (with decomposition) T_i 450.11 K (176.96°C), T_p 455.20 (182.05°C); decomposition peak T_p 471.46 K (198.31°C).

Reference data

M.p. 450.5 K (177.3°C) [57], 449.4 K (176.2°C) (decomposition) [58]; T_d 413 K (140°C) [59].

Sample

Hexogen (RDX); 1,3,5-trinitro-1,3,5-triazacyclohexane.

Measurements

Sample mass, 2.0 mg; apparatus, LCT.

Results

Melting peak (with decomposition) T_i 451 K (178°C), T_c 472 K (199°C), T_p 477 K (204°C); decomposition peak T_{si} 498 K (225°C), T_p 507 K (234°C).

The curve in the inset shows that an exothermic process proceeds at first and then it is transformed into an endothermic process and finally it undergoes a rapid exothermic reaction with decomposition. Therefore, there are two points of heat balance.

Reference data

M.p. 477.7–478 K (204.5 – 205°C) [61], 476 K (203°C) [62], 477 K (204°C) [63]; T_d 488 K

(continued)

(215 °C) [63]; 100 °C, 48 h, α 0.09%; 120 °C, 48 h, α 0.19% [61].

Others

Decomposition of the sample followed by melting [64].

In dynamic air (5.8 l h^{-1}), sample mass 21.80 mg, heating rate $6 \text{ }^{\circ}\text{C min}^{-1}$, the DTA curve shows that initial melting starts at 203 °C, explosion takes place at 216 °C, and T_i for mass loss on the TG curve (simultaneous TG-DTA) is ca 188 °C [63].

The decomposition mechanism suggested by analysis of FTIR-Raman spectra is as follows [65]: during the decomposition of RDX cleavage of N—NO₂ bonds take place first with evolution of large amounts of NO and HONO, followed by cleavage of C—N bonds, and NO₂ takes part in the reaction simultaneously with the cleavage of C—N bonds; HONO would exist for only a very short time ($2\text{HONO} \rightarrow \text{NO} + \text{NO}_2 + \text{H}_2\text{O}$). The rate-controlling step for liquid decomposition is the cleavage of C—H bonds [66].

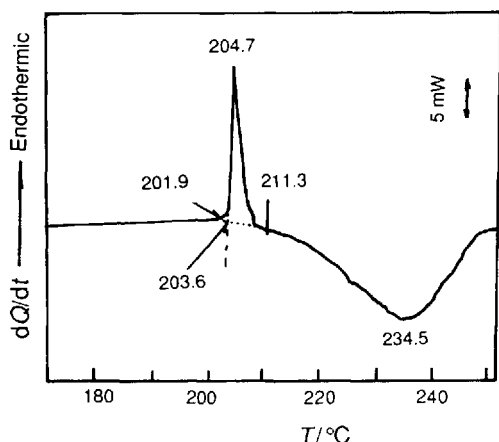


Figure 11.24 DSC curve of hexogen in dynamic argon

Sample

Hexogen (RDX); 1,3,5-trinitro-1,3,5-triazacyclohexane.

Measurements

Sample mass 2.0 mg; apparatus, Perkin-Elmer DSC-7; heating rate, $10 \text{ }^{\circ}\text{C min}^{-1}$; atmosphere, argon; flow-rate, 25 ml min^{-1} .

Results

Melting peak (with decomposition) T_i 475.1 K (201.9 min⁻¹), T_e 476.8 K (203.6 °C), T_p 477.9 K (204.7 °C); height of peak 20.64 mW; decomposition peak T_i 484.5 K (211.3 °C), T_p 507.7 K (234.5 °C).

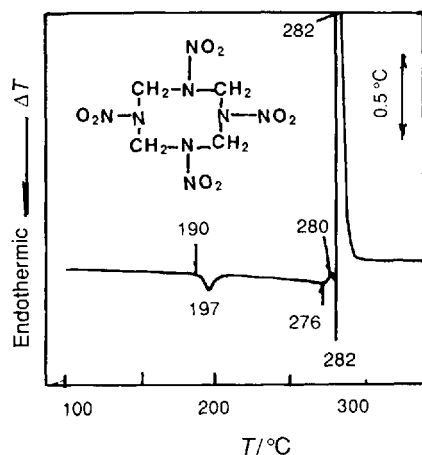


Figure 11.25 DTA curve of cyclotetramethylenetetranitramine in static air

Sample

Cyclotetramethylenetetranitramine (HMX); octahydro-1,3,5,7-tetranitro-1,3,5,7-tetrazocine; 1,3,5,7-tetranitro-1,3,5,7-tetra-azacyclooctane.

Measurements

Sample mass, 2.0 mg; apparatus, LCT.

Results

Crystal line transition peak (β - δ) T_i 463 K (190 °C), T_p 470 K (197 °C); decomposition peak (with melting) T_i 549 K (276 °C), T_{pl} (heat balance point of decomposition and melting) 553 K (280 °C), T_{p2} (heat balance point of melting and decomposition) 555 K (282 °C), T_{ig} 555 K (282 °C).

Reference data

M.p. 551 K (278 °C) (decomposition) [67], 555 K (282 °C) [68], 100 °C, 48 h, α 0.025%; 120 °C, 48 h, α , 0.035% [69].

Others

There are four forms of crystals for HMX (α , β , γ and δ) [70].

The thermal decomposition process of HMX was studied by time-of-flight mass spectrometry (Model Zhp-6 spectrometer) [71]. It is suggested that the decomposition of HMX involves three stages, i.e. initial decomposition of the solid phase at about 160 °C, decomposition with melting and decomposition of the liquid phase. The products which have been confirmed are NO_2 , NO , HCN and CHO .

The rate-controlling step of the decomposition of HMX in the liquid phase is cleavage of C-N bonds [72].

When the heating rate is $< 3^\circ\text{C min}^{-1}$, the melting peak on the DTA curve disappears because the total heat of decomposition is higher than that of melting [73].

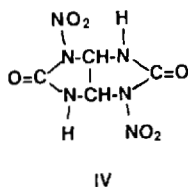
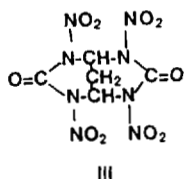
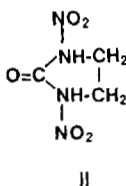
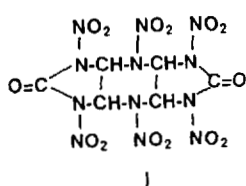
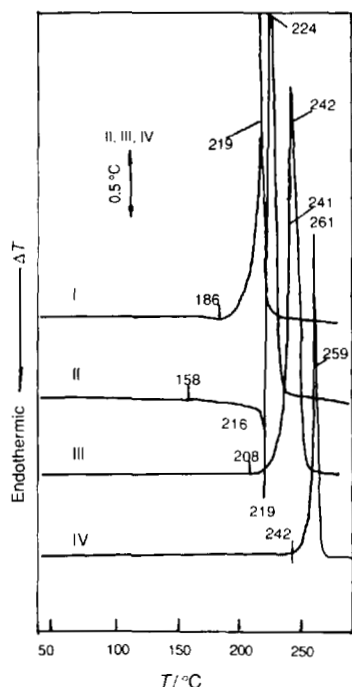


Figure 11.26 DTA curve of four kinds of cyclourea nitroamine compounds in static air

Samples

I, 2,4,6,8,10,12-Hexanitro-2,4,6,8,10,12-hexaazatricyclo[7.3.0.0.3.7]-5,11-dodecanedione; II, *N,N'*-dinitroethyleneurea-2,5-dinitro-2,5-diazacyclo-pentaneone; III, 2,4,6,8-tetranitro-2,4,6,8-tetraazadicyclo[3.3.1]-3,7-nonanedione; IV, 1,4-dinitro-2,4,6,8-tetraazadicyclo[3.3.0]-3,7-octanedione. All supplied by Xian Modern Chemistry Research Institute.

Measurements

Sample mass, 2.0 mg (each). DTA sensitivity (total deflection): I, $\pm 50 \mu\text{V}$; II–IV, $\pm 25 \mu\text{V}$.

Results

I. Decomposition peak T_i 459 K (186 °C), T_{si} 492 K (219 °C), T_{ig} 492 K (219 °C), T_p 492 K (219 °C). II. Melting peak (with decomposition) T_i 431 K (158 °C), T_c 491 K (218 °C), T_p (heat balance point of melting and decomposition) 492 K (219 °C); decomposition peak T_{ig} 497 K (224 °C). III. Decomposition peak T_i 481 K (208 °C), T_{si} 514 K (241 °C), T_p 515 K (242 °C), T_{ig} 515 K (242 °C). IV. Decomposition peak T_i 515 K (242 °C), T_{si} 532 K (259 °C), T_p 534 K (261 °C).

Reference data

I. M.p. 481 K (208 °C) (type A), 469 K (196 °C) (type B) [74], 100 °C 48 h, α 0.1% [74]. III M.p. 523 K (250 °C) (decomposition) [74]; 80 °C 48 h, α 0.026% [74]. IV M.p. 513 K (240 °C) (decomposition) [75]; 100 °C 100 h, α 0.23% [75].

Others

In static air, heating rate 5°C min^{-1} , T_p on DTA curves are [76] I, 481 K (208 °C) II, 486 K (213 °C); III, 497 K (224 °C); IV, 506 K (233 °C).

By evolved gas analysis, the main products that have been identified are N_2O , CO_2 , NO and H_2O . The order of relative amounts of products for I and II is $\text{N}_2\text{O} > \text{CO}_2 > \text{NO}_2 > \text{H}_2\text{O}$ and for III and IV $\text{CO}_2 > \text{NO}_2 > \text{N}_2\text{O} > \text{H}_2\text{O}$.

Table 11.8

Peak No.	T_i/K	T_p/K	Remarks
1	321	322	unstable IV' \rightarrow II''
2	359	362	Crystal phase III \rightarrow II
3	400	404	Crystal phase II \rightarrow I
4	436	445	T_e (for melting of crystal phase I) 443 K
5	486		T_{p2} (for exothermic decomposition) 559 K

tetragonal crystal $\xrightleftharpoons{-18^\circ\text{C}}$ α (5)orthorhombic crystal $\xrightleftharpoons{32.1^\circ\text{C}}$ β (4)orthorhombic crystal $\xrightleftharpoons{84.2^\circ\text{C}}$ γ (3)tetragonal crystal $\xrightleftharpoons{125.2^\circ\text{C}}$ δ (2)cubic crystal $\xrightleftharpoons{169.6^\circ\text{C}}$ liquid ϵ (1)

Others

Completely anhydrous ammonium nitrate will not decompose even at temperatures up to 300 °C [78].

Ammonium nitrate begins to decompose into NH_3 and HNO_3 at 110 °C; it decomposes into nitrogen oxide and water between 200 and 270 °C; the reaction is very rapid when at temperatures >400 °C, with a violent explosion and giving NH_3 and H_2O [79].

In vacuum [77], peak 5' is the peak of comprehensive heat effects of vaporization, dissociation and decomposition of liquid NH_4NO_3 . The dissociation process is as follows: $\text{NH}_4\text{NO}_3(\text{l}) \rightarrow \text{NH}_3(\text{g}) + \text{HNO}_3(\text{g})$; decomposition proceeds according to $\text{NH}_4\text{NO}_3(\text{l}) \rightarrow \text{N}_2\text{O}(\text{g}) + 2\text{H}_2\text{O}(\text{g})$.

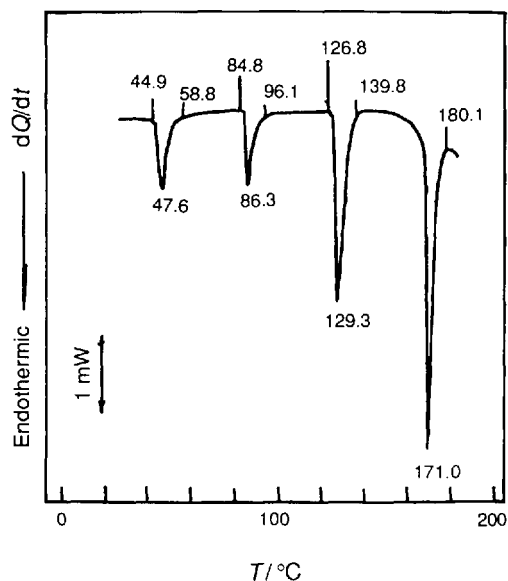


Figure 11.29 DSC curve of ammonium nitrate in dynamic nitrogen. The test results were obtained by promptly remeasuring the sample which had been heated to about 148 °C followed by cooling to room temperature

Sample

Ammonium nitrate. Source, chemically pure reagent recrystallized once from water.

Measurements

Sample mass, 1.367 mg; apparatus, Shimadzu DSC-50.

Results

Characteristic temperatures are given in Table 11.9

Table 11.9

Peak No.	T_i/K ($t/^\circ\text{C}$)	T_p/K ($t/^\circ\text{C}$)	Remarks
1	318.02 (44.87)	320.70 (47.55)	
2	357.95 (84.80)	359.47 (86.32)	
3	399.93 (126.78)	402.44 (129.29)	
4	412.98 (139.83)	444.19 (171.04) ^a	

^a T_e (for melting peak) 442.54 K (169.39 °C).

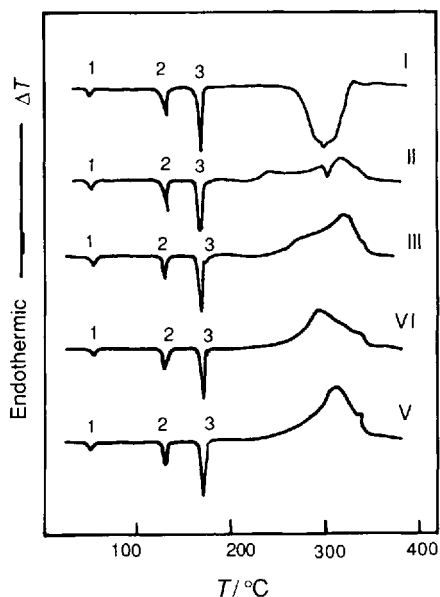


Figure 11.30 DTA curve of ammonium nitrate in argon under different pressures. Reproduced by permission of the *Journal of the Japanese Explosives Society* from Ref. 80

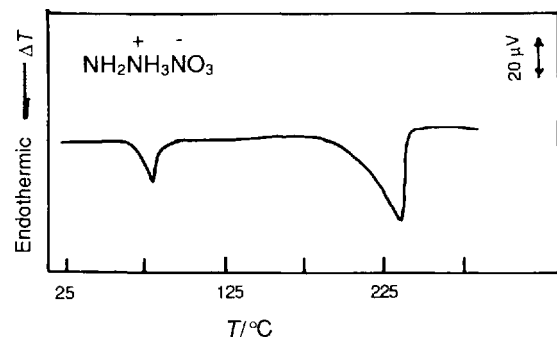


Figure 11.31 DTA curve of hydrazinium nitrate in vacuum (replotted from Ref. 77)

Sample

Ammonium nitrate, Source, chemically pure reagent, recrystallized from water and dried, then passed through a 100 mesh (147 μm) sieve.

Measurements

Sample mass, ca 5 mg; apparatus, Rigakudenki high-pressure DTA; crucible, hermetically sealed aluminum crucible with a pinhole in the center of the cover; atmosphere pressure (gauge pressure): I, 0 MPa; II, 0.5 MPa; III, 1.0 MPa; IV, 5.0 MPa; V, 10.0 MPa.

Results

Crystal line transition peaks (peaks 1 and 2) and melting peak (peak 3) did not show evident changes at different pressures. The DTA curve shows an exothermic effect from about 0.5 MPa and the exothermic peak becomes more and more evident with increase in pressure.

Sample

Hydrazinium nitrate (purity >99%).

Measurements

Sample mass, 75.65 mg; apparatus, Shimadzu DT-2A DTA; heating rate, 3 $^{\circ}\text{C min}^{-1}$; DTA sensitivity (told deflection), $\pm 100 \mu\text{V}$; paper speed, 250 mm h^{-1} ; reference material for melting-condensation, SiO_2 ; crucible, platinum; thermocouple, Pt-PtRh.

Results

Melting peak T_i 344.3 K (71.1 $^{\circ}\text{C}$), T_e 345.5 K (72.3 $^{\circ}\text{C}$), T_p 353.8 K (80.6 $^{\circ}\text{C}$); decomposition peak with vaporization T_i 463 K (190 $^{\circ}\text{C}$), T_e ca 483 K ca 210 $^{\circ}\text{C}$, T_p 510 K (237 $^{\circ}\text{C}$).

Reference data

M.p. 343.9 K (70.7 $^{\circ}\text{C}$) (stable form), 335.3 K (62.1 $^{\circ}\text{C}$) (unstable form); 75 $^{\circ}\text{C}$ 9 months, α 0.7%; no explosion on heating to 360 $^{\circ}\text{C}$ [81].

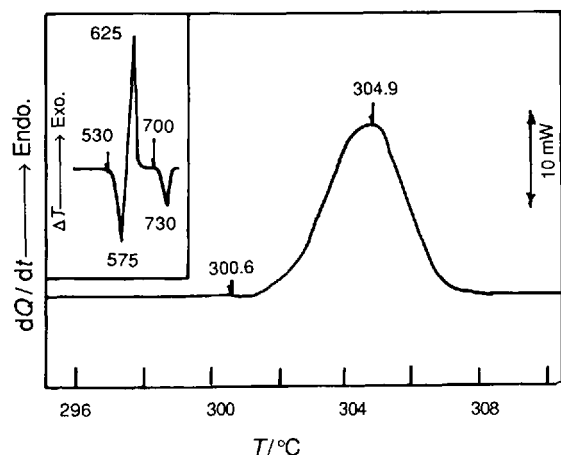


Figure 11.32 DSC curve of potassium perchlorate for crystalline transition in dynamic argon. The inset [82] is part of the DTA curve after crystalline transition under conditions of sample mass 199.0 mg, static air, $10\text{ }^{\circ}\text{C min}^{-1}$

Sample

Potassium perchlorate (analytically pure reagent), KClO_4 .

Measurements

Sample mass, 3.00 mg; apparatus, Perkin-Elmer DSC-7; heating rate, $10\text{ }^{\circ}\text{C min}^{-1}$; atmosphere, argon; flow-rate, 45 ml min^{-1} .

Results

Crystalline transition peak T_i 573.8 K (300.6 min^{-1}), T_e 575.5 K ($302.3\text{ }^{\circ}\text{C}$), T_p 578.1 K ($304.9\text{ }^{\circ}\text{C}$).

Reference data

α - β -transformation at 572.7 K ($299.5\text{ }^{\circ}\text{C}$).

Others

Melting peak (in static air) [82] T_i ca 803 K (ca $530\text{ }^{\circ}\text{C}$), T_p (heat balance point of melting and decomposition) ca 848 K (ca $575\text{ }^{\circ}\text{C}$), decomposition peak T_p ca 898 K (ca $625\text{ }^{\circ}\text{C}$); melting peak of decomposition product KCl T_i ca 973 K (ca $700\text{ }^{\circ}\text{C}$), T_p ca 1003 K (ca $730\text{ }^{\circ}\text{C}$).

Isothermal decomposition at $549\text{--}569\text{ }^{\circ}\text{C}$ proceeds in three stages: in the initial stage decomposition occurs after partial melting at the unsteady site on the crystal surface; in the intermediate stage, decomposition occurs in the molten phase after entire melting to liquid; in the last stage, decomposition of liquid takes place at the surface of the new phase KCl. The reaction proceeds as $\text{KClO}_4 \rightarrow \text{KCl} + 2\text{O}_2$.

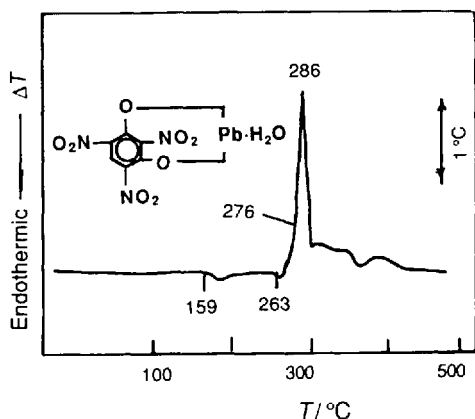


Figure 11.33 DTA curve of lead 2,4,6-tetranitroresorcinate in static air. Reproduced from Ref. 84

Sample

Lead styphnate; lead 2,4,6-trinitroresorcinate (LTNR). Source, neutral crystal obtained by sodium salt method.

Measurements

Sample mass, 10.3 mg; dilution ratio, 1:10 (sample: reference material); padded at the bottom of the crucible with 130 mg of α - Al_2O_3 ; apparatus, simultaneous DTA-TG (Model 4.1) (Beijing Optical Instrument Factory); DTA sensitivity (total deflection), $\pm 50 \mu\text{V}$; heating rate, $5.6^\circ\text{C min}^{-1}$, paper speed, 57 mm min^{-1} ; thermocouple, Pt-PtRh10; crucible, platinum (height 18 mm, diameter 7.5 mm).

Results

Dehydration peak T_i 432 K (159°C); decomposition peak T_i 532 K (259°C), T_e 547 K (274°C), T_{si} 549 K (276°C), T_p 559 K (286°C); α 52.4% and residue is P_6O (at final temperature 485°C).

Reference data

Test results with undiluted sample of 5.4 mg; dehydration peak T_i 434 K (161°C), T_p 448 K (175°C); decomposition peak T_i 538 K (265°C), T_{exp} 560 K (287°C) (with explosive sound) [85].

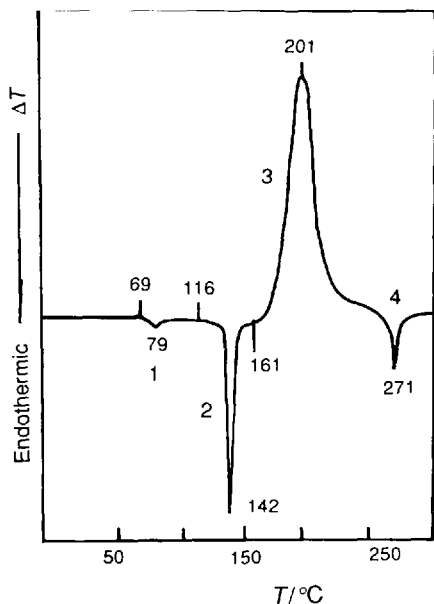


Figure 11.34 DTA curve of desensitized pentaerythritol tetranitrate

Sample

Desensitized pentaerythritol tetranitrate (PETN)
(PETN: desensitizer = 95 : 15, mass ratio).

Measurements

Sample mass, 3.0 mg; apparatus, LCT.

Results

Characteristic temperatures are given in Table 11.10.

Table 11.10

Peak No.	T_i/K ($t/^\circ\text{C}$)	T_p/K ($t/^\circ\text{C}$)	Remarks
1	342 (69)	352 (79)	Melting of desensitized PETN
2	389 (116)	415 (142)	PETN melting, T_i 414 K
3	434 (161)	474 (201)	Decomposition peak
4		544 (271)	Endothermic peak of the decomposition products

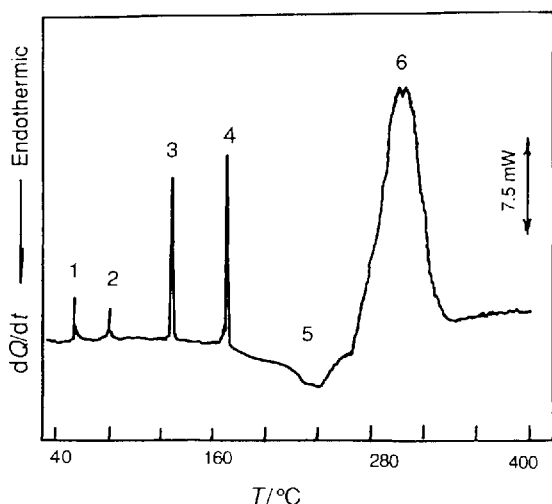


Figure 11.35 DSC curve of No. 2 industrial explosive. Reproduced by permission of Lu Guiying

Sample

No. 2 rock ammonium nitrate explosive (ammonium nitrate: TNT: wood flour = 83.5–86.5 : 10.0–12.0 : 3.5–4.5, mass ratio).

Measurements

Sample mass, 1.280 mg; apparatus, Perkin-Elmer DSC-7; heating rate, $20^{\circ}\text{C min}^{-1}$; atmosphere, nitrogen; flow-rate, 20 ml min^{-1} .

Results

Approximate values of T_p on the DTA curves are given in Table 11.11.

Table 11.11

Peak No.	$T_p/\text{K} (t/^{\circ}\text{C})$	Remarks ^a
1	328 (55)	Crystalline transition of AN IV–II
2	354 (81)	Crystalline transition of AN III–I
3	402 (129)	Crystalline transition of AN II–I
4	463 (190)	Melting peak of AN
5	514 (241)	Exothermic peak
6	540 (267)	Endothermic peak

^a AN = ammonium nitrate.

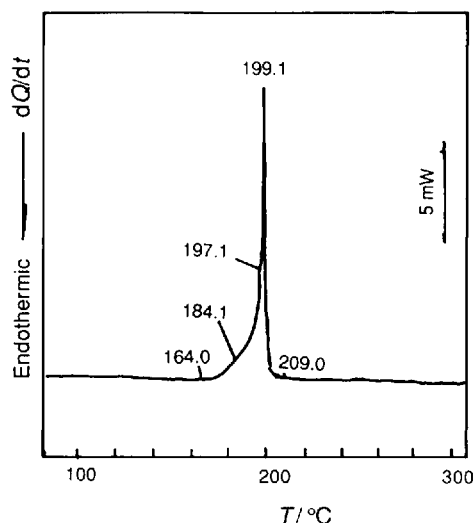


Figure 11.36 DSC curve of 2/1 single-base propellant in dynamic nitrogen

Sample

A 2/1 single-base propellant with desensitizing components (mass fraction %) nitrocellulose (degree of nitration $209.0\text{ ml}^1\text{g}$) *ca* 91%, diphenylamine 1.0–2.0%, camphor > 1.8%, graphite > 0.4% and others.

Measurements

Sample mass, 0.830 mg; apparatus, Shimadzu DSC-50.

Results

Decomposition peak T_i 437.11 K (163.96°C), T_{ig} 470.27 K (197.12°C), T_p 472.21 K (199.0°C). There is a discernible shoulder at 184.14°C .

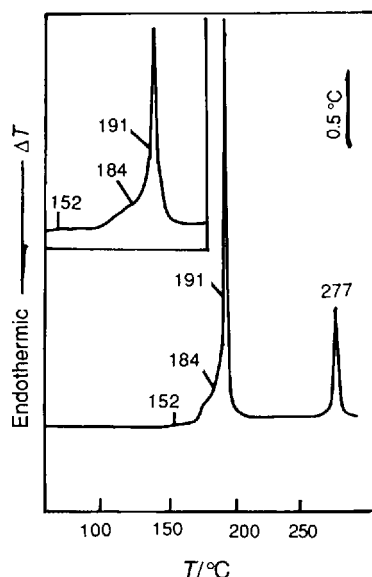


Figure 11.37 DTA curve of 4/7 single-base propellant in static air. The inset is the DTA curve of sample mass 3.0 mg, paper speed 15 mm min⁻¹

Sample

A 4/7 single-base propellant with components (mass fraction %) nitrocellulose (degree of nitration ≥ 208.0 ml g⁻¹) ca 95%; dipheylamine 1–2%, total volatiles $\geq 3.5\%$.

Measurements

Sample mass, 2.0 mg; apparatus, LCT.

Results

Decomposition peak T_i 425 K (152 °C) T_{ig} 464 K (191 °C). It decomposes slowly in the range 152–184 °C. The peak at 277 °C is the exothermic peak of the decomposition products.

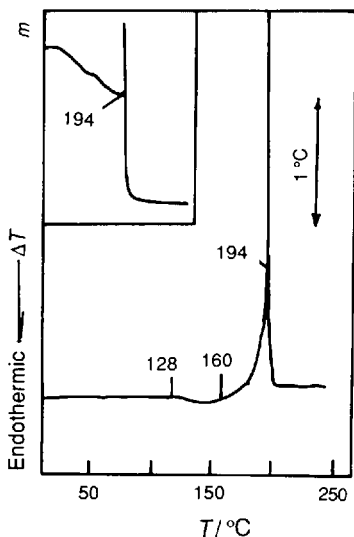


Figure 11.38 DTA curve of double-base propellant in static air. The inset is the TG curve obtained with LCT apparatus

Sample

Double-base propellant with components (mass fraction %) No. 3 nitrocellulose 50%, nitroglycerine 26.5%, Centralite 3.0% and others.

Measurements

Sample mass, 2.0 mg; apparatus, LCT.

Results

Decomposition peak (with a slow endothermic process in the initial stage) T_i 401 K (128 °C), T_{p1} 433 K (160 °C), T_{ig} 467 K (194 °C). A slow mass loss with several steps occurred below 194 °C, and at 194 °C it changed to a rapid mass increase and mass loss (the mass increase is an apparent mass increase; nitrocellulose and some propellants also show a similar phenomenon).

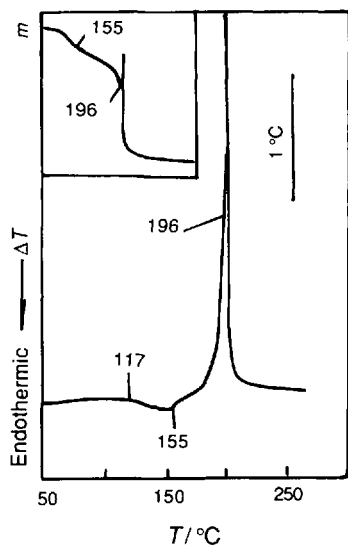


Figure 11.39 DTA curve of ribbon double-base propellant in static air. The inset is the TG curve obtained with LCT apparatus

Sample

Ribbon double-base propellant used in mortar projectiles with components (mass %) No. 3 nitrocellulose 58.5%, nitroglycerine 40%, centralite 0.8% and others.

Measurements

Sample mass, 2.0 mg; apparatus, LCT.

Results

Decomposition peak (with a slow endothermic process in the initial stage) T_i 390 K (117 °C), T_{p1} 428 K (155 °C); T_{ig} 469 K (196 °C). The mass loss below 196 °C occurs in approximately two steps and changes into a rapid mass increase and mass loss at 196 °C.

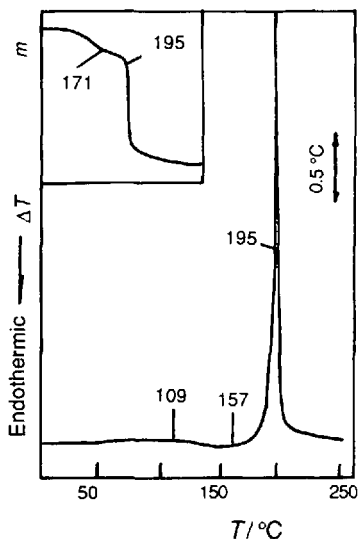


Figure 11.40 DTA curve of triple-base propellant containing nitroguanidine in static air. The inset is the TG curve obtained with LCT apparatus

Sample

Triple-base propellant containing nitroguanidine, with components (mass %) pyrocellulose 28%, nitroglycerine 22.5%, nitroguanidine 47.7%, stabilizer, etc.

Measurements

Sample mass, 2.0 mg; apparatus, LCT.

Results

Decomposition peak (with a slow endothermic process in the initial stage) T_i 482 K (109 °C), T_{p1} 430 K (157 °C); T_{ig} 468 K (195 °C). A mass loss in two steps occurs below 195 °C and at 195 °C it changes into a rapid mass loss.

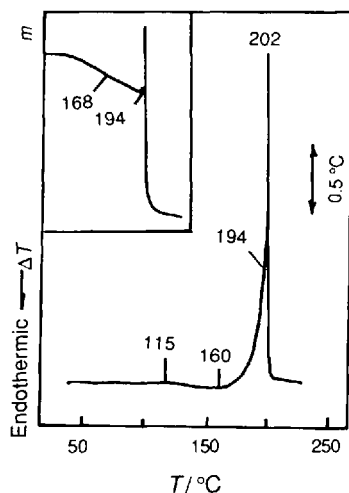


Figure 11.41 DTA curve of triple-base propellant containing nitrotriglycol in static air. The inset is the TG curve obtained with LCT apparatus

Sample

Triple-base propellant containing nitrotriglycol (TAGEN) with components (mass fraction %) nitrocellulose 65.5%, TAGEN 11%, nitroglycerine 21%, Centralite, etc.

Measurements

Sample mass, 2.0 mg; apparatus, LCT.

Results

Decomposition peak (with a slow endothermic process in the initial stage) T_i 388 K (115 °C), T_{p1} 433 K (160 °C), T_{ig} 467 K (194 °C). A slow mass loss in two steps occurs below 194 °C and at 194 °C it changes into a rapid mass increase and mass loss.

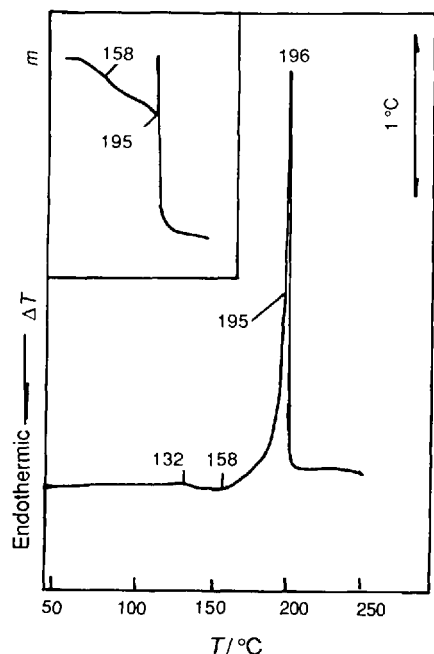


Figure 11.42 DTA curve of SQ-2 double base propellant in static air. The inset is the TG curve obtained with LCT apparatus

Sample

SQ-2 double-base propellant; with components (mass fraction %) nitrocellulose 59.2%, nitroglycerine 25.3%, Centralite II 2.9% and others.

Measurements

Sample mass, 2.0 mg; apparatus LCT.

Results

Decomposition peak (with a slow endothermic process in the initial stage) T_i 405 K (132 °C), T_{p1} 431 K (158 °C), T_{ig} 468 K (195 °C), T_{p2} 469 K (196 °C).

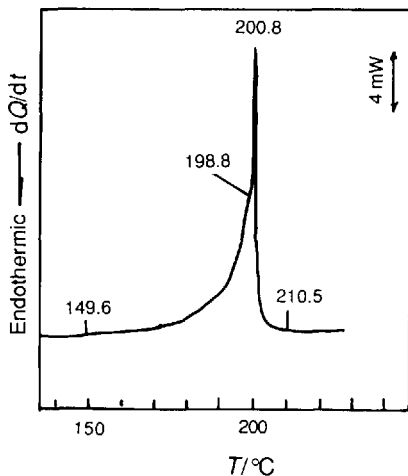


Figure 11.43 DSC curve of SS-2 double-base propellant in dynamic nitrogen

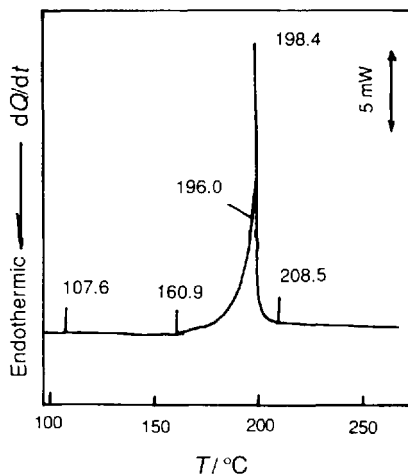


Figure 11.44 DSC curve of double-base propellant containing aluminum powder in dynamic nitrogen

Samples

SS-2 double-base propellant with components (mass fraction %) nitrocellulose 55%, nitroglycerine 29.3%, dinitrotoluene 10.0%, Centralite II 3.0%, graphite 0.5% and others.

Measurements

Sample mass, 1.107 mg; apparatus, Shimadzu DSC-50.

Results

Decomposition peak T_i 422.76 K (149.61 °C), T_{ig} 471.99 K (198.84 °C), T_p 473.95 K (200.80 °C), T_f 483.63 K (210.48 °C).

Sample

Double-base propellant containing Al powder with components (mass fraction %) nitrocellulose 51%, nitroglycerine 27%, DINA (diethanol-nitramine dinitrate) 13%, Al powder 5%, Centralite II 1% and others.

Measurements

Sample mass 1.187 mg; apparatus, Shimadzu DSC-50.

Results

Decomposition peak T_i ca 434.09 K (ca 160.94 °C), T_{ig} 469.19 K (196.04 °C), T_p 471.55 K (198.40 °C). A slow endothermic process occurs from 107.63 to nearly 160.94 °C.

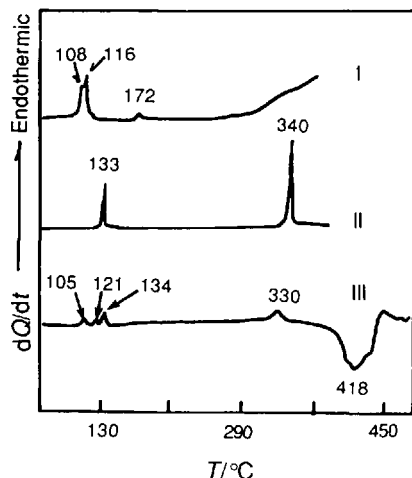


Figure 11.45 DSC curve of black powder and its ingredients. Reproduced by permission of VCH Verlagsgesellschaft from Ref. 86

Samples

I, Sulfur (purity 99.999%); II, potassium nitrate (purity > 99.5%), III, black powder (KNO_3 : C : S = 75 : 15 : 10, mass ratio).

Measurements

Sample masses, I 5 mg, II 3.2 mg and III 1 mg; apparatus, Perkin-Elmer DSC-2; heating rate, $20^\circ\text{C min}^{-1}$; crucible, sealed aluminum; reference crucible empty (with lid); purge gas, nitrogen at a pressure of 138 kPa.

Results

I. Crystalline transition peak (orthogonal system to monoclinic system), T_i ca 368 K (ca 95°C), T_p 381 K (108°C ; melting peak T_p 389 K (116°C); liquid-liquid transition peak T_i ca 433 K (ca 160°C), T_p 445 K (172°C). When heated to 120°C followed by cooling to room temperature and remeasurement, the peak at 108°C disappears and the peak at 116°C shifts to 112°C . II. Crystalline transition peak ($\alpha \rightarrow \beta$) T_i ca 403 K (ca 130°C), T_p 406 K (133°C); melting peak T_i ca 603 K (ca 330°C), T_p 613 K (340°C). III. Crystalline transition peak of S T_p 378 K (105°C), melting peak of S T_p 394 K (121°C); crystalline transition peak of KNO_3 T_p 407 K (134°C); melting peak of KNO_3 T_p 603 K (330°C). A broad peak formed by the reaction of the constituents in black powder covers the temperature range 663–723 K (390 – 450°C).

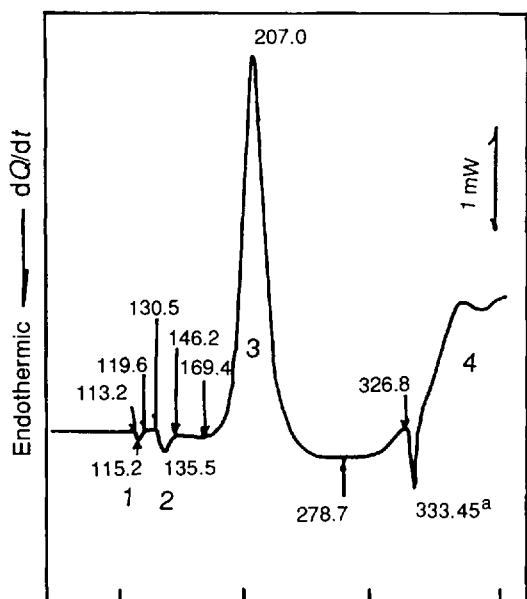


Figure 11.46 DSC curve of benite powder in dynamic nitrogen

Sample

Benite; black powder: nitrocellulose = 60 : 40 (mass ratio).

Measurements

Sample mass, 0.668 mg; apparatus, Shimadzu DSC-50.

Results

Characteristic temperatures are given in Table 11.12.

Table 11.12

Peak No.	T_i/K ($t/^\circ\text{C}$)	T_p/K ($t/^\circ\text{C}$)	Remarks
1	386.35 (113.20)	388.32 (115.17)	Melting of S
2	403.63 (130.48)	408.62 (135.47)	Crystalline transition of KNO_3
3	442.58 (169.43)	480.13 (206.98)	Decomposition of nitrocellulose
4	551.84 (278.69)		Reaction between constituents

^a peak at 333.45 $^\circ\text{C}$ results from the melting of KNO_3 .

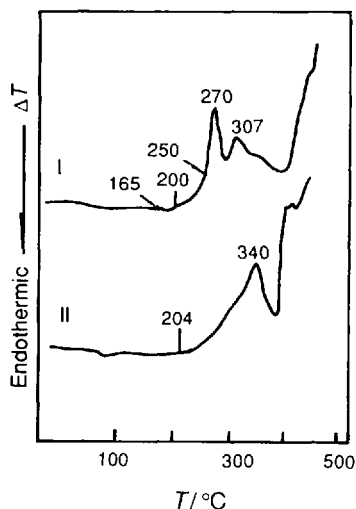


Figure 11.47 DTA curves of lead trinitroresorcinate coated with shellac and shellac itself. Reproduced from Ref. 84

Samples

I, Lead trinitroresorcinate (LTNR) coated with shellac (LTNR:Shellac = 1:1, mass ratio); II, shellac.

Measurements

Sample masses, I 18.0 mg and II 14.2 mg; apparatus and the conditions for measurement as in Figure 11.33.

Results

I. Dehydration peak T_i 438 K (165 °C); decomposition peak T_i 473 K (200 °C), T_{si} 523 K (250 °C), T_p 543 K (270 °C). II. decomposition peak T_i 477 K (204 °C), T_p 613 K (340 °C).

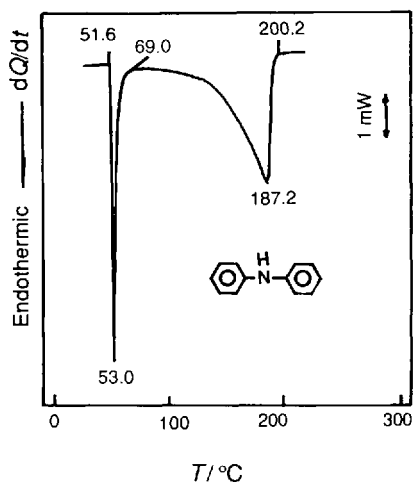


Figure 11.48 DSC curve of diphenylamine in dynamic nitrogen

Sample

Diphenylamine (DPA).

Measurements

Sample mass, 1.514 mg; apparatus, Shimadzu DSC-50.

Results

Melting peak T_i 324.78 K (51.63 °C), T_p 326.22 K (53.07 °C); vaporization peak T_i ca 353 K (ca 80 °C), T_p 460.38 K (187.23 °C), T_i 473.34 K (200.19 °C).

Reference data

M.p. 327 K (54 °C) [87], b.p. 575 K (302 °C) [87].

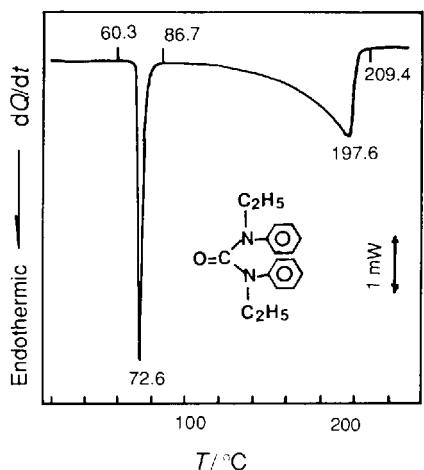


Figure 11.49 DSC curve of Centralite I in dynamic nitrogen

Sample

Centralite I.

Measurements

Sample Mass 1.038 mg; apparatus, Shimadzu DSC-50.

Results

Melting peak T_i 333.47 K (60.32 °C), T_e 344.4 K (71.32 °C), T_p 345.73 K (72.58 °C); vaporization peak T_i ca 368 K (ca 95 °C), T_p 470.79 K (197.64 °C), T_f 482.56 K (209.41 °C).

Reference data

M.p. 344.7–345 K (71.5–72 °C) [88]; b.p. 599–603 K (326–330 °C) [88].

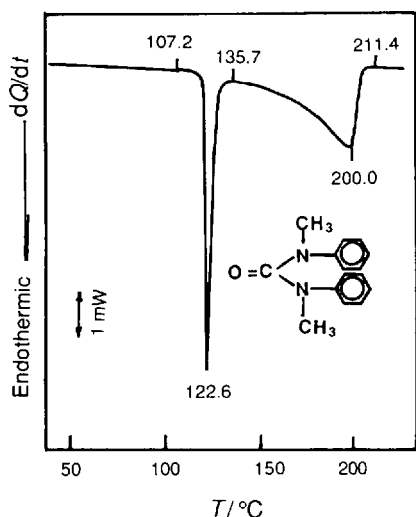


Figure 11.50 DSC curve of Centralite II in dynamic nitrogen

Sample

Centralite II.

Measurements

Sample mass, 1.036 mg; apparatus, Shinadzu DSC-50.

Results

Melting peak T_i 380.31 K (107.16 °C), T_e 394.52 K (121.37 °C), T_p 395.73 K (122.58 °C); vaporization peak T_i 408.86 K (135.71 °C), T_p 472.90 K (199.75 °C), T_f 484.54 K (211.39 °C).

Reference data

M.p. 394–394.7 K (121–121.5 °C) [89]; b.p. 623 K (350 °C) [89].

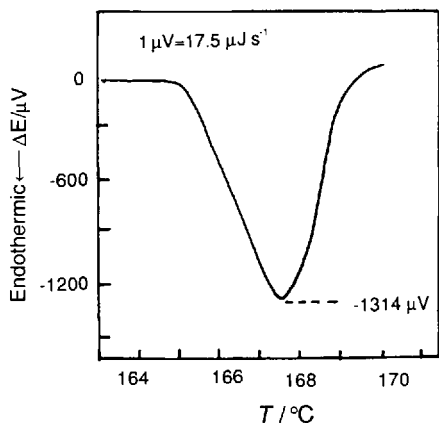


Figure 11.51 Microcalorimetry curve of crystalline transition of β -HMX. Reproduced from Ref. 90

Sample

β -HMX.

Measurements

Apparatus, Calvet microcalorimeter, low-temperature type; heating rate, 0.5°C h^{-1} .

Results

Initial temperature of β to α transformation 438 K (165°C), final temperature 442 K (169°C), Above 169°C , β -HMX decomposes immediately (exotherm).

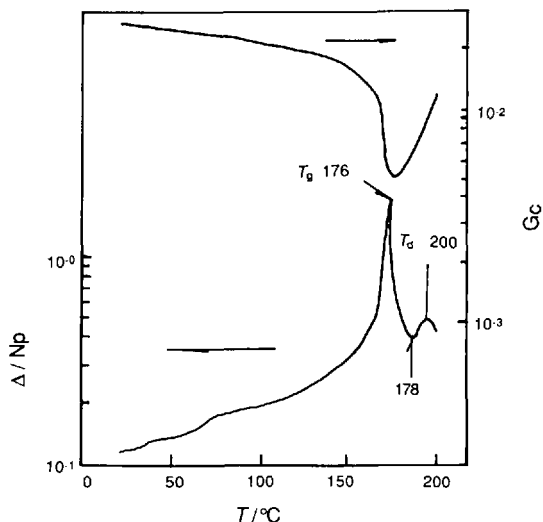


Figure 11.52 Dynamic thermomechanical (TBA) curves of No. 3 nitrocellulose. Reproduced from Ref. 91

Sample

No. 3 nitrocellulose; the specimen braid was composed of 3600 loose single filaments, each about 200 mm long. Glass-fiber braid was subjected to heat treatment at 400 – 500°C for 2 hours before the experiment. A 20–100 mg amount of sample solution was impregnated in the braid and then the solvent on the braid was removed. The braid was prepared for use in the following experiment.

Measurements

Heating rate, 1°C min^{-1} (or 2°C min^{-1}); atmosphere, high-purity nitrogen or vacuum.

Results

Maximum damping peak (glass transition of nitrocellulose) 446 – 451 K (173 – 178°C), relative modulus decreases by 2–3 orders of magnitude; sub-damping peak (decomposition and cross-linking of nitrocellulose) $ca\ 456$ – 483 K ($ca\ 183$ – 210°C), relative modulus increases.

11.1 References

- 1 Krien, G., *Thermoanalytische Ergebnisse der Untersuchung von Sprengstoffen (Einheitliche Sprengstoffe)*, AZ: 3.0-3/3960/76. Bonn, Bundesinstitut für Chemisch-technische Untersuchungen, 1976, p. 35.
- 2 Krien, G., *Thermoanalytische Ergebnisse der Untersuchung von Sprengstoffen (Einheitliche Sprengstoffe)*, AZ: 3.0-3/3960/76. Bonn, Bundesinstitut für Chemisch-technische Untersuchungen, 1976, p. 182.
- 3 Sun Rongkang, Ren Teshung and Gao Huailin, *Chemistry and Technology of Secondary Explosives*. Beijing, National Defense Industry Press, 1981 Vol. I, 337 (in Chinese).
- 4 Dong Haishan and Zhou Fenfen, *Properties of High Energy Explosives and Relavent Materials*. Beijing, Science Press, 1989, p. 275 (in Chinese).
- 5 Zhang Houshen, Hu Rongzu and Yan Desuo, *Abstracts of Proceedings of the Third Symposium on Solution Chemistry, Thermodynamics, Thermochemistry and Thermal Analysis*. Hongzhou, Chinese Chemical Society, 1986, p. 476.
- 6 Zhang Sigui (editor), *Technical Handbook of Fine Organic Chemicals (I)*. Beijing, Science Press, 1991, p. 788 (in Chinese).
- 7 Krien, G., *Thermoanalytische Ergebnisse der Untersuchung von Sprengstoffen (Einheitliche Sprengstoffe)*, AZ: 3.0-3/3960/76. Bonn, Bundesinstitut für Chemisch-technische Untersuchungen, 1976, p. 216.
- 8 *Handbook of Explosives and Propellants*. Xian, Research Institute No. 204, 1981, p. 51.
- 9 Itoh, M., Yoshida, T., Nakamura, M., and Uetake, K., *J. Ind. Explos. Soc. Jpn.*, 1977, 1, 17.
- 10 Hara, Y., Matsubara, H. and Osada, H., *J. Ind. Explos. Soc. Jpn.*, 1977(6), 338.
- 11 Sun Rongkang, Ren Teshung and Gao Huailin, *Chemistry and Technology of Secondary Explosives*. Beijing, National Defence Industry Press, Vol. I, 1981, 193 (in Chinese).
- 12 Hara, Y. and Osada, H., *J. Ind. Explos. Soc. Jpn.* 1978, (3), 100.
- 13 Krien, G., *Thermoanalytische Ergebnisse der Untersuchung von Sprengstoffen (Einheitliche Sprengstoffe)*, AZ: 3.0-3/3960/76. Bonn: Bundesinstitut für Chemisch-technische Untersuchungen, 1976, p. 59.
- 14 Sun Rongkang, Ren Teshung and Gao Huailin, *Chemistry and Technology of Secondary Explosives*. Beijing, National Defense Industry Press, Vol. I, p. 112 (in Chinese).
- 15 Urbanski, T. (Sun Rongkang, transl.) *Chemistry and Technology of Propellants and Explosives*. Beijing, National Defense Industry Press, 1976, Vol. 1, p. 343 (in Chinese).
- 16 Sun Rongkang, Ren Teshung and Gao Huailin, *Chemistry and Technology of Secondary Explosives*. Beijing, National Defense Industry Press, 1981, Vol. I, p. 352 (in Chinese).
- 17 Hara, Y., Matsubara, H., and Osada, H., *J. Ind. Explos. Soc. Jpn.*, 1975, (5), 266.
- 18 Sun Rongkang, Ren Teshung and Gao Huailin, *Chemistry and Technology of Secondary Explosives*. Beijing, National Defence Industry Press, 1981, Vol. 1, p. 353 (in Chinese).
- 19 Urbanski, T. (Sun Rongkang, transl.), *Chemistry and Technology of Propellants and Explosives*. Beijing, National Defense Industry Press, 1976, Vol. 1, p. 349 (in Chinese).
- 20 Meyer, R. (Chen Zhengheng and Zhu Xiwu, transl.) *Handbook of Explosives*. Beijing, Coal Industry Ministry Press, 1980, p. 288 (in Chinese).
- 22 Urbanski, T. (Sun Rongkang, transl.), *Chemistry and Technology of Propellants and Explosives*. Beijing, National Defense Industry Press, 1976, Vol. 1, p. 424 (in Chinese).
- 23 Krien, G., *Thermoanalytische Ergebnisse der Untersuchung von Sprengstoffen (Einheitliche Sprengstoffe)* AZ: 3.0-3/3960/76. Bonn, Bundesinstitut für Chemisch-technische Untersuchungen, 1976, p. 174.
- 24 Hara, Y., Kawano, F., and Osada, H., *J. Ind. Explos. Soc. Jpn.*, 1976, (5), 233.
- 25 Krien, G., *Thermoanalytische Ergebnisse der Untersuchung von Sprengstoffen (Einheitliche Sprengstoffe)*, AZ: 3.0-3/3960/76. Bonn, Bundesinstitut für Chemisch-technische Untersuchungen, 1976, p. 179.
- 26 Krien, G., *Thermoanalytische Ergebnisse der Untersuchung von Sprengstoffen (Einheitliche Sprengstoffe)*, AZ: 3.0-3/3960/76. Bonn, Bundesinstitut für Chemisch-technische Untersuchungen, 1976, p. 200.
- 27 Urbanski, T. (Sun Rongkang, transl.), *Chemistry and Technology of Propellants and Explosives*. Beijing, National Defense Industry Press, 1976, Vol. 1, 249 (in Chinese).
- 28 Dong Haishan and Zhou Fenfen, *Properties of High Energy Explosives and Relevant Materials*. Beijing, Science Press, 1989, p. 278 (in Chinese).
- 29 Sun Rongkang, Ren Teshung and Gao Huailin, *Chemistry and Technology of Secondary Explosives*. Beijing, National Defense Industry Press, 1981, Vol. 1, p. 228.
- 30 Krien, G., *Thermoanalytische Ergebnisse der Untersuchung von Sprengstoffen (Einheitliche Sprengstoffe)*, AZ: 3.0-3/3960/76. Bonn, Bundesinstitut für Chemisch-technische Untersuchungen, 1976, p. 148.
- 31 Urbanski, T. Sun Rongkang (transl.), *Chemistry and Technology of Propellants and Explosives*.

- Beijing, National Defense Industry Press, 1976, Vol. 1, p. 371.
- 32 Dong Haishan and Zhou Fenfen, *Properties of High Energy Explosives and Relevant Materials*. Beijing, Science Press, 1989, p. 255 (in Chinese).
 - 33 Sun Rongkang, Ren Teshung and Gao Huailin, *Chemistry and Technology of Secondary Explosives*. Beijing, National Defense Industry Press, 1981, Vol. I, p. 388 (in Chinese).
 - 34 Krien, G., *Thermoanalytische Ergebnisse der Untersuchung von Sprengstoffen (Einheitliche Sprengstoffe)*, AZ: 3.0-3/3960/76. Bonn, Bundesinstitut für Chemisch-technische Untersuchungen, 1976, p. 101.
 - 35 Krien, G., *Thermoanalytische Ergebnisse der Untersuchung von Sprengstoffen (Einheitliche Sprengstoffe)*, AL: 3.0-3/3960/76. Bonn, Bundesinstitut für Chemisch-technische Untersuchungen, 1976, p. 100.
 - 36 Krien, G., *Thermoanalytische Ergebnisse der Untersuchung von Sprengstoffen (Einheitliche Sprengstoffe)*, AZ: 3.0-3/3960/76. Bonn, Bundesinstitut für Chemisch-technische Untersuchungen, 1976, p. 78.
 - 37 Sun Rongkang, Ren Teshung and Gao Huailin, *Chemistry and Technology of Secondary Explosives*. Beijing, National Defense Industry Press, 1981, Vol. I, p. 703 (in Chinese).
 - 38 Luo Binghe and Yao Zeyuin, *Special Issue of Thermal Analysis*. Beijing, Beijing Optical Instrument Factory, 1984, Vol. 1, p. 31 (in Chinese).
 - 39 Bai Lin and Luo Binghe, in *Abstracts of Proceedings of the Second Symposium on Solution Chemistry, Thermodynamics, Thermochemistry and Thermal Analysis*. Wuhan, Chinese Chemical Society, Wuhan 1984, p. 373.
 - 40 Yang Zhongyi, *Explosives Used in Propellants*. Nanjing, East China Institute of Engineering, 1977, p. 73 (in Chinese).
 - 41 Krien, G., *Thermoanalytische Ergebnisse der Untersuchung von Sprengstoffen (Einheitliche Sprengstoffe)*, AZ: 3.0-3/3960/76. Bonn, Bundesinstitut für Chemisch-technische Untersuchungen, 1976, p. 27.
 - 42 *Handbook of Explosives and Propellants*. Xian, Research Institute No. 204, 1981, p. 112 (in Chinese).
 - 43 Krien, G., *Thermoanalytische Ergebnisse der Untersuchung von Sprengstoffen (Einheitliche Sprengstoffe)*, AZ: 3.0-3/3960/76. Bonn, Bundesinstitut für Chemisch-technische Untersuchungen, 1976, p. 141.
 - 44 Wang Xiaochuan, Huang Henjian, Wang Liu and Wang Zhaomin, *Rep. Explos.*, 1992, (4), 8 (in Chinese).
 - 45 Yang Zhongyi, *Explosives Used in Propellants*. Nanjing, East China Institute of Engineering, 1977, p. 84 (in Chinese).
 - 46 Sun Rongkang, Ren Teshung and Gao Huailin, *Chemistry and Technology of Secondary Explosives*. Beijing, National Defense Industry Press, 1981, Vol. I, p. 659 (in Chinese).
 - 47 Krien, G., *Thermoanalytische Ergebnisse der Untersuchung von Sprengstoffen (Einheitliche Sprengstoffe)*, AZ: 3.0-3/3960/76. Bonn, Bundesinstitut für Chemisch-technische Untersuchungen, 1976, p. 76.
 - 48 Cai Zhengqian, *Technology of Nitrocellulose*. Nanjing, East China Institute of Engineering, 1977, p. 32 (in Chinese).
 - 49 Cai Zhengqian, *Technology of Nitrocellulose*. Nanjing, East China Institute of Engineering, 1977, p. 74 (in Chinese).
 - 50 Krien, G., *Thermoanalytische Ergebnisse der Untersuchung von Sprengstoffen (Einheitliche Sprengstoffe)*, AZ: 3.0-3/3960/76. Bonn, Bundesinstitut für Chemisch-technische Untersuchungen, 1976, p. 125.
 - 51 Yang Zhongyi, *Explosives Used in Propellants*. Nanjing, East China Institute of Engineering, 1977, p. 97 (in Chinese).
 - 52 Dong Haishan and Zhou Fenfen, *Properties of High Energy Explosives and Relevant Materials*. Beijing, Science Press, 1989, 261 (in Chinese).
 - 53 Gibbs, T. R. and Popolato, A. *LASL Explosive Property Data*. Beijing, Research Institute No. 903 (transl.), 1982, p. 44.
 - 54 Dong Haishan and Zhou Fenfen, *Properties of High Energy Explosives and Relevant Materials*. Beijing, Science Press, 1989, p. 273 (in Chinese).
 - 55 Krien, G., *Thermoanalytische Ergebnisse der Untersuchung von Sprengstoffen (Einheitliche Sprengstoffe)*, AZ: 3.0-3/3960/76. Bonn, Bundesinstitut für Chemisch-technische Untersuchungen, 1976, p. 166.
 - 56 Meyer, R. (Chen Zhengheng and Zhu Xiwu, transl.), *Handbook of Explosives*. Beijing, Coal Industry Ministry Press, 1980, p. 242 (in Chinese).
 - 57 *Handbook of Explosives and Propellants*. Xian, Research Institute No. 204, 1981, p. 91 (in Chinese).
 - 58 Meyer, R., (Chen Zhengheng and Zhu Xiwu, transl.), *Handbook of Explosives*. Beijing, Coal Industry Ministry Press, 1980, p. 88 (in Chinese).
 - 59 Krien, G., *Thermoanalytische Ergebnisse der Untersuchung von Sprengstoffen (Einheitliche Sprengstoffe)*, AZ: 3.0-3/3960/76. Bonn, Bundesinstitut für Chemisch-technische Untersuchungen, 1976, p. 7.
 - 60 Cai Zhengqian, *Explos. Propellants*, 1991, (2), 37 (in Chinese).
 - 61 Dong Haishan and Zhou Fenfen, *Properties of*

- High Energy Explosives and Relevant Materials. Beijing, Science Press, 1989, p. 266 (in Chinese).
- 62 *Handbook of Explosives and Propellants*. Xian, Research Institute No. 204, 1981, p. 78 (in Chinese).
 - 63 Krien, G., *Thermoanalytische Ergebnisse der Untersuchung von Sprengstoffen (Einheitliche Sprengstoffe)*, AZ: 3.0-3/3960/76. Bonn, Bundesinstitut für Chemisch-technische Untersuchungen, 1976, p. 103.
 - 64 Sun Rongkang, Ren Teshung and Gao Huailin, *Chemistry and Technology of Secondary Explosives*. Beijing, National Defense Industry Press, 1981, Vol. I, p. 522.
 - 65 Wang Xiaochuan, *Rep. Explos.*, 1992, (3), 27 (in Chinese).
 - 66 Yang Dong, Song Hongchang and Li Shangwen, *Explos. Propellants*, 1994, (1), 21 (in Chinese).
 - 67 Sun Rongkang, Ren Teshung and Gao Huailin, *Chemistry and Technology of Secondary Explosives*. Beijing, National Defense Industry Press, 1981, Vol. I, p. 593 (in Chinese).
 - 68 Krien, G., *Thermoanalytische Ergebnisse der Untersuchung von Sprengstoffen (Einheitliche Sprengstoffe)* AZ: 3.0-3/3960/76. Bonn, Bundesinstitut für Chemisch-technische Untersuchungen, 1976, p. 137.
 - 69 Dong Haishan and Zhou Fenfen, *Properties of High Energy Explosives and Relevant Materials*. Beijing, Science Press, 1989, p. 252 (in Chinese).
 - 70 *Handbook of Explosives and Propellants*. Xian, Research Institute No. 204, 1981, p. 82 (in Chinese).
 - 71 Jing Zhongxing and Bai Mulay, *Rep. Chem. Eng., Beijing Inst. Eng.*, 1984, (1), 12 (in Chinese).
 - 72 Yang Dong, Song Hongchang and Li Shangwen, *Explos. Propellants*, 1994, (1), 23 (in Chinese).
 - 73 Chun Shijin, *Thermal Analysis of Explosives*. Beijing, Science Press, 1994, p. 142 (in Chinese).
 - 74 *Handbook of Explosives and Propellants*. Xian, Research Institute No. 204, 1981, p. 110 (in Chinese).
 - 75 Dong Haishan and Zhou Fenfen, *Properties of High Energy Explosives and Relevant Materials*. Beijing, Science Press, 1989, p. 247 (in Chinese).
 - 76 Xi Yuye, Cai Zhengqian, Wang Naiyan, Xiao Heming, Tang Zehua and Yu Mahong, *Anal. Chem.* 1991, (12), 1387 (in Chinese).
 - 77 Wang Bangning, *Acta Chim. Sin.* 1982, (11), 1001.
 - 78 Urbanski, T. (Niu Bingyi and Chen Shaoliang transl.) *Chemistry and Technology of Propellants and Explosives*. Beijing, National Defence Industry Press, 1976, Vol. 2, p. 330 (in Chinese).
 - 79 *Encyclopedia of Chinese Chemical Products*. Beijing, Chemical Industry Press, 1994, Vol. I, p. 423 (in Chinese).
 - 80 Nakamura, H., Kamo, K., Aramaki, S., and Hara, Y., *J. Explos. Soc. Jpn.*, 1994, (4), 147.
 - 81 Urbanski, T. (Niu Bingyi and Chen Shaoliang transl.) *Chemistry and Technology of Propellants and Explosives*. Beijing, National Defense Industry Press, 1976, Vol. 2, 339 (in Chinese).
 - 82 Liptay, G. (Weng Fuqi, transl.), *Figure Collection of Thermal Analysis Curves*. Jiangsu, Jiangyin Chang Jing Instrument Factory, 1978, p. 12 (in Chinese).
 - 83 Nakamura, H., Nakamura, S., and Nakamari, I., *J. Ind. Explos. Soc. Jpn.*, 1975, (1), 27.
 - 84 Cai Zhengqian, *Explos. Propellants* 1995, (2), 19 (in Chinese).
 - 85 Cai Zhengqian, *Thermal Analysis*. Beijing, Higher Education Press, 1993, p. 90 (in Chinese).
 - 86 Hussain, G. and Rees, G. J., *Propellants Explos. Protect.*, 1990, 15, 43.
 - 87 Meyer, R. (Chen Zhengheng and Zhu Xiwu, transl.), *Handbook of Explosives*. Beijing, Coal Industry Ministry Press, 1980, p. 76 (in Chinese).
 - 88 Meyer, R. (Chen Zhengheng and Zhu Xiwu, transl.), *Handbook of Explosives*. Beijing, Coal Industry Ministry Press, 1980, p. 35 (in Chinese).
 - 89 Meyer, R. (Chen Zhengheng and Zhu Xiwu, transl.), *Handbook of Explosives*. Beijing, Coal Industry Ministry Press, 1980, p. 36 (in Chinese).
 - 90 Chu Shijin, *Thermal Analysis of Explosives*. Beijing, Science Press, 1994, p. 96 (in Chinese).
 - 91 Jia Zhanning and Zhou Qihai, *J. Beijing Inst. Technol.*, 1984, 3, 72 (in Chinese).

Thermal Analysis Curves of Inorganic Materials

12.1 Thermal Analysis Curves of Complexes of Rare Earth Bromides with Glycine (Gly) and Alanine (Ala)

Samples were prepared by Sun Tongshan and co-workers [1-3]; their general formulas are $\text{REBr}_3 \cdot 3\text{Gly} \cdot 3\text{H}_2\text{O}$ (RE = La, Ce, Pr, Nd, Sm, Eu,

Gd, Tb, Dy and Y) and $\text{REBr}_3 \cdot 3\text{Al} \cdot n\text{H}_2\text{O}$ (RE = La, Ce, Pr, Nd, Sm, Eu, Gd and Tb, $n = 3$; RE = Dy and Y, $n = 2.5$).

Measurements: were performed under the following conditions: Perkin-Elmer TGS-2 thermogravimetric analyzer; heating rate $10^\circ\text{C min}^{-1}$; sample mass 3-9 mg; N_2 atmosphere (40 ml min^{-1}).

Table 12.1 The common forms of $f(x)$ and $g(x)$

Function No.	Mechanism	$g(x)$	$f(x)$
1	P1	$\alpha^{1/4}$	$4\alpha^{1/4}$
2	A1.5	$[-\ln(1-\alpha)]^{2/3}$	$1.5(1-\alpha)[- \ln(1-\alpha)]^{1/3}$
3	A2	$[-\ln(1-\alpha)]^{1/2}$	$2(1-\alpha)[- \ln(1-\alpha)]^{1/2}$
4	A3	$[-\ln(1-\alpha)]^{1/3}$	$3(1-\alpha)[- \ln(1-\alpha)]^{2/3}$
5	A4	$[-\ln(1-\alpha)]^{1/4}$	$4(1-\alpha)[- \ln(1-\alpha)]^{3/4}$
6	R2	$1 - (1-\alpha)^{1/2}$	$2(1-\alpha)^{1/2}$
7	R3	$1 - (1-\alpha)^{1/3}$	$3(1-\alpha)^{2/3}$
8	D1	α^2	$1/2\alpha$
9	D2	$(1-\alpha)\ln(1-\alpha) + \alpha$	$-[\ln(1-\alpha)]^{-1}$
10	D3	$[1 - (1-\alpha)^{-1/3}]^2$	$1.5[1 - \ln(1-\alpha)^{1/3}]^{-1}(1-\alpha)^{2/3}$
11	D4	$(1 - 2\alpha/3) - (1-\alpha)^{2/3}$	$1.5[1 - \ln(1-\alpha)^{1/3} - 1]^{-1}$
12	F1	$-\ln(1-\alpha)$	$(1-\alpha)$
13	F2	$(1-\alpha)^{-1} - 1$	$(1-\alpha)^2$
14	F3	$(1-\alpha)^{-2} - 1$	$0.5(1-\alpha)^3$

Note:

Func. No. Mechanism $g(x) \sim f(x)$

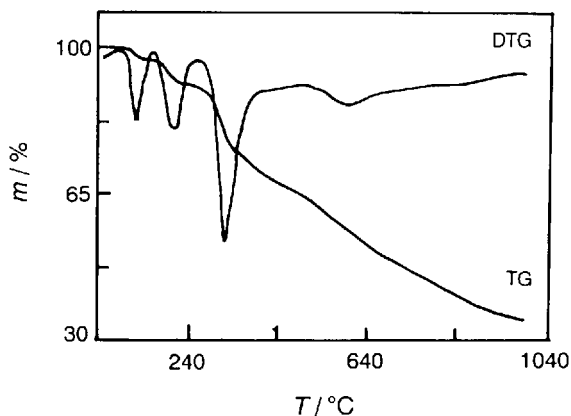
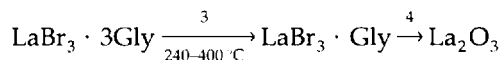
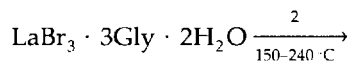
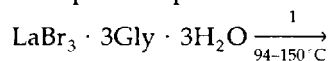


Figure 12.1 TG and DTG curves of complex of lanthanum bromide with glycine [1,3]

Results

Thermal decomposition processes:



Kinetic parameters and thermal decomposition mechanisms (for a definition of mechanism functions, see Table 12.1):

Process 1: $E = 194.1 \text{ kJ mol}^{-1}$, $\ln[A/(s^{-1})] = 57.2$, mechanism is F1.

Process 2: $E = 257.0 \text{ kJ mol}^{-1}$, $\ln[A/(s^{-1})] = 62.0$, mechanism is D3.

Process 3: $E = 173.9 \text{ kJ mol}^{-1}$, $\ln[A/(s^{-1})] = 33.2$, mechanism is F2.

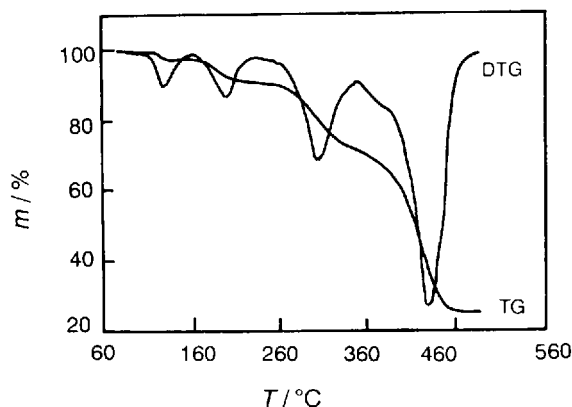
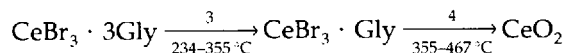
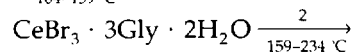
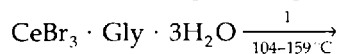


Figure 12.2 TG and DTG curves of complex of cerium bromide with glycine [2]

Results:

Thermal decomposition processes:



Kinetic parameters and thermal decomposition mechanisms:

Process 1: $E = 186.6 \text{ kJ mol}^{-1}$, $\ln[A/(s^{-1})] = 53.7$, mechanism is F1.

Process 2: $E = 283.0 \text{ kJ mol}^{-1}$, $\ln[A/(s^{-1})] = 67.2$, mechanism is D3.

Process 3: $E = 312.5 \text{ kJ mol}^{-1}$, $\ln[A/(s^{-1})] = 59.2$, mechanism is D3.

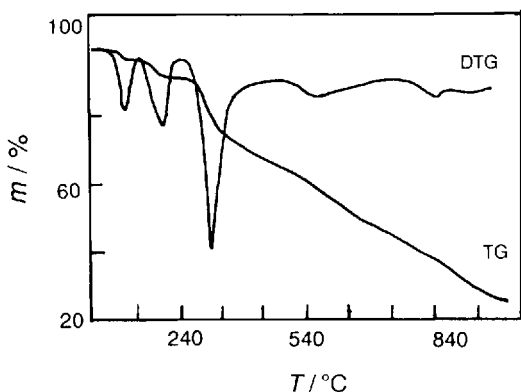


Figure 12.3 TG and DTG curves of complex of praseodymium bromide with glycine [2]

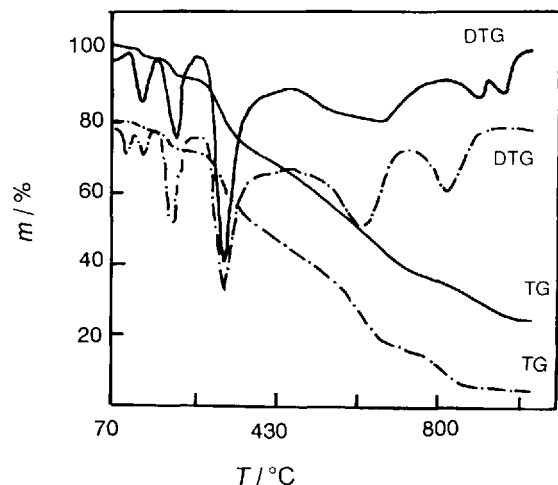
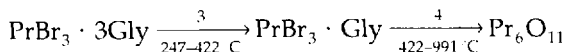
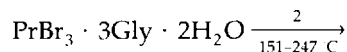
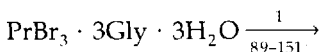


Figure 12.4 TG and DTG curves of complexes of neodymium bromide (—) and gadolinium bromide (---) with glycine [1-3]

Results:

Thermal decomposition processes:



Kinetic parameters and thermal decomposition mechanisms:

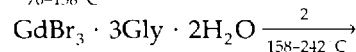
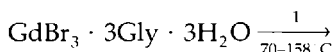
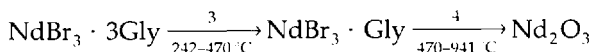
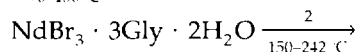
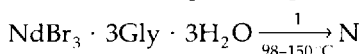
Process 1: $E = 170.6 \text{ kJ mol}^{-1}$, $\ln[A/(s^{-1})] = 50.6$, mechanism is F1.

Process 2: $E = 231.4 \text{ kJ mol}^{-1}$, $\ln[A/(s^{-1})] = 54.4$, mechanism is D3.

Process 3: $E = 198.8 \text{ kJ mol}^{-1}$, $\ln[A/(s^{-1})] = 36.7$, mechanism is F2.

Results

Thermal decomposition processes:



Kinetic parameters and thermal decomposition mechanisms:

Neodymium:

Process 1: $E = 160.5 \text{ kJ mol}^{-1}$, $\ln[A/(s^{-1})] = 47.1$, mechanism is F1.

Process 2: $E = 222.7 \text{ kJ mol}^{-1}$, $\ln[A/(s^{-1})] = 53.0$, mechanism is D3.

Process 3: $E = 198.7 \text{ kJ mol}^{-1}$, $\ln[A/(s^{-1})] = 38.4$, mechanism is F2.

Gadolinium:

Process 2: $E = 366.3 \text{ kJ mol}^{-1}$, $\ln[A/(s^{-1})] = 90.1$, mechanism is D3.

Process 3: $E = 166.9 \text{ kJ mol}^{-1}$, $\ln[A/(s^{-1})] = 30.6$, mechanism is F2.

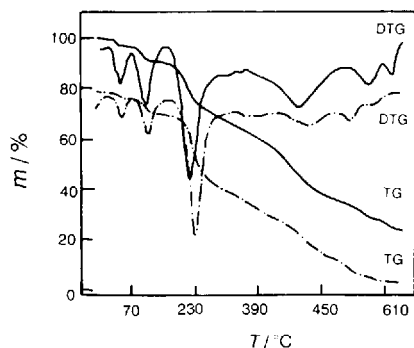
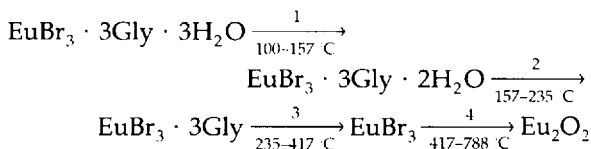
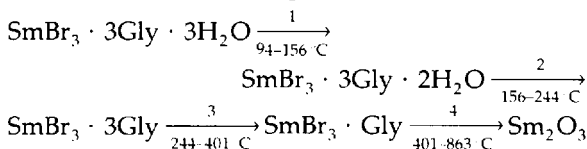


Figure 12.5 TG and DTG curves of complexes of samarium bromide (—) and europium bromide (---) with glycine [2]

Results

Thermal decomposition processes:



Kinetic parameters and thermal decomposition mechanisms:

Samarium:

Process 1: $E = 148.8\text{ kJ mol}^{-1}$, $\ln[A/(s^{-1})] = 42.6$, mechanism is F1.

Process 2: $E = 256.8\text{ kJ mol}^{-1}$, $\ln[A/(s^{-1})] = 61.1$, mechanism is D3.

Process 3: $E = 172.7\text{ kJ mol}^{-1}$, $\ln[A/(s^{-1})] = 31.9$, mechanism is F2.

Europium:

Process 1: $E = 146.4\text{ kJ mol}^{-1}$, $\ln[A/(s^{-1})] = 41.5$, mechanism is F1.

Process 2: $E = 272.8\text{ kJ mol}^{-1}$, $\ln[A/(s^{-1})] = 65.4$, mechanism is D3.

Process 3: $E = 171.6\text{ kJ mol}^{-1}$, $\ln[A/(s^{-1})] = 31.7$, mechanism is F2.

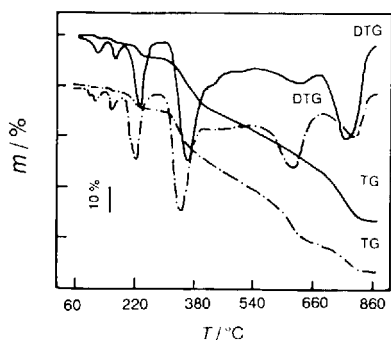
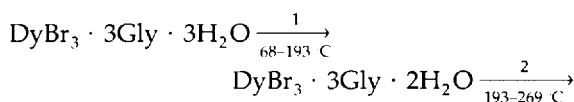
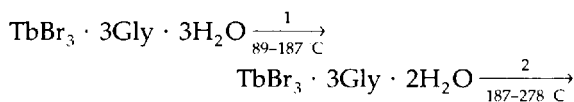


Figure 12.6 TG and DTG curves of complexes of terbium bromide (—) and dysprosium bromide (---) with glycine [2].

Results

Thermal decomposition processes:



(continued)

Kinetic parameters and thermal decomposition mechanisms:

Terbium:

Process 2: $E = 323.1 \text{ kJ mol}^{-1}$, $\ln[A/(s^{-1})] = 73.3$, mechanism is D3.

Process 3: $E = 183.7 \text{ kJ mol}^{-1}$, $\ln[A/(s^{-1})] = 31.9$, mechanism is F2.

Dysprosium:

Process 2: $E = 339.2 \text{ kJ mol}^{-1}$, $\ln[A/(s^{-1})] = 77.6$, mechanism is D3.

Process 2: $E = 198.2 \text{ kJ mol}^{-1}$, $\ln[A/(s^{-1})] = 35.0$, mechanism is F2.

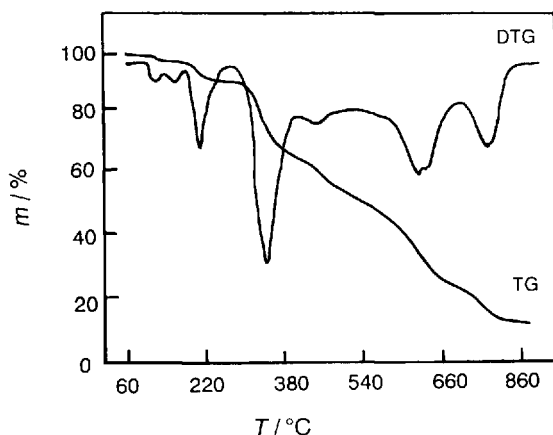


Figure 12.7 TG and DTG curves of complex of yttrium bromide with glycine [2].

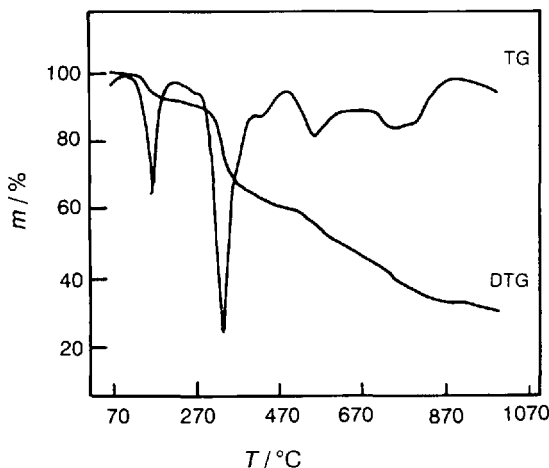
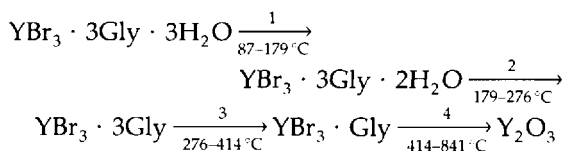


Figure 12.8 TG and DTG curves of complex of lanthanum bromide with alanine [1,3].

Results

Thermal decomposition processes:



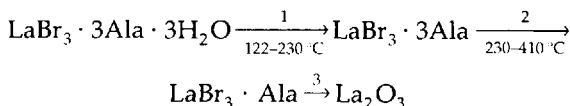
Kinetic parameters and thermal decomposition mechanisms:

Process 2: $E = 380.7 \text{ kJ mol}^{-1}$, $\ln[A/(s^{-1})] = 90.3$, mechanism is D3.

Process 3: $E = 216.3 \text{ kJ mol}^{-1}$, $\ln[A/(s^{-1})] = 39.1$, mechanism is F2.

Results

Thermal decomposition processes:



Kinetic parameters and thermal decomposition mechanisms:

Process 1: $E = 243.2 \text{ kJ mol}^{-1}$, $\ln[A/(s^{-1})] = 60.8$, mechanism is D3.

Process 2: $E = 206.2 \text{ kJ mol}^{-1}$, $\ln[A/(s^{-1})] = 38.3$, mechanism is F2.

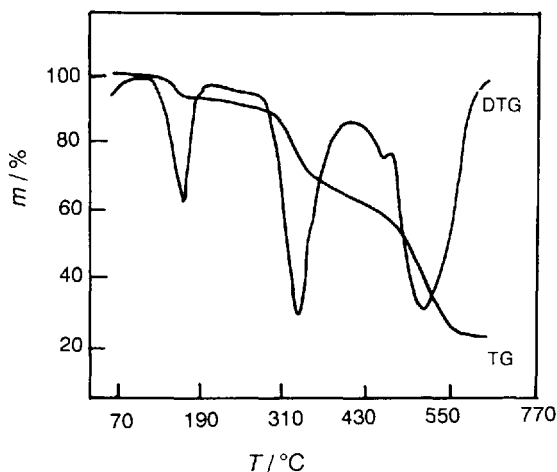


Figure 12.9 TG and DTG curves of complex of cerium bromide with alanine [3].

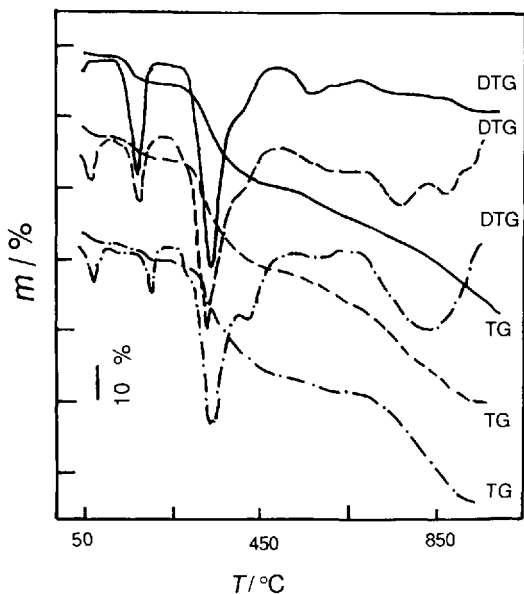
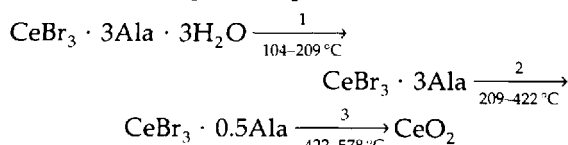


Figure 12.10 TG and DTG curves of complexes of praseodymium bromide (—), samarium bromide (----) and terbium bromide (— · — · —) with alanine [3].

Results

Thermal decomposition processes:



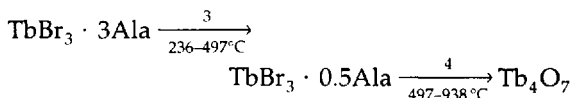
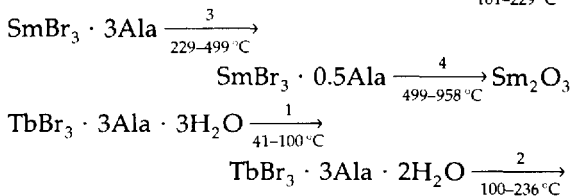
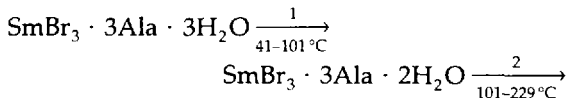
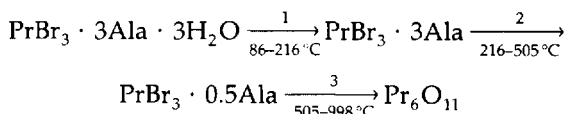
Kinetic parameters and thermal decomposition mechanisms:

Process 1: $E = 219.0 \text{ kJ mol}^{-1}$, $\ln[A/(s^{-1})] = 56.2$, mechanism is D2.

Process 2: $E = 222.2 \text{ kJ mol}^{-1}$, $\ln[A/(s^{-1})] = 37.7$, mechanism is D3.

Results

Thermal decomposition processes:



Kinetic parameters and thermal decomposition mechanisms:

Praseodymium:

Process 1: $E = 188.1 \text{ kJ mol}^{-1}$, $\ln[A/(s^{-1})] = 46.8$, mechanism is D2.

Process 2: $E = 143.7 \text{ kJ mol}^{-1}$, $\ln[A/(s^{-1})] = 24.3$, mechanism is F2.

Samarium:

Process 3: $E = 123.5 \text{ kJ mol}^{-1}$, $\ln[A/(s^{-1})] = 20.2$, mechanism is F2.

Terbium:

Process 3: $E = 108.0 \text{ kJ mol}^{-1}$, $\ln[A/(s^{-1})] = 16.9$, mechanism is F2.

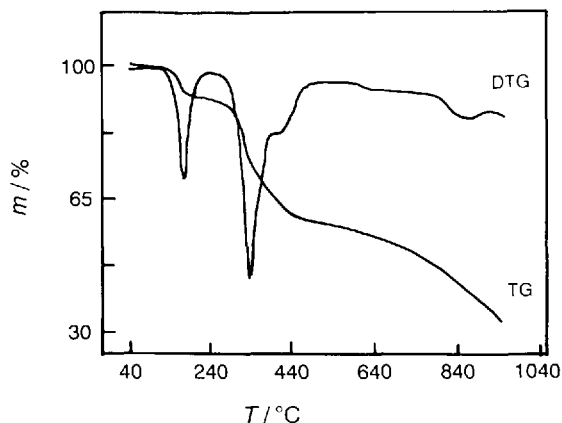
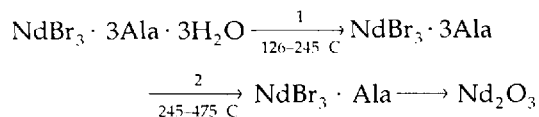


Figure 12.11 TG and DTG curves of complex of neodymium bromide with alanine [1,3]

Results

Thermal decomposition processes:



Kinetic parameters and thermal decomposition mechanisms:

Process 1: $E = 257.2 \text{ kJ mol}^{-1}$, $\ln[A/(s^{-1})] = 64.7$, mechanism is D3.

Process 2: $E = 139.9 \text{ kJ mol}^{-1}$, $\ln[A/(s^{-1})] = 24.8$, mechanism is F2.

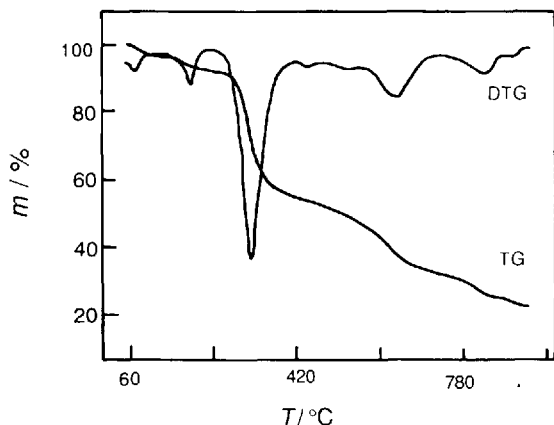
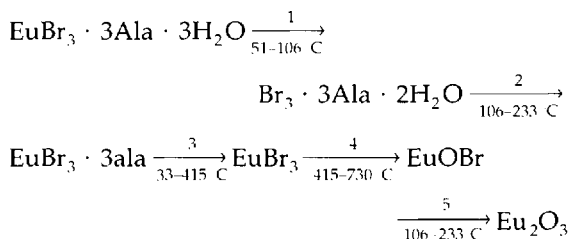


Figure 12.12 TG and DTG curves of complex of europium bromide with Alanine [3]

Results

Thermal decomposition processes:



Kinetic parameters and thermal decomposition mechanism:

Process 3: $E = 155.9 \text{ kJ mol}^{-1}$, $\ln[A/(s^{-1})] = 27.6$, mechanism is F1.

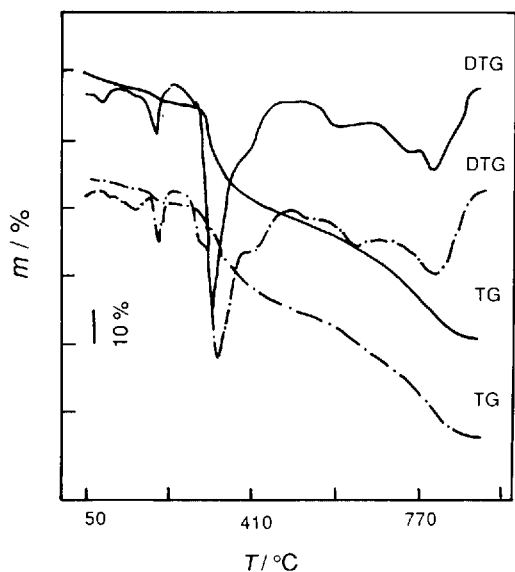


Figure 12.13 TG and DTC curves of complexes of gadolinium bromide (—) and dysprosium bromide (---) with alanine [3]

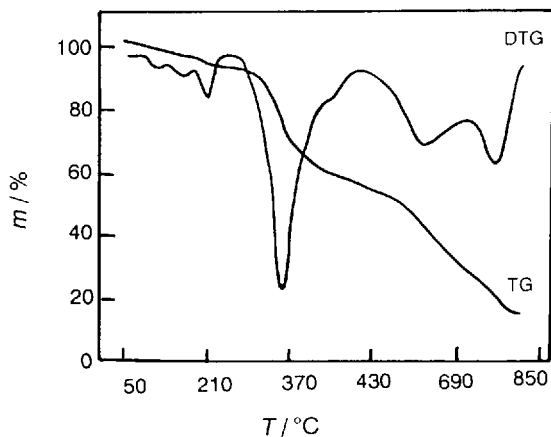
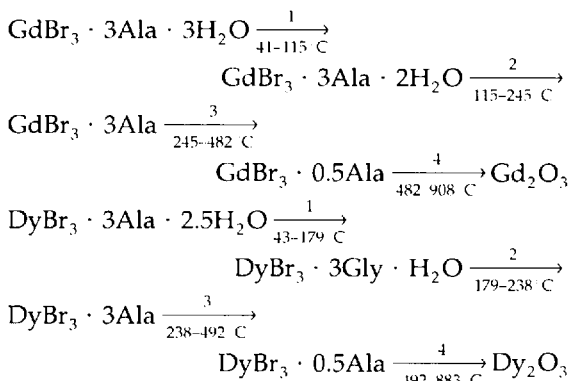


Figure 12.14 TG and DTG curves of complex of yttrium bromide with alanine [3]

Results

Thermal decomposition processes:



Kinetic parameters and thermal decomposition mechanisms

Gadolinium:

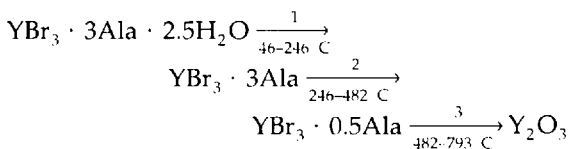
Process 3: $E = 183.7\text{ kJ mol}^{-1}$, $\ln[A/(s^{-1})] = 31.9$, mechanism is F2.

Dysprosium:

Process 3: $E = 198.2\text{ kJ mol}^{-1}$, $\ln[A/(s^{-1})] = 35.0$, mechanism is F2.

Results

Thermal decomposition processes:



Kinetic parameters and thermal decomposition mechanism:

Process 2: $E = 120.4\text{ kJ mol}^{-1}$, $\ln[A/(s^{-1})] = 19.6$, mechanism is F2.

12.2 Thermal Analysis Curves of Complexes of Transition Metals with Schiff Bases

Samples

The four complexes were prepared by Li Shulan *et al.*; their molecular formulas are (a) $\text{Cu}(\text{C}_8\text{H}_7\text{O}_2)_2(\text{C}_6\text{H}_4\text{N}_2)(\text{H}_2\text{O})$, (b) $\text{Ni}(\text{C}_8\text{H}_7\text{O}_2)(\text{C}_6\text{H}_4\text{N}_2)(\text{H}_2\text{O})$, (c) $\text{Cu}(\text{C}_8\text{H}_7\text{O}_2)_2(\text{C}_2\text{H}_4\text{N}_2)(\text{H}_2\text{O})$ and (d) $\text{Ni}(\text{C}_8\text{H}_7\text{O}_2)(\text{C}_2\text{H}_4\text{N}_2)(\text{H}_2\text{O})$.

Measurements

Perkin-Elmer TGS-2 thermogravimetric analyzer, heating rate $10^\circ\text{C min}^{-1}$, sample mass 1–4 mg, N_2 atmosphere (40 ml min^{-1}).

Results

Thermal decomposition temperature and mass-loss rates (%)

- (a) 139–175 $^\circ\text{C}$, 3.85%; 213–396 $^\circ\text{C}$, 32.97%; 396–980 $^\circ\text{C}$, 46.16%.
- (b) 70–138 $^\circ\text{C}$, 3.75%; 317–511 $^\circ\text{C}$, 29.67%; 511–780 $^\circ\text{C}$, 51.06%.
- (c) 108–241 $^\circ\text{C}$, 4.57%; 245–380 $^\circ\text{C}$, 32.00%; 380–668 $^\circ\text{C}$, 43.83%.
- (d) 81–238 $^\circ\text{C}$, 5.10%; 326–425 $^\circ\text{C}$, 32.46%; 425–795.5 $^\circ\text{C}$, 44.59%.

Thermal decomposition mechanisms:

- (a) Step 2: Mampel equation.
- (b), (c) Steps 2: Avrami–Erofeev equation (nucleation and growth, $n = 1.5$).
- (d) Step 2: contraction geometry shape (cylinder symmetry).

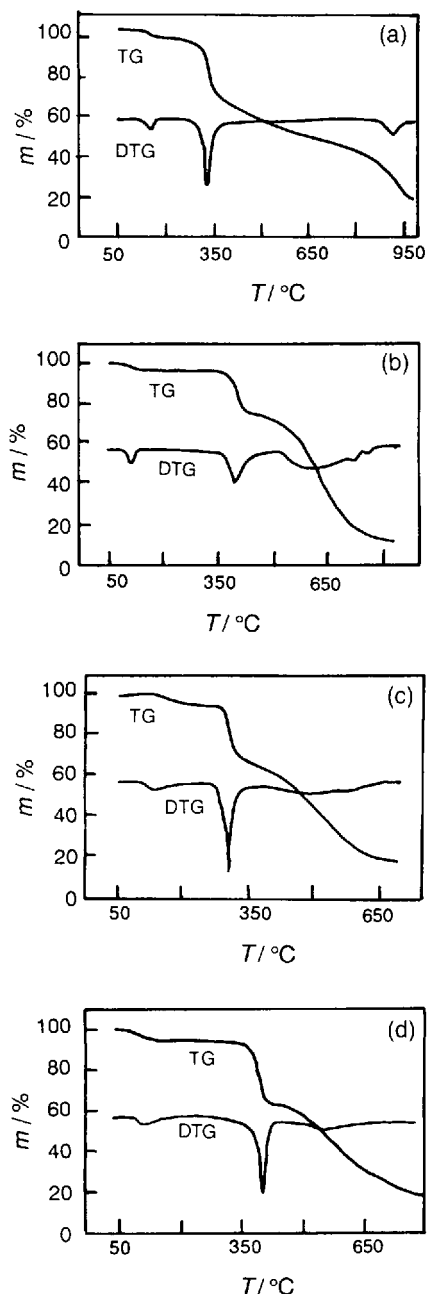


Figure 12.15 TG and DTG curves of (a) monoqua-3-methoxysalicylaldehyde-*o*-phenyldiaminecopper(II), (b) 3-methoxysalicylaldehyde-*o*-phenyldiamine nickel(II) monohydrate, (c) monoqua 3-methoxysalicylaldehyde-diethyldiaminecopper(II) and (d) 3-methoxysalicylaldehyde-diethyldiaminenickel(II) monohydrate (d)[4]

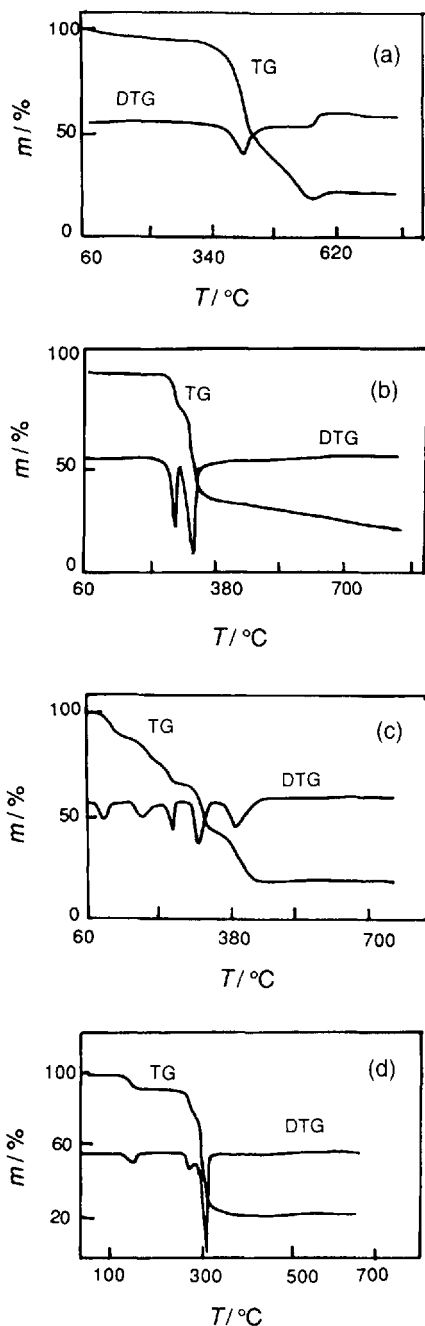


Figure 12.16 TG and DTG curves of (a) salicylaldehyde-*o*-aminobenzoic acid nickel(II) monohydrate, (b) salicylaldehyde-*o*-aminobenzoic acid copper (II) monoacetate, (c) N-salicylaldehyde-*o*-aminobenzoic acid dipyrindine copper(II) monohydrate and (d) *o*-vanillin-*o*-aminobenzoic acid copper(II) monohydrate [5–7]

Samples

The four complexes were prepared by Li Shulan *et al.*; their molecular formulas are

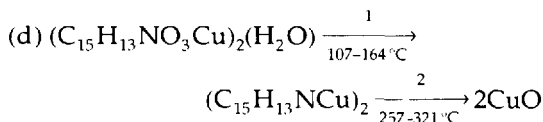
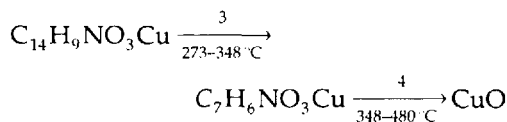
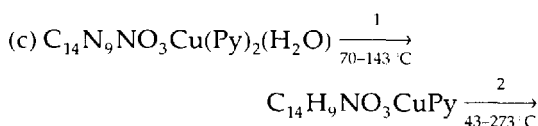
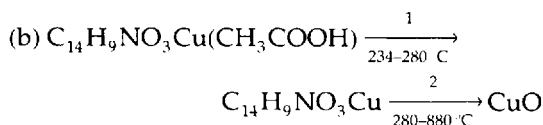
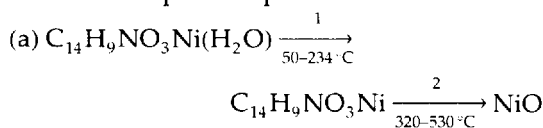
- (a) $C_{14}H_9NO_3Ni(H_2O)$,
- (b) $C_{14}H_9NO_3Cu(CH_3COOH)$,
- (c) $C_{14}H_9NO_3Cu(Py)_2(H_2O)$,
- (d) $(C_{15}H_{13}NO_3Cu)_2(H_2O)$.

Measurements

Perkin-Elmer TGS-2 thermogravimetric analyzer, heating rate $10^\circ C \text{ min}^{-1}$, sample mass 2–4 mg, N_2 atmosphere (40 ml min^{-1}).

Results

Thermal decomposition processes:



Thermal decomposition mechanisms and activation energies:

(a) Step 2: second-order chemical reaction, $E = 180.5 \text{ kJ mol}^{-1}$

(b) Steps 2: Avrami–Erofeev equation (coring and growth, $n = 1.5$), $E = 212.5 \text{ kJ mol}^{-1}$.

(c) Step 4: Avrami–Erofeev equation (coring and growth, $n = 2$), $E = 197.5 \text{ kJ mol}^{-1}$

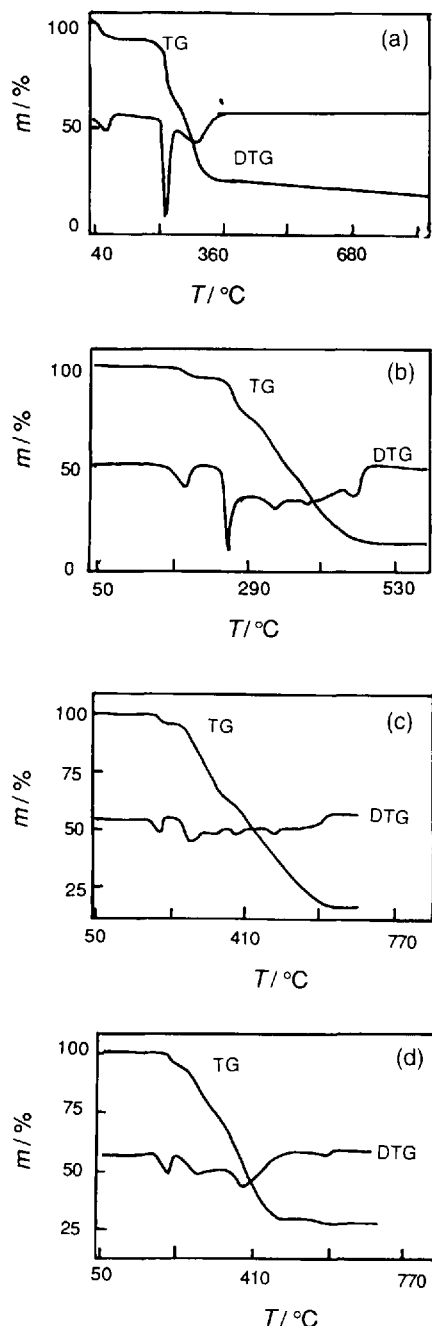


Figure 12.17 TG and DTG curves of (a) 3-methoxysalicylaldehydeleucinecopper(II) monoethylate, (b) 3-methoxysalicylaldehydeleucinenickel(II) monohydrate, (c) 3-methoxysalicylaldehydephenylalaninenickel(II) monohydrate and (d) 3-methoxysalicylaldehydealaninezinc(II) monohydrate[8]

Samples

The four complexes were prepared by Li Shulan *et al.*; their molecular formulae are (a) $\text{Cu}(\text{C}_7\text{H}_6\text{O}_2\text{CH}=\text{NC}_6\text{H}_{10}\text{O}_2)(\text{C}_2\text{H}_5\text{OH})$, (b) $\text{Ni}(\text{C}_7\text{H}_6\text{O}_2\text{CH}=\text{NC}_6\text{H}_{10}\text{O}_2)(\text{H}_2\text{O})$, (c) $\text{Ni}(\text{C}_7\text{H}_6\text{O}_2\text{CH}=\text{NC}_9\text{H}_8\text{O}_2)(\text{H}_2\text{O})$ and (d) $\text{Zn}(\text{C}_7\text{H}_6\text{O}_2\text{CH}=\text{NC}_3\text{H}_4\text{O}_2)(\text{H}_2\text{O})$.

Measurements

Perkin-Elmer TGS-2 thermogravimetric analyzer, heating rate $10^\circ\text{C min}^{-1}$; sample mass 2–4 mg, N_2 atmosphere (40 ml min^{-1}).

Results

Thermal decomposition temperatures and mass-loss rates (%):

(a) $40\text{--}90^\circ\text{C}$, 11.48%; $185\text{--}347^\circ\text{C}$, 70.64%.

(b) $134\text{--}225^\circ\text{C}$, 5.56%; $230\text{--}475^\circ\text{C}$, 74.91%.

(c) $183\text{--}232^\circ\text{C}$, 5.21%; $240\text{--}526^\circ\text{C}$, 79.86%.

(d) $172\text{--}230^\circ\text{C}$, 6.39%; $230\text{--}672^\circ\text{C}$, 67.36%.

Thermal decomposition mechanisms and activation energies:

(a) Step 1: second-order chemical reaction, $E = 135.4 \text{ kJ mol}^{-1}$.

(b) Step 1: Avrami-Erofeev equation (coring and growth, $n = 1$), $E = 145.2 \text{ kJ mol}^{-1}$.

(c) Step 1: Avrami-Erofeev equation (coring and growth, $n = 1$), $E = 233.5 \text{ kJ mol}^{-1}$.

(d) Step 1: contraction of geometrical shape (ball symmetry), $E = 181.6 \text{ kJ mol}^{-1}$;

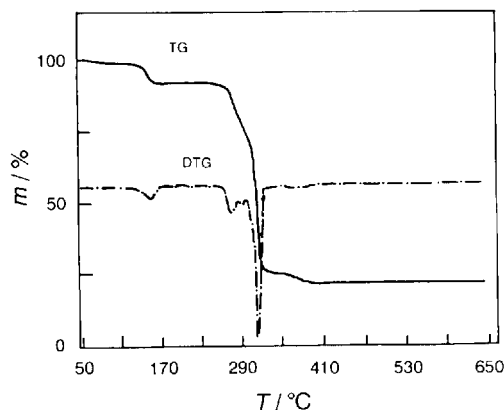


Figure 12.18 TG and DTG curves of bis[monoqua(3-methoxysalicylaldehyde-*o*-aminobenzoic acid copper(II)) monohydrate [6]

Sample

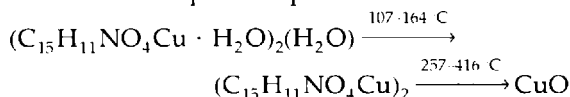
The complex was prepared by Wang Hong *et al.*; the molecular formula is $(C_{15}H_{11}NO_4Cu \cdot H_2O)_2(H_2O)$.

Measurements

Perkin-Elmer TGS-2 thermogravimetric analyzer, heating rate $10^\circ C \min^{-1}$; sample mass 4.6160 mg; N_2 atmosphere (40 ml min^{-1}).

Results

Thermal decomposition processes:



Thermal decomposition mechanism and activation energy:

Step 1: contraction of geometrical shape (ball symmetry), $E = 161.8 \text{ kJ mol}^{-1}$

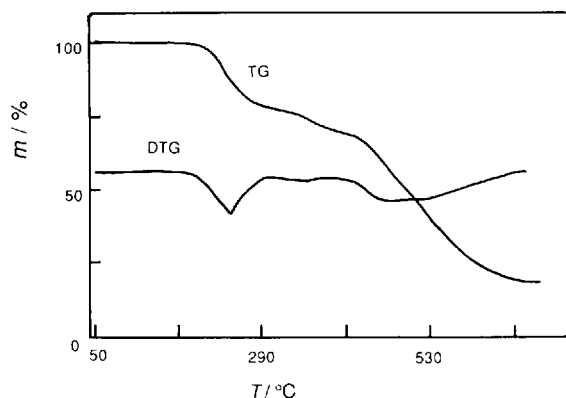


Figure 12.19 TG and DTG curves of bis[N-(2-hydroxyethyl)-*o*-vanillindiamino]zinc(II) [9]

Sample

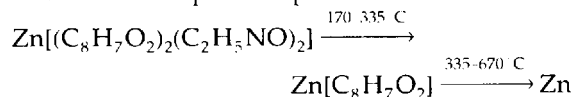
The complex was prepared by Wang Hong *et al.*; the molecular formula is $Zn[(C_8H_7O_2)_2(C_2H_5NO)_2]$

Measurements

Perkin-Elmer TGS-2 thermogravimetric analyzer, heating rate $10^\circ C \min^{-1}$, sample mass 5.2182 mg, N_2 atmosphere (40 ml min^{-1}).

Results

Thermal decomposition processes:



Thermal decomposition mechanism:

Step 1: second-order chemical reaction.

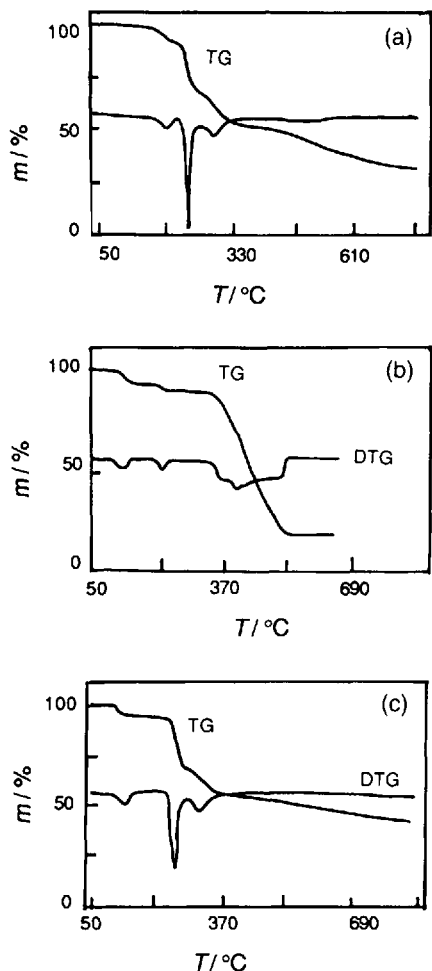


Figure 12.20 TG and DTG curves of (a) *o*-vanillinylicinecopper(II), (b) 2,4-dihydroxyacetophenoneethylenediiminatocopper(II) and (c) 2,4-dihydroxyacetophenoneethylenediaminonickel (II) [10]

Samples

The three complexes were prepared by Li Shulan *et al.*; their molecular formulas are (a) $\text{Cu}(\text{C}_7\text{H}_6\text{O}_2\text{CH}=\text{NC}_2\text{H}_2\text{O}_2)(\text{H}_2\text{O})$, (b) $\text{Cu}[\text{C}_6\text{H}_4\text{O}_2\text{C}(\text{CH}_3)=\text{NC}_2\text{H}_4\text{N}=\text{C}(\text{CH}_3)\text{C}_6\text{H}_4\text{O}_2](\text{H}_2\text{O})$ and (c) $\text{Ni}[\text{C}_6\text{H}_4\text{O}_2\text{C}(\text{CH}_3)=\text{NC}_2\text{H}_4\text{N}=\text{C}(\text{CH}_3)\text{C}_6\text{H}_4\text{O}_2]-(0.5\text{CH}_3\text{COOH})(\text{H}_2\text{O})$.

Measurements

Perkin-Elmer TGS-2 thermogravimetric analyzer, heating rate 10°C min , sample mass 2–5 mg, N_2 atmosphere (40 ml min^{-1}).

Results

Thermal decomposition temperatures:

(a) $123\text{--}221^\circ\text{C}$; $221\text{--}294^\circ\text{C}$; $294\text{--}745^\circ\text{C}$.

(b) $77\text{--}156^\circ\text{C}$; $229\text{--}288^\circ\text{C}$; $288\text{--}850^\circ\text{C}$.

(c) $80\text{--}101^\circ\text{C}$; $101\text{--}178^\circ\text{C}$; $178\text{--}603^\circ\text{C}$.

Thermal decomposition mechanisms:

(a) Step 2: Avrami-Erofeev equation (coring and growth, $n = 2$).

(b) Step 2: Avrami-Erofeev equation (coring and growth, $n = 1.5$).

(c) Step 2: Avrami-Erofeev equation (coring and growth, $n = 1.5$).

12.3 Thermal Analysis Curves of Other Complexes

Sample

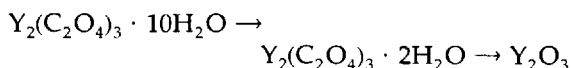
Yttrium oxalate decahydrate,
 $\text{Y}_2(\text{C}_2\text{O}_4)_3 \cdot 10\text{H}_2\text{O}$.

Measurements

Shimadzu DT-30, heating rate $10^\circ\text{C min}^{-1}$, sample mass 10 mg, air atmosphere (50 ml min^{-1}) or steam atmosphere (50 ml min^{-1}).

Results

Thermal decomposition processes under steam atmosphere:



Activation energy of dehydration process of $\text{Y}_2(\text{C}_2\text{O}_4)_3 \cdot 10\text{H}_2\text{O}$ under a steam atmosphere, $E = 36.6 \text{ kJ mol}^{-1}$.

There is no intermediate of $\text{Y}_2\text{O}_2\text{CO}_3$ in the decomposition processes, which makes the temperature of decomposition lower.

Y_2O_3 ultrafine powders with diameters of about 0.03 μm were obtained.

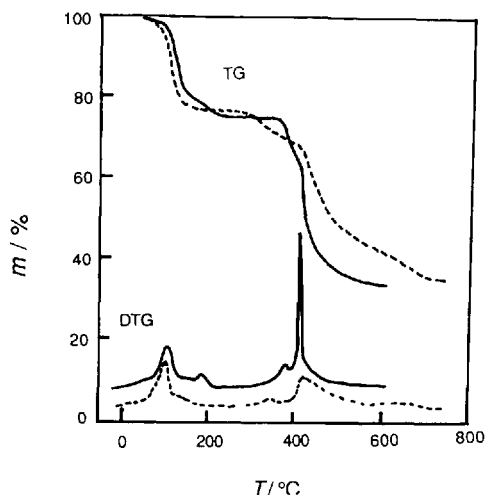


Figure 12.21 TG-DTG curves of yttrium oxalate decahydrate under an air atmosphere (---) and a steam atmosphere (—)

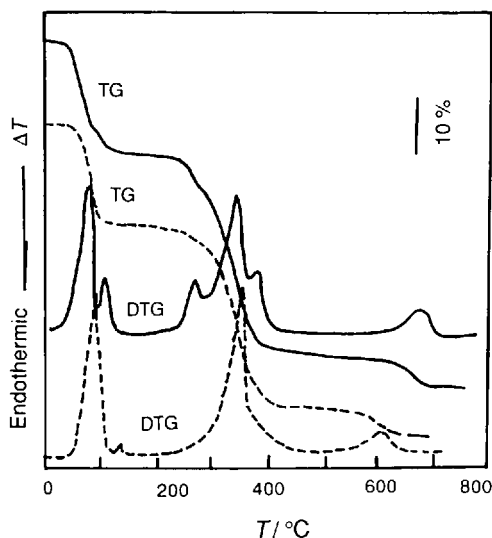


Figure 12.22 TG-DTA curves of rare earth acetates, $\text{Nd}(\text{CH}_3\text{COO})_3 \cdot 4\text{H}_2\text{O}$ (—) and $\text{Gd}(\text{CH}_3\text{COO})_3 \cdot 4\text{H}_2\text{O}$ (---) [12,13]

Samples

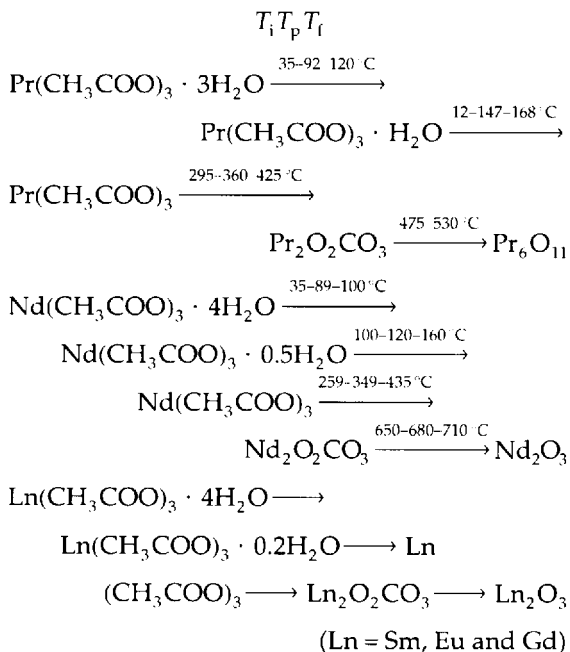
Rare earth acetates, $\text{Ln}(\text{CH}_3\text{COO})_3 \cdot 4\text{H}_2\text{O}$, $\text{Ln} = \text{Pr, Nd, Sm, Eu, Gd}$.

Measurements

Shimadzu DT-30, heating rate $10^\circ\text{C min}^{-1}$, sample mass 10 mg, air atmosphere (50 ml min^{-1}).

Results

Thermal decomposition processes:



Activation energies of dehydration processes, $E = 66.5-84 \text{ kJ/mol}^{-1}$; activation energies of decomposition processes, $E = 225.4-244.9 \text{ kJ mol}^{-1}$.

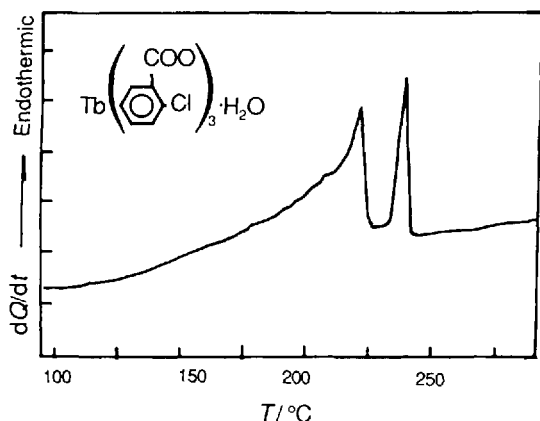


Figure 12.23 DSC curve of terbium *o*-chlorobenzoate [14]

Sample

Terbium chlorobenzoate, $\text{Tb}(\text{ClC}_6\text{H}_4\text{COO})_3 \cdot \text{H}_2\text{O}$.

Measurements

Perkin-Elmer DSC-7; heating rate $30^\circ\text{C min}^{-1}$, sample mass 15.2 mg, N_2 atmosphere (50 ml min^{-1}).

Results

Temperature of peak of dehydration process, $T = 221^\circ\text{C}$. Enthalpy change of dehydration process, $\Delta H = 73.0 \text{ kJ mol}^{-1}$. Solid-state transition of the complex occurs at 239°C , the enthalpy change for the process, $\Delta H = 16.0 \text{ kJ mol}^{-1}$.

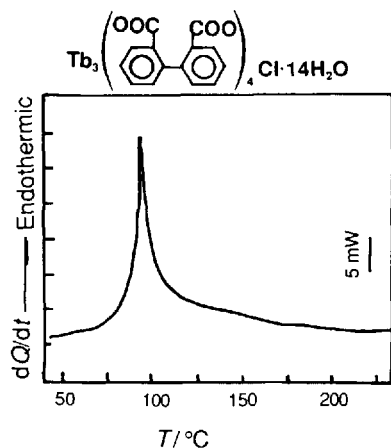


Figure 12.24 DSC curve of tetrakis(dibenzoate)tetradecaaquatriserbium chloride [14]

Sample

Tetrakis(dibenzoate)tetradecaaquatriserbium chloride, $\text{Tb}_3(\text{OOC}_6\text{H}_4\text{C}_6\text{H}_4\text{COO})_4\text{Cl} \cdot 14\text{H}_2\text{O}$.

Measurements

Perkin-Elmer DSC-7; heating rate $30^\circ\text{C min}^{-1}$, sample mass 7.5 mg, N_2 atmosphere (50 ml min^{-1}).

Results

The dehydration reaction of the complex involves only one step; temperature of peak of dehydration reaction, $T = 93.4^\circ\text{C}$. Enthalpy change for dehydration reaction, $\Delta H = 582.8 \text{ kJ mol}^{-1}$.

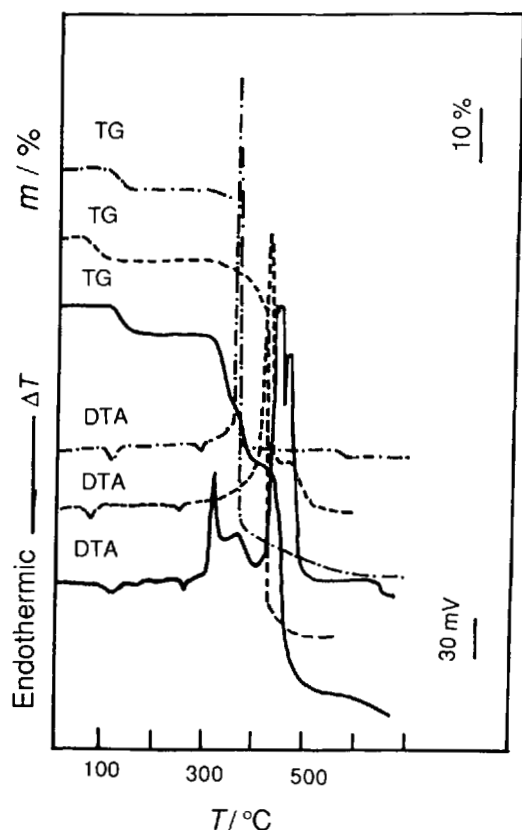


Figure 12.25 TG-DTA curves of rare earth *m*-nitrobenzoates $\text{LaL}_3 \cdot 2\text{H}_2\text{O}$ (—), $\text{LuL}_3 \cdot 2\text{H}_2\text{O}$ (---) and $\text{NdL}_3 \cdot 2\text{H}_2\text{O}$ (-.-) [14]

Samples

Rare earth *m*-nitrobenzoates, $\text{LnL}_3 \cdot n\text{H}_2\text{O}$ ($n = 2$, $\text{Ln} = \text{La} \rightarrow \text{Lu}$, Y ; $n = 0$, $\text{Ln} = \text{Sc}$).

Measurements

Shimadzu DT-30, heating rate $10^\circ\text{C min}^{-1}$, sample mass 10 mg; air atmosphere (50 ml min^{-1}).

Results

Dehydration reactions of hydrous complexes involve only one step.

Solid-state transition of the complexes occurs at about 300°C .

Dehydration temperatures of the complexes decrease with increase in atomic number of the rare earths, but decomposition temperatures increase.

The relationship between activation energies for dehydration processes and atomic numbers of the rare earths shows a 'W effect'.

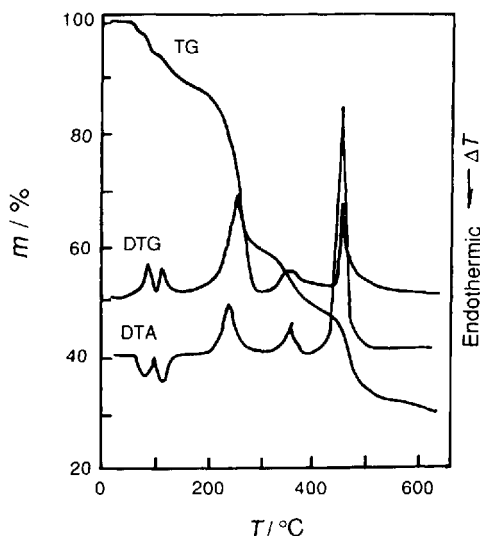


Figure 12.26 TG-DTG-DTA curves of terbium *o*-hydroxybenzoate [14]

Sample

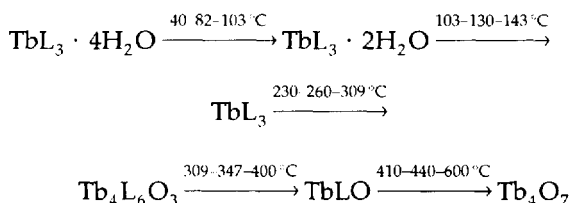
Terbium *o*-hydroxybenzoate,
 $\text{Tb}(\text{OOCCH}_6\text{H}_4\text{OH})_3 \cdot 4\text{H}_2\text{O}$.

Measurements

Shimadzu DT-30, heating rate $10^\circ\text{C min}^{-1}$, sample mass 10 mg; air atmosphere (50 ml min^{-1}).

Results

Thermal decomposition processes:



Activation energies for dehydration processes are 40.1 and 58.8 kJ mol^{-1} , respectively.

Enthalpy changes for dehydration processes are 70.0 and 85.3 kJ mol^{-1} , respectively.

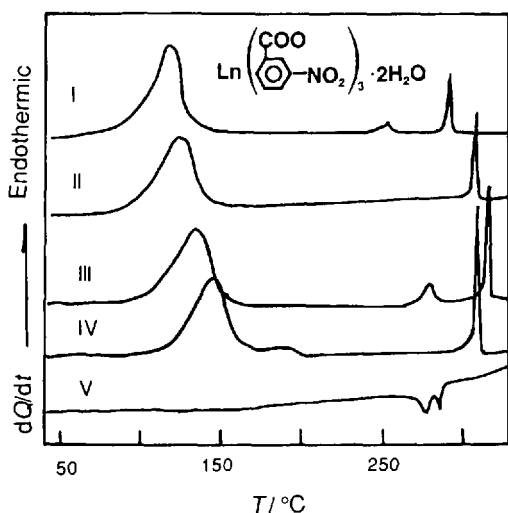


Figure 12.27 DSC curves of rare earth *m*-nitrobenzoates [15,16].

Samples

Rare earth *m*-nitrobenzoates, $\text{Ln}(\text{OOCCH}_4\text{NO}_2)_3 \cdot 2\text{H}_2\text{O}$ (Ln = I, Y; II, Ho; III, Tb; IV, Pr; V, Ho). V-cooling DSC curve

Measurements

Perkin-Elmer DSC-7, heating rate $30^\circ\text{C min}^{-1}$, cooling rate $300^\circ\text{C min}^{-1}$ for sample 5, sample mass 15 mg, N_2 atmosphere (50 ml min^{-1}).

Results

Enthalpy changes for dehydration processes of the complexes, $\Delta H = 119.4\text{--}152.4 \text{ kJ mol}^{-1}$.

LnL_3 (Ln = Nd \rightarrow Dy, Er, Tm and Y) show two solid-state transitions at about 300°C and total enthalpy changes $\Delta H = 14.0\text{--}30.0 \text{ kJ mol}^{-1}$.

Sample

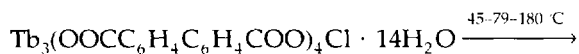
Tetrakis(dibenzoate)tetradecaquatristerbium chloride, $\text{Tb}_3(\text{OOC}_6\text{H}_4\text{C}_6\text{H}_4\text{COO})_4\text{Cl} \cdot 14\text{H}_2\text{O}$.

Measurements

Shimadzu DT-30, heating rate $10^\circ\text{C min}^{-1}$, sample mass 10 mg, air atmosphere (50 ml min^{-1}).

Results

Thermal decomposition processes:



Activation energies for dehydration process of the complex are $E = 70.8\text{ kJ mol}^{-1}$ (Ozawa method) and 66.2 kJ mol^{-1} (Kissinger method).

The terbium oxide formed is an ultrafine powder.

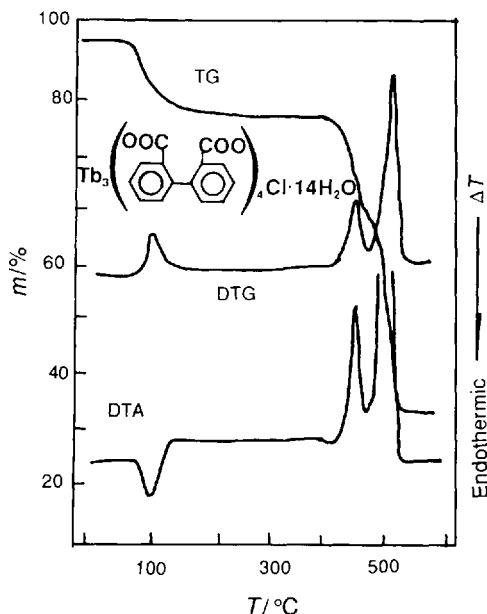


Figure 12.28 TG-DTG-DTA curves of tetrakis(dibenzoate)tetradecaquatristerbium chloride [14]

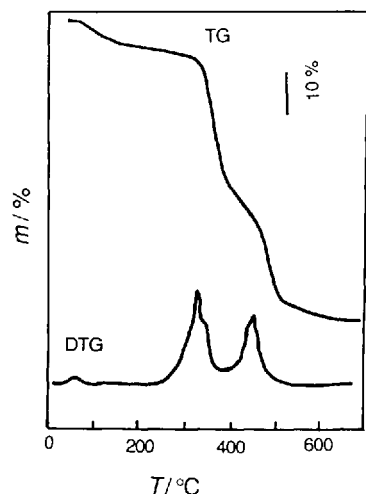


Figure 12.29 TG-DTG curves of europium *N*-acetylalanate [17]

Sample

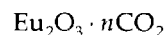
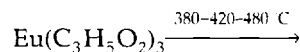
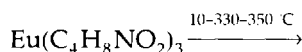
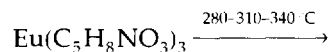
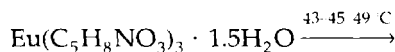
Europium *N*-acetylalanate, $\text{Eu}(\text{CH}_3\text{CH}(\text{NHCOCH}_3)\text{COO})_3 \cdot 1.5\text{H}_2\text{O}$

Measurements

Shimadzu DT-30, heating rate 5°C min^{-1} , sample mass 2.1 m, air atmosphere (60 ml min^{-1}).

Results

Thermal decomposition processes:



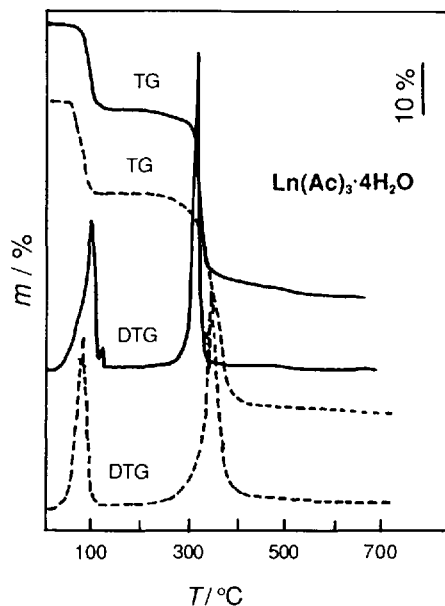


Figure 12.31 TG-DTG curves of heavy rare earth acetates, $\text{Tb}(\text{OAc})_3 \cdot 4\text{H}_2\text{O}$ (—) and $\text{Yb}(\text{OAc})_3 \cdot 4\text{H}_2\text{O}$ (---) [18]

Samples

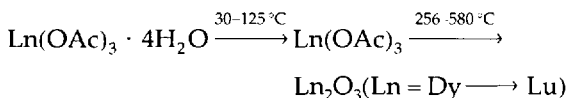
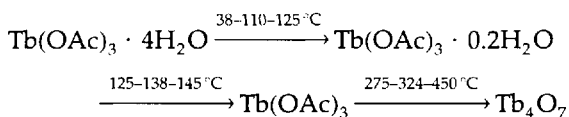
Heavy rare earth acetates, $\text{Ln}(\text{OAc})_3 \cdot 4\text{H}_2\text{O}$ ($\text{Ln} = \text{Tb-Lu}$).

Measurements

Shimadzu DT-30, heating rate $10^\circ\text{C min}^{-1}$, sample mass 10 mg; air atmosphere (50 ml min^{-1}).

Results

Thermal decomposition processes:



Activation energy for dehydration process of terbium acetate, $E = 81.3 \text{ kJ mol}^{-1}$ the activation energies for the others, $E = 78-99 \text{ kJ mol}^{-1}$; Enthalpy changes for dehydration processes of the complexes, $\Delta H = -183$ to -225 kJ mol^{-1} .

For decomposition processes of the complexes, $E = 126-179 \text{ kJ mol}^{-1}$, $\Delta H = 341-576.9 \text{ kJ mol}^{-1}$.

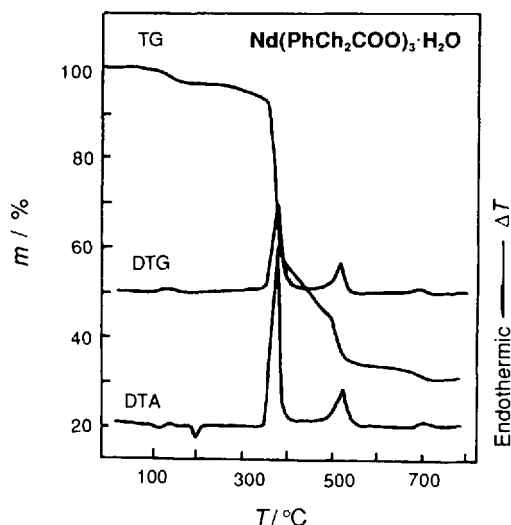


Figure 12.32 TG-DTG-DTA curves of neodymium phenylacetate [19]

Sample

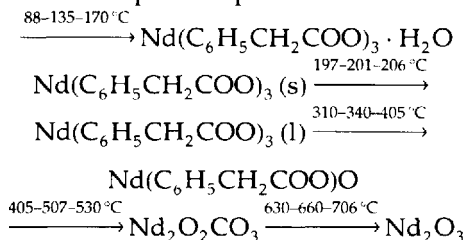
Neodymium phenylacetate, $\text{Nd}(\text{C}_6\text{H}_5\text{CH}_2\text{COO})_3 \cdot \text{H}_2\text{O}$.

Measurements

Shimadzu DT-30, heating rate $10^\circ\text{C min}^{-1}$, sample mass 10 mg, air atmosphere (50 ml min^{-1}).

Results

Thermal decomposition processes:



The enthalpy change for dehydration process, $\Delta H = 30.0 \text{ kJ mol}^{-1}$. Enthalpy change and entropy change for melting, $\Delta H = 25.3 \text{ kJ mol}^{-1}$ and $\Delta S = 53.4 \text{ J mol}^{-1} \text{ K}^{-1}$.

Sample

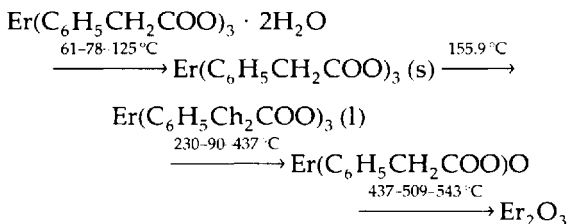
Erbium phenylacetate, $\text{Er}(\text{C}_6\text{H}_5\text{CH}_2\text{COO})_3 \cdot 2\text{H}_2\text{O}$.

Measurements

Shimadzu DT-30, heating rate $10^\circ\text{C min}^{-1}$, sample mass 10 mg, air atmosphere (50 ml min^{-1}).

Results

Thermal decomposition processes:



Activation energy and enthalpy change for dehydration process, $E = 97.2 \text{ kJ mol}^{-1}$ ($n = 2$) and $\Delta H = 82.2 \text{ kJ mol}^{-1}$. Enthalpy change and entropy change for melting process, $\Delta H = 38.1 \text{ kJ mol}^{-1}$ and $\Delta S = 88.9 \text{ J mol}^{-1} \text{ K}^{-1}$.

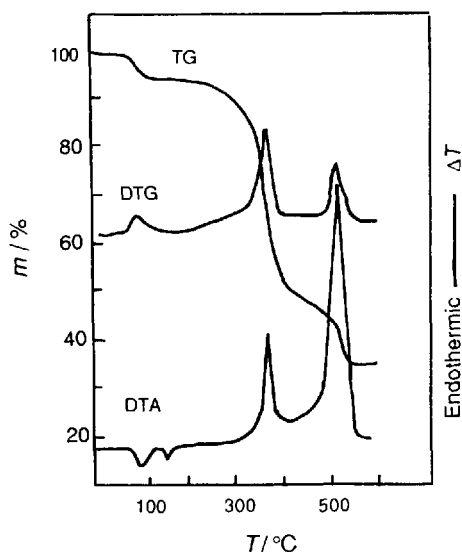


Figure 12.33 TG-DTG-DTA curves of erbium phenylacetate [20]

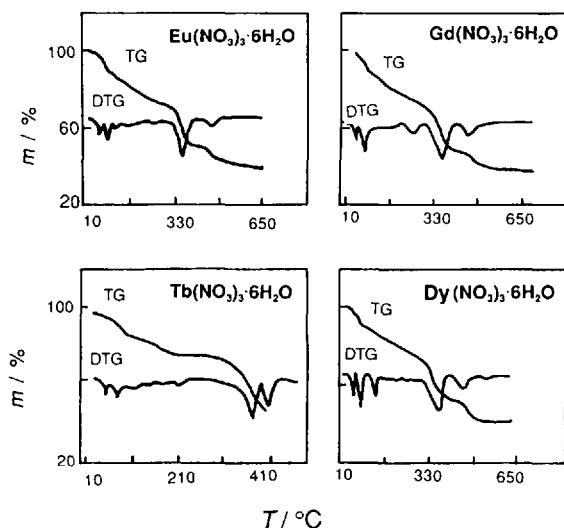


Figure 12.34 TG-DTG curves of hydrous medium rare earth nitrates [21]

Samples

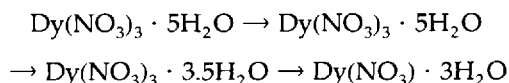
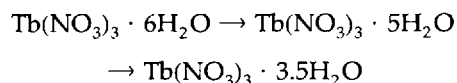
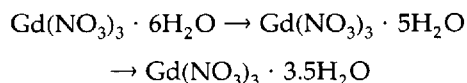
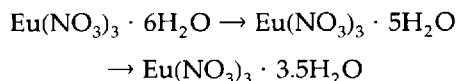
Hydrous medium rare earth nitrates, $\text{Ln}(\text{NO}_3)_3 \cdot 6\text{H}_2\text{O}$ ($\text{Ln} = \text{Eu, Gd, Tb and Dy}$).

Measurements

Perkin-Elmer TG-2, heating rate $10^\circ\text{C}\cdot\text{min}^{-1}$, sample mass 10 mg, N_2 atmosphere (50 ml min^{-1}).

Results

Dehydration processes:



Activation energies for dehydration processes, $E = 80170\text{ kJ/mol}$

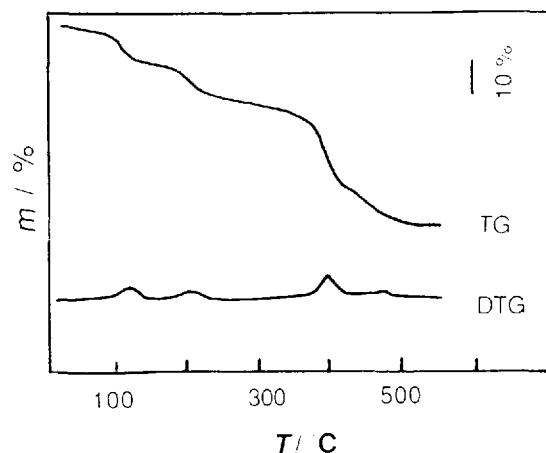


Figure 12.35 TG and DTG curves of monoserinethulium nitrilotriacetate [22]

Sample

Monoserinethulium nitrilotriacetate, $\text{Tm}(\text{NTA})$ (Ser); $\text{Tm}[\text{N}(\text{CH}_2\text{COO})_3][\text{HOCH}_2\text{CH}(\text{NH}_2)\text{COOH}]$.

Measurements

Shimadzu DT-30, heating rate 5°C min^{-1} , sample mass 3.58 mg, air atmosphere (60 ml min^{-1}).

Results

Thermal decomposition processes: $\text{Tm}(\text{NTA})$ (Ser) $\rightarrow \text{Tm}(\text{NTA})(\text{HOCH}_2\text{CH}_3 \rightarrow \text{Tm}(\text{NTA}) \rightarrow \text{Tm}(\text{HCOO})_3 \rightarrow \text{Tm}_2(\text{CO}_3)_3 \rightarrow \text{Tm}_2\text{O}_3$

12.4 References

- 1 Sun Tonshan, Zhao Yuting, Jin Jiahui and Wang Daqing, *J. Thermal Anal.*, 1995, **45**, 317.
- 2 Sun Tongshan, Xio Yumei, Wang Daqing, Wang Fenglian and Zhao Yuting, *Thermochim. Acta*, 1996, **287**, 199.
- 3 Xio Yumei, MS., Thesis, Shangong University, Jinan, 1996.
- 4 Li Shulan, Liu Dexin, Zhang Shengqiang, Wang Hong, and Yang Zhaohe, *Thermochim. Acta*, 1996, **275**, 215.
- 5 Li Shulan, Liu Dexin, Zhou Alanhua, Zhang Shengqiang, Liu Liang and Yang Zhaohe, *Chem. Res. Chin. Univ.*, 1996, **12**(2), 194.
- 6 Wang Hong, Li Shulan, Liu Dexin, Cui Xuegui, Li Xiaoyan and Yang Zhaohe, *Chem. J. Chin. Univ.*, 1994, **15**(4), 485.
- 7 Li Shulan, Liu Dexin, Meng Fanqin, Zhou Jianhua and, Yang Zhaohe, *Chin. J. Struct. Chem.*, 1995, **1**, 55.
- 8 Li Shulan, Wang Hong, Liu Dexin, Cui Xuegui, Li Xiaoyan and Yang Zhaohe, *Acta Chim. Sin.*, 1995, **53**, 455.
- 9 Wang Hong, Li Shulan, Liu Dexin and Yang Zhaohe, *J. Shandong Univ.*, 1995, **30**(4), 474.
- 10 Li Shulan, Liu Dexi, Cui Xuegui, Li Xiaoyan and Sun Hongjian, *J. Shandong Univ.*, 1993, **28**(4), 442.
- 11 Wang Zenglin, Tang Gongben and Sun Wanming, *Chin. J. Less-Common Met.* 1991, **15**, 272 (in Chinese).
- 12 Sun Wanming, Wang Zenglin, Tang Gongben and Ni Jiazuan, *Chin. J. Rare Earths*, 1992, **10**, 120 (in Chinese).
- 13 Wang Zenglin, Sun Wanming, Tang Gongben and Ni Jiazuan, *Chin. J. Rare Earths*, 1992, **10**, 18 (in Chinese).
- 14 Wang Zenglin, Ma Jiafang, Niu Chunji and Ni Jiazuan, *Chin. J. Inorg. Chem.*, 1992, **8**, 396 (in Chinese).
- 15 Wang Zenglin, Niu Chunji, Ma Jianfang and Ni Jiazuan, *Chin. J. Appl. Chem.*, 1993, **10**, 28 (in Chinese).
- 16 Wang Zenglin, Niu Chunji, Ma Jiafang and Ni Jiazuan, *J. Thermal Anal.*, 1994, **41**, 899.
- 17 Jia Yuqing, Sun Wanming and Niu Chunji, *Thermochim. Acta*, 1992, **196**, 85.
- 18 Wang Zenglin, Zhuang Wende, Sun Wanming and Ni Jiazuan, *Chin. J. Rare Earths*, 1991, **9**, 104 (in Chinese).
- 19 Wang Zenglin, Jin Zhongsheng, Niu Chunji and Ni Jianzuan, *Chin. J. Rare Earths*, 1992, **10**, 102 (in Chinese).
- 20 Wang Zenglin, Hu Ninghai, Niu Chunji and Ni Jianzuan, *Acta Phys.-Chim.*, 1992, **8**, 642. (in Chinese).
- 21 Gao Shenglin, Yang Zupei and Wang Zenglin, *Chin. J. Rare Earths*, 1990, **8**, 110 (in Chinese).
- 22 Sun Wangming, Niu Chungji and Jia Yuqing, *Thermochim. Acta*, 1992, **208**, 18.

DTA–EGD–GC Coupled Simultaneous Thermal Analysis Curves

The DTA–EGD–GC on-line coupled simultaneous technique and associated equipment have been in use since the 1980s [1–3]. The principles and applications in various areas of science of the DTA–EGD–GC technique were outlined in Part I, Sections 2.4.3 and 5.3.1.

The following functions can be delineated:

1. The EGD curve traces the variations on the DTA curve. The feature of an endotherm or exotherm on the DTA curve enables one to detect whether it is due to a physical process or a chemical process.
2. According to the calibration line of the evolved gas which was released in the process of the thermal decomposition of samples, each chemical reaction can be detected while applying the quantitative method of EGD, i.e. the QEGD method [3].
3. According to the variations on the DTA–EGD curves, relevant components of the reaction gases evolved at any temperature can be intercepted and analyzed by GC by operating a sampling valve at certain intervals.
4. The sampling of the reaction gases evolved can be employed not only under programmed heating, but also under programmed cooling and with a predetermined isothermal temperature of reaction.
5. The information and data on the above four aspects of DTA–EGD–GC and temperature can be obtained by one test on a single sample of milligram size under the same conditions.
6. The apparatus also enables one to evaluate DTA–EGD (or QEGD) curves or DTA–GC curves according to the experimental purpose.
7. The DTA–EGD–GC on-line coupled simultaneous technique provides a microscale experimental method that is precise and rapid for the investigation of the reaction processes involved in the thermal decomposition of samples. The variations of the composition of reaction gases evolved can be traced and the mechanism of gas–solid phase and gas–gas phase thermal reactions in an inert gas or reactant gas can be studied.

This chapter presents DTA–EGD–GC curves and data in areas such as solid catalysts, anti-oxidant additives in petroleum, minerals and thermal properties of coal.

13.1 Solid Catalysts

Sample

The sample was provided by the Research Institute of Industrial Catalysis (ECUST), China.

Measurements

DTA— $\pm 100 \mu\text{V}$; heating rate, $10^\circ\text{C min}^{-1}$ isothermal reaction temperatures, 400, 350, 300 250 $^\circ\text{C}$; reference material, empty crucible; composition of reaction gases, volume ratio (%) of $\text{CO}:\text{O}_2:\text{N}_2 = 2.7:5:92.3$ flow-rate, 35 ml min^{-1} ; LaMnO mass, 2.16 mg.

GC—TCD₂—Bridge current, 140 mA cell temperature, 60°C ; chromatographic columns in series, 401—organic support and 5A molecular sieve; carrier gas, argon; flow-rate, 20 ml min^{-1} .

Results

$\text{CO} + \frac{1}{2} \text{O}_2 \rightarrow \text{CO}_2$ as a model reaction (exotherm).

The conversion degree (%) of $\text{CO} \rightarrow \text{CO}_2$ at various isothermal temperatures is shown in the figure.

The oxidative activity of LaMnO_3 is lower than those of LaCoO_3 (Figure 13.2) and $\text{La}_{0.7}\text{Sr}_{0.3}\text{CoO}_3$ (Figure 13.3).

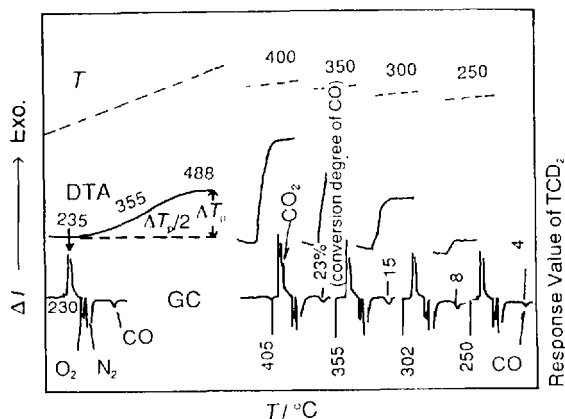


Figure 13.1 DTA-GC curves of LaMnO_3 catalyst for purification of exhaust gases [4-6]

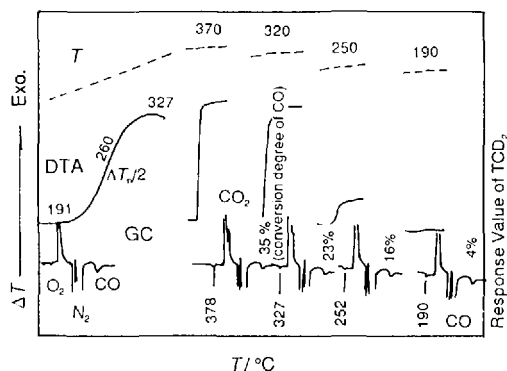


Figure 13.2 DTA-GC curve of LaCoO_3 catalyst for purification of exhaust gases [4-6]

Sample and measurements

LaCoO_3 mass, 2.08 mg.

Isothermal reaction temperature 370, 320, 290 and 190 °C.

Sample source and measurement conditions as in Figure 13.1.

Results

The conversion degree (%) of CO to CO_2 at various isothermal temperatures are shown in Figure 13.2.

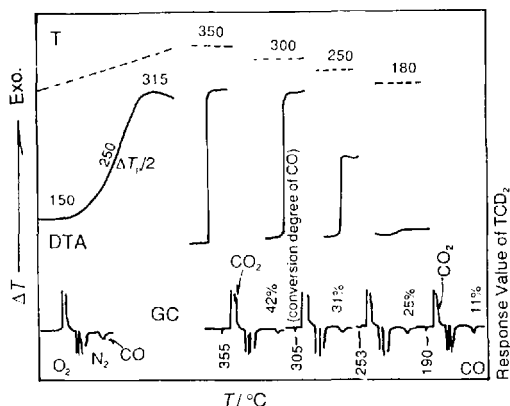


Figure 13.3 DTA-GC curves of $\text{La}_{0.7}\text{Sr}_{0.3}\text{CoO}_3$ catalyst for purification of exhaust gases [4-6]

Sample and measurements

$\text{La}_{0.7}\text{Sr}_{0.3}\text{CoO}_3$ mass, 2.00 mg. Isothermal reaction temperatures, 350, 300, 250 and 180 °C. Sample source and measurement conditions as in Figure 13.1.

Results

The conversion degree (%) of CO to CO_2 at various isothermal temperatures is shown in Figure 13.3.

The experimental results indicated that the order of oxidation activity for the purification of automotive exhaust gases of three perovskite catalysts containing rare earth is as follows: $\text{La}_{0.7}\text{Sr}_{0.3}\text{CoO}_3 > \text{LaCoO}_3 > \text{LaMnO}_3$. The results were confirmed by evaluation using a reactor.

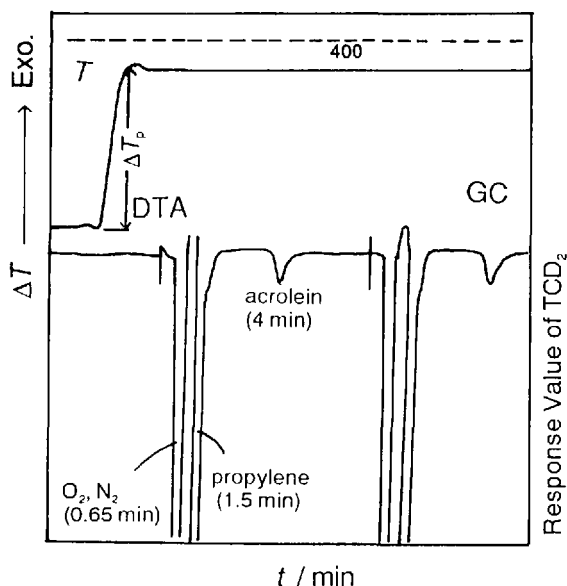


Figure 13.4 DTA-GC curves for screening the calcination conditions for a multicomponent oxide catalyst [7]

Sample

The multicomponent oxide catalyst $\text{Co}_a\text{Fe}_b\text{Bi}_c\text{Mo}_d$ was used for the oxidation of dilute propylene to acrolein. The catalyst was provided by Research Institute of Industrial Catalysis, (ECUST).

Measurements

DTA— $\pm 100 \mu\text{V}$; isothermal reaction temperature, 400°C ; reference material, empty crucible; sample mass, 20 mg; composition ratio (%) of reaction gases of propylene $\text{CO} : \text{O}_2 : \text{N}_2 = 2 : 4 : 94$.

GC-TCD₂—Bridge current, 240 mA; cell temperature, 130°C ; carrier gas, H_2 ; flow-rate, 25 ml min^{-1} ; chromatographic column, Porapak-QS.

Results

Owing to a number of by-products in the reaction products, the height of the exothermic peak on the DTA curve does not bear a direct relationship to the peak area of acrolein on the gas chromatogram. When the calcination temperature was $T + 50^\circ\text{C}$ and the calcination time at $t + 1 \text{ h}$, the peak area of acrolein on the gas chromatogram increased although the peak height on the DTA trace decreased.

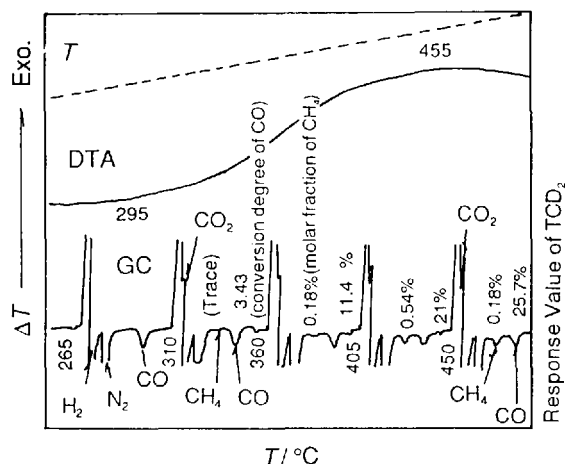


Figure 13.5 DTA–GC curves for screening the methanation activity of an Ni/Al₂O₃ catalyst

Sample

The sample was provided by Research Institute of Industrial Catalysis (ECUST).

Measurements

DTA— ± 100 mV; $10^\circ\text{C min}^{-1}$; composition ratio (%) of reaction gases CO:H₂: N₂ = 4.6 : 15.4 : 80%; flow-rate, 20 ml min^{-1} ; sample mass, 5.39 mg; reference material, empty crucible;

GC–TCD₂—Bridge current, 160 mA; cell temperature, 60°C ; chromatographic columns in series; carrier gas, argon; flow-rate, 40 ml min^{-1} .

Results

The conversion degree (%) of CO and molar fraction (%) of CH₄ in tail gases are shown on the GC plot at various temperatures (265, 310, 360, 405 and 450°C). The methanation activity of the Ni/Al₂O₃ catalyst is low.

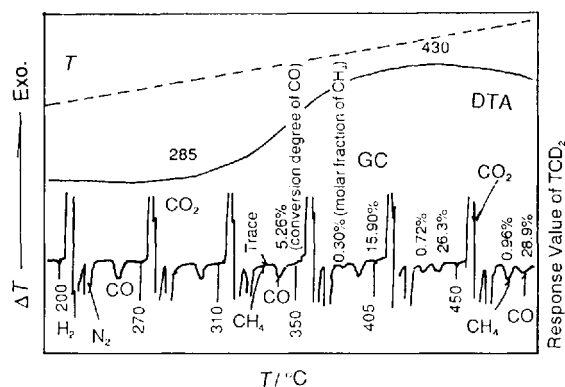


Figure 13.6 DTA–GC curves for screening the methanation activity of an Ni–La₂O₃/Al₂O₃ catalyst [8]

Sample and measurements

Sample mass, 5.40 mg. Sample source and measurement conditions as in Figure 13–5.

Results

The initial reaction temperature and ΔT_{max} are shown in the figure. The CO conversion degree (%) and the molar fraction (%) of CH₄ in the tail gases at various temperatures are shown in the figure. The methanation activity of the Ni–La₂O₃/Al₂O₃ catalyst is moderate.

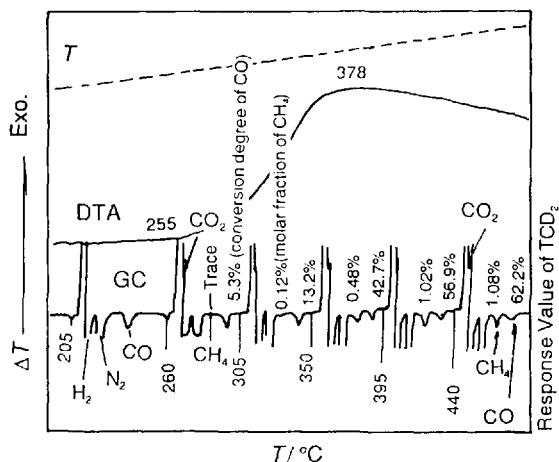


Figure 13.7 DTA-GC curves for screening the methanation activity of an Ni-La₂O₃-Pd/Al₂O₃ catalyst

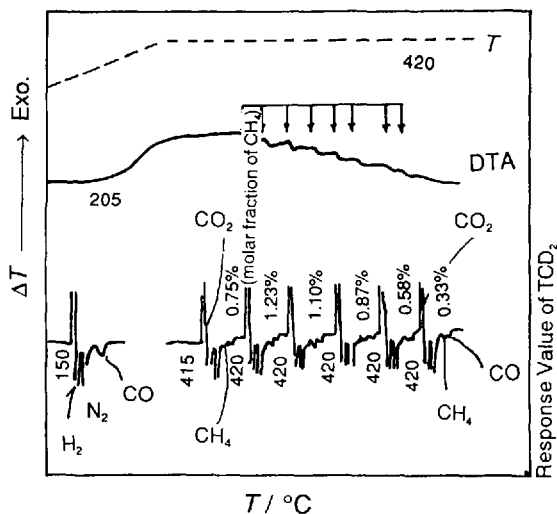


Figure 13.8 DTA-GC curves of poisoning effect by pulsing SO₂ on a Ni/Al₂O₃ catalyst. Arrows indicate that catalyst was poisoned 8 times by volume fraction 0.86% SO₂, every time 2 ml, total amount 16 ml

Sample and measurements

Sample mass, 5.41 mg. Sample source and measurement conditions as in Figure 13.5.

Results

The conversion (%) of CO and the molar fraction (%) of CH₄ (mol%) in the tail gases at various temperatures (205, 260, 305, 350, 395 and 440 °C) are shown in the figure. The order of the activity and selectivity for the above three methanation catalysts is Ni-La₂O₃-Pd/Al₂O₃ » Ni-La₂O₃/Al₂O₃ > Ni/Al₂O₃.

Samples and measurements

Sample mass, 5.39 mg. Sample source and measurement conditions as in Figure 13.4.

Results

By pulsing SO₂ eight times with 16 ml of the titrant for 30 min, the Ni/Al₂O₃ catalyst lost its activity. When Figure 5.19 is compared with Figure 13.8, the resistance to sulfur of the Ni-La₂O₃-Pd/Al₂O₃ catalyst is one order of magnitude higher than that of Ni/Al₂O₃.

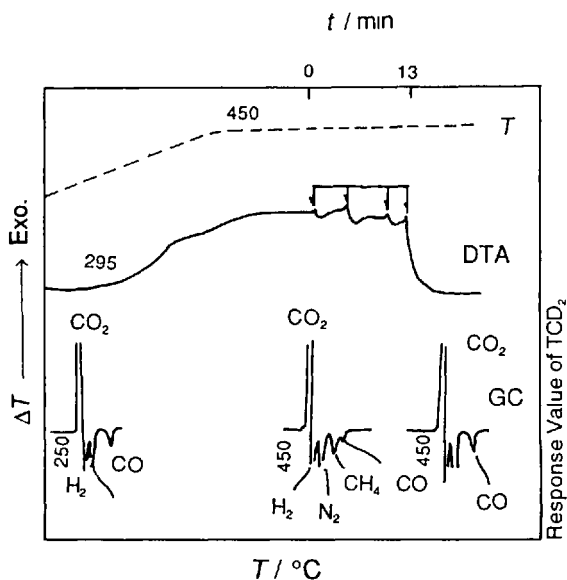


Figure 13.9 DTA-GC curves of poisoning effect by pulsing H_2S on an $\text{Ni-La}_2\text{O}_3\text{-Pd/Al}_2\text{O}_3$ catalyst [9]. Arrows indicate impulse poisoning by higher concentration H_2S , titration amount 16 ml in all

Samples and measurements

Sample mass, 5.38 mg. The poisoning effect of high concentration H_2S on the $\text{Ni/Al}_2\text{O}_3$ catalyst was examined under isothermal conditions at 450 °C. Sample source and measurement conditions as in Figure 13-5.

Results

By pulsing H_2S four times with 16 ml of the titrant for 13 min, the $\text{Ni/Al}_2\text{O}_3$ catalyst lost its activity. The exothermic curve decreased rapidly, the CH_4 peak disappeared and the CO peak maintained its original height on the gas chromatogram.

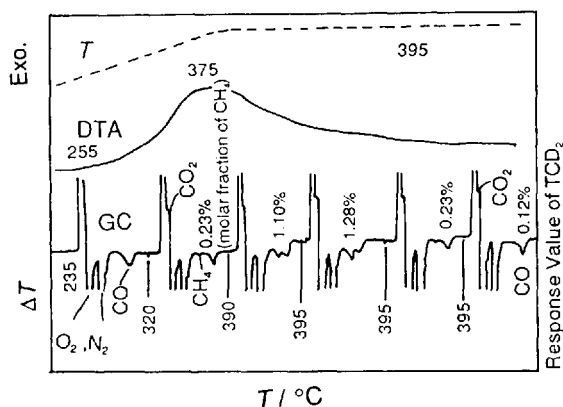


Figure 13.10 DTA-GC curves of Ni-La₂O₃-Pd/Al₂O₃ catalyst after regeneration following sulfur poisoning [10]

Sample and measurements

Sample mass, 2.95 mg. Method of regeneration as in Section 5.3. Sample source and measurement conditions as in Figure 13.5.

Results

The methanation activity of the Ni-La₂O₃-Pd/Al₂O₃ catalyst after regeneration following sulfur poisoning can be restored slightly (see Section 5.3).

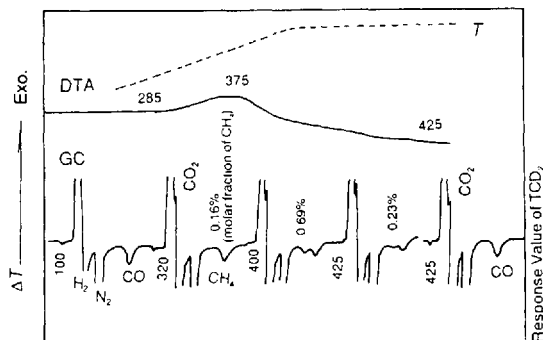


Figure 13.11 DTA-GC curves of Ni/Al₂O₃ catalyst after regeneration following sulfur poisoning [8]

Sample and measurements

Sample mass, 3.35 mg. Measurement conditions as in Section 5.3.

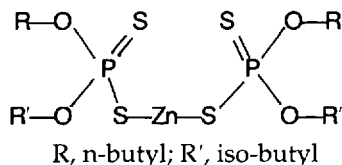
Results

If the regeneration conditions are changed by increasing the regeneration temperature and reducing reaction in a flowing atmosphere, the regeneration effect of the poisoned catalyst increases.

13.2 Anti-oxidant Additives in Petroleum

Sample

The ZDDP sample, ZDDP was provided by Lei Zhou, Institute of Petroleum Refining, Beijing, China:



Measurements

DTA— ± 100 mV; heating rate, $20^\circ\text{C min}^{-1}$; atmosphere, air; flow-rate, 45 ml min^{-1} ; sample mass, 12.57 mg; reference material, empty crucible.

GC/TCD₂—Bridge current, 240 mA; cell temperature, 130°C ; chromatographic column, Porapak-QS; carrier gas, air; flow-rate, 25 ml min^{-1} .

Results

The first exotherm ($205\text{--}250^\circ\text{C}$) is caused by oxidation of ZDDP after its oxidative induction period, leading to the reaction of intramolecular isomerization. The second exotherm ($250\text{--}280^\circ\text{C}$) is thermal degradation of the ZDDP. A number of products of the thermal degradation at 280°C can be seen in the gas chromatogram.

Sample and measurements

Sample mass 10–12 mg. Sample source and the measurement conditions as in Figure 13.12. Decomposition temperature is shown in the figure.

Results

According to the information provided by the DTA–GC curves, the mechanism of the thermal oxidative decomposition of ZDDP can be explored [5]. Figure 13.13 indicates that $\text{C}_8\text{H}_{12}\text{SH}$ is unstable at $280\text{--}300^\circ\text{C}$ in air.

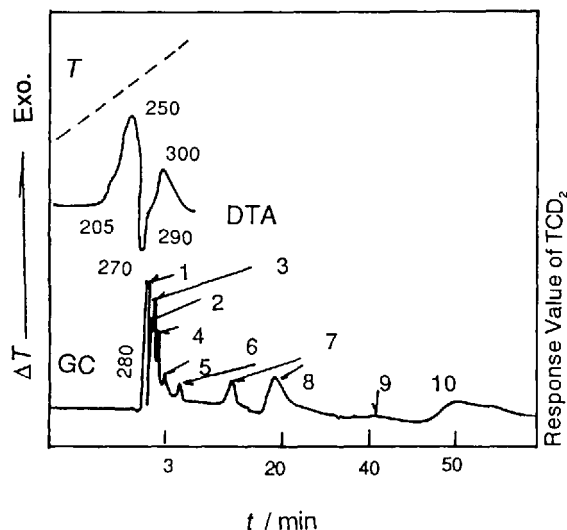


Figure 13.12 DTA–GC curves of thermal oxidative decomposition of ZDDP anti-oxidant additive at 280°C [11, 12]. 1, Air (0.65 min); 2, H_2S (1.35 min); 3, COS (1.75 min); 4, SO_2 (1.95 min); 5, iC_4/nC_4 (2.7–3.2 min); 6, ? (4.3–4.6 min); 7, ? (9.3–10.4 min); 8, $\text{C}_8\text{H}_{17}\text{SH}$ (22.6–23.5 min); 9, $\text{C}_8\text{H}_{17}\text{SC}_4\text{H}_9$ (42.9–43.6 min); 10, 1-octene (50.1–52.3 min) (iC_4 , iso-butylene; nC_4 , n-butylene)

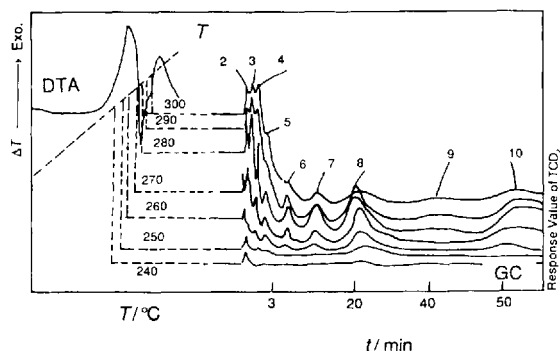


Figure 13.13 (a) DTA–GC curves of thermal oxidative decomposition of ZDDP anti-oxidant additive

(continued)

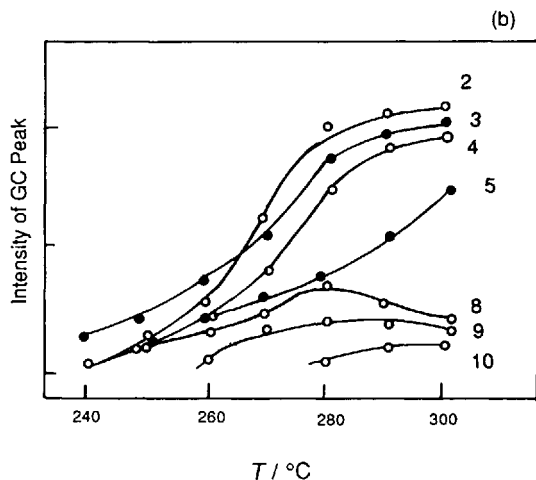


Figure 13.13 (b) Relationships between GC intensity and temperature. 2, COS; 3, H_2S ; 4, SO_2 ; 5, $i\text{C}_4^-/n\text{C}_4^-$; 8, $\text{C}_8\text{H}_{17}\text{SH}$; 9, $i\text{C}_8^-$; 10, $\text{C}_8\text{H}_{17}\text{SC}_4\text{H}_9$; peaks 6 and 7 not identified ($i\text{C}_4^-$, iso-butylene; $n\text{C}_4^-$, n-butylene; $i\text{C}_8^-$, i-octane)

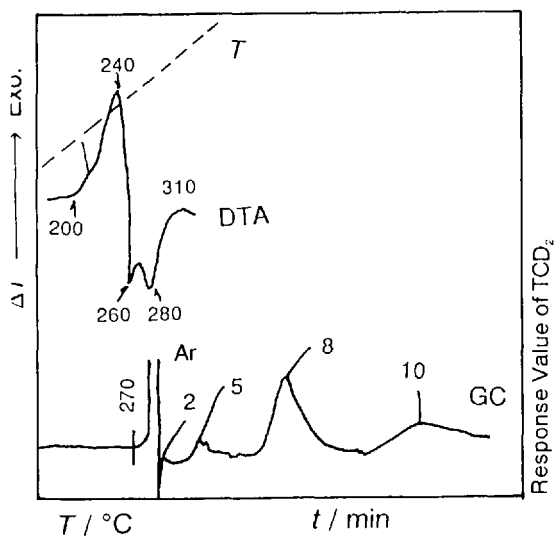


Figure 13.14 DTA-GC curves of thermal decomposition of ZDDP antioxidant additive at 280 °C [13]

Sample and measurements

Sample mass, 12.25 mg; atmosphere, argon; flow-rate, 45 ml min⁻¹. Sample source and the measurement conditions as in Figure 13.12.

Results

On the gas chromatogram relating to the endothermic peak observed at about 270 °C, a small amount of H_2S , $i\text{C}_4^-/n\text{C}_4^-$ and a large amount of $\text{C}_8\text{H}_{17}\text{SH} + 1-\text{C}_8^-$ are detected. $\text{C}_8\text{H}_{17}\text{SH}$ and $1-\text{C}_{10}^-$ are the main primary products of the thermal decomposition of ZDDP at temperatures lower than 270 °C and are comparably stable in an inert atmosphere ($1-\text{C}_{10}^-$, 1-decene; others see Figure 13.13).

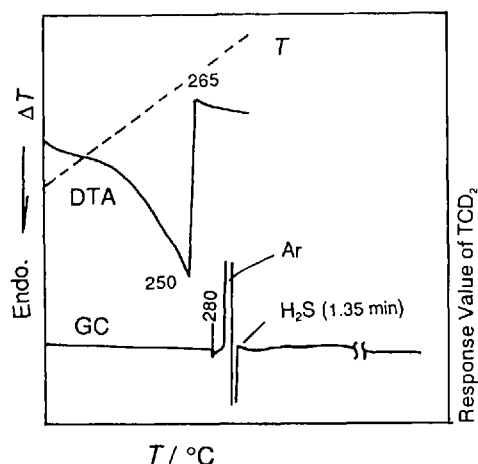


Figure 13.15 DTA-GC curves of thermal decomposition of $C_{12}H_{25}SH$ at 280 °C [5]

Sample and measurements

Sample, $C_{12}H_{25}SH$; sample mass, 11.96 mg. DTA: $\pm 250 \mu V$. Other conditions as in Figure 13.12.

Results

On the gas chromatogram, relating to the wide endothermic peak at 250 °C, a micro amount of H_2S is detected. Figure 13.15 indicates that the thiol is stable in an inert atmosphere.

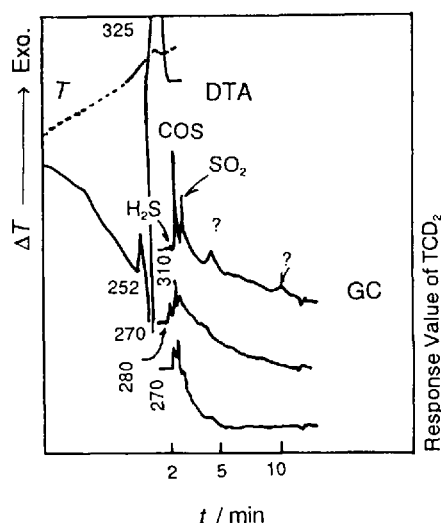


Figure 13.16 DTA-GC curves of thermal oxidative decomposition of $C_{12}H_{25}SH$ at 270, 280 and 300 °C [5]

Sample and measurements

Sample mass, 10–12 mg. Measurement conditions as in Figure 13–12.

Results

The endothermic peak at 270 °C is followed by a large exothermic peak at 325 °C. The peak intensities of H_2S , COS, SO_2 and peaks 6 and 7 on the gas chromatogram increase with increasing decomposition temperature. The thiol is unstable at temperatures higher than 280 °C in air.

13.3 Coal

Sample

Yanzhou candle coal was provided by the Institute of Chemical Technology of Coal (ECUST).

Measurements

DTA— $\pm 250 \mu\text{V}$; heating rate, $10^\circ\text{C min}^{-1}$; atmosphere, air; flow-rate, 15 ml min^{-1} ; sample mass, 2.08 mg; reference material, empty crucible.

EGD-TCD₁—Bridge current, 100 mA; cell temperature, 110°C .

CG-TCD₂—Bridge current, 160 mA; cell temperature, 110°C .

Chromatographic column, 401 organic support; carrier gas, N_2 at 60 ml min^{-1} .

Results

The various characteristic burning temperatures of candle coal are shown in the DTA curve. The O_2 consumption relating to the evolved CO_2 and H_2O peaks is shown on the gas chromatogram. Around the characteristic burning temperature at $T_D \approx T_E$, the O_2 consumption is high, corresponding to an O_2 peak height decrease on the gas chromatogram.

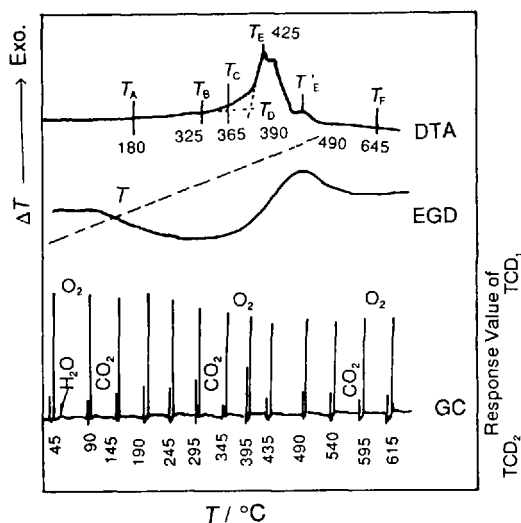


Figure 13.17 DTA-EGD-GC characteristic burning curves of candle coal [14–16]

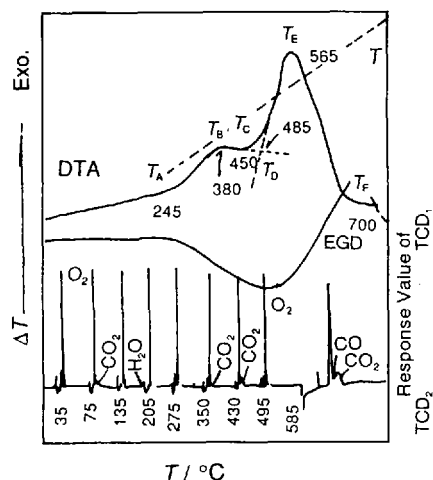


Figure 13.18 DTA-EGD-GC characteristic burning curves of bitumite coal [6]

Samples and measurements

Sample, Zhouzhuang bitumite coal, China; sample mass, 1.98 mg; heating rate, $20\text{ }^{\circ}\text{C min}^{-1}$. Sample source and measurement conditions as in Figure 13.17.

Results

The various characteristic burning temperatures of bitumite coal are shown in the DTA curve. The shoulder peak (from T_B to T_C) is the characteristic shape of plastic bitumite coal.

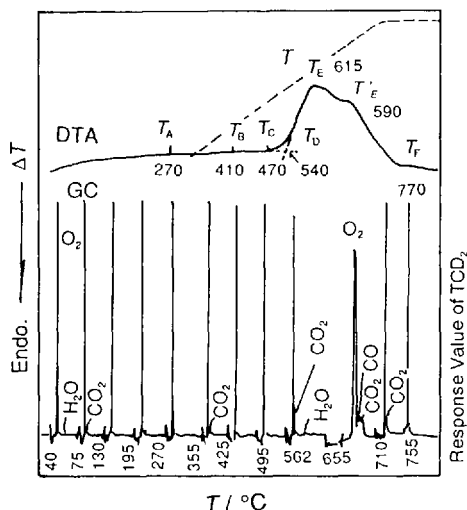


Figure 13.19 DTA-EGD-GC characteristic burning curves of anthracite coal [6]

Sample and measurements

Sample, Jingcheng anthracite coal, China; sample mass, 2.04 mg; heating rate, $20\text{ }^{\circ}\text{C min}^{-1}$. Sample source and measurement conditions as in Figure 13.17.

Results

The various characteristic burning temperatures of anthracite coal are shown on the DTA curve. At temperatures from T_A to T_C , a drift of the horizontal line occurs. This is caused by anthracite coal having a high fixed carbon and a low volatile matter content.

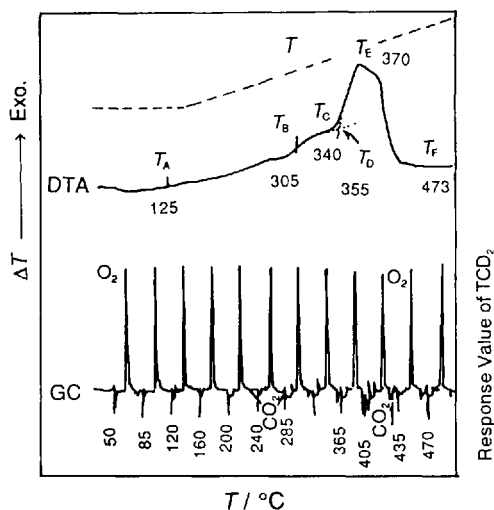


Figure 13.20 DTA-EG-GC pyrolysis characteristic curves of bituminous coal [14-17]

Sample

Sample, bituminous coal, CDR-104(12), provided by the Institute of Coal Chemistry, Chinese Academy of Sciences, Taiyan, China.

Measurements

DTA— $\pm 100 \mu\text{V}$; heating rate, $20^\circ\text{C min}^{-1}$, atmosphere, N_2 flow-rate, 20 ml min^{-1} ; sample mass, 125.19 mg; reference material, coke powder.

EGD-TCD₁—Bridge current, 100 mA; cell temperature, 110°C .

GC-TCD₂—Bridge current, 160 mA; cell temperature, 110°C .

Chromatographic column, 401 organic support; carrier gas, N_2 ; flow-rate, 60 ml min^{-1} .

Results

The endotherm observed at temperatures lower than 125°C represents the loss of adsorbed water associated with low molecular mass volatile gas. The second broad endotherm at $300\text{--}465^\circ\text{C}$ is due to the formation of a metaplastic system. The large exotherm at $465\text{--}510^\circ\text{C}$ is attributed to a primary carbonization stage as a result of the formation of semi-coke. In the pyrolyzed gas evolved in the primary carbonization stage, H_2 , CH_4 and $\text{C}_2\text{C}_3/\text{C}_3$, H_2O , etc, are detected on the gas chromatogram. The second carbonization stage at about $510\text{--}750^\circ\text{C}$ is a transient process from semi-coke to coke ($\text{C}_2^=$, ethylene; $\text{C}_3^=$, propylene; C_3 , propane).

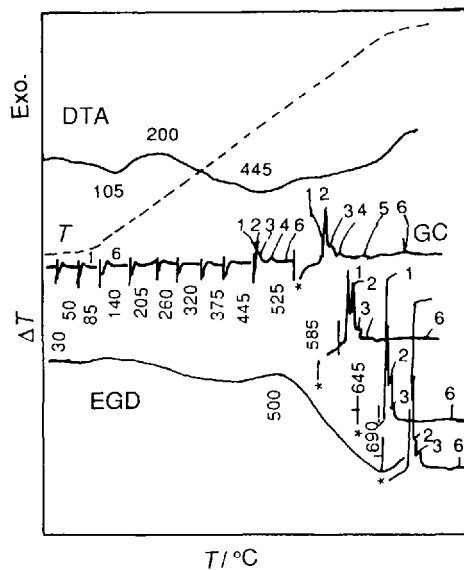


Figure 13.21 DTA-EGD-GC characteristic pyrolysis curves of gas coal

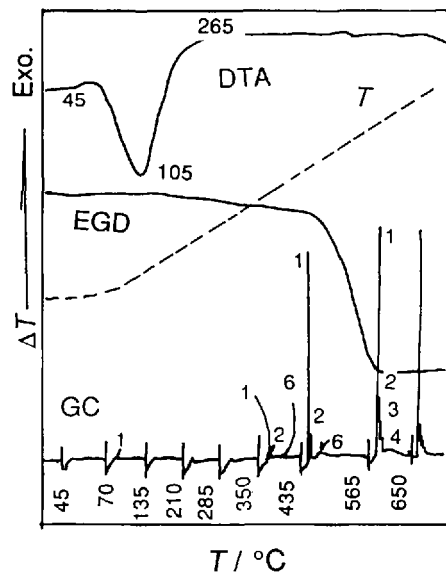


Figure 13.22 DTA-EGD-GC pyrolysis characteristic curves of lignite coal

Sample and measurements

Sample, Datong gas coal, China; sample mass, 25.35 mg; reference material, coke powder. Sample source and measurement conditions as in Figure 13.20.

Results

The first endotherm at a temperature lower than 200 °C is attributed to water desorption. The primary carbonization at a temperature lower than 500 °C and the second carbonization from 500 to 769 °C are shown on the DTA curve.

The gas coal is not thermally stable, and on this account large amounts of H_2 , CH_4 and C_2/C_3 and H_2O are detected on the gas chromatogram. The residue shows weak stickability and is breakable and non-diluted.

Sample and measurements

Sample, Neimeng (Inner Mongolia) lignite coal, China; sample mass, 25.08 mg; reference material, coke powder. Sample source and measurement conditions as in Figure 13.20.

Results

The exotherm at 49–205 °C is attributed to evaporation of absorbed H_2O and pyrolyzed H_2O . This is due to the fact that the lignite is a low-rank coal containing a large amount of OH groups. The thermal stability of the metaplastic system formed is low. According to the EGD-GC curves, the temperature range of primary and second carbonization is from 265 to 435 °C. The residual coal is breakable, non-stickable and rigid.

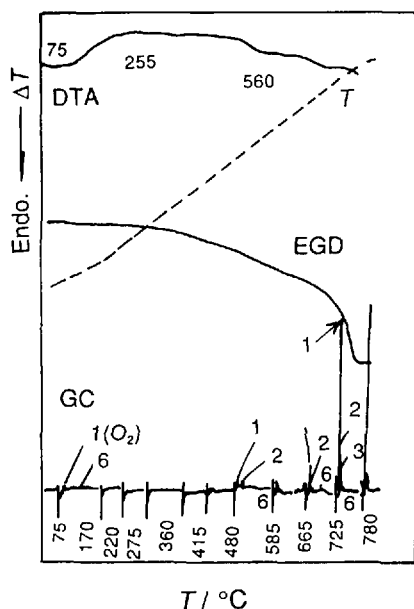


Figure 13.23 DTA-EGD-GC characteristic pyrolysis curves of anthracite coal

Sample and measurements

Sample, Jingcheng anthracite coal, China; sample mass, 25.28 mg. Sample source and measurement conditions as in Figure 13.20.

Results

As the carbon content of the anthracite is about 92%, a metaplastic system cannot be formed in the pyrolysis process. On this account, the DTA curve drifts gradually. The EGD curve does not decrease rapidly until 700 °C. Large amounts of H_2 , C_1 , C_2^+ , H_2O , etc., are detected at 725 and 780 °C on the gas chromatogram. The residual coke is rigid and powdery.

13.4 Minerals

Sample

The sample was provided by the Department of Inorganic Material/Specimen Room of Minerals (ECUST), China.

Measurements

DTA— $\pm 100 \mu\text{V}$; heating rate, $20^\circ\text{C min}^{-1}$; atmosphere, air- $\text{CO}_2(1:1)$ mixed gas; flow-rate, 30 ml min^{-1} ; reference material, $\alpha\text{-Al}_2\text{O}_3$; sample mass, (a) 2.72 mg, (b) 4.11 mg.

GC/TCD₂—Bridge current, 120 mA; cell temperature, 110°C .

EGD/TCD₂—Bridge current, 120 mA; cell temperature, 100°C .

Chromatographic column, 401 organic support; carrier gas, N_2 ; flow-rate, 30 ml min^{-1} .

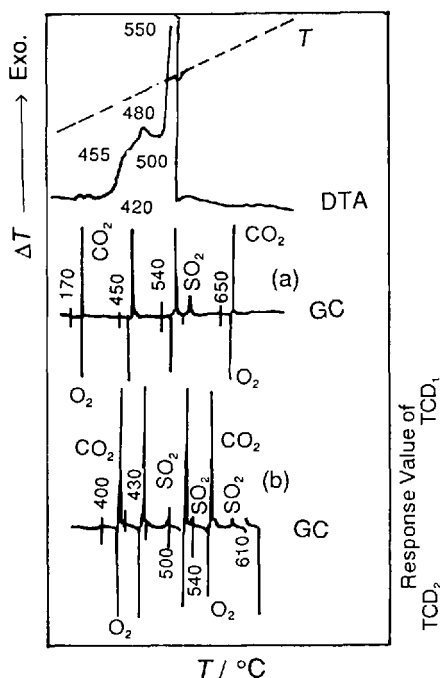
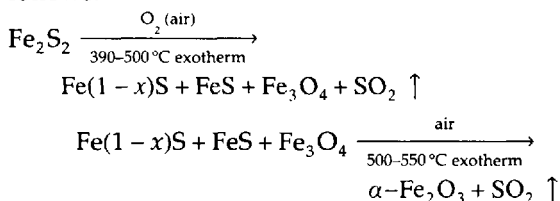


Figure 13.24 DTA-GC curves of pyrite [18–20]

Results

In gas chromatograms (a) and (b), relating to DTA curve, an SO_2 peak is detected at 430, 500 and 540°C and the O_2 peak decreases continuously. The reaction process of pyrite in air is as follows:



The residue is red powder, non-magnetic; yield, 70.75%.

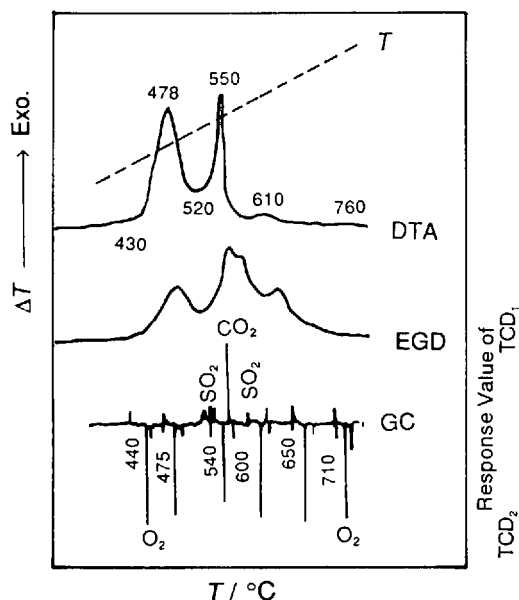


Figure 13.25 DTA-EGD-GC curves of siderite containing micropyrrite in air

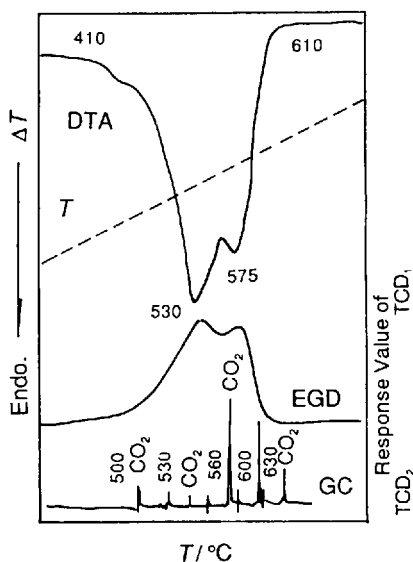


Figure 13.26 DTA-EGD-GC curves of siderite containing micropyrrite in N_2 [18]

Sample and measurements

Sample mass, 27.16 mg; atmosphere, air; flow-rate, 30 ml min⁻¹. EGD-TCD₁: bridge current, 120 mA; cell temperature, 80 °C. Sample source and other conditions as in Figure 13.24.

Results

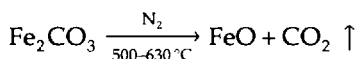
An exothermic peak is observed at 478 °C on DTA the curve. On the gas chromatogram, the SO₂ peak is detected in the same temperature range and the O₂ peak decreases at 475 °C. (The reaction process is the same as in Figure 13.24). At ca 550 °C (the second peak on the DTA curve), a large amount of CO₂ and a small amount of SO₂ are detected on the gas chromatogram. The O₂ peak decreases gradually at the same time.

Sample and measurements

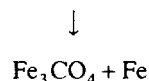
Sample mass, 35.96 mg; atmosphere, N_2 ; flow-rate, 30 ml min⁻¹. GC-CD₂: bridge current, 160 mA; cell temperature, 80 °C. Other conditions as in Figure 13.24.

Results

In the inert atmosphere, the siderite containing pyrite cannot produce the oxidized reaction of pyrite. The reaction equation of Fe₂CO₃ is as follows:



exothermic effect



The residue is a black powder showing strong magnetism; yield, 70.33%.

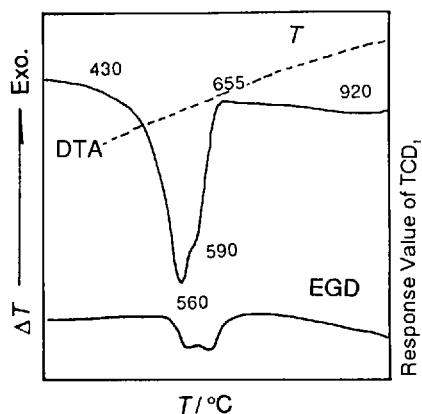


Figure 13.27 DTA-EGD-GC curves of siderite containing micropyrrite in CO_2 [21]

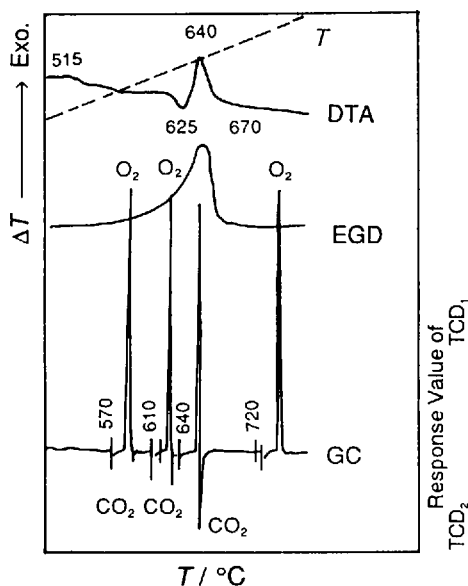


Figure 13.28 DTA-EGD-GC curves of siderite containing microkaolinite in air

Sample and measurements

Sample mass, 38.98 mg; atmosphere, CO_2 ; flow-rate, 30 ml min^{-1} . Other conditions as in Figure 13.26.

Results

The EGD curve traces the variations on the DTA curve. Because of the pressure sharing of the carrier gas, CO_2 , the endothermic peak with a shoulder at 560, 590°C shifts to the high-temperature side, in contrast to Figure 13.26. The residue is a black powder, ferromagnetic; yield, 70.29%.

Sample

Sample, FeCO_3 provided by Nan Jing College of Geology, Specimen Room of Minerals, China.

Measurements

DTA— $\pm 100 \mu\text{V}$, $20^\circ\text{C min}^{-1}$; atmosphere, air; flow-rate, 30 ml min^{-1} ; sample mass, 21.17 mg; reference material, coke powder.

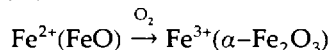
EGD/ TCD_1 —Bridge current, 120 mA; cell temperature, 110°C .

GC/ TCD_2 —Bridge current, 140 mA; cell temperature, 110°C .

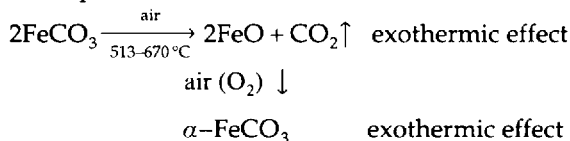
Other conditions as in Figure 13.26.

Results

The DTA-GC curves suggest that the oxidative decomposition reaction of siderite is almost simultaneous with



The equation is as follows:



The residue is a black powder showing strong magnetism; yield, 70.39%.

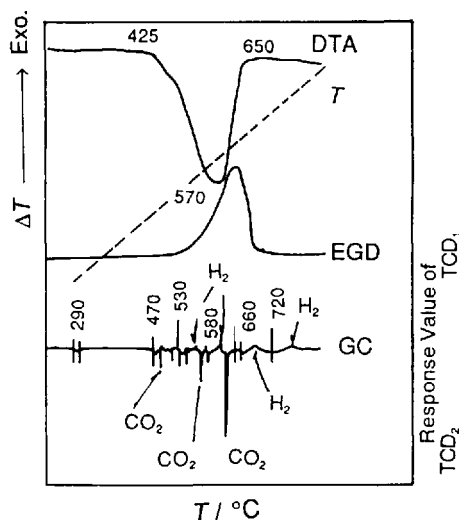


Figure 13.29 DTA-EGD-GC curves of siderite 2 containing microkaolinite in N_2 [11, 20, 22]

Sample and measurements

Sample mass, 22.30 mg. DTA, $\pm 250 \mu V$; heating rate, $40^\circ C \min^{-1}$; atmosphere, N_2 ; flow-rate, 30 ml min^{-1} . Sample source and other conditions as in Figure 13.28.

Results

On the gas chromatogram, the CO_2 peak and micro H_2 peaks are detected at 470, 530 and 580 $^\circ C$. The mechanism of the production of H_2 is the same as in Figure 13.26 [20, 22].

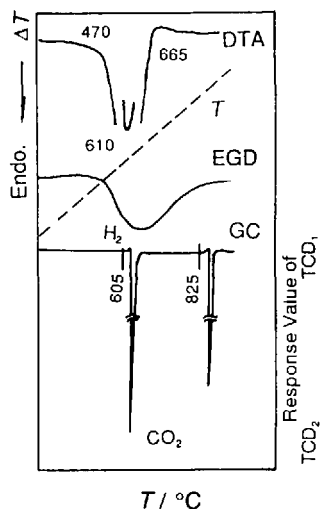


Figure 13.30 DTA-EGD-GC curves of siderite 2 containing microkaolinite in CO_2 [9]

Sample and measurements

Sample mass, 22.31 mg. DTA: $\pm 100 \mu V$; heating rate, $40^\circ C \min^{-1}$; atmosphere, CO_2 ; flow-rate, 15 ml min^{-1} ; Sample source and other conditions as in Figure 13.28.

Results

Comparing the results in Figures 13.30 and 13.31 with these results, it is concluded that H_2 is produced by the reaction of FeO with H_2O in the inert atmosphere. The mechanism of H_2 production is the same as in Figure 13.26.

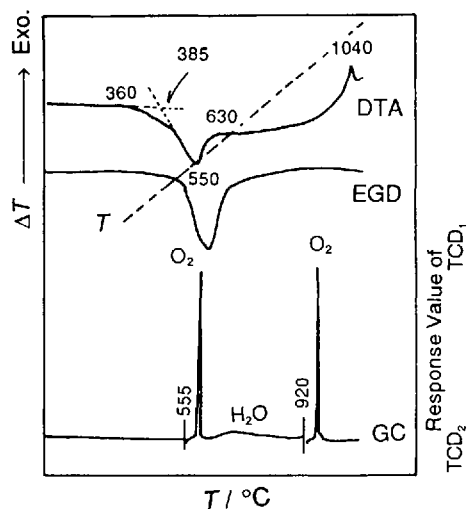


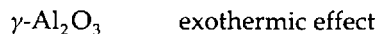
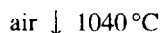
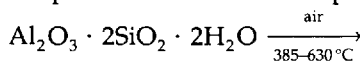
Figure 13.31 DTA-EGD-GC curves of kaolinite in air

Sample and measurements

Shouzhou Kaolinite, China; sample mass, 18.06 mg; atmosphere, air; flow-rate, 30 ml min⁻¹. DTA: ±250 μV; heating rate, 20 °C min⁻¹; DTA ±100 μV. Other conditions as in Figure 13.28.

Results

The exothermic peak at 1040 °C on the DTA curve is caused by the transformation of metakaolinite, hence α-Al₂O₃ is formed at high temperature. The reaction equation is as follows:



The residue is a greyish white powder; yield, 89.09%.

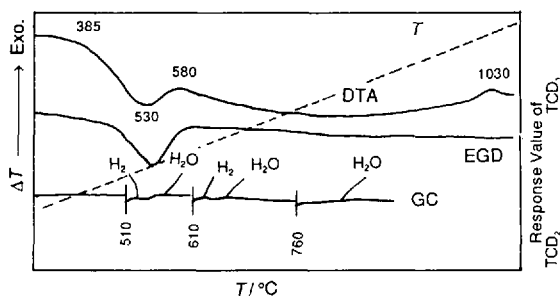


Figure 13.32 DTA-EGD-GC curves of kaolinite in N₂

Sample and measurements

Sample mass, 14.51 mg; atmosphere, N₂; flow-rate, 30 ml min⁻¹. Sample source and conditions as in Figure 13.28.

Results

The gas chromatogram indicates that the dehydroxylic H₂O peak is detected at 510, 610 and 760 °C. The small exothermic peak at 1030 °C on the DTA curve is attributed to the production of γ-Al₂O₃. The experimental results indicate that the kaolinite tested contained a trace amount of FeO as impurity. The mechanism of H₂ production is the same as in Figure 13.26.

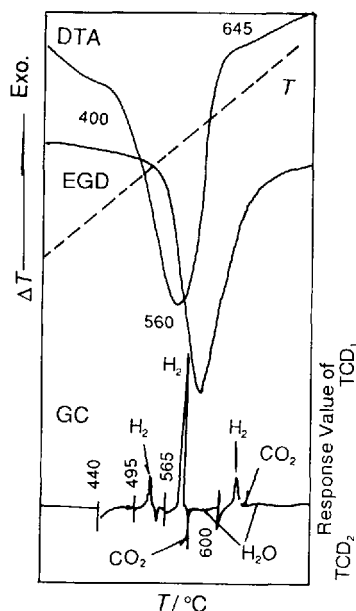


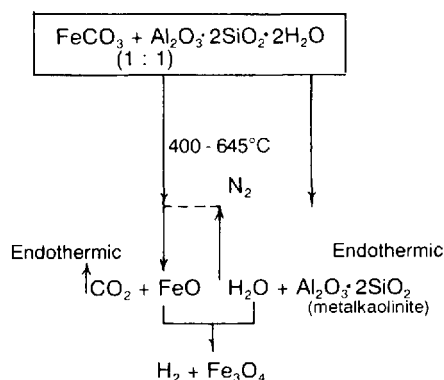
Figure 13.33 DTA-EGD-GC curves of kaolinite-siderite (1 : 1) [20, 22]

Sample and measurements

Sample mass, 22.83 mg. DTA: $\pm 100 \mu\text{V}$; heating rate, $40^\circ\text{C min}^{-1}$; atmosphere, N_2 ; flow-rate, 30 ml min^{-1} . Other conditions as in Figure 13.28.

Results

The endothermic peak at 560°C is attributed to the thermal decomposition of siderite and kaolinite. On the gas chromatogram, CO_2 , H_2O and a large H_2 peak are detected at 495, 565 and 600°C . The mechanism of H_2 production can be expressed by



13.5 References

- Cai Gencai, *J. East China Inst. Chem. Technol.*, 1981, 7, 468.
- Cai Gencai, *J. East China Inst. Chem. Technol.*, 1982, 1, 88.
- Cai Gencai, *Anal. Instrum.*, 1992, 4, 10.
- Cai Gencai and Zhu Xiaolin, *J. East China Inst. Technol.*, 1987, 13(4), 437.
- Cai Gencai, *J. East China Inst. Chem. Technol.*, 1987, 13(4), 438.
- Cai Gencai, *J. Fuel Chem. Technol.*, 1989, 17(14), 329.
- Cai Gencai, *J. Fuel Chem. Technol.*, 1992, 20(3), 318.
- Cai Gencai, *J. Fuel Chem. Technol.*, 1985 13(4), 358.
- Huang Boling, *DTA Handbook of Minerals*. Beijing, Science Press, 1987.
- Cai Gencai, *J. Fuel Chem Technol.*, 1995, 13(4), 385.
- Cai Gencai, *J. East China Inst. Chem. Technol.*, 1992, 18(3), 404.
- Cai Gencai, *J. East China Univ. Sci. Technol.*, 1995, 21(2), 256.
- Cai Gencai, *J. East China Inst. Chem. Technol.*, 1989, 9, 330.
- Cai Gencai, *J. East China Univ. Sci. Technol.*, 1995, 21(2), 262.
- Cai Gencai, Qian Yanlong, Huang Jiling, Huang Jiazheng *et al.*, *J. East China Univ. Sci. Technol.*, 1997, 23(1).
- Cheng Jinghong, He Zijian, Li Jiansheng and Cai Gencai, in *Proceedings of the 2nd Symposium on STTT of the Chinese Chemical Society*, 1984, p. 439.
- Cai Gencai, Qian Yanlong, Huang Jiling, Huang Jiazheng *et al.*, *J. East China Univ. Sci. Technol.*, 1997, 23(1).
- Cai Gencai, *J. Mineral.*, 1989, 9, 330.
- Morgan, D. J., *Thermochim. Acta*, 1988, 135, 207.
- Paulik, J., Paulik, M., and Arnold, M., *J. Thermal Anal.*, 1984, 29, 345.
- Huang Kelong, *J. Mineral.*, 1979, 4, 331.
- Morgan, D. J., *Anal. Proc.*, 1984, 21, 3.

Appendix 1

Specific Heat Capacity of Pure α -Alumina in the Temperature Region from 120 to 780 K

Temperature		Specific heat capacity (J g ⁻¹ °C ⁻¹)	Temperature		Specific heat capacity (J g ⁻¹ °C ⁻¹)
(K)	(°C)		(K)	(°C)	
120.00	-153.15	0.196 9	440.00	166.85	0.987 5
130.00	-143.15	0.235 0	450.00	176.85	0.997 5
140.00	-133.15	0.274 0	460.00	186.85	1.007 0
150.00	-123.15	0.313 3	470.00	196.85	1.016 0
160.00	-113.15	0.352 5	480.00	206.85	1.024 7
170.00	-103.15	0.391 3	490.00	216.85	1.033 0
180.00	-93.15	0.429 1	500.00	226.85	1.040 8
190.00	-83.15	0.465 9	510.00	236.85	1.048 4
200.00	-73.15	0.501 4	520.00	246.85	1.055 6
210.00	-63.15	0.535 5	530.00	256.85	1.062 6
220.00	-53.15	0.568 2	540.00	266.85	1.069 2
230.00	-43.15	0.599 4	550.00	276.85	1.075 6
240.00	-33.15	0.629 2	560.00	286.85	1.081 6
250.00	-23.15	0.657 6	570.00	296.85	1.087 5
260.00	-13.15	0.684 5	580.00	306.85	1.093 1
270.00	-3.15	0.710 1	590.00	316.85	1.098 6
280.00	6.85	0.734 2	600.00	326.85	1.103 8
290.00	16.85	0.757 1	610.00	336.85	1.108 8
300.00	26.85	0.778 8	620.00	346.85	1.113 6
310.00	36.85	0.799 4	630.00	356.85	1.118 2
320.00	46.85	0.818 6	640.00	366.85	1.122 7
330.00	56.85	0.837 2	650.00	376.85	1.127 0
340.00	66.85	0.854 8	660.00	386.85	1.131 3
350.00	76.85	0.8713	670.00	396.85	1.135 3
360.00	86.85	0.887 1	680.00	406.85	1.139 2
370.00	96.85	0.902 0	690.00	416.85	1.143 0
380.00	106.85	0.916 1	700.00	426.85	1.146 7
390.00	116.85	0.929 5	720.00	446.85	1.153 7
400.00	126.85	0.942 3	740.00	466.85	1.160 4
410.00	136.85	0.954 4	760.00	486.85	1.166 7
420.00	146.85	0.966 0	780.00	506.85	1.172 6
430.00	156.85	0.977 0			

See also Appendix 2.

www.iran-mavad.com

مرجع دانشجویان و مهندسين مواد

Appendix 2

An Approximate Expression of Specific Heat Capacity of Pure α -Alumina

The specific heat capacity values in Appendix 1 are approximated with the following equations:

$$c_p = A_0 + A_1x + A_2x^2 + A_3x^3 + A_4x^4 + A_5x^5 + A_6x^6 + A_7x^7 + A_8x^8 + A_9x^9 + A_{10}x^{10} \quad (1)$$

$$x = (T - 650 \text{ K})/550 \text{ K} \quad (2)$$

$$= (\theta - 376.85 \text{ }^\circ\text{C})/550 \text{ }^\circ\text{C} \quad (2a)$$

$$\theta = (T - 273.15 \text{ K}) \text{ }^\circ\text{C/K} \quad (3)$$

where $100 \text{ K} \leq T \leq 1200 \text{ K}$

$$A_0 = 1.127 \text{ 05}$$

$$A_1 = 0.232 \text{ 60}$$

$$A_2 = -0.217 \text{ 04}$$

$$A_3 = 0.264 \text{ 10}$$

$$A_4 = -0.237 \text{ 78}$$

$$A_5 = -0.100 \text{ 23}$$

$$A_6 = 0.153 \text{ 93}$$

$$A_7 = 0.545 \text{ 79}$$

$$A_8 = -0.478 \text{ 24}$$

$$A_9 = -0.376 \text{ 23}$$

$$A_{10} = 0.344 \text{ 07}$$

c_p and A_i ($i = 1, 2, \dots$) in $\text{J }^\circ\text{C}^{-1} \text{ g}^{-1}$, T in K, θ in $^\circ\text{C}$

The respective two coefficients in Equations (2) and (2a) are for normalizing the temperature variables T and θ . The standard deviation from the values in Table 2 is $0.00013 \text{ J }^\circ\text{C}^{-1} \text{ g}^{-1}$. The maximum deviation is 0.071% at 140 K. The deviations at temperatures higher than 300 K are less than 0.02%.

www.iran-mavad.com

مرجع دانشجویان و مهندسين مواد

Appendix 3

Physical Constants and Conversion Tables

A3.1 Table of Physical Constants

Table 2.1

Quantity	Symbol	Value
Permeability of vacuum	μ_0	$4\pi \times 10^{-7} \text{ H m}^{-1}$
Velocity of light	c	$299\,792\,458 \text{ m/s}$
Dielectric constant of vacuum	$\epsilon_0(\mu_0 c^2)^{-1}$	$8.854\,187\,816 \times 10^{-12} \text{ F m}^{-1}$
Fine-structure constant	$\alpha = \mu_0 c e^2 / 2h$ α^{-1}	$7.297\,353\,08(33) \times 10^{-3}$ $137.035\,989\,5(61)$
Electronic charge	e	$1.602\,177\,33(49) \times 10^{-19} \text{ C}$
Planck's constant	h $\hbar = h/2\pi$	$6.626\,075\,5(40) \times 10^{-34} \text{ Js}$ $1.054\,572\,66(63) \times 10^{-34} \text{ Js}$
Avogadro's number	L, N_A	$6.022\,136\,7(36) \times 10^{23} \text{ mol}^{-1}$
Atomic mass unit	amu	$1.660\,540\,2(10) \times 10^{-27} \text{ kg}$
Electron rest mass	m_e	$9.109\,389\,7(54) \times 10^{-31} \text{ kg}$
Proton rest mass	m_p	$1.672\,623\,1(10) \times 10^{-27} \text{ kg}$
Neutron rest mass	m_n	$1.674\,928\,6(10) \times 10^{-27} \text{ kg}$
Faraday's constant	$F = Le$	$9.648\,530\,9(29) \times 10^4 \text{ C mol}^{-1}$
Rydberg constant for infinite mass	$R_\infty = \mu_0^2 m_e c^4 / 8h^3$	$1.097\,373\,153\,4(13) \times 10^7 \text{ m}^{-1}$
Hartree energy	$E_a = 2hcR_\infty$	$4.359\,748\,2(26) \times 10^{-18} \text{ J}$
First Bohr radius	$a_0 = \alpha/4\pi R_\infty$	$5.291\,772\,49(24) \times 10^{-11} \text{ m}$
Bohr magneton	$\mu_B = eh/2m_e$	$9.274\,015\,4(31) \times 10^{-24} \text{ J T}^{-1}$
Nuclear magneton	$\mu_N = eh/2m_p$	$5.050\,786\,6(17) \times 10^{-27} \text{ J T}^{-1}$
Magnetic moment of electron	μ_e	$9.284\,770\,1(31) \times 10^{-24} \text{ J T}^{-1}$
Landé g-factor for free electron	$g_e = 2\mu_e/\mu_B$	$2.002\,319\,304\,386(20)$
Proton gyromagnetic ratio	γ_p	$2.675\,221\,28(81) \times 10^8 \text{ s}^{-1} \text{ T}^{-1}$
Gas constant	R	$8.314\,510(70) \text{ J K}^{-1} \text{ mol}^{-1}$
0°C in Kelvin	T_0 RT_0	273.15 K $2.271\,108(19) \times 10^3 \text{ J mol}^{-1}$
Atmospheric pressure	p_0	$101\,325 \text{ Pa}$
Molar volume of ideal gas	$V_0 = RT_0/p_0$	$2.241\,410(19) \times 10^{-2} \text{ m}^3 \text{ mol}^{-1}$
Boltzmann's constant	$k = R/L$	$1.380\,658(12) \times 10^{-23} \text{ J K}^{-1}$
Acceleration due to gravity	g	$9.806\,65 \text{ m/s}^2$

A3.2 Energy Conversion Table

J	cal	BTU	kWh	atm	kg m
1	0.239 006	$0.947\,831 \times 10^{-3}$	$2.777\,778 \times 10^{-7}$	9.86896×10^{-3}	0.101 972
4.184	1	$3.965\,73 \times 10^{-3}$	$1.162\,222 \times 10^{-6}$	$4.129\,29 \times 10^{-2}$	0.426 649
$1.055\,040 \times 10^3$	$2.521\,61 \times 10^2$	1	$2.930\,667 \times 10^{-4}$	10.412 44	$1.075\,84 \times 10^2$
3.6×10^6	8.60421×10^5	$3.412\,19 \times 10^3$	1	$13.552\,92 \times 10^4$	$3.670\,98 \times 10^5$
$1.013\,25 \times 10^2$	24.2173	$9.603\,90 \times 10^{-2}$	$2.814\,583 \times 10^{-5}$	1	10.332 23
9.806 65	2.343 85	$9.295\,05 \times 10^{-3}$	$2.724\,069 \times 10^{-6}$	$9.678\,41 \times 10^{-2}$	1

A3.3 Molar Energy Conversion Table

J mol ⁻¹	erg mol ⁻¹	cal mol ⁻¹	eV mol ⁻¹	cm ⁻¹	K
1	$1.660\,566 \times 10^{-17}$	0.239 006	$1.036\,435 \times 10^{-5}$	$8.359\,348 \times 10^{-2}$	0.120 273 1
$6.022\,045 \times 10^{16}$	1	$1.493\,03 \times 10^{16}$	$6.241\,461 \times 10^{11}$	$5.034\,037 \times 10^{15}$	$0.724\,290 \times 10^{16}$
4.184	$6.947\,806 \times 10^{-17}$	1	$4.336\,444 \times 10^{-5}$	0.349 755	0.503 222
$9.648\,455 \times 10^4$	$1.602\,189 \times 10^{-12}$	$2.306\,036 \times 10^4$	1	$8.065\,479 \times 10^3$	$1.160\,450 \times 10^4$
11.962 655	$1.986\,477 \times 10^{-16}$	2.859 143	$1.239\,852 \times 10^4$	1	1.438 786
8.314 41	$1.380\,663 \times 10^{-16}$	1.987 192	$8.617\,347 \times 10^{-3}$	0.695 030 4	1

A3.4 Pressure Conversion Table

Pa, N m ⁻²	Torr, mmHg	bar	kg cm ⁻²	psi	atm
1	$7.500\,62 \times 10^{-3}$	10^{-5}	$1.019\,72 \times 10^{-5}$	$1.450\,38 \times 10^{-4}$	$9.869\,23 \times 10^{-6}$
133.322	1	1.3322×10^{-3}	$1.359\,51 \times 10^{-3}$	$1.933\,68 \times 10^{-2}$	$1.315\,79 \times 10^{-3}$
10^5	750.062	1	1.019 72	14.5038	0.986 932
$9.806\,65 \times 10^4$	735.559	0.980 665	1	14.2233	0.967 841
$6.894\,76 \times 10^3$	51.7149	$6.894\,76 \times 10^{-2}$	$7.030\,70 \times 10^{-2}$	1	$6.804\,60 \times 10^{-2}$
$1.013\,25 \times 10^5$	760	1.013 25	1.033 23	14.6959	1

A3.5 Thermal Conductivity Conversion Table

J/s m K	kcal/m h °C	cal/cm s °C
1	0.860 421	$2.390\,06 \times 10^{-3}$
1.162 22	1	$2.777\,78 \times 10^{-3}$
418.4	360	1

A3.6 Temperature Conversion Equations

$$T/^{\circ}\text{C} = T/\text{K} - 273.15 = (T/^{\circ}\text{F} - 32) \times 5/9$$

$$T/^{\circ}\text{F} = (T/\text{K}) \times 9/5 - 459.67 = (T/^{\circ}\text{C}) \times 9/5 + 32$$

$$T/\text{K} = T/^{\circ}\text{C} + 273.15 = (T/^{\circ}\text{F} + 459.67) \times 5/9$$

www.iran-mavad.com

مرجع دانشجویان و مهندسين مواد

Index of Contributors

Numbers indicate chapter and/or section. Numbers in parentheses are relevant pages

- Cai Gencai 2.4.3.1-3 (34-37); 2.4.6 (38); 5.3.1 (136-141); 12 (378-401)
- Cai Zhenqian 11 (337-374)
- Cong Guangmin 4.3.5 (99-100)
- Guo Quipeng 4.3.1-4 (92-99)
- Hashimoto Toshimasa 2.3.2-4 (28-32); 7.66-67 (205)
- Hatakeyama Hyoe 5.4.1-3 (142-144)
- Hatakeyama Tatsuko 1.1-1.2(3-4); 1.4.1 (6); 1.5 (8-11); 2.1-2.2.1(15-17); 2.2.2.7 (24); 2.2.3-4 (24-27); 2.3.1 (27-28); 2.4.3.3-4 (36-38); 2.5 (39); 3.1 (42-47); 3.5 (63-64); 4.1.3-5 (68); 4.2.25-26 (90-91); 4.4.7 (107); 4.5.1-3 (107-109); 6.1.1-2 (155-157); 7.1.2-2 (165-166); 7.5-8 (167-169); 7.11 (171); 7.14-16 (173-174); 7.20 (176); 7.22-29 (177-182); 7.44 (190-191); 7.48 (193); 7.55-57 (199-200)
- He Guanhu 6.1.3-4 (157-159)
- Hua Rong 7.58-60 (200-201); 7.63-65 (203-204)
- Huang Kelong 5.6 (149-150); 10 (247-334)
- Huang Yuhui 4.3.5 (99-100)
- Jian Qing 4.6.1-5 (112-124)
- Jian Yinshan 5.6 (149-150); 10 (247-334)
- Ling Yue 11 (337-374)
- Liu Jingjian 4.1.7 (70-71); 4.1.8 (71); 4.2.2 (74); 4.2.4-5 (77); 4.2.9 (79-80); 4.2.10 (80); 4.2.16 (84); 4.3.6-7 (100-101); 4.4.4-5 (104-106); 4.4.6 (106-107); 7.10 (170); 7.12-13 (171-173); 7.61-62 (202-203);
- Liu Yan 8.8 (223-237)
- Liu Zhenhai 1.1- 3 (3-6); 1.4.2 (7-8); 1.5 -6 (8-13); 3.1-3.5 (42-64); 4.1.1-2 (66-68); 4.1.6 (68-69); 4.2.1 (72-73); 4.2.3 (74-76); 4.2.6-8 (77-79); 4.2.10-13 (80-82); 4.2.14-15 (82-84); 4.2.17-25 (84-90); 4.2.27 (91-92); 4.3.8 (101-102); 4.4.1-3 (102-104); 4.4.6 (106-107); 4.5.4-6 (110-111); 4.7.2-4 (125-126); 5.1-5.2.3 (129-136); 5.3.2 (141-142); 5.5.2-4 (147-149); 5.7.2-5 (151-153); 6.1.2 (156-157); 6.2-6.3 (159-161); 7.3-4 (166-167); 7.9 (169-170); 7.17-19 (175-176); 7.21 (177); 7.30-43 (182-190); 7.45-47 (191-192); 7.49-54 (193-198);
- Lu Zhenrong 3.3.7 (56-61); 4.2.27 (91-92); 4.4.1-3 (102-104); 4.5.4-6 (110-111); 4.7.2-4 (125-126); 5.2.1-3 (133-136); 5.5.2 (147-148); 5.7.2-4 (151-152); 6.1.2 (156-157)
- Nishinari Katatsuyoshi 8.1 (212-223)
- Niu Chunji 12.3 (391-400)
- Peng Xinheng* 5.2.1 (133-135)
- Qian Yixiang 4.5.7 (112); 4.7.1 (124-125); 5.5.1 (146); 5.7.1 (150)
- Qu Guijie 4.1.7-8 (70-71); 4.2.2 (74); 4.2.4 (76); 4.2.9-10 (79-80); 4.3.6-7 (100-101); 4.4.4-5 (104-106); 4.4.6 (106-107)
- Quinn, Francis X. 2.2.1-3 (17-26); 2.4.1-2 (32-33); 2.4.3.1 (34-35); 2.4.3.4 (37-38); 2.4.4 (39); 2.4.6 (40)
- Sun Tongshan 12.1-12.2 (378-390)
- Wang Zenglin 12.3 (391-400)
- Wei Xueli 4.6.1-5 (112-124)
- Yang Shulin 8.8 (223-237)
- Ye Chunmin 7.10 (170); 7.12-13 (171-173); 7.61-62 (202-203)
- Ye Su 5.4.4-6 (144-146); 9 (239-246)
- Zhang Hongfang 3.3.4 (51-53)
- Zhao Min 4.6.1-5 (112-124)

General Index

Note: Figures and Tables are indicated [in this index] by *italic page numbers*; abbreviations used:

DMA = dynamic mechanical analysis
DSC = differential scanning calorimetry
DTA = differential thermal analysis
DTG = differential thermogravimetry
EGD = evolved gas detection
GC = gas chromatography
TA = thermal analysis
TG = thermogravimetry
TMA = thermomechanical analysis

Acid hydrolysis, of cellulose, 144–5

Activation energy

dehydration processes, 391, 392, 395, 398, 399, 400

determination of

by DSC, 118

by iso-conversion methods, 47–8, 57–8

for metals and alloys, 118–19

by rate-jump method of CRTA, 61

for thermosetting resins, 54, 56

glass transition of amorphous alloys, 114

oxidation of polyethylene, 132, 182

phase transformations of metals and alloys,
118–19

polymer transitions, 26, 168, 194–8

transport of polymer segments across solid–liquid
interface, 80–1

Adiabatic HS-DSC, 23

Alcoholic drinks, quality control of, 110

Alloys, *see* Metals and alloys

Alternating current calorimetry (ACC)

apparatus, 16, 27, 27

measurements, 27–8

Alternating current thermal diffusivity

measurement analyzer, 16

Alternating temperature, 27

Aluminium crucibles/sample vessels, 46, 107, 108,
118, 132, 147, 148, 155, 182

Aluminium nitride crucibles/sample vessels, 46

Aluminium wire, coated, 132

Amorphous alloys

glass transition of, 114–15, 122

specific heat capacity determined for, 122

thermal expansion curves for, 123–4, 124

Anti-oxidant additives [for petroleum], 410–12

Anti-oxidant properties of metals and alloys, 123

Apparatus

basic conformation, 15

commercial apparatus, 15–16

computer software for, 16–17

Arrhenius equation, 26, 54, 69, 152

applicability to solid-state kinetics, 56–7

Arrhenius plots

oxidative induction time, 132, 182

secondary relaxation of cross-linked polymer, 106

Arsenate minerals, thermal analysis of, 312–13

ASTM adiabatic bomb calorimeter, 149

ASTM standards, 12, 66, 72

Atmospheric effects, 44–5

Austenitic transformation, 113

Avrami equation, 50, 52, 78, 82

combined with Ozawa equation, 53

Avrami–Erofeev equation, 386, 387, 388, 390

Avrami rate parameters, 80, 82, 101, 119

Barton method, 56

Binary systems, phase diagrams for, 91–2

Biomaterials, water content of, 111

Borate minerals, thermal analysis of, 301–8

Buoyancy effects, 45

Calcination conditions of multicomponent catalysts,
139–40

- Calibration methods, 8–11
 - calorimetric calibration, 11
 - dimensional calibration, 11
 - enthalpy calibration, 9–11
 - temperature calibration, 8–9, 11
- Calorimetric calibration methods, 11
- Calorimetric purity method, 159
- Carbon black in rubber, measurement of, 151–2, 185
- Carbon crucibles/sample vessels, 46
- Carbonate minerals, 149, 150, 293–300, 419–22
- Catalysts
 - burning coke on, 141
 - DTA–EGD–GC curves, 141, 403–9
 - evaluation of metal catalysts by pressure DSC, 141–2
 - evaluation in solid state by DTA–EGD–GC coupled technique, 136–41, 403–9
 - methanation catalysts, 140, 406–7
 - poisoning of, 140–1, 407–8
 - regeneration after sulfur poisoning, 409
 - multicomponent catalysts, 139–40, 405
- Cell suspensions, cryobehavior of, 124–5
- Cellulose
 - acid hydrolysis of, 144–5
 - thermal decomposition of, 142–3
- Certified Magnetic Reference Material GM 761, magnetic transition temperatures, 8
- Certified Reference Materials (CRMs), 9, 10
- Charring, thermosetting resins, 133, 134
- Chemico-thermal stability, of polymeric materials, 129
- Chinese National Standards, 12
- Chromate minerals, thermal analysis of, 314
- Clearing point, liquid crystals, 88
- Clerk–Taylor method [for determination of thermal diffusivity], 159
- Cloud point curves
 - polymer blends, 93
 - see also* Turbidity
- Coal
 - determination of heat content, 148–9
 - DTA–EGD–GC curves, 413–17
 - proximate analysis of, 148
- Coke, proximate analysis of, 148
- Commercial apparatus, 15–16
 - non-standard thermal analyzers, 16
 - standard thermal analyzers, 16
- Continuous temperature–transformation (CTT) diagrams, 120
 - see also* Time–temperature–transformation (TTT) diagrams
- Controlled rate thermogravimetry (CRTG), 19
- Controlled transformation rate thermal analysis (CRTA) method, 60–1
- Convection currents, effect on TA, 45
- Conversion factors listed, 426–7
- Copper crucibles/sample vessels, 132, 182
- Copper oxide catalysts, oxidative activity of, 137–8
- Copper wire, coated, 132
- Corrosion resistance of metals and alloys, study by TGA, 123
- Cowen method [for determination of thermal diffusivity], 159
- Critical cooling rate, metals and alloys, 120
- Cross-linked polymers
 - effect of cross-linked density on glass transition temperature, 68, 179
 - secondary relaxation of, 106
 - thermal analysis of, 133–6, 179
- Crucibles [in TG], 18–19, 19, 45
 - see also* Sample vessels
- Cryopreservation of cells, 124–5
- Crystallinity of polymers
 - determination of, 83–4
 - effect on glass transition temperature, 68
 - effect of processing conditions, 84–5
 - in polymer blends, 93–4, 95–6, 97
- Crystallization enthalpy, amorphous alloys, 114
- Crystallization of metals and alloys, 118
- Crystallization of polymers
 - heat of crystallization determined by DSC, 74–6, 79
 - isothermal crystallization, 77–8
 - determination of crystallization rate, 78
 - growth rate of polymer spherulites, 81, 82–3, 82, 101
 - kinetic parameters, 82
 - measurement of heat of crystallization, 78–9
 - of miscible polymer blends, 100–1
 - surface free energies of developing crystals, 80
 - transition regions of melt-crystallized polymers, 79–80
 - transport activation energy of polymer segments, 80–1
 - non-isothermal kinetics, 51–3
- Crystallization temperature
 - determination by DSC/DTA, 72–3
 - end temperature of crystallization, 73, 73
 - onset temperature of crystallization, 73, 73
 - peak temperature, 73, 73
 - in polymer blends, 94, 95, 96–7
- Crystals, liquid crystals, 87–9
- Curie point, 8, 19, 115, 116
- Curve, meaning of term, 5
- Dehydration, of inorganic salts, 64, 391, 392, 395, 398, 399, 400
- Denaturation of proteins, 90–1, 125
- Derivative, meaning of term, 5
- Derivative TA curves, 49, 61–2
- Devitrification, 133, 134
- Dielectric loss spectra, polymers, 106
- Dielectric measurement analyzer, 16, 106
- Difference-differential methods, 48
 - see also* Freeman–Carroll method
- Differential, meaning of term, 5

- Differential scanning calorimetry (DSC), 6
 - acid hydrolysis of cellulose studied using, 144–5
 - apparatus, 16, 19, 20, 45
 - determination of apparatus constant, 78–9
 - installation considerations, 39
 - sample vessels, 45, 118
 - software for, 16, 119, 156
 - automated sample supplier, 39
 - calorimetric calibration of, 11
 - compared with TMDSC, 22
 - composition of polymer blends determined using, 101–2
 - coupled with EGD, 34–5
 - crystallinity of polymers determined using, 83–5
 - crystallization temperature determined using, 72–3
 - curing of thermosetting resins studied using, 135
 - data reporting of, 7
 - definition, 4
 - energetic materials studied using, 147–8, 343–6, 350, 354–5, 358–60, 362, 365, 369–73
 - enthalpy calibration of, 9–11
 - enthalpy of melting of perfect polymer crystals determined using, 76
 - enthalpy relaxation of polymers studied using, 68–9, 168
 - fat [animal fat] studied by, 89–90, 125
 - food components studied using, 212–36
 - with Fourier transform infrared spectrometry (DSC–FTIR), 165–6
 - glass transition temperature determined using, 66–7
 - gypsum converting to plaster of Paris studied by, 153
 - heat-conductive oils studied using, 150
 - heat-flux DSC, 4
 - apparatus, 16, 19, 20
 - data reporting of, 7
 - sample vessels, 20, 21
 - triple-cell heat flux DSC, 20–1
 - heats of fusion/crystallization of polymers determined using, 74–6
 - high-pressure DSC, 112, 141–2, 148
 - applications, 145, 340
 - high-sensitivity DSC, 23
 - inorganic materials studied using, 393, 395
 - isothermal crystallization of polymers studied using, 77–9, 101
 - iso-thermosetting reaction of resin, 54
 - lipids studied using, 90, 91
 - liquid crystals studied using, 33, 87–8, 89
 - low-temperature operation, 24, 124
 - meat analysis using, 125–6
 - melting temperature determination using, 72–3
 - mixed edible fat studied using, 125
 - multiple melting peaks of polyethylene studied using, 85–6
 - non-isothermal crystallization kinetics of
 - polymers studied using, 51–3
 - oxidative stability determined using
 - for polymers, 132
 - for rosins, 145
 - phase diagrams constructed using, 91–2, 93, 109
 - photopolymerized polymers studied using, 136
 - plant materials studied using, 240–3, 245–6
 - polymer blends studied using, 92–102
 - polymers studied using, 168–83, 185
 - polymorphism of long-chain hydrocarbons studied using, 86, 87
 - pore size distribution determination using, 161
 - power compensation DSC, 4
 - apparatus, 21, 21
 - compared with heat-flux DSC, 21
 - data reporting of, 7
 - maximum sensitivity, 21
 - pressurized DSC (PDSC), 112, 141–2, 148
 - purity determined using, 159–60
 - sample vessels, 46, 107, 108, 118, 147, 148, 155, 182
 - self-reacting substances studied using, 147–8
 - silicone rubber studied using, 126
 - simultaneous DSC–RLI instrument, 32, 33
 - simultaneous DSC–TLI instrument, 32–3
 - solid fat index determined using, 89–90
 - specific heat capacity determined using, 22–3, 120–1, 122, 155–6
 - step heating technique, 90
 - sub-ambient operation, 24, 124
 - temperature calibration of, 8–9
 - temperature-modulated DSC, 21–3
 - compared with DSC, 22
 - experimental precautions, 22
 - heat capacity determination using, 22–3
 - thermodynamic equilibrium melting temperature of polymer crystals determined using, 74
 - transport activation energy of polymer segments measured using, 80–1
 - water in biomaterials determined using, 111
 - water content of polymers determined using, 107–8
 - water–ethanol mixtures measured using, 110
 - water–polymer systems studied using, 109, 110
 - wax content of lubricants determined using, 90
 - with X-ray analysis, 33
- Differential thermal analysis (DTA), 6
 - apparatus, 16, 17, 20, 45
 - installation considerations, 39
 - software for, 16
 - borate minerals studied using, 304–7
 - coupled with EGD, 34–5
 - coupled with EGD and GC, 35–6, 402
 - applications, 403–23
 - crystallization temperature determination using, 72–3
 - data reporting of, 7
 - definition, 4

- Differential thermal analysis (DTA) (*continued*)
 DTA-EGD-GC on-line coupled simultaneous technique, 35-6, 402
 applications, 36, 136-41, 403-23
 energetic materials studied using, 147, 338-42, 344, 344-9, 347-9, 351-4, 351-8, 356-8, 361, 363-4, 366-8, 372
 enthalpy calibration of, 9-11
 glass transition temperature determined using, 66-7
 high-pressure DTA, 16, 23-4, 24
 applications, 174, 176, 344, 346, 349, 361
 liquid crystals studied using, 88
 lowest separation temperature determined using, 63
 melting temperature determination using, 72-3
 phase diagrams constructed using, 116-17
 with polarizing light microscopy (DTA-POL), 16
 polymers studied using, 174, 176, 177
 silicone rubber, 126
 temperature-time curve, 19-20, 20
 temperature calibration of, 8-9
 characteristics required of reference standards, 9
 terminated point [for transition or reaction]
 determined using, 62
 thermal time constant determined using, 62-3
 with thermogravimetry (TG-DTA), 16, 17, 18, 108-9, 111, 112, 126, 149
 arsenate minerals, 312-13
 borate minerals, 300-3, 308
 carbonate minerals, 293-300
 chromate minerals, 314
 for elements, 248-52
 and Fourier transform infrared spectrometry (TG-DTA-FTIR), 37-8, 142-4
 halide minerals, 252-6
 and mass spectrometry (TG-DTA-MS), 36-7
 oxide minerals, 271-80
 phosphate minerals, 308-12
 silicate minerals, 315-36
 sulfate minerals, 280-93
 sulfide minerals, 256-70
 and thermo-gas titrimetry (TG-DTA-TGT), 38
 tungstenate minerals, 315
 vanadate minerals, 314
 with X-ray diffractometry, 16
see also DTA-EGD-GC...; TG-DTA-MS coupled technique
- Differential thermogravimetry (DTG)
 silicone rubber, 126
 water sorbed on polymers, 109
- Dilatometry, 26-7
see also Thermodilatometry
- Dimensional calibration, of TMA, 11
- DIN standards, 12
- Dotriacontane, polymorphism of, 86
- Doyle's [approximate] expression, 47, 131
- DTA-EGD-GC on-line coupled simultaneous technique, 35-6
 apparatus, 35-6
 applications, 36, 136-41, 403-23
 procedures, 36
see also Differential thermal analysis; Evolved gas detection; Gas chromatography
- DTA-GC coupled technique, copper oxide catalysts studied using, 137-8
- DTA-NDIR coupled technique, 38
see also Differential thermal analysis; Non-dispersive infrared spectrometry
- DTA/DSC-EGD coupled technique, 34-5
see also Differential scanning calorimetry; Differential thermal analysis; Evolved gas detection
- Dynamic mechanical analysis (DMA), 4, 25-6
 apparatus, 16, 26, 26
 software for, 16
 DMA curves, 26, 26
 polymers studied using, 104-5, 106-7, 193-204
 theory, 25
 transition maps, 26, 26
 TTT isothermal cure diagram constructed using, 133
- Dynamic mechanical storage modulus, polymers, 106, 107
- Dynamic rate controlled method, 64
- Dynamic thermomechanometry, 6
 definition, 4
see also Dynamic mechanical analysis (DMA)
- Edible fat, thermal analysis of, 125
- Edible meat, DSC measurement of, 125-6
- Elastomers
 glass transition temperatures, 166
 specific heat capacities, 167
 thermal stability, 186-7
 WLF equation constants for, 70
see also Rubbers
- Electrically insulating materials
 thermal index estimated for
 by TG-secant method, 131
 by Toop method, 129-31
- Electron traps, 29
- Elements, thermal analysis of, 247-52
- Ellerstein method, 55-6
- Emanation thermal analysis, 6
- Energetic/energy-stored materials
 monitoring instantaneous change of, 146
 thermal analysis of, 146-9, 337-77
- Energy, conversion factors, 427
- Enthalpy *see* Crystallization...; Fusion/melting...; Mixing...; Transition enthalpy
- Enthalpy calibration, of DSC/DTA, 9-11
- Enthalpy changes, dehydration processes, 393, 395, 398, 399

- Enthalpy method, specific heat capacity determined using, 121, 156
- Enthalpy relaxation, 66, 68–9, 168
- Entropy *see* Mixing entropy
- Epoxy-amine resins, kinetics of thermosetting, 53–4
- Epoxy resins, curing of, 135
- Equilibrium melting temperature, of polymer crystals, 74
- Evolved gas analysis (EGA), 6
 - coupled with thermal analysis, 33, 36–9, 143, 144, 357
- Evolved gas detection (EGD), 6
 - coupled with DSC/DTA, 34–5
 - coupled with DTA and GC, 35–6, 402
 - applications, 403–23
 - coupled with thermal analysis, 33, 34–6
 - quantitative method, 34–5, 402
- Experimental factors, effect on TA, 42–7
- Explosives, thermal analysis of, 146–8, 337–77
- Fat
 - mixed fat, 125
 - solid fat index determined for, 89–90
- Ferromagnetic materials, magnetic transition temperatures of, 8, 115–16
- Fibers *see* Polymer fibers
- Films, polymer, study by TMA, 102–4
- Flame-retardant wood, combustion characteristics, 145–6
- Flory-Huggins theory, 99
- Food additives, thermal analysis of, 223–37
- Foods, thermal analysis of, 212–23
- Fourier-Biot equation, 157
- Fourier transform dielectric spectrometry, 16
- Fourier transform infrared spectrometry (FTIR)
 - with differential scanning calorimetry (DSC-FTIR), 165–6
 - with Raman spectroscopy, 355
 - with thermogravimetry (TG-FTIR), 16, 37–8, 142–4, 351
- Fox equation, 92, 93, 95
- Freeman-Carroll method [for determination of kinetic parameters], 48–9, 55
- Fusible links temperature calibration data, 9
- Fusion/melting enthalpy
 - data listed for reference materials, 10, 11, 75
 - of perfect polymer crystals
 - determination by DSC, 76
 - determination by solvent dilution, 76–7
 - of polymers, determination by DSC, 74–6
 - of rare-earth compounds, 399
- Gas chromatography
 - with DTA (DTA-EGD-GC), 35–6, 403–23
 - with thermogravimetry (TG-GC), 16
- Gases, thermal conductivities, 158
- Gelatinization, effect on DSC curves for starch, 111
- Gelation, 133
- Gibbs free energy of mixing, 99
- Gibbs free enthalpy difference, crystallization and melting of metals and alloys, 112
- Ginstling-Brounshtein equation, 50, 58
- Glass crucibles, 122
- Glass-forming ability (GFA) of alloys, 114, 118
- Glass transition
 - of amorphous alloys, 114–15
 - meaning of term, 114
 - of polymers
 - activation energy, 71, 194, 196–8
 - resolution by TMDSC, 22
- Glass transition temperatures
 - of copolymers, 167
 - determination by DSC/DTA, 66–7
 - of elastomers, 166
 - end temperature of glass transition, 66, 67
 - mid-point glass transition temperature, 66, 67, 166
 - onset temperature of glass transition, 66, 67
 - of polymer blends, 68, 92–3, 98
 - of polymers, factors affecting, 67–8
 - of thermosetting resins, 133, 134
- Gold crucibles/sample vessels, 46, 144
- Gordon-Taylor equation, 92, 92, 93
- Gray's definition of least separation temperature, 63
- Greases, oxidative stability of, 132–3
- Gypsum, conversion to plaster of Paris, 152–3
- Halide minerals, thermal analysis of, 252–6
- Heat capacity
 - determination of, 22–3, 27, 155–6
 - see also* Specific heat capacity
- Heat conduction equation, 158
- Heat-conductive oils, thermal decomposition of, 150
- Heat content, of coal, determination by PDSC, 148–9
- Heat of crystallization
 - of polymers, determination by DSC, 74–6, 79
 - see also* Enthalpy of crystallization
- Heat-flux DSC, 4
 - apparatus, 16
 - data reporting of, 7
 - triple-cell heat-flux DSC, 20–1
- Heat of fusion
 - data listed for standard materials, 11, 75
 - for polymer blends, 93
 - for polymers, 74–6, 94
 - see also* Enthalpy of fusion
- Heat-resistant polymers
 - structures, 130
 - thermal stability of, 129
- Heating-curve determination, 6
- Heating rate
 - effect on TA, 42–3, 46, 48
 - meaning of term, 5–6
- High-pressure DSC, 112, 141–2, 148
 - applications, 145, 340

- High-pressure DTA
 apparatus, 16, 23–4, 24
 applications, 174, 344, 346, 349, 361
- High-sensitivity DSC (HS-DSC), 23
- Hoffman–Weeks plots, 74, 94, 96
- Humidity
 viscoelasticity of polymers affected using, 107
see also Water vapor
- Hydrated polymer systems, water content of, 107–9
- Hydrocarbons, long-chain, polymorphism studied by DSC, 86, 87
- Hydrogen, iron oxide reduced by, 152
- Hydrogen sulfide, catalysts affected by, 408
- ICTA–NBS Standard Reference Materials (SRMs), 9
- Indium
 determination of thermal time constant, 63
 enthalpy/heat of fusion/melting, 10, 11, 75, 160
 melting DSC curve, 112, 160
 melting temperature, 10, 10, 11, 75, 112
 effect of heating rate, 42
 as fusible link, 9
- Inorganic materials
 dehydration of, 64
 thermal analysis of, 378–400
- Interaction energy density, polymer blends, 94, 94, 95, 97
- International Confederation for Thermal Analysis (ICTA)
 first established, 4
 Standard Reference Materials, 9
see also ICTA–NBS...SRMs
- Interpenetrating polymer networks (IPNs), 200
- Isobaric mass-change determination, 6
- Isoentropic diagram, 118
- Isothermal crystallization
 DSC curves, 78, 79
 of miscible polymer blends, 100–1
 of polymers, 77–8
 crystallization rate determined by DSC, 78
 growth rate of spherulites, 81, 82–3, 82
 heat of crystallization determined by DSC, 78–9
 transport activation energy of polymer segments, 80–1
- Isothermal solid-state reactions, 50–1
- Jander equation, 50, 58
- Japanese Industrial Standards (JIS), 12, 66, 72
- Johnson–Mehl–Avrami (JMA) kinetic model, 58, 59, 119
- Kauzmann temperature, 118
- Kinetic compensation effect, 57
- Kinetic model function, 57
 determination of, 58–9
 functional forms, 50, 58
- Kinetics
 isothermal crystallization of polymers, 80–1
 non-isothermal crystallization kinetics of polymers, 51–3
 of thermal analysis, 47–9
 Kirchhoff's equation, 91
 Kissinger method [for determination of activation energy], 42, 48, 56, 396
- Laser pulse method, thermal measurement by, 159
- Least separation temperature
 determination using DTA, 63
 Gray's definition, 63
- Lifetime–temperature relationship, electrically insulating materials, 131
- Lignin, thermal decomposition of, 143–4
- Linear expansion coefficients, determination of, 27, 123–4, 156–7
- Lipids, thermal phase transition of, 90, 91
- Liquid crystals, 87
 study using DSC, 33, 87–8, 89
see also Thermotropic liquid crystals
- Long-chain hydrocarbons
 polymorphism studied by DSC, 86, 87
 thermal diffusivity, 159
- Loss factor, polymers, 104, 105, 193–204
- Loss modulus *see* Shear loss modulus
- Low-temperature DSC, 24, 124–5
- Lower critical solution temperature (LCST), for polymer blends, 97, 99
- Lubricants
 oxidative stability of, 132
 wax content of, 90
see also Oils and greases
- Magnetic transition temperatures [of ferromagnetic materials], 8, 115–16
 determination by specific heat method, 115, 115–16
 determination by TG, 115
- Malek–Šmrcka method [of kinetic analysis of TA data], 57
- Mampel equation, 386
- Martensitic transformation of shape memory alloys, 113–14
- Mass of sample, effect on TA, 43
- Mass spectrometry, 36
 with thermogravimetry (TG–MS), 16, 356
 with thermogravimetry and gas chromatography (TG–MS–GC), 16
- Melting enthalpy *see* Fusion/melting enthalpy
- Melting entropy, rare-earth compounds, 399
- Melting temperature
 data listed for reference materials, 10, 10, 11, 75
 determination by DSC/DTA, 72–3
 end temperature of melting, 72, 73
 onset temperature of melting, 72, 73
 peak temperature, 72, 73
 polyethylene, 86
 polymer blends, 94, 97–8

- thermodynamic equilibrium melting temperature, of polymer crystals, 74
- Metal catalysts, evaluation of, 141–2
- Metals and alloys
 - corrosion resistance of, 123
 - crystallization and melting of, 112–13
 - magnetic transition of, 115–16
 - phase transformation of, determination of kinetic parameters for, 117–20
 - reaction with gases, 152
 - specific heat capacities determined for, 120–3
 - thermal conductivities, 158
 - thermal diffusivity data, 159
 - thermal expansion coefficients, 157
- Metastable phase diagram, 117–18
- Metastable solids, specific heat capacity determined for, 121–2
- Methacrylate polymers
 - apparent activation energy of enthalpy relaxation, 69
 - WLF equation constants for, 70
- Methanation catalysts
 - activity and selectivity of, 140, 406–7
 - poisoning of, 140–1, 407–8
 - regeneration after poisoning, 409
- Minerals
 - arsenate minerals, 312–13
 - borate minerals, 301–8
 - carbonate minerals, 293–300, 419–21
 - chromate minerals, 314
 - determination of composition of minerals showing isomorphism, 149–50
 - DTA–EGD–GC curves, 418–23
 - halide minerals, 252–6
 - oxide minerals, 271–80
 - phosphate minerals, 308–12
 - quantitative analysis of, by TG, 149
 - silicate minerals, 315–36
 - sulfate minerals, 280–93
 - sulfide minerals, 256–70, 418–19
 - thermal analysis of, 252–336
 - tungstenate minerals, 315
 - vanadate minerals, 314
- Mixing enthalpy, metallic liquids, 117
- Mixing entropy, metallic liquids, 117
- Mixture testing, liquid crystals studied using, 88
- Multicomponent systems, phase diagram for, 91
- Multi-step process, distinguished from derivative TA curve, 62
- Nanostructure alloys, specific heat capacity determined for, 122
- National Bureau of Standards (NBS), *see also* ICTA–NBS Standard Reference Materials
- Nichrome heating coil, 17
- Nishi–Wang plots, 94, 96
- Nitrobenzenes, 338–9
- Nomenclature, developments in, 4, 5
- Non-dispersive infrared (NDIR) spectrometry, 33
 - coupled with DTA, 38
- Non-isothermal crystallization kinetics of polymers, 51–3
- Non-isothermal kinetic analysis [of TA data], 57–60
- Non-metallic materials
 - thermal conductivities, 158
 - thermal diffusivity data, 159
 - thermal expansion coefficients, 157
- Oils, heat-conductive oil, 150
- Oils and fats, oxidation of, 152
- Oils and greases, oxidative stability of, 132–3
- One-dimensional diffusion, 50
- Opto-thermal transient emission radiometry (OTTER), 39
- Organic materials, oxidative stability of, 132–3, 187–8
- Oxidative induction time (OIT), 132
 - of polyethylene, 132, 182
- Oxidative stability
 - of organic materials, 132–3, 187–8
 - of polymers, 132, 188
- Oxide minerals, thermal analysis of, 271–80
- Oxidizing atmosphere, 45
- Oxyluminescence, 29
- Ozawa–Flynn–Wall method [for determination of activation energy], 42, 47–8, 56, 131, 396
- Ozawa method [for non-isothermal crystallization kinetics], 52
 - modified Ozawa method, 52–3
- Packing density [of sample], effect on TA, 46–7
- Particle size of sample, effect on TA, 43–4
- PE function line, 147–8
- Peak area
 - liquid crystal transition enthalpy determined using, 88
 - measurement of
 - cut-and-weigh method, 10, 153
 - integrator method, 10
 - planimeter method, 10, 153
 - particle size effects, 43
 - sample mass effects, 43
- Peak values
 - kinetic parameters determined using, 49
 - for thermosetting resins, 56
- Perovskite-type catalysts, oxidative activity of, 138–9
- Petroleum anti-oxidant additives, DTA–EGD–GC curves, 410–12
- Phase boundary reaction, 50
- Phase diagrams
 - construction using DSC, 91–2, 93, 109
 - construction using DTA, 116–17
 - of metals and alloys, 116–17, 117–18
 - metastable phase diagram, 117–18
 - of polymer blends, 91–2, 93

- Phase diagrams (*continued*)
 - stable phase diagram, 117
 - unstable phases, 118
 - of water-polymer systems, 109, 110
- Phase separation, polymer blends, 92-3, 96-9
- Phosphate minerals, thermal analysis of, 308-12
- Photopolymerization reactions, 135-6
- Physical constants
 - conversion factors, 426
 - symbols, 426
- Plant materials, thermal analysis of, 239-46
- Plaster of Paris, production of, 152-3
- Platinum-rhodium alloy crucibles/sample vessels, 46
- Platinum-rhodium alloy heating coils, 17
- Platinum crucibles/sample vessels, 46
- Platinum heating coils, 17
- Polarizing light microscopy
 - with DSC, 80-1, 88
 - with DTA, 16
 - liquid crystals studied using, 88
 - polymer blends studied using, 101
- Polyethylene
 - degree of crystallinity, 86
 - density, 86
 - DTA curve of melting, 62, 63
 - heat of melting, 86
 - multiple melting peaks, 85-6
 - oxidative stability, 132, 182
 - types, 85
- Polyimides
 - structures, 130
 - thermal stability of, 129
- Polymer blends
 - amorphous polymer blends, 92-3
 - composition determined by DSC, 101-2
 - glass transition temperatures of, 68, 92-3, 98
 - lower critical solution temperature for, 99
 - miscible blends containing one (or more) crystalline polymers, 93-6
 - phase separation in, 96-9
 - upper critical solution temperature for, 99
- Polymer crystals
 - enthalpy of melting, 76-7
 - melting temperature determined by DSC, 74
 - surface free energies during isothermal crystallization, 80
- Polymer fibers, effect of spinning speed, 174, 190-1
- Polymer films
 - anisotropy measured using TMA, 102-3
 - effect of reinforcing agents on mechanical properties, 103
 - penetration and tension measurements by TMA, 103-4
- Polymer glasses, relaxation times of, 69
- Polymer liquid crystals, 88-9
- Polymer-solvent systems, upper and lower critical solution temperatures for, 99
- Polymerization reactions, thermal analysis of, 133-6, 183-5
- Polymers
 - chain molecular motions studied, 29
 - characteristic temperature, 72
 - crystallinity of
 - determination by dynamic heating method, 83-4
 - determination by isothermal crystallization method, 84
 - effect on glass transition temperature, 68
 - effect of processing conditions, 84-5
 - polyethylene, 86
 - crystallization kinetics
 - isothermal crystallization, 80-1
 - non-isothermal crystallization, 51-3
 - dynamic mechanical spectra, 104-5, 194-8, 200-1
 - enthalpy relaxation of, 68-9, 168
 - free volume fraction, 71-2
 - glass transition of
 - activation energy, 71, 194, 196-8
 - relaxation times, 69
 - temperature dependence, 70
 - resolution by TMDSC, 22
 - glass transition temperature
 - determination by DSC/DTA, 66-7, 166-7
 - effect of cross-linking density, 68
 - effect of crystallinity, 68
 - effect of plasticizer, 67-8
 - effect of random copolymers, 68
 - effect of relative molecular mass, 68
 - isothermal crystallization of, 77-82
 - crystallinity determined by DSC, 84
 - crystallization rate determined by DSC, 78
 - growth rate of polymer spherulites, 81, 82-3, 82
 - heat of crystallization determined by DSC, 78-9
 - kinetic parameters, 82
 - surface free energies of developing polymer crystals, 80
 - transition regions of melt-crystallized polymer, 79-80
 - melting temperature, factors affecting, 168-73, 179
 - molecular relaxation processes studied, 28
 - non-isothermal crystallization kinetics, 51-3
 - oxidative stability of, 132, 182
 - phase transition of
 - heating rate effects, 43
 - measurement by high-pressure DTA, 23, 24
 - plasticizers, effect on glass transition temperature, 67-8
 - thermal analysis curves, 165-211
 - thermal diffusivity data, 159, 205
 - thermal expansion coefficients, 72, 157
 - thermal stability of, 129
 - transition maps, 26, 26, 206-10
 - TSC spectra, 28
- Polymorphous diagram, 118
- Pore size distribution determination, 161

- Power compensation DSC, 4
 apparatus, 21, 21
 compared with heat-flux DSC, 21
 data reporting of, 7
 maximum sensitivity, 21
- Precious-metal catalysts, evaluation of, 141–2
- Pressure, conversion factors, 427
- Pressurized differential scanning calorimetry (PDSC), 112, 141–2, 148
- Privalov calorimeter, 23, 91
- Propylene, catalytic oxidation of, 139, 139–40, 405
- Proteins, denaturation of, 90–1, 125
- Proximate analysis, coal and coke, 148
- Quantitative differential thermal analysis (QDTA)
 apparatus, 20
 maximum sensitivity, 20
- Quantitative evolved gas detection (QEGD) method, 34–5, 402
- Quenched glasses, 122
 thermal expansion curves for, 124
- Raman spectroscopy, with FTIR spectroscopy, 355
- Random nucleation, 50
- Rare-earth-containing perovskite-type catalysts, 138–9
- Reaction enthalpy, gypsum to plaster of Paris, 153
- Reaction mechanism, effect on TA, 49–50
- Reaction order (RO) kinetic model, 58, 59
- Reducing atmosphere, 45
- Reflected light intensity, combined with DSC (RLI–DSC) analysis, 32, 33
- Relaxation activation energy, polymers, 71, 105–6
- Relaxed glasses, 122
 thermal expansion curves for, 124
- Resolution of apparatus, 47
- Retrogradation ratio, 217
- Rosins, oxidative stability of, 145
- Rubbers
 carbon-black content measurement
 continuous heating method, 151, 185
 double heating method, 151–2
 thermal analysis of, 126
 vulcanization of, 183
 WLF equation constants for, 70
 see also Elastomers
- Sample vessels [in DSC/DTA], 20, 21, 45, 107, 108, 118, 147, 148, 155
 maximum operating temperatures, 46
- Sensitivity
 high-sensitivity DSC, 23
 power compensation DSC, 21
 quantitative DTA, 20
- Sestak–Berggren (SB) kinetic model, 57, 58, 59–60
- Shape memory alloys, martensitic transformation of, 113–14
- Shape memory effect, 113
- Shear loss modulus, polymers, 104, 194–8, 202
- Shear storage modulus, polymers, 104, 105, 194–200, 202–3
- Silicate minerals, thermal analysis of, 315–36
- Silicon carbide heating coil, 17
- Silicone rubber, thermal analysis of, 126
- Silver crucibles/sample vessels, 46, 107, 147
- Simultaneous TA analysis, 15, 16, 32–9
- Small-angle X-ray scattering (SAXS), analysis simultaneous with DSC, 33, 74
- Software, 16–17, 119, 156
- Solid fat index (SFI), determination by DSC, 89–90
- Solid-state reactions, isothermal reactions, 50–1
- Solvent dilution, enthalpy of melting of perfect polymer crystals determined using, 76–7
- Specific heat capacity
 of α -alumina, 424–5
 of cellulose and related compounds, 178
 changes
 at glass transition, 66, 69
 on denaturation of proteins, 91
 determination of, 22–3, 27, 120–1, 155–6
 enthalpy method, 121, 156
 for magnetic transition of alloys, 115–16
 measuring error estimated, 121
 for metals and alloys, 120–3
 for metastable solids, 121–2
 scanning method, 120–1, 155–6
 of elastomers, 167
- Spinel-type catalysts, 136–7
- Spinning speed, polymer fibers, 174, 190–1
- Stability limit of phases, 118
- Stable phase diagram, 117
- Stainless-steel crucibles/sample vessels, 46, 144, 147, 150
- Standard Reference Materials (SRMs), 9
- Standard test methods, for thermal analysis, 12–13
- Storage modulus *see* Shear storage modulus
- Subscripts, meaning of term, 5
- Sulfate minerals, 280–93
- Sulfide minerals, 256–70, 418–19
- Sulfur dioxide, catalysts affected by, 140–1, 407
- Superheated crystals, specific heat capacity determined for, 121–2
- Surface free energies
 during isothermal crystallization
 polymer blends, 100–1
 polymer crystals, 80
- Synchrotron orbital radiation (SOR), analysis simultaneous with DSC, 33
- Temperature, conversion factors, 427
- Temperature calibration
 of DSC, 8–9, 109
 of DTA, 8–9
 of TG, 8, 19
 of TMA, 11

- Temperature-modulated DSC (TMDSC), 21–3
 - compared with DSC, 22
 - experimental precautions, 22
 - heat capacity determination using, 22–3
- Temperature wave analysis (TWA) method, 30–2
 - apparatus, 31
 - measurements, 31–2
 - samples, 31
 - theory, 30–1
- Terminology, 4–6
- TG-DTA-FTIR coupled technique, 37–8
 - see also* Differential thermal analysis; Fourier transform infrared spectrometry; Thermogravimetry
- TG-DTA-MS coupled technique, 36–7
 - see also* Differential thermal analysis; Mass spectrometry; Thermogravimetry
- TG-secant method, thermal index of electrically insulating materials determined using, 131
- Thermal analysis (TA)
 - apparatus
 - automated systems, 39
 - basic configuration, 15
 - commercial apparatus, 15–16
 - for energetic materials, 337
 - installation and maintenance considerations, 39–40
 - for minerals, 247
 - non-standard apparatus, 16, 27–32
 - resolution of apparatus, 47
 - simultaneous analyzers, 16, 32–9
 - simultaneous operation of several instruments, 15, 16, 32–9
 - standard apparatus, 16, 17–27
 - applications
 - carbon black in rubber, 151–2
 - catalysts evaluation, 136–42
 - coal and coke, 148–9
 - cross-linking and polymerization reactions, 133–6
 - crystallization and melting, 72–92
 - explosives, 146–8
 - glass transitions, 66–72
 - gypsum/plaster-of-Paris reaction, 152–3
 - heat-conductive oils, 150
 - metals and alloys, 112–24
 - metals reacting with gases, 152
 - minerals analysis, 149–50
 - miscibility and phase behavior of polymer blends, 92–102
 - oils and fats oxidation, 152
 - thermal stability studies, 129–33
 - thermomechanometry, 102–7
 - water content measurement, 107–12
 - wood, 142–6
 - characteristics, 6–7
 - classification of techniques, 6
 - coupled with EGD/EGA, 33–8
 - curves, types, 61–2
 - data reporting of, 7–8
 - definitions, 4, 5
 - experimental factors affecting, 43–7
 - with Fourier transform infrared spectrometry, 16, 33, 37–8
 - with gas chromatography, 16, 33, 35–6
 - historical background, 3–4
 - kinetics, 47–9
 - advances in, 56–61
 - with mass spectrometry, 16, 33, 36–7
 - meaning of term, 3, 4
 - meaning of various TA terms, 5–6
 - with non-dispersive infrared spectrometry, 33, 38
 - purity determined using, 159–61
 - standard test methods, 12–13
 - with thermo-gas titrimetry, 33, 38
 - thermodynamic parameters determined using, 155–9
- Thermal conductivity
 - conversion factors, 427
 - determination of, 157–8
 - ranges quoted for various materials, 158
- Thermal conductivity detectors (TCDs), 33, 34
 - applications, 403–20
- Thermal depolarization current measurement, 28
- Thermal diffusivity
 - determination of, 30–2, 158–9
 - values quoted for various materials, 159, 205
- Thermal expansion coefficients
 - determination of, 27, 123–4, 156–7
 - values quoted for various materials, 157
- Thermal index for electrically insulating materials
 - determination by TG-secant method, 131
 - determination by Toop method, 129–31
- Thermal stability
 - of elastomers, 186–7
 - of electrically insulating materials, 129–31
 - oxidative stability
 - of cotton, 187–8
 - of polymers, 132–3, 188
 - of polymeric materials, 129, 189
- Thermal time constant, determination using DTA, 62–3
- Thermally stimulated current (TSC) analyzer *see* Thermally stimulated current (TSC) analysis
- Thermoacoustimetry, 6
- Thermocurrent measurement, 28
- Thermodilatometry, 6, 24, 26–7
- Thermodynamic equilibrium melting temperature, of polymer crystals, 74
- Thermodynamic parameters, measurement using TA, 155–9
- Thermoelectrometry, 6
- Thermo-gas titrimetry (TGT), 33
 - coupled with TG and DTA, 38
- Thermogravimetry (TG), 6, 17
 - apparatus, 17–19

- above-balance sample arrangement, 18
- basic configuration, 17
- below-balance sample arrangement, 18
- commercially available apparatus, 16, 18
- crucibles, 18–19, 19, 45
- microbalance, 17–18
- parallel-balance sample arrangement, 18
- simultaneous measurements, 17
- software for, 16
- atmospheric conditions for measurements, 19
- carbon black in rubber measured using, 151
- coal/coke analysed using, 148
- corrosion resistance of metals and alloys studied using, 123
- data reporting of, 7
- definition, 4
- with differential thermal analysis (TG–DTA), 16, 17, 18, 108–9, 111, 112, 126, 149
 - arsenate minerals, 312–13
 - borate minerals, 300–3, 308
 - carbonate minerals, 293–300
 - chromate minerals, 314
 - and Fourier transform infrared spectrometry (TG–DTA–FTIR), 37–8, 142–4
 - halide minerals, 252–6
 - and mass spectrometry (TG–DTA–MS), 36–7
 - oxide minerals, 271–80
 - phosphate minerals, 308–12
 - silicate minerals, 315–36
 - sulfate minerals, 280–93
 - sulfide minerals, 256–70
 - and thermo-gas titrimetry (TG–DTA–TGT), 38
 - tungstenate minerals, 315
 - vanadate minerals, 314
- energy-stored materials studied using, 146
- with Fourier transform infrared spectrometry (TG–FTIR), 16, 37–8, 142–4, 351
- with gas chromatography (TG–GC), 16
- high-resolution TG, 19
- inorganic materials studied using, 379–92, 394–400
- and magnetic transition of metals and alloys, 8, 115
- with mass spectrometry (TG–MS), 16, 36–7
 - and gas chromatography (TG–MS–GC), 16
- metals reacting with gases studied by, 152
- minerals analysed using, 149
- oxidation of oils and fats studied using, 152
- plant materials studied using, 239–42, 244–5
- polymers studied using, 185–6, 188–9
- quantitative treatment of data, 63–4
- silicone rubbers studied using, 126
- temperature calibration of, 8, 19
 - Curie point method, 8, 19
 - dropping weight method, 8
- thermal index of electrically insulating materials determined using, 131
- with thermo-gas titrimetry (TG–DTA–TGT), 38
- water content of manganese dioxide determined using, 111, 112
- water content of polymers determined using, 108–9
 - see also* TG–DTA–MS...; TG–DTA–TGT coupled technique
- Thermoluminescence (TL)
 - apparatus, 16, 29, 30
 - measurements, 29–30
 - and oxyluminescence, 29
 - samples, 29
 - theory, 29
 - TL curves, 30
- Thermomagnetometry, 6
- Thermomechanical analysis (TMA), 6, 24
 - apparatus, 16
 - basic configuration, 25, 25
 - sample probes, 25, 25
 - software for, 16
 - applications, 102–4, 374
 - data reporting of, 7–8
 - dimensional/size calibration of, 11, 25
 - linear expansion coefficients measured using, 123–4, 156–7
 - polymer films studied using, 102–4
 - temperature calibration of, 11, 25
- Thermomechanometry, 15–16, 24–6
 - applications, polymers, 102–7
 - see also* Dynamic mechanical analysis; Thermomechanical analysis; Viscoelastic measurements
- Thermomicroscopy, 32–3
 - applications, 33
- Thermoparticulate analysis, 6
- Thermoporosimetry, 161
- Thermoptometry, 6
- Thermosetting resins
 - curing of, 135
 - determination of kinetic parameters, 55–6
 - glass transition temperatures, 133, 135
 - kinetics under isothermal conditions, 53–5
 - photopolymerization of, 135–6
 - TTT isothermal cure diagram used, 133–5
- Thermosonimetry, 6
- Thermostimulated current (TSC) analysis, 28–9
 - apparatus, 16, 28
 - applications, 28
 - experimental procedure, 28
 - thermal sampling method, 28–9
- Thermotropic liquid crystals, 87–8
- Thermotropic polymeric liquid crystals, 88–9
 - main-chain liquid crystalline polymers (MCLCP), 88–9
 - side-chain liquid crystalline polymers (SCLCP), 88, 89
 - transition temperature regions, 88
- Thomas–Staveley equation, 80
- Three-dimensional diffusion, 50

- Time-temperature-transformation (TTT) diagrams, 120
- Time-temperature-transformation (TTT) isothermal cure diagram, 13
- Toop method, 129–31
- Transition enthalpy, liquid crystals, 88
- Transition maps, polymers, 26, 26, 206–10
- Transition temperature of standard metals, 11
- Transmitted light intensity, combined with DSC (TLI-DSC) analysis, 32–3
- Transport activation energy, of polymer segments during isothermal crystallization, 80–1
- Triple-cell heat-flux DSC, 20–1
- Tungstenate minerals, thermal analysis of, 315
- Turbidity
 - crystalline polymer blends, 96
 - see also* Cloud point curves
- Turbulence effects, 45
- Two-dimensional diffusion, 50, 58

- Undercooled liquids, specific heat capacity determined for, 122–3
- Upper critical solution temperature (UCST), for polymer blends, 99

- Vanadate minerals, thermal analysis of, 314
- Van't Hoff equation, 159, 161
- Viscoelastic measurement analyzer, 16
- Viscoelastic parameters
 - for polymers, 106–7, 204
 - effect of humidity, 107
- Vitrification, 133, 134
- Vogel-Fulcher law, 119
- Vulcanization enthalpy, 183

- Water content
 - bound water content, 108–9, 111, 181
 - freezing bound water content, 108, 109
 - freezing water content, 108, 109
 - measurement of, 107–12
 - in aluminium oxide, 112
 - in biomaterials, 111
 - in manganese dioxide, 111, 112
 - in polymers, 107–9
 - in water-ethanol mixtures, 110
 - non-freezing water content, 108, 109
- Water vapor
 - dehydration process affected using, 44, 391
 - see also* Humidity
- Wax content of lubricants, determination by DSC, 90
- Weight-drop method [for temperature calibration of TG], 8
- Wide-angle X-ray diffraction (WAXD), analysis simultaneous with DSC, 33
- Williams-Landel-Ferry (WLF) equation, 26, 70, 71, 107
 - macromolecular constants in, 70–1
- Wire coatings, 132
- Wood
 - flame-retardant wood, 145–6
 - thermal decomposition of, 144
- Wood and wood components, thermal analysis of, 142–6

- X-ray diffractometry
 - with DSC, 33
 - with DTA, 16
 - liquid crystals studied using, 88
 - spinel-type catalysts studied using, 137
- Ziabicki method [for non-isothermal crystallization kinetics], 51–2

Index compiled by Paul Nash

Materials Index

Note: Figures and Tables are indicated [in this index] by *italic page numbers*

- ABS, 159
Acacia senegal powder, 220–1
Acanthite, 263
Adularia, 321
Adzuki bean cotyledon cells, 221
Adzuki protein, 222
Aegirine, 318
 Ag_3AsS_3 , 265
 AgAuTe_4 , 263
 AgCuS , 269
 AgSbS_3 , 265
Air, 159
Aksaite, 304
Alabandite, 261
 $\text{Al}(\text{AlSiO}_3)_2$, 323
 $\text{Al}_2\text{Al}(\text{SiO}_4)\text{O}$, 323
Alanine, complexes with rare earth bromides, 378, 382–5
Albite, 321
 $\text{Al}(\text{H}_2\text{O})_2(\text{AsO}_4)$, 313
 $\text{Al}_4(\text{H}_2\text{O})_4(\text{Si}_4\text{O}_{10})(\text{OH})_8$, 324
 $\text{AlK}(\text{SO}_4)_2 \cdot 12\text{H}_2\text{O}$, 232
Allanite, 333
Almandine, 322
 $\text{AlNH}_4(\text{SO}_4)_2 \cdot 12\text{H}_2\text{O}$, 233, 288
 $\text{Al}(\text{OH})_3$, 275
 AlOOH , 275
 $\text{AlO}(\text{OH})$, 275
 $\text{Al}_3(\text{PO}_4)(\text{OH})_6 \cdot 6\text{H}_2\text{O}$, 312
 $\text{Al}_2(\text{SiO}_4)(\text{F},\text{OH})_2$, 336
 $\text{Al}_2(\text{SiO}_4)\text{O}$, 323
 $\text{Al}_2\text{Si}_3\text{O}_7(\text{OH})_4$, 335
 $\text{Al}_2(\text{Si}_4\text{O}_{10})(\text{OH})_2$, 324
 $\text{Al}_4(\text{Si}_4\text{O}_{10})(\text{OH})_8$, 324
 $\text{Al}(\text{SO}_4)(\text{OH}) \cdot 5\text{H}_2\text{O}$, 291
 $\text{Al}_2(\text{SO}_4)(\text{OH})_4 \cdot 5\text{H}_2\text{O}$, 291
 $\text{Al}_4(\text{SO}_4)(\text{OH})_{10} \cdot 5\text{H}_2\text{O}$, 291
Alum, 288
 α -Alumina, 424–5
hydrated, 112
Aluminite, 291
Aluminum, 9, 11, 157, 159, 250
Aluminum chloride hexahydrate, 255
Aluminum powder, in propellant, 369
Aluminum sulfate heptadecahydrate, 285
Alunite, 289
Alunogen, 285
Ammoniac, 253
Ammonium chloride, 253
Ammonium nitrate, 358–61
Ammonium nitrate based explosive, 365
Analcime, 332
Anatase, 278
Anauxite, 335
Andalusite, 323
Andradite, 323
Anglesite, 280
Anhydrite, 282
Ankerite, 298
Anorthite, 321
Anthophyllite, 319
Anthracite coal, 414, 417
 α -Antigorite, 329
 β -Antigorite, 329
Antimony trioxide, 272
Antimony(III) sulfide, 258
Antlerite, 293
Aragonite, 296
Arbocel, 142–3
Arkanite, 280, 281
Arsenic sulfides, 258, 260
Arsenic trioxide, 272
Arsenolite, 272
Arsenopyrite, 268
Astrakanite, 286
Aurichalcite, 299
Avicennite, 272
Azal grapes, 222

- Azurite, 299
 $\text{Ba}(\text{AlSi}_3\text{O}_8)_2 \cdot 6\text{H}_2\text{O}$, 331
 $\text{BaCa}(\text{CO}_3)_2$, 297
 Baddeleyite, 278
 $\text{BaMg}(\text{CO}_3)_2$, 297
 Barite, 282
 Barium carbonate, 10, 293
 Barium sulfate, 282
 Bark and components, 242–3
 Barytocalcite, 298
 Basaluminite, 297
 Bassanite, 284
 see also Calcium sulfate hemihydrate
 BeAl_2O_4 , 279
 Bean oil, 152
 Beef fat, 125
 Beef tallow, 90
 Benite, 371
 Benzoic acid, 11, 75, 224
 sodium salt, 225
 Benzoin methyl ether, 135
 Benzoyl peroxide (BPO), 147
 Berthierite, 267
 Beryllium oxide, 277
 Beryllonite, 308
 Berzelite, 312
 Biotite, 326
 Bischafite, 255
 $\text{Bis}[N-(2\text{-hydroxyethyl})\text{-}o\text{-vanillindiamino}]\text{zinc(II)}$, 389
 Bismite, 271
 $\text{Bis}[\text{monaqua-3-methoxysalicylaldehyde-}o\text{-aminobenzoic acid copper(II)}]\text{ monohydrate}$, 389
 Bismuth, 248
 Bismuth oxide, 271
 Bismuth silicate, 334
 Bismuth sulfide, 258
 Bismuthinite, 258
 Bismutotantalite, 279
 BiTaO_4 , 279
 Bituminous coal, 415
 Bitumite coal, 414
 Black powder, 370
 in benite, 371
 Boehmite, 275
Bombyx mori silk fibroin, 177, 199
Bombyx mori silk sericin, blend with PVA, 200
 Borax, 302
 Bornite, 265, 266
 Borosilicate glass, 11
 Boulangerite, 268
 Brazilianite, 311
 Britholite, 309
 Bromellite, 277
 Brycite, 275
 Bunsenite, 277
 Butadiene–styrene rubber, 185, 203
 Butlerite, 290
n-Butyl acrylate, 167
 Butyl rubber, 70, 166, 186
 $\text{CaAl}_2(\text{Al}_2\text{Si}_2)\text{O}_{10}(\text{OH})_2$, 327
 $\text{Ca}_3\text{AlAl}_2(\text{Si}_2\text{O}_7)(\text{SiO}_4)\text{O}(\text{OH})$, 333
 $\text{CaAl}_2(\text{F,OH})_8$, 256
 $\text{Ca}(\text{Al}_2\text{Si}_3\text{O}_8)$, 321
 $\text{Ca}(\text{Al}_2\text{Si}_3\text{O}_{10}) \cdot 3\text{H}_2\text{O}$, 331
 $\text{Ca}_2\text{Al}_2\text{Si}_3\text{O}_{10}(\text{OH})_2$, 335
 $\text{Ca}_3\text{Al}_3(\text{Si}_2\text{O}_7)(\text{SiO}_4)\text{O}(\text{OH})$, 333
 $\text{Ca}_3\text{Al}_2(\text{SiO}_4)_3$, 323
 $\text{Ca}_2\text{Al}_2\text{V}(\text{Si}_2\text{O}_7)(\text{SiO}_4)\text{O}(\text{OH})$, 333
 $\text{Ca}_7[\text{B}_4\text{BSiO}_6(\text{OH})_5]$, 308
 $\text{Ca}[\text{B}_2\text{O}(\text{OH})_6]$, 307
 $\text{Ca}[\text{B}_2\text{O}_2(\text{OH})_4]$, 305
 $\text{CaB}_2\text{O}_3(\text{OH})_2$, 304
 $\text{CaB}_3\text{O}_3(\text{OH})_5$, 304
 Cabrerite, 313
 $\text{Ca}_2\text{Ca}_3[(\text{PO}_4)(\text{CO}_3)]_3(\text{OH})$, 309
 $\text{Ca}_2\text{Ca}_3(\text{PO}_4)_3(\text{OH})$, 309
 $\text{Ca}_2\text{Ce}_3[(\text{Si,P})\text{O}_4]_3(\text{F,OH})$, 309
 $[\text{Ca,Ce,Th}][(\text{P,Si})\text{O}_4]$, 308
 Cadmium carbonate, 295
 $\text{Ca}_3\text{FeAl}_3(\text{Si}_2\text{O}_7)(\text{SiO}_4)\text{O}(\text{OH})$, 333
 $\text{Ca}_3\text{Fe(III)}_2(\text{SiO}_4)_3$, 323
 $\text{Ca}(\text{H}_2\text{O})_4[\text{B}_2\text{BO}_3(\text{OH})_5]$, 303
 $\text{Ca}_2(\text{H}_2\text{O})[\text{B}_4\text{BO}_7(\text{OH})_5]$, 307
 $\text{Ca}(\text{H}_2\text{O})_5[\text{B}(\text{OH})_4]_2$, 304
 Calaverite, 257
 Calcite, 149, 296
 Calcium carbonate, 35, 64, 149, 296
 Calcium fluoride, 253
 Calcium montmorillonite, 325
 Calcium oxalate, anhydrous, 35, 64
 Calcium oxalate monohydrate, 34, 47, 63–4
 Calcium oxide, 277
 Calcium propionate, 226
 Calcium sulfate, 231, 282
 Calcium sulfate dihydrate, 43, 44, 45, 153, 284
 Calcium sulfate hemihydrate, 152, 284
 Calcium tungstenate, 315
 $\text{CaMg}(\text{CO}_3)_2$, 149, 297
 $\text{CaMg}_3(\text{CO}_3)_4$, 297
 $\text{Ca}(\text{Mg,Fe(II),Al})(\text{Si,Al})_2\text{O}_6$, 317
 $\text{Ca}(\text{Mg,Fe})(\text{CO}_3)_2$, 298
 $\text{Ca}(\text{Mg}_{0.0-0.25}\text{Fe}_{1-0.75})(\text{Si}_2\text{O}_6)$, 317
 $\text{Ca}(\text{Mg}_{1-0.75}\text{Fe}_{0.0-0.25})(\text{Si}_2\text{O}_6)$, 317
 $\text{Ca}_2[\text{Mg,Fe(II)}]_2[\text{Si}_8\text{O}_{22}][\text{OH}]_2$, 320
 $\text{CaMg}(\text{H}_2\text{O})_3[\text{B}_2\text{BO}_4(\text{OH})_3]_2$, 307
 $\text{CaMg}(\text{H}_2\text{O})_6[\text{B}_2\text{BO}_3(\text{OH})_5]_2$, 305
 $\text{Ca}_2\text{Mn(III)Al}_2(\text{Si}_2\text{O}_7)(\text{SiO}_4)\text{O}(\text{OH})$, 333
 $(\text{Ca,Mn,Ce,La,Y,Th})_2[\text{Fe(II),Fe(III),Ti}](\text{Al,Fe})_2(\text{Si}_2\text{O}_7)(\text{SiO}_4)\text{O}(\text{OH})$, 333
 $\text{CaMn}(\text{Si}_2\text{O}_6)$, 317
 Camphor [in propellant], 365
 $(\text{Ca,Na}_2)(\text{Al,Si}_2\text{O}_6) \cdot 6\text{H}_2\text{O}$, 331

- $(\text{Ca}, \text{Na}_2)(\text{AlSi}_2\text{O}_6) \cdot 6\text{H}_2\text{O}$, 331
 $(\text{Ca}, \text{Na}_2)(\text{Al}_2\text{Si}_7\text{O}_{18}) \cdot 6\text{H}_2\text{O}$, 330
 $(\text{Ca}, \text{Na}_2, \text{K}_2)(\text{Al}_2\text{Si}_7\text{O}_{18}) \cdot 7\text{H}_2\text{O}$, 332
 $(\text{Ca}, \text{Na})(\text{Mg}, \text{Fe(II)}, \text{Fe(III)}, \text{Al})(\text{Si}_2\text{O}_6)$, 317
 $(\text{Ca}, \text{Nb})_2\text{Nb}_2\text{O}_6(\text{OH}, \text{F})$, 280
 Candle coal, 413
 Carboborite, 307
 Carbonate-hydroxyapatite, 309
 Carboxylated poly(2,6-dimethyl-1,4-phenylene-polystyrene blends, 99
 Carboxylated poly(phenylene oxide)-polystyrene (CPPO-PS) blends, 100
 Carboxymethylcellulose (CMC), sodium salt, 109, 110, 233
 Carnalite, 255
 κ -Carrageenan (CAR), 217-18
 Cassiterite, 278
 Castor oil-polyepichlorohydrin (PECH-CO) blends, 201
 $\text{Ca}(\text{WO}_4)$, 315
 Celestine, 282
 Cellobiose, 178
 Cellophane film, 193
 Cellulose, 143, 145, 178, 181, 239-40
 amorphous, 178
 regenerated cellulose, 107, 180-1
 Cellulose ester, *see also* PHB-CE blends
 Cellulose nitrate, 70
 Cellulose tributyrates, 70
 Centralite, 373
 in propellants, 366-9
 Cerianite, 278
 Cerium bromide
 complex with alanine, 383
 complex with glycine, 379
 Cerium dioxide, 278
 Cervantite, 272
 Chabazite, 331
 Chaidamuite, 292
 Chalcantite, 284
 Chalcocite, 263
 Chalcopyrite, 265
 Cheralite, 308
 Chloragyrite, 253
 Chloraluminite, 255
 Chlorinated polyethylene (CPE) blends, 99
 Chromium trioxide, 278
 Chrysoberyl, 279
 Chrysolite, 316
 α -Chrysotile, 329
 β -Chrysotile, 329
 $\text{C}_{12}\text{H}_{25}\text{SH}$, 412
 Cinnabar, 260
 Citric acid, 230
 Clinocllore, 328
 Clinostatite, 317
 Clinoptilolite, 330
 Clinoziosite, 333
 Coal, 148, 413-17
 Cobalt arsenosulfide, 269
 Cobalt carbonate, 295
 Cobaltite, 269
 Coesite, 273
 Co-Fe-Bi-Mo-A-B-C-O catalyst, 405
 $\text{Co}_3(\text{H}_2\text{O})_8(\text{AsO}_4)_2$, 313
 Colemanite, 304
 Coloradoite, 263
 β -Conglycinin, 214-15
 Cookeite, 328, 329
 $\text{CoO}(\text{OH})$, 276
 Copper, 157, 159, 250
 Copper-based spinels, 137
 Copper chloride, 254
 Copper iodide, 254
 Copper oxalate monohydrate, 43-4, 44
 Copper oxide, 274
 Copper oxide catalysts, 138, 139
 Copper sulfate pentahydrate, 284
 Copper sulfide, 263
 Coquimbite, 285
 Corn starch, 219, 220
 Cotton, 187
 flame-retardant, 188
 Cotton cellulose, 181, 239-40
 Cotton lint cellulose, 181
 COVTPU50St50, 71-2, 71, 106
 CPPO-PS blends, 100
 Cristobalite, 273
 Cryolite, 256
 $\text{CuAl}_6(\text{H}_2\text{O})_4(\text{PO}_4)_4(\text{OH})_8$, 310
 Cu-Al-Ni single crystals, 114
 Cu_3AsS_4 , 264
 $\text{Cu}_{12}\text{As}_4\text{S}_{13}$, 267
 $\text{Cu}_2(\text{CO}_3)(\text{OH})_2$, 299
 $\text{Cu}_3(\text{CO}_3)_2(\text{OH})_2$, 299
 Cu-Cr-O spinel, 137
 Cu-Fe-O spinel, 137
 CuFeS_2 , 265
 Cu_5FeS_4 , 265
 $\text{Cu}_2\text{FeSnS}_4$, 269
 Cupra rayon, 181
 Cuprite, 274
 $\text{Cu}_{12}\text{Sb}_4\text{S}_{13}$, 270
 $\text{Cu}_3(\text{SO}_4)(\text{OH})_4$, 293
 $\text{Cu}_4(\text{SO}_4)(\text{OH})_6 \cdot \text{H}_2\text{O}$, 293
 Cyclotetramethylenetetranitramine, 356
 Cyclourea nitroamine compounds, 357
 Cylindrite, 270
 Dextrin gel, 111
 Diamond, 157, 159
 synthetic, 252
 Diaspore, 275
 4,4'-Dichlorodiphenyl sulfone, 160
 Dickite, 324
 Diethanolnitramine dinitrate (DINA), 351

- Diethylene glycol dinitrate (DEGDN/DEGN), 350
 Di-4'-heptoxybenzal-1,4-phenylenediamine, 87-8
 2,4-Dihydroxyacetophenoneethylenediiminato-copper(II) monohydrate, 390
 2,4-Dihydroxyacetophenoneethylenediiminato-nickel(II) monohydrate, 390
 Dimyristoylphosphatidylcholine (DMPC), 91
 Dinitrato(di-*N*-alkylcaprolactams)uranyl(II), 60
 Dinitrato(*N,N,N',N'*-tetra-*n*-butyl aliphatic diamide)uranyl(II), 60
 1,2-Dinitrobenzene, 339
 1,3-Dinitrobenzene (1,3-DNB), 338
 1,4-Dinitrobenzene (1,4-DNB), 339
 Dinitrocellulose, in propellants, 365, 369
 2,4-Dinitrochlorobenzene (2,4-DNCB), 343
 2,6-Dinitrochlorobenzene (2,6-DNCB), 343
 3,4-Dinitrochlorobenzene (3,4-DNCB), 343
 Di(nitroethyl) nitramine, 351
N,N'-Dinitroethyleurea-2,5-dinitro-2,5-diazacyclopentan-1-one, 357
 1,4-Dinitroglycoluril (1,4-DINGU), 357
 2,6-Dinitro-2,4,6,8-tetraazadicyclo[3.3.0]-octanedione, 357
 2,3-Dinitrotoluene (2,3-DNT), 341
 2,4-Dinitrotoluene (2,4-DNT), 147, 341
 2,5-Dinitrotoluene (2,5-DNT), 341
 2,6-Dinitrotoluene (2,6-DNT), 341
 3,4-Dinitrotoluene (3,4-DNT), 341
 3,5-Dinitrotoluene (3,5-DNT), 341
 Diopside, 317
 Diphenylamine (DPA), 372
 in propellants, 365-6
 Dolomite, 44, 61, 149, 298
 Dotriacontane, 87
 Double-base propellants, 366-7, 368-9
 Dravite, 335
 Dysprosium bromide
 complex with alanine, 385
 complex with glycine, 381
 Dysprosium nitrate, 400

 Elbaite, 335
 Enargite, 264
 Engineering plastics, 168
 Epidote, 333
 Epoxy resin (EP), 135, 159, 184
 glass-fiber reinforced, 103
 Epoxy resin-phenol formaldehyde (EP-PF), 204
 Epsomite, 283
 Erbium phenylacetate, 399
 Erythrite, 313
 Eskolaite, 278
 Ethanol-water mixtures, 110
 Ethyl *p*-hydroxybenzoate, 227
 Ethylenedinitramine (EDNA), 354
 Ethylene-propylene copolymer, 70
 Eulytite, 334
 Europium acetate, 392
 Europium *N*-acetylalanate, 396
 Europium acetylvalinate, 397
 Europium bromide
 complex with alanine, 384
 complex with glycine, 381
 Europium nitrate, 400
 Evansite, 312
 EVEA rubber, 70

 Fassaitite, 317
 Faustite, 310
 Fayalite, 315
 Fe(II)Al₂(SO₄)₄ · 22H₂O, 288
 Fe(II)₃Al₂(Si₄O)₃, 322
 FeAsS, 267
 FeCl₃ · 6H₂O, 255
 Fe-Co-Si-B alloys, 124
 Fe15Cr alloy, 123
 Fe(III)₂Fe(II)BO₅, 301
 [Fe(II)₃ · Fe(III)₃][H₂O]₈₋₁₁[PO₄]₂[OH]₁₇, 312
 Fe(II)Fe(III)₂O₄, 274
 [Fe(II)]_{1-0.7} · Mg_{0-0.3}][Si₈O₂₂][OH]₂, 320
 (Fe(II)Mn)₂(PO₄)F, 309
 α-FeO(HO), 275
 γ-FeO(OH), 275
 Ferrinatriite, 286
 Ferrohortonlite, 316
 Fe-Si-B alloys, 115
 Fe(III)(SO₄)(OH) · 2H₂O, 290
 Fe(III)(SO₄)(OH) · 5H₂O, 290
 Fe(III)₂(SO₄)₂(OH)₂ · 7H₂O, 290
 FeS · Sb₂S₃, 267
 Fe-Ti alloys, 117
 Fiberboard, 146
 Fibers *see* Cellulose; Cotton; Jute; Linen; Rayon; Silk
 Fibroferrite, 290
 Flame-retardant cotton, 188
 Fluorinated elastomer, 186
 Fluorite, 253
 Forsterite, 315
 Franckeite, 270
 Franklinite, 279
 Fumaric acid, 230

 Gadolinium acetate, 392
 Gadolinium bromide
 complex with alanine, 385
 complex with glycine, 380
 Gadolinium-cobalt alloys, 116
 Gadolinium nitrate, 400
 Gahnite, 279
 Galena, 261
 Galenobismutite, 268
 Gas coal, 416
 Gellan gum, 218
 Gellan gusodium-type, 212-14
 Gibbsite, 275
 Glass-fiber reinforced epoxy resin, 103

- Glauberite, 281
 Glauconite, 325
 Glaucophane, 319
 Gluconic acid, zinc salt, 236, 237
 Glucono-delta-lactone, 228
 Glucose, 38, 178
 Glutamic acid, sodium salt, 236
 Glycerin monostearate, 235
 Glycerine trinitrate, 349
 Glycine, complexes with rare earth bromides, 378, 379–82
 Goethite, 275
 Gold, 9, 11, 157, 159, 251
 Gold telluride, 257
 Goslarite, 283
 Grapes, 222
 Graphite [clay-like], 251
 Graphite [flakes], 252
 Graphite [in propellant], 365
 Grossular, 323
 Grunerite, 320
 Gypsum, 153, 284
 see also Calcium sulfate dihydrate

 H_3BPO_3 , 301
 Halite, 253
 Halloysite, 324
 Halotrichite, 288
 Harmotome, 331
 Hastingsite, 320
 Hauerite, 256, 257
 Healandite, 330
 Heat-conductive oil, 150
 Hedenbergerite, 317
 Hematite, 273
 Hemicellulose, wheat straw, 244–6
 Heterogenite, 276
 Hexacosane, 43
 2,4,6,8,10,12-Hexanitro-2,4,6,8,10,12-hexaazatricyclo [7.3.0.03.7]-dodecane-5,11-dione, 357
 2,2',4,4',6,6'-Hexanitrostilbene (HNS), 348
 Hexogen, 354, 355
 $HgS_2 \cdot Sb_4S_6$, 267
 High-density polyethylene (HDPE), 77, 85, 159, 193–4
 HMX, 356, 374
 Hoernesite, 313
 Hohmannite, 290
 Holmium *m*-nitrobenzoate, 395
 Holmquistite, 319
 Holocellulose
 bark holocellulose, 242–3
 wheat straw holocellulose, 244–6
 Hortonlite, 316
 Howlite, 308
 Hungchaoite, 306
 Huntite, 297
 Hyaluronic acid (HA) hydrogel, 179
 Hydrazinium nitrate, 361
 Hydrobiotite, 326
 Hydroboracite, 307
 Hydromolysite, 255
 Hydromuscovite, 326
 Hydrotalcite, 300
 Hydroxyapatite, 309

 Illite, 327
 Inderborite, 305
 Inderite, 303
 Indium, 9, 10, 10, 11, 42, 63, 75, 112, 160
 Inyoite, 303
 Iron, 157, 159, 251
 Iron(II) aluminum sulfate dodecahydrate, 288
 Iron(II) carbonate, 297
 Iron(III) chloride hexahydrate, 255
 Iron–chromium alloys, 123
 Iron–cobalt–silicon–boron alloy, 124
 Iron disulfide, 256
 Iron(II) oxide, 274
 Iron(III) oxide, 152, 273
 Iron(II) silicate, 315
 Iron–silicon–boron alloy, 115
 Iron(II) sulfate heptahydrate, 282
 Iron(III) sulfate decahydrate, 285
 Iron(III) sulfate nonahydrate, 285
 Iron sulfide, 259
 Iron–titanium alloys, 117

 Jadeite, 318
 Jamesonite, 270
 Jarosite, 289
 Johannsenite, 317
 Jordanite, 264
 Jute cellulose, 181

 $KAl_2[(Al, Si_3)O_{10}](OH)_2$, 326
 $K_{1-x}(Al, Fe)_2(Al_{1-x}Si_{3-x}O_{10})(OH)_2$, 325
 Kaliborite, 306
 $K(AlSi_2O_6)$, 322
 $K(AlSi_3O_8)$, 321
 $KAl(SO_4)_2 \cdot 12H_2O$, 288
 $KAl(SO_4)_2(OH)_6$, 289
 Kaolinite, 51, 324, 422
 with siderite, 420–1, 423
 Kapok cellulose, 181
 Kapton [polyimide], 129, 159
 $K_2Ca(SO_4)_2 \cdot H_2O$, 286
 $KFe(III)_3(SO_4)_2(OH)_6$, 289
 $KHMg_2(H_2O)_4[IB_3B_3O_8(OH)_5]_2$, 306
 $K_{1-x}(H_2O)_xAl_2[AlSi_3O_{10}](OH)_{2-x}(H_2O)_x$, 327
 Kieserite, 283
 $KMg_3(AlSi_3O_{10})(OH)_2$, 327
 $K_2MgCa_2(SO_4)_4 \cdot 2H_2O$, 286
 $K(Mg, Fe, Al)_{2-x}[(Al, Si_3)O_{10}](OH)_2$, 326
 $K_2Mg_2(SO_4)_2 \cdot 4H_2O$, 287
 $K_2Mg_2(SO_4)_2 \cdot 6H_2O$, 287

- Konjac glucomannan (KGM), 217–18, 220
 Kozhinskite, 304
 Kraft lignin (KL), 143–4
 Krennerite, 257
 Kurnakovite, 306
 Kyanite, 323

 LaCoO₃ catalyst, 139, 404
 LaMnO₃ catalyst, 139, 403
 Langbeinite, 281
 Lanthanum bromide
 complex with alanine, 382
 complex with glycine, 379
 Lanthanum *m*-nitrobenzoate, 394, 395
 Lanthanum oxide, 83, 172–3
 Larc-TPI, 129
 Larch wood, 240–2
 Lard, 125
 La_{0.7}Sr_{0.3}CoO₃ catalyst, 139, 404
 Lead, 9, 11, 75, 249
 Lead(II) oxide, 271
 Lead styphnate, 363
 Lead(II) sulfate, 280
 Lead(II) sulfide, 261
 Lead 2,4,6-trinitroresorcinate (LTNR), 363
 coated with shellac, 372
 Leonite, 287
 Lepidocrocite, 275
 Leucite, 322
 LiAl₂(OH)₆Al₂[(AlSi₃O₁₀)(OH)₂], 328
 LiAl(PO₄)(OH), 311
 LiAl(Si₂O₆), 318
 Li(AlSi₄O₁₀), 322
 Lignin
 wheat straw lignin, 244–6
 wood lignin, 144
 Lignite coal, 416
 Lignocell, 144
 Lime, 277
 Li₂[Mg,Fe(II)]₃Al₂Si₃O₂₂[OH]₂, 319
 Linen cellulose, 181
 Litharge, 271
 Livingstonite, 267
 Long-chain hydrocarbons, 87, 159
 Lopezite, 314
 Lorandite, 267
 Low-density polyethylene (LDPE), 85, 193–4
 Lueneburgite, 305
 Lutetium *m*-nitrobenzoate, 394
 Lysozyme, 91

 McCoy's 5A medium with AB serum, 124
 Magnesite, 296
 Magnesium aluminum sulfate dodecahydrate, 288
 Magnesium carbonate, 149, 296
 Magnesium chloride hexahydrate, 255
 Magnesium hydroxide, 49, 275
 Magnesium oxide, 277

 Magnesium potassium chloride hexahydrate, 255
 Magnesium siderite, 150
 Magnesium silicate, 315
 Magnesium sulfate heptahydrate, 64, 282
 Magnesium sulfate monohydrate, 283
 Magnetite, 274
 Malachite, 299
 Maleic anhydride modified polypropylene, 170, 199
 Malic acid, 237
 Manganese carbonate, 297
 Manganese dioxide, 111, 112, 274
 Manganese disulfide, 256
 Manganese silicate, 315
 Manganese sulfate monohydrate, 283
 Manganese sulfide, 261
 Manganite, 276
 Manganosite, 274
 Manganotantalite, 279
 Mansfieldite, 313
 Margarite, 327
 Marshite, 254
 Massicot, 271
 Maucherite, 262
 Melantherite, 282
 Mercury sulfide, 260
 Mercury telluride, 263
 Metacinnabar, 260
 Metasequoia wood, 240–2
 Methacrylic acid, 136
 3-Methoxysalicylaldehydealaninezinc(II)
 monohydrate, 388
 3-Methoxysalicylaldehydeethyldiaminenickel(II)
 monohydrate, 386
 3-Methoxysalicylaldehydeleucinecopper(II)
 monoethanoate, 388
 3-Methoxysalicylaldehydeleucinenickel(II)
 monohydrate, 388
 3-Methoxysalicylaldehydephenylalaninenickel(II)
 monohydrate, 388
 3-Methoxysalicylaldehyde-*o*-
 phenyldiaminenickel(II) monohydrate, 386
N-Methyl-*N*,2,4,6-tetranitroaniline, 353
 Mg₆Al₂(CO₃)(OH)₁₆ · 4H₂O, 300
 MgAl₂O₄, 279
 Mg₃Al₂(SiO₄)₃, 323
 MgAl₂(SO₄)₄ · 22H₂O, 288
 Mg₃B₂O₅, 301
 Mg[B₂O(OH)₆], 305
 Mg₂[B₂O₄(OH)](OH), 308
 MgCa₂[HCO₃]₂[B(OH)₄]₂(OH)₂ · 2H₂O, 307
 Mg₆Cr₂(CO₃)(OH)₁₆ · 4H₂O, 300
 [Mg,Fe(III),Al]₃(AlSi₄O₁₀)(OH)₂ · *n*H₂O, 330
 (Mg,Fe,Al)₃(OH)₆(Mg,Fe,Al)₃[(Si,Al)₄O₁₀](OH)₂, 328
 (Mg,Fe,Al)₃(OH)₆[Mg,Fe(II),Al]₃[(Si,Al)₄O₁₀](OH)₂,
 328
 (Mg,Fe_{1-x})CO₃, 150
 Mg₆Fe(III)₂(CO₃)(OH)₁₆ · 4H₂O, 300
 (Mg_{0.25}Fe_{0.75})₂SiO₄, 316

- $(\text{Mg,Fe})_2\text{SiO}_4$, 316
 $(\text{Mg}_{0.75}\text{Fe}_{0.25})_2\text{SiO}_4$, 316
 $[\text{Mg,Fe(II)}]_7[\text{Si}_8\text{O}_{22}][\text{OH}]_2$, 319
 $\text{Mg}_3(\text{H}_2\text{O})_8(\text{AsO}_4)_2$, 313
 $\text{Mg}(\text{H}_2\text{O})_5[\text{B}_2\text{B}_3(\text{OH})_5]$, 306
 $\text{Mg}(\text{H}_2\text{O})_3[\text{BB}_2\text{O}_4(\text{OH})_2]_2$, 304
 $\text{Mg}(\text{H}_2\text{O})_5[\text{B}_2\text{BO}_3(\text{OH})_5]$, 303
 $\text{Mg}(\text{H}_2\text{O})_6[\text{B}_2\text{B}_2\text{O}_5(\text{OH})_4]$, 306
 $\text{Mg}_3(\text{H}_2\text{O})[\text{B}_3\text{B}_2\text{O}_7(\text{OH})_4]_2$, 308
 $\text{Mg}_3(\text{H}_2\text{O})_4(\text{PO}_4)_2[\text{B}_2\text{O}(\text{OH})_4]$, 305
 $\text{Mg}_8(\text{H}_2\text{O})_4(\text{Si}_6\text{O}_{15})_2(\text{OH})_4 \cdot 8\text{H}_2\text{O}$, 330
 $\text{Mg}_3(\text{OH})[\text{Al}_3[(\text{Si,Al})_4\text{O}_{10}(\text{OH})_2]]$, 328
 Mg_2SiO_4 , 315
 $\text{Mg}_2\text{Si}_2\text{O}_6$, 317
 $\text{Mg}_3(\text{Si}_4\text{O}_{10})(\text{OH})_2$, 324
 $\text{Mg}_6(\text{Si}_4\text{O}_{10})(\text{OH})_8$, 329
Microkaolinite, 420–1
Micropyrrite, 419–20
Mimetite, 312
Mirabilite, 280, 281
 $\text{Mn}_3\text{Al}_2(\text{Si}_3\text{O})_3$, 322
 $(\text{Mn,Fe})_2(\text{PO}_4)\text{F}$, 309
 $(\text{Mn,Fe})(\text{WO}_4)_3$, 315
 $\text{Mn} \cdot \text{MnO}_2(\text{OH})_2$, 276
 MnTa_2O_6 , 279
Molybdenite, 257
Molybdenum disulfide, 256
Molybdenum oxide, 271
Molybdite, 271
Monaqua-3-methoxysalicylaldehydeethyl-
diaminecopper(II), 386
Monaqua-3-methoxysalicylaldehyde-o-
phenyldiaminecopper(II), 386
Monoserinethulium nitrilotriacetate, 400
Montbrasite, 311
Montmorillonite, 325
Mordenite, 330
Morenosite, 282
Mortar projectile propellant, 367
Mottramite, 314
Mukhinite, 333
Mumetal, 8
Muscovite, 326

 $\text{NaAl}_2(\text{AlSi}_3)\text{O}_{10}(\text{OH})_2$, 27
 NaAlF_6 , 256
 $\text{NaAl}_3(\text{PO}_4)_2(\text{OH})_4$, 311
 $\text{NaAl}(\text{Si}_2\text{O}_6)$, 318
 $\text{Na}(\text{AlSi}_3\text{O}_8)$, 321
 $\text{Na}_2(\text{AlSi}_2\text{O}_6)_2 \cdot 2\text{H}_2\text{O}$, 332
 $\text{Na}_2(\text{Al}_2\text{Si}_3\text{O}_{10}) \cdot 2\text{H}_2\text{O}$, 332
 $\text{Na}_8(\text{AlSiO}_4)_6(\text{SO}_4)_3$, 336
 $\text{Na}[\text{Be}(\text{PO}_4)]$, 308
 $\text{Na}_2\text{B}_4\text{O}_5(\text{OH})_4 \cdot 3\text{H}_2\text{O}$, 302
 $\text{Na}_2\text{B}_4\text{O}_5(\text{OH})_4 \cdot 8\text{H}_2\text{O}$, 302
 $(\text{Na,Ca})_{0.33}(\text{Al,Mg})_2(\text{Si}_4\text{O}_{10})(\text{OH})_2 \cdot n\text{H}_2\text{O}$, 325
 $\text{Na}_2\text{Ca}(\text{AlSi}_5\text{O}_{12})_4 \cdot 12\text{H}_2\text{O}$, 330
 $\text{NaCa}[\text{B}_5\text{O}_7(\text{OH})_4] \cdot 6\text{H}_2\text{O}$, 303

 $\text{NaCa}_2[\text{Fe(II),Mg}]_4[\text{Fe(III)}][\text{Si}_6\text{Al}_2\text{O}_{22}][\text{OH}]_2$, 320
 $\text{NaCa}(\text{H}_2\text{O})_3[\text{B}_3\text{B}_2\text{O}_7(\text{OH})_4]$, 306
 $\text{NaCa}_2[\text{Mg,Fe(II)}]_4[\text{Al}][\text{Si}_6\text{Al}_2\text{O}_{22}][\text{OH}]_2$, 320
 $\text{NaCa}_2(\text{MgMn})_2(\text{AsO}_4)_3$, 312
 $\text{NaCa}_2[\text{Si}_3\text{O}_8(\text{OH})]$, 335
 $\text{NaCO}_3 \cdot \text{H}_2\text{O}$, 294
 $\text{Na}_2[\text{Fe(II),Mg}]_3\text{Fe(III)}_2[\text{Si}_8\text{O}_{22}][\text{OH}]_2$, 319
 $\text{NaFe(III)}(\text{Si}_2\text{O}_6)$, 318
 $\text{Na}_3\text{Fe}(\text{SO}_4)_3 \cdot 3\text{H}_2\text{O}$, 286
 $\text{NaFe(III)}_3(\text{SO}_4)_2(\text{OH})_6$, 289
 NaHCO_3 , 294
 $\text{Na}_3\text{H}(\text{CO}_3)_2 \cdot 2\text{H}_2\text{O}$, 294
Nahcolite, 294
 $\text{Na}_x(\text{H}_2\text{O})_4[\text{Mg}_2(\text{Al}_x\text{Si}_{4-x}\text{O}_{10})(\text{OH})_2]$, 325
 $(\text{Na,K,Ca})_{2-3}[\text{Al}_3(\text{Al,Si})_2\text{Si}_{13}\text{O}_{36}] \cdot 12\text{H}_2\text{O}$, 330
 $\text{NaLiAl}_2\text{Al}_6(\text{Si}_6\text{O}_{18})(\text{BO}_3)_3(\text{OH})_4$, 335
 $\text{NaMg}_3\text{Al}_6(\text{Si}_4\text{O}_{18})(\text{BO}_3)_3(\text{OH})_4$, 335
 $\text{Na}[\text{Mg,Fe(II)}]_3\text{Al}_2\text{Si}_8\text{O}_{22}[\text{OH}]_2$, 319
 $\text{Na}_2\text{Mg}(\text{SO}_4)_2 \cdot 4\text{H}_2\text{O}$, 286
Nantokite, 254
Naphthalene, 11
 Na_2SO_4 , 280
 $\text{Na}_2\text{SO}_4 \cdot 10\text{H}_2\text{O}$, 280
Natrojarosite, 289
Natrolite, 332
Natural rubber, 151, 157, 167, 186
Neodymium acetate, 392
Neodymium bromide
 complex with alanine, 384
 complex with glycine, 380
Neodymium *m*-nitrobenzoate, 394
Neodymium phenylacetate, 399
Neoprene, 166, 186
 $\text{NH}_4\text{Al}(\text{SO}_4)_2 \cdot 12\text{H}_2\text{O}$, 233, 288
 $\text{Ni}_{11}\text{As}_8$, 262
 $\text{Ni}/\text{Al}_2\text{O}_3$ catalyst, 140, 406, 407, 409
 $(\text{Ni,Al})_3(\text{OH})_6[\text{Ni,Al}]_3[(\text{AlSi}_3\text{O}_{10})(\text{OH})_2]$, 328
Nickel, 8, 252
Nickel arsenide, 262
Nickel oxide, 277
Nickel sulfate heptahydrate, 282
Nickel sulfate hexahydrate, 284
Nickeline, 262
Nifontovite, 307
 $\text{Ni-La}_2\text{O}_3/\text{Al}_2\text{O}_3$ catalyst, 140, 406
 $\text{Ni-La}_2\text{O}_3\text{-Pd}/\text{Al}_2\text{O}_3$ catalyst, 140, 141, 407, 408, 409
 $(\text{Ni,Mg})_3(\text{H}_2\text{O})_8(\text{AsO}_4)_2$, 313
Nimite, 328
Ni-P alloy, 119
Ni-Pd alloy, 116
Nitrate explosive, 365
Nitrile elastomer, 186
m-Nitroaniline, 344
Nitrocellulose, 352, 374
 in benite, 371
 in propellants, 366–9
m-Nitrochlorobenzene, 343
o-Nitrochlorobenzene, 343

- p*-Nitrochlorobenzene, 343
 Nitroglycerine, 349
 in propellants, 366–9
 Nitroguanidine, 352
 in propellant, 367
m-Nitrotoluene, (*m*-MNT), 340
o-Nitrotoluene, (*o*-MNT), 340
p-Nitrotoluene, (*p*-MNT), 340, 341
 Nitrotriglycol (TAGEN), in propellant, 368
 Norsethite, 297
 Nosean, 336
 Novax, 129
 Nylon 6, 82, 157, 159, 210
 blends with polypropylene, 171, 199
 Nylon 66, 157, 210
 blends with PEI, 105
 blends with PEV, 105
 Nylon 1010, 51, 52
 Nylon film, 104

 Octahydro-1,3,5,7-tetranitro-1,3,5,7-tetrazocine, 356
 Omphacite, 317
 Orpiment, 258
 Orthoclase, 321
 Otavite, 295

 Paragonite, 327
 Paratellurite, 271
 Pargasite, 320
 PbAs_2S_4 , 264
 $\text{Pb}_{14}(\text{As,Sb})_6\text{S}_{23}$, 264
 PbBi_2S_4 , 268
 $\text{PbCu}(\text{VO}_4)(\text{OH})$, 314
 $\text{Pb}_4\text{FeSb}_6\text{S}_{14}$, 270
 $\text{Pb}_2\text{Pb}_3(\text{AsO}_4)_3\text{Cl}$, 312
 $\text{Pb}_5\text{Sb}_4\text{S}_{11}$, 268
 $\text{Pb}_5\text{Sb}_8\text{S}_{17}$, 266
 $\text{Pb}_9\text{Sb}_8\text{S}_{21}$, 266
 $\text{Pb}_3\text{Sb}_2\text{Sn}_4\text{S}_{14}$, 270
 $\text{Pb}_5\text{Sb}_2\text{Sn}_3\text{S}_{14}$, 270
 PbSnS_2 , 269
 $\text{Pb}_5(\text{VO}_4)_3\text{Cl}$, 314
 PCL–Penton blends, 95–6
 PdO/carbon catalyst, 142
 PE–PP blends, 102, 103
 PECH–CO blends, 201
 PECH–PMMA IPNs, 200
 PECH–PU blends, 201
 PECH–St–MMA–BMA blends, 204
 Pectolite, 335
 PEEK, 80, 81, 129, 159, 175–6
 blends with PEK-C, 101
 PEI–nylon 66 blends, 105
 Pentaerythritol tetranitrate (PETN), 147, 350
 desensitized PETN, 364
 Pentahydroborite, 304
 Penton, 95
 PEO–PHE blends, 53

 PEO–PU blends, 93, 94
 Perbunan [elastomer], 186
 Periclase, 277
 Permanorm 3, 8
 Permanorm 5, 8
 PES–C–PEO blends, 96–9
 PESF, 129
 Petalite, 322
 Petroleum anti-oxidant additives, 410–12
 PEV–nylon 66 blends, 105
 PHB–CE blends, 102
 Phenol formaldehyde–epoxy resin (PF–EP), 204
 Phenolic resin, 185
 Phenolphthalein poly(ether ether sulfone)–poly(ethylene oxide) (PES–C–PEO) blends, 96–9
 Phlogopite, 327
 PI-2080, 129
 Pickeringite, 288
 Picric acid (PA), 347
 Picryl chloride, 344
 Piemontite, 333
 Pine wood, 240–2
 Pinnoite, 305
 Plagionite, 266
 Plaster of Paris, 153
 see also Calcium sulfate hemihydrate
 Platinum–nickel–phosphorus alloys, 120, 123
 PMMA–PVAc blends, 93
 POD, 129
 Polyacetaldehyde, 70
 Polyacrylonitrile, 189
 Polyamides
 blends with polypropylene, 171, 199
 modified by acrylonitrile–butadiene epoxy resin, 47, 48
 Polyarylate, 196
 Poly(aryl ether sulfone), 205
 Polyarylsulfone, 48
 Poly(γ -benzyl L-glutamate), 210
 Poly[3,3-bis(chloromethyl)oxetane]–poly(ϵ -caprolactone) blends, 95–6
 Poly(bisphenol-A carbonate), 209
 Polybutadiene, 43, 70, 166, 186, 187, 203
 Polybutadiene–(methyl methacrylate) cross-linked polymer, 71, 72
 Polybutadiene–polystyrene-*co*-butadiene blends, 99
 Polybut-1-ene (PB), 83
 isotactic (iPB-1), 173
 Poly(*n*-butyl acrylate), 208
 Poly(*n*-butyl methacrylate), 70
 Poly(ϵ -caprolactone)–poly[3,3-bis(chloromethyl)oxetane] blends, 95–6
 Polycarbonate (PC), 159
 Polychloroprene, 167, 186
 Polychlorotrifluoroethylene, 74, 75, 82
 Polydimethylsiloxane, 70
 Polyepichlorohydrin–castor oil blends, 201

- Polyepichlorohydrin–poly(methyl methacrylate) interpenetrating polymer networks, 200
- Polyepichlorohydrin–polyurethane blends, 201
- Polyepichlorohydrin–styrene–methyl methacrylate–butyl methacrylate blends, 204
- Poly(ether ether ketone) (PEEK), 81, 129, 159, 175–6
- Poly(ether imide) (PEI), 105, 198, 205
blends with nylon 66, 105
- Poly(ethyl methacrylate), 70
- Polyethylene (PE), 24, 77, 83, 85–6, 86, 132, 157, 182, 206
blends with polypropylene, 102, 103
film, 103, 104
high-density polyethylene, 77, 85, 159, 193–4
low-density polyethylene, 85, 193–4
see also Chlorinated polyethylene
- Poly(ethylene naphthalenedi-2,6-carboxylate) (PEN), 174, 190
- Poly(ethylene oxide) (PEO), 210
blends with phenolphthalein poly(ether ether sulfone), 96–9
blends with polyurethane, 93, 94
- Polyethylene–propylene copolymer, 70
- Poly(ethylene terephthalate) (PET), 52, 53, 84, 159, 174, 190, 205, 209
- Poly(2-ethylhexyl methacrylate), 70
- Polyhalite, 286
- Poly-1-hexene, 70
- Poly(*n*-hexyl methacrylate), 70
- Polyimides, 129, 159, 191–2
- Polyisobutylene, 70, 206
- Polyisocyanate, 184
- Polyisoprene, 83, 183
- Poly(methyl acrylate), 70, 207
- Poly(methyl methacrylate) (PMMA), 70, 106, 107, 159, 207, 208
blends with poly(styrene-*co*-acrylonitrile), 99
blends with poly(vinyl acetate), 93
interpenetrating polymer networks with polyepichlorohydrin, 200
- Poly- α -methylstyrene, 70
- Polynosic rayon, 181
- Poly(*n*-octyl methacrylate), 70
- Polyol, 184
- Polyoxyethylene, 83
- Polyoxymethylene (POM), 46, 83, 159, 192, 209
- Polyoxypropylene, 82
- Poly(phenylene oxide) (PPO), 69
- Poly(phenylene sulfide) (PPS), 176–7, 191
- Polypropylene (PP), 82, 83, 157, 159, 169–70, 206
blends with polyamide-6, 171, 199
film, 104
isotactic polypropylene, 76, 79–80, 82, 84, 172–3, 203
maleic anhydride modified, 170, 199
with rare earth oxide fillers, 83, 172–3, 203
with wollastonite, 171–2, 202
- Poly(propylene oxide), 70
- Polystyrene (PS), 68, 70, 155, 157, 159, 165, 166, 207
- Poly(styrene-*co*-acrylonitrile) (SAN), 205
- Poly(styrene-*co*-acrylonitrile)–poly(methyl methacrylate) blends, 99
- Polystyrene-*co*-butadiene copolymer, 70
- Polystyrene-*co*-butadiene-*cis*-1,4-polybutadiene blends, 99
- Polystyrene–carbon disulfide gels, 178
- Polystyrene–carboxylated poly(2,6-dimethyl-1,4-phenylene blends, 99
- Polystyrene–carboxylated poly(phenylene oxide) blends, 100
- Polystyrene–polyurethane copolymer, 71, 106
- Poly sulfone, 196
- Polytetrafluoroethylene (PTFE), 159, 188–9, 195, 209
- Poly(tetrahydrofuran), oligomer with styrene, 55
- Polytrifluorochloroethylene, 209
- Polyurethane (PU), 70, 184
blends with polyepichlorohydrin, 201
blends with poly(ethylene oxide), 93, 94
- Polyurethane–polystyrene copolymer, 71, 106
- Poly(vinyl acetate) (PVAc), 70, 208
- Poly(vinyl acetate)–poly(methyl methacrylate) blends, 93
- Poly(vinyl alcohol) (PVA), 26, 159, 208
blend with silk sericin, 200
gels, 179
- Poly(vinyl chloride) (PVC), 37, 157, 159, 194, 207
- Poly(vinyl chloride)–poly(*N*-vinyl-2-pyrrolidone) blends, 92
- Poly(vinyl chloroacetate), 70
- Poly(vinylidene chloride), 208
- Poly(vinylidene fluoride), 209
- Poly(*N*-vinyl-2-pyrrolidone–poly(vinyl chloride) blends, 92
- Poplar wood, 240–2
- Pork meat, 125
- Potassium aluminum sulfate dodecahydrate, 288
- Potassium chloride, 253
- Potassium chromate, 10, 314
- Potassium dichromate, 314
- Potassium nitrate, 10, 370
- Potassium perchlorate, 10, 362
- Potassium sorbate, 226
- Potassium sulfate, 10, 47, 280
- Poznyakite, 293
- PPX, 129
- Praseodymium acetate, 392
- Praseodymium bromide
complex with alanine, 383
complex with glycine, 380
- Praseodymium *m*-nitrobenzoate, 395
- Prehnite, 335
- Preobrazhenskite, 308
- Priceite, 307
- Probertite, 306
- Propionic acid, calcium salt, 226
- Propyl gallate, 228

- Propyl *p*-hydroxybenzoate, 227
 Prosopite, 256
 Proustite, 265
 PSF, 129
 PVA-sericin blends, 200
 PVAc-PMMA blends, 93
 PVP-PVC blends, 92
 Pyargyrite, 265
 Pyrite, 256, 418
 with siderite, 419–20
 Pyroaurite, 300
 Pyrocellulose, 352
 in propellant, 367
 Pyrochlore, 280
 Pyrolusite, 274
 Pyrope, 323
 Pyrophyllite, 324
 Pyrrhotite, 259

 Quartz, 11, 273
 Quenstedtite, 285

 Rare earth acetates, 392, 398
 Rare earth bromides
 complexes with alanine, 378, 382–5
 complexes with glycine, 378, 379–82
 Rare earth catalyst systems, 203, 403–4, 406–9
 Rare earth nitrates, 400
 Rare earth *m*-nitrobenzoates, 394, 395
 Rare earth oxides [as polymer fillers], 83, 172–3, 203
 Rayon, 181
 RDX, 354, 355
 Realgar, 260
 Regenerated cellulose, 107, 180, 181
 Retgersite, 284
 Rhodochrosite, 297
 Ribbon double-base propellant, 367
 Riebeckite, 319
 Ripidolite, 328
 Rock ammonium nitrate explosive, 365
 Rosasite, 299
 Rosin, 145
 Rostite, 291
 Rubber, 151, 157, 167, 186
 Rutile, 278
 Ryton GR-02, 176

 Saccharin, sodium salt, 234
 Salicylaldehyde-*o*-aminobenzoic acid copper(II)
 monoacetate, 387
N-Salicylaldehyde-*o*-aminobenzoic acid
 dipyridinecopper(II) monohydrate, 387
 Salicylaldehyde-*o*-aminobenzoic acid nickel(II)
 monohydrate, 387
 Samarium acetate, 392
 Samarium bromide
 complex with alanine, 383
 complex with glycine, 381

 Sanidine, 321
 Saponite, 325
 Sapphire, 32, 156, 159
 Sartorite, 264
 Sassolite, 301
 Sb(III)Sb(V)O₄, 272
 Sb(III)Sb(V)₂O₆, 272
 Scheelite, 315
 Schiff bases, complexes with transition metals,
 386–90
 Schonite, 287
 Scolecite, 331
 Selenium, 83, 248
 Semseyite, 266
 Sepiolite, 330
 Sericite, 327
 Shellac, 372
 LTNR coated with, 372
 Sheridanite, 328
 SI polymer, 159
 Siderite, 42, 149–50, 297
 with kaolinite, 420–1, 423
 with pyrite, 419–20
 Sideropilestone, 150
 Silica, 10, 47, 273
 Silicone elastomer/rubber, 126, 186
 Silk fibroin, 177, 199
 Silk sericin, blend with PVA, 200
 Sillimanite, 323
 Silver, 9, 11, 157, 159, 250
 Silver chloride, 253
 Silver sulfide, 263
 Silver sulphate, 10
 Single-base propellants, 365–6
 Sjögrenite, 300
 Smithsonite, 296
 (Sn,Fe)(O,OH)₂, 280
 Sodium aluminofluoride, 256
 Sodium benzoate, 225
 Sodium carbonate monohydrate, 294
 Sodium carboxymethylcellulose, 233
 Sodium chloride, 253
 Sodium fluoride, 253
 Sodium glutamate, 236
 Sodium montmorillonite, 325
 Sodium nitrate, 229
 Sodium nitrite, 229
 Sodium saccharin, 234
 Sodium sulfate, 280
 Sodium sulfate decahydrate, 280
 Sodium-type gellan gum, 212–14
 Softwood, 240–2
 Softwood Kraft lignin, 143–4
 Softwood powder, 144
 Sorbic acid, 225
 potassium salt, 226
 Soybean (Enrei) β -conglycinin, 214–15
 Spessartine, 322

- Sphalerite, 261
 Spherochalcite, 295
 Spinel, 279
 Spodumene, 318
 Spruce wood, 240–2
 SQ-2 double-base propellant, 368
 SS-2 double-base propellant, 369
 Stainless steel, 157, 159
 Stannite, 269
 Starch, 111, 222
 corn starch, 219, 220
 Stibiconite, 272
 Stibnite, 258
 Stichite, 300
 Stilbite, 332
 Straw, wheat, 244–6
 Stromeyerite, 269
 Strontianite, 296
 Strontium carbonate, 10, 296
 Strontium sulfate, 282
 Styrene-butadiene (SB) copolymer, 70, 159, 183, 203
 Styrene monomers, 168
 Styrene oligomers, 165
 Suanite, 301
 Sucrose, 223
 Sulfur, 247, 370
 Sweet potato starch, 216–17
 Sylvanite, 263
 Sylvite, 253
 Syngenite, 286
 Szaibelyite, 308
 Szmikite, 283
- Talc, 324
 Tallow, beef, 90
 Tarapacaite, 314
 Tarbuttite, 311
 Teallite, 269
 Teflon, 188
 Tellurium, 249
 Tellurium dioxide, 271
 Tennentite, 267
 Tenorite, 274
 Tephroite, 315
 Terbium acetate, 398
 Terbium bromide
 complex with alanine, 383
 complex with glycine, 381
 Terbium *o*-chlorobenzoate, 393
 Terbium *o*-hydroxybenzoate, 395
 Terbium nitrate, 400
 Terbium *m*-nitrobenzoate, 395
 Tetrahedrite, 270
 Tetrakis(dibenzoate)tetradecaaquatristerbium
 chloride, 393, 396
 1,3,5,7-Tetranitro-1,3,5,7-tetraazacyclooctane, 356
 2,4,6,8-Tetranitro-2,4,6,8-tetraazadicyclo[3.3.1]-
 nonane-3,7-dione, 357
- Tetrayl, 353
 Thallium trioxide, 272
 Thenardite, 280, 281
 Thermonatrite, 294
 Thorianite, 278
 Thorite, 334
 Thorium dioxide, 278
 Thorium silicate, 334
 Tin, 10, 11, 75, 248
 Tin dioxide, 278
 Tincalconite, 302
 Titanium dioxide, 278
 TlAsS₂, 267
 TMSMMA-*n*-BA copolymers, 167
 Topaz, 336
 Trafoperm, 8
 Transition metals
 catalysts, 140–1, 406–9
 complexes with Schiff bases, 386–90
 Tremolite, 320
 Tridymite, 273
 (Trimethylsilyl)methyl methacrylate, copolymers
 with *n*-BA, 167
 2,4,6-Trinitroaniline, 345
 1,2,3-Trinitrobenzene, 339
 1,2,4-Trinitrobenzene, 339
 1,3,5-Trinitrobenzene (1,3,5-TNB), 338
 2,4,6-Trinitrobenzoic acid, 345
 2,4,6-Trinitrochlorobenzene (2,4,6-TNCB), 344
 2,4,6-Trinitrophenol, 347
 2,4,6-Trinitrophenylmethylnitramine, 353
 2,3,4-Trinitrotoluene, 346
 2,3,5-Trinitrotoluene, 346
 2,3,6-Trinitrotoluene, 346
 2,4,5-Trinitrotoluene, 346
 2,4,6-Trinitrotoluene (α -TNT), 346, 365
 3,4,5-Trinitrotoluene, 346
 1,3,5-Trinitro-1,3,5-triazacyclohexane, 354, 355
 2,4,6-Trinitro-2,4,6-triazacyclohexa-1-one, 358
 2,4,6-Trinitro-*m*-xylene (TNX), 339
 Triple-base propellants, 367–8
 Triplite, 309
 Trisalanylaninetetrakisaeuropium chloride,
 397
 Trona, 294
 Tschermigite, 288
 Tungsten disulfide, 256
 Tungstenite, 257
 Turquoise, 310
- Ulexite, 303
 Ultem, 105, 129, 198
 see also Poly(ether imide)
 Upilex R, 129
 Upilex S, 129
 U-polymer, 129, 196
 Uralborite, 305
 Uranyl(II) complexes, 60

- Uvarovite, 323
- Valentinite, 272
- Vanadinite, 314
- o*-Vanillin-*o*-aminobenzoic acid copper(II) monohydrate, 387
- o*-Vanillinglycinecopper(II) monohydrate, 390
- Vavlamoffite, 280
- Vermiculite, 330
- Victrix PEEK 450G, 175–6
- Vigna angularis* cotyledon cells, 221
- Villaumite, 253
- Viscose rayon, 180, 181
- Vitis vinifera*, 222
- Viton [elastomer], 186
- Vivianite, 312
- Vonsenite, 301
- Water, 157
- Wheat straw and components, 244–6
- Whewellite, 43–4, 44
- Whisky, 110
- Willemite, 334
- Witherite, 293
- Wolframite, 315
- Wollastonite, in polypropylene composites, 171–2, 202
- Wood, 240–2
- Wood cellulose, 143, 181
- Wood flour [in explosive], 365
- Wood lignin, 144
- Wuestite, 274
- Xenotime, 308
- Xylitol, 235
- Ytterbium acetate, 398
- Yttrium bromide
 complex with alanine, 385
 complex with glycine, 382
- Yttrium *m*-nitrobenzoate, 395
- Yttrium oxalate decahydrate, 391
- Yttrium oxide [as polymer filler], 83, 172–3, 203
- Yttrium phosphate, 308
- ZDDP anti-oxidant [petroleum] additive, 410–11
- Zinc, 9, 11, 75, 157, 159, 249
- Zinc carbonate, 296
- Zinc gluconate, 236, 237
- Zinc hydroxide carbonate, 46
- Zinc oxide, 277
- Zinc phosphinate polymer, 70
- Zinc silicate, 334
- Zinc sulfate heptahydrate, 282
- Zinc sulfide, 261
- Zincite, 277
- Zincobotryogen, 292
- Zincocopiapite, 292
- Zircon, 334
- Zirconium dioxide, 278
- Zirconium silicate, 334
- $\text{ZnAl}_6(\text{H}_2\text{O})_4(\text{PO}_4)_4(\text{OH})_8$, 310
- ZnAl_2O_4 , 279
- $\text{ZnCu}(\text{CO}_3)(\text{OH})_2$, 299
- $\text{Zn}_3\text{Cu}_2(\text{CO}_3)_2(\text{OH})_6$, 299
- ZnFe_2O_4 , 279
- $\text{ZnFe(III)}(\text{SO}_4)_2(\text{OH}) \cdot 4\text{H}_2\text{O}$, 292
- $\text{ZnFe(III)}(\text{SO}_4)_2(\text{OH}) \cdot 7\text{H}_2\text{O}$, 292
- $\text{ZnFe(III)}_4(\text{SO}_4)_6(\text{OH})_2 \cdot 18\text{H}_2\text{O}$, 292
- $\text{Zn}_2(\text{PO}_4)(\text{OH})$, 311
- Zoisite, 333
- Zr–Al–Ni–Cu–Co alloys, 114, 115, 120, 122
- ZSM-5A molecular sieve catalyst, 141
- Zwieselite, 309

Index compiled by Paul Nash